GRUPPO NAZIONALE DI GEOFISICA DELLA TERRA SOLIDA

Atti del 32° Convegno Nazionale

Trieste, 19–21 novembre 2013
Palazzo dei Congressi
della Stazione Marittima

Tema 3: Geofisica applicata

ISTITUTO NAZIONALE DI OCEANOGRAFIA E DI GEOFISICA SPERIMENTALE

EAGE EUROPEAN ASSOCIATION OF GEOSCIENTISTS & ENGINEERS
SEZIONE ITALIANA

13° Convegno Nazionale

GRUPPO NAZIONALE DI GEOFISICA DELLA TERRA SOLIDA

32° convegno nazionale

Trieste

19-21 novembre 2013
Stazione Marittima

ATTI
Tema 3: Geofisica Applicata

ISTITUTO NAZIONALE DI OCEANOGRAFIA E DI GEOFISICA SPERIMENTALE

In collaborazione con

EAGE EUROPEAN ASSOCIATION OF GEOSCIENTISTS & ENGINEERS
SEG
SEZIONE ITALIANA
13° Convegno Nazionale

GRUPPO NAZIONALE DI GEOFISICA DELLA TERRA SOLIDA

32° Convegno Nazionale
Atti - Tema 3: Geofisica Applicata

Comitato organizzatore

D. Slejko
D. Albarello
A. Argnani
E. Del Pezzo
M. Dolce
M. Fedi
P. Galli
S. Grimaz
E. Loinger
L. Martelli
A. Masi
G. Naso
R. Petrini
L. Sambuelli
G. Santarato
E. Serpelloni
S. Solarino
U. Tinivella
A. Vesnaver

ISBN 978-88-902101-9-8 collezione completa
ISBN 978-88-902101-8-1 questo volume

A cura di: D. Slejko, A. Rebez, A. Riggio, M. Fedi, E. Loinger, L. Sambuelli, G. Santarato, U. Tinivella, A. Vesnaver

Con la collaborazione di:
M. Bobbio, P. Giurco e L. Riosa

Copertina: M. Sedmach

Impaginazione e stampa:
Mosetti Tecniche Grafiche, Trieste

Finito di stampare nel mese di novembre 2013

Alla fine del film "Intrigo a Stoccolma" di Mark Robson, l'organizzatore del premio Nobel dice qualcosa come: "Mi preoccupo ogni anno per l'organizzazione del premio e poi tutto fila sempre liscio" nel frattempo, a sua insaputa, era successo tutto quello che ci si può aspettare in un film d'azione. Così per me è per il GNGTS, anche se è il sedicesimo anno che lo organizzo e nel passato "tutto è filato liscio", temo sempre in avvio che il convegno possa riuscire male, con pochi partecipanti e di scarso interesse. E quest'anno ce ne sarebbe ben stato motivo, visti i finanziamenti sempre scarsi per la ricerca e la concomitanza con altre manifestazioni geofisiche di respiro nazionale tenutesi recentemente.

Invece, anche quest'anno sembrerebbe (condizionale d'obbligo) che la partecipazione sarà nutrita, visto l'alto numero di note ricevute per la presentazione. Sarà merito della città di Trieste, che ospiterà quest'anno la manifestazione, che richiama numerosi partecipanti o saranno gli enigmi, che ogni terremoto propone, che invogliano i ricercatori al confronto, fatto sta che per tre giorni si parlerà di Geofisica e, anche se novità eclatanti non usciranno, conto che tanti ricercatori saranno un po' più ricchi di conoscenza.

Le prospettive, come dicevo, sembrano positive anche stavolta, con un numero di pre-iscritti che un mese prima del convegno ha già superato le 250 unità. Volente o nolente devo pensare al futuro e perciò a lasciare presto in altre mani l'organizzazione di questo convegno: chiudere in bellezza potrebbe essere una saggia soluzione.

La strutturazione del convegno su 3 temi, proposta negli ultimi anni, é stata mantenuta: ci sembra rispecchi le principali discipline geofisiche e risulta di semplice organizzazione. Le presentazioni sono state suddivise nei tre temi generali: Geodinamica, Caratterizzazione sismica del territorio e Geofisica Applicata, che sintetizzano i grandi filoni lungo i quali si articola la ricerca geofisica italiana. Ogni tema, poi, si sviluppa in tre sessioni specifiche con apertura sia alla componente geologica che a quella ingegneristica.

Anche quest'anno è stata fatta la scelta di raccogliere note estese (ma non troppo) a formare gli atti del convegno. Questa scelta, che in parte rinnega quanto si è scritto nel passato a favore dei riassunti estesi, è stata dettata dalla necessità di produrre un volume utilizzabile per la valutazione ufficiale dell'attività scientifica dei ricercatori e degli enti. Poteva essere una scelta azzardata con scarsa partecipazione, viste le recenti valutazioni ANVUR, che avrebbero potuto indirizzare soprattutto i giovani ricercatori a pubblicare su riviste con alto

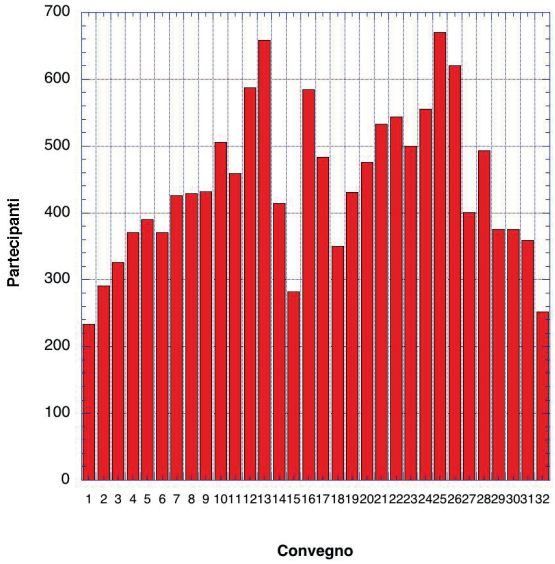

Fig. 1 – Numero di partecipanti ai convegni GNGTS. Il primo convegno si è tenuto nel 1981 e, in seguito, ha avuto cadenza annuale con l'eccezione del 1982. Il numero dei partecipanti all'ultimo convegno è aggiornato ad un mese prima dell'inizio del convegno stesso.

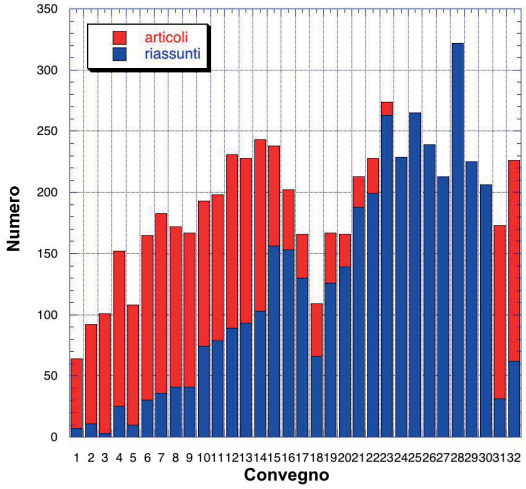

Fig. 2 – Numero di note presentate nei convegni GNGTS. Fino al 2004 è stato pubblicato il volume (dal 1997 sotto forma di CD-Rom) degli atti del convegno contenente in forma estesa le note presentate (barre rosse). In seguito, si è deciso di pubblicare soltanto il volume dei riassunti estesi (barre blu).

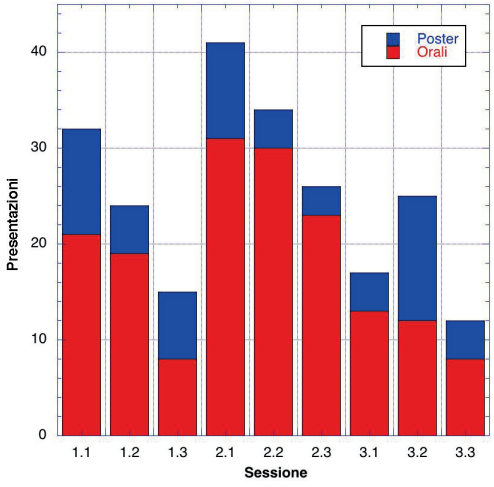

Fig. 3 – Numero di note presentate nelle varie sessioni del 32° convegno. Vengono indicate le comunicazioni orali con il colore rosso e quelle in forma di poster con il colore blu.

Impact Factor: bollino blu dell'eccellenza e panacea per la valutazione o solo parziale criterio speditivo di confronto senza garanzia di qualità? Invece il presente volume raccoglie ben 164 note, delle 226 che verranno presentate al convegno. Si tratta di una percentuale (73%) abbastanza alta che premia la scelta fatta. La produzione di atti di rilevanza scientifica ha determinato la necessità di avviare un processo di referaggio di tutti i testi. I convenor se ne sono fatti carico e, pertanto, risultano responsabili della qualità del materiale presentato. L'aumentata mole di materiale da stampare, rispetto a quella degli anni precedenti in cui venivano prodotti dei riassunti estesi, ha condizionato la scelta di suddividere gli atti in tre volumi, ciascuno dei quali raccoglie le note relative ad uno dei tre temi. Molte note (108) sono in lingua inglese: ciò permette una diffusione del presente volume anche all'estero. Delle 226 note in programma, ben 165 sono destinate alla presentazione orale.

Anche quest'anno alcune sessioni del convegno GNGTS (quelle di Geofisica Applicata) sono state organizzate in collaborazione con la Sezione Italiana EAGE-SEG, che realizza così il suo 13° Convegno Nazionale.

Una segnalazione degna di nota va all'Associazione Geofisica Licio Cernobori, che ha scelto anche quest'anno il convegno GNGTS quale sede per l'attribuzione del premio in memoria di un caro collega ed amico prematuramente scomparso anni or sono.

Un ringraziamento particolare va ai convenor (Dario Albarello, Andrea Argnani, Edoardo Del Pezzo, Mauro Dolce, Maurizio Fedi, Paolo Galli, Stefano Grimaz, Eugenio Loinger, Luca Martelli, Angelo Masi, Giuseppe Naso, Riccardo Petrini, Luigi Sambuelli, Giovanni Santarato, Enrico Serpelloni, Stefano Solarino, Umberta Tinivella e Aldo Vesnaver), che hanno proposto e organizzato le varie sessioni e hanno curato il referaggio dei testi, ed alla Segreteria Organizzativa (Muzio Bobbio, Paolo Giurco e Laura Riosa, oltre ad Alessandro Rebez e Anna Riggio, che firmano con me e con i convenor questi atti), che ha raccolto e preparato tutto il materiale qui stampato. Desidero ringraziare, infine e soprattutto, il Presidente dell'OGS, che ha accolto ancora una volta con entusiasmo e con generosità l'idea di finanziare il convegno GNGTS, nonostante le difficoltà economiche con cui tutti gli enti di ricerca devono scontrarsi.

Dario Slejko

"...cerco qualcosa: un briciolo di conoscenza in questo nostro piccolo grande pianeta. E in me stesso..." L. C. 1989.

PREMIO DELL'ASSOCIAZIONE PER LA GEOFISICA "LICIO CERNOBORI" - 2013

L'**Associazione per la Geofisica Licio Cernobori – AGLC**, nata il 30 ottobre del 2000 per ricordare Licio Cernobori, geofisico prematuramente scomparso, ed il suo entusiasmo contagioso, ha come fine la promozione degli studi geofisici e soprattutto la formazione scientifica e la crescita dei più giovani.

Tale fine è stato perseguito attraverso l'elargizione di un premio di studio presso l'Università di Trieste, aperto anche a laureandi/laureati in Geofisica Applicata di altre università o strutture scientifiche coinvolte in progetti comuni con l'Ateneo di Trieste. Si ricordano i vincitori degli anni passati Giulio Paoli (2001), Sara Cisilin (2002), Marica Calabrese (2003), Manfredi Scozzi (2004), Ivan Gladich (2006), Manuela Zuliani (2006), Andreika Starec (2008), Sara Ferrante (2009).

Oltre all'attività didattica/divulgativa che i componenti dell'Associazione svolgono in diverse occasioni, sono stati finanziati negli anni diversi convegni, scuole, progetti, iniziative, in Italia e all'estero:

- Copie degli Atti del Convegno TRANSALP (Trieste, Febbraio 2003) per le biblioteche universitarie;
- Agevolazioni per gli studenti al Congresso: STRUCTURES IN THE CONTINENTAL CRUST AND GEOTHERMAL RESOURCES (Siena, 24-27 September 2003);
- Sovvenzione di uno studente, Alberto Gaudio dell'università di Urbino per la Scuola di Processing dati sismici marini (Trieste, ottobre 2004);
- Agevolazioni per studenti del terzo mondo alla partecipazione del Workshop IRIS-Orfeus "Understanding and managing information from seismological networks" (Palmanova (UD) 28 Febbraio – 6 marzo 2005);
- Finanziamento di € 400 Euro ad Andrejka Starec (2006), allora studentessa, per garantirle un altro mese presso il TNO (Paesi Bassi) a conclusione della sua borsa e consentirle la conclusione della tesi sullo stoccaggio geologico della CO_2, con la guida di Pascal Winthaegen e del chiar.mo Prof. Rinaldo Nicolich dell'Università di Trieste.
- Finanziamento annuale di € 400 per la partecipazione di un insegnante ai seminari GIFT per gli insegnanti delle scuole elementari e secondarie nell'ambito del convegno dell' European Geosciences Union - Geophysical Information for Teachers (GIFT): Giovanni Banchelli (2007), Pier Paolo Caputo (2008), Giovanni Aglialoro (2009), Francesco Gobbo (2010), Giulia Realdon (2011), Eva Godini (2012), Maria Barbera (2013).

Nell'occasione del decennale (2010) si è istituito un premio per i giovani relatori al Congresso annuale GNGTS, ripetuto nel 2011. Nel 2010 il premio di 2000,00 € è andato alla dottoressa **Marina Pastori**, per il lavoro "***Crustal fracturing field and presence of fluid as revealed by seismic anisotropy: case-histories from seismogenic areas in the Apennines",*** selezionato tra 40 lavori e 8 finalisti, nel 2011 al **dott. Edoardo Peronace**, per il lavoro "***Shallow geophysical imaging of the mt. Marzano fault zone; a kaleidoscopic view through ERT, GPR and HVSR analyses***", selezionato tra 38 lavori e 13 finalisti.

Dal 2012 il premio è stato suddiviso in tre premi di 700,00 €, uno per ciascuno dei Temi del convegno: *Geodinamica, Caratterizzazione sismica del territorio e Geofisica applicata*. I vincitori sono stati:

Lorenzo Bonini, per il lavoro: **"*Comprendere la gerarchia delle faglie attive per migliorare la caratterizzazione sismica del territorio: l'esempio del terremoto di L'Aquila del 2009 (Mw 6.3)*", Rocco Ditommaso,** per il lavoro **"*Risposta sismica delle strutture: dalla non stazionarietà alla non linearità apparente*", Gianluca Fiandaca,** per il lavoro **"*Time domain induced polarization: 2D inversion for spectral information*"**, selezionati tra 31 lavori presentati.

Quest'anno i lavori presentati sono 27. I riassunti e le presentazioni preliminari sono attualmente all'esame delle tre commissioni, che stanno lavorando per scegliere i tre vincitori, che verranno annunciati e premiati nel corso dell'Assemblea del Convegno (20 novembre 2013).

Per altre informazioni, per diventare socio e contribuire a continuare e migliorare le iniziative dell'Associazione per la Geofisica Licio Cernobori – AGLC, http://www2.units.it/cernobor/.

Il Presidente dell'Associazione
Marco Romanelli

Indice

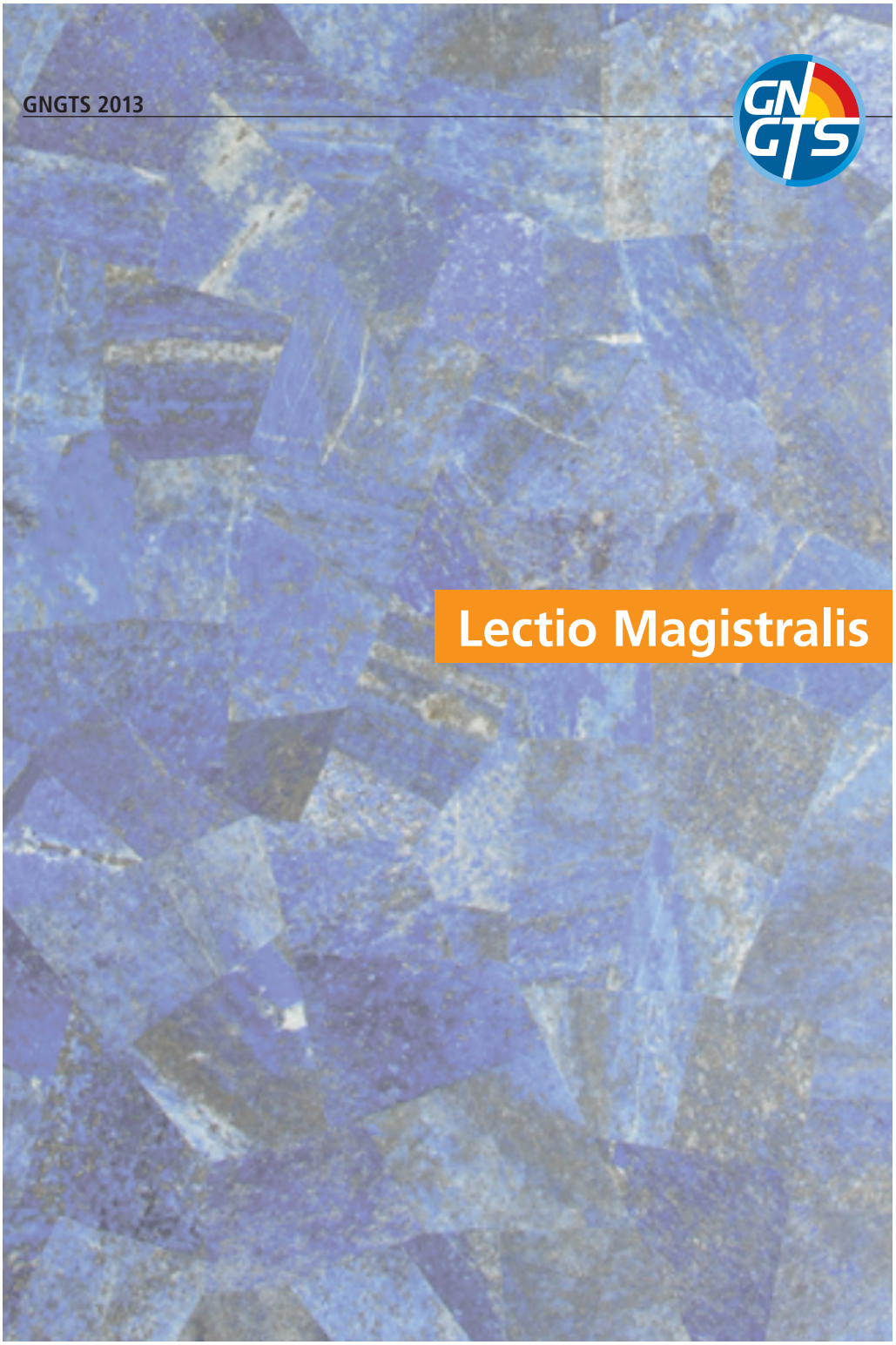

Lectio Magistralis

THE CRUST IN ITALY FROM SEISMIC PROSPECTING AND ADDITIONAL INVESTIGATING TECHNIQUES

R. Nicolich
DIA, University of Trieste, Italy

The near-vertical reflection seismic method was the most appropriate exploration tool utilized in the crustal exploration of Italy and neighbouring Seas with the CROP (CROsta Profonda) project and with similar programs. The method, subsequent to the improvements in data acquisition and processing with increased dynamic range of digital data and more powerful processing software, provides signal easily interpreted in geological terms. To complete the information needed for major geological synthesis a combination of different geophysical investigating techniques were required and added. Significant the wide-angle refraction/reflection method (WAR/R), which yield propagation velocities at depth with greater accuracy. Both reflection and refraction techniques, separately used, supply results which are different in nature though complementary.

Examples of the current interpretation and the open debates about the structure and geodynamics of the crust of the Italian area will be presented with regard to: first, the definition of the seismic nature of the Moho discontinuity, in terms of its position, topography, smoothness and continuity; second, the lower crust contribution in the complexities of the collision mechanisms; third, the presence of decoupling levels within the subducting lithosphere or the intracrustal ones, related to the Neogenic evolution, an insight into the processes that built the geological structures of the upper crust; fourth, what to do and future improvements to crustal exploration.

Active seismic prospecting can give major information in the first 50-60 km of the lithosphere, with limited data quality in the collision zones where the utilization of the receiver functions analysis can help in the precise indication of the positions in the crust-mantle transitions of the colliding plates. The tectonic melange may dominate the thickened crust after collision, making difficult to isolate the different bodies because the physical differences are small. Larger depths are investigated by earthquake hypocentre distribution or by tomographic analysis of teleseismic events, outside of my presentation.

Of interest, the acquisition of wide-angle reflection fans, successfully employed for imaging the complex geometries of the M-interface on collision belts once information was available about an approximate position at depth of the target.

The study of the crust started in Italy with controlled source refraction profiles in the Western Alps in 1956, in replay to requests for international collaboration among the confining countries. Analog recorders were used, and the spacing between stations, the number of the acquired profiles, were related to the availability of instruments and operators (students) from different participating countries. Reliable results were obtained only on the gross changes in crustal thickness and on the main velocity structures, but the data quality increased as years go following the technological evolution (from the initial coffins to the Coca-Cola cans of ALP-2000).

The deep seismic soundings covered the whole Italian Peninsula with profiles integrated with other pertinent geophysical methods. This activity was concluded with the long N-S transect of the European GeoTraverse (EGT) program in 1986 (Ansorge *et al.*, 1992).

We returned to the Alpine chain with reflection seismics updated technologies in joint international multidisciplinary programs, exploring Western Alps in 1985-1986, first with a French-Italian joint venture (CROP-ECORS), followed by a co-operation with the Swiss NRP20 project in the Central Alps. The Eastern Alps were explored from 1999-2000 by partner institutions of Italy, Austria and Germany acquiring data along the TRANSALP profile. In the mean time the CROP venture programmed acquisitions across the Apenninic chain; Sicily was explored in 2009, but with different funding following the CROP-11 solution.

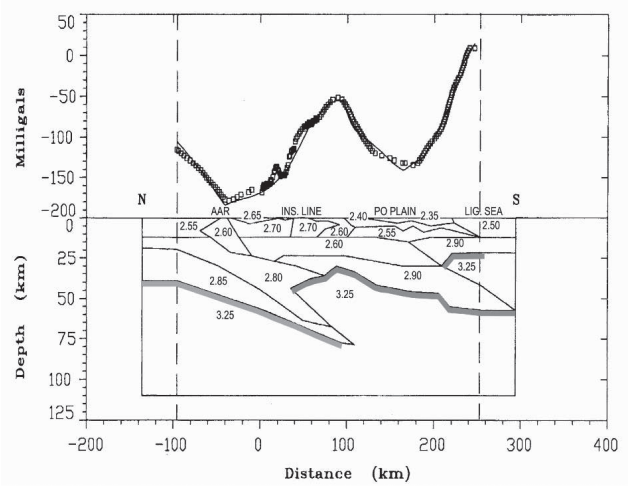

Fig. 1 – The gravimetric model (from Marson *et al.*, 1994) along the European GeoTraverse, crossing the Alps, the Po Plain and the Apennines, down to the Ligurian Sea. The model settles the European Moho at 60 km or more beneath the Po Plain with Adria Moho down-bended to about 40 km by the Apennines overthrust, Apennines here characterized by a vertical Moho uplift. Density values in gr/cm^3.

The deep exploration of the marine areas started in 1988 in the Provenzal Basin (again a CROP-ECORS joint venture) and after covered all the Italian neighbouring seas with CROP and with similar projects (ETNASEIS, SINBUS, PROFILES, IMERSE, ...).

The dynamite source was employed in several transects, but also heavy vibrators were used, for ex. in the narrow mountain valleys, but still adding explosive shots to aid imaging the deepest reflecting markers. The depth penetration of vibroseis signals is turned up to be particularly low in such areas where high-impedance rocks are exposed at the surface. The use of complementary wide-angle acquisitions continued about everywhere with in-line profiling or with fans or again designing cross-lines to enable 3D images extracted from a wide corridor centred on the main profile. The operative parameters employed in the acquisition were modified with the continuous improvements of the recording technologies and the gained experiences, varying the number of the active recording channels, the group intervals, the offsets; all parameters choice limited by the available funding.

The addition of the gravity information with the Bouguer anomalies can help to position the deep basins, the deep roots of the orogenies and of the high density bodies at shallow depths. Both the seismic and gravity interpretation take mutual advantage by iterative use of the two data sets and of the constraints posed to fulfill both observed data. The gravity field can be used to extend the interpretative models beyond the seismic profile and 3D gravity models have been presented to control the laterally variable crustal architecture. In Fig. 1 an example of a gravimetric model, which utilized the seismic information along a sector of the EGT transect from the internal crystalline massif in Switzerland to the Ligurian Sea, crossing the Milano belt, the western Po plain and the northern Apennine arc. The structural setting of the Adria domain results from the convergence of the plate margins producing a foreland-foredeep domain consumed by the advancing neighbouring chains with vertical offset of respective Moho's.

In Fig. 2 an example of wide-angle fan profiling, which were of primary importance for the interpretation of the deep interfaces disclosed in the reflection seismic sections of the CROP-ECORS project (Damotte *et al.*, 1990), revealing a dramatic imbrication of the upper mantle and crust. Organizing the sampling interval of reflectors along the cross sections and the shot-receivers distance in fan to have reflecting points around the critical distance corresponding to the common depth point of the near vertical reflection profile, the wavelet from the base of the crust is known to be very energetic and can be identified by the maximum amplitude signal. The root zone of the chain was outlined down to 55 km depth with the flaking of the lithosphere under the chain in the Briançonnais zone, while the hinterland Moho is raising stepwise from the Po plain up to about 13 km depth, the base of the outcropping rise known as the Ivrea lower crust body.

The exploration of the Alpine chain reached the peak with the TRANSALP transect, which utilized again multidisciplinary approaches: a) seismic multichannel acquisition with vibroseis and explosives, b) a 3D control of the deep structures utilizing a supplementary spread, c) wide-angle profiles, d) gravity measurements with compilation of a new map of cross-borders Bouguer anomalies covering NE-Italy, W-Austria and Bavaria, e) recording of seismological data with a permanent stations network.

Along TRANSALP profile the geophysical/geological models and the reflection seismic images with their well resolved small-scale heterogeneities (Lueschen *et al.*, 2006) have been extended on larger depths by teleseismic "receivers functions", P to S converted signals, illuminating the lithosphere from below which can give information on the main converter, the M-discontinuity, or on wide velocity gradient zone. An example is given in Kummerow *et al.* (2004), where the base of the crust and intracrustal structures in the Eastern Alps are recognized (Fig. 3), confirming the interpretation of the Transalp seismic sections (Castellarin *et al.*, 2006) with a south-dipping polarity of the Europe subducted mantle. It is not so immediate with the initially presented lower resolution teleseismic tomography procedures (Lippitsch *et al.*, 2003), probably with a poor control of the upper crust velocities and heterogeneities and construction of tomographic sections along direction where it is difficult to resolve the laterally variable structures (old, recent).

ALP 2002 experiment came again to WAR/R technique, but with many shots, several profiles and a large number of narrow spaced recording instruments, to complete the investigation of the Eastern Alps and Central Europe (Brückl *et al.*, 2010). The compression between Europe and the indenting Adria microplate generated the tectonic forces for the Dinaric orogeny, active from Cretaceous to Miocene, and for the extrusion and escape of the Eastern Alps towards the unconstrained Pannonian basin. Adria is moving towards north, obliquely thrusting

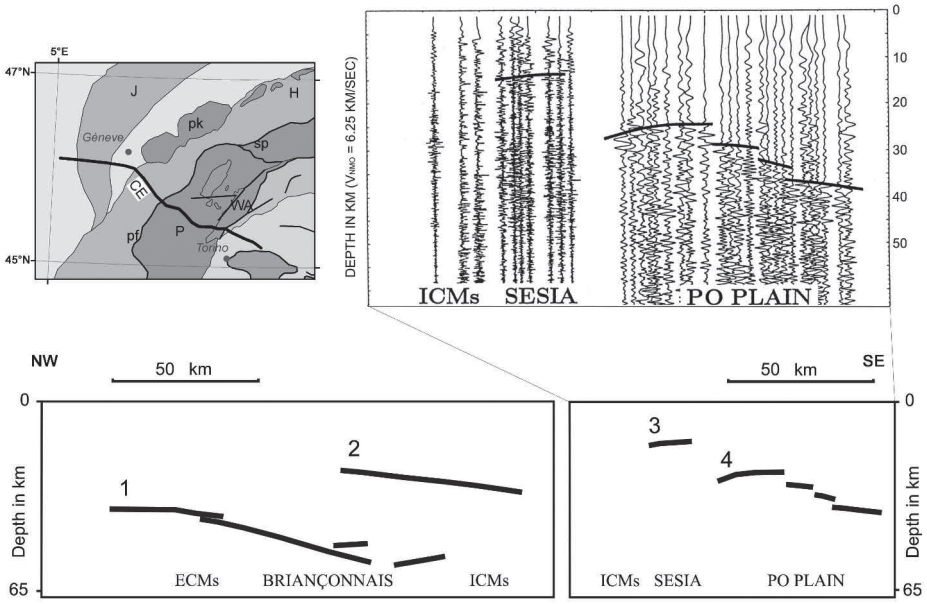

Fig. 2 – An example of the utilization of wide-angle fans with the crustal model and a stepwise M-discontinuity reflection images along a transect from the Po Plain to Gran Paradiso (from Thouvenot *et al.*, 1990, modified), intersecting Sesia-Lanzo zone and Canavese line, which marks the eastern limit of the chain (CE = seismic profile CROP-ECORS). Reflections are picked on the seismic section using a maximum amplitude criterion and traces correlation. ICMs = internal crystalline massif; ECMs= external crystalline massif. At the bottom the crustal scheme with main discontinuities across the whole Western Alpine chain: 1- European Moho, 2- Brianconnais Moho, 3 - base of the Ivrea body, 4- Adria Moho.

under the Pannonian fragment corresponding to the Dinaric chain. The upper crust is here characterized by the Dinaric thrusts (upper plate) moving westwards, opposed by the Istria massive Mesozoic shelf domain, the stable part of Adria that emerge from the Adriatic Sea. Europe is in the position of lower plate beneath Adria overthrust by a Pannonian fragment with vertical offsets of the respective Moho's, in the north; in front of the Adriatic coasts and beneath the Dinaric chain, the Moho surface seems to remain rather smooth and continuous from the foreland to the hinterland and down-bended towards the culmination of the Dinaric chain (Velebit mountains), suggesting that a major decoupling operates at or near the Moho between the Adria and Pannonian and the respective former mantle lithospheres (Šumanovac *et al.*, 2002). The lower crust of Adria probably plays a major role in the definition of the crust structure and evolution. The joint deep reflection seismic profiles with the WAR/R velocities could be the winning solution and give an answer to the role of the Adria indenter in a key area for crucial seismotectonic modelling.

The Adria collision with the Apennines developed from late Miocene to Quaternary. Unlike in the Alps, where a major lithosphere scale fault accounts for vertical offset of the Moho between the upper and lower plate, along the Apenninic chain facing the Adriatic Sea, the Moho surface remain rather smooth and nearly continuous, gently bended, from the foreland towards the Apennine chain and up to the hinterland mantle dome. A major decoupling is operating near the Moho and only the continental lithosphere of Adria seems to be currently involved in the subduction process presently active with a nearly south-eastward directed subduction plane, as proposed by Di Stefano *et al.* (2009) with earthquakes tomography analysis. These authors accept the upwelling of the asthenosphere and the related thermal softening of the crust on the Tyrrhenian side. Therefore the back-arc extension and the asthenosphere upwelling, in addition to the slab pull, constitute the major driving force in the Apennine-Adria collision.

The mobilized and uplifted asthenosphere, a not depleted mantle wedge, can be responsible of the lower crust lamination by magmatic intrusion. The mantle derived magmas releases heat at the base of the crust, induces anatexis in the overlying crustal rocks and produce granitoids melts, quickly migrating towards higher levels (Locardi and Nicolich, 2005). Wide-angle refraction/reflection acquisitions (Giese *et al.*, 1976) across the Tuscany Geothermal Province revealed a peculiar velocity structure with alternate velocity/density variations in the lower crust and a seismic waves propagation velocity not higher than 7.8 km/s, assigned to the Moho discontinuity. Crustal reflection seismic profiles give a well resolved image of the lower crust and of the brittle/ductile transition interval utilizing seismic attributes and the evaluation of strength (Accaino *et al.*, 2006).

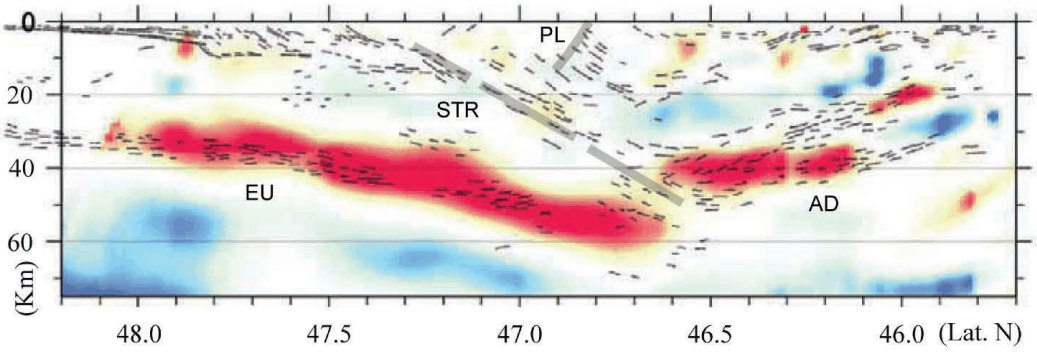

Fig. 3 – Receivers function and combined explosive and vibroseis depth migrated data line drawing along TRANSALP transect (from Lueschen *et al.*, 2006, modified). The presence of decoupling levels (the Sub Tauern Ramp: STR) within the subducted lithosphere poses an insight into the processes that built the geological structures of the upper crust. EU = Europe; AD = Adria; PL = Periadriatic Line.

The reprocessing of the CROP profiles in the region, let us to apply the wave equation datuming technique (Barison *et al.*, 2011; Giustiniani *et al.*, 2013) extracting information previously hidden by approximate static corrections and surface noise. From picked first arrivals, a tomography inversion created a near surface velocity model by iterative ray-tracing and travel time calculations. Then, the wave equation was applied to move shots and receivers to a given datum plane, removing time shifts related to topography and to near-surface velocity variations. Basically, WED is the process of upward or downward continuation of the wave-field between two arbitrarily-shaped surfaces; a process useful to attenuate ground roll, enhance higher frequencies, increase the resolution and improve the signal/noise ratio.

The new outputs show evidence of regional continuity of high amplitude horizons, a better fitting with the surface geological setting and with well data, resembling the local industry investigations; the results confirm the role of overpressured fluids, better define the tectonic setting as well as the contribution to the reflectivity of lithology and of hydrothermal fluids or thermo-metamorphic minerals.

The wave equation datuming is now applied to the SIRIPRO profile crossing central Sicily from the Tyrrhenian Sea to the Sicily Channel. This reprocessing requires large computers, parallel processors, because of the long listening times. The profile was acquired without additional complementary geophysical tools, like new wide-angle experiments, offshore-onshore continuation, … It shows the crustal flexure from the Hyblean foreland towards the Caltanisetta through, accompanied by crustal thinning: from an already thinned crust (around 30 km the Moho depth on coast of the Sicily Channel) to about 16-17 km thickness of the same interval beneath Caltanisetta. North of the collision zone the Maghrebides chain includes units of the African margin in a similar way to the crustal setting in the North-Algeria facing the Algerian basin. It is necessary to better resolve the structures of Maghrebides chain, north of the Caltanisetta through in the collision zone, where a Moho uplift is possible, as confirmed by the gravity anomalies and old deep refraction data. Again a bended continuous crust-mantle interface from hinterland to foreland is suggested, with delaminations and the decoupled mantle lithosphere still locally subducted and recycled in the asthenosphere, but more complex structures cannot be excluded. Moreover, contraction events are currently active at the toe of the North Sicilian margins, possibly accounting for the initiation of a new underthrusting/subduction zone along the southern margin of the Tyrrhenian basin, that will accomodate further convergence between Africa and Europe.

A crustal flexure has been observed moving from the Hyblean domain to the Ionian deep basin, where the crust-mantle transition interval is characterized by a curious high amplitude reflectors in the low frequency band (around 10 Hz). The crustal thinning from the Sicily channel to the Ionian basin across the Malta Escarpment is shown in reflection seismic profiles as well as the presence of a crustal transcurrent fault accounting for a major dextral lateral escape of the Calabria Block during the Plio-Quaternary opening of the Tyrrhenian Sea. The fault separates the eastward thinning continental crust from the deep Ionian domain, which crust is proposed as oceanic from many authors. The interpretation of the seismic data is still under debate and the presence of a wide oceanic domain or of an area still belonging to a distal portion of the North African continental margin cannot be confirmed or plainly denied. Following the exposed Tethian ophiolitic suture (in Albania, Western Greece, Crete, Western Turkey, …) the Tethian ocean has been already recycled within the asthenosphere. The Cretaceous rifting, presently recognized offshore Libia, is a possible origin of the thinning of the crust of a north African margin widely extended in the Ionian Sea with the presence of pull-apart basin up to oceanic openings; once more, the eclogitization of the upper mantle can account for the high velocities and high densities necessary to justify the positive Bouguer anomalies. The tectonic loading of the Africa foreland lithosphere by the Calabrian (and Aegean) arcs is not sufficient to account for the 4 km water depth in the Ionian abyssal plain. Other forces, like slab pull, lateral push of the asthenosphere upwelling in the Tyrrhenian

and Aegean back-arcs are likely to account for the retreat of the deep mantle slabs and must therefore contribute to the decoupling operating close to the Moho. The decoupling of the crust is confirmed by the thrust-top pull-apart basins currently developing above the back-stop of the Hellenic Arc (Wardell *et al*., 2013; Barison and Nicolich, 2013).

The combined utilization of morphological analysis plus high resolution and deep penetration multichannel seismic jointly with OBS for wide-angle recordings and part of a permanent network of seismological station in connection with on land positioned recording points, is the optimum solution for the lithosphere exploration in subduction or collision zones. A first project was Etnaseis with marine and land synchronized operations (Laiglè *et al*., 2000). The SeaHellarc project followed these ideas studying the western continental margin of Peloponnesus. Thales project investigated the Lesser Antilles with European and French funding (Laiglè *et al*., 2013). This area was the target of a complete set of active and passive offshore seismic experiment: multichannel reflection seismic with air gun source organized in the Single Bubble mode, OBS WAR/R seismic profiles, OBS and land permanent seismological stations for earthquakes location, receiver functions analysis imaging the slab top and the LVL. The objective were the geometries of interplate boundary zone constrained from the subduction deformation front and the possible generation of mega-thrust earthquakes.

References

Accaino F., Nicolich R. and Tinivella U.; 2006: *Highlighting the crustal structure of the Tuscan Geothermal Province*. Boll. di Geof. teor. ed appl., **47**, 3, 425-445.

Ansorge L., Blundell D. and Mueller St.; 1992: *Europe's Lithosphere-Seismic Structure.* In: Blundell D., Freeman R. and Mueller St. (eds.) A Continent Revealed, The European Geotraverse. Cambridge University Press ISBN 0-521-42948X.

Brűckl E., Behm M., Decker K., Grad M., Guterch A., Keller GR. and Thybo H.; 2010: *Crustal structure and active tectonics in the Eastern Alps.* Tectonics, **29**, TC2011, doi:10.1029/2009TC002491, 1-17

Barison E., Brancatelli G., Nicolich R., Accaino F., Giustiniani M. and Tinivella U.; 2011: *Wave equation datuming to marine OBS data and to land high resolution seismic profiling.* J. Appl. Geophys., **73**, 267-277, doi: 10.1016/j.jappgeo 2011.01.009.

Barison E. and Nicolich R.; 2013: *Reflection seismic images from OBSs profiling across External Hellenides.* Boll. Geof. teor. appl., in press.

Castellarin A., Nicolich R., Fantoni R., Cantelli L., Sella M. and Selli L.; 2006*: Structure of the lithosphere beneath the Eastern Alps (southern sector of the Transalp transect)*. Tectonophysics, **414,** 1-4, 259-282.

Damotte B., Nicolich R., Cazes M. and Guellec S.; 1990: *Mise en oeuvre, traitment et présentation du profil plaine du Po-Massif Central*. In: Roure F *et al.* (eds.) Deep Structure of the Alps. Soc. Geol. de France, de Suisse, Ital., vol. spec. **1**: 65-76.

Di Stefano R., Kissling E., Chiarabba C., Amato A. and Giardini D.; 2000: *Shallow subduction beneath Italy: three-dimensional images of the Adriatic-European-Tyrrhenian lithosphere system based on high-quality P wave arrival times*. JGR, **114**, B05305, doi: 1029/2008JB005641.

Giese P., Wigger P., Morelli C. and Nicolich R.; 1981: *Seismische Studien zur Bestimmung der Krustenstruktur im Bereich der geothermischen Anomalie der Toskana*. EUR 7578, de MF: pp 1-108.

Giustiniani M., Nicolich R.and Tinivella U.; 2013: *The seismic image of the upper crust of the Tuscan geothermal province from CROP profiles.* Proceedings of Geoitalia 2013 - Session 12, Pisa.

Ismail Zadeh A.T., Nicolich R. and Cernobori, L.; 1998: *Modelling of geodynamic evolution of the Ionian Sea basin*. Computational Seismology and Geodynamic, **30**, 32-50.

Kummerow J. *et al*.; 2004: *A natural and controlled source seismic profile through the Eastern Alps: TRANSALP*. Earth Planet. Sci. Lett., **225**,115-129.

Laiglè M., Hirn A., Sapin M., Bécel A., Charvis P., Flueh E., Diaz J., Lebrun J.-F., Gesret A., Raffaele R., Galvé A., Evain M., Ruiz M., Kopp H., Bayrakci G., Weinzierl W., Hello Y., J.-C. Lèpine, Viodé J.-P., Sachpazi M., Gallart J., Kissling E. and Nicolich R.; 2013: *Seismic structure and activity of the north-central Lesser Antilles subduction zone from an integrated approach: Similarities with the Tohoku forearc*. Tectonophysics, **603**, 1-20.

Laiglè M., Hirn A., Sapin M., Lepine J.-C., Diaz J., Gallart J. and Nicolich R.; 2000: *Mt Etna dense-array local earthquake P and S tomography and implications for volcanic plumbing.* J. of Geophys. Res., B9, Solid Earth and Planets, **105**, 21.633-21.646.

Lippitsch R., Kissling E. and Ansorge J.; 2003: *Upper mantle structure beneath the Alpine orogen from high-resolution teleseismic tomography*. J. Geophys. Res., **108,** B8, 2376, ESE 5, 1-15.

Locardi E. and Nicolich R.; 2005: *Crust-Mantle structures and Neogene-Quaternary magmatism in Italy.* Boll. Geof. teor. appl., **46**, 2-3, 169-180.

Lueschen E., Borrini D. Gebrande H., Lammerer B., Millahn K. and Nicolich R.; 2006: *TRANSALP-deep crustal vibroseis and explosive seismic profiling in the Eastern Alps*. Tectonophysics, **414,**1-4, 9-38.

Marson I., Orlando L. and Stoka M.;1994: *Gravity model on the CROP profile*. In: Montrasio A. and Sciesa E. (eds.) Proceedings of Symp. "CROP-Alpi Centrali". Quaderni di Geodinamica Alpina e Quaternaria, vol. spec. **2**,161-169.

Thouvenot F., Senechal G., Hirn A. and Nicolich R.; 1990: *ECORS-CROP wide-angle reflection seismics: constraints on deep interfaces beneath the Alps.* In: F. Roure *et al.* (eds.) Deep Structure of the Alps. Soc. Geol. de France, de Suisse, Italiana, spec. vol. **1**: 97-106.

Šumanovac F., Orešković J., Grad M. and ALP 2002 W.G.; 2009: *Crustal structure at the contact of the Dinarides and Pannonian basin based on 2-D seismic and gravity interpretation of the Alp07 profile in the ALP 2002 experiment*. Geophys. J. int. **179**: 615-633.

Wardell N., Camera L., Mascle J., Nicolich R., Marchi M., Anagnostou C., Barison E. and SeaHellarc team; 2013: *The Peloponnesus Continental Margin from Zakynthos Island to Pylos area, Part 2: Structural framework from seismic reflection and morpho-bathymetric data.* Boll. Geof. teor. appl., in press.

Tema 3

Geofisica Applicata

sessione 3.1

Sismica superficiale e profonda

Convenor: E. Loinger e U. Tinivella

co-organizzata con Sezione Italiana Eage-Seg

A NEW DETAILED SEISMIC STRATIGRAPHY OF THE GULF OF POZZUOLI (NAPLES BAY, SOUTHERN TYRRHENIAN SEA) BASED ON HIGH RESOLUTION SEISMIC REFLECTION PROFILES: INSIGHTS INTO THE OFFSHORE VOLCANOLOGY OF THE PHLEGREAN FIELD VOLCANIC COMPLEX

G. Aiello, E. Marsella
Istituto per l'Ambiente Marino Costiero (IAMC), Consiglio Nazionale delle Ricerche (CNR), Napoli, Italy

Introduction. A new detailed seismic stratigraphy of the Gulf of Pozzuoli (Naples Bay, southern Tyrrhenian sea, Italy) is here purposed and discussed based on the geological interpretation of high resolution seismic reflection profiles, recently collected in the frame of research programmes of marine geological mapping. This offshore stratigraphy is utilized to put some new insights on the marine volcanology of the Phlegrean Fields volcanic complex, deeply studied onshore through field volcanological data. The new stratigraphic setting here purposed will improve the geological and geophysical knowledge on the active volcanic area of the Phlegrean Fields and the adjacent offshore sectors. The tectonic framework of the area will also be discussed based on seismic interpretation and identification of main fault systems and their relationships to the main regional unconformities in the Pozzuoli basin filling.

The stratigraphy and geology of volcanic areas, such as the Gulf of Pozzuoli, has been recently studied in detail (Groppelli and Goette, 2010), focussing on several aspects. Some results mainly deal with the types of mappable stratigraphic units and unconformity bounded units (Lucchi *et al.*, 2010; Tibaldi, 2010; Bonomo and Ricci, 2010; Palladino *et al.*, 2010), centering on Italian volcanoes and showing the use of different applications in the concept of mapping on the base of stratigraphic units, with the aim to define the evolution of a volcanic area. These studies have applied in the field survey the lithosomatic and synthemic units (or

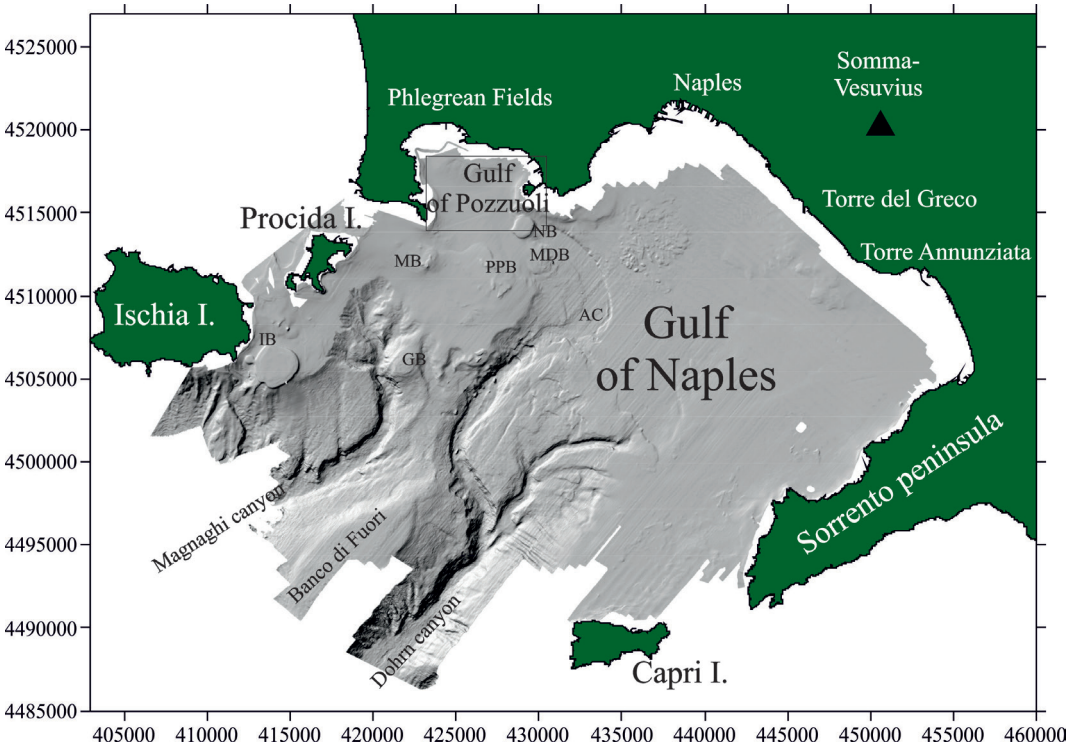

Fig. 1 – Shaded relief map of the Multibeam bathymetry (ELAC, Bottomchart MK2) recorded in the Bay of Naples by the CNR-IAMC Institute (reported from Aiello et al., 2001 and D'Argenio et al., 2004).

Unconformity Bounded Stratigraphic Units or UBSU) to synthesize the volcanic evolution of the area. The relative importance of a volcanic unconformity depends on its geographic extension, the duration of an associated hiatus, or its volcano-structural significance. The application of unconformity-bounded units to synthesize detailed lithostratigraphic units has been carried out in the south-western sector of the Phlegrean Fields volcanic complex (Perrotta *et al.*, 2010). The integration of field data by seismo-stratigraphic analysis of the Bay of Naples and wells drilled in the city of Naples (Milia, 2010) has allowed the reconstruction of the stratigraphic evolution of the southern margin of the Phlegrean Fields, highlighting the close relationships among volcanic activity, marine sedimentation and sea level fluctuations. This allowed to distinguish magmatic features, such as dykes, domes and tuff cones, deciphering the complex stratal architecture as an interplay between the syneruptive and intereruptive stratigraphic units.

In this paper, a correlation with the onshore geology of the Phlegrean Fields has been carried out in order to highlight tectonic and magmatic implications in the geological evolution of the Phlegrean Fields volcanic complex, intensively studied through field geology (Rosi and Sbrana, 1987; Morhange *et al.*, 2005; Bellucci *et al.*, 2006; De Natale *et al.*, 2007; Bodnar *et al.*, 2007; Aiello *et al.*, 2013).

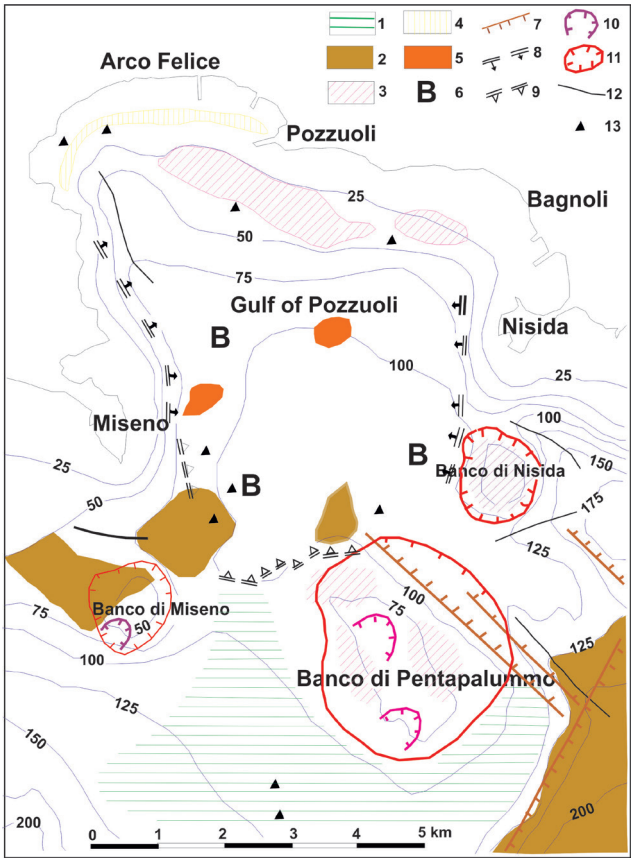

Fig. 2 – Sketch morphological map of the Pozzuoli Bay (modified after Aiello et al., 2012). Key. 1: Wurmian regressive unconformity. 2: Depositional areas at the base of slopes. 3: Post-wurmian terraces. 4: Beach of Roman age. 5: Saddles buried between basins.. B: Intraplatform basins. 6: Morpho-structural slopes along regional faults. 7: Volcano-tectonic morpho-structural slopes. 8: Caldera rims. 9: Crateric rims. 10: Volcanic edifices. 11: Canyon's heads and thalwegs. 12: Gas manifestations. 13: Physiographic margin of the inner shelf. 14: Physiographic margin of the central basin..

Geologic setting. The Gulf of Pozzuoli, offshore the Phlegrean Fields volcanic complex (Naples Bay, southern Tyrrhenian sea) is an inlet with limited dimensions, bounded seawards by several submerged volcanic banks (Pentapalummo Bank; Nisida Bank; Miseno Bank; Fig. 1; Aiello *et al.*, 2012, 2013).

The Phlegrean Fields is an active volcanic center near Naples, Italy (Fig. 2). Numerous eruptions occurred in this volcanic complex during the Late Quaternary (Fig. 2) and repeated episodes of slow vertical ground movement (bradyseism) have been documented since Roman times. Vertical ground movements have been observed since the nineteenth century, when the sea level marks left on the ruins of a Roman market called "Serapeo" in the Pozzuoli town indicated a strong volcano-tectonic subsidence of the area (Dvorak and Mastrolorenzo, 1991; Morhange *et al.*, 2005). The sea level measurements made within the Phlegrean Fields from 1819 to 1968 give an average subsidence rate of 14 mm/yr. Thermal cooling and contraction of a large magmatic body beneath this caldera have been

proposed as a possible cause for local subsidence within the Phlegrean Fields volcanic complex (Dvorak and Mastrolorenzo, 1991). The episodic uplift of some sectors of the Phlegrean Fields is clearly indicated onshore. These sectors include the most recent eruptive vents, including the Monte Nuovo vent, historically erupted during the 1538. Geophysical evidence suggests that the uplift at the Phlegrean Fields is caused by the periodic reactivation of a shallow magmatic body, possibly by intrusion of additional magma or alternatively, hydrothermal mechanisms (Dvorak and Mastrolorenzo, 1991).

The Phlegrean Fields are a young explosive caldera having a diameter of about 12 km, created by the volcano-tectonic collapse during two main volcanic events (Rosi and Sbrana, 1987). This caldera was the source of two large volcanic deposits in the Campania Plain, i.e. the Campanian Ignimbrite (35 ky B.P.) and the Neapolitan Yellow Tuff (12 ky B.P.). After the formation of the Neapolitan Yellow Tuff, representing the main bulk of the Naples town, two periods of eruptive activity occurred in the Phlegrean Fields from 10 to 8 ky B.P. and again from 4.5 to 3.7 ky B.P. (Rosi and Sbrana, 1987). Each eruptive period was followed by a period of quiescence that lasted a few thousand years.

Some deep well data (Mofete and San Vito geothermal areas: Aiello *et al.*, 2012) have been also taken into account for a better correlation with the volcanic products of the Phlegrean Fields volcanic complex. A deep stratigraphic section in the Mofete geothermal area (northern Phlegrean Fields: Aiello *et al.*, 2012) has shown the occurrence of deep trachytic subvolcanic bodies, overlain by siltites, sandstones and shales and then by tuffites, tuffs and lavas interbedded. Pre-calderic products superimpose on these ones and are represented by latitic and trachytic lavas, overlain by the Campanian Ignimbrite. Post-calderic products, overlying the Campanian Ignimbrite are constituted of chaotic tuffites, the Mofete yellow tuffs and the Baia pyroclastites. Another stratigraphic section has been constructed in the San Vito geothermal area (Gulf of Pozzuoli: Aiello *et al.*, 2012). The deep products are represented by silts and sandstones interbedded overlain by tuffites, tuffs and lavas interbedded, both in a submarine environment. Pre-calderic volcanites consist of trachytic lava domes, overlain by chaotic tuffs. Post-caldera products are represented by the Gauro yellow tuff, overlain by latitic scoria and pumices and then by incoherent pyroclastic rocks.

Data and methods. The interpreted Sparker grid consist of seven seismic sections recorded in the Pozzuoli Gulf, both parallel and perpendicular to the shoreline. Seismic acquisition was carried out by using a multielectrode sparker system (SAM96), including shorter pulse lengths for an equivalent energy discharge, increasing the peak pressure and the amplitude of the acoustic wave. The seismic sections were graphically recorded on continuous paper sheets with a vertical recording scale of 0.25. The resolution of the seismic data was about 1 m.

The ability of Multitip Sparker systems to record high resolution seismic data on continental shelf and deeper waters has been revealed and their technical characteristics have been measured in laboratory using different arrangements of energy storage and salinity of water (Rutgers and de Jong, 2003). Sparkers can be used for the production of acoustic pulses as seismic source for sub-bottom profiling in the sea. A multi-tip (200-800 tips) sparker has been developed, which makes high-resolution seismic profiling possible in deep water. The characteristics of the multi-tip sparker system have been measured in a basin in the laboratory using different arrangements of the capacitive energy storage and salinity of the water. A model in Matlab has been used to calculate the current waveform in the spark array for different layouts of the power supply (Rutgers and de Jong, 2003).

The geological techniques of high resolution seismic stratigraphy have been applied in the geological interpretation of seismic profiles (Mitchum *et al.*, 1977; Vail *et al.*, 1977). The stratigraphic interpretation of the seismic data for a particular geologic setting is based on the evaluation of variations in acoustic characteristics reflecting changes in sedimentary processes, tectonic setting and position of sea level. Parallel reflectors, usually continuous and distinct reflectors draping the sea floor typically indicate fine-grained pelagic and

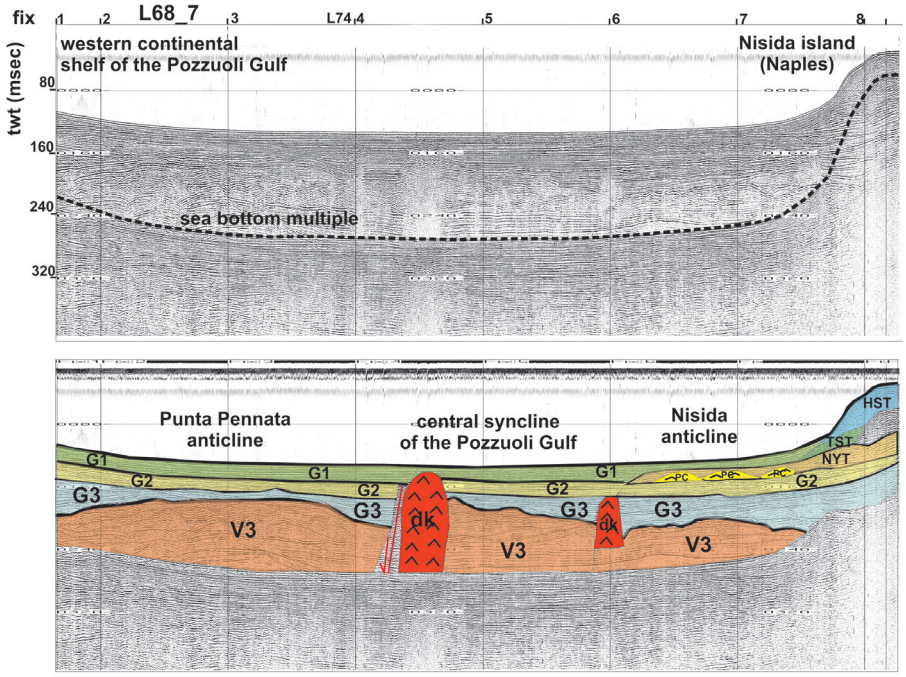

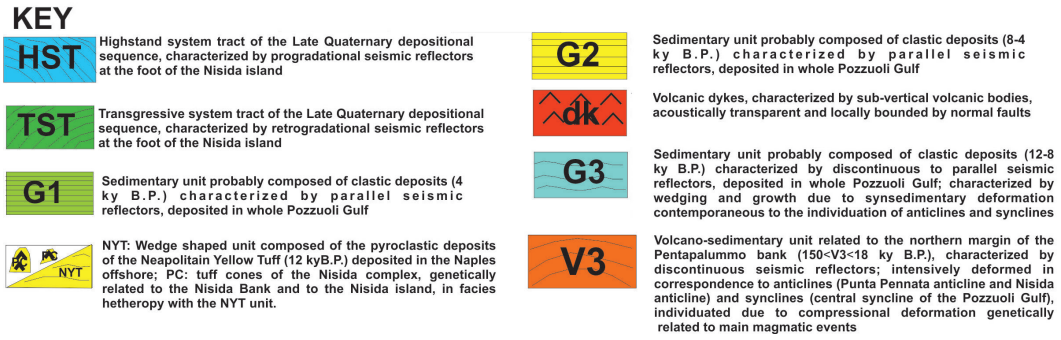

Fig. 3 – Seismic profile L68_7 and corresponding geologic interpretation (modified after Aiello *et al.*, 2012). Note the occurrence of a wide antiformal structure, composed of the Punta Pennata and Nisida anticlines, distinguishing respectively the western and eastern continental shelves of the Gulf of Pozzuoli and the central syncline of the Gulf of Pozzuoli. Volcanic dykes, characterized by sub-vertical, acoustically-transparent and locally bounded by normal faults have been identified through seismic interpretation..

hemipelagic sedimentation deposited during the last stages of a sea level rising or during sea level highstands. Discontinuous, more or less parallel reflectors often indicate mud turbidites deposited during a sea level rising, onlapping or draping depending on geological conditions. Acoustically transparent reflectors vary according to geological setting and sediment type and generally indicate silty-mud turbidites, debris flow deposits and small slumps and finally, channel fill deposits restricted within associated levees or structural walls. Unorganized chaotic reflectors indicate slump masses and possibly high density debris flow deposits, often onlapping but sometimes unconfined. Broken wavy seismic reflectors are typical of slump masses or sediment creep. Acoustical voids, characterized by an inverted U shape are usually acoustically transparent and occurring in the shallow subbottom and are interpreted as gas-charged sediments.

High resolution seismic stratigraphy in the Gulf of Pozzuoli. The seismic profile L68_07 (Fig. 3), running from the western continental shelf of Pozzuoli Gulf and Nisida island

has been interpreted to show the main stratigraphic and structural features of the Pozzuoli Gulf, reported in the geologic interpretation (in the lower inset of the figure). The seismo-stratigraphic analysis has allowed to distinguish eight seismic units. The V3 unit is the oldest one (Fig. 3) and has been interpreted as a volcaniclastic unit genetically related to the northern margin of the Pentapalummo Bank, characterized by discontinuous seismic reflectors. It appears involved in compressional deformation in correspondence to the Punta Pennata and Nisida anticlines. The unit is overlain by the G3 unit, a sedimentary unit composed of clastic deposits, ranging in age from 12 and 8 ky B.P. It is characterized by discontinuous to parallel reflectors and synsedimentary wedging and growth contemporary with folding. The dk unit denominates volcanic dykes, categorized by acoustically transparent vertical bodies, locally bounded by normal faults. The overlying G2 unit is the second unit of the basin filling and is a sedimentary unit composed of clastic deposits, ranging in age from 8 and 4 ky B.P. The NYT/PC unit categorizes the pyroclastic deposits of the Neapolitan Yellow Tuff, while the PC unit represents the tuff cones of the Nisida volcanic complex. The G1 unit is represented by a sedimentary unit composed of clastic deposits (4 ky B.P.). The transgressive and highstand deposits have also been identified (Fig. 3).

High resolution seismic stratigraphy in correspondence to the Capo Miseno volcanic edifice has also been studied through the geological interpretation of the L67_7 seismic profile. A land-sea correlation of the volcanic sequences of Capo Miseno has been attempted based on seismo-stratigraphic criteria. The Capo Miseno volcanic edifice is composed of stratified yellow tuffs, i.e. the Bacoli-Isola Pennata-Capo Miseno yellow tuffs (Rosi and Sbrana, 1987). Field geo-volcanological survey of the Capo Miseno volcanic edifice (Rosi and Sbrana, 1987) has suggested that these units consist of pumiceous tuffs, regularly stratified and very highly lithified. The mass is formed by layers of pumice set in an altered ashy matrix, frequently vesciculated and pisolitic. The volcanic layers are medium to thickly bedded and are poorly sorted with a stratification ranging from subparallel to low-angle cross bedding. At the Capo Miseno tuff cone the sedimentary structures include gravity flowage ripples and slumping. Field observation suggests the emplacement of muddy material from wet eruptive clouds, resulting from hydromagmatic activity (Rosi and Sbrana, 1987). The presence of both massive and cross-bedded layers suggests the eruption of alternating pyroclastic flow and wet surges. The offshore elongment of the Capo Miseno-Isola Pennata and Bacoli yellow tuffs is represented by a thick volcanic unit, acoustically transparent and exposed over a large area and identified offshore the Capo Miseno volcanic promontory. The unit is interpreted as genetically related to the yellow tuffs cropping out onshore. On the slopes of the volcanic bank, deformed by normal faulting, the seismic unit is put in lateral contact with a pyroclastic unit, characterized by discontinuous and sub-parallel seismic reflectors.

Tectonic setting. The tectonic setting of the Pozzuoli seismic units is herein briefly discussed. The V3 volcaniclastic unit is intensively deformed in correspondence to three anticlinalic structures in the Gulf of Pozzuoli, respectively named the Punta Pennata anticline, the Pozzuoli anticline and the Nisida anticline. The same unit is deformed in correspondence to two synclines, namely the central syncline of the Pozzuoli Gulf and the Epitaffio syncline, individuated due to the compressional deformation genetically related to the main magmatic events of the Phlegrean Fields volcanic complex. The G3 sedimentary unit is strongly involved by wedging and growth in correspondence to older anticlines, involving the V3 unit and related synclines. The deposition of the pyr1 unit, pyroclastic in nature, is controlled by normal faulting, since it has been deposited in a structural depression located under the Capo Miseno volcanic edifice. The dk volcanic unit is represented by several dykes whose emplacement has been controlled by normal faulting in the eastern and central Pozzuoli Gulf, inducing the magma uprising along preferential pathways represented by tectonic lineaments. The pyr2 pyroclastic unit has been deposited in the eastern Pozzuoli Gulf, where it is involved by wedging and growth, testifying its deposition during vertical down throwing of normal

faults. The G2 marine seismic unit is characterized by wedging and growth in correspondence to the above mentioned anticlines and synclines. The Capo Miseno seismic unit is deformed in correspondence to both the slopes of the bank by normal faulting. A structural depression is individuated under the volcanic edifice of Capo Miseno, in which a thick pyroclastic unit deposits.

Conclusions. The Gulf of Pozzuoli represents the submerged border of the Phlegrean caldera, resulting from the volcano-tectonic collapse induced from the pyroclastic flow deposits of the Campanian Ignimbrite (35 ky B.P.). Several morpho-depositional units have been identified, i.e., the inner continental shelf, the central basin, the submerged volcanic banks and the outer continental shelf. The stratigraphic relationships between the Quaternary volcanic units related to the offshore caldera border and the overlying deposits of the Late Quaternary depositional sequence in the Gulf of Pozzuoli have been highlighted. Fourteen main seismic units, both volcanic and sedimentary, tectonically controlled due to contemporaneous folding and normal faulting have been revealed by geologic interpretation. These units are herein resumed, from the oldest to the youngest. The V3 unit, located in the Pozzuoli Gulf is characterized by acoustically transparent to discontinous seismic facies and is strongly eroded at its top. It is a volcaniclastic unit related to the northern margin of the Pentapalummo bank. The G3 unit, located in the Pozzuoli Gulf is characterized by discontinuous to parallel seismic reflectors, representing the lower sedimentary unit of the basin fill, composed of clastic deposits. The pyrl unit, located in the Eastern Pozzuoli Gulf, is characterized by discontinuous to sub-parallel seismic reflectors. It represents a pyroclastic unit, uncertain in attribution, deposited in a structural depression under the Capo Miseno volcanic edifice. The dk unit is represented by sub-vertical volcanic bodies, acoustically transparent and locally bounded by normal faults. This unit, detected in the eastern and central Pozzuoli Gulf, is represented by volcanic dykes due to magma uprising in correspondence to normal faults, as already suggested for the whole Naples Bay (Fusi, 1996; Fusi *et al.*, 1991). The pyr2 unit, interpreted in the eastern Pozzuoli Gulf, is characterized by a seismic facies with continuous progradational to parallel seismic reflectors. This pyroclastic unit, uncertain in attribution, has been deposited from the offshore surrounding the Capo Miseno volcanic edifice to the Miseno volcanic bank. The lsl1 unit is represented by a wedge-shaped, chaotic to discontinuous seismic unit, occurring in the eastern Pozzuoli Gulf. It is represented by a wide palaeo-landslide, overlying the V3 volcaniclastic unit and coeval with the basal part of the G2 marine unit. The G2 marine unit, identified in the Pozzuoli Gulf, is characterized by parallel and continuous seismic reflectors. It represents the intermediate unit of the basin fill, probably composed of clastic deposits. The NYT/PC seismic unit is a complex volcanic unit recognized in both the Naples and Pozzuoli Bays. The NYT unit is represented by the pyroclastic deposits of the Neapolitan Yellow Tuff (12 ky), showing a wedge-shaped, acoustically transparent, volcanic seismic unit. The PC unit is characterized by a seismic facies with mound-shaped, acoustically-transparent, volcanic bodies interlayered with parallel reflectors. The PC unit is represented by the tuff cones of the Nisida volcanic complex in facies hetheropy with the Neapolitan Yellow Tuffs and interstratified with the G3 marine deposits. The lsl2 unit is represented by a wedge-shaped, chaotic to discontinuous seismic unit. It is represented by a fossil landslide overlying the G2 marine unit and underlying the Lowstand System Tract of the Late Quaternary depositional sequence and has been interpreted in the eastern Pozzuoli Gulf. The G1 marine unit is characterized by a seismic facies with parallel and continuous seismic reflectors and has been detected in the whole Gulf of Pozzuoli. It represents the upper sedimentary unit of the basin fill, attaining a maximum thickness in the depocenter of the central basin. The LST seismic unit is characterized by progradational seismic reflectors, erosionally truncated at their top. It represents the lowstand system tract of the Late Quaternary depositional sequence and has been detected in the inner continental shelf off Pozzuoli. The lsl unit is a wedge-shaped, chaotic to discontinuous, seismic unit, detected in the Gulf of Pozzuoli, south of the Miseno Cape. It is represented by landslide

deposits intercalated in the upper part of the lowstand system tract, locally characterized by the occurrence of palaeo-channels. The TST unit is characterized by the occurrence of retrogradational seismic reflectors. It has been detected in the eastern Pozzuoli Gulf and is represented by the transgressive system tract of the Late Quaternary depositional sequence. The HST unit, characterized by progradational to parallel seismic reflectors, has been detected in the Eastern Pozzuoli Gulf and represents the highstand system tract of the Late Quaternary depositional sequence.

References

Aiello G., Marsella E. & Di Fiore V.; (2012): *New seismo-stratigraphic and marine magnetic data of the Gulf of Pozzuoli (Naples Bay, Tyrrhenian sea, Italy).* Marine Geophysical Research, **33 (2)**, pp. 97-125.

Aiello G., Marsella E. & Di Fiore V.; (2013): *Dati sismostratigrafici e magnetici marini sul golfo di Pozzuoli (Tirreno meridionale): implicazioni sugli eventi tettonici e magmatici del complesso vulcanico dei Campi Flegrei (Campania).* Miscellanea INGV, **19**, pp. 137-138.

Aiello G., Barra D., Carlino S., De Natale G., De Vita S., Di Vito M.A., Isaia R., Marturano A., Molisso F., Mormone A., Piochi M., Sacchi M., Somma R., Troise C. and Wiersberg T.; (2013): *I risultati preliminari della perforazione recente a Bagnoli (CFDDP): contributi per lo studio dell'evoluzione della linea di costa nell'area orientale della caldera dei Campi Flegrei*. Miscellanea INGV, **19**: pp. 79-80.

Bellucci F., Woo J., Kilburn R.J. and Rolandi G.; (2006): *Ground deformation at Campi Flegrei, Italy: implications for hazard assessment*. Geological Society of London Special Publication, **269:** pp. 141-157.

Bodnar R.J., Cannatelli C., De Vivo B., Lima A., Belkin H.E. and Milia A.; (2007): *Quantitative model and magma degassing and ground deformation (bradyseism) at Campi Flegrei, Italy: implications for future eruptions.* Geology, **35 (9)**: pp. 791-794.

Bonomo R. and Ricci V.; (2010): *Application of unconformity-bounded (UBSU) unit to the geological survey of the volcanic island Ustica (Italy).* In: Groppelli G. and Goette L.V. (Eds.) *Stratigraphy and geology of volcanic areas.* GSA Special Papers, ISBN 97808137224645.

De Natale G., Troise C. & Sacchi M.; (2007): *The Campi Flegrei deep drilling project*. Scientific Drilling, **4:** pp. 48-50.

Dvorak J.J. and Mastrolorenzo G., (1991): *The mechanisms of recent vertical crustal movements in Campi Flegrei caldera, southern Italy.* Geological Society of America Special Paper, **263**: pp. 1-47.

Fusi N., (1996): *Structural setting of the carbonatic basement and its relationships with the magma uprising in the Gulf of Naples, Italy.* Annals of Geophysics, **39 (3).**

Fusi N., Mirabile L., Camerlenghi A. & Ranieri G., (1991): *Marine geophysical survey of the Gulf of Naples (Italy): relationship between submarine volcanic activity and sedimentation*. Memorie della Società Geologica Italiana, **47**: pp. 95-114.

Groppelli G. and Goette L.V.M; (2010): *Stratigraphy and geology of volcanic areas*. GSA Special Papers, ISBN 9780813724645, pp. 1-291.

Lucchi F., Tranne C.A. and Rossi P.L.; (2010): *Stratigraphic approach to geological mapping of Late Quaternary volcanic island of Lipari (Aeolian Archipelago, southern Italy).* In: Groppelli G. and Goette L.V. (Eds.) *Stratigraphy and geology of volcanic areas.* GSA Special Papers, ISBN 97808137224645.

Milia A.; (2010): *The stratigraphic signature of volcanism off Campi Flegrei (Bay of Naples, Italy).* In: Groppelli G. and Goette L.V. (Eds.) *Stratigraphy and geology of volcanic areas.* GSA Special Papers, ISBN 97808137224645.

Mitchum J.R., Vail P.R. & Sangree J.B.; (1977): *Stratigraphic interpretation of seismic reflection pattern in depositional sequences*. In: Payton C.E. *Seismic stratigraphy - Applications to hydrocarbon exploration*. AAPG Mem. **26**: pp. 117-134.

Morhange C., Marriner R., Laborel J., Todesco M. and Oberlin C.; (2005): *Rapid sea-level movements and noneruptive crustal deformations in the Phlegrean Fields caldera, Italy.* Geology, **34 (2)**: pp. 93-96.

Palladino D.M., Simei S., Sottili G. & Trigila R.; (2010): *Integrated approach for the reconstruction of stratigraphy and geology of Quaternary volcanic terrains: an application to the Vulsini volcanoes (Central Italy).* In: Groppelli G. and Goette L.V. (Eds.) *Stratigraphy and geology of volcanic areas.* GSA Special Papers, ISBN 97808137224645.

Perrotta A., Scarpati C., Luongo G. and Morra V.; (2010): *Stratigraphy and volcanological evolution of the southwestern sector of Campi Flegrei and Procida island.* In: Groppelli G. and Goette L.V. (Eds.) *Stratigraphy and geology of volcanic areas.* GSA Special Papers, ISBN 97808137224645.

Rosi M. and Sbrana A.; (1987): *Phlegrean Fields.* CNR, Quaderni De La Ricerca Scientifica, Roma, Italy.

Rutgers W.R. and de Jong I.; (2003): *Multi-tip sparker for the generation of acoustic pulses*. Sensor Review, **23 (1):** pp. 55-59.

Tibaldi A.; (2010): *A new geological map of Stromboli volcano (Tyrrhenian sea, Italy) based on the application of lithostratigraphic and unconformity bounded (UBSU) units.* In: Groppelli G. and Goette L.V. (Eds.) *Stratigraphy and geology of volcanic areas.* GSA Special Papers, ISBN 97808137224645.

Vail P.R., Mitchum R.M., Todd R.G., Widmier J.M., Thompson S., Sangree J.B. and Bubb J.N.; (1977): *Seismic stratigraphy and global change of sea level.* In: Payton C.E. (Ed.) *Seismic stratigraphy - Applications to hydrocarbon exploration.* AAPG Mem. **26**: pp. 49-116.

COMPARISON BETWEEN ULTRASHALLOW REFLECTION AND REFRACTION TOMOGRAPHY IN A GEOTECHNICAL CASE STUDY

R. Balia
Dipartimento di Ingegneria Civile, Ambientale e Architettura-DICAAR, Università degli Studi di Cagliari, Italy

Introduction. From the last decades of the past century, an intense research to investigate the possibility and convenience of using the ultra-shallow reflection technique in engineering and environment - both with P- and SH-wave - has been developed, as witnessed by the abundant literature including theoretical papers and technical papers dealing with real case studies (e.g. Steeples *et al.*, 1997; Ghose *et al.*, 1998; Miller *et al.*, 1998; Miller and Xia, 1998; Steeples and Miller, 1998; Baker *et al.*, 2000; Deidda and Balia, 2001; Balia *et al.*, 2001, 2003; Balia and Gavaudò, 2003; Schmelzbach *et al.*, 2005; Balia and Littarru, 2010).

Almost at the same time there has been a significant evolution of refraction seismology, with the final transition from classical techniques, based on the analysis and interpretation of the traveltime curves, to refraction tomography (e.g. White, 1988; Moser, 1991; Hole, 1992; Mandal, 1992; Boschetti *et al.*, 1996; Sheehan *et al.*, 2005).

Presently, there is the feeling that, in spite of the continuous development of the shallow and ultra-shallow reflection, the use of this technique for operational, non-scientific purposes is still relatively uncommon. Very likely, this is also due to the greater ease of use and the effectiveness attained with refraction tomography so that in most of the cases, especially in engineering and environmental problems in which more often than not the targets are just a few meters deep, the latter technique is preferred.

As known, ultra-shallow reflection requires specific instruments and field procedures: high natural frequency geophones, when available, placed at very short spacing, CMP cables, very short shot-point spacing; the problems become even more challenging in the processing: strong interference with refractions, ground-roll and air-wave, data sets generally characterized by poor signal-to-noise ratio, great difficulty for compensation of static effects and for velocity analysis, and so on. Of course, a good processing package is strictly necessary.

Even refraction tomography requires a good processing package, but: geophone interval and shot interval can be less, the spread management is less demanding and nowadays processing simply requires the coordinates of detectors and shot-points, and obviously the first-arrival times; moreover the most complete processing packages allow to process jointly surface data and down-hole/up-hole/cross-hole data.

The aim of this paper is to show, analyze and discuss the results obtained along one same profile by means of shallow reflection and refraction tomography respectively, using the same base materials and, obviously, the respective processing packages.

Experimental site and instruments. The experimental site is located in the old town of the city of Cagliari (Sardinia, Italy). In this case, the accurate knowledge of the subsoil to a depth of 10-15 m from the ground level was requested for designing an underground car parking. Apart from the road paving (0.3 m thick) the near-surface geological scheme of the site is constituted, top to bottom, by: 1) a more or less compacted backfill made up of sand, gravel and abundant clay, with thickness from zero to several meters, 2) a bedrock constituted by Miocene argillaceous limestone, more or less fractured and weathered, more than twenty meters thick, belonging to the intermediate member of the so-called "Miocene Cagliaritano", and named "Tramezzario" (Barrocu *et al.*, 1981). The excavation for the parking should have a depth of about 12 m, and therefore the aim of the survey was to define the depth to Miocene limestone bedrock and to identify both characteristics and possible changes especially within the bedrock, at least in the first fifteen meters from ground surface. The ground surface of the site is regular and the line along which seismic data acquisition has been performed, about North-South oriented, has a dip of 5%. The basic equipment employed for the two surveys is listed below:

- geophones with natural frequency of 14 Hz, un-damped;
- data acquisition system ABEM - Seistronix RAS 24, two units with a maximum of 48 active channels;
- energy source: 5 kg sledge hammer with vertical stacking for refraction; accelerated dropping weight, single shot, for reflection;
- CMP cables and accessories.
- refraction data processing has been performed by means of the SeisOptPro V5.0 package which simply requires the first-arrival times and the acquisition geometry, and works through a non-linear optimization technique, the so-called Adaptive Simulated Annealing (e.g. Lindsay and Chapman, 1993). Ultra-shallow reflection data have been processed by means of the SPW - Seismic Processing Workshop package.

Ultra-shallow reflection section. The reflection section is shown in Fig. 1. It has been obtained with:

- 36 channel off-end spread;
- geophone interval = shot interval 1 m; maximum CMP fold 1800%;
- in-line minimum offset 6 m, maximum offset 41 m;
- shots 100; acquisition time 3,5 hours, spread assembly-disassembly included;
- processing time, record uploading included, one full day.

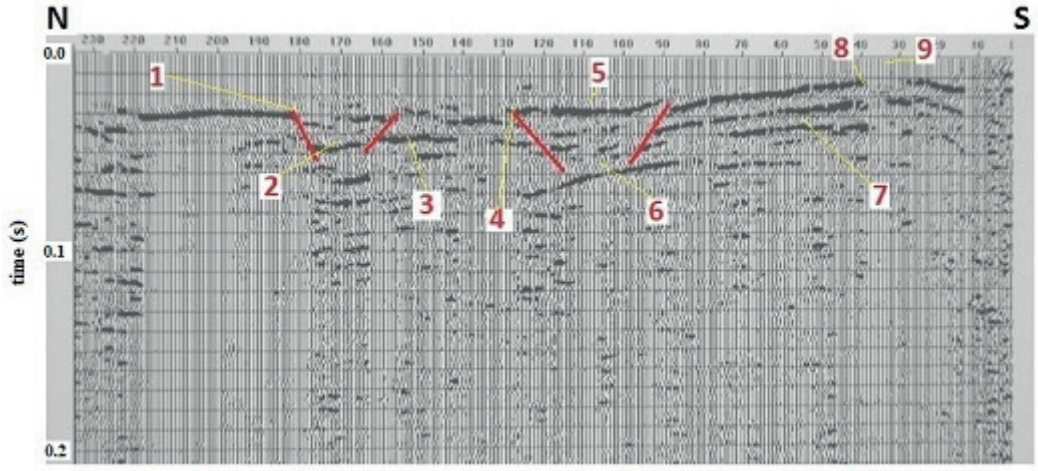

Fig. 1 – The utrashallow reflection section. CMP trace interval 0.5 m; red lines represent faults; red numbers indicate reflectors and structural details.

The processing flow has been rather simple and included the following main steps: trace edit, frequency analysis and filtering, spectral whitening, sorting into CMP gathers, velocity analysis, NMO correction and brute stack, spatial noise filtering, 2-traces horizontal stack. Though ambient noise level was very low, reflections were not very clearly detectable and several attempts to apply more sophisticated processing steps have not provided satisfactory results; eventually, the most convenient way for velocity analysis revealed the constant velocity sections method (CVS): the seismic section at hand has been obtained with a constant stack velocity of 850 m/s. At a glance, a near surface reflector affected by several discontinuities can be individuated; the dominant frequency of reflections is of the order of 100-170 Hz. It is located at a depth of 3-12 m from South to North, values estimated on the basis of the stack velocity which is the only available information for time-to-depth conversion. Several faults are also visible but, for the same lack of information said above, quantifying their possible throw is not easy. Actually, taking into account the geological information, namely the good knowledge of

the base geology in the study area, the raw geotechnical model can be described as constituted by a more or less shallow bedrock, more or less fractured, made up of Miocene limestone and covered by loose, soft materials: that's not exactly a high detail information. However, the seismic section shows several interesting details as indicated in the figure: a small step affecting the shallowest reflector (1), a deeper reflector (2) (3), another step (4), another portion of the shallowest reflector (5), a deeper reflector (6) (7), a sudden lack of reflections close to surface (8) (9); but it must be said that both identification and significance of these details are largely dependent on what has resulted from the next refraction survey.

Refraction tomography. The refraction tomography section is shown in Fig. 2, where the position of the reflection section is also indicated. It has been obtained with:

- 48 channel single spread;
- geophone interval 3 m, shot interval 6 m;
- shots 27; acquisition time 2 hours, spread assembly-disassembly included;
- first-break picking (manual) and uploading: 2 days;
- processing time 9 hours overnight.

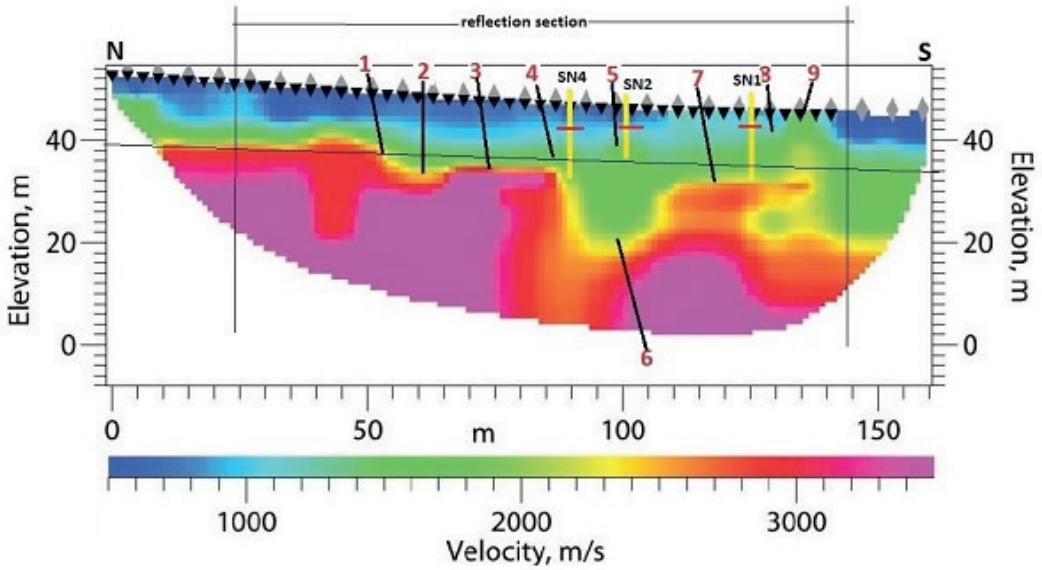

Fig. 2 – The refraction tomography. Grey triangles and black triangles represent shot-points and geophones respectively. Boreholes are indicated with the yellow lines and the red dashes represent the backfill-to-limestone transition; red numbers indicate relevant details and the black line parallel to ground-surface is the bottom of the excavation for the car park to be built.

The immediate feeling is that the tomography contains four primary velocity fields, namely, top to bottom: 1) a dark-blue field, corresponding to P-wave velocity of 500-1000 m/s; 2) a green field, corresponding to 1300-1900 m/s; 3) a red field, corresponding to 2800-3100 m/s; a purple field, corresponding to velocity exceeding 3400 m/s. The secondary fields (light-blue and yellow) appear to represent essentially the transitions from a primary field to the other. The geotechnical interpretation is made easier thanks to three boreholes drilled along the seismic line -though not exactly coincident with the line itself- whose position and depth are shown in Fig. 2 (SN1, SN2 and SN4); these boreholes are not very deep, but they provide the depth of the backfill-to-limestone transition, marked with the red horizontal dashes in Fig. 2. As can be seen, this transition roughly corresponds to transition from dark-blue to light-blue,

which means that the light-blue field doesn't represent the simple graphical effect of a velocity gradient, but the nearest-to-surface limestone, highly weathered and fractured, with P-wave velocity of the order of 1000 m/s. Based on this evidence, it can be said that the green, red and purple fields represent the progressive improvement with depth of the limestone quality. The P-wave velocity associated with the green field is 1300-1900 m/s, then corresponding to still highly fractured material: in fact P-wave velocity laboratory measurements on integer limestone samples give velocity exceeding 3000 m/s, that is in the red and purple fields. Apart from this short description, the meaning of the refraction tomography will be further discussed in the next paragraph.

All the features numbered in the reflection section can be easily located in the refraction tomography. Apart from the apparent slope inversion of the structures from one section to the other -essentially due to the fact that the refraction tomography is referred to the real ground surface, while the reflection section is drawn with respect to a horizontal reference line- it must be admitted that the correspondence between the two sections is beyond all expectations. However one must ask: would have been possible to give a reliable interpretation of the reflection section, in the absence of the refraction tomography? And again: what is the level of information of each of the two products, especially in geotechnical terms?

Discussion and conclusions. First of all must be recalled that, in agreement with a decision declared in the introduction, the two surveys have been purposely carried out using the same basic equipment and with acquisition-processing sequences equivalent in terms of time and overall effort. Actually a more challenging work could have been made for the ultrashallow reflection profile, but one cannot be sure that the additional effort would have given an adequate improvement of the results. This said, let us consider the whole information given by each of the two surveys.

The shallow reflection section appears attractive due to the inherent ability of the reflection method to provide a visual representation intuitively associated with the real structures of the subsoil. Actually it contains very good information as far as the structural conditions are concerned, since faults and main geological transitions are clearly depicted. However the velocity field, rather uncertain and approximate, is substantially useless for geotechnical purposes. To this must be added that the reliable interpretation of the section is strongly dependent on the availability of the refraction tomography: for example, only after examining the refraction tomography it can be concluded that the closest-to-surface reflector does not represent the same geotechnical transition everywhere along the line and, without considering the tomography, the capability of interpreting the reflection section improves just a little even considering the information from the three boreholes.

On the other hand the refraction tomography, probably less attractive in spite of its multicolor structure, seems also less real, probably due to the smoothing of the abrupt velocity changes inherent in the processing technique. But it shows a highly detailed and reliable velocity field and, at least in the case at hand, its meaning in geotechnical terms is clearly understandable, and more with the contribution of the even few and shallow boreholes. In Fig. 2, the black thin line drawn at elevation of 41-33 m and parallel to ground surface represents the bottom of the excavation that must be realized for building the car parking. Thus, from the refraction tomography one can deduct that the volume to be removed is constituted by a loose backfill with thickness of 1-6 m, and by weathered and fractured limestone: both easily workable materials, removable with digging machines, without need for high energy systems such as dynamite or demolition hammer. It is also clear that the deepest level of the car park will be based on the limestone, which is a further very useful information for designers.

Summing up, if one is forced to choose between the ultrashallow reflection and the refraction tomography, very likely the latter must be preferred thanks to the completeness and the high detail that can be reached with this technique, mainly regarding the velocity field, and also for the ease of use of the results. But eventually the base response from the comparison

between the results provided by the two techniques, at least in the case at hand, is that they are strongly complementary and mutually explaining and validating. Therefore, since the two products can be obtained by means of the same basic equipment, better with some additional not very expensive equipment -such as higher frequency geophones for the reflection survey-, the conclusion could be that whenever possible and justified, both surveys should be executed.

Acknowledgements. The work has been carried out with the financial support of the City of Cagliari. Special thanks are due to Dr. Mario Mossa, Dr. Maria Luisa Mulliri, Dr. Mauro Fanni, Dr. Roberto Follesa, and to the lab-technicians at DICAAR Mr. Gianni Andrea Uda, Mr. Maurizio Serci and Mr. Claudio Zara for their fundamental contribution in data acquisition.

References

Baker G. S., Steeples D. W., Schmeissner C. and Spikes K. T.; 2000: *Collecting seismic-reflection data from depths shallower than three meters*. Proceedings of the Annual Symposium on the Application of Geophysics to Engineering and Environmental Problems (SAGEEP 2000), EEGS publication, 1207-1214.

Balia R. and Gavaudò E.; 2003: *Seismic reflection imaging of an ultrashallow interface from a P-wave data set with a poor signal-to-noise ratio*. Near Surface Geophysics, **1**, 183-191.

Balia R., Gavaudò E., Ardau F. and Ghiglieri G.; 2003: *Geophysical approach to the environmental study of a coastal plain*. Geophysics, **68**, 1446-1459.

Balia R., Gavaudò E. and Ghiglieri G.; 2001: *Geophysical survey of a karst area - A case study from Sardinia, Italy*. European Journal of Environmental and Engineering Geophysics, **6**, 167-180.

Balia R. and Littarru B.; 2010: *Geophysical experiments for the pre-reclamation assessment of industrial and municipal waste landfills*. J. Geophys. Eng., **7**, 64-74.

Barrocu G., Crespellani T. and Loi; 1981: *Caratteristiche geologico-tecniche del sottosuolo dell'area urbana di Cagliari*. Rivista italiana di Geotecnica, **Anno XV**, **2**, 98-144.

Boschetti F., Dentith M. C. and List R. D.; 1996: *Inversion of seismic refraction data using genetic algorithms*. Geophysics, **61**, 1715-1727.

Deidda G. P. and Balia R.; 2001: *An ultrashallow SH-wave seismic reflection experiment on a subsurface ground model. Geophysics*, **66**, 183-191.

Ghose R., Nijhof V., Brouwer J., Matsubara Y., Kaida Y. and Takahashi T.; 1998: *Shallow to very shallow, high resolution reflection seismic using a portable vibrator system*. Geophysics, **63**, 1295-1309.

Hole J. A.; 1992: *Nonlinear high-resolution three-dimensional travel time tomography*. J. Geophys. Res., **97**, 6553-6562.

Lindsay C. E. and Chapman N. R.; 1993: *Matched field inversion for geoacoustic model parameters using Adaptive Simulated Annealing*. IEEE Journal of Oceanic Engineering, **18**, 224-231.

Mandal B.; 1992: *Forward modeling for tomography: triangular grid-based Huygens' principle method*. J. Seis. Exp, **1**, 239-250.

Miller K. C., Harder S. H., Adams S.C. and O'Donnel Jr. T.; 1998: *Integrating high-resolution refraction data into near-surface seismic reflection data processing an interpretation*. Geophysics, **63**, 1339-1347.

Miller R. D. and Xia J.; 1998: *Large near-surface velocity gradients on shallow seismic reflection data*. Geophysics, **63**, 1348-1356.

Moser T. J.; 1991: *Shortest path calculation of seismic rays*. Geophysics, **56**, 59-67.

Schmelzbach C:, Green A. G. and Horstmeyer H.; 2005: *Ultra-shallow seismic reflection imaging in a region characterized by high source-generated noise*. Near Surface Geophysics, **3**, 33-46.

Sheehan J. R., Doll W. E. and Mandell W. A.; 2005: *An evaluation of methods and available software for refraction tomography analysis*. JEEG, **10**, 21-34.

Steeples D. W., Green A. G., McEvily T. V., Miller R. D., Doll W. E. and Rector J. W.; 1997: *A workshop examination of shallow seismic reflection surveying*. The Leading Edge, **16**, 1641-1647.

Steeples D. W. and Miller R. D.; 1998: *Avoiding pitfalls in shallow seismic reflection surveys*. Geophysics, **63**, 1213-1224.

White D. J.; 1989: *Two-dimensional seismic refraction tomography*. Geophysical Journal, **97**, 223-245.

ITERATIVE DECONVOLUTIONS TO COMPENSATE WAVELET STRETCHING ON 4TH ORDER TRAVELTIME KINEMATIC

E. Biondi[1], E. Stucchi[1], A. Mazzotti[2]
[1] Department of Earth Sciences, Geophysics, University of Milan, Italy
[2] Department of Earth Sciences, Geophysics, University of Pisa, Italy

Introduction. Normal move-out (NMO) correction applied to common-midpoint (CMP) gathers is needed for stacking, AVO analysis and for other seismic processing steps. The result of this operation are CMP gathers where the offset and velocity effects have been removed and thus all the traces, recorded at variable source to receiver offset, simulate a zero-offset kinematic. The NMO corrected CMP gathers are then employed for AVO analysis and for building stacked images. However, it is well known that the traditional sample by sample NMO correction introduces the stretching of the reflected wavelets (Buchholtz, 1972). These distortions are caused by the non-parallelism of the local traveltime of each reflected event, or, in the frequency domain, as the consequence of the nonphysical energy changes introduced by the non-stationary time shifts applied. Additionally, there are other drawbacks of the standard NMO correction, such as the partial duplication of the recorded events and the time inversion of the samples of a reflection (Masoomzadeh *et al*., 2010). Typically, in order to avoid such negative effects, which may compromise the quality of the stacked images, a mute function is applied to the distorted part of the corrected CMP gathers. Yet, the application of the mute function limits the stacking process to only the near vertical reflections. For example, in case of long-offset acquisitions the wavelets used in the stacking process are constrained to a limited portion of the recorded data and therefore the muting reduces the exploitable information provided by the wide-angle wavelets. As a matter of fact, there are many instances where long-offset acquisitions are crucial, such as sub-basalt exploration or seismic undershooting. In these cases the far offset reflections on the CMP gathers are necessary for imaging purposes (Colombo, 2005).

Since in exploration seismology it is now common to acquire and process data with more than 10 km of offset, a nostretch NMO correction procedure is of interest. Many authors have proposed alternative methods (e.g. Perroud and Tygel, 2004; Masoomzadeh, 2010). However, these techniques are affected by limitations, in particular they do not account for interfering reflections and offset variations of the waveforms, which are commonly present in wide-angle CMP gathers. Moreover, they may introduce horizontal coherent noise that after stacking can mimic true reflected events. In this paper we propose an extension of the algorithm of the normal moveout through iterative partial corrections and deconvolutions which deals with long-offset data and offset varying waveforms (Mazzotti *et al*., 2005). We test our method on a synthetic seismic gather which presents long-offset traces, interfering events and amplitude and phase variations with offset of the reflected waveforms. In addition to these features, we add random noise to the gather and we simulate under-shooting acquisitions using offsets greater than 1000 m (Fig. 1). We also apply our nostretch algorithm to a subset of an offshore marine line (Rocchi *et al*., 2007) simulating again an under-shooting pattern by muting the short offset traces. We start illustrating the normal moveout through partial corrections (NMOPC) and then we show the synthetic and real applications.

Method. The Normal Moveout through partial corrections can be divided into three phases: wavelet estimation, partial NMO correction and shaping deconvolution. We based our algorithm on the 4th order traveltime approximation proposed by Taner and Koehler (1969). For the wavelet estimation, we employ temporal-offset windows which slide both in time and offset. The short-offset window is projected along the 4th order curve corresponding to the central time of the window. These windows enable to select portions of the wavefield where the reflected wavelets can be considered as stationary. The time samples and the traces within each window constitute a matrix which contains reflected and interfering events plus random noise.

The singular value decomposition (SVD) is then applied to each of these matrices and from the 1st eigenvalue the reflected waveform can be separated from interfering events and random noise. Finally, an average across the columns is computed to obtain the estimated wavelet. The short-offset window is then shifted by a predetermined time amount, which ranges between 50% and 80% of the window's time length, and the whole estimation procedure is repeated. Thus, we end up with an estimation of the offset variant wavelets for each 4th order traveltime curve derived from the velocity analysis spectrum. These time and offset variant wavelets will constitute our desired output in the successive deconvolution steps that will be carried out in an iterative fashion after the application of each partial NMO correction.

It is worth noting that in order to avoid edge effects on the representative wavelets, all the adjacent estimation windows are both time and offset overlapped, typically this overlap is between 20% and 50% of the considered dimension. The short-offset window time length is approximately equal to the wavelet duration, while the offset width depends on whether the waveform variations along the offset are strong or mild.

The second phase of our method is the NMO partial correction. The purpose of this operation is to limit the waveform distortions, which would be greater if the corrections were performed in a single step. We regulate the amount of NMO correction by means of the NMO percentage parameter that is defined as follow:

$$\alpha = \frac{t_1 - t_{1\text{new}}}{t_1 - t_0} \qquad (1)$$

where t_1 is the traveltime at the maximum offset for the uncorrected trajectory, $t_{1\text{new}}$ is the traveltime at the same offset for the partially corrected trajectory and t_0 is the final correction time.

Once α has been set, it is possible to move the original traveltime curve t_{old} to the partially NMO corrected trajectory t_{new} using the following equations:

$$\beta = \frac{t_{1\text{new}}^2 - t_0^2}{c_{2\text{old}} X^2 + c_{3\text{old}} X^4} \qquad (2)$$

$$t_{\text{new}} = \sqrt{t_0^2 + \beta c_{2\text{old}} x^2 + \beta c_{3\text{old}} x^4} \qquad (3)$$

where $c_{2\text{old}}$ and $c_{3\text{old}}$ are the coefficients of the fourth order equation, X is the maximum offset and x is the offset. The result of the partial correction is a CMP where the reflections have been only partly moved to their final horizontal alignment so that they have been subjected to only a minimal stretch.

The limited distortions introduced by the partial correction can be removed by shaping the stretched wavelets to their original (unstretched) status by the application of Wiener shaping filters. In fact, knowing the relations between the old and the new traveltime curves (equation 3) and using the estimated wavelets, it is possible to build the partially corrected unstretched CMP gather which constitutes the desired output. To enhance the coherent reflections and to attenuate the influence of the noise we may weigh the samples of the desired output CMP with the semblance values computed from the velocity analysis.

To create the unstretched CMP gather, that is our desired output, the estimated wavelets are inserted into an empty CMP panel centered along the corresponding partially corrected 4th order curves. We employ the same time and offset overlaps we used in the wavelet estimation. Then we apply a trace by trace shaping deconvolution to the partially corrected and stretched CMP gather having as the desired output the partially corrected unstretched CMP. The procedure of partial NMO correction and shaping deconvolution is then reiterated until a complete NMO correction is achieved.

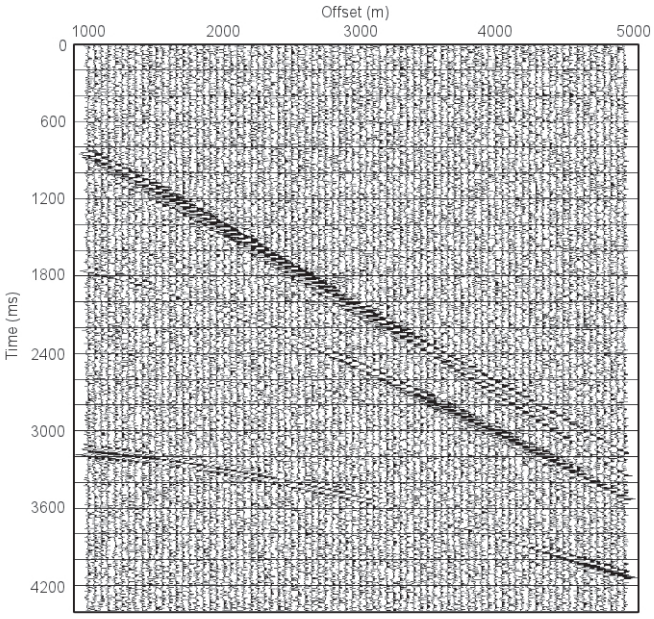

Fig. 1 – Synthetic gather with random noise obtained using a ray-tracing routine (Cerveny, 1985) on the six layers earth model of Tab. 1. To demonstrate the efficacy of the NMOPC the traces up to 1000 m offset have been removed.

Synthetic example. To test our nostretch routine, we apply the NMOPC to a synthetic gather where the near-offset traces are completely missing, in fact, the minimum offset in the CMP of Fig. 1 is 1000 m. In this example the receiver interval is 50 m and the maximum offset is 5000 m. This synthetic gather is built using the earth layered model of Tab. 1. In this model at far offset the traveltimes deviate from the hyperbolic trajectories particularly for the second reflection. Note that the ray-tracing algorithm we used (Cerveny, 1985) properly computes the amplitude and phase variations with offset of the reflected waveforms. Six reflections with offset variations are present, and the two deeper events are nearly overlapped due to the small thickness of the sixth layer (50 m only). Moreover, the noise level is such that the fourth reflection is almost buried in the noise.

Tab. 1 – Earth layered model used for the computation of the synthetic CMP gather of Fig. 1.

Thickness (m)	Velocity (m/s)
400	1500
200	1700
700	1600
500	2000
1000	2100
50	2400
∞	3600

Fig. 2a shows the NMO corrected synthetic data without any mute applied, obtained employing the conventional NMO technique. Several well known artifacts can be observed in this image. First, the two shallower reflections are affected by significant over-stretching and distortions in the interfering part. Second, the traveltime curves which do not correspond to

a reflected event but are nevertheless used by the NMO procedure, cause wavelet repetitions, as indicated by the arrows in the corrected panel. Finally, the other reflections are affected by waveform stretching in particular at far offset. The superimposed red line indicates the mute function with a 50% of stretching mute. This mute function rejects completely the first and the second corrected events and the long-offset part of the gather as well. Conversely, the synthetic gather corrected using the NMOPC does not present the distortions of the traditionally corrected CMP (Fig. 2b). The long-offset waveforms are not stretched, the intersecting events are completely separated, there are not any spurious wavelets and also the corrected events have retained much of their amplitude and phase characteristics. Furthermore, since the NMOPC is based on a SVD estimation process and on a series of shaping deconvolutions that use semblance weighted wavelets, the random noise is highly damped. Note that the fourth reflection, which is completely obscured in Fig. 2a, can be detected in this corrected CMP. The minor artifacts that do appear would be effectively attenuated by the stacking process.

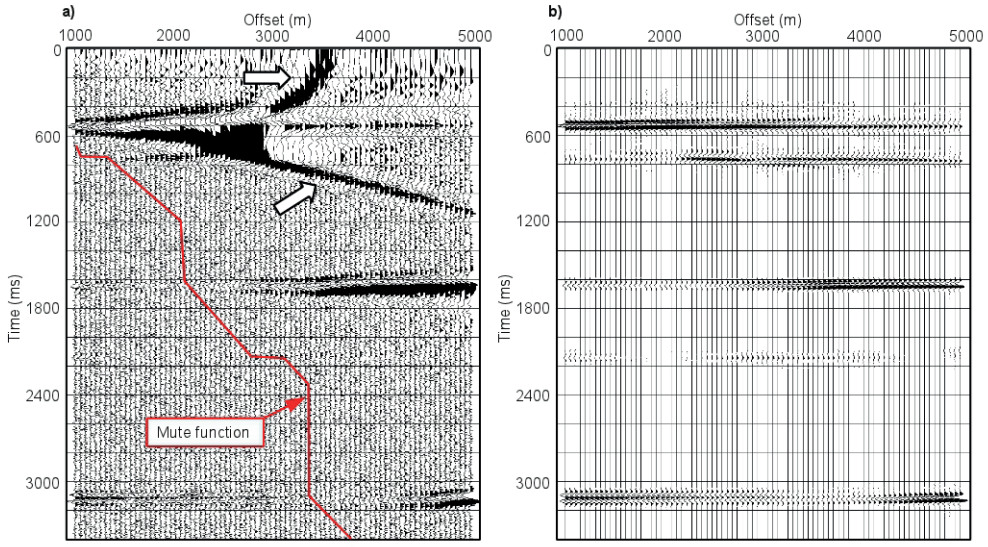

Fig. 2 – a) Synthetic gather corrected using the traditional NMO correction with superimposed a mute function of 50% stretching threshold. b) Result of the application of the NMOPC on the synthetic gather with noise. Note that the fourth reflection, which was buried in the noise before correction, has been highlighted by the SVD and the shaping deconvolutions.

Real data application. We carry out a real data application on a marine seismic line which pertains to a subset of the 3D data set described in Rocchi *et al.* (2007) and acquired on the Senegal passive margin. The acquisition parameters for this line are: source interval 100 m, receivers interval 12.5 m, minimum offset 380 m, maximum offset 8100 m and fold coverage of 125. The result of the stacking procedure employing the whole offset range is shown on Fig. 3a. To test the NMOPC, we simulate an undershooting configuration dropping the data acquired with offset shorter than 2300 m. To this data set we apply the conventional NMO technique and the NMOPC to proceed with the stacking process. The stacked section obtained with the traditional NMO correction and mute (30% of stretching threshold) is displayed on Fig. 3b. Many reflected events are muted in this sections, especially in the right hand part, where a low velocity anticline is present. Therefore, the shallow structure is completely lost. On the contrary, the NMOPC stacked section (Fig. 3c) presents all the reflected events, including the shallow ones and shows a signal-to-noise ratio comparable with the full offset section of Fig. 3a.

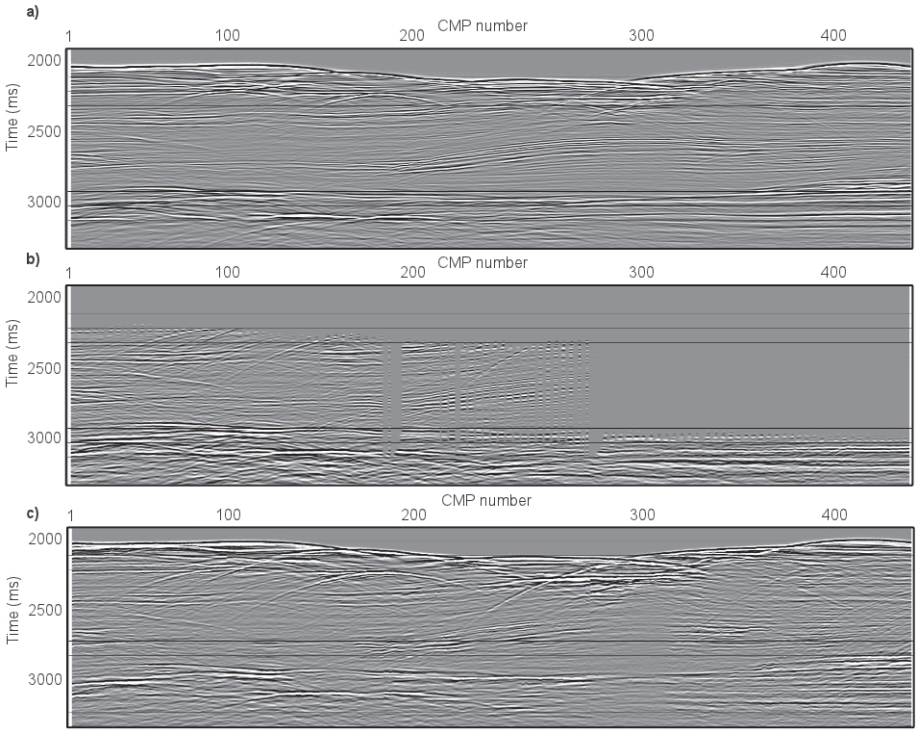

Fig. 3 – a) Stacked section of a subset of the data described in Rocchi *et al.* (2007) employing all the recorded traces. b) Stacked section obtained using the undershooting test data after correction with the traditional NMO algorithm. c) Stacked section obtained using the NMOPC routine applied on the undershooting test data.

Conclusion. The conventional NMO correction cannot deal with long-offset recordings and may causes serious problem when it is applied to interfering events and data with amplitude and phase variations with offset. Not only is the NMOPC effective in avoiding stretching distortions caused by the NMO corrections, but it is also able to maintain much of the amplitude and phase features of the reflected wavelets. This can turn out useful in many situations such as when employing undershooting techniques or when useful reflections occur at large source-receiver offsets. Moreover, the NMOPC corrected CMPs can be employed for AVO and PVO analysis. The efficacy of our method is demonstrated by either the synthetic example and the real data application. The NMOPC is rather flexible and can adapt to different data. In fact the estimation window dimension and overlaps can be varied according to specific needs and targets. The same applies to the number of iterations controlled by the NMO percentage. The main purpose of the NMOPC is not to replace the traditional NMO correction, but to provide information in such cases when the over-stretch distortions cannot be avoided unless by the application of a muting function.

Acknowledgements. We gratefully acknowledge the support of Landmark/Halliburton for the use of their Promax/Landmark seismic software.

References

Buchholtz H.; 1972: *A note on signal distorsion due to dynamic (nmo) correction.* Geophysical Prospecting, **20**, no. 2, pp. 395-402.

Cerveny V.; 1985: *Ray synthetic seismograms for complex two-dimensional and three-dimensional structures.* Journal of Geophysics, **58**, pp. 2-26.

Colombo D.; 2005: *Benefits of wide-offset seismic for commercial exploration targets and implications for data analysis.* The Leading Edge, **24**, no. 4, pp. 352-363.

Masoomzadeh H., Barton P. J. and Singh S. C.; 2010: *Nonstretch moveout correction of long-offset multichannel seismic data for subbasalt imaging: Example from the North Atlantic.* Geophysics, **75**, no. 4, pp. R83-R91.

Mazzotti A., Stucchi E. and Clementi M.; 2005: *Normal Moveout through partial corrections.* 67th EAGE Conference & Exhibition, EAGE, Extended Abstracts, Z-99 pp.

Perroud H. and Tygel M.; 2004: *Nonstretch NMO.* Geophysics, **69**, no. 2, pp. 599-607.

Rocchi S., Mazzotti A., Marroni M., Pandolfi L., Costantini P., Di Biase D., Bertozzi G., Federici F. and Lo Papa G.; 2007: *Detection of Miocene saucer-shaped sills (offshore Senegal) via integrated interpretation of seismic, magnetic and gravity.* Terra Nova, **19**, no. 4, pp. 232-239.

Taner M.T. and Koehler F.; 1969: *Velocity spectra-digital computer derivation and applications of velocity functions.* Geophysics, **34**, no. 6, pp. 859-881.

THE IMPACT OF RAYLEIGH WAVES ELLIPTICITY IN MODE MISIDENTIFICATION

J. Boaga[1], G. Cassiani[1], C. Strobbia[2], G. Vignoli[3]

[1] Dipartimento di Geoscienze, Università degli Studi di Padova, Italy

[2] Total E&P, Pau, France

[3] Aarhus University, Hydrogeophysics Group, Aarhus C, Denmark

Introduction. The surface wave method is widely diffused for shear wave velocity estimation. It is based on the dispersion properties of vertically heterogeneous media (Arai *et al.*, 2004; Foti, 2002; Tokimatsu, 1995; Strobbia, 2002; Socco and Strobbia, 2004). Every surface wave technique requires firstly an high quality recorded seismograms to be analysed, From the data we can estimate the dispersive properties of surface waves, and then go forward with an inversion process of the dispersion curve, controlling the observed Rayleigh wave dispersion, in order to estimate a realistic shear wave velocity profile. One of the most neglected problem in surface wave analyses is the complexity of the multimodal wave propagation which can lead to modes misidentification (Tuan *et al.*, 2011). Even if several issues must be fronted, e.g. attention must be paid to the presence of subsurface structure more complex than simple one-dimensional layering (Strobbia and Foti, 2006; Vignoli *et al.*, 2009, 2011), the inversion of the dispersion curve remains one of the most critical aspect of all the procedure (see Lai *et al.*, 2005, Maraschini *et al.*, 2010). Commonly dispersion curves are identified as energy density maxima in transformed domains, for example the frequency-wavenumber or the frequency-velocity domain. For each frequency the energy maxima are identified in correspondence of certain modal wavenumbers k or velocities v, and it is commonly assumed that the highest modal k, corresponding to the lowest phase velocity v, belongs to fundamental mode of propagation (Weaver *et al.*, 1982; Karray *et al.*, 2008; Park *et al.*, 1999). Generally common surface wave users consider only the largest spectrum energy frequency by frequency, and the fundamental mode is assumed as dominant even if this is not always verified (Foti *et al.*, 2002; Zhang *et al.*, 2003). Often from surface wave analyses we observe only an apparent dispersion curve which represent the contribution of several modes. The focus of this study is on evaluating the effects of mode mis-identification, in particular as a consequence of the well known 'osculation' phenomenon (Malischewsky *et al.*, 2008). Osculation points are point at which two modal dispersion curves get very close and often have the appearance of crossing each other (Cercato, 2009). We want here to show as the osculation phenomenon is strictly related with the polarization of Rayleigh motion in the case of strong impedance contrast in the first subsoil (Boaga *et al.*, 2013). The use of a multi components analyses of motion can be really useful in certain particular geological conditions.

Osculation and velocity contrasts. The errors in terms of depth and velocity of the bedrock can be large if modes identification is wrong, and these parameters are of interest in engineering surveys. When strong impedance contrast is present energy shift from the fundamental to the first higher mode at the so call 'osculation' point. In the case of 'perfect osculation' even with ideal noise-free modal synthetics, a standard data analysis will extract an apparent continuous curve resulting from the two adjacent modes. But in the applied practice of multi-channels analysis of Rayleigh wave (MASW, Park *et al.*, 1999), given the measurement noise, and the

limited spectral resolution of finite array lengths, this ambiguity can be expected even with larger velocity differences between the two osculating modes.

In order to investigate this situation we test synthetic cases with and without a large velocity contrast. The synthetic datasets (full-waveform seismic records) are generated using the SEM2DPACK software (Ampuero, 2008). The excitation source is, in all cases, a Ricker wavelet with 20 Hz frequency peak, located at the ground surface and corresponding to a vertical motion. The simulated recorded data are considered reliable up to 50 Hz. At the bottom and at the lateral boundaries we applied Stacey (1988) absorbing conditions. In order to assess purely the effects of the geological conditions which generate mode contamination, we simulated an optimal surface wave acquisition without spatial aliasing and spectral resolution issues, using a 640 m long acquisition array with 1 m receiver spacing.

We consider 3 simple cases of the same subsoil model with a soft layer resting on top of a stiffer half space; we applied an increasing impedance contrast with the aim of generating the well known case of mode mis-identification as in Fig. 1. As in this simple modal synthetic case, a large velocity contrast shows an 'osculation point', which is the frequency around the two modes have a 'kissing' point. For frequencies smaller than the osculation frequency most energy is located on the first higher mode rather than on the fundamental mode, while for frequencies larger than the osculation frequency, energy remains on the fundamental mode.

The behaviour of the high impedance contrast case can lead to serious misinterpretation of the dispersion curve, with very large overestimation of the bedrock shear wave velocity. Note that this erroneous velocity estimation is acting against precaution, that can have detrimental impacts on seismic amplification assessment. Inverting the apparent curve assuming that the curve belongs to a fundamental mode will lead to a large overestimation of the half-space velocity. This in turn can have a severe impact on seismic response analysis (e.g. Boaga *et al.*, 2011, 2012a).

In practical cases, in presence of coherent and incoherent noise, with the loss of spectral resolution due to the limited array length and the geophone spacing, the identification of the

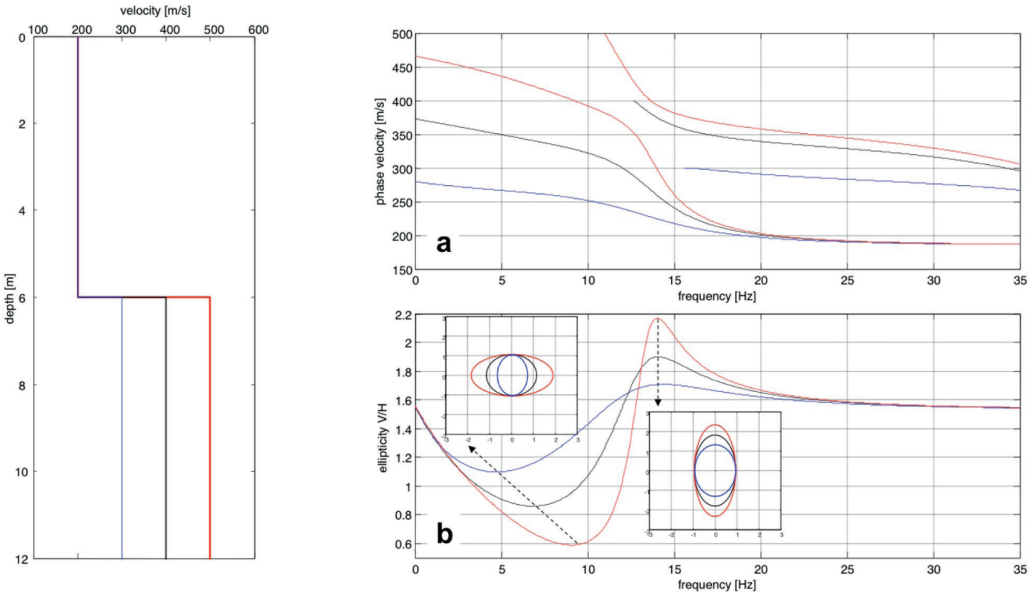

Fig. 1 – Modal curves and ellipticity of the fundamental mode for three models with varying velocity contrasts: a 6m layer with shear wave velocity equal to 200 m/s layer resting on a half space having shear wave velocity equal to 300 m/s (blue), 400 m/s (black) and 500 m/s (red) respectively.

two separate modes can become even harder. The discontinuity of the picked maxima in correspondence of the osculation point can totally disappears: with a poorer f-k resolution the osculation point is often not recognizable.

The apparent dispersion curve seems continuous in velocity, and the spectral amplitude distribution is continuous as well. The amplitude of the recorded vertical particle velocity results from the smooth transition between the contribution of the fundamental mode and the first higher mode.

Polarization and osculation. As discussed by Tuan *et al.* (2011) and Malischewsky *et al.* (2008), the osculation phenomenon occurs only for certain impedance contrast cases, and has consequences also for seismic response analysis (Konno and Omachi, 1988; Castellaro and Mulargia, 2009; Mucciarelli *et al.*, 2009; Boaga *et al.*, 2011). High impedance contrasts have, in fact, also a strong impact onto seismic amplification, and are a primary target for the site characterization (Nogoshi *et al.*, 1970; Nakamura, 1989; Fah *et al.*, 2011; Bonnefoy-Claudet *et al.*, 2008; Hobiger *et al.*, 2009).

It is well known that the Rayleigh wave particle motion is elliptical; the ratio between the vertical and the horizontal components, the *vertical ellipticity*, depends on the velocity profile. In a homogeneous half space, the ellipticity is constant for all frequencies, and a function of the Poisson's ratio. In vertically heterogeneous media, the ellipticity is a function of frequency, and its character is strongly dependent on the velocity contrasts.

The polarization of surface waves is related to the velocity structure, and the signature of the velocity structure on the polarization becomes larger with larger velocity contrast. Therefore several characterization techniques have been devised to take advantage of motion polarization. It can be shown that the magnitude of the ellipticity peak is directly related to the velocity contrast. But we want to show here that also the relationship between polarization and osculation is direct.

In absence of sharp velocity contrasts, modes are well separated and the ellipticity curve is fairly flat. In presence of a strong velocity contrast, the distance between the modes is reduced and the ellipticity peak becomes more pronounced.

It is evident that the cases with large velocity contrast are the most dangerous for the possible mode mis-identification. And in these cases, the ellipticity exhibits behaviour progressively more extreme as the velocity contrast increases. It can be observed as at certain frequency f_V the horizontal particle motion vanishes, and the Rayleigh wave is purely vertically polarized, and one frequency f_H the vertical particle motion vanishes, and the polarization becomes horizontal. These singularities are also points where the direction of the elliptical particle motion changes: from counter-clockwise to clockwise and to counter-clockwise again. The peak of the vertical ellipticity takes place very close to the osculation frequency. It is important to enhance how the ellipticity discussed here refers to the fundamental mode only. The polarization of the first higher mode has an opposite behaviour, becoming vertical for frequencies smaller than the osculation frequency.

Large contrasts in the subsurface produce both the mode osculation and a high peak of vertical ellipticity. Therefore, existence of such peak indicates the presence of a large velocity contrast, and the risk of osculation. The frequencies at which these two phenomena occur are related, even in multilayer models. The osculation happens because of a drop of amplitude of the vertical component, and below the osculation the vertical component reaches a zero.

A Monte Carlo simulation of 2000 cases with 3 layers over a bedrock, with a large velocity contrast, is performed and analysed, and the results show the direct relationship between these frequencies (Boaga *et al.*, 2013).

The osculation happens at a frequency between to the frequency f_H of the horizontal polarization and the frequency f_V of vertical polarization, the peak of vertical ellipticity curve of the fundamental mode. As a consequence we aim at demonstrating that the mode osculation

problem can be predicted and solved studying the ellipticity. The use of multichannel, passive single station data and multicomponent active multichannel data can be a practical solution.

Multi-component surface wave data.

Passive data. Site characterization techniques base on the spectral relationship between horizontal and vertical components of ambient noise have become very popular, being fast and efficient especially in mapping and zonation projects. The Horizontal to Vertical Spectral Ratio (HVSR) has been proven to be an efficient detector of impedance contrasts, even if the nature of the spectral peaks is still debated. Even neglecting the intricacies of the λ/4 hypothesis (Konno and Omachi, 1988; Lachet and Bard, 1994; Chatelain *et al.*, 2007), body wave contribution and HVSR amplitude interpretation (Bard, 1998), measurements of single station noise is certainly capable of excluding or confirming the presence of a strong impedance contrast (Bonnefoy-Claudet *et al.*, 2008). Consequently, single station noise measurements can also be useful in the identification of a subsoil that can induce modal misidentification in surface wave dispersion study.

It has been proven that, under some hypotheses (or conditions) the average spectral ratio is a reliable measure of the Rayleigh wave ellipticity (Hobiger *et al.*, 2009; Malischewsky and Scherbaum, 2004). With strong velocity contrasts, and with near sources of ambient noise, the noise wavefield is dominated by surface waves, and the spectral ratio can be considered as an experimental ellipticity curve.

We created some simple synthetic ReMi data, using a model with 5 m of sediments (Vs=300 m/s) over a bedrock of (Vs=1100 m/s). The source distribution is random and uniform in azimuth around a linear array, composed of 48 channels, spaced 2 meters. The resulting frequency-normalized ReMi spectrum is shown in Fig. 2. The generation of pure Rayleigh wave data and the computation of the spectrum follow the approach of Strobbia and Cassiani (2011). We notice that at the osculation point, the different energy ratio between the two modes changes the shape of the averaged spectrum. The peak becomes closer to the higher mode, due to the effect of the energy shift, but the spectrum is more skewed. The inspection of two slices at constant frequency, at 23 Hz and 28 Hz, above and below the osculation frequency, shows the relationship between the spectral maxima and the true wavenumber of the fundamental and higher modes (Figs. 2b and 2c). If some evidence of lower velocity is present, the ambiguities

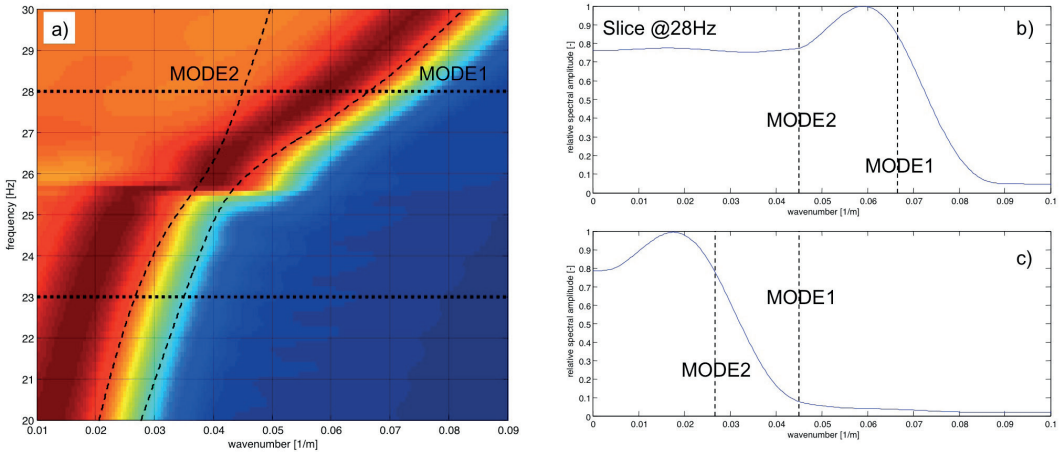

Fig. 2 – F-K analysis of synthetic ReMi f-k spectrum generated with 5000 sources uniformly and randomly distributed around a linear 48 channels with 2 m spacing array for (5 m of sediments with Vs =300 m/s over a bedrock of Vs=1100 m/s). Two slices at 28 Hz and 23 Hz are plotted respectively in panels b) and c). Below the osculation frequency the peak of the spectrum is closer to mode2, thus also these ReMi data suffer from the osculation problem.

of picking such spectrum do not reduce the uncertainty on the extracted dispersion. To pick the fundamental mode, one should peak at 80% of the spectral maximum at 28 Hz, and at 10% of the spectral maximum at 23 Hz. We conclude that also passive ReMi data suffer from the osculation problem. Less ambiguous is the use of a different measurement of the same active wavefield, and the use of the horizontal component can help in solving the osculation issues.

Active data. As shown above, the energy shift between modes is related to the different ellipticity for frequencies smaller and larger than the osculation frequency. In particular below the osculation point the Rayleigh wave ellipticity makes the first higher mode much more energetic in the vertical component than the fundamental mode. This implies that if only the vertical component of soil motion is acquired and analysed in the multi channel seismic records, energy seems to shift from the fundamental mode (at frequencies larger than the osculation frequency) to the first higher mode (below the osculation frequency). This can potentially lead to severe errors in dispersion curve identification, but is only due to the traditional use of vertical geophones only. Fig. 3 shows the spectra from the vertical and horizontal component data for the same model of Fig. 2, with a limited length array. The horizontal component allows the identification of the fundamental mode, even below the osculation frequency, with no ambiguity.

Note that the horizontal components do not present the disturbing osculation phenomenon so important in the vertical components. In particular, below the osculation frequency, energy maxima still remain on the fundamental mode, except for the very low frequencies, and thus produce an easily identifiable dispersion curve. This is in agreement with the ellipticity polarization shown in Fig. 8, in which the horizontal component of the fundamental mode maintains high amplitudes below the osculation frequency.

These synthetic results and the supporting theory indicate that the use of horizontal component receivers in multichannel arrays can allow a correct definition of the fundamental mode dispersion down to low frequencies, well below the osculation point. This conclusion can lead to the design of alternative operational practice that can avoid any overestimation of bedrock seismic velocity as a consequence of the osculation problem. The same linear array can be used with multi-component receivers acquiring multiple shots.

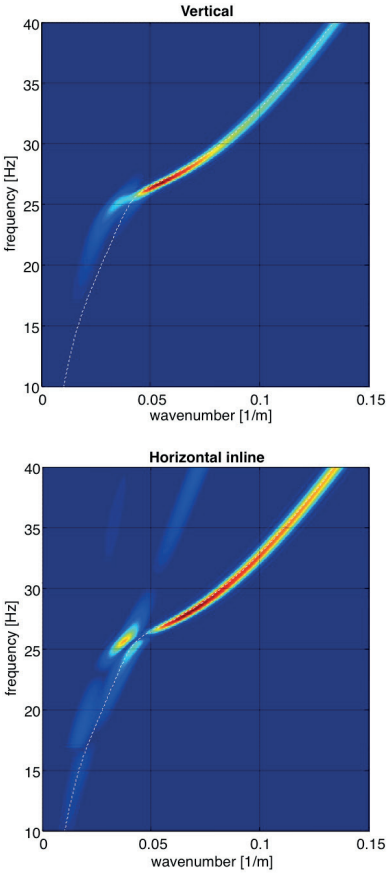

Fig. 3 – f-k spectra of the horizontal and vertical inline components over the same array. Top) f-k spectrum of the vertical component active seismic records for the same model of Fig. 2 (bottom) f-k spectrum of the horizontal component seismic records for for the same model of Fig. 2.

Conclusions. Below the osculation frequency the f-k spectrum energy maxima of the vertical component of motion do not insist on the only fundamental theoretical mode. This can lead to large errors in the inverted models if modes contribution is not considered, with large over estimation of bedrock velocity. The osculation frequency is directly related to the thickness and the velocities of the layers and a similar behaviour is observed in the theoretical Rayleigh ellipticity. Our synthetic tests show that the osculation frequency is practically the same frequency at which Rayleigh ellipticity

fundamental mode has a minimum. We note how the osculation frequency, at which we observe the shift of energy between fundamental and first higher mode, is the same frequency at which fundamental and first higher mode have similar ellipticity. We described as the fundamental mode below that singular frequency has a predominantly horizontal motion, while first mode has a predominantly vertical motion. If we look only on the vertical component energy seems to shift from the fundamental to the first mode while, on the contrary, the use of horizontal components can help to avoid mode misidentification. This evidence has been experimentally demonstrated in Boaga *et al.* (2013).

These synthetic results and the supporting theory indicate that the use of horizontal component receivers in multichannel arrays can allow a correct definition of the fundamental mode dispersion down to low frequencies, well below the osculation point. This is the reason to employ a Multi-components Analyses of Surface Wave (McASW). This approach can lead to the design of alternative operational practice that can avoid any overestimation of bedrock seismic velocity as a consequence of the osculation problem. Since one of the main use of shear wave profiles is for the seismic amplification analysis, and that bedrock velocity overestimation could lead to serious misleading, the value of McASW approach here proposed is evident.

Tab. 1 – Properties of the synthetic models.

Case 1	V_p (m/s)	V_s (m/s)	density (g/cm^3)	thickness (m)
top layer	600	300	1.8	5
bedrock	1000	500	1.9	-

Case 2	V_p (m/s)	V_s (m/s)	density (g/cm^3)	thickness [m]
top layer	600	300	1.8	5
bedrock	2200	1100	2.2	-

Tab. 2 – Subsoil model for the Belluno site.

Belluno Site	V_p (m/s)	V_s (m/s)	density (g/cm^3)	thickness [m]
Layer1	700	350	1.8	6
Layer2	2100	1050	1.9	-

References

Ampuero J.-P., 2008, SEM2DPACK: A spectral element method tool for 2D wave propagation and earthquake source dynamics - User's Guide Version 2.3.4. Available at http://sourceforge.net/projects/sem2d/

Arai H. and K. Tokimatsu, 2004, S-Wave Velocity Profiling by Inversion of Microtremor H/V Spectrum, Bulletin of the Seismological Society of America; v. 94; no. 1; p. 53-63; DOI: 10.1785/0120030028Bard P.Y., 1998, " Microtremor Measurements: A Tool For Site Effect Estimation?", Manuscript for Proc. of 2nd International Symposium on the Effect of Surface Geology on Seismic Motion, Yokohama, Japan, 1-3 Dec, 1998.

Boaga J., Cassiani G., Strobbia L.C. and G. Vignoli 2013. Mode misidentification in Rayleigh waves: Ellipticity as a cause and a cure, Geophysics, 78, 4, 2013

Boaga J., G. Vignoli and G. Cassiani, 2011, Shear wave profiles from surface wave inversion: the impact of uncertainty onto seismic site response analysis, Journal of Geophysics and Engineering, 8, 162-174, doi:10.1088/1742-2132/8/2/004.

Boaga J., S. Renzi, G. Vignoli, R. Deiana and G. Cassiani, 2012a, From surface wave inversion to seismic site response prediction: beyond the 1D approach, Soil Dynamics and Earthquake Engineering, doi:10.1016/j.soildyn.2012.01.001.

Boaga J., G. Vignoli, R. Deiana and G. Cassiani, 2012b, The influence of subsoil structure and acquisition parameters on surface wave mode contamination, *submitted, J. of Applied Geophysics*.

Bonnefoy-Claudet, S., Koeler, A., Cornou, C., Wathelet, M., And Bard, P.-Y., 2008, Effects of Love waves on microtremor H/V ratio, Bull. Seismol. Soc. Am. 98, 288-300.

Castellaro S. and Mulargia F., 2009, The Effect of Velocity Inversions on H/V. Pure and Applied Geophysiscs, Vol. 166, 4, 567-592.

Cercato M., 2009, Addressing non-uniqueness in linearized multichannel surface wave inversion Geophysical Prospecting, Volume 57, Issue 1, pages 27-47.

Chatelain, J.L., Guiller, B., Cara, F., Duval, A., Atakan, K., Bard, P.-Y., and the WP02 SESAME TEAM, 2007, Evaluation of the influence of experimental conditions on H/V results from ambient noise, Bull. Earthq. Eng. DOI 10.1007/s10518-007-9040-7.

Fah D., F. Kind and D. Giardini, 2011, A theoretical investigation of average H/V ratios, Geophys. J. Int. 145, 535-549, doi: 10.1046/j.0956-540x.2001.01406.x

Forbriger T., 2003, Inversion of shallow-seismic wavefields: I. Wavefield transformation Geophys. J. Int., 153, 719-734

Foti S., 2000, Multistation Methods for Geotechnical Characterization using Surface Waves. PhD dissertation, Politecnico di Torino, Italy

Foti S., 2003, Small Strain Stiffness and Damping Ratio of Pisa Clay from Surface Wave Tests. *Geotechnique*, 53(5): 455-461

Foti S., L. Sambuelli, L.V. Socco, C. Strobbia, 2002, Spatial sampling issues in fk analysis of surface waves. Proc. of SAGEEP2002. Las Vegas. USA. February 10-14. CD-Rom

Hobiger M., N. Le Bihan, C. Cornou and P.-Y. Bard, 2009, Rayleigh wave ellipticity estimation from ambient seismic noise using single and multiple vector-sensor techniques 17th European Signal Processing Conference (EUSIPCO 2009) Glasgow, Scotland, August 24-28, 2009

Karray M and G. Lefebvre, 2008, Techniques for mode separation in Rayleigh wave testing. Soil Dyn Earthquake Eng, doi:10.1016/j.soildyn.2008.07.005

Konno K., T. Omachi, 1998, Ground motion characteristics estimated from spectral ratio between horizontal and vertical components of microtremors. Bull. Seism. Soc. Am. 88, pp. 228-241. 386

Lachet C and P.-Y. Bard, 1994, Numerical and Theoretical investigations on the possibilities and limitations of Nakamura's Technique. J. Phys. Earth 42, pp. 377-397.

Lai C.G., S. Foti and G.J. Rix, 2005, Propagation of Data Uncertainty in Surface Wave Inversion. JEEG, Vol.10, Issue 2, pp. 219-228.

Malischewsky P.G. and F. Scherbaum, 2004, Love's formula and H/V-ratio (ellipticity) of Rayleigh waves, Wave Motion 40 (2004) 57-67

Malischewsky P.G, F. Scherbaum, C. Lomnitz, T. Tran Thanh, F. Wuttke and G. Shamir, 2008, The domain of existence of prograde Rayleigh-wave particle motion for simple models, Wave Motion, 45, 556-564.

Maraschini M., F. Ernst, S. Foti, L.V. Socco, 2010 A new misfit function for multimodal inversion of surface waves, Geophysics, VOL. 75, NO. 4, G31-43 doi: 10.1190/1.3436539. Mucciarelli, M., M. Herak, and J. Cassidy (Eds.), 2009, Increasing Seismic Safety by Combining Engineering Technologies and Seismological Data, Springer, Dordrecht.

Mulargia, F. and S. Castellaro, 2008, Passive imaging in nondiffuse acoustic wavefields, Phys. Rev. Lett. 100, 218501(1-4).

Nakamura Y., 1989, A method for dynamic characteristics estimation of subsurface using microtremors on the ground surface. Quaterly Rept. RTRI, Japan 33, pp. 25-33.

Nogoshi M., T. Igarashi, 1970, On the propagation characteristics of the microtremors. J. Seism. Soc. Japan 24, pp. 24-40.

Park C.B., R. D. Miller and J. Xia, 1999, Multichannel analysis of surface waves. Geophysics; June 1999; v. 64; no. 3; p. 800-808; DOI: 10.1190/1.1444590

Socco L.V., C. Strobbia and S. Foti, 2002, Multimodal Interpretation of Surface Wave Data, VIII EEGS 8 - 14 September 2002, Aveiro.

Socco L.V. and C. Strobbia, 2004, Surface Wave Methods for near-surface characterisation: a tutorial, Near Surface Geophysics, 2, pp.165-185.

Socco L.V., S. Foti and D. Boiero, 2010, Surface-wave analysis for building near-surface velocity models -Established approaches and new perspectives, *Geophysics*, 75(5); P. 75A83-75A102, 10.1190/1.3479491

Stacey R. 1988, Improved transparent boundary formulations for the elastic-wave equation. Bulletin of the Seismological Society of America, 78(6).

Strobbia, C., 2002, Surface wave methods, Acquisition, processing and inversion. PhD Thesis Politecnico di Torino, Turin, Italy.

Strobbia C. and S. Foti, 2006, Multi-offset phase analysis of surface wave data (MOPA). J. Appl. Geophys., 59, 300-313.

Strobbia C., A. Laake, P.L. Vermeer, A. Glushchenko, 2011, Surface Waves: Use Them Then lose them. Surface wave analysis, inversion and attenuation in land reflection seismic surveying, Near Surface Geophysics, 9

Thomson W.T., 1950, "Transmission of Elastic Waves Through a Stratified Soil Medium", J.Appl.Phys., 21:89-93

Tokimatsu K., 1995, Geotechnical Site Characterisation using Surface Waves. Proc. IS Tokyo 1995, Balkema, 1333-1368

Tuan T.T., F. Scherbaum, P.G. Malischewsky, 2011, On the relationship of peaks and troughs of the ellipticity (H/V) of Rayleigh waves and the transmission response of single layer over half-space models. Geophysical Journal International Volume 184, Issue 2, pages 793-800.

Vignoli, C. Strobbia, G. Cassiani, P. Vermeer, 2011, Statistical multi-offset phase analysis for surface wave processing in laterally varying media, Geophysics 76, U1.

Vignoli G. and G. Cassiani, 2009, Identification of lateral discontinuities via multi-offset phase analysis of surface wave data, Geophysical Prospecting, 58, pp. 389-413.

Weaver, R.L., 1982, On diffuse waves in solid media, J. Acoust. Soc. Am. 71, 1608

Zhang S.X. and L.S. Chan, 2003, Possible effects of misidentified mode number on Rayleigh wave inversion Journal of Applied Geophysics 53 (2003) 17-29.

NEOTECTONIC REACTIVATION OF MESO-CENOZOIC STRUCTURES IN THE GULF OF TRIESTE AND ITS RELATIONSHIP WITH FLUID SEEPINGS

M. Busetti[1], F. Zgur[1], M. Vrabec[2], L. Facchin[1], C. Pelos[1], R. Romeo[1], L. Sormani[1], P. Slavec[3], I. Tomini[1], G. Visnovich[1], A. Zerial[3]

[1] OGS - Istituto Nazionale di Oceanografia e di Geofisica Sperimentale, Italy
[2] Faculty of Natural Sciences and Engineering, University of Ljubljana, Slovenija
[3] Harpha Sea d.o.o. Koper, Slovenija

Introduction. In 2005 and 2009 the Italian part of the Gulf of Trieste was investigated by geophysical survey, which provided insight into the deep structure and stratigraphy of the area, and also suggested the possibility of recent tectonic activity (Busetti *et al.*, 2010a, b). The existing survey was recently extended to Slovenian waters with the 2013 multichannel seismic and high resolution seismic data, collected in Italian - Slovenian collaboration. The complete datas*et al*lows the correlation of offshore geological structures with the structures that are exposed in the coastal part of the Istria peninsula. The seismic profiles provide evidences of not only of the deep structure, but also of neotectonic deformation that drives, along the main active fault zones, the migration of fluids, such as biogenic gas seeping and thermal springs.

Geological setting. The Gulf of Trieste and the surrounding coastal areas belong to the northern part of the Adriatic Foreland, consisting of the Mesozoic-Paleogene carbonate platform, overlaid by Eocene turbidites, and buried below the Plio-Quaternary marine and continental sediments of the Friuli Plain and the Northern Adriatic Sea.

During the Jurassic rifting the extensive carbonate platform of Triassic Dolomia Principale fragmented into separate paleogeographic units. In the Belluno Basin to the west, deepwater carbonates (Jurassic-Cretaceous) were deposited, followed by the Scaglia Alpina marly limestones (Eocene-lower Aptian), and Gallare Marls (Eocene) which filled the basin. In the east, the Friuli Carbonate Platform, a northern part of the Adriatic carbonate platform, persisted until Cretaceous.

In the Tertiary Dinaric and Alpine compressive phases, the carbonate platform was flexured and buried by Eocene turbidites (Flysch) and by Late Miocene continental and coastal Molassa deposits.

During the Messinian marine regression the subaerial exposure and erosion produced complex morphology with valleys and ridges. In the western part of the Gulf of Trieste, Pliocene marine progradation draped the Messinian erosional topography with marine sediments, followed by further regression in the Late Pliocene.

In the Pleistocene regression and transgression cycles, forced by glacial and interglacial periods, the alternation of marine, transitional and continental sediments was deposited (Busetti *et al.*, 2010a, b).

The pronounced NW-SE-trending structural grain of the area is defined by compressional structures of the Dinaric fold-and-thrust system. The main structure is the topographically prominent Dinaric frontal ramp, running along the north-eastern coast of the Gulf. Belonging to the same system structural system is the Palmanova Thrust in the Friuli Plain and its eastward continuation along the north-eastern boundary of the Istria Peninsula (Busetti *et al.*, 2010a, b; Placer *et al.*, 2010). The foredeep in front of the ramp has been inverted by compressional tectonic, with thrusts dissecting and deforming the Flysch, such as the Buzet and Buje thrusts that were mapped onshore (Placer *et al.*, 2010). The main detachment of this frontal thust system is following the contact of Flysch with the underlying carbonates (Busetti *et al.*, 2010a, b).

The seismic dataset. The offshore geology of the Gulf of Trieste has been investigated in several geophysical surveys. In the Italian part of the Gulf, in 2005 and 2009 were acquired 524 km of multichannel seismic (MCS) and high resolution Chirp profiles. The 2013 survey in Slovenian territorial waters, done in collaboration with the University of Ljubljana and the

Harpha Sea d.o.o. of Koper, acquired 132 km of multichannel seismic and 150 km of Chirp data (Fig. 1). All geophysical surveys were conducted with the R/V OGS Explora.

Major lithologic units in the subsurface were identified on seismic reflection profiles by Busetti *et al.* (2010a, b). Additional subsurface data were provided from the Grado-1 well,

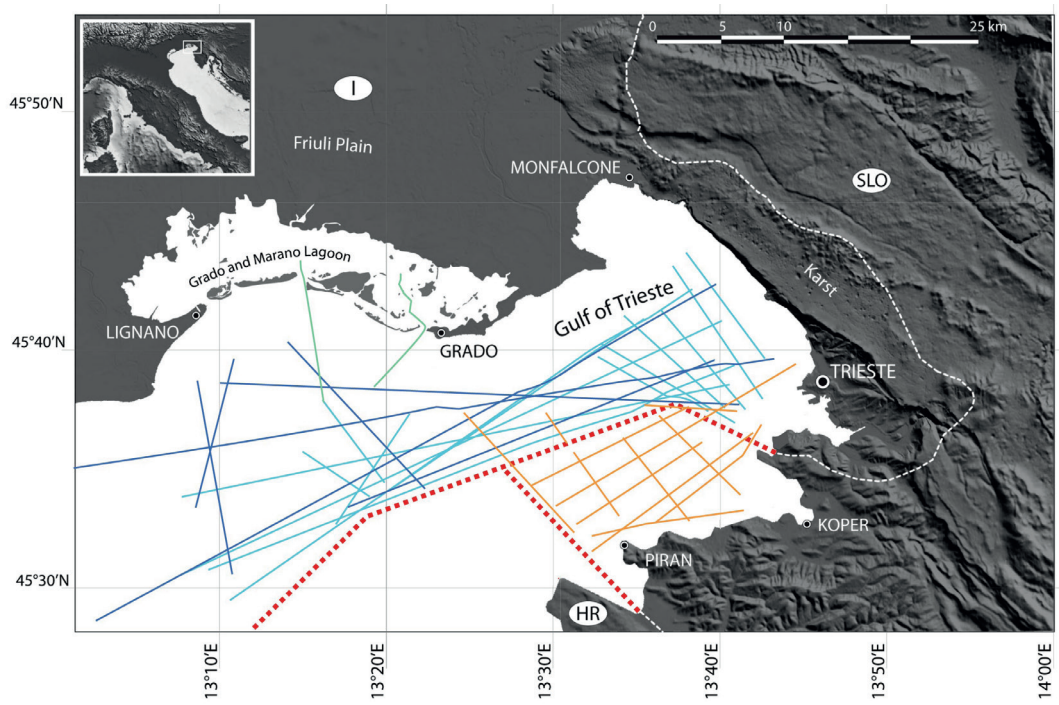

Fig. 1 – Position map of the multichannel seismic and high resolution Chirp data collected by N/R OGS Explora in 2005 (blu lines), in 2009 (light blue lines), and in 2013 (orange lines), for a total of 656 km. Dashed red lines are the offshore national borders.

drilled in 2008 for geothermal surveys on the northern coast of the Gulf (Della Vedova *et al.*, 2008; Cimolino *et al.*, 2010). The Grado-1 well recovered Upper Cretaceous platform carbonates from the well-bottom depth of 1108 up to 1007 m, and Paleogene carbonates from 1001 to 616,5 m. Those two units correspond to similar rocks outcropping in the Karst and Istria. Salty hot water at 42°C occur in two major fracture zones, encountered at 736-740 m, and from 1040 to the well bottom. Carbonates are followed by about 300 m of terrigenous sediment, interpreted to comprise 50-60 m of Eocene Flysch, followed by about 250 m of Miocene Molassa. The topmost sedimentary unit consists of Plio-Quaternary sediments with less than 300 m of thickness (Della Vedova *et al.*, 2008; Cimolino *et al.*, 2010).

Results and discussion. The main seismo-stratigraphic units and horizons interpreted from the multi-channel seismic profiles (MCS) are the Carnian Unconformity, the Meso-Cenozoic carbonates (Friuli Carbonate Platform in the east, and Scaglia in the west in Belluno basinal area), the Eocene turbidites of the Flysch, the Eocene Gallare Marls, the Pliocene progradation sequence and the Quaternary sediments of continental and marine origin (Busetti *et al.*, 2010a, b).

The Carnian Unconformity was encountered in the Amanda well (drilled offshore westward the study area) at 5340 m, and marks the base of the Late Triassic Dolomia Principale. The Carnian Unconformity is a well-known horizon in the seismic exploration data of the Friuli Plain, where it is considered to be one of the detachment levels of the thrusts (Poli and

Zanferrari, 2008). In the MCS collected in the gulf, the Carnian Unconformity is a prominent, well-defined reflector, and is also the lowest interpretable horizon, occurring at about 1.8 - 2.0 seconds.

The Friuli Carbonate Platform developed mainly in the Mesozoic. During the Paleogene, carbonate deposition occurred locally in intraplatform basins, as documented by the Grado-1 well that recovered about 400 meter of Paleogene limestones, similar to those present on land in the Karst and Istria (Cimolino *et al*., 2010). On the seismic reflection profiles from our study area, several kilometres wide tectonically-controlled intraplatform basins occur, filled by well-stratified horizons (Fig. 2).

The Mesozoic extensional phase with NW-SE oriented extensional faults is still recognizable at the paleomargin of the carbonate platform, in the western part of the Gulf of Trieste. The tectonic structure of the margin-slope carbonate system is characterized by the master normal fault verging westward, associated with antithetic east-verging normal faults exhibiting block rotation and syntectonic sedimentation.

The south-westward propagation of the Dinaric thrust system that started in the late Cretaceous reached the study area in the Eocene. The foredeep of the External Dinarides thrust system was filled by the turbidites of the Eocene Flysch. Presently the Dinaric frontal ramp is located at the coastline, where it is called the Trieste Thrust, that involves both the carbonates and the overlying Flysch with a vertical component of displacement exceeding 1000 m (Busetti *et al*, 2010a, b). North-westward contination of this structure, covered by the Plio-Quaternary sediments of the Friuli Plain, is the Palmanova Thrust, that is separated from the Trieste Thrust by the sinistral Sistiana Fault. The Palmanova Thrust originated in the Dinaric thrusting episode and was subsequently reactivated as a frontal structure of the Late Cenozoic South Alpine thrust system (Poli and Zanferrari, 2008). South-eastward into Slovenia and Croatia, the Dinaric frontal ramp continues into the Črni Kal Thrust (Placer, 2008; Placer *et al*., 2010).

The foredeep was affected by compressional tectonic, producing a series of folds and thrusts in approximately NW-SE orientation, with the detachment level at the top of carbonates (Busetti *et al*., 2010a, b). A post-thrusting tectonic phase produced subvertical transpressional

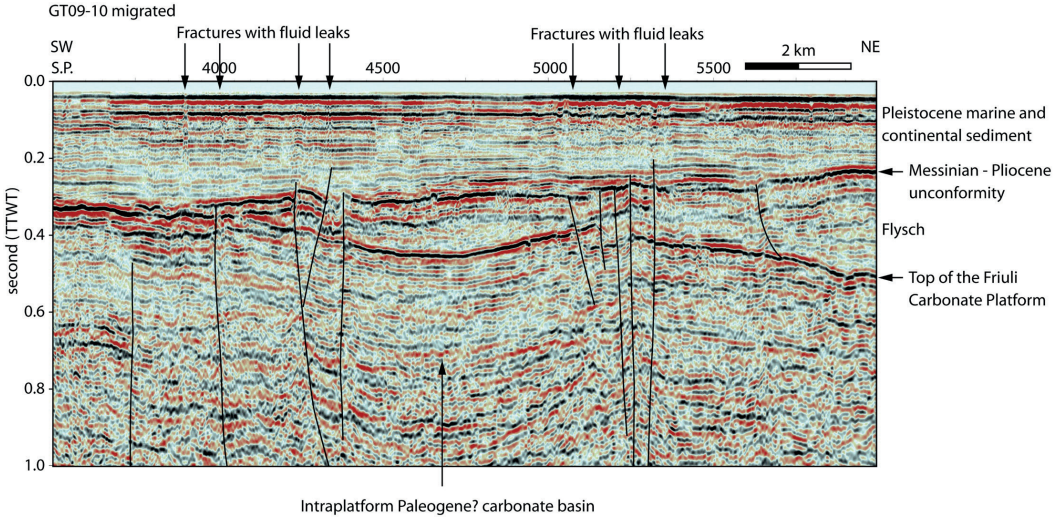

Fig. 2 – Multichannel seismic profiles across the intraplatform basin filled by Paleogene carbonate recovered in the Grado-1 well. The tectonically controlled basin is filled by well stratified limestones. In the post Miocene the faults were reactivated in a transpressional style. The fault strands disrupted the Messinian-Pliocene unconformity with 10-20 meter of vertical displacement. Above the fault zones, the Quaternary sediment have low amplitude signals, suggesting pervasive occurrence of fluids seeping through fracture zones.

faults, that cut the previous Dinaric thrusts, involving the Mesozoic carbonates, which produced a series of positive flower structures and related structural highs. Neotectonic activity of the flower structures is indicated by fault strands which displace the Messinian-Pliocene erosional surface at the top of the Flysch with several meters of throw. As suggested by Busetti *et al.* (2010a, b) these structures are the northwestward continuation of the Hrastovlje Thrust that deforms the outcropping Flysch in the Istria Peninsula in the foreland of the Dinaric Frontal Ramp (Placer *et al.*, 2010).

The newly acquired MCS dataset clearly shows that the structures outcropping along the southeastern coast of the Gulf of Trieste continue westward into the offshore area. For example, one of the most prominent structures is a several kilometers wide anticline in the carbonates, that corresponds to the Izola anticline, a small isolated limestone outcrop along the coast entirely surrounded by the Flysch (Fig. 3). Our seismic profiles show that the axis of the anticline continues into the gulf in the NW-SE direction and plunges moderately towards the NW. The conformably overlying Flysch layers on the top of the carbonates are affected by folding, and the anticline is covered by sub-horizontal Quaternary sediments, which demonstrates that the onset of folding postdates the deposition of the Flysch, and that the deformation terminated by the Quaternary.

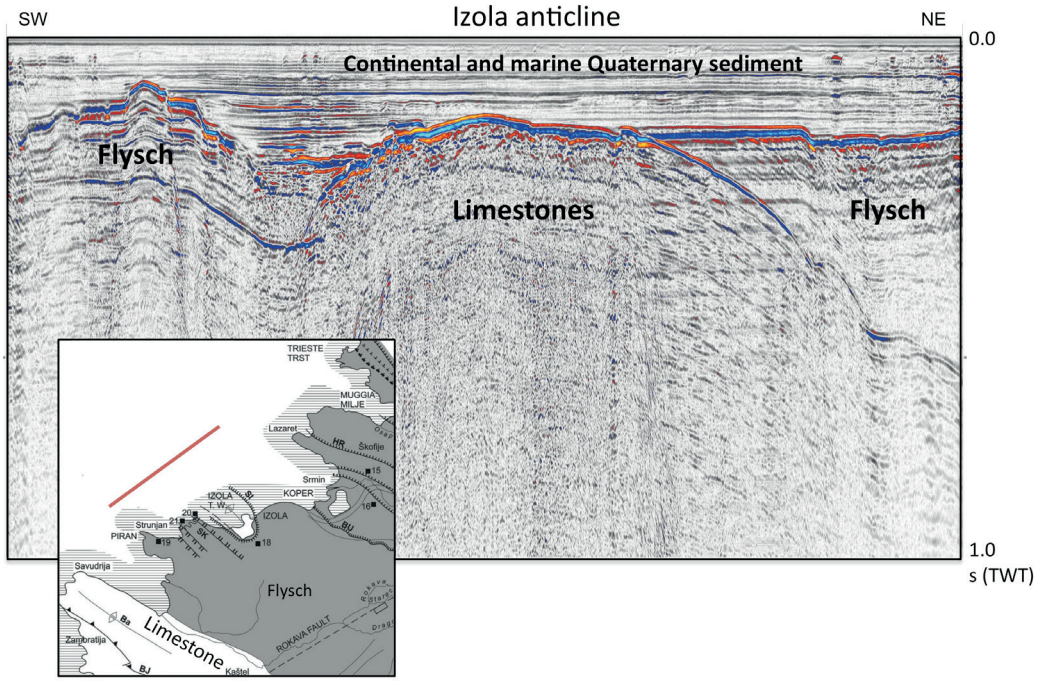

Fig. 3 – Brute stack of the multichannel seismic profiles acquired along the Istrian coasts, across the Izola Anticline. Inset map with onshore location of the Izola Anticline and the seismic profiles (red line).

Post-thrusting transpressional reactivation affected both the Mesozoic extensional faults at the paleoshelf margin and slope system of the carbonate platform, and the faults controlling the Paleogene intraplatform carbonate basins, as well as the Cenozoic thrusts and folds. These faults are subvertical and displace the Carnian Unconformity, and are associated with transpressional flower structures that deform the carbonates and the Eocene Flysch. Additionally, the fault strands clearly vertically offset the Pliocene Unconformity for several meters to several tens of meters. Weak deformation of the overlying marine and continental Quaternary sediments can also be inferred. We attribute this transpressional activity to the ongoing northward movement

of the Adria microplate, well documented by GPS data (i.e. Weber *et al.*, 2010). In the Gulf of Trieste and its immediate surroundings, no historical records of local seismic events are known, and only low magnitude events (< M 4) with both shallow and deep hypocenters have been recorded by the Sismometric Network of the OGS, operating since 1977. However, the very modest seismic record may be influenced by the low deformation rate and/or long recurrence times of earthquakes.

Both the MCS and Chirp data show seismic evidence of fluid occurrences and migration in the Quaternary sediment covering the main fault zones (Fig. 2). These fluids can be related to either water or gas occurence, as the presence of both is well documented in the area.

Low enthalpy waters occur within the carbonates and constitute the geothermal reservoir of the region (Calore *et al.*, 1995). They are well known in the coastal Friuli Plain, were they are already used as geothermal resources. To further exploit the geothermal potential, the Grado-1 well was drilled in 2008. The well encountered thermal water in fractured carbonates at 42-45° C at depths between 736 and 740 meters, and from 1040 to downhole at 1108 meters (Della Vedova *et al.*, 2008; Cimolino *et al.*, 2010). Low-entalphy (about 40°C) natural springs of sulphurous-salty-alkaline waters (Doro, 1939) are present on land close to the northeastern coast of the gulf at the Roman Baths of Monfalcone, which are exploited since ancient times. The springs are located few meters below the plain, and are coming out along faults and karstic conduits. On the southeastern coast of the Gulf, close to the town of Izola, eight submarine thermal springs occur with temperature from 22 to 30°C (Žumer, 2004).

The low-frequency horizons in the carbonate sequence, seen in our multichannel seismic profiles, are usually considered as an indication of the presence of fluids. They may indicate the occurrences of salty low-enthalpy waters, belonging to the same reservoir system that was drilled in the Grado-1 well. The Izola hot springs are located close to the crest of the Izola anticline. This geological setting provides suitable conditions for the rising of the thermal water from the reservoir to the sea floor.

Fluid seepings from the sea floor, mainly related to gas, are also quite frequent in the Gulf. They are well known to the local population in the Northern Adriatic, as they favour the development of carbonatic concretions that form up to a few meters of relief on the seabed and are called *trezze* or *grebeni* by local population (Gordini *et al.*, 2004, 2010). High-resolution seismic data show the presence of biogenic gas pockets in surface sediments, which chemical analyses revealed that the gas consists primarily of methane (81-84%), nitrogen (15-18%) and oxygen (0.7-1.3%) (Gordini *et al.*, 2004, 2010).

In multichannel seismic profiles, up to several hundred metres wide areas with very low amplitude signals occur in the Quaternary sedimentary sequence. These low-amplitude areas may indicate the presence of fluids within the sediment. In Chirp profiles, fluid accumulation zones in the late Pleistocene sediments are characterized by transparent acoustic facies. Accumulations of fluids are usually associated with major fault zones occurring in the underlying pre-Quaternary carbonate and turbidite sequence, especially with the faults that indicate Quaternary activity. We therefore speculate that the origin of accumulations is related to fluid migration along the main fracture/fault zones.

Fluids can also rise up to the sea floor as plumes in the water column that were recorded in the Chirp profiles. Fluid seepings produce small relief forms on the seabed, such as the abovementioned *trezze* or *tegnue*, but also small mud volcanoes and small pockmarks a few meters in diameter. As already documented by Gordini *et al.* (2004, 2010) these resiliences are constituted mainly of methane of biogenic origin.

The fracture systems may therefore facilitate the migration of both deep and shallow fluids, that constitute of low enthalpy thermal waters in carbonates, as well as of gas, primarily methane, occurring in the Quaternary and Neogene sediments.

Conclusions. Interpretation of seismic data demonstrated a polyphase tectonic evolution of the area, which started by Mesozoic rifting and deposition of a several km thick carbonate

succession, dissected by normal faults. During Cenozoic orogeny, the gulf area represented the frontal part of the SW-ward advancing Dinaric thrust system, and was initially buried by foredeep flysch sediments of Eocene age, then affected by thrusts in the final stage of Dinaric deformation. In Late Cenozoic continuing convergence of the Adriatic microplate towards Eurasia produced transpressional reactivation of the faults, which might be continuing into the present time, as seismic profiles have revealed that tectonic deformation is affecting the Quaternary marine and continental sediments. We found geophysical evidence of fluid migrations through the sedimentary units, that are spatially associated with major neotectonic fault zones. Neotectonic activity provides permeable fracture systems along which the fluids migrate. The fluids may come both from the low-enthalphy carbonate reservoir, as well as from the terrigenous sedimentary sequence bearing biogenic gas.

Acknowledgements. The authors acknowledge the crew and the scientific party of the R/V OGS Explora and of the Harpha Sea support vessel, for collecting the geophysical data.

References

Busetti M., Volpi V., Barison E., Giustiniani M., Marchi M., Ramella R., Wardell N. and Zanolla C., 2010a: *Meso-Cenozoic seismic stratigraphy and the tectonic setting of the Gulf of Trieste (northern Adriatic)*. GeoActa, SP**3**, 1-14.

Busetti M., Volpi V., Nicolich R., Barison E, R. Romeo, L. Baradello, Brancatelli G., Giustiniani M., Marchi M., Zanolla C., Wardell N., D. Nieto, and Ramella R.; 2010b: *Dinaric tectonic features in the Gulf of Trieste (Northern Adriatic)*. Boll. Geof. Teor. Appl., **51**(2-3), 117-128.

Calore C, Della Vedova B, Grassi S, Marson I, Nicolich R, Squarci P (1995) *A hydrotermal system along the coastal area of Friuli–Venezia Giulia Region (NE Italy)*. In: Proceedings of the World Geothermal Congress, Florence, 2, 1269–1274.

Cimolino A., Della Vedova B., Nicolich R., Barison E. and Brancatelli G.; 2010: *New Evidence of the outer Dinaric deformation front in the Grado area (NE-Italy)*. Rend. Fis. Acc. Lincei 21-Suppl. 1: S167-S179. DOI 10.1007/s12210-010-0096-y.

Della Vedova B., Castelli E., Cimolino A., Vecellio C., Nicolich R. and Barison E.; 2008: *La valutazione e lo sfruttamento delle acque geotermiche per il riscaldamento degli edifici pubblici*. Rassegna Tecnica del Friuli Venezia Giulia, **6**/2008, 16-19.

Doro, 1939. *Analisi chimica e chimico-fisica delle acque delle Terme di Monfalcone*. Annali di Chimica Applicata, XXIX.

Gordini E., Marocco R., Tunis G., and Ramella R., 2004. *I depositi cementati del Golfo diTrieste (Adriatico Settentrionale): Distribuzione areale, caratteri geomorfologici e indagini acustiche ad alta risoluzione*. Il Quaternario, **17**(2/2), 555-563.

Gordini E., Ciriaco S., Borme D., Cibic T., Falace A., Faresi L., Marocco r., Odorico R., Poloniato D., and Kaleb S., 2010: *Trezze o "Grebeni": biotopi e geotopi dell'Alto Adriatico*. OGS, 246 pp.

Fantoni R., Catellani D., Merlini S., Rogledi S., and Venturini S., 2002: *La registrazione degli eventi deformativi cenozoici nell'avampaese veneto-friulano.* Mem. Soc. Geol. Italiana, **57**, 301-313.

Placer L.; 2008: *Principles of the tectonic subdivision of Slovenia*. Geologija **51**(2), 205-217.

Placer L., Vrabec M., and Celarc B., 2010. The base for understanding of the NW Dinarides and Istria Peninsula Tectonics. Geologija 53/1, 55-86, doi:10.5474/geologija.2010.005

Poli E., and Zanferrari A., 2008: *Inquadramento geologico e lineamenti strutturali*. In: Note Illustrative della Carta Geologica d'Italia alla scala1:50.000, Foglio 066 Udine. 23-34.

Weber, J., Vrabec, M., Pavlovčič-Prešeren, P., Dixon, T., Jiang, Y., Stopar, B., 2010: *GPS-derived motion of the Adriatic microplate from Istria Peninsula and Po Plain sites, and geodynamic implications*. Tectonophysics 483, 214-222, doi:10.1016/j.tecto.2009.09.001

Žumer J., 2004: *Odkritje podmorskih termalnih izvirov*. Geografski Obzornik, **51**(2), 11-17.

IMAGING OF MULTIPLE REFLECTIONS

C. Fortini, V. Lipari
Dipartimento di Elettronica, Informazione e Bioingegneria, Politecnico di Milano, Italy

Introduction. Conventional seismic imaging algorithms are based on single-scattering hypothesis. The reverberations that generates during the wavefield propagation in the subsurface of a seismic experiment (*multiple reflections*) are usually considered as unwanted noise. In marine seismic acquisition, both primary reflections and sea *surface-related* multiples are recorded. The most common approach used to handle with the presence of multiple reflections in the acquired seismic data is to try to eliminate them. First, a model of the multiples is built by means of either *model-based* or *data-driven* methods and then the noise model is adaptively subtracted from the original data (Verschuur, 2006; Verschuur *et al*., 1992; Lipari *et al*., 2012).

Although multiple reflections affect the recorded primary reflections, they also had interacted with the subsurface discontinuities and they thus carry information about the Earth's structure. Recently, researches on multiples (especially surface-related multiples) had shifted their focus on the exploitation on what has been often considered only as noise. Berkhout and Verschuur (2006) showed that multiple reflections can be used to re-create the associated primaries and then exploited for imaging purposes. They also proved that multiples carry useful information and can thus enhance the overall understanding of the subsurface structure. Guitton (2002) and Muijs (2007) showed that WE (Wavefield Extrapolation) migration algorithms can be effectively used for the imaging of the multiple reflections. Alkhalifah (2011) showed that it is possible to use the whole recorded seismic field to correctly image the subsurface discontinuities, avoiding the costly steps of multiples prediction and subtraction. In Shaoping *et al*. (2011) the new dual-sensor acquisition devices are exploited to separate up-going and down-going fields. The separated wavefields are then used for the migration of both primaries and surface-related multiples. Moreover, also in the context of seismic *full waveform inversion* multiples are now included in the inversion process as a source of valuable information.

In this work we review how it is possible to adapt WE migration techniques to effectively exploit the information contained in the surface-related multiples recorded in a seismic experiment. We developed a new WE migration algorithm that provides the ability to migrate both primary and multiple reflections. The migrated section coming from the migration of multiples is shown to provide a wider illumination of the subsurface in most of the cases or, at least, to illuminate the Earth with different angles with respect of those of the primary reflections. In order to prove this statement, we analyzed the migration results also in the A-CIG (Angle Common Image Gather) domain. Moreover, some preliminary results about the discrimination of the artifacts that generates in the multiples imaging are shown. This document is organized as follows: in first section we explain the underlying interpretation of the seismic experiment used throughout the whole work. In sections two and three we show, respectively, the modifications we made to adapt the WE migration algorithm for dealing with the surface-related multiples and the main issues involved in the proposed imaging technique. Section four contains the results obtained on two different synthetic dataset. One was created ad-hoc for the validation of the new migration while the other is the more realistic Sigsbee2b synthetic dataset, often used as benchmark for the multiples prediction and attenuation. Section five concludes the document with some final remarks and the outlook about the possible future developments.

Earth's impulse response. In Yilmaz (2001) the concept of the *convolutional model* for the characterization of the seismic experiment was introduced. According with the proposed interpretation, the recorded seismogram can be modeled as the convolution of the Earth's impulse response with the injected source wavelet. The injected source is the elastic (or acoustic for marine seismic surveys) impulse sent into the ground, while the recorded primaries (the reflections) constitute the Earth's response to the injected source. Also the surface-related

multiples can be accounted for by using this model. Surface-related multiples generates when primary reflections reach the acquisition surface and undergo to an additional downward bounce that send them again into the subsurface. This mainly happen in the context of marine acquisition, where the interface between the water and the air has an high reflection coefficient. The multiple reflections (at least the surface-related) can thus be viewed as the Earth's impulse response to the primaries that now act as a source wavefield.

These considerations lead to the multiples imaging procedure explained in the next section.

WE imaging of multiples. As already said, our goal was to modify pre-existing imaging techniques in order to be able to exploit the information carried by the multiple reflections. Even though Kirchhoff migration is still widely used in the industrial world, our choice fell on the WE (Wavefield Extrapolation) migration algorithms that provide a better accuracy and can handle more complex environments. Both WEM and RTM belong to this class of imaging procedures and can be modified to image multiples as explained here below.

The underlying idea of all the WE migration algorithms is to simulate the seismic wavefield that traveled in the subsurface before and after its interaction with the discontinuities, in order to correctly move the recorded reflection events at the location where they were generated. The concept was firstly introduced by Claerbout in his 1971 paper "Towards a unified theory of reflector mapping" where he stated his famous *imaging principle*: "reflectors exist at points in the ground where the first arrival of downgoing wave is time coincident with an upgoing wave". The *downgoing wavefield* is the pressure (or particle velocity) field generated by the source that propagates downward into the subsurface. The *upgoing wavefield* correspond to reflected energy, traveling upwards towards the recording surface. The whole imaging procedure involved in WE migration algorithms can be summarized by the following three steps:

1) emulation of the downgoing field U_D (t, $\mathbf{x}$);

2) emulation of the upgoing field U_{UP} (t, $\mathbf{x}$);

3) application of the *imaging principle*;

where $\mathbf{x}$ is the vector of the space coordinates $\mathbf{x} = (x, y, z)$. Depending on the chosen algorithm (WEM or RTM), U_D and U_{UP} are extrapolated, respectively, in depth or in time even though the variations needed to correctly image the surface-related multiples are irrespective of the choice of the specific algorithm. If we assume to know the subsurface model (that is the situation when one performs the seismic migration), steps 1 and 2 are simply a modeling exercise. Step 3 implies the analysis of the matching between the two traveling wavefields to determine if they coincide in time and space and to retrieve the information about the reflection coefficient. The imaging principle is implemented by means of an *imaging condition*. The matching between the two wavefield can be evaluated by using a simple cross-correlation between the two fields, as expressed in the following formula:

$$I(\mathbf{x}) = U_D * U_{UP} = \sum_{\omega} U_D(\mathbf{x},\omega)\overline{UA_{UP}(\mathbf{x},\omega)} \qquad (1)$$

where the cross-correlation is expressed in the temporal frequency (ω) domain.

In the conventional migration, the downgoing wavefield is reconstructed by propagating *forward-in-time* an estimated source function S (t, $\mathbf{x}$). The upgoing wavefield is reconstructed by *backward-in-time* extrapolation of the seismic recording R (t, $\mathbf{x}$). Eq. (1), for the conventional migration, can be written as:

$$I(\mathbf{x}) = U_D * U_{UP} = S(t,\mathbf{x}) * R(t,\mathbf{x}) \qquad (2)$$

Following the idea expressed in the previous section, one could migrate the surface-related multiples by simply substituting the data used in step 1 and step 2. For the downgoing field, instead of using S (t, $\mathbf{x}$), we inject and forward propagate the seismic recording R (t, $\mathbf{x}$). For the

upgoing wavefield reconstruction we use an estimation of the surface-related multiples $M(t, \mathbf{x})$ in place of the recorded primaries and we propagate this field backward in time. This way the downgoing wavefield would contain the primary reflections, regarded as a virtual source for the surface related multiples $M(t, \mathbf{x})$. The multiples field can be retrieved using one of the many multiples prediction methods. In our work we used both the well-known SRME algorithm (Verschuur *et al.*, 1992) and an original model-based prediction algorithm (Lipari *et al.*, 2012).

Eq. (1) for the case of multiples imaging becomes:

$$I(\mathbf{x}) = U_D * U_{UP} = S(t,\mathbf{x}) * M(t,\mathbf{x}) \tag{3}$$

Surface-related multiples had followed different propagation paths with respect to the primary reflections and then they carry a different information about the Earth's structure. Moreover, multiples can produce better illumination. For the case of conventional migration, the source illumination is basically determined by the source-receivers geometry and covers approximately half of the receivers coverage. On the other hand, in imaging of multiples, every receiver is treated as a source and almost the whole region covered by the receivers is illuminated (see Fig. 1). In particular, multiples tend to reach the subsurface discontinuities with lower angle on incidence with respect to the primaries (Fig. 3). These considerations makes the use of multiples reflections attractive for improving the overall picture of the subsurface.

Cross-talk. Each one of the two terms involved in Eq. (3) can be re-written expanded in its components:

$$R(t,\mathbf{x}) = \left(P_A + P_B + ... + P_n + M_A^1 + M_B^1 + ... + M_A^2 + M_B^2 + ... + IM\right) \tag{4}$$

$$M(t,\mathbf{x}) = \left(M_A^1 + M_B^1 + ... + M_A^2 + M_B^2 + ... + IM\right) \tag{5}$$

where the subscript letters ($A,B,...,n$) refer to different interfaces in the subsurface, while the superscript numbers indicate the order of the multiple events. We indicated the primary events with the letter P and the multiples with M. IM indicates all the others events not accounted in the present work (diffractions, internal multiples, etc.). Useful contributions to the migrated section only come from the combination of primaries and multiples corresponding to the same reflector. All the others terms in the summation of Eq. (6) have to be regarded as noise and they are commonly called *cross-talk terms*. We can consider the seismic image obtained from the multiples migration to be composed by two terms: the desired image $\hat{I}(\mathbf{x})$ and the image of the artifacts $I_N(\mathbf{x})$:

$$\hat{I}(\mathbf{x}) = P_A * M_A^1 + P_B * M_B^1 + ... + M_A^1 * M_A^2 + M_B^1 * M_B^2 + ... \tag{6}$$

$$I_N(\mathbf{x}) = P_A * M_B^1 + P_B * M_A^1 + ... + P_A * M_A^2 + P_B * M_B^2 + ... \tag{7}$$

In Eq. (7) it is possible to notice that the cross talk terms are of two types: those events that come from the interaction of primaries and multiples of order higher that the first and those events generated by the cross-correlation of primary reflections of one interfaces and multiples of a different reflector. The former produce the same effect of the cross-correlation of a source function $S(t, \mathbf{x})$ with the surface-related multiples recorded in the original data. The latter show up as unwanted virtual interfaces in the final migrated image. Both type of artifacts seem to have a different moveout with respect to the one of the desired events in the A-CIG domain (see Fig. 3) even if more studies are needed for their identification and removal. As a matter of fact, cross-talk attenuation is still an open topic in the area of seismic imaging.

Tests. For the testing phase we developed a WE migration code based on the use of Kirchhoff extrapolation for the simulation of the downgoing and upgoing wavefields. Being based on Kirchhoff extrapolation it lacks of the accuracy provided by the more effective finite difference extrapolation engines commonly used in WEM and RTM. Nevertheless,

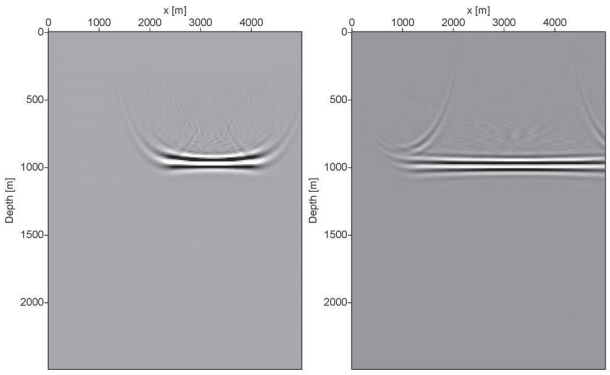

Fig. 1 – Imaging results on a simple synthetic data. Left: Conventional migrated section of a single shot gather. Right: Migration of multiples of the same single shot gather of the left-hand-side picture. It is possible to notice the wider illumination provided by the new migration procedure.

for the purpose of validating the new procedure for the multiples migration, the implemented code still produces acceptable results.

We first tested our migration procedure on a very simple synthetic dataset created ad-hoc for the experiment. The data were generated using a FD (Finite Difference) software. The model used for the simulation provides a single flat reflector in a constant velocity medium. Fig. 1 shows the migrated sections obtained with both the standard imaging procedure and the migration of multiples. Only a single CSG (Common Shot Gather) was processed. The acquisition geometry of the shot gather under analysis provides a split-spread arrangement of the receivers (from x=1000 m to x=5000 m) while the source is placed at x=3000 m. It is possible to notice that the multiples migration not only is able to reconstruct the subsurface discontinuity but it also provides a much wider illumination.

We tested our new imaging algorithm also on the more realistic synthetic dataset Sigsbee2b. Fig. 2 shows the comparison between the conventional migration result and the migrated section obtained by migrating the multiples. The two images are very similar thus confirming the feasibility of the proposed procedure. Moreover there are areas where the multiples migration produces better results, especially in terms of vertical resolution. The yellow arrows superimposed onto the images point to some artifacts coming from the cross-talk terms that generate in the multiples imaging while the yellow box highlight the area where the main improvements occur.

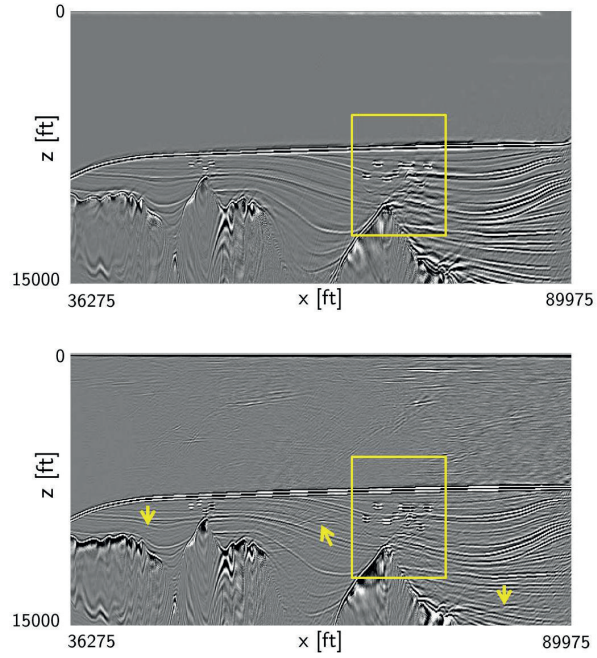

Fig. 2 – Imaging results on the Sigsbee2b dataset (close-up). Top: Image from conventional imaging of primaries. Bottom: Migration of multiples. The yellow arrows indicate the cross-talk noise. In the highlighted area in the yellow box it is possible to notice the better results produced by the migration of multiples in terms of spatial resolution with respect of the primaries image.

Fig. 3 show an example of two A-CIGs (Angle Common Image Gathers) extracted from both the migrated sections obtained with the migration of primaries and the multiples image. It is possible to notice the different illumination provided by the multiple reflections.

Final remarks. A new migration technique able to correctly account for surface-related multiples was presented with examples on both a simple ad-hoc synthetic data and on

a more realistic synthetic dataset. The multiples recorded in the data were successfully treated as a source of valuable information of the subsurface discontinuities and it was possible to create a migrated section using this new information. The main issue related to the migration of multiples is the cross-talk between primaries and multiples relative to different reflectors. More studies are needed to better characterize the cross-talk events and to implement some techniques for their removal or attenuation even though their analysis in the A-CIG domain seems to promising. Nevertheless, the performed tests showed that the seismic image constructed using the surface-related multiple reflections could be very useful to complement the conventional migrated section. As a matter of fact, the illumination provided by the multiples is often wider than the one of the primaries. Moreover, the multiples arrive at the subsurface discontinuities with different angles with respect to the primaries, thus providing additional information that could be useful for the migration velocity analysis.

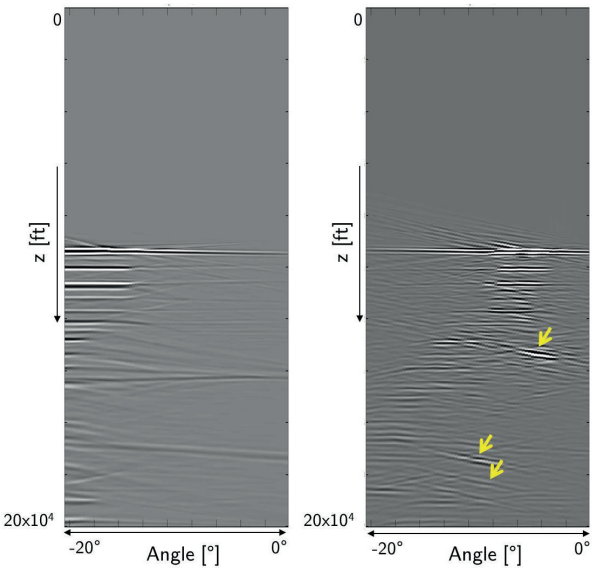

Fig. 3 – Angle gathers panels from the Sigsbee2b dataset with the conventional migration (left) and with the migration of multiples (right). The yellow arrows indicate the events associated with the cross-talk noise. It is possible to notice that for the case of the multiples migration the energy is concentrated at smaller angles than in the case of the conventional migration.

Acknowledgements. This work has been done in collaboration with Eni. The authors would like to thank Eni to the permission to publish this work.

References

Alkhalifah, T., Zuberi, M.; 2011: *Imaging by Forward Propagating the Recorded Data - An Analysis*. 73rd EAGE Conference & Exhibition incorporating SPE EUROPEC 2011 Vienna, Austria, 23-26 May 2011

Berkhout, A.J., Vershuur, E.; 2006: *Imaging of multiple reflections*. Geophysics, 71, no. 4, SI209-SI220.

Claerbout, J. F.; 1971: *Toward a unified theory of reflector mapping*. Geophysics, 36, no. 3, 467-481.

Guitton, A.; 2002: *Shot-profile migration of multiple reflections*. Stanford Exploration Project, Report 111.

Lipari, V., Fortini, C., Spadavecchia, E., Bienati, N.; 2012: *Prediction of surface-related and inter-bed multiples via Kirchhoff extrapolation*. Istanbul 2012 - International Geophysical Conference and Oil & Gas Exhibition: pp. 1-4.

Muijs, R., Robertsson, J. O. A., Holliger, K.; 2007: *Prestack depth migration of primary and surface-related multiple reflections: Part I – Imaging*. Geophysics 72, S59-S69.

Shaoping, L., Whitmore, N.D., Valenciano, A.A., Chemingui, N.; 2011: *Imaging of Primaries and Multiples with 3D SEAM Synthetic*.

Verschuur, E.; 2006: *Seismic multiple removal techniques - past, present and future*. EAGE publications, ISBN 90-73781-51-5.

Verschuur, D.J., Berkhout, A.J., Wapenaar, C.P.A.; 1992: *Adaptive surface-related multiple elimination*. Geophysics 57, 1166-1177.

Yilmaz, O.; 2011: *Seismic Data Analysis: Processing, Inversion, and Interpretation of Seismic Data*. Society of Exploration Geophysicists, ISBN 978-1-56080-094-1

EVOLUZIONE GEOMORFOLOGICA E STRUTTURALE DI UN'ANTICLINALE DELLA PIANURA PADANA DA DATI SISMICI 3D A RIFLESSIONE

A. Gennari[1], M. R. Barchi[3], M. Galbiati[2], P. Rocchini[1]
[1] *Eni e&p, S. Donato Milanese, Italy*
[2] *Eni UK, London, United Kingdom*
[3] *Dipartimento di Scienze della Terra, Università di Perugia, Italy*

Introduzione. La Geomorfologia Sismica (Seismic Geomorphology) viene definita come l'applicazione di tecniche analitiche pertinenti allo studio di forme terrestri attuali, applicate a superfici antiche e sepolte, derivate da dati sismici 3D (Davis *et al.*, 2007). L'analisi è basata sull'estrazione di attributi sismici (come ampiezza, continuità, curvatura ecc.) lungo orizzonti rappresentativi di superfici geologiche. Questo nuovo approccio, basato sull'*imaging* sismico in tre dimensioni, è diventato, negli ultimi anni, un'importante metodologia per l'esplorazione, la comprensione e la caratterizzazione di *reservoir* di idrocarburi.

Il presente lavoro è il risultato di una Tesi di Laurea Magistrale in Geologia degli Idrocarburi, svolta a seguito di uno stage formativo della durata di tre mesi, presso Eni, divisione Exploration & Production.

Il lavoro si è occupato del trattamento e dell'interpretazione di un volume sismico 3D, esteso su un'area di circa 70 km^2, localizzato all'interno del bacino di avanfossa padano, nel settore delle "pieghe emiliane" (Fig. 1). Scopo della ricerca è la ricostruzione dell'evoluzione tettonico-sedimentaria di questa porzione di bacino, tra il Pliocene superiore e l'attuale, sulla base di analisi geomorfologiche e strutturali.

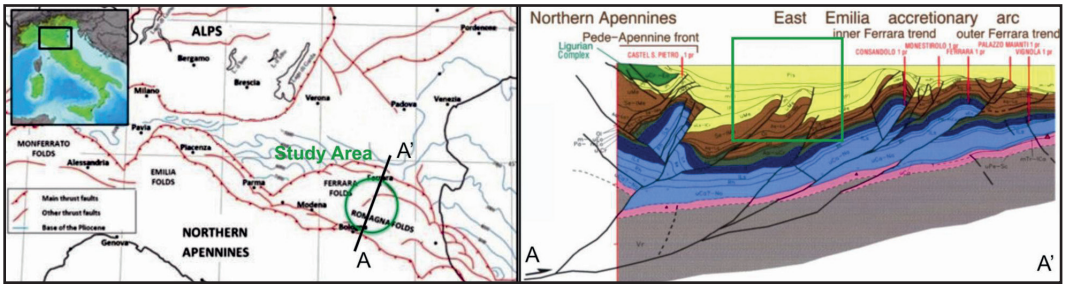

Fig. 1 – A sinistra: localizzazione dell'area di studio. A destra: sezione regionale attraversante l'area oggetto di studio evidenziata in verde (Fantoni e Franciosi 2009).

L'analisi sismico-geomorfologica si è concentrata nell'intervallo che va dal Pliocene sup. all'attuale. Si sono qui riconosciute 5 Unità Sismo-stratigrafiche, che corrispondono in prima approssimazione a sequenze deposizionali già definite a scala regionale (Ghielmi *et al.*, 2010). Le prime tre Unità sono deposte in un bacino profondo, la cui morfologia è condizionata dalla tettonica sin-sedimentaria, molto attiva nel Pliocene superiore-Pleistocene inferiore: la prima unità è sabbioso argillosa, la seconda prevalentemente argillosa, la terza prevalentemente sabbiosa. La quarta Unità è costituita dalla cosiddetta Progradazione Padana, cioè dai depositi di colmamento della pianura che segnano il passaggio dall'ambiente francamente marino a quello transizionale e successivamente continentale. La quinta Unità, infine, è costituita dalle alluvioni recenti.

Dal punto di vista strutturale, l'area di studio è caratterizzata dalla presenza di un thrust principale, con direzione WNW-ESE, al cui tetto si sviluppa un'anticlinale asimmetrica, che rappresenta anche la principale struttura morfologica, che influenza il bacino di sedimentazione. L'anticlinale risulta compresa tra una "sinclinale esterna" (a nord) e una "sinclinale interna" (a sud).

Per l'elaborazione, la visualizzazione e l'interpretazione dei dati sono stati utilizzati alcuni software dedicati (Petrel, Paleoscan), che hanno reso possibile la creazione di un modello

geologico 3D del sottosuolo. A partire da una prima fase di interpretazione manuale di alcuni marker particolarmente significativi, la procedura semi-automatica ha consentito l'estrazione di circa 300 orizzonti sismici (*horizon slices*). Gli orizzonti sismici sono stati in seguito convertiti in mappe/superfici tempi (tempi doppi di riflessione, TWT) sulle quali sono stati calcolati gli attributi sismici di ampiezza e continuità. Tra queste 300 superfici ne sono state selezionate circa 70, tutte riferibili alla successione Plio-Pleistocenica, oggetto di questo studio.

Le analisi geo-morfologiche e strutturali si sono infatti basate sul riconoscimento e l'interpretazione delle principali *features* geo-morfologiche e strutturali ben evidenziate dalle mappe di ampiezza e continuità per ciascun orizzonte sismico.

Metodologia. Lo studio è stato condotto utilizzando principalmente il rilievo sismico 3D acquisito e processato in eni nel 2011. Oltre ai convenzionali volumi sismici, *stack* e migrazione, sono stati generati quegli attributi sismici risultati più efficaci nell'analisi strutturale e stratigrafica della sequenza oggetto di studio.

L'interpretazione sismica dell'area è stata condotta per fasi successive. La prima fase, condotta con il software *Petrel,* è stata dedicata alla comprensione delle principali caratteristiche stratigrafico-strutturali dell'area di studio e per l'individuazione delle principali *features sismo-deposizionali* in essa presenti. L'utilizzo di tale software ha permesso inoltre di interpretare i principali orizzonti sismici, selezionati in base alle buone caratteristiche di continuità laterale, delle geometrie interne ed esterne e dei parametri sismici quali, in particolare, la continuità. Conoscenze stratigrafico-deposizionali derivanti dall'ampia documentazione disponibile hanno permesso la ricostruzione del *Framework* stratigrafico e strutturale del volume sismico.

La seconda fase, condotta con il software *Paleoscan*, ha permesso l'interpretazione semiautomatica del volume sismico e la costruzione del modello geologico del sottosuolo (Geomodel). Il modello ottenuto è stato successivamente ri-computato, dopo l'importazione degli orizzonti interpretati nella fase precedente, che fungono da *constraint* per i rapporti geometrici e stratigrafici. Il modello geologico finale, così ottenuto, comprende circa 300 orizzonti, per ciascuno dei quali il software ha automaticamente generato delle mappe di ampiezza e continuità.

La terza e ultima fase di interpretazione è consistita nella selezione manuale di circa 70 dei 300 orizzonti computati, sulla base della loro continuità laterale e del contenuto di informazioni sismico-geomorfologiche e strutturali. I 70 orizzonti interpretati sono stati trasformati in mappe-tempi, sulle quali sono stati calcolati gli attributi di continuità ed ampiezza (Fig. 2).

L'attributo di continuità è la misura della similitudine della forma d'onda, espressa in ampiezza e fase, tra una traccia sismica e quelle vicine. Porzioni di tracce simili produrranno alti valori di continuità (colore bianco in figura), viceversa, porzioni di tracce diverse saranno mappate con bassi valori di continuità (colore nero in figura). Quando le condizioni geologiche modificano lateralmente la risposta sismica nel sottosuolo, come ad esempio in presenza di faglie, di scarpate o di improvvise variazioni di facies, la continuità diminuisce bruscamente: la mappa di continuità tende quindi ad evidenziare strutture e forme. L'ampiezza delle riflessioni simiche, invece, esprime il contrasto di impedenza acustica tra litologie a contatto, mettendo quindi in evidenza sia le variazioni litologiche che la possibile presenza e tipologia di fluidi che riempiono le porosità delle rocce.

In base alla qualità delle mappe, alla presenza o meno di particolari *features* e alla loro posizione all'interno della successione studiata, sono state ri-selezionate una serie di *Horizon Slice* sulle quali è stata effettuata l'interpretazione di tipo sismico-geomorfologico. Inoltre, laddove presente il dato di pozzo e dove questo intercetta importanti *features* geomorfologiche, è stata effettuata la calibrazione litologica delle stesse, utilizzando principalmente il log di potenziale spontaneo (Sp). Questo log risponde in modo affidabile in contesti deposizionali di tipo clastico come l'avanfossa padana, evidenziando alternanze di sabbie e argille, caratterizzate rispettivamente da bassi e alti valori di potenziale spontaneo.

Il flusso di lavoro precedentemente descritto ha portato alla caratterizzazione sismico-geomorfologica e strutturale delle principali sequenze deposizionali all'interno dell'area di studio.

Risultati. Con lo sviluppo e l'acquisizione di rilievi sismici 3D, l'opportunità di estrarre immagini sismiche in mappa ha aperto il campo ad un nuovo tipo di approccio basato sull'interpretazione sismico-geomorfologica (Posamentier, 2000). Inoltre l'estrazione degli attributi sismici permette una migliore caratterizzazione degli elementi morfo-deposizionali presenti in diversi contesti geologici, quali ad esempio il bacino di avanfossa, oggetto di questo studio.

La successione plio-pleistocenica studiata è stata suddivisa in 5 Unità Sismo-stratigrafiche principali, che riflettono le principali fasi tettonico-deposizionali che hanno caratterizzato questa porzione del bacino di avanfossa padano. Esse vengono di seguito descritte, dal basso verso l'alto.

Unità Sismo-stratigrafica I (Pliocene sup. – Pleistocene inf. basale). È costituita da depositi torbiditici prevalentemente sabbiosi con alternanze di argille. Questa caratteristica le conferisce una facies sismica distinta da elevati contrasti di impedenza acustica e da riflettori continui lateralmente, anche se altamente deformati o localmente tagliati dal sovrascorrimento principale. In questa sequenza si evidenziano una serie di canali rettilinei, provenienti da NO, che vengono convogliati nel depocentro della sinclinale esterna e che risultano quindi fortemente influenzati dalla presenza dell'alto strutturale. Sono canali principalmente erosivi, privi di levee o depositi laterali e poco aggradanti. I canali risultano essere sincroni alla deformazione prodotta dal sovrascorrimento e la loro posizione migra nel tempo verso NE, in accordo con la migrazione della deformazione e quindi del depocentro del bacino.

L'ambiente deposizionale è riferibile ad un bacino confinato.

Unità Sismo-stratigrafica II (Pleistocene inferiore). Questa Unità (Fig. 2) è formata da argille di frangia di lobo torbiditico nelle zone di alto strutturale e da depositi torbiditici sabbiosi

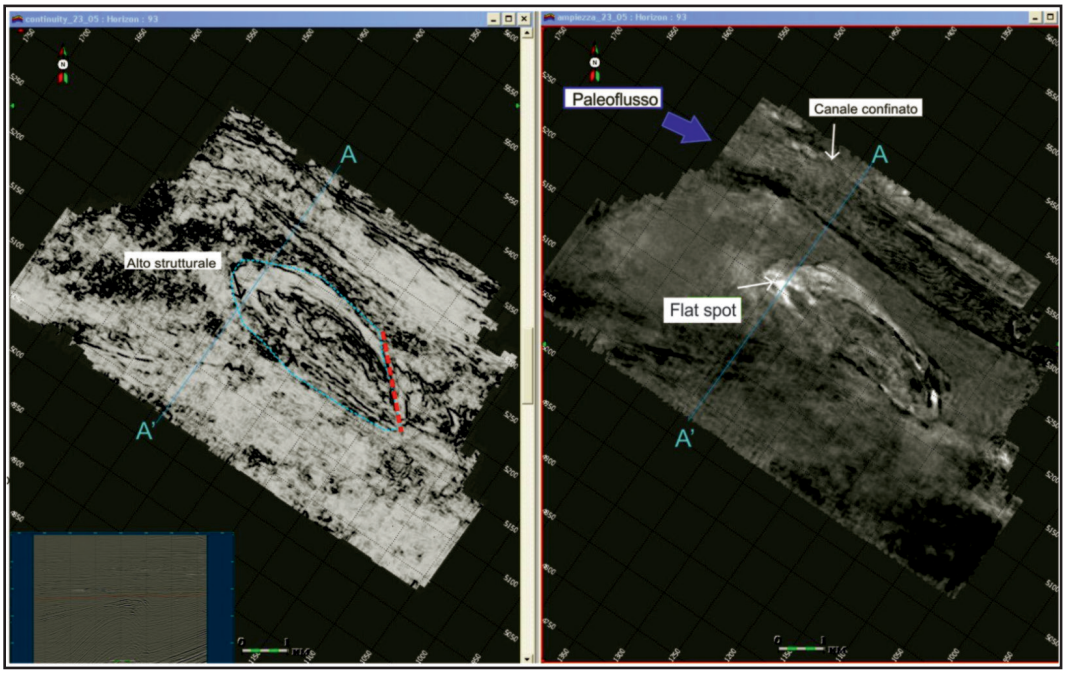

Fig. 2 – Mappa di continuità (a sinistra) e di ampiezza (a destra), relative ad un orizzonte delle argille Calabriane, estratta dall'Unità Sismo-stratigrafica II. Il massimo di ampiezza (Flat spot) alla terminazione settentrionale della piega è riferibile ad una interfaccia acqua-gas nel sottosuolo.

canalizzati all'interno delle sinclinali principali. La sequenza assume perciò una caratteristica facies sismica semitrasparente, interrotta lateralmente da evidenti corpi canalizzati, costituiti da sedimenti con elevati rinforzi di ampiezza. Questi corpi assumono geometrie rettilinee e si osservano principalmente all'interno della sinclinale esterna. Sono caratterizzati da paleoflussi provenienti da NO che deviano intorno all'anticlinale principale e che risultano quindi ancora fortemente influenzati da essa, anche se in questa fase si registra una stasi tettonica della struttura oggetto di studio.

Al termine di questa sequenza si registra un improvviso cambiamento delle condizioni morfo-climatiche, segnalato dalla formazione di un imponente canyon sottomarino (1500 m di larghezza), con un profilo tipicamente a V che erode circa 150 ms di sedimenti all'interno del bacino studiato. L'estensione regionale di questa struttura è stata dedotta da precedenti studi Eni, attraverso l'interpretazione regionale di linee sismiche 2D, dalle quali si evince che il canyon si estende dal bacino compreso tra le "pieghe romagnole" e "le pieghe ferraresi", passando nel depocentro della Sinclinale Esterna, fino alla paleo-linea di costa adriatica. Questa struttura sarebbe quindi associabile ad un forte abbassamento del profilo di equilibrio che, in questa fase di relativa stasi tettonica dell'anticlinale principale e data la sua estensione, potrebbe essere dovuto o a variazioni climatiche o a variazioni tettoniche a scala regionale. Le curve delle variazioni isotopiche dell'O^{18} indicano infatti che la parte sommitale del Calabriano è caratterizzata da forti variazioni nella segnatura isotopica, associabili a importanti variazioni climatiche che nella parte alta del Pleistocene inferiore segnano una progressiva fase di raffreddamento climatico con forti variazioni del livello eustatico.

L'ambiente deposizionale di questa sequenza è riferibile ad un bacino confinato.

Unità Sismo-stratigrafica III (Pleistocene inf. – Pleistocene medio basale). È costituita da depositi torbiditici di tipo I (Mutti, 1985), ricchi in sabbie. Alla base della sequenza si registra un netto cambiamento sia nella facies log che in quella sismica, che assume un aspetto omogeneo interrotto da riflettori tabulari con scarsa continuità laterale e elevati rinforzi di ampiezza, riferibili a depositi più argillosi. Alla base di questa sequenza si registra anche un cambiamento nella direzione dei paleoflussi, qui provenienti principalmente da ovest. Questi flussi torbiditici depositano parte del sedimento preso in carico in prossimità dell'alto strutturale formando degli *splay* frontali che, come evidenziato dai log di pozzo, mostrano una litologia prevalentemente sabbiosa. La loro posizione sembrerebbe indicare che l'anticlinale principale, seppur sepolta sotto la Sequenza II, produce ancora un controllo strutturale sulla sedimentazione del bacino studiato, forse anche a causa della compattazione differenziale dei sedimenti precedentemente deposti.

Verso l'alto questa sequenza registra un aumento nella sinuosità dei corpi canalizzati, che sono caratterizzati da una scarsa aggradazione in tutto l'intervallo. Questi corpi formano dei caratteristici depositi laterali di *overbank*, testimoniati nei log di pozzo da sequenze *fining-upward* dello spessore di circa 40 m. Questi lobi assumono una posizione leggermente più arretrata rispetto ai precedenti, ma sempre in corrispondenza dall'anticlinale principale.

Da questo momento in poi i successivi apporti, provenienti prevalentemente da ovest, non appaiono più influenzati dall'anticlinale sepolta. Nella parte centrale dell'Unità si osservano prima una serie di canali meandriformi sovrapposti ed interferenti, difficilmente risolvibili singolarmente, cui fanno seguito caratteristici sistemi di *channel-levee*.

Verso l'alto la Sequenza III registra un nuovo cambiamento nella direzione principale degli apporti, che tornano a provenire da NO. Questi sono caratterizzati da canali rettilinei di dimensioni intorno al chilometro e anch'essi poco aggradanti, forse sintomo di elevate velocità di sedimentazione e ingenti apporti di sedimenti.

La Sequenza III nel suo complesso, registra un sostanziale colmamento del bacino studiato e una stasi tettonica della struttura anticlinalica. I depositi sono formati da torbiditi di piana bacinale, in posizione ancora distale rispetto allo slope, alla base della sequenza. Verso l'alto, vengono ricoperti da torbiditi sempre più prossimali, che precedono la progradazione.

L'ambiente deposizionale è quindi riferibile ad un bacino non confinato, che viene progressivamente colmato.

Unità Sismo-stratigrafica IV (Pleistocene medio). È costituita dai sedimenti marini e di transizione della progradazione padana. Il prograding è caratterizzato da *foreset* molto inclinati, la cui presenza ostacola l'estrazione degli attributi sismici di continuità ed ampiezza. Ciononostante si possono osservare una serie di erosioni rettilinee o *chutes* (Farre *et al.*, 1985) in prossimità della zona di scarpata che danno origine verso il bacino a stretti canali sinuosi e a depositi conoidali di fondo scarpata.

Contrariamente a quanto avviene solitamente, la geometria dello *shelf break* risulta essere convessa verso il retro-paese: questo potrebbe essere spiegato in parte con la doppia direzione dei paleoflussi, provenienti da NO e da ovest ed in parte con un controllo strutturale all'interno del bacino, prodotto ancora dall'anticlinale sepolta, che per compattazione differenziale ai suoi fianchi, costituisce ancora un ostacolo nella migrazione della progradazione.

Unità Sismo-stratigrafica V (Pleistocene medio sommitale - attuale). È formata dai sedimenti di transizione e continentali delle alluvioni padane. I principali elementi deposizionali presenti in questa Unità sono dei piccoli canali sinuosi di pianura alluvionale. Sono difficilmente caratterizzabili, in quanto l'intervallo si trova nella parte più superficiale del volume dove la qualità del dato sismico si presenta decisamente scarsa.

La deposizione della successione sopradescritta è accompagnata dalla enucleazione e sviluppo di un complesso set di strutture tettoniche (Fig. 3), tutte associabili ad un campo di stress compressivo con una direzione di massimo raccorciamento SO-NE. Le strutture principali sono: il Sovrascorrimento Principale; un retro scorrimento (*backthrust*), sviluppato al tetto del sovrascorrimento principale; l'Anticlinale Principale e le due Sinclinali, Esterna ed Interna.

Al tetto del sovrascorrimento è presente anche un'importante faglia trastensiva destra con geometria anastomizzata, che accomoda parte del rigetto differenziale lungo il Sovrascorrimento Principale.

All'interno della Sinclinale Esterna sono presenti una serie di faglie sub-verticali a cinematica trascorrente e all'interno della Sinclinale Interna si osservano dei set di faglie dirette, localizzate sulle zone di chiusura periclinale dell'anticlinale principale.

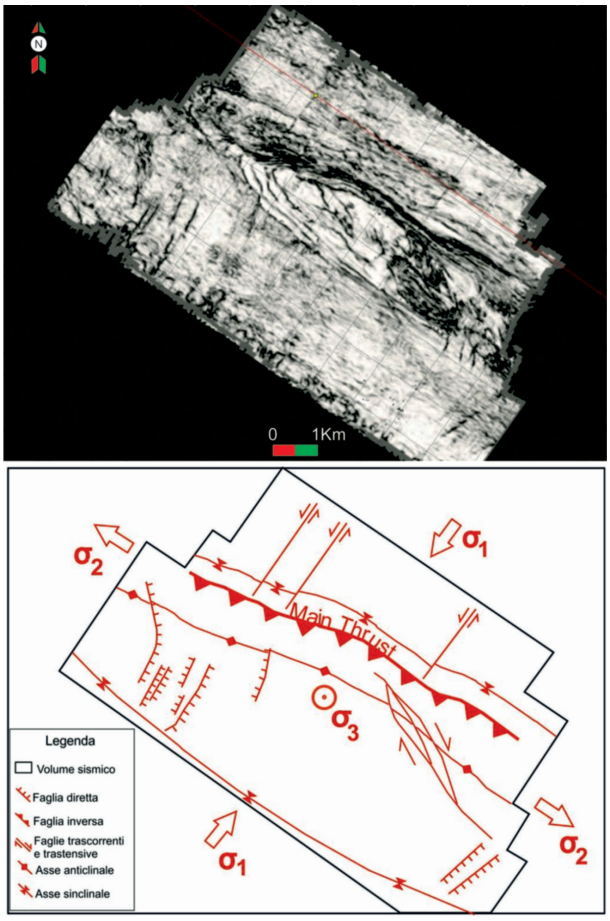

Fig. 3 – In alto: Mappa di continuità di un orizzonte sismico estratto nell'intervallo del Pleistocene inferiore. Il principale flusso canalizzato, quasi rettilineo, si localizza al letto del sovrascorrimento nordvergente, che delimita verso NE l'anticlinale principale. In basso: Associazioni strutturali che caratterizzano l'area di studio e i loro rapporti geometrici con il campo di stress compressivo.

Questa complessità strutturale si inserisce nel contesto regionale del settore esterno della Catena a Pieghe e Sovrascorrimenti dell'Appennino Settentrionale. Nello specifico ci troviamo nella zona in compressione tuttora attiva, sepolta al di sotto della Pianura Padana.

Le nostre osservazioni, confrontate con i risultati già pubblicati da altri Autori (p.es. Fantoni e Franciosi, 2009; Ghielmi *et al*., 2010), consentono di concludere che l'Unità Sismo-stratigrafica I risulta essere sin-tettonica e contemporanea alla principale fase deformativa compressiva che caratterizza l'area di studio e che genera il Sovrascorrimento Principale, attivo almeno fino alla base del Pleistocene. Si osserva anche che parte dell'Unità Sismo-stratigrafica II, anch'essa sin-tettonica, risulta fagliata da strutture tettoniche oblique, attive anche dopo la principale fase tettonica che genera il Sovrascorrimento Principale, che tuttavia non sembrano influenzare in modo significativo la sedimentazione all'interno del bacino studiato.

La deposizione delle successive Unità sismo-stratigrafiche studiate risulta influenzata passivamente dalle strutture tettoniche compressive precedentemente formate, almeno fino alla porzione centrale dell'Unità Sismo-stratigrafica III. Dal dato sismico si osserva come i riflettori risultino deformati e lateralmente piegati al di sopra dell'Anticlinale Principale.

La parte alta dell'Unità Sismsostratigrafica III e le successive Unità Sismo-stratigrafiche IV e V risultano essere post-tettoniche ed influenzate solo da compattazione differenziale dei sedimenti torbiditici ed infine alluvionali, che colmano e modellano la paleo-topografia del bacino studiato.

Considerazioni finali. Questo lavoro mostra le potenzialità dell'analisi sismica 3D nello studio dell'evoluzione tettonico-sedimentaria di un settore complesso del sottosuolo padano.

L'utilizzo di tecnologie innovative per l'interpretazione sismica (*Paleoscan e Petrel*) è risultato decisivo per l'efficacia dell'interpretazione stessa e per la gestione di un data-set sismico 3D.

Questo lavoro conferma come l'integrazione delle analisi sismico-geomorfologica e strutturale siano uno strumento sicuramente efficace, a volte indispensabile, per comprendere l'evoluzione dei processi e dei sistemi deposizionali all'interno di un bacino tettonicamente attivo.

Riconoscimenti. Le elaborazioni presentate in questo lavoro sono ricavate dalla Tesi di Laurea Magistrale (Corso in Geologia degli Idrocarburi, Università di Perugia) di Andrea Gennari prodotta durante lo Stage, svolto presso ENI Exploration and Production. Si ringraziano ENI E&P e Stogit S.p.A. per la possibilità di utilizzare e riprodurre i dati sismici.

Bibliografia

Davies R.J., Posamentier H.W., Wood L J., Cartwright J.A (2007). *Seismic Geomorphology: Applications to Hydrocarbon Exploration and Production*. Geological Society of London. Special publications, 277, 2007, pp. 1-14.

Fantoni R. & Franciosi R. (2009). *Mesozoic extension and Cenozoic compression in Po Plain and Adriatic foreland*. Rendiconti online Soc. Geol. It., Vol. … (2009)

Farre J.A. & William B. (1985). *3D View of Erosional Scars on U.S. Mid-Atlantic Continental Margin*. A.A.P.G. Bullettin. Volume 69.

Ghielmi M., Minervin M., Nini C., Rogledi S., Rossi M. (2010) – *Sedimentary and Tectonic evolution in the eastern Po Plain and northern Adriatic Sea area from Messinian to Middle Pleistocene (Italy).* In Sassi, F.P. (Ed.), *Nature and Geodynamics of the Litosphere in Northern Adriatic*. Rend. Fis. Acc. Lincei, 21, 2010 (Suppl. 1), pp.131-166.

Mutti E. (1985) - *Turbidite systems and their relations to depositional sequences*. In: Zuffa, G.G. (Ed.), *Provenance of arenites*. NATO-ASI Series, Reidel, Dordrecht, 65-93.

Posamentier (2000) - *H. W. Posamentier, Seismic stratigraphy into the next millennium; a focus on 3D seismic data*. American Association of Petroleum Geologists Annual Convention, New Orleans, Abstracts Volume vol. 9 (2000), p. A118.

CHARACTERIZATION OF THE SUBSOIL IN THE AREA OF THE FRIARS MINOR CONVENT OF ISPICA (SOUTH-EASTERN SICILY)

S. Grassi[1], S. Imposa[1], G. Coco[2], M. Corrao[2]

[1] Dip. di Scienze Biologiche, Geologiche e Ambientali, Sezione di Scienze della Terra, Università di Catania, Italy

[2] Geocheck s.r.l., Aci Sant'Antonio, Catania, Italy

Introduction. The main goal of this work has been the characterization of the subsoil beneath the convent of the Friars Minor of Ispica, a village located in south-eastern Sicily. This building, located on top of a calcarenitic cliff, shows evidence of failure and instability.

To achieve this target, we have estimated the Vs_{30} in three mechanical drillings using the down-hole technique (DHT) and carried out a seismic tomography survey. The present study complements previous geognostic and structural surveys published by Imposa *et al.* (2010).

Considerable advancement has had, recently, the analysis of refraction data for the characterization of rocky terrains in terms of seismic waves velocity and amplitude, for the identification of deep interfaces and the determination of the degree of fracturing. The degree of fracturing in a medium affects the propagation of seismic waves: fractured volumes of rocks show lower P and S waves velocity, dispersion and attenuation, anisotropy of velocity (e.g., Abu-Zeid and Vuillermin, 1996); mapping Vs variations allows to infer variations of mechanical properties throughout the medium.

Above the calcareous cliff where the Franciscan convent stands, the morphology is rather flat and of karstic type, interrupted by long and deep stream incisions locally called caves ("cave"). Ispica is in fact located at the farest end of a ~ 12-km long, ~ 100 m deep, stream incision called Cava d'Ispica (Ispica Cave), a renowned archaeological site with caves inhabited some 2,000 years BC and hundreds of graves of Christian age (IV–V century). The study area is characterized by outcrops of alternating calcarenites and marls of the Ragusa Formation, with levels of calcarenites belonging to the Irminio Member (Carbone *et al.*, 1982; Grasso *et al.*, 2000). It is located within the Hyblaean calcareous highland that is part of the foreland domain outcropping in southeastern Sicily (Fig. 1). The foreland units deepen northward beneath the Gela nappe that represents the most external front of the chain.

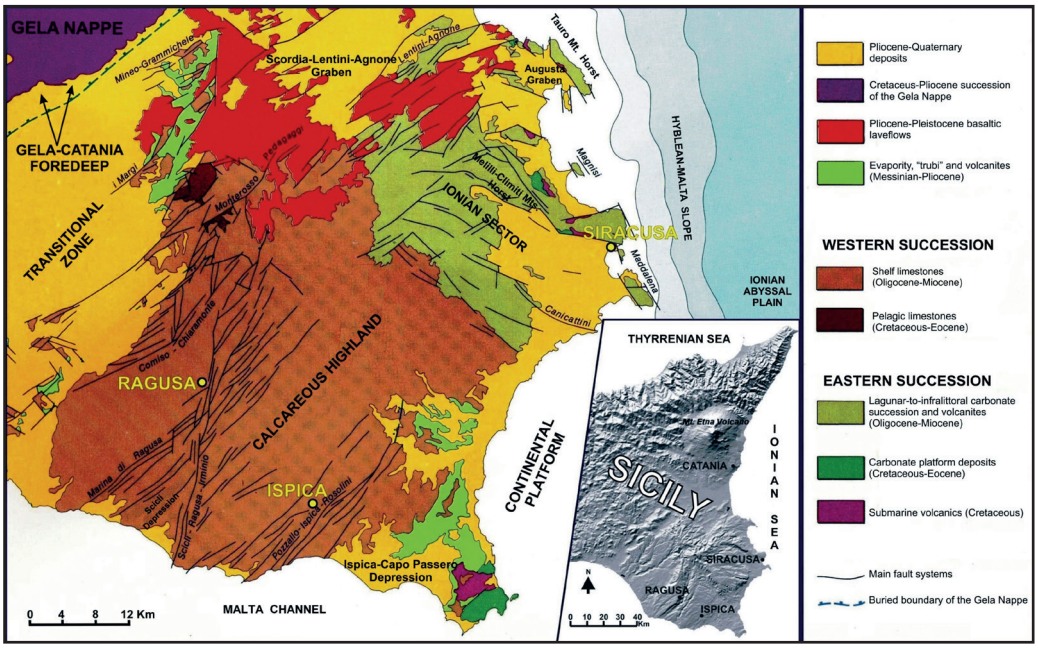

Fig. 1 – Geological map of south-eastern Sicily (Lentini *et al.*, 1987).

The dominant structure in the study area is the Ispica (known also as Pozzallo-Ispica-Rosolini) fault zone that extends NE-SW for about 20 km adjoining the marls and calcarenites of the Ragusa Formation (lower Miocene) to the west with the blue clays of the Tellaro Formation (middle Miocene) to the east (Ghisetti and Vezzani, 1980; Carbone *et al.*, 1982; Grasso *et al.*, 2000) (Fig. 1). Fault planes dip on average ~80° toward the SW with a maximum vertical offset of 100 m, forming the Ispica-Capo Passero depression to the west. The NE-SW slope above which stands the convent corresponds to the Ispica fault plane (Fig. 1).

Methodologies. In the last twenty years, down-hole seismic surveys has proven to be a valuable tool for the physical and dynamic characterization of soils. The down-hole technique allows to determine the average and interval seismic velocity of compressional (P) and shear (S) waves. In a down-hole seismic survey, a seismic source is placed on the surface near a borehole, and two tri-axial geophones are placed at selected depths in the borehole, to measure seismic velocity at fixed space intervals (Sambuelli *et al.*, 2004). The raw data obtained from a downhole survey are the travel times for compressional and shear waves from the source to the geophones and the distance between the source and geophones.

The down-hole techniques do not require that seismic velocity increases with depth, because the arrival times are estimated as far as waves penetrate into the medium. Therefore, these methods are suitable to detect velocity inversions along the hole, as well as fractured volumes of rocks (Cosma *et al.*, 2001).

We have carried out a down-hole survey in the 30m deep mechanical drillings S1-S3 (Fig. 2). Two 3-D geophones with natural frequency of 4.5 Hz are fastened to the walls of the hole through a pneumatic system. To measure shear waves velocity, the soil is energized by a hammer that hits transversely an iron plate placed at 2 meters of distance from the hole axis. Seismic signals are recorded in digital format and analyzed in the time domain with a dedicated software for P and S waves picking (CWP/SU). The arrival time of the S wave train is identified using the procedure of Boathwright (1987) that consists in rotating the two horizontal components of the ground motion until the maximum amplitude of the waves is reached, i.e. the source and the receiver are aligned. This point coincides with the arrival of the S waves recorded on the two horizontal components that will have opposite peaks at the same time.

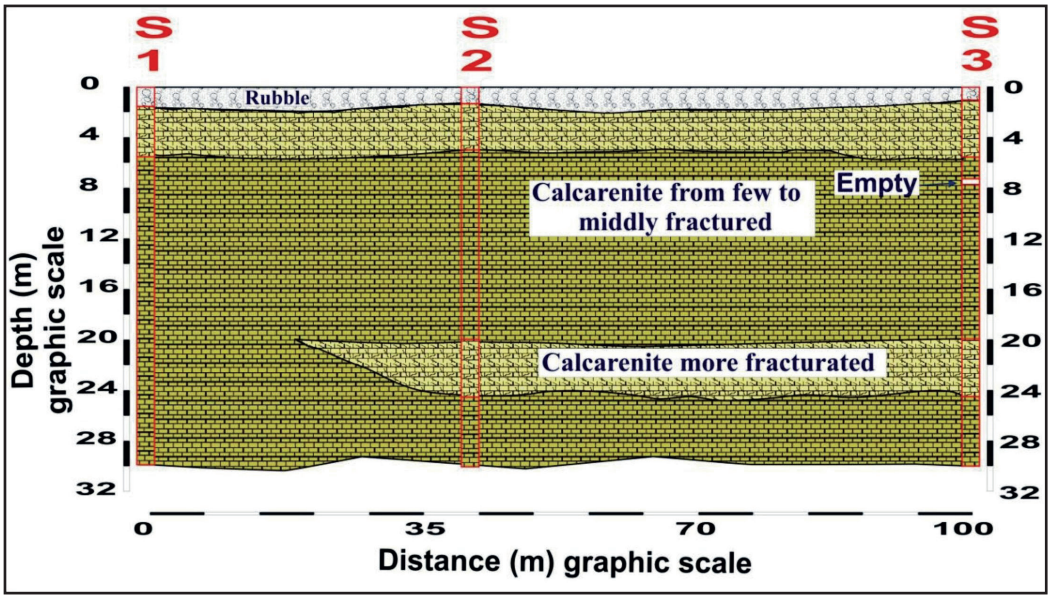

Fig. 2 – Lithostratigraphic profile reconstructed along the mechanical drillings S1-S3 (Imposa *et al.*, 2010).

To evaluate the heterogeneity of the seismic layers, we determined the true interval velocity V_i, i.e. the velocity the wave would propagate vertically between two adjacent positions *Zn* and *Z(n-1)* of the geophone:

$$V_i = S_z/t_v \quad (1)$$

where S_z is the partial distance equal to *Zn - Z(n-1)*.

A seismic transient correspond to an impulsive stress of low energy; therefore, soils and rocks traversed by seismic waves undergo elastic-type deformation; P and S waves velocity are related to the elastic and mechanical properties of the geologic medium through which they propagate. From the estimated seismic velocities *Vp* and *Vs*, we have computed the following elastic and seismic parameters: γ_{din}, geophysical density, indicating the status of aggregation of soils; *G*, rigidity modulus; K, compressibility modulus; *E*, Young or elasticity modulus; *M*, contrast modulus; σ, Poisson ratio. The seismic parameters describe the dynamic behavior of a litho-stratigraphic unit in terms of transmission of seismic energy from a formation to another. I.S., seismic impedance, defined as the shear wave velocity for the density of the medium, related to the local amplification of ground motion; refraction (t) and reflection (ξ) coefficients, related to the rigidity of the ground, representing the ratio between the amplitude of the reflected and refracted wave with respect to the incident wave. They are related to the amount of the energy transmitted from one lithotype to the other.

To classify the soils according to the current regulation O.P.C.M. 3274/2003 ("First elements on general criteria for the seismic classification of the national territory and technical regulations for construction in seismic areas") we have identified 4 seismic zones characterized by different values of horizontal acceleration (α_g/g) of the response spectrum as follows: seismic zone 1, with acceleration 0.35 g; seismic zone 2, with acceleration 0.25 g; seismic zone 3, with acceleration 0.15 g; seismic zone 4, with acceleration 0.05 g.

The down-hole technique is the most reliable because it allows to get evaluations of the seismic amplifications using as datum of base the profile of the Vs with the depth. In absence of a specific study of the site, the parameter *Vs30*, introduced from the „D.M. 14/01/2008", is used for defining the interaction between the structure and the studied area, it represents the average shear wave velocity in the first 30 meters of depth.

In the mechanical drillings S1-S3 we have computed the weighted average shear wave velocity Vs_{30} in the first 30 m of depth, defined as:

$$V_{S30} = \frac{30}{\sum_{i=1,N} \frac{h}{V_i}} \quad (2)$$

where h and V indicate thickness (in meters) and shear wave velocity in the *i*-th of the *N* layers that have been drilled in the first 30 meters. The Vs_{30} is used to classify the rigidity of a soil, since shear wave velocity is directly related to the rigidity modulus μ as:

$$\mu = \rho * V_s^2 \quad (3)$$

where ρ is the density.

In addition, we used the seismic tomography method to distinguish highly fractured volumes of rocks from intact or little fractured rocks. We used a cross-up hole configuration of multishots type, with 21 vertical geophones, located along the calcarenitic cliff, with natural frequency of 14 Hz and interspacing of 5 meters; was covered a total distance of 105 meters. A seismic gun has been used as seismic source. Have been carried out seven shots, inside the mechanical drilling S2, with interspacing of 4 meters, up to a depth of 28 meters (Fig. 3). Data were analyzed using the G.S.A.O. (Generalized Simulated Annealing-Optimization) method (Pullammanappallil and Louie, 1994). The G.S.A.O. allows a nonlinear optimization of the inversion of the arrival times of the direct and refracted seismic waves. The advantage of this

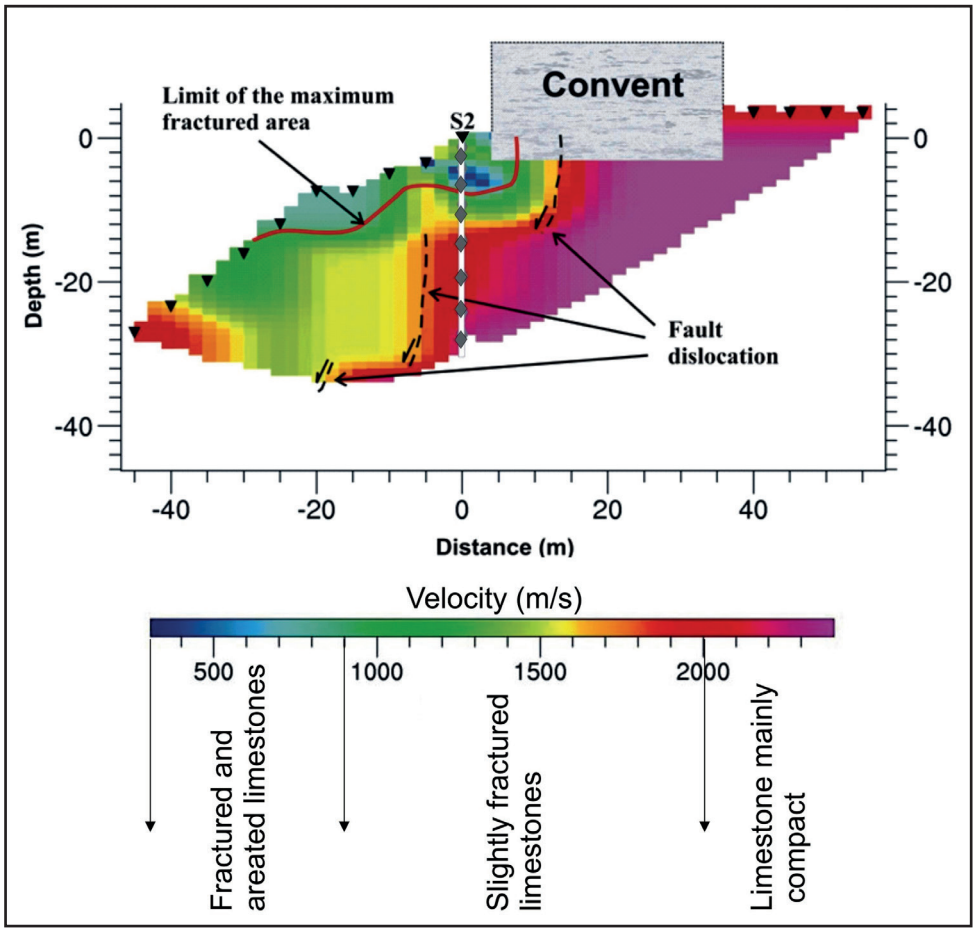

Fig. 3 – Sismo-stratigraphic section. The black triangles show the distribution of the geophones; gray diamonds represent the shot points.

technique is the independence from the initial velocity model. The data processing can be summarized in the following steps: i) travel times are computed from a given initial velocity model, and the least-square error E_i between computed and observed traveltimes is determined for each iteration i as follows:

$$E_i = \frac{1}{N}\left[\sum_{j=1}^{N}(t_j^{obs} - t_j^{cal})^2\right] \qquad (4)$$

where N is the number of observations, j indicates each observation, t^{obs} and t^{cal} are observed and calculated traveltime, respectively; ii) the velocity model is perturbed by including a random velocity constant and calculating the new least-square error E_1; iii) the probability P that the new model is acceptable is determined:

$$\mathrm{P} = 1; \quad E_1 \le E_0 \qquad (5)$$

$$P = P_c = \exp\left[\frac{(E_{\min} - E_1)^q \, \Delta E}{T}\right]; \quad E_1 > E_0 \qquad (6)$$

where *Pc* is the probability to accept the condition $\Delta E = E_0 - E_1$, *q* is an integration constant determined empirically, E_{min} is the objective value of the function of the total minima. In theory $E_{min} = 0$.

Results. From the seismic velocities Vp and Vs estimated at 1 m intervals along the three mechanical drillings we have computed elastic and seismic parameters. The stratigraphy of the study area is characterized by more or less fractured calcareous lithotypes (Fig. 2). Seismic velocity is irregular with depth (Fig. 3). We have identified 4 seismic layers referred to different lithotypes, characterized by the physical parameters listed in Tab. 1.

Tab. 1 – Characteristics of the lithotypes.

Seismic layer	Lithology	Vp (m/s)	Vs (m/s)	γ^{din} (gr/cm^3)	Coeff. τ	Coeff. ξ
hFr_C	Highly Fractured Calcarenite	1279.49	477.50	1.98	1.20	-0.20
mFr_C	Moderately Fractured Calcarenite	1758.18	757.12	2.11	0.83	0.17
lFr_C	Little Fractured Calcarenite	2308.98	1092.73	2.22	0.92	0.08
wPr_C	Well preserved Calcarenite	3202.42	1572.29	2.36	0.96	0.04

Seismic layer	μ (kg/cm^2)	K (kg/cm^2)	E (kg/cm^2)	M (kg/cm^2)	S.I. (t*m^{-*}s^{-1})	σ
hFr_C	4771.49	27578.86	13383.85	33940.84	949.62	0.41
mFr_C	12558.74	49709.38	34603.28	66454.37	1599.29	0.39
lFr_C	27345.35	85291.60	73909.50	121752.06	2430.40	0.35
wPr_C	59897.23	167823.70	160397.04	247686.68	3720.13	0.34

The velocity image of the substrate resulting from the tomography survey is characterized by several seismic layers with irregular geometry (Fig. 3). Lateral and vertical velocity changes define three seismic layers. The shallower layer extends from 0 to 2 m from the ground surface with seismic velocities of 500-900 m/s; it corresponds to the altered portion of the substrate; the second layer is characterized by an average P-wave velocity of 1000-2000 m/s and extends from 5.5 m west of S2 to the end of the tomography array; the third layer shows seismic velocity of 2000-3000 m/s. The imaged velocity shows a step-like pattern that can be ascribed to the dislocation along the Ispica fault plane.

Conclusion. The study area lies on a calcareous rocky terrain composed of banks of limestones with white-grayish and white-yellowish colors intercalated with soft marly layers. This unit represents the lower portion of the Irminio Member of the Ragusa Formation, of Aquitanian-Burdigalian age.

In three mechanical drillings, 30 m deep and aligned along the edge of the cliff, we have carried out down-hole measurements of seismic velocity (*Vs30*); we have also collected cross-up hole seismic tomography profiles. From the results of these surveys we identified four seismic layers characterized by a different degree of fracturing laterally varying in the NW-SE direction. The fractured portion, that correspond to the fault zone determining the offset of the rocky terrain object of this study, extends in part beneath the Minor Friars Convent.

The down-hole measurements and the V_{S30} allows us to define the study area, in accordance with the OPCM 3274/2003, D.M. 14/01/2008 "Categories of ground" and with the elasto-dynamical parameters, as a B-type soil.

Acknowledgement. This work was funded by a financial support of the Catania University (PRA n. 20104001082, Scientific Responsible: Imposa S.).

References

Abu-Zeid N., Vuillermin F. 1996. Analiysis of possible relationships between seismic properties and some of Rock mass geomechanic properties of the outcropping carbonate rock masses in Wadi El-kaffrien dam site (Jordan). Proceedings of the Application of Geophysics to Engineering and Enviromental Problems, pp. 605-616.

Boatwright J., Porcella R., Fumal T., Liu Hsi-Ping 1987, Direct estimates of shear wave amplification from a borehole near Coalinga, California, Earthquake Notes, v. 57, 8 p.

Carbone S., Di Geronimo I., Grasso M., Iozzia S., Lentini F. 1982. I terrazzi marini quaternari dell'area iblea. Contr. alla realizzazione della Carta Neotettonica d'Italia C.N.R., P.F. Geodinamica, N° 506, (Giannini Ed.) Napoli.

Cosma C., Heikkinen P., Keskinen J., Enescu N. 2001. VSP in crystalline rocks from down-hole velocity pro.ling to 3D fracture mapping. International Journal of Rock Mechanics & Mining Sciences, 38, 843-850.

Ghisetti F., Vezzani L. 1980. The structural features of the Hyblean Plateau and of the Mount Judica area (South-Eastern Sicily): a microtectonic contribution to the deformation history of the Calabrian Arc. Bull. Soc. Geol. It., 99, 57-102.

Grasso M., Pedley H.M., Maniscalco R., Ruggieri R. 2000. Geological context and explanatory notes of the "Geological Map of central-southern sector of the Hyblean Plateau." Mem. Soc. Geol. It., 55, 45-52.

Imposa S., Corrao M., Barone F., Coco G., Occhipinti R., Mozzicato P. 2010. Geostructural and geognostic survey for a stability analysis of the calcareous cliff of Ispica (Hyblean plateau, southeastern Sicily). Bulletin of Engineering Geology and the Environment, 69, 2, 247-256, ISSN: 1435-9529, doi: 10.1007/s10064-009-0257-3.

Sambuelli L., Godio A., Socco L.V., Dall'Ara A., Vaira G., Deidda G. 2004. Metodi geofisici per la caratterizzazione degli ammassi rocciosi, In: La caratterizzazione degli ammassi rocciosi nella progettazione geotecnica, PATRON (ITA), MIR 2004, Torino 24-25 novembre 2004, pp. 47-90, Vol. 1, ISBN: 88-555-2782-7.

Pullammanappallil S. K., Louie J. N. 1994. "A Generalized Simulated- Annealing Optimization for Inversion of First-Arrival Times". Bulletin of the Seismological Society of America, Vol. 84, No. 5, pp. 1397-1409.

O.P.C.M. 3274/2003. Ordinanza del Consiglio dei Ministri 3274 del 20/3/2003,"Primi elementi in materia di criteri generali per la classificazione sismica del territorio nazionale e normative tecniche per la costruzione in zona sismica", pubblicata nel Supplemento n. 72 alla Gazzetta Ufficiale n. 105 del 08/05/2003.

HIGH RESOLUTION SEISMIC REFLECTION/REFRACTION PROFILING ACROSS A LARGE DEBRIS FLOW FAN (VINSCHGAU/VENOSTA VALLEY, ITALIAN ALPS)

S. Maraio[1], P.P.G. Bruno[2], V. Picotti[1]

[1] Dipartimento di Scienze della Terra e Geologico-Ambientali, Università di Bologna, Italy

[2] INGV, Istituto Nazionale di Geofisica e Vulcanologia, Napoli, Italy

Introduction and approach. Fan-shaped deposits are common in formerly glaciated mountains, especially where steep tributary valleys join broad troughs; this being a classic locus where high volumes of mobilized sediment suffer a sudden loss of transport power. The term 'alluvial fan' generally includes both fluvial and debris-flow-dominated deposits. A group of exceptionally large alluvial fans occurs in Val Venosta, a major glacial trough in the east-central Alps, Italy. The Val Venosta group is the largest group in the Alps; concentrated glacial erosion in conducive geology among the probable cause explaining anomalous fans number and size. In this work, our attention is focused on the "Allitz/Laas" fan; it is one of the largest symmetrical fans in the Alps: it deflects the Adige River to the opposite slope foot and dominates Val Venosta as an extraordinary half-barrier. We have acquired and processed an ~4 km long high-resolution seismic reflection profile across the Allitz/Laas fan, crossing the residential area of the village of Laas. The target of this work is the study of the shallow portion (about 500 m deep) of this alluvial fan. We had two principal investigation aims. First aim is the imaging of the bedrock, in order to define its depth and consequently to estimate the thickness of sediment accumulation, as well as to analyze the morphology of the bedrock and the valley engraving. Second investigation aim is the analysis of the sediment's stratigraphy, in order to retrace the formation history of the alluvial fan. This information will provide us with important knowledge about the debated genesis of Adige Valley. Seismic stratigraphic

analysis on seismic sections will also provide information about the interaction between the sedimentation rate and the glacier evolution.

Alluvial fan environments, often present significant challenges for high-resolution seismic exploration. The main factors hindering seismic imaging are: 1) strong lateral velocity contrasts in heterogeneous sediments of the shallow portion of subsurface; 2) unfavorable topographic conditions along the profile and 3) presence of dipping reflectors representing the bedrock. A dense wide-aperture acquisition geometry, allowing nonstandard processing and a meaningful interaction and comparison between refraction and reflection data has been proven capable of overcome most of the above-mentioned limiting factors (Improta and Bruno, 2007; Bruno *et al*., 2010, 2011, 2012). A dense wide-aperture acquisition geometry differs from typical common-midpoint small aperture reflection because it allows recording both multi-fold reflection data spanning a large range of offsets (from small-offset near-vertical reflections to large-offset large amplitude post-critical reflections) and deep penetrating refracted waves, which are suitable for first-arrival travel-time tomography. Tomography not only contributes information about the subsurface structure but also provides a good control on the near-surface velocity structure that is crucial for improving the quality of static corrections and, ultimately, the stacking of shallow reflections.

Local setting. Val Venosta is a major glacial trough of the east-central Italian Alps. Its lower part trends west-east for 42 km, decreasing its main altitude from 900 to 500 m above sea level moving toward East end above Meran and it is obstructed by a large fan complex into the Adige gorge. At its West end, the Upper Val Venosta ascends north into the lowest gap in the main Alpine divide west of Brenner, the Reschen Pass (1500 m). The terrain character falls into three elevation ranges, reflecting Quaternary glacial impact over an orogenic landscape that had become generally 'mature' and well adjusted to late Tertiary base levels. Below 2400 m altitude, steep slopes fall to the Venosta glacial trough, without high rock-walls; tributary valleys are more V-shaped than U-shaped because of gravitational and fluvial overprinting. The geology is predominantly represented by Austro-Alpine metamorphic units (Agliardi *et al*., 2009b), comprising metapelites and metapsammites, with subordinate orthogneiss, metabasites and calcschists. slices of sedimentary Upper Palaeozoic-Mesozoic cover occur around the Upper Val Venosta. The entire stack is cut by north, east-, NE-and SW-trending fractures, strongly constraining the drainage pattern and the strength of rock masses. (Jarman *et al*., 2011) The valley bottom hosts the biggest group of anomalously large fans within the European Alps, the origin of which is still matter of debate. If on one hand Jarman *et al*. (2011) hypothesize a catastrophic formation of the fans modulated by large, rapid slope failures, on the other hand, a mechanism of paraglacial progradation, mainly mediated by debris flows, represents the alternate theory. The latter interpretation would be sustained by the high contemporary rates of debris-flow transport recorded in basins covered by glacial and glacio-fluvial deposits across the entire AltoAdige/Sudtirol region (Brardinoni *et al*., 2012).

Data acquisition and processing. We acquired four seismic profiles, with a total profile length of ~4 km. Three profiles (Lasa_1, Lasa_2, Lasa_3) are longitudinal to the valley, and one profile (Lasa_4) cuts the alluvial fan as a transverse section, crossing profile Lasa_1 (Fig. 1). The logistic of line acquisition was very hard on profiles Lasa_2 and Lasa_3, because these profiles come across the residential area of the village of Laas. P-wave seismic reflection data were collected using a single 6382-kg IVI-Minivib® truck. At each vibration point we stacked 2, 15 s long, 10–200 Hz sweeps generating a 1s correlated record with 1ms sample interval. Source move-up was 5 m. Single 10-Hz vertical geophones were also placed at 5 m intervals. Tight spacing of both geophone and vibration points ensured a very regular and dense subsurface coverage, with common midpoints spaced of only 2.5 m. The acquisition parameters were expressly designed to keep maximum data redundancy.

The identification of the optimal processing sequence depends on the quality and characteristics of the data recorded. The reflection processing was performed through Landmark

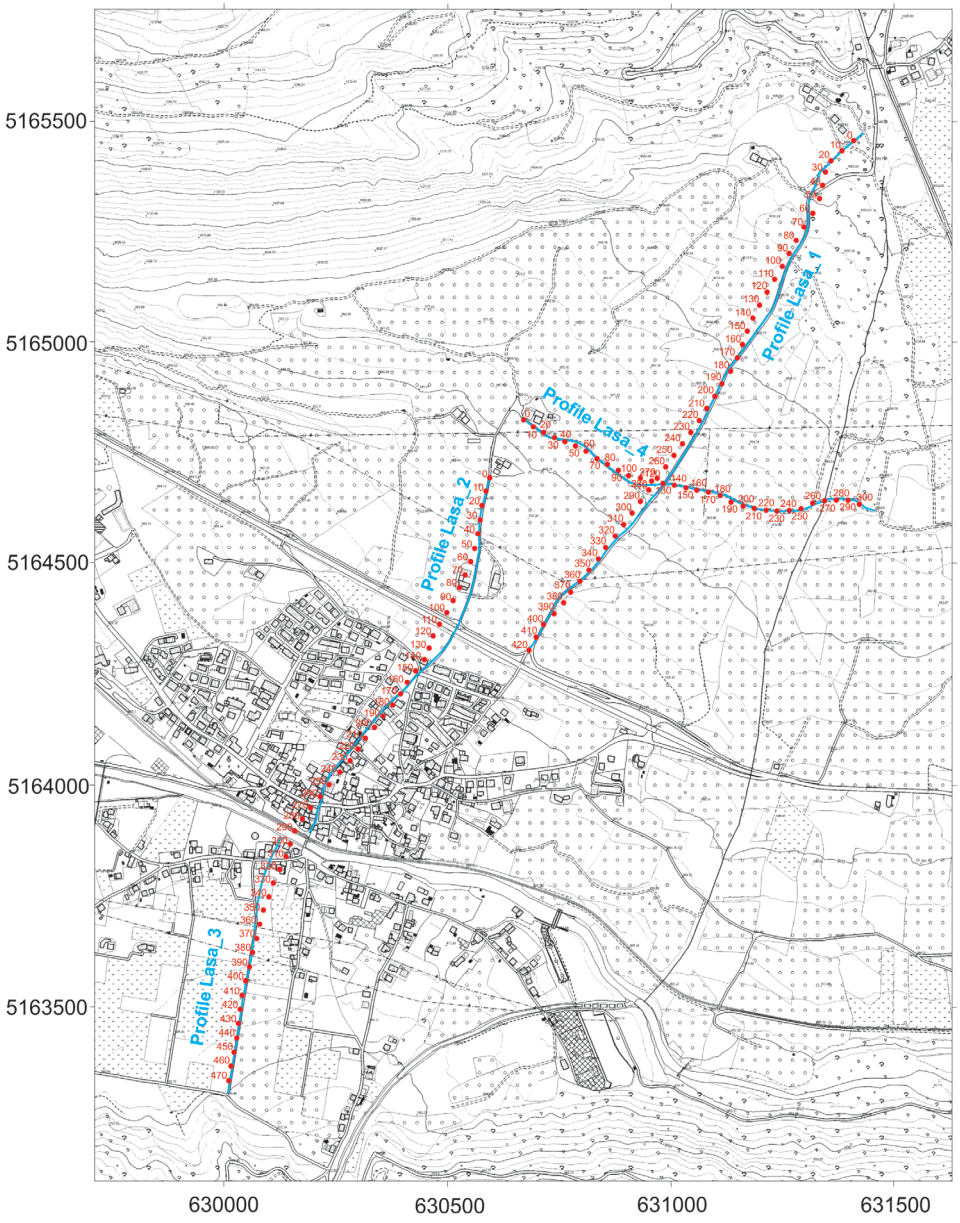

Fig. 1 – Profile location on topographic map 1:5000, Acquired profile in blue and elaboration profile (CDP) in red. Topographic map by Autonomous Province of Bolzano - Alto Adige - Informatic geographical and statistical office.

commercial software ProMAX. The data processing consisted of three main phases: 1) pre-processing, 2) velocity analysis and stacking; 3) post-stack migration. First operation was the cross-correlation between the wave function generated by the source (sweep) with the seismic array seismograms. Subsequently, we assigned to all traces a geometry in UTM WGS84 coordinates. The profiles were acquired and therefore processed with a crooked line geometry. A minimum phase filter was estimated by the source sweeps. The main and longer part of refraction processing was the picking of the first arrivals. The reading of the first arrival phases was performed on the entire dataset, consisting of about 110,500 traces. The first arrivals were

checked for consistency using the reciprocity rules of Ackermann *et al.* (1986) and then inverted using a commercial software, that is part of the SeisImager ®package, distributed by Oyo Corporation Ltd. and based on the work of Hayashi and Takahashi (2001). The tomographic models, not only provide important information for interpretation of the seismic profiles, but are also used in the reflection processing sequence, integrating the semblance-based velocity models used for the normal moveout correction. First break picks were also used to apply refraction static corrections (Taner *et al.*, 1998). The preliminary velocity models were obtained by picking the maximum of semblance (Neidell and Taner, 1971). The preliminary velocity models and the resulting stacks were refined by two cycles of residual static corrections and velocity analysis (Clerabout and Ronen, 1985). The final stack sections were processed with a spatial filtering algorithm, and depth migrated using a Kirchhoff post-stack depth migration.

Discussion and conclusions. The data acquired in Laas (BZ) are characterized by good signal-to-noise ratio. The use of a "dense wide aperture" geometry, allowed us to sample reflected and refracted phases in a wide offset range, therefore reaching a comparable depth penetration for both reflected and refracted phases. Combination of seismic reflection and first-arrival tomography provided overlapping and matching information in terms of reflectivity models and P-wave tomographic velocity models along our profiles, and allowing us to imaging from the topographic surface down to the top of the basement. All tomographic models show heterogeneous P wave velocities and strong gradients: P-wave velocities vary from a minimum of about 0.5 km/s at the surface and increase up to over 4.5 km/s at top of the metamorphic bedrock. The comparison between tomographic models and depth migrated sections, emphasize a perfect agreement between the trend and the geometry of seismic-stratigraphic units on the migrated sections with the P-wave velocity models from the first-arrival tomography.

The migrated profile "Lasa_1" shows a very shallow reflector with high amplitude at an average depth of 150-200 m (Fig. 2). Its amplitude characteristics and the high stacking velocity associated with this reflector (V_{RMS}> 3500 m/s), suggest that this event is generated by the reflection from the top of metamorphic bedrock. This interpretation is supported by the agreement between the reflection event and the high velocity (Vp > 4 km/s) of seismic tomography.

The migrated profiles of Lasa2_3 (Fig. 2) clearly image the structure of the valley and the trend of the top of the metamorphic bedrock below. The profiles also show an a sub-horizontal

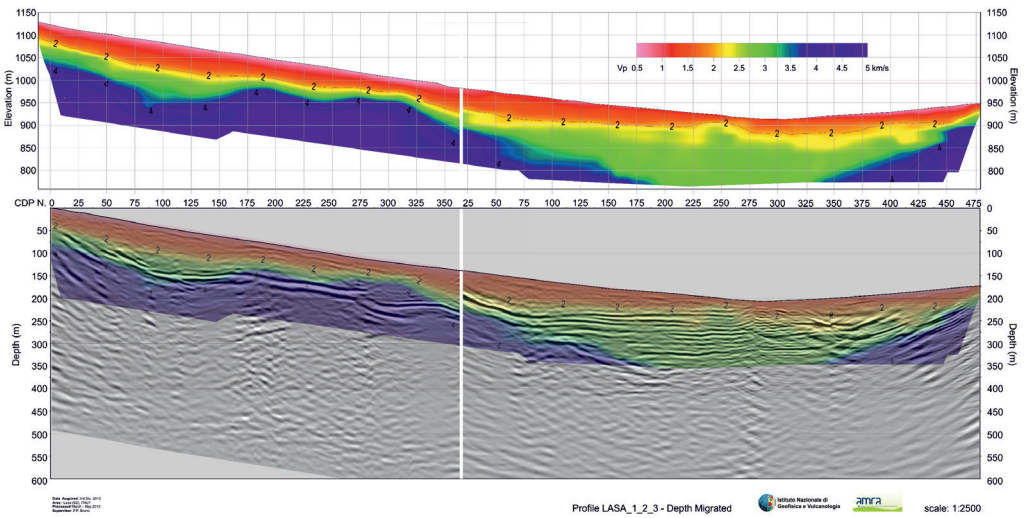

Fig. 2 – Depth migrated sections of profiles Lasa_1 and Lasa_2_3 with respective tomographic models.

reflective series, probably related to the Adige River fluvial deposits which fill the more depressed portion of the valley, where at present there is the Adige River bed. The thickness of this sub-horizontal reflective series is about 100 m. Below CDP 25 the bedrock undergoes a sudden increase in dip towards the south and its apparent depth becomes ~200 m below CDP 150. From this point forward, the bedrock top is no longer visible on the seismic section, and reappears below CDP 350 at about the same depth of (i.e. ~150 m from surface) with an opposite dip, therefore decreasing its depth (~40-50 m) towards the end of the profile. Seismic tomography velocity information is perfect agreement with seismic reflection data. The contour line 4 km/s (interpreted as indicative of the bedrock top) shows indeed a clear and distinct trend to deepen rapidly towards the central part of the profile, with a maximum depth of more than 200m, between metric progressives 600-1150 m, below the surface location of Adige River (Fig.2). Between CDPs 0-250 and CDPs 325-479, the fluvial deposits, are covered by an area of poor reflectivity, similar to those present in the upper part of profiles "Lasa_1" and "Lasa_4". Based also on the P-wave velocity form tomographic models these seismic facies can probably be associated with dry, nonreflective alluvial fan deposits (Fig. 2).

Along tomographic profile "Lasa_4", ray penetration is lower (on average between 50 and 100 m) because the basement is shallower than on the other profiles. Lasa_4 profile also shows the maximum vertical gradients of velocity, certainly caused by a shallow bedrock (with the top at about 50 m from surface) that tends to deepen toward the east. These features are in agreement with the reflection image, which confirms both the depth of the bedrock top, and its clear dip towards the east. This dip of the top of the basement explains a step of ~35 m in Fig 2 affecting the top of bedrock between the adjacent parts of profiles "Lasa_1" and "Lasa_2_3". In fact, by analyzing the depth migrated and tomography profiles of "Lasa_2_3" and comparing them with those of "Lasa_1" it is evident a 35 m vertical offset of the top of the bedrock. This vertical offset is well justified by the lateral offset (about 300 m) between the two profiles (see Fig. 1), and by the slope towards the east of the bedrock top on "Lasa_4" migrated profile.

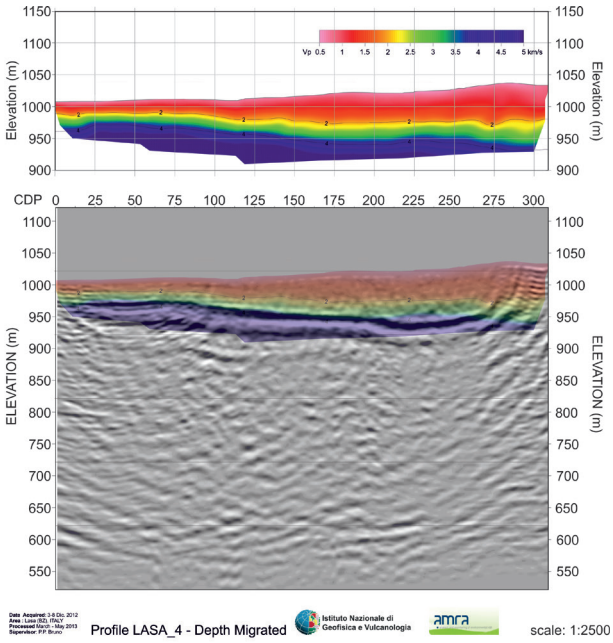

Fig. 3 – Depth migrated section of profile Lasa_4 with respective tomographic model.

References

Ackermann H. D., Pankratz L. W. and Dansereau D. (1986). *Resolution of ambiguities of seismic refraction traveltime curves*. Geophysics, Vol. 51, N. 2; P. 223-235.

Agliardi, F., Zanchi, A. & Crosta, G. B. 2009b. *Tectonic vs. gravitational morphostructures in the central Eastern Alps (Italy): constraints on the recent evolution of the mountain range.* Tectonophysics, 474, 250 – 270.

Brardinoni F., Church M., Simoni A., and Macconi P. 2012. *Lithologic and glacially conditioned controls on regional debris-flow sediment dynamics*. Geology, 40, 455-458.

Bruno P.P., A. Castiello, F. Villani & L. Improta, 2013, *High-resolution densely spaced wide-aperture seismic profiling as a tool to aid seismic hazards assessments of fault-bounded intramontane basins: application to Vallo di Diano, Southern Italy*, Bull. Seismol. Soc. America, Vol. 103, No. 3, doi: 10.1785/0120120071.

Bruno P.P, Castiello A., Improta L. (2010) - *Ultrashallow seismic imaging of the causative fault of the 1980, M6.9, southern Italy earthquake by Pre-Stack Depth Migration of dense wide-aperture data*, Geophys. Res. Lett., 37.

Bruno P.P., Improta L., Castiello A., Villani F.and Montone, P. (2010). *The Vallo di Diano fault system; new evidence for an active range-bounding fault in southern Italy using shallow, high-resolution seismic profiling.* B. Seismol. Soc. Am., 100(2):882-890.

Bruno P.P., Pazzaglia F.J., Picotti V. (2011). *Evidence for active folding and faulting at the northern Apennines mountain front near Bologna, Italy from high resolution seismic reflection profiling.* Geophysical Research Letters, vol. 38.

Hayashi K. and Takahashi T. (2001). *High Resolution Seismic Refraction Method Using Surface and Borehole Data for Site Characterization of Rocks*. International Journal of Rock Mechanics and Mining Sciences, Vol. 38, pp. 807-813.

L. Improta e P.P. Bruno (2007) - *Combining seismic reflection with multifold wide-aperture profiling: An effective strategy for high-resolution shallow imaging of active faults.* Geophys. Res. Lett., 34.

Jarman D., Agliardi F., Crosta G.B. (2011). *Megafans and outsize fans from catastrophic slope failures in Alpine glacial troughs: the Malser Haide and the Val Venosta cluster, Italy.* Geological Society, London, Special Publications 2011; v. 351; p. 253-277

Neidell N.S. and Taner. (1971). *Semblance and other coherency measures for multichannel data.* Geophysics, v. 36, no. 3, p. 482-497Quinn R., Bull J.M. and Dix J.K. (1988). Optimal Processing of Marine High Resolution Seismic Reflection (Chirp) data. Marine Geophysical Research -Volume 20, Number 1, 13-20, DOI: 10.1023/A:1004349805280.

Ronen J. and Clerabout. (1985). *Surface-consistent residual statics estimation by stack-power maximization*. Geophyics, v. 50, no. 12, pp. 2759-2767. doi: 10.1190/1.1441896

Taner M.T., Wagner D.E. and Baysal E. (1998). *A unified method for 2-D and 3-D refraction statics*. Geophysics, v. 63, no. 1, p. 260–274.

SEISMIC SIGNATURE OF MESSINIAN EVENT IN THE MEDITERRANEAN BASINS

A. Mocnik[1], A. Del Ben[1], R. Geletti[2]

[1] University of Trieste, Dip. Matematica e Geoscienze, Trieste, Italy

[2] OGS, Borgo Grotta Gigante-Sgonico, Trieste, Italy

Introduction. In this study we interpret deep penetration multichannel seismic profiles (Fig. 1) to analyze the Messinian Salinity Crisis (MSC) markers in the different domains of the Mediterranean basins.

The MSC represents a huge succession of events that modified the entire Mediterranean region in a relative short period of time (Hsü *et al.*, 1973); it produced a thick deposition of evaporate lithologies in the deep basins and an erosional unconformity on the marginal and onshore domains.

This study is based on the analysis of both old and new seismic profiles in order to correlate the different seismic evidences of the MSC markers across the several different basins of the Mediterranean Sea.

Seismic dataset. We used multichannel MS lines, sponsored by National Council of Research (CNR) and acquired and processed by OGS in 1972; deep crustal MCS profiles of the Italian Deep Crustal Exploration Project (CROP) (Scrocca *et al.*, 2003; Finetti, 2005),

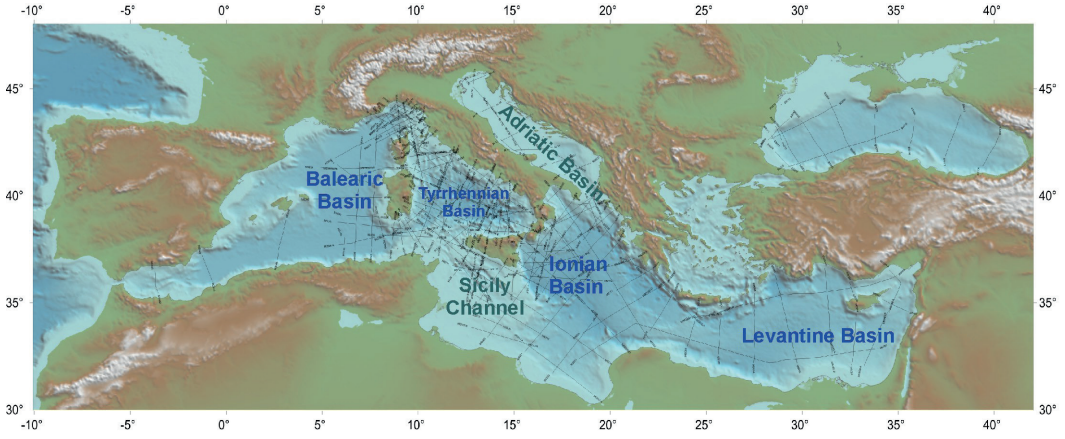

Fig. 1 - Map of the Mediterranean Sea with the position of the MS and CROP profiles. The deep basins are highlighted with blue color, the shallow basins with green color.

sponsored by CNR, Ente Nazionale Energia Elettrica (ENEL) and Ente Nazionale Idrocarburi (ENI); high resolution seismic profiles of the WS10 Project acquired and processed in 2010 by the R/V OGS Explora in the western Sardinian offshore.

Geological setting. Seismic profiles of the Mediterranean basins have been analysed by many Authors (CIESM, 2008; Lofi *et al.*, 2012 with cited references) to reconstruct the different seismic signature of the Messinian Units. The "Messinian trilogy" recognized in the Balearic abyssal plain (Rehault *et al.*, 1984), has been expanded on with the interpretation of the different seismic facies that form the Lower evaporite Unit (LU), the salt Mobile Unit (MU) and the Upper evaporite mainly gypsiferous Unit (UU). On the lower continental slope of the West Sardinia margin, which represents the eastern passive margin of the Balearic Basin, a thinning salt layer overlayed by the Upper Unit, turns into the Messinian Erosional Surface (MES): it is generally characterized by a strong reflector which truncates the top lapping pre-Messinian reflectors.

The Ionian oceanic crust underthrusts below the Calabrian and Hellenic Arcs forming active subducting slabs. In the deep basin the Messinian event is commonly evidenced by gypsum and salt layer that was piled up by compressive tectonics for a total thickness of some hundred meters (Finetti, 1982). The Ionian Basin represents, with the Levantine Basin in the Eastern Mediterranean Sea, the remnant of the Permo-Triassic Neo-Tethys (Finetti, 2005; Stampfli, 2005); the basin is characterized by a thick sedimentary package overlying the oceanic crust where the Messinian salt is often affected by plastic deformation. The Messinian trilogy seems to be absent and only MU, with some internal reflectors, has been recognized (Lofi *et al.*, 2012), bounded by two erosional surfaces on the top and on the bottom.

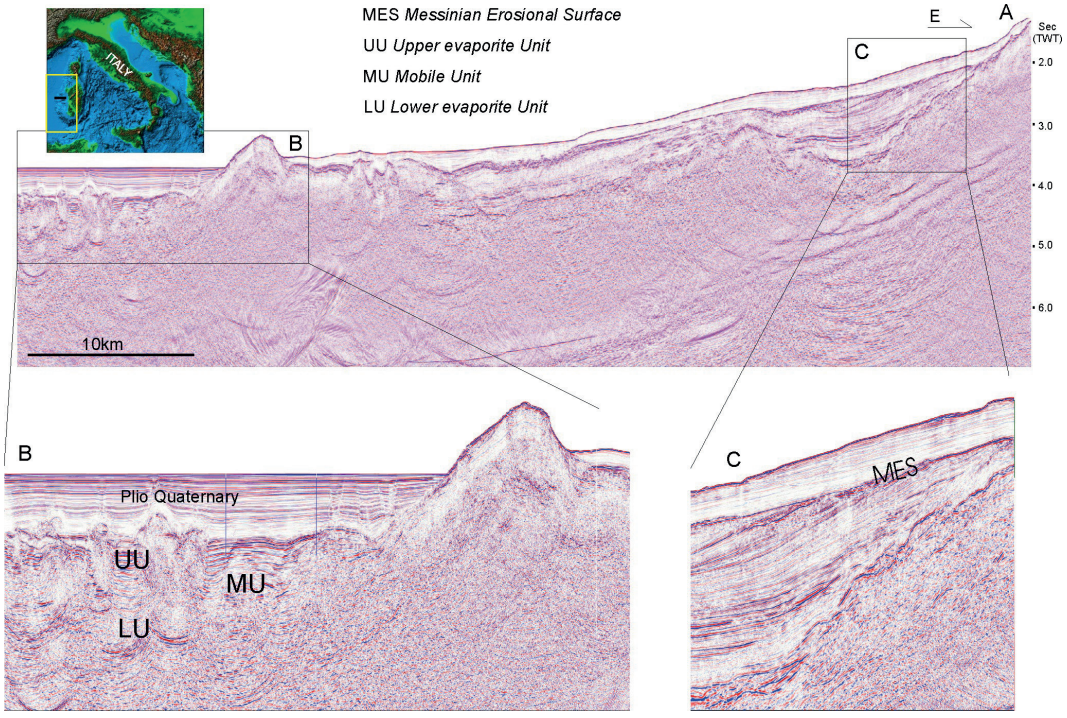

Fig. 2 - A:seismic profile WS 10-07 located in map where the continental slope and basin domains are respectively highlighted in frames B and C. In B the stratified Plio Quaternary sequence covers the Upper Units (UU) deformed by salt tectonics where the Mobile Unit (MU) is evidenced with transparent facies. The underlying Lower Unit (LU) is weakly reflecting, due to the high absorption by the diapir structures. In C the Messinian Erosional Surface (MES) on the slope clearly truncates the pre-Messinian horizons.

No seismic evidences of Messinian trilogy have been recorded in the present shallow basins. In the Adriatic Basin the Messinian sequence is absent or mainly represented by gypsum and anhydrite with marls intercalation, named Gessoso Solfifera formation. It is calibrated by a great number of boreholes and reaches a thickness of about 120m. Also in the Sicily Channel we can recognize hiatus related to the MES or, alternatively, the Gessoso Solfifera layer, calibrated by some boreholes.

The Tyrrhenian Basin opened, from west to east, since the Tortonian age. No relevant presence of Messinian evaporite units has been recorded, just some samples of gypsum lithologies are testified along the continental margins (Fabbri and Curzi, 1980).

Discussion. In Fig. 2 the WS10-07 seismic profile crosses with an east-west direction the Sardinian slope of the continental margin till the deep Balearic Basin. In the detail B we have highlighted the Messinian trilogy where the thick and high reflecting UU covers the MU which is deformed by halokinetics processes; the LU is partially masked by the signal absorption due to the diapir presence. In the frame C the typical seismic signature of the MES is evident along the upper continental slope by a prominent reflector that truncates the pre-Messinian horizons.

In Fig. 3 four seismic portions of a virtual profile starting from the Adriatic Basin, crossing the Ionian Basin and reaching the Levantine Basin are described.

A portion of seismic profile ADRIA-95 (Fig. 3A) shows the Messinian layer as a prominent reflector that encompasses the entire gypsum deposits of about 100 m, as calibrated by Eterno 1 borehole. It is covered by the thick low reflecting Pliocene sediments and by the Quaternary prograding sequences originated by the erosion of the Apennine Chain.

Moving to the deep Ionian Basin the Gessoso Solfifera formation turns on the thick salt layer of the abyssal plain, as shown along the seismic profile CROP-22 (Fig. 3B); the bottom of its characteristic transparent facies is well evidenced by a prominent reflector, west-tilted and giving a structural high. The pre-Messinian horizons show toplap terminations on the salt bottom that is probably associated to a sub-aerial exposure due to the joint effects of the Messinian sea level drop and of the tilting. Toward west the compressive tectonics originate more and more irregular reflectors on the top and inner the salt layer producing typical diffractions.

The thick layer of Messinian salt is proved to be present till the eastern sector of the Mediterranean Sea: the portion of the seismic profile MS-50 (Fig. 3C) shows an eastward increasing of salt deformation, where the deep Nile fan delta has been deposited after the Messinian crisis. The underlying salt layer is squeezed by the Plio-Quaternary sediment load and a single high amplitude reflector identifies the remaining discontinuity .

In the West Cilicia Basin, along the seismic profile MS-49 (Fig. 3D) the salt layer clearly pinches out toward the margin. A high reflecting upper sequence, interpreted by Bertoni and Cartwright (2006) as deep-water clastic sediments, are very similar to the seismic facies of the UU in the Balearic Basin, suggesting their possible ascription to gypsum layer.

Conclusions. The MSC, even if it is well documented in the whole Mediterranean Sea by several different seismic markers, is a still open question. The interpretation of the seismic signatures let to distinguish alternated phases of exposure and flooding of the different basins which often result to be hardly correlated to one another.

In the Adriatic basin and in the Sicily Channel the Messinian layer, where it is not replaced by an erosional surface, is present as a thin evaporate layer mainly constituted by Gessoso Solfifera formation. The Messinian trilogy has been observed only in the deep Balearic Basin, while in the Ionian and Levantine Basins it shows a mainly salt seismic facies.

The presented seismic data aim to contribute to the recognition of the different seismic facies which characterize the different units; their comparison could improve the comprehension of the processes that affected the Messinian events in the Mediterranean region, specially because of the critical lacking of boreholes.

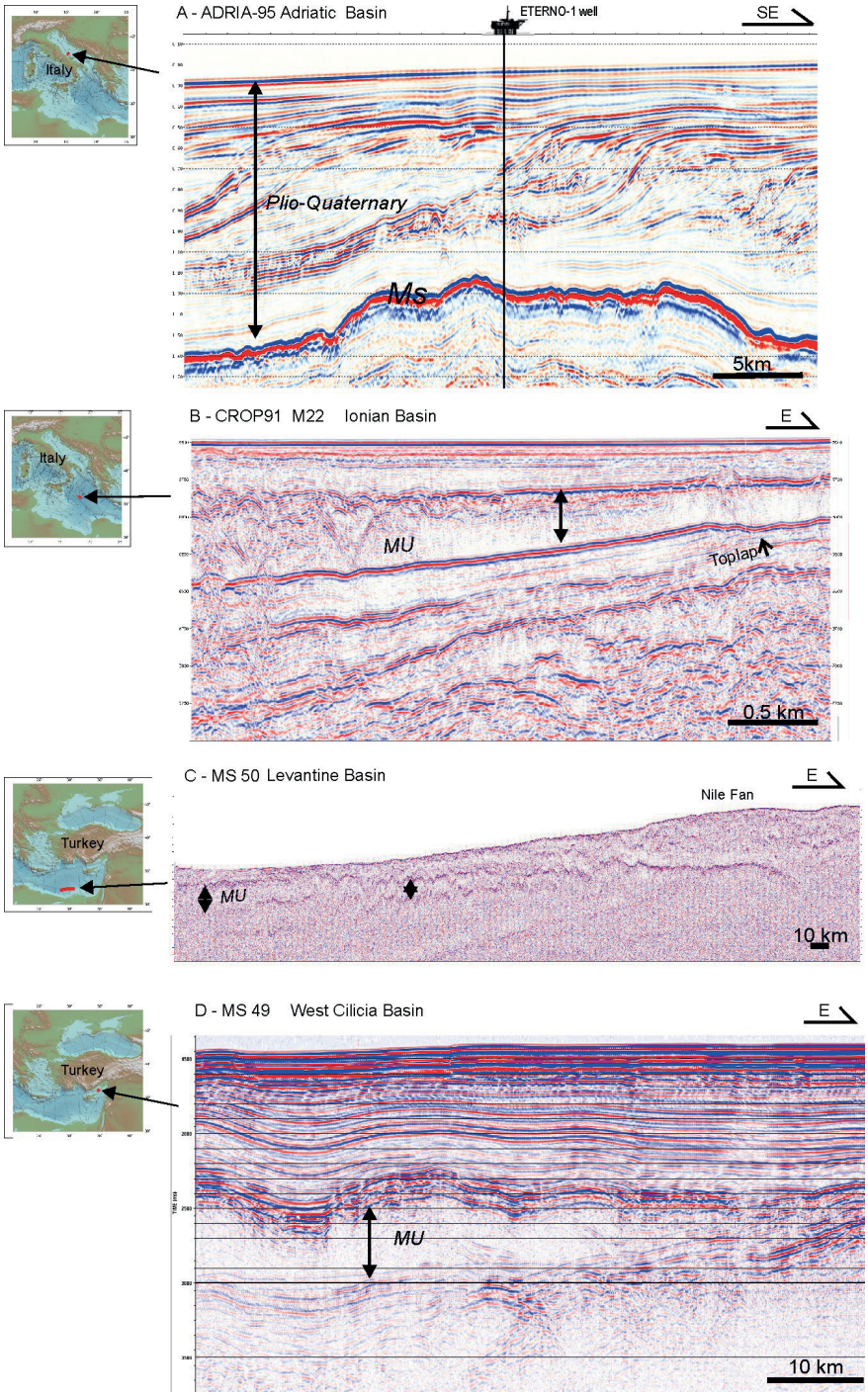

Fig. 3 - A:portion of seismic profile ADRIA-95 located in the Central Adriatic Basin where the Messinian layer is evidenced by reflector Ms; B: portion of CROP-22 seismic profile located in the Ionian Basin with a wes-tilted Mobile Unit (MU); C: portion of seismic profile MS-50 located in the Levantine Basin where the salt layer is deformed by the deep Nile fan deposits; D: portion of seismic profile MS-49 located in the West Cilicia Basin, where the transparent facies of the Messinian salt pinches out on the basin's margin.

References

Bertoni C. and Cartwright J.A.; 2006: *Controls on the basinwide architecture of late Miocene (Messinian) evaporites on the Levant margin (Eastern Mediterranean*). Sedimentary Geology, **188-189**, 93-114.

CIESM; 2008: *The Messinian Salinity Crisis from mega-deposits to microbiology* - A consensus report N.33 in CIESM Workshop Monographs (F. Briand, Ed.), 168 pp, Monaco.

Fabbri A. and Curzi P.; 1980: *The Messinian of the Tyrrhenian Sea: seismic evidence and dynamic implications*. Giorn. Geol., ser.2, 43, 1, 215-248.

Finetti I.; 1982: *Structure, stratigraphy and evolution of Central Mediterranean.* Boll. Geof. Teor. Appl., **24**, 75-155.

Finetti I.R. (ed.); 2005a: CROP Project: *Deep seismic exploration of the Central Mediterranean and Italy.* Atlases in Geoscience 1, Elsevier, 794 pp.

Hsü, K. J., Cita, M. B., and Ryan, W.B.F; 1973: *The Origin of the Mediterranean Evaporites*. In Ryan, W.B.F, Hsu, K. J., *et al*., Init. Repts. DSDP, 13, Pt. 2: Washington (U.S. Govt. Printing Office), 1203-1231.

Lofi J., Déverchère J., Gaullier V., Gorini C., Guennoc P., Loncke L., Maillard A., Sage F., Thinon I.; with contr. J. Benkhelil *et al*..; 2011: *Seismic atlas of the "Messinian salinity crisis" markers in the Mediterranean and Black Seas Paris*. Memoire de la Société Géologique de France, **179**, 71 pp. ISBNs:2853630978, 9782853630979, 9782853630979 .

Rehault J. P., Boillot G., Mauffret A.; 1984: *The Western Mediterranean Basin geological evolution*. Mar. Geol., **55**, 447-477.

Scrocca D., Doglioni C., Innocenti F., Manetti P., Mazzotti A., Bertelli L., Burbi L. and D'Offizi S. Eds; 2003: *CROPAtlas – Seismic Reflection Profiles of the Italian Crust*. Memorie descrittive della Carta Geologica d'Italia, 52.

Stampfli G.M.; 2005: *Plate Tectonics of the Apulia-Adria microplate.* In: Finetti I.R. (ed), CROP Project: Deep seismic exploration of the Central Mediterranean and Italy, Atlases in Geoscience 1, Elsevier, pp. 747-766.

COMPARISON BETWEEN NEIGHBORHOOD AND GENETIC ALGORITHMS ON TWO ANALYTICAL OBJECTIVE FUNCTIONS AND ON A 2.5D SYNTHETIC SEISMIC INVERSE PROBLEM

A. Sajeva[1], M. Aleardi[1], A. Mazzotti[1], E. Stucchi[2]

[1] Earth Sciences Department, University of Pisa, Italy

[2] Earth Sciences Department, University of Milan, Italy

Introduction. A geophysical inverse problem consists in obtaining the earth model for which the predicted data best fit the observed one (Tarantola, 1986). The problem is often non-linear and can be solved using a local linearization method (such as Gauss-Newton, steepest descent or conjugate gradient) or using a global optimization method (such as Grid Search, Simulated Annealing, Genetic Algorithms, Particle Swarm and Neighborhood Algorithm). In this work we compared and evaluated the efficiency and the limits of a Genetic Algorithm (GA) and of the Neighbourhood Algorithm (NA) varying the dimensions of the model space. We first tested these methods on two analytical objective functions: a multidimensional convex parabola and a more complex egg-box functional. Lastly we performed an acoustic full waveform inversion considering a small and smoothed portion of the Marmousi model.

The Neighborhood Algorithm. The Neighborhood Algorithm is a direct search method which is based on the concept of proximity. The method is composed by two parts which deal with two different stages of the optimization problem: the sampling of the model space (Sambridge, 1999a), and the appraising of the ensemble (Sambridge, 1999b).

The sampling part deals with finding models of acceptable data fit in a multidimensional parameter space. One of its key ideas is to be best guided by all previous models for which the forward problem has already been solved. Therefore, it makes use of the previous models to approximate the misfit function everywhere in model space. The misfit functional is interpolated to the value of its nearest neighborhood in model space. The method uses Voronoi cells (Voronoi, 1908) to determine the nearest model space sample. The algorithm is conceptually simple, in fact, it requires just two 'tuning parameters': the number of new models to be generated per iteration *ns*; and the number of best fitting models to be selected among these new models per iteration *nr*. The user can also set *ns* to decrease as the number of iterations increases. Furthermore, the method makes use of only the rank of a data fit error rather than its numerical value.

The objective of the method is to generate an acceptable ensemble of "good fitting" models, rather than seeking a single optimal model. For this reason, a subsequent appraising stage is provided to extract information from the ensemble (Sambridge, 1999b). Several authors have proposed methods for analyzing an ensemble of data-acceptable models, primary using cluster analysis techniques (e.g. Kennett, 1978). In this algorithm, the appraising stage is developed in the framework of Bayesian Inference, that is, the input ensemble is reinterpolated to construct an approximate PPD, thus, such approximated PPD is importance sampled via a Gibbs sampler (Geman and Geman, 1984).

Genetic Algorithms. Genetic Algorithms are search algorithms developed by Holland (1975) belonging to the larger class of evolutionary algorithms, and are based on the mechanics of natural selection and evolution to search through model space for optimal solutions. In a genetic algorithm, a population of strings (called chromosomes), which encodes candidate solutions (called individuals, or phenotypes) to an optimization problem, is evolved toward better solutions during the evolution process which starts from a population of randomly generated individuals. In each generation, the fitness (the error associated to each possible solution) of every individual is evaluated, then multiple individuals are stochastically selected from the current population on the basis of their fitness. Then they are modified (using crossover and mutation operators) to form a new population which is used in the next iteration. The algorithm terminates when either a maximum number of generations has been produced, or a satisfactory fitness level has been reached for the current population.

Following the theory of the "punctuated equilibria" (Gould and Eldredge, 1977) it has been formulated a more sophisticated version of the GA, the so called Niched-Genetic Algorithms (N-GA), where the initial random population is divided in multiple subpopulation which are subjected to separated selection and evolution processes. Only for a fixed number of iterations the different populations can exchange some individuals to simulate the natural migration process. Therefore, a niching method must be able to form and maintain multiple diverse solutions and preserve them for the entire duration of the GA run. This method avoids the so called genetic drift (Horn, 1993), that is the loss of diversity inside a single population which can lead to convergence toward a local minimum in case of multimodal objective function (Sen and Stoffa, 1992). More details about GA can be found in Goldberg (1989) and Mitchell (1996).

Inversion in case of Analytical Objective functionals. Convex Objective Functional. In this first test we compared the GA and the NA optimization methods on a very simple multidimensional parabolic objective function, which can be expressed by the following formula:

$$e = \sqrt{\frac{\sum_{i=1}^{nd} m_i^2}{nd}}$$

where nd is the dimension of the model space and the n-dimensional model is m=[m_1,m_2,...., m_{nd}].

The accepted values of each variable range between -10 and +10. Since the misfit function is convex, we selected a single best models for each iteration for NA and a single population without niching for GA.

Fig. 1a shows the number of model evaluations needed to ensure an optimal convergence toward the unique minimum with an accuracy of 1e-6. The red circles and blue crosses represent the NA and GA, respectively, while the red and blue dotted lines represent a fourth degree polynomial fit for NA and GA respectively. For model space dimensions less than 16, the NA requires a smaller number of misfit evaluations. On the other hand, the curve fitting evidences the high number of model evaluations needed for convergence in case of high dimension model

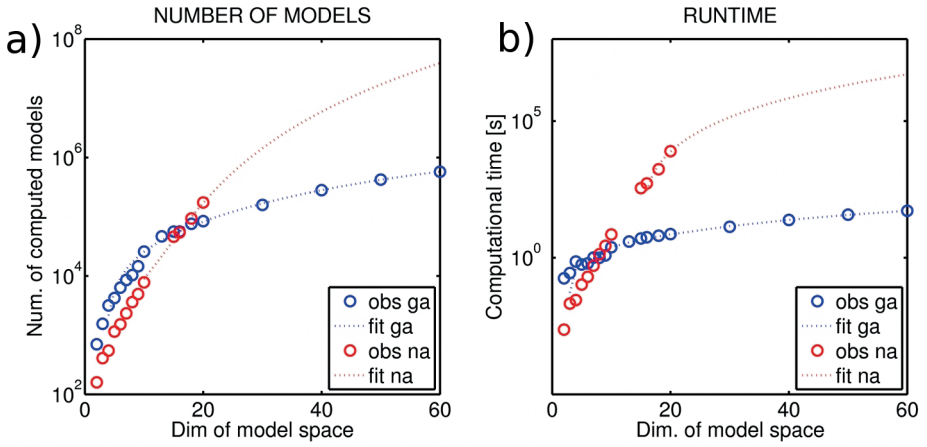

Fig. 1 – Convex misfit functional: (a) comparison of number of models computed to reach convergence for GA (blue) and NA (red); (b) comparison of runtime occurred to reach convergence for GA (blue) and NA (red). Each experimental dataset in the graphs was fitted with a polynomial of 4th degree.

space. This is a crucial limit of the NA method, in fact, we stopped the NA inversions at nd=20 due to the very high computational cost of the inversion procedure.

Fig. 1b shows the computational time of the two different optimization methods tested on a esa-core Intel(R) Xeon(R) CPU E5645 @2.40GHz, 48 GB RAM. In such a simple inversion, no forward model computation is requested, therefore the computation time only depends on the internal algorithm operations. This figure shows a trend very similar to that previously observed in Fig. 1a. One can note a better performance of the NA method below *nd*=9 while the GA appears to overtake the NA for high-dimension model spaces.

In case of NA, the most time consuming operation is the computation of the Voronoi cells which is linearly dependent on the space dimension and is proportional to the square of the number of models: (Sambridge, 1999a):

$$t \propto nd \cdot ne^2$$

where *t* is the computational time and *ne* is the number of evaluated models.

Multiminima Objective Functional. In this second test we compared the GA and the NA optimization methods on a more challenging multidimensional objective functional which consists in a so-called multidimensional egg-box, that is, a product of sinusoids which we weighted with a *n*-dimensional gaussian centered on the true model, in order to enhance a single minimum with respect to the others. The analytical misfit can be expressed by the following formula:

$$e = \prod_{i=1}^{nd} sin\left(\frac{2\pi m_i}{l}\right) \prod_{i=1}^{nd} exp\left(\frac{-\left(m_i - m_{true,i}\right)^2}{2\sigma^2}\right)$$

where l is the wavelength of the sinusoid, σ is the width of the gaussian, $m_{true,i}$ is the i-th component of the true model. We chose l=8, σ=2, and we located m_{true} on one of the minima of the multidimensional sinusoid, at position (*l*/4,*l*/4). As in the first test each parameter ranges between -10 and +10, while we convergence to 1e-2.

When performing the GA inversions we used the same values for the control parameters independently of the dimension of the parameter space, namely a number of individuals of 100, 10 subpopulation, selection rate of 80% and a mutation rate of 1%. In addition, we set the migration process to take place every ten generations.

Differently, in the NA inversion the small set of free-parameters (*ns* and *nr*) must be adjusted depending on the dimensions of the model space in order to guarantee convergence. Roughly they must increase along with the dimension of model space proportionally to the number of minima of the misfit functional. As a rule of thumb, we multiplied each value (*ns, nr*) by 6 when adding a new dimension in the inversion, because, in this particular case, the number of minima increases by a factor of 6 when a new dimension is added. Notwithstanding the effort, we noted that the convergence is not assured, even setting ns and nr to high values (e.g., $ns=10^3$, $nr=10^2$ for $nd=4$), and the method is subjected to fall on local minima.

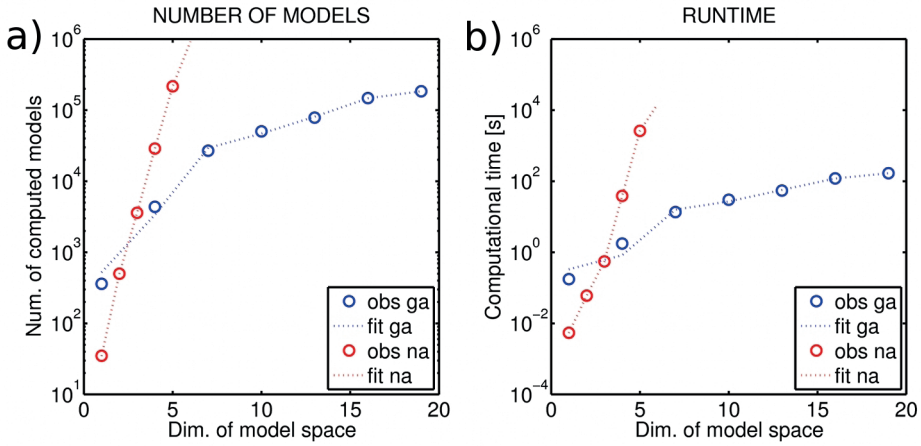

Fig. 2 – Multi-minima misfit functional: (a) comparison of number of models computed to reach convergence for GA (blue) and NA (red); (b) comparison of runtime occurred to reach convergence for GA (blue) and NA (red). Each experimental dataset in the graphs was fitted with a polynomial of 5th degree.

Fig. 2a shows the number of model evaluations needed to ensure convergence for the two methods. The red and blue crosses represent the NA and GA respectively, while the red and blue dotted lines represent a five degree polynomial fit for NA and GA respectively. Note that the same behavior of the first test occurs, i.e., NA is better performing for smaller dimensions while GA is more effective in case of higher dimension model spaces. However, in this case the GA results to be better performing than NA already for very small model space dimensions (around 2 in Fig. 2a) so that the GA implementation results to be the best for almost every dimensions. We stopped the NA inversion at $nd=5$ due to the high computational cost of the inversion procedure.

Fig. 2b shows the computational time of the two different optimization methods, which have been tested on the same hardware of the first test. Note a better performance of the NA method below $nd=3$, where the cross-point takes place, and then a better behavior of GA for higher dimensions.

As we already pointed out, NA inversions appear to need high values for the free-parameters to ensure convergence in case of high dimensional spaces (e.g. $ns > 10^3$ for $nd=5$). Furthermore, based on the results in these tests, it seems that it is best to choose a *nr* value, the number of selected models per iteration, at least as big as the number of local minima of the functional. Obviously this information would not be available when performing an actual inversion. Differently, GA seemed to be less sensitive to the specific values of the user defined parameters, and to better escape local minima even with a relatively small population (100 models) per generation.

Synthetic seismic inversion. Full-waveform inversion is a relatively novel variant of seismic tomography characterized by the numerical solution of the equations of motions (Fichtner, 2011). We performed our test simulating very low seismic frequencies (<1 Hz) and assuming

an acoustic approximation. This low frequency range combined with a finite difference seismic propagator allowed us to use a very wide grid (where the distance between each node is 288 m in every spatial direction) without dealing with numerical dispersion during the forward model computations. The consequent low number of model parameters (16 cells along the x direction and 4 in the z direction) allowed us to use a global optimization method.

We simulated a 3D seismic propagation on a 2D model with in-line extension of 4600 m, and a maximum depth of roughly 800 m (see Fig. 3a). Regarding the seismic acquisition parameters, we used 15 shot points and 60 geophones, a source interval of 288 m and a receiver distance equal to 72 m.

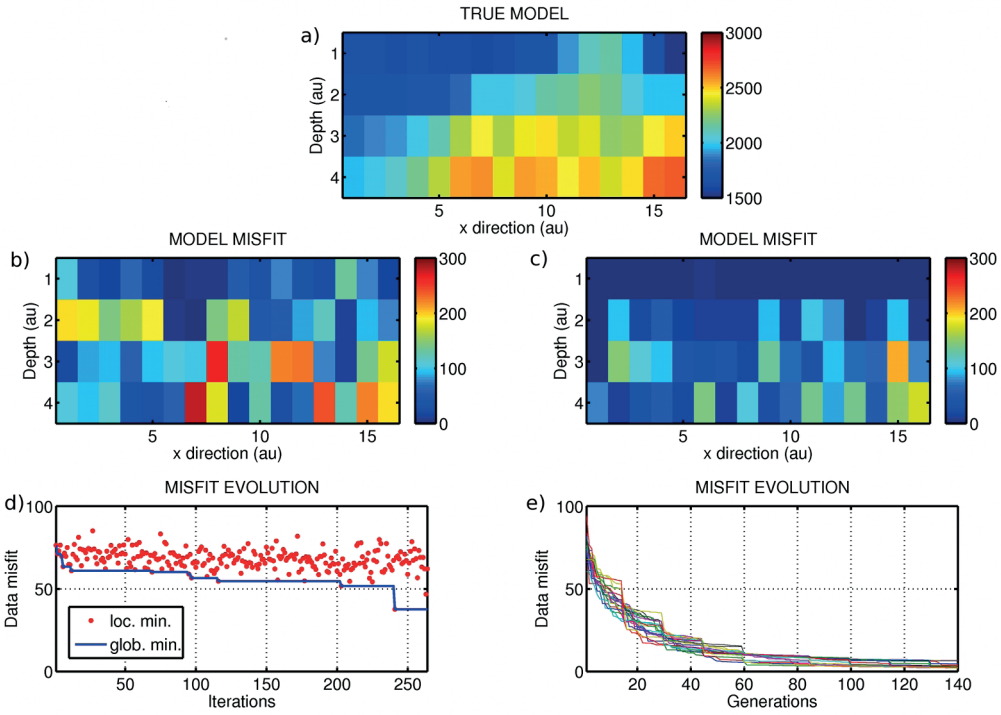

Fig. 3 – The true acoustic model (a); difference between the true model and the final computed model for NA (b) and for GA (c) inversions, respectively. The evolution of the misfit with respect to the iterations in the NA inversion (d), and with respect to the generations in the GA inversion (e). In (d) the current minimum misfit per iteration and the global current minimum misfit per iteration are shown. In (e) each colored line represents the misfit evolution of a different subpopulation.

For the inversions, we considered the admissible range for each model parameter to be 400 m/s wide and set around the true value. In the NA inversion, the user defined parameters were set to *ns*=128 and *nr*=32 for 320 iterations. This parameters were chosen following the rule of thumb given by Sambridge (1999a) that links the free-parameters to the dimension of the model space. With the GA we chose the following control parameters: 300 individuals for the population of each generation and maximum number of 30 generations; a selection rate of 0.8 (which means that for each generation we replaced the 80% of models, while the remaining best 20% survived unchanged); we used a mutation rate of 10%, and a selection pressure of 2 over a linear ranking. We divided the population in 20 subpopulations, that migrated every 15 generations into each other.

Figs. 3b and 3c show the differences between the true and the inverted model for both the GA and NA optimization, respectively. Note a better convergence of GA with respect to NA.

The shallowest part of the model is better resolved in either the inversions. This is due to the better illumination of the near surface part of the model with respect to the deeper elements.

Figs. 3d and 3e graph the misfit evolution for the NA and GA, respectively. Note the slow rate of convergence of the NA, and a better performance of GA. In the GA inversion, the misfit evolution is different for each subpopulation that explores a different part of the model space, and jumps can be seen in the plot in correspondence of the generations at which the migration algorithm takes place. In particular NA does not show a significant decrease of the misfit with the iterations and this is likely due to an entrapment into a local minimum. Therefore the GA method seems to be characterized by a more efficient exploration of the entire model space. In conclusion, also this synthetic seismic inversion test confirms the previously obtained results by means of the analytical objective functions.

Conclusions. In this work we compared two different global optimization methods: Genetic Algorithm and the Neighborhood algorithm.

The tests on the convex analytical misfit function highlighted the better performance of the NA technique in case of a low dimensional model space, and, vice versa, a better performance of the GA for higher dimension model spaces. The cross-point at which the number of models needed for convergence for the GA is less than that needed for the NA occurs approximately at a dimension of 16 unknowns (that is for a dimension 16 of the model space). Analogously, the computational time at which GA starts converging faster than NA takes place at dimensions greater than 9.

The tests on the multi-minima analytic function showed a more problematic reliability of the NA method, in fact, it resulted that the cross-point moved toward smaller dimensions of the model space (2-3) and that generally GA outperformed NA. Furthermore NA seemed to be subjected to be trapped in local minima if the model space is not adequately sampled by the previous set of models. In order to avoid it, the number of models computed for each iteration, must be set to increase at least linearly with the number of dimensions of the model space.

Focusing on the computational time, the inversions on the analytical misfit functionals showed a steeper curve for NA than for GA against the parameter dimensions. The high computational costs of the NA is likely due to the time needed to evaluate the Voronoi cells, which is proportional to the square of the number of evaluated models. Thus, the computational cost of the NA increases dramatically along with the number of dimensions. In comparison, the GA computational time is significantly lower for high dimension model spaces.

The synthetic seismic inversions performed with model space of dimension 64, confirmed the results obtained with the analytic functionals, that is, the better performance of GA in case of higher dimensional parameter spaces. The bad performance of NA in terms of convergence toward a good model is likely due to the small values chosen for the free parameters in the test, values that we took from the literature, but that must be probably set to higher values when moving towards higher dimension parameter spaces (*nd*=30-60). In conclusion, the global optimization method must be carefully chosen depending on the expected dimension of the model space.

Acknowledgements. These results were obtained within a research project with ENI. We thank ENI for the permission to publish this paper.

References

Fichtner A.; 2011: *Full Seismic Waveform Modelling and Inversion*. Springer.

Geman S. and Geman D.; 1984: *Stochastic Relaxation, Gibbs distributions and the Bayesian Restoration of images*. IEEE Trans. Patt. Analysis Mach. Int., 6, 721-741.

Goldberg D.E.; 1989: *Genetic algorithm in search, optimization and machine learning*, Kluwer Academic Publishers.

Gould S. J. and Eldredge N.; 1977: *Punctuated equilibria: the tempo and mode of evolution reconsidered, Paleobiology.* **3** (2), 115-151.

Holland J.H.; 1975: *Adaptation in natural and artificial systems*. University of Michigan Press.

Horn J.; 1993: *Finite Markov Chain Analysis of genetic Algorithms with Niching.* Proceedings of the 5th international Conference on genetic algorithms, 110-117.

Kennett B.L.N.; 1978: *Some aspects of non-linearity in inversion*. Geophys. J. R. Astr. Soc., 55, 373-391.
Mitchell M.; 1996: *An introduction to genetic algorithms*. MIT Press.
Sambridge M.; 1999a: *Geophysical inversion with a neighborhood algorithm-- II. Searching a parameter space*. Geoph. J. Int. 138, 479-494.
Sambridge M.; 1999b: *Geophysical inversion with a neighborhood algorithm-- II. Appraising the ensemble*. Geoph. J. Int. 138, 727-746.
Sen M. K. and Stoffa P. L.; 1992: *Rapid sampling of model space using genetic algorithms: examples from seismic waveform inversion*. Geophysical journal International, 108, 281-292.
Tarantola A.; 1986: *A strategy for nonlinear elastic inversion of seismic reflection data*. Geophysics, **51**,10, 1893-1903.
Voronoi M. G.; 1908: *Nouvelles applications des paramètres continus à la théorie des formes quadratiques*. J. reine Angew. Math., 134, 198-287.

CHEBYSHEV ARRAY FORMING FOR NEAR SURFACE INVESTIGATIONS

A. Tognarelli[1], E. Stucchi[2]
[1] *Earth Sciences Department, University of Pisa, Italy*
[2] *Earth Sciences Department, University of Milan, Italy*

Introduction. In recent years, reflection seismics has increasingly been extended to near surface investigations to help in better delineate the subsurface properties, in particular the shallow layers geometry. The applications of shallow reflection surveys range from hydrogeological prospecting (Pugin *et al.*, 2009; Ge *et al.*, 2010), environmental and engineering problems (Miller and Steeples, 1994; Shtivelman, 2003), landslide characterization (Malemhir *et al.*, 2013; Stucchi *et al.*, in press) to mention but just a few.

The generally limited availability of recording hardware when compared to oil or mining exploration, and the often poor performance of the energy sources, are two problems that add to the known difficulties inherent to the near surface exploration (Steeples and Miller, 1998). It is quite common to employ recording equipment using only 24 or 48 active channels, with single vertical or horizontal geophone (for P- or S-wave survey), and simple energy sources such as the sledgehammer or the weight drop. This results in a poor depth penetration of the seismic signal and in a severe source related noise contamination (ground roll and air blast) of the acquired data. However, it may be possible to turn these hardware weaknesses into potential advantages. In fact, the relative facility of striking blows with the sledgehammer and the flexibility aptitude of 24-48 channel short spreads allow the geophysicist to acquire a plentiful quantity of data and to leave to the processing lab the task to appropriately stack them to increase the signal-to-noise (S/N) ratio. This corresponds to performing source and/or receiver array simulations, where the output can be optimized on the basis of specific criteria such as noise attenuation or resolution. Indeed, contrarily to what happens in the field where the arrays would be fixed along the entire profile, the simulation of arrays in the processing can be time and space variant and their responses can be changed according to the changing characteristics of the data.

In our work we demonstrate how effective spatial filters can be easily obtained by properly mixing and weighting different traces and how this turns out in a fair improvement in the data quality. The optimal weights are computed by means of Chebyshev polynomials (Carlini and Mazzotti, 1989; Holzman, 1963), where “optimal” is intended as more efficient and uniform noise attenuation in the array filter stop-band region compared to the un-weighted array. The real data pertain to a reflection survey carried out to delineate the subsurface structure of a huge landslide located in the Northern Apennine, Italy (Stucchi *et al.*, in press). A 10 kg sledgehammer and a 48 channels single geophone spread were used as the energy source and the recording devices in the production phase.

Field acquisition. The spread configuration was designed on the basis of synthetic traveltimes (Zelt and Smith, 1992) computed on a three layers model built from previous geophysical and geotechnical data (Federici *et al.*, 2002). Tests were carried out in the first days

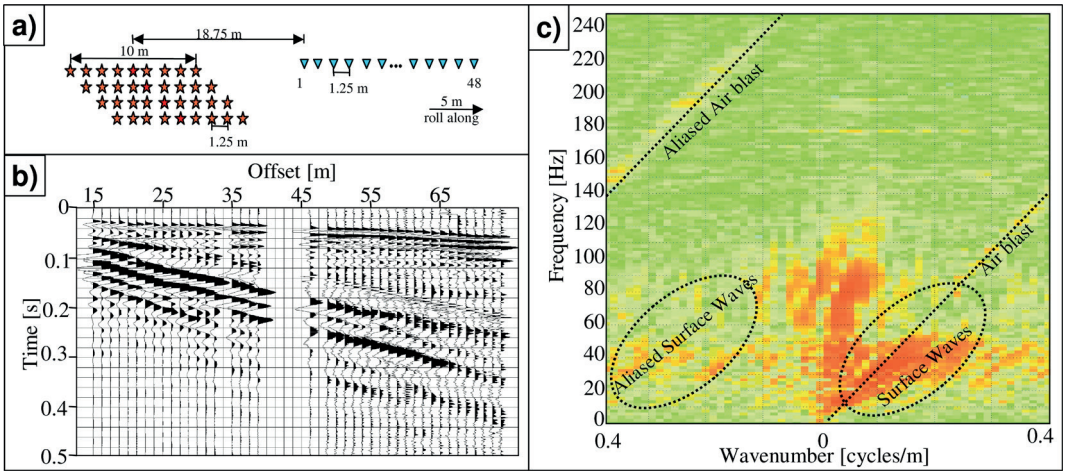

Fig. 1 – a) Acquisition layout. The stars represent the source locations and the triangles represent the receiver locations. b) An example of a single blow gather. A trace by trace normalization is applied to the seismogram. c) f-k spectrum of the seismogram showed in frame b).

of the survey to check the design parameters and to properly set the minimum and maximum offset. Fig. 1a) shows the acquisition layout used in the field. The receiver spacing was 1.25 m to reduce the surface waves and air wave aliasing effects. As many as 36 source records corresponding to 36 single blows spaced of 1.25 m were recorded, leaving the receiver spread in the indicated position. The whole source-receiver layout was then advanced of 5 m downhill along the profile and the acquisition procedure was repeated again.

The flexibility of the hardware equipment and in particular of the source, allowed us to record the data with a source-array geometry. From an estimate of the velocity and of the frequency content of the surface waves in the test records, which were found to be approximately 350 m/s and 35 Hz as the pick frequency respectively, we decided to realize the source-array layout shown in Fig. 1a), which is characterized by the first notch at k≈0.1 [cycles/m]. Recording each single blow separately we left the task of array-forming for spatial filtering to the processing lab. We ended up having 868 single blow gathers for a total profile length of about 200 m.

A typical single blow gather is shown in Fig. 1b) after a trace by trace normalization. Some reflections are clearly visible between 80 ms and 100 ms at far offset, but the high amplitude coherent noise due to the air blast wave and, particularly, to the surface waves (ground roll) that contaminate the data overwhelm any signal outside the optimum window. Fig. 1c) illustrates the corresponding f-k spectrum. The high amplitudes of the ground roll, its partially aliased nature and the partly overlapping frequencies of the ground roll with the useful signal make it difficult for subsequent processing tools to achieve a satisfactory noise attenuation and we may often have to resort to drastic measures such as the muting of entire portions of the observed data.

Chebyshev polynomials. The Chebyshev polynomials are defined using the following recursion formula (Holzman, 1963):

$$T_0(u) = 1$$

$$T_1(u) = u$$

$$T_{m+1}(u) = 2uT_m(u) - T_{m+1}(u) \qquad (1)$$

Some examples are: $T_2(u) = 2u^2 - 1$, $T_3(u) = 4u^3 - 3u$, $T_4(u) = 8u^4 - 8u^2 + 1$ ...

$$T_8(u) = 128u^8 - 256u^6 + 160u^4 - 32u^2 + 1, \text{ etc.}$$

In general the following properties are of interest: in the rage $-1 \le u \le 1$ and $m > 0$, all the polynomials oscillate about zero even- or odd- symmetrically (for m even or odd respectively) with maximum amplitude of the oscillations equal to 1. For $u > 1$, $T_m(u)$ increases monotonically; for $u < -1$, $T_m(u)$ increases monotonically if m is even and decreases monotonically if m is odd. For all the polynomials: $T_m(1) = 1$.

Given the acquisition parameters used in the field, we exploit these properties for determining the weights of the source and receiver arrays and the maximum rejection ratio R possible. Here below we briefly outline the procedure for the source array weights computation.

The polynomial variable u is set to $u = \sigma x$ where x is given by $x = \cos(\pi D_0 \lambda_l)$ with D_0 the distance between two consecutive elements of the array (1.25 m) and $1/\lambda_l$ the wavenumber at which the first notch of the array will occur. In our case with 9 elements of the array ($m = 8$), we choose $\lambda_l \approx 9m$, slightly softening the indications suggested by the ground roll characteristics in the test but achieving a higher rejection ratio R. This gives $\sigma = 1/x \approx 1.1$ and $R \approx 22$. The array coefficients can now be computed by means of the following formula (Holzman, 1963 eq. 35):

$$a_k = \frac{2}{N} \sum_{s=0}^{[m/2]} \varepsilon_s T_m[\sigma \cos(\frac{s\pi}{N})] T_{m-2k}[\cos(\frac{s\pi}{N})] \qquad (2)$$

where: [] is the floor function, $m = 8, N = m + 1$, and $\varepsilon_s = 1$ if s=0 otherwise $\varepsilon_s = 2$, giving for the a_k:

0.3682, 0.5261, 0.7610, 0.9355, 1.0000, 0.9355, 0.7610, 0.5261, 0.3682 for k=1...9.

Array simulations. The redundant number of single blow gathers with closely spaced sources and receivers acquired, allow now to perform source and/or receiver array simulations in the processing lab that achieve the desired spatial filter responses. As an example, the blue line in Fig. 2 illustrates the spectrum of the simulated array composed by 9 evenly spaced and equally weighted sources. It is evident the performance of the array in attenuating the wavenumber components above 0.1 [cycles/m], which are mainly due to the surface waves noise and air wave. However, as shown by the lobe amplitudes in the stop-band region, the array response is not uniform, suggesting that the equal weights array performance can be improved in the lab. Indeed, an even more effective noise attenuation is achieved by the application of a simulated array composed by 9 evenly spaced but weighted blows, where the weights are computed using the procedure described in the previous paragraph based on the Chebyshev polynomials. The corresponding filter response is shown by the red line in Fig. 2. Note the uniform maximum amplitude of the lobes in the stop-band region at the expense of a slight higher position of the first notch due to the $\lambda_l = 9m$ used.

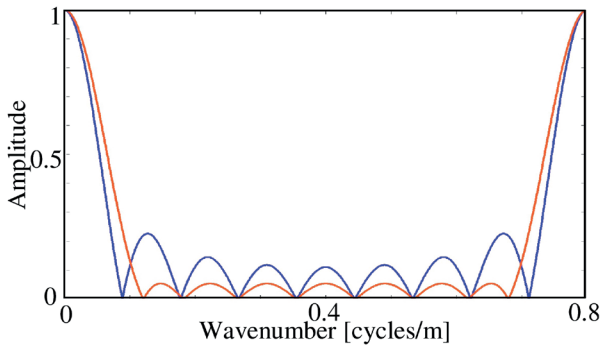

Fig. 2 – Comparison between the spatial response of the simulated array composed by 9 evenly spaced and equally weighted sources (blue) and by the optimal Chebyshev weighted sources (red).

Results. The results obtained filtering the data with equally and optimized (Chebyshev) weighted spatial filters are checked on shot gathers and on stacked data. On shot gathers the surface waves noise attenuation is appreciable both in offset-time *(x,t)* and in frequency *(f,k)* domain, even if at short offsets residuals still remain. Concerning the stacked data, the close-ups

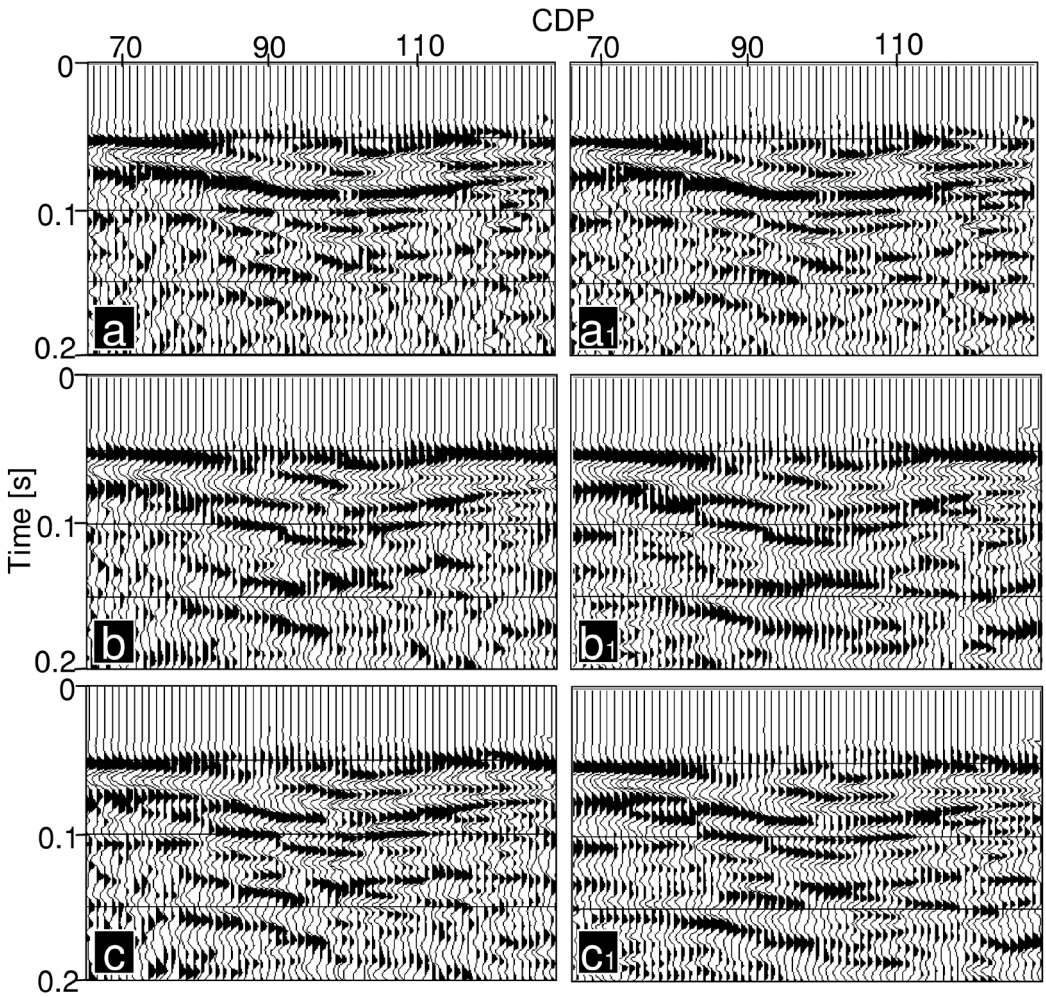

Fig. 3 – Close-ups of the stack sections obtained after a basic processing sequence. Frames a), b) and c) compare the unfiltered data, the data after the application of the equally weighted source array, the filtered data with the weighted Chebyshev source array, respectively. Frames a1), b1) and c1) illustrate the same close-ups where the traces at short offset are muted and where the receiver spatial array filters with equal weights (b1) and optimal Chebyshev weights (c1) are applied.

in Figs. 3 a, b, c illustrate the outcomes of the spatial filters application on the more interesting part of the Patigno landslide stacked section. A basic processing sequence consisting of band-pass filter (10-20-140-160 Hz), statics corrections, velocity analysis, NMO correction (30% stretch mute), AGC (25 ms), surface consistent residual statics and stack was applied to the data to obtain the section in a). An attenuation of the surface waves noise is achieved when the step of equally weighted array forming is introduced in the processing sequence, (compare frame a) with frame b)), and a further attenuation is evident when the Chebyshev weighted array is used instead (frame c). The noise attenuation in the equally weighted array stack comes with a little decrease in resolution of the upper events, an effect that do not appear in the Chebyshev weighted array stack. Frames a1,b1,c1 display the same close-ups after the application of the weighted spatial filters on the receiver side (5 receivers equally weighted in b1) and Chebyshev weighted in c1 and a mute of the shortest offset traces (a1,b1,c1). The beneficial effects of the

whole procedure is appreciable in frame c1, where an improvement in the continuity of the reflections, preserving the available resolution, is clearly evident.

Conclusions. Source and/or receiver array simulation is widely employed in deep seismic reflection surveys to tackle the high level of source related noise that may affect the reflection records. This methodology can also be extended to near surface reflection seismic investigations, where simple energy sources such as sledgehammers or weight drops are used along with equipment of limited recording channels. In general, due to the operational flexibility of the low channel number recording spread and to the low cost energy source, it is possible to acquire a redundant number of single source – single receiver gathers with only a small additional effort in the field work. This implies just a slight increase of the acquisition time and leaves untouched the budget, laying the basis for the application of this technique.

The availability of many traces pertaining to closely spaced sources and receivers allows to simulate source and/or receiver arrays that act as spatial filters aimed at attenuating the source related coherent noise. The desired array response may be attained by properly weighing the array elements and the optimal weights can be determined through the use of Chebyshev polynomials. Because of the uniform response of the polynomials in the stop-band region, Chebyshev weighted arrays prove to be more effective than equal weighted arrays in the noise attenuation even if a less restrictive notch was set.

From the experience we carried out it results that simulating arrays in the processing lab brings an improvement in the data quality and can be achieved at the expense of a slight increase in the acquisition effort and in the processing work. Finally, through the array simulation we can either achieve a data reduction (for instance we can halve the number of source gathers), maintaining proper anti-aliasing conditions, or else we can keep as many simulated array source gathers as many original single blow gathers. The same applies for receiver simulated arrays.

Acknowledgements. The seismic data processing was carried out using the ProMax® software of Landmark Graphics Corporation that is gratefully acknowledged. The code for the array simulation has been developed internally. We would also like to thank Prof. Alfredo Mazzotti for his useful suggestions and interesting discussion.

References

Carlini A. and Mazzotti A.; 1989: Optimized receiver array simulation based upon resolution constraints. Geophysical Prospecting, 37, 607-621.

Federici P. R., Puccinelli A., Chelli A., D'Amato Avanzi G., Ribolini A. and Verani M.; 2002: The Large Landslide of Patigno (Northern Apennines, Italy): geological, geomorphological and geognostic integrated analysis. In Rybar, Stemberg and Wagner (eds), "Landslides", Swets and Zeitlinger, Lisse, pp. 547-552.

Ge J., Magnani M.B. and Waldron B.; 2010: Imaging a shallow aquitard with seismic reflection data in Memphis, Tennessee, USA. Part II: data analysis, interpretation and traveltime tomography. Near surface Geophysics, 8, 341-351. DOI: 10.3997/1873-0604.2010025.

Holzman M.; 1963: Chebyshev optimized geophone arrays. Geophysics, 28, 145-155.

Malehmir A., Bastani M., Krawczyk C.M., Gurk M., Ismail N., Polom U. and Persson L.; 2013: Geophysical assessment and geotechnical investigation of quick-clay landslides – a Swedish case study. Near surface Geophysics, 11, 341-350. DOI: 10.3997/1873-0604.2013010

Miller R. and Steeples D.; 1994: Applications of shallow high-resolution seismic reflection to various environmental problems. Journal of Applied Geophysics, 31, 65-72.

Pugin A., Pullan S., Hunter L. and Oldenborger G.; 2009: Hydrogeological prospecting using P- and S-wave landstreamer seismic reflection methods. Near surface Geophysics, 7, 315-327. DOI: 10.3997/1873-0604.2009033.

Shtivelman V.; 2003: Application of shallow seismic methods to engineering, environmental and groundwater investigations. Bolletino di Geofisica Teorica ed Applicata, 44, 209-222.

Steeples D. and Miller R.; 1998: Avoiding pitfalls in shallow seismic reflection surveys. Geophysics, 63(4), 1213-1224.

Stucchi E., Ribolini A. and Anfuso A.; 2013: High resolution reflection seismic at the Patigno landslide, Northern Apennines, Italy. Accepted for publication in Near Surface Geophysics.

Zelt C. A. and Smith R.B.; 1992: Seismic traveltime inversion for 2-D crustal velocity structure. Geophysical Journal International, 108, 16-34.

SEPARATION AND IMAGING OF SEISMIC DIFFRACTIONS

D. Urbano, V. Lipari
Dipartimento di Elettronica, Informazione e Bioingegneria, Politecnico di Milano, Italy

Introduction. Diffracted and reflected seismic waves are different physical phenomena originating from different kinds of subsurface features. Usually, in seismic exploration, the focus is on seismic reflections because they carry most of the information about subsurface.

However, sometimes the goal of seismic processing consists in identifying small subsurface features (e.g. faults, fractures and rough edges of salt bodies) or small changes in reflectivity. In all these cases it is diffracted waves which contain the most valuable information (Kanasewich, and Phadke, 1988; Landa and Keydar, 1998). Over the last decade there has been an increasing interest in using diffractions as a direct indicator of different kinds of discontinuities. The energy carried by diffractions can be also used to refine velocity models (Harlan *et al*., 1984; Landa *et al*., 2008; Reshef and Landa, 2009). Tsingas *et al.* (2012) proposed to use diffraction imaging as a tool for helping interpretation in fractured reservoirs.

Typically diffracted energy is one or even two order of magnitude weaker than reflected one and often it is not easy to distinguish the diffracted events in a full dataset or to identify the image of diffractors in a full seismic migrated image. Therefore, diffractions have to be separated from reflections for imaging or other kind of processing and this still represents one of the main issues when handling diffractions.

Several approaches were proposed for the separation of reflections and diffractions, and several different domains were used for this purpose.

Khaidukov *et al.* (2004) take advantage of the different propagation properties of the waves. The recorded wavefield is focused back to the imaginary source location in a pseudo-depth domain and then the reflections are muted out. After defocusing of this muted data they obtain a wavefield where reflection events have been suppressed. Taner *et al.* (2006) show how to separate reflections and diffractions using plane-wave constant p sections. In this domain reflection energy can be filtered out by the method of plane-wave destructors (PWD) (Claerbout, 1992; Fomel, 2002). Separation of diffractions and reflections and imaging of diffractions by dip-filtering via the same PWD operator, but this time in the post-stack migrated domain, is discussed by Fomel *et al.* (2007).

Separation in the post-migration dip-angle gathers, where reflections always have a concave shape (Audebert *et al*., 2002) and diffraction have a different shape (horizontal if migration was performed with the correct velocity) has been proposed by Landa *et al.* (2008) and Reshef and Landa (2009).

In this work we analyze separation of diffractions in the migrated image domain via two algorithms belonging to the last two mentioned methodologies. First we analyze the peculiarities of the separation via dip-filtering of the migrated image. We introduce a different filtering technique based on the local image gradient. Then we illustrate the properties of the dip-angle common image gathers and we analyze the behavior of this domain in the context of separation of diffractions. Finally, we propose to combine these methodologies in an original technique that aims to take advantage of both. The effectiveness of the method has been tested on both synthetic and field datasets. Here we show an example on the synthetic Sigsbee dataset.

Separation of diffractions via dip-filtering in the depth image domain. The first studied technique is a variation of the method proposed by Fomel *et al.* (2007) which performs separation of diffractions by dip filtering in the post-stack domain.

The use of dip-filtering in the depth migrated image domain as a method for separating diffractions is based on the underlying assumption that, in a migrated section, reflections are imaged as strong coherent events with a dip that changes with continuity. On the contrary diffractions are imaged as very localized coherent events that do not show any identifiable dip.

Thus, once the events that show clearly identifiable and slowly variable dip are removed, the remaining coherent events are interpreted as diffractions.

The result of dip filtering is an image that shows an approximation of all those events that do not follow the dominant trend of dips. Therefore we can use this result as an estimation of the migrated image of the diffractions. Even in the case of incorrect migration velocity the diffractions can be identified and separated by this methodology because they appear as little "smiles" (in the case of overestimated migration velocity) or "frowns" (in the case of underestimated migration velocity) and they still do not follow the dominant trend of dips. This peculiarity means that, after the separation of diffractions, this domain could be suitable for a velocity analysis based on the focusing of diffraction events.

Fomel *et al.* (2007) use the method of plane-wave destructors (Claerbout, 1992; Fomel, 2002) for dip filtering. In our study we use a different filter based on the gradient squared tensor (GST) as a tool for dip estimation (van Vliet and Verbeek, 1995), because of the easier parametrization, the lower computational complexity, and the presence of a dip coherency output.

GST exploits the eigenvectors of the dyadic product of the gradient vector with itself ($g \bullet g^t$) to estimate the local slopes. The additional feature of dip estimation by the GST method is that it gives the coherency of the local estimate as an auxiliary output, originally called "anisotropy" (van Vliet and Verbeek, 1995). The value of the local dip coherency varies from 0 to 1. A value of 0 corresponds to a perfect isotropy: no dominant dip has been clearly identified, therefore the estimated dip value is not reliable. A value of 1 means that the local neighborhood of the examined point exhibits the same behavior; therefore the estimated dip is very reliable.

Local gradients, GST eigenvectors and local dip coherency can be used to build very accurate dip filters (Hale, 2007), which can be used to properly enhance or remove events showing a certain dip, respectively emphasizing coherent events or revealing underlying information (residual image).

This methodology works quite well in eliminating reflection events. However, the residual image can also contain noise, effects of uneven illumination, edge effects due to limited migration aperture and other kinds of spurious events besides the desired diffractions.

Separation of diffractions in the migrated dip angle domain. The second methodology studied consists in separation of diffractions and reflections in the dip angles domain at the depth point.

Among the well-known reflection angle common image gathers (CIGs), it is possible to obtain, as an output of the migration process, the so called dip-angle CIGs which show the image of the events as a function of the imaged reflector's dip (i.e. the dip of the vector obtained by summing the incident and the reflected slowness vectors). The dip-angle CIGs have been used as a tool for equalization of illumination in depth migrated images, for true amplitude migration (Audebert *et al.*, 2000), for optimal migration aperture estimation (Bienati *et al.*, 2009) and for velocity analysis (Reshef and Ruger, 2005)

In this domain we are essentially looking at the direction in which the incident energy is sent back. In the case of a reflector the wavefield follows the Snell's law, therefore it is sent back in a single direction, which is univocally identified by the actual reflector's dip. In the case of a point diffractor the incident energy is sent back in all directions. In the dip angle domain these directions are identified by the stationarity of the events' moveout. The stationary points are preserved when summing over the dips according with the stationary phase principle.

To be more precise, when migrated with the correct velocity, a diffraction appears as a flat horizontal event if the dip-angle CIG is located exactly above the point diffractor, and as a dipping event if the CIG is relative to an horizontal position near the diffractor. On the contrary the reflections appears as concave events where the apex indicates the actual reflector's dip. The different behavior of diffractions and reflections in this domain can be exploited for the separation of diffractions e.g. by means of dip filtering of flat horizontal events.

The moveouts of reflection and diffractions are different and clearly recognizable even in the case of migration with wrong velocity. In this case the imprint of a reflection is still a

concave event. The analytical expressions of reflection and diffraction moveouts in constant velocity media can be found in Landa *et al.* (2008).

In particular, in the zero offset case, the imprint of a flat reflector in the dip-angle gather located at x is the following:

$$z(x,\alpha) = \frac{(z_0 \cos\alpha_0 + x \sin\alpha_0) v_M \cos\alpha}{v - v_M \sin\alpha_0 \cos\alpha}$$

Here v is the medium velocity, v_M is the migration velocity, α is the dip angle, α_0 is the actual reflector's dip. The reflector is described by the equation: $z(x) = z_0 + x \tan\alpha_0$. Note that, if the migration is performed with the correct velocity ($v_M = v$), then the stationary point occurs at the actual reflector's dip: $\alpha = \alpha_0$.

The shape of a diffractor point in the dip-angle gather located at x is:

$$z(x,\alpha) = \frac{v_M \cos\alpha [(x - x_0) v_M \sin\alpha + D]}{v^2 - v_M^2 \sin^2\alpha_0}$$

where $D = \sqrt{z_0^2 (v^2 - v_M^2 \sin^2\alpha) + (x - x_0)^2 v^2}$. Thus, when migrating with the correct velocity, the shape of a diffraction point in the gather located exactly above is a horizontal flat line which corresponds to illuminating the diffractor uniformly from all directions. If the gather is not located just above the diffractor the shape is a curve with no stationary points.

It is possible to take advantage of the local discrepancy between reflection and diffraction events and use dip-filtering in this domain, in order to separate diffractions which do not follow the dominant trend of dips.

Being substantially a pre-stack domain, the dip-angle gathers are more prone to noise with respect to the post-stack image domain and this can lead to an incorrect dip estimation which causes artifacts in the dip-filtered gather and in the subsequent migrated image of the diffractors (i. e. the stack over the dip angles). On the other hand the dip-angles domain has the advantage that the shape of diffractions is clearly identified and other kind of spurious events cannot be mistaken for them. Diffractions look significantly different from reflections in the common-image gathers and unlike reflections, they are affected by velocity errors in the conventional way. These two characteristics mean that also this domain could be used to perform effective migration velocity analysis by using the moveout of diffraction events.

Combined separation technique. The aim of our work was to unify the two methodologies mentioned above in order to exploit the peculiarity of each. The input data is depth migrated image in the dip-angle CIG domain. The algorithm is made of the three following steps:

1. local slopes are estimated on the stack image through a filter based on the gradient square tensor method;
2. dip filtering of each constant dip angle image is performed. It removes strong coherent events with continuously variable slopes calculated at step 1. In this way, being the filter a linear operator, we obtain the contribution of each common angle panel to the final residual consisting in all events, including seismic diffractions, that do not follow the dominant slope pattern. After this step we have eliminated the reflection but, besides the diffractions, there are still spurious events due to migration artifacts, uneven illumination or noise;
3. each dip-angle CIG is then further processed, this time in a way that emphasizes the coherent events through the local coherency of the filter. Indeed, in the dip angle domain, the diffracted events are strong coherent events (horizontal events if migrated with the correct velocity), on the other hand the remaining spurious events do not usually show a clearly identifiable dip. Therefore by applying a mask proportional to the local coherency of the dips estimated in the dip angle CIGs the true diffractions are emphasized compared with the spurious events.

If the energy of the reflections has been correctly removed in the dip filtering step it is possible to emphasize only the true diffractions with a low computational effort. This is also a drawback of the algorithm: also the residual reflections which survive to the dip filtering step (e.g. due to an incorrect dip estimation) could be emphasized through the application of the mask, being coherent events as well.

Example. As an example we show the synthetic Sigsbee 2A dataset released by the SMAART JV consortium.

This model contains a sedimentary sequence broken up by a number of normal and thrust faults. In the sedimentary sequence are embedded two dozens of point diffractors, regularly

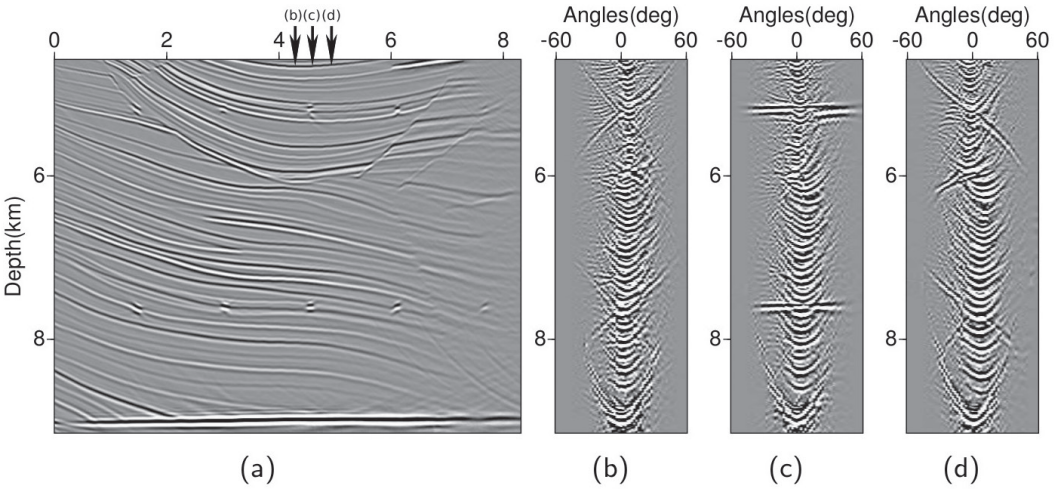

Fig. 1 – Migrated image of the Sigsbee 2A synthetic dataset: image 1-a is a zoom of the zone with the diffractor point. The black arrows b c and d point to the location of the dip-angle common image gathers of images 1-b, 1-c and 1-d respectively.

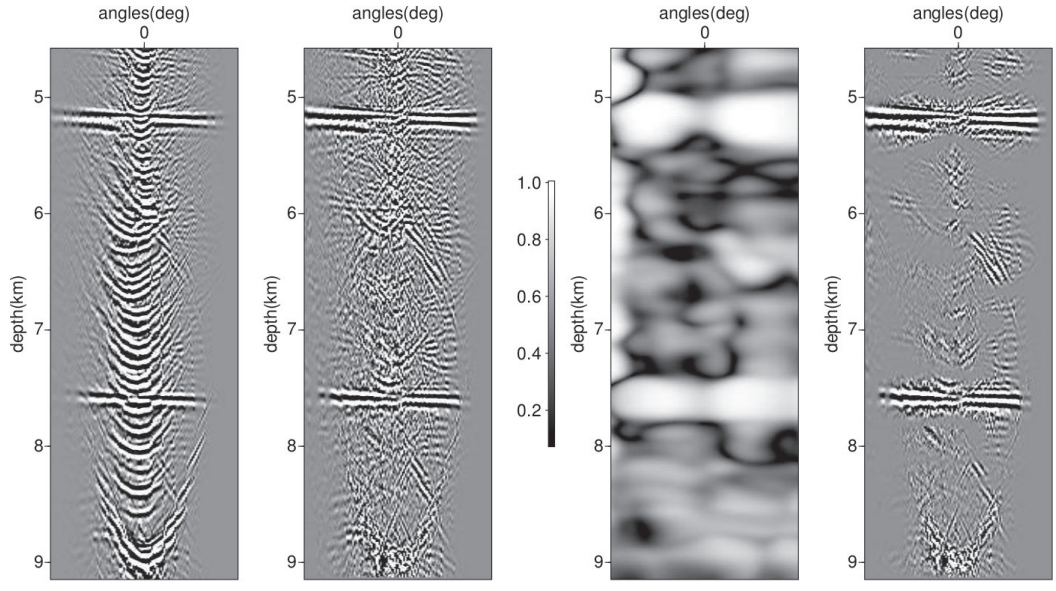

Fig. 2 – From left to right: first, a dip-angle CIG located exactly in correspondence of two diffractor points. Second, a dip-angle CIG in the same location after removal of reflection via dip-filtering. Third, local dip coherency estimated on the previous CIG. Fourth, enhancement of diffraction on the second dip-angle CIG.

positioned at two different depths. As an additional issue, there is a complex salt structure found within the model that causes illumination problems when migrating the data.

In Fig. 1 a part of the migrated section is shown in the image at left. The 3 arrows on top of the image indicate the locations of the three dip-angle CIGs shown in the images at right. In particular panel 1c is located exactly above two isolated diffractor points. The diffractions are clearly visible in panel 1c as two strong horizontal events embedded in a pattern of concave events. Being this gather located on a sedimentary sequence, it is noticeable how the apex of the concave events are positioned approximately at the same lateral position in the gather. This is what we expected for a sequence of approximately parallel events. Images 2b and 2d show two dip-angle gathers located at the right and at the left of the same point diffractors. Also in these gathers diffractions are easy to distinguish from the dominant pattern of concave reflections. Here they appear as dipping events whose slopes are determined by the horizontal distance between the location of the gather and the location of the diffractor.

The images of Fig. 2 illustrates, from left to right, the effect of three steps of the proposed procedure in the dip-angle gathers. First the original dip-angle CIG, on a location exactly above two point diffractors, is shown. The diffractors are quite noticeable as the strong horizontal events. Also the concave events corresponding to reflections are easily identifiable. The second image shows a CIG correspond to the same location, this time after dip-filtering on the common dip images: the concave events corresponding to reflections have been correctly removed while the diffractors have been properly preserved. However, several other events with no easy interpretation are present in addition to the two evident diffractions. In the third image from left the estimated local coherency computed on the previous CIG is shown. It is quite evident that the two strong diffractors are clearly identified as large zones of high coherency. Finally in the last image the regions of high coherency have been emphasized leading to an enhancement of the actual diffraction events.

In Fig. 3 we show a depth migrated section of the Sigsbee 2A dataset in the zone of the point diffractors. In the left image the result of the depth migration is shown. In the image at right the migrated image of enhanced diffractions is shown (i.e. the stack over dip angles of the enhanced CIGs). It is noticeable that most of the reflectors have been properly removed and that diffractor points have been highlighted.

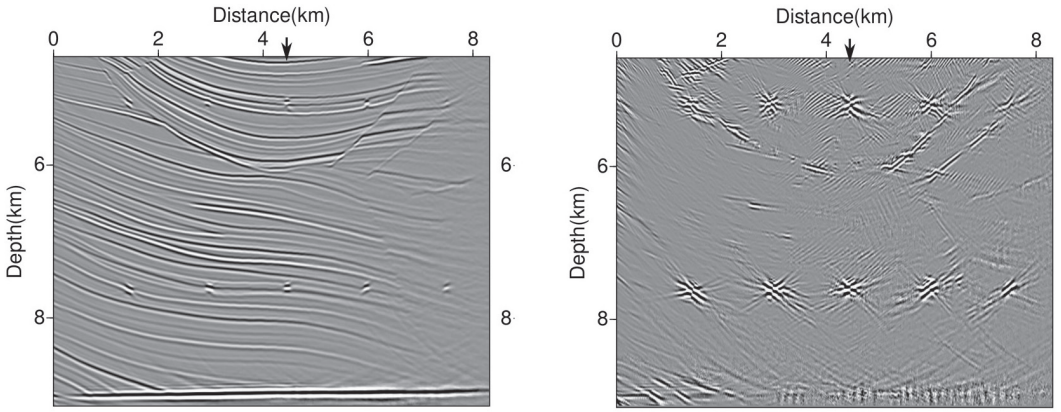

Fig. 3 – Migrated section of the Sigsbee 2A dataset. Zoom of the zone of the point diffractors, before (left) and after (right) separation and enhancement of diffractions. The arrow refers to the position where the common image gather in Fig. 2 is placed.

Conclusions and future works. Diffractions are reliable indicators of small structural and lithological elements of the subsurface. However, since they are order of magnitudes less

energetic than reflections, it is necessary to separate diffraction from reflections in order to perform diffraction imaging and processing.

We analyzed separation of diffractions by dip-filtering in the post-stack domain and separation in the dip-angle gathers. Then a strategy for separation of diffractions from reflections in the depth migrated images has been developed, based on a combination of the previously analyzed algorithms and taking advantage of the virtues of both. The strategy has been tested with promising results on both synthetic and field data. Although separation of reflection and diffraction energy can never be exact, the proposed methodology achieves the practical purpose of enhancing diffractive response of small subsurface discontinuities. Here an example of separation of diffraction in the synthetic Sigsbee 2A dataset is shown. Future works will be focused on the study of methodologies for the actual use of diffraction for velocity analysis, both in the post-stack depth migrated image and in the dip-angle gathers.

Acknowledgements. The authors wish to thank the Smaart JV consortium for releasing the Sigsbee 2A synthetic dataset.

References

Audebert F., Froidevaux P., Huard I., Nicoletis L. and Svay-Lucas J.; 2000: *A multi-angle toolbox for restored amplitude images and AVA-Gathers*. SEG Expanded Abstracts, MIG 10.4.

Audebert, F., Froidevaux,P., Racotoarisoa, H., Svay-Lucas, J.; 2002: *Insights into migration in the angle domain*. SEG Expanded Abstracts, 1188-1191.

Bienati N., Andreoletti C., Perrone F., Lipari V., Giboli M.; 2009: *Limited Aperture Migration in the Angle Domain*. 71st EAGE Conference & Exhibition

Fomel S.; 2002: *Applications of plane-wave destruction filters*. Geophysics, 67, 1946–1960.

Fomel S., Landa E., and Taner M.T.; 2007: *Poststack velocity analysis by separation and imaging of seismic diffractions*. Geophysics, 72, U89–U94

Hale D., 2007: *Local dip filtering with directional laplacians*. CWP Report, 567

Harlan, W. S., Claerbout J. F., and Rocca F.; 1984: *Signal/noise separation and velocity estimation: Geophysics*. 49, 1869-1880.

Kanasewich, E. R., and Phadke S. M.; 1988: *Imaging discontinuities on seismic sections*. Geophysics, 53, 334–345.

Khaidukov V., Landa E., and T. J. Moser T.J.; 2004: *Diffraction imaging by focusing-defocusing: An outlook on seismic superresolution*. Geophysics, 69, 1478–1490

Landa E., Fomel S., and Reshef M.; 2008: *Separation, imaging, and velocity analysis of seismic diffractions using migrated dip-angle gathers*. SEG Expanded Abstracts, 27, 2176.

Landa, E., and S. Keydar,; 1998: *Seismic monitoring of diffraction images for detection of local heterogeneities*. Geophysics, 63, 1093–1100.

Reshef M. and Landa E.; 2009: *Post-stack velocity analysis in the dip-angle domain using diffractions*. Geophysical Prospecting, 2009, 57, 811–821

Reshef, M., and Ruger A.; 2005: *Influence of structural dip on interval velocity analysis*. 75th Annual International Meeting, SEG, Expanded Abstracts, 2245–2248.

Taner M.T., Fomel S., and Landa E.; 2006: *Prestack separation of seismic diffractions using plane-wave decomposition*. SEG Expanded Abstracts, 25, 2401

Tsingas C., El Marfhoul B., and Dajani A.; 2010 *Fracture Detection by Diffraction Imaging*. 71st EAGE Conference & Exhibition

van Vliet L. J., and Verbeek P. W.; 1995: *Estimators for Orientation and Anisotropy in Digitized Images*, ASCI, 442-450

CALIBRATION OF A NEW UNCOUPLED ACOUSTIC SENSOR FOR GROUND MOTION DETECTION

A. Vesnaver[1,2], E. Poggiagliolmi[3], F. Brunetti[1], D. Zuliani[1]
[1] *OGS - Istituto Nazionale di Oceanografia e di Geofisica Sperimentale, Trieste, Italy*
[2] *King Fahd University of Petroleum and Minerals, Dhahran, Saudi Arabia*
[3] *Entec Integrated Technologies, London, United Kingdom*

Introduction. A standard geophone for seismic surveys is coupled to the ground by a spike. This device records the ground motion with respect to an inertial mass attached to a coil in a magnetic field, both suspended by a spring. Geophones have been used for decades in the oil and gas exploration industry and they are currently being employed in seismic recording systems with a number of channels exceeding 200,000. Even larger systems, totaling 1 million receivers, have been announced to be commercially available in the coming months. The number of geophones equals the channel number only in the uncommon case of single-sensor recording: more often, a small array of geophones is connected to each channel (e.g., a dozen). Consequently, the total number of geophones to be planted and retrieved during these surveys exceeds already 1 million. The ensuing field operations require crews composed of hundreds of people, which result in high costs and demanding logistics. In desert areas (as in the Middle East and North Africa, or Arctic) mobilizing people and instruments is the main problem, while in urban areas planting spikes into the ground may be unfeasible, because it may damage roads, yards and building. Uncoupled sensors are much less invasive and, if properly miniaturized, their weight and volume may be significantly smaller than standard geophones based on a moving coil.

Removing the coupling of sensors to the ground not only reduces the required man-power significantly, but also improves the signal quality. The coupling with the ground may be very poor in the sandy deserts of North Africa and Middle East, or in the permafrost of Canada and Siberia, where a major share of hydrocarbon reserves are located. For these reasons, we have been developing an uncoupled acoustic sensor that should provide better signal quality at lower costs of surveys on land (Poggiagliolmi *et al.*, 2012, 2013). In this paper, we present the basic principles and the calibration results obtained in the laboratory to compare the performance of the new device with that one of standard geophones for land seismic surveys.

Uncoupled sensor description. Fig. 1 shows the basic principle of the proposed uncoupled sensor. A piezoelectric transmitter emits a continuous acoustic carrier frequency, which impinges on the ground surface where it is Doppler modulated by the ground's vibrations. The back-scattered signal is recorded by a piezoelectric receiver, and the resulting Doppler frequency shift is used to measure the ground displacement or velocity.

A few prototypes of the new sensors have been made and tested both in the field and the lab. Field tests were carried out for different ground types: glass panes, cotto tiles, fine and coarse gravel, sand, leaves, pine needles, among others (Poggiagliolmi *et al.*, 2012, 2013), with very encouraging results. Quite surprisingly, the energy of the back-scattered signal is not decreasing so much with the roughness of the target surface; instead, the main effect observed is a less sensitive dependence on the dip angle of such a surface with respect to the source. For very flat surfaces (as glass panes or cotto tiles) such angular dependence is much higher. The back-scattered signal is strong in two

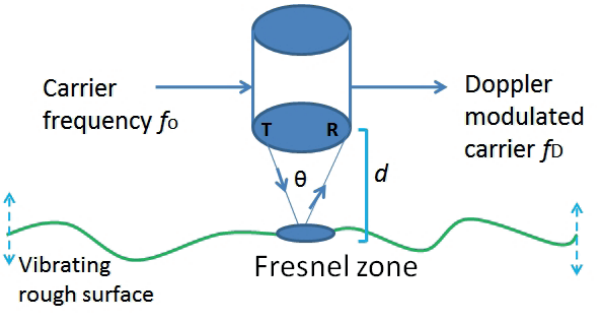

Fig. 1 – General scheme for an acoustic uncoupled sensor.

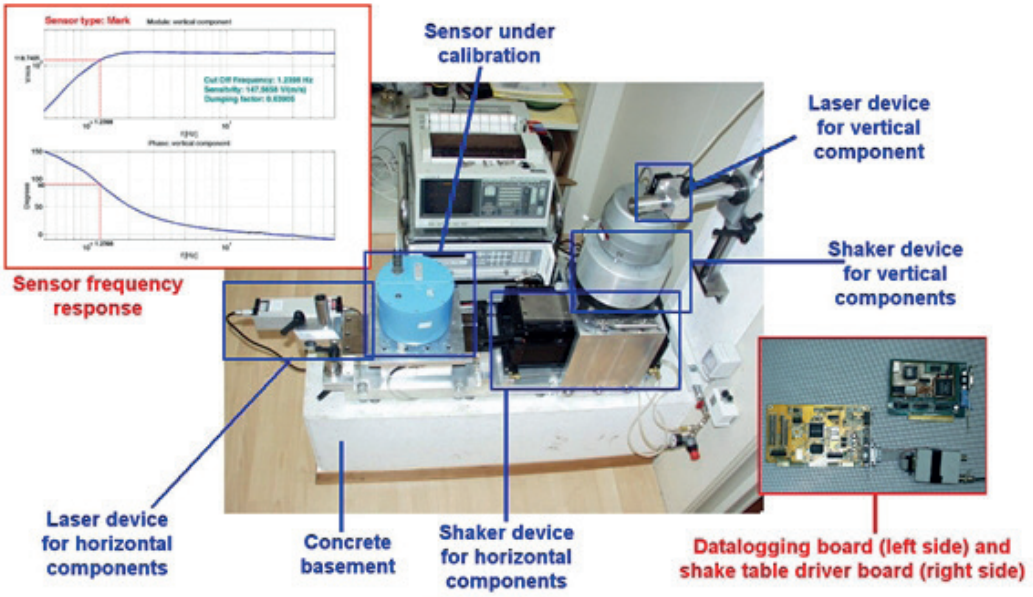

Fig. 2 – Shaker table system at the OGS Centre of Seismological Research in Udine.

extreme cases: either for very smooth surface (as glass or tiles) for a narrow incidence angle close to the orthogonal direction, or for very rough surfaces (as coarse gravel) for dipping angles exceeding 15 degrees. For more realistic surfaces found in nature, e.g., sand, the signal strength was considerably above the minimum threshold required for reliable detection of Doppler shift.

As part of the ongoing uncoupled sensor development and characterization program, field tests were followed by quantitative laboratory measurements on the most recent prototype. The particular measurements described herein consisted of comparisons between the performance of the new prototype and that of a conventional 10-Hz geophone, which is normally used for large scale seismic surveys for oil and gas exploration and production. Needless to say, this and other geophone types require planting by a spike. Fig. 2 displays the shaker table apparatus built and used at the Seismological Research Centre of OGS in Udine, able to generate controlled frequency signals in the range from 0.3 to 100 Hz (Ponton *et al.*, 2002). This setup was employed to calibrate the response of the uncoupled sensor for a range of spot frequencies.

The calibration system hardware includes a shaker table, a laser interferometer, a custom-made interface board that allows for A/D conversion between the laser interferometer and a personal computer. An audio board and a M24 Lennartz data logger is also included (Fig. 2). The shaker table is mounted on a 500 kg reinforced cement base. The system software has been written using MatLab. An automatic procedure was devised to determine the response curves of the sensors. The input, broadband signal, used to drive the shaker table, is designed to fit the characteristics of the sensor type being calibrated (i.e., velocimeter or accelerometer), its nominal peak frequency response and the target frequency range. For short period instruments, reliable response curves can be estimated in the time span of a few minutes, whereas longer acquisition times are required for broadband sensors.

Spectral response. Further calibration tests were carried out at the Oceanographic Calibration Laboratory of OGS in Trieste, because its accurate temperature control and good acoustic insulation can minimize the environmental noise. A 24-bit multi-channel acquisition system was used to collect data from a standard geophone and the uncoupled sensor. No filters were applied as our goal was to study the signal properties without distortions. Both sensors measured signals with a level well above the noise floor. The measurements carried out with this system are optimal above 5 Hz, because the shaker tabled used in that case was built and optimized for standard 10-Hz geophones, commonly used for seismic surveys. Instead, the calibration system available at the Centre of Seismological Research in Udine is targeting quite lower frequencies, up to 0.1 Hz, which are relevant for earthquake monitoring. The integration of these two frequency ranges was needed, therefore, for appreciating the capabilities of the new device.

Fig. 3 shows the amplitude spectra of signals provided by a 10-Hz geophone and the uncoupled acoustic sensor. The spectra obtained from both receivers display a major peak at the expected frequency of 10 Hz, and a similar trend for the noise at other frequencies. Away from the peak the standard geophone shows essentially the ambient noise above the acquisition system noise floor. Assuming that the ambient noise is identical for both the geophone and the new sensor, the noise level of the latter is higher (about 20 dB) within the band of frequencies between 1 and 100 Hz. We expect that by

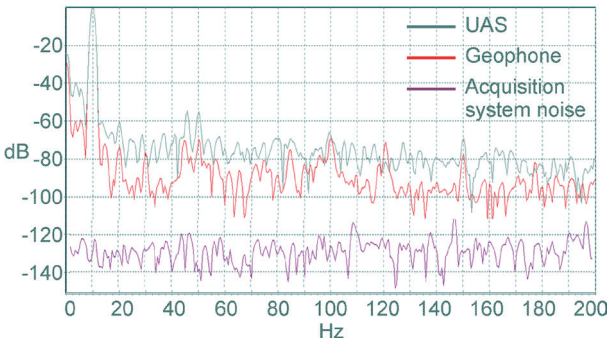

Fig. 3 – Response at shaker table for 10 Hz from the uncoupled acoustic sensor (grey), a 10-Hz standard geophone (red) and the acquisition system noise (magenta).

improving some of the prototype electronics, and in particular the low-noise circuitry, the performance of the new sensor to be very close or to out-perform the acquisition system employing conventional geophones. This is expected at the lowest frequencies below the geophone natural frequency, where the sensitivity of the standard geophone declines sharply, unlike the new prototype.

Further measurements and manufacturing improvements are ongoing. We expect possible drawbacks due to temperature changes between the sensor and the vibrating surface, because in principle these changes could affect the sound speed and, consequently, the observed time shifts. Fortunately, our early tests show that such a phenomenon is barely observable, when temperature changes are not extreme. Systematic laboratory and field tests are needed (and planned) to quantify precisely this effect.

Conclusions. Uncoupled acoustic sensors have relevant potential applications both for active seismic on land and for seismological recording. In the first case, a faster and cheaper data acquisition is envisaged, as well as a reduction of signal distortions due to coupling with loose grounds (see e.g. Robinson and Husseini, 1982, among others). In the second case, the direct recording of the displacement, instead of velocity or acceleration, may provide more accurate data for estimating earthquakes' magnitude.

Acknowledgements. Our work was partially supported by the Grant n. 11-OIL1638-04 in the NSTIP Program by KACST, Riyadh, Saudi Arabia. We thank Stefano Gustin (Microsum) for his contribution to the prototype development, and Luca Baradello, Daniel Nieto, Lorenzo Petronio and Franco Zgauc (OGS) for their valuable help.

References

Poggiagliolmi E., Vesnaver A., Nieto D. and Baradello L.; 2012: The application of uncoupled sensors to seismic exploration, Expanded Abstracts, SEG/KOC Workshop on Global Single Sensor Acquisition, Kuwait City (Kuwait).

Poggiagliolmi E., Vesnaver A., Nieto D. and Baradello L.; 2013: An uncoupled acoustic sensor for land seismic acquisition, 75th EAGE Meeting, Extended Abstracts, London (United Kingdom), We 04 16.

Ponton F., Di Bartolomeo P., A. Govoni and D. Zuliani; 2002: Seismometer calibration at OGS, XXVIII General Assembly of the European Seismological Commission, University of Genoa, September 2-8 2002.

Robinson D. K. and Husseini M. I.; 1982: Technique for reflection prospecting in the Rub' Al-Khali. Geophysics 18, 54-69.

sessione 3.2

Metodi elettro-magnetici e gravimetrici

Convenor: M. Fedi e G. Santarato

co-organizzata con Sezione Italiana Eage-Seg

IMAGING AUTOMATICO DI CAMPI DI POTENZIALE

M.A. Abbas[1,2] e M. Fedi[1]

[1] *Dipartimento di Scienze della Terra, Università di Napoli Federico II, Napoli, Italy*

[2] *Geology Department, South Valley University, Qena, Egypt*

Introduzione. Fedi (2007) ha introdotto il metodo *DEXP* (*Depth from Extreme Points*) per stimare la profondità delle sorgenti dei campi di potenziale scalando il campo o le sue derivate parziali con una legge di scala determinata a partire dai dati stessi. Tale legge di scala dipende dall'indice strutturale, che è l'opposto del grado di omogeneità per i campi che soddisfano l'equazione di omogeneità. Il metodo è stato applicato ai dati gravimetrici, magnetici e di potenziale spontaneo, per fornire un'immagine della distribuzione delle sorgenti (Fedi, 2007; Fedi e Abbas, 2013; Fedi e Pilkington, 2012). In questa nota descriviamo una versione automatica del metodo DEXP che ha due notevoli caratteristiche: a) utilizza una legge di scala che non dipende dall'indice strutturale delle sorgenti, b) è completamente automatico in modo che possa essere implementato come un veloce metodo di imaging.

Teoria. Il concetto fondamentale della teoria DEXP è la funzione di scala τ, definita come la derivata del logaritmo del campo potenziale, f, o una delle sue derivate parziali, rispetto a $log\,(z)$ (Fedi, 2007):

$$\tau = \frac{\partial \log(f)}{\partial \log(z)} \qquad (1)$$

Quindi, la funzione di scala per i campi omogenei, a $x = x_0$ e $y = y_0$, o lungo le linee definite dagli zeri della derivata orizzontale del campo (Fedi *et al.*, 2009) è la seguente:

$$\tau = -\frac{Nz}{z - z_0} \qquad (2)$$

dove N è l'indice strutturale, una quantità correlata alla geometria della sorgente.

Questa relazione può essere generalizzata a qualsiasi ordine p^o di derivata di f attraverso la legge:

$$\tau_p = -\frac{(N + p)z}{z - z_0} \qquad (3)$$

Fedi (2007) ha mostrato che la trasformazione DEXP può essere utilizzata per valutare nei suoi punti estremi la profondità delle sorgenti. Ha definito la trasformazione DEXP Ω come:

$$\Omega = z^{N_p/2} f \qquad (4)$$

dove

$$N_p = N + p \qquad (5)$$

Dall'Eq. (4), notiamo che la legge di scala dipende dal valore dell'indice strutturale. Questa caratteristica rende questo metodo più versatile e preciso rispetto ad altri metodi di imaging quali la migrazione, la correlazione e altri, che utilizzano un weighting prefissato nelle loro leggi di scala (Fedi e Pilkington, 2012). La qualità del risultato dipende dalla scelta di N, che può tuttavia essere facilmente valutato prima di eseguire la trasformazione (ad esempio, Fedi, 2007;. Cella *et al*, 2009).

Il metodo proposto in questa nota è una modifica del metodo DEXP, sulla base dell'Eq. (5), che assicura proprietà importanti per la funzione di scala del rapporto di due derivate di f di differente ordine.

Per dimostrare questo, consideriamo il rapporto $\Re_{mn} = f_m / f_n$, tra due derivate parziali di diverso ordine di un campo omogeneo f ; f_m e f_n, dove m ed n sono i rispettivi ordini di differenziazione. Dall'Eq. (1) si trova facilmente che la funzione di scala di $\Re_{mn}$ è:

$$\tau(\Re_{mn}) = \tau\left(\frac{f_m}{f_n}\right) = \frac{\partial \log\left(\frac{f_m}{f_n}\right)}{\partial \log(z)} = \frac{\partial \log(f_m)}{\partial \log(z)} - \frac{\partial \log(f_n)}{\partial \log(z)} = \tau(f_m) - \tau(f_n) \qquad (6)$$

Dalle Eqq. (3) e (6), si nota che in $x = x_0$ e $y = y_0$, $\tau(\Re_{mn})$ assume la forma:

$$\tau(\Re_{mn}) = -\frac{(m-n)z}{z - z_0} \qquad (7)$$

Il punto interessante nell'Eq. (7) è che t è indipendente dall'indice strutturale e dipende solo dalla differenza tra gli ordini delle due derivate. In particolare, quando $z = -z_0$, t è data da:

$$\tau(\Re_{mn})\Big|_{z=-z_0} = -\frac{(m-n)}{2} \qquad (8)$$

Così, la trasformata DEXP del rapporto tra due ordini di campo omogeneo *f* è semplicemente:

$$\Omega = z^{(m-n)/2}\,\Re_{mn} \qquad (9)$$

Poiché l'esponente (*m*-*n*)/2 è determinato, la trasformazione DEXP è completamente automatica. Come mostrato in Fedi (2007), la profondità alle sorgenti può quindi essere ottenuta semplicemente stimando le posizioni degli estremi di Ω, cioè dell'immagine DEXP. Questo tipo di DEXP automatica può essere quindi applicata al rapporto tra due derivate di diverso ordine del campo gravimetrico, magnetico o del potenziale spontaneo.

Un altro modo per applicare il metodo DEXP è quello di considerare la trasformazione DEXP della derivata dell' *l*-ordine del rapporto. Infatti, essendo il rapporto $\Re_{mn}$ omogeneo di ordine *m*-*n*, la sua derivata l^{ma} sarà omogenea di ordine *m*-*n*+*l*. La funzione di scala corrispondente e la trasformazione DEXP saranno date da:

$$\tau\left(\frac{\partial^l}{\partial z^l}(\Re_{mn})\right) = -\frac{(m-n+l)z}{(z-z_0)} \qquad (10)$$

$$\Omega = z^{(m-n+l)/2}\,\frac{\partial^l}{\partial z^l}(\Re_{mn}) \qquad (11)$$

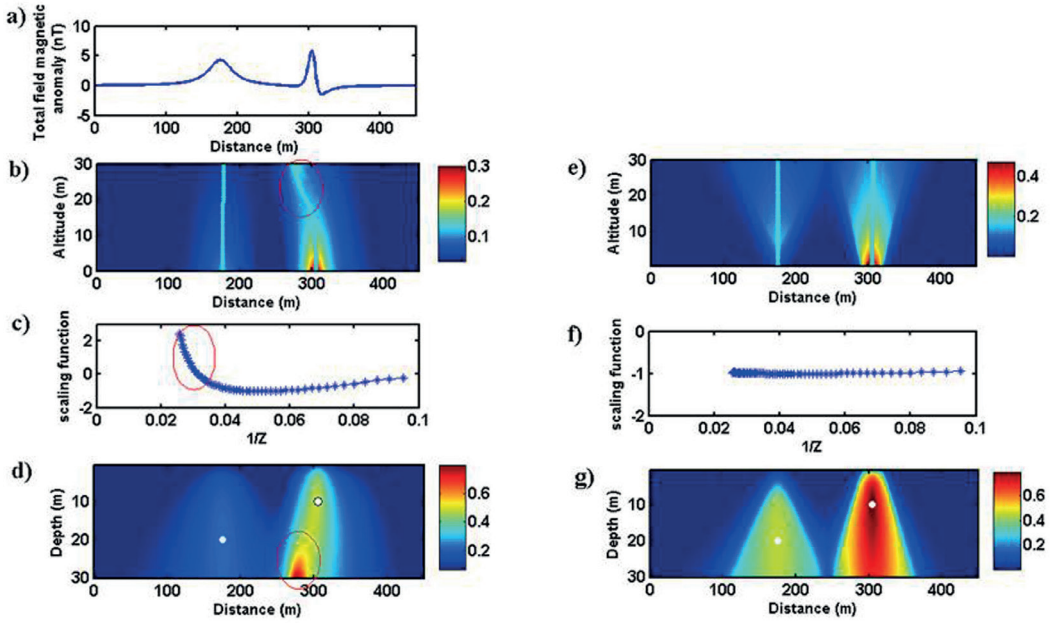

Fig. 1 – La trasformazione automatica DEXP applicata al campo magnetico di un modello multi-sorgente (cilindro orizzontale e dicco). a) Il profilo del campo magnetico totale anomalia, b) il rapporto R_{2l} a diverse quote e le linee di estremi (linee continue in azzurro), c) la funzione di scala lungo la linea di estremi destra in 'b', d) l'immagine DEXP del rapporto R_{2l}, i cerchi rossi indicano la zona di effetti di non-linearità a causa della interferenza. e) Il rapporto R_{43} diverse quote e le linee i estremi (linee continue in azzurro); f) la funzione di scala lungo la linea di estremi in 'e'; g) l'immagine DEXP del rapporto R_{43}. I punti bianchi indicano i massimi della DEXP, corrispondenti alla profondità corretta per entrambe le sorgenti.

Esempio. Abbiamo applicato il metodo al campo magnetico di un modello multi-sorgente (Fig. 1a): un cilindro orizzontale con un momento di dipolo 600 A/m^2 a (x_0, z_0) = (305,10) m, e un dicco verticale con 50 A/m^2 momento di dipolo a (x_0, z_0) = (175, 20) m. L'inclinazione magnetica è di 60° e la declinazione è 0°. Abbiamo applicato la trasformazione DEXP al rapporto $\Re_{21}$ tra il secondo e il primo ordine segnale analitico del campo. Innanzitutto notiamo una linea di estremi curva, in relazione al cilindro orizzontale (Fig. 1b). Anche la funzione di scala non è una linea retta (Fig. 1c). Questo comportamento dimostra che il problema è non lineare. Abbiamo quindi deciso di considerare derivate di ordine superiore e utilizzare la trasformazione DEXP al rapporto $\Re_{43}$ tra i segnali analitici del quarto e terzo ordine. Le Figg. 1e ed 1f mostrano che la linea di estremi è ora retta (Fig. 1e), così come la funzione di scala (Fig. 1f). Ciò significa che la DEXP di $\Re_{43}$ ha una risoluzione sufficiente a rendere la non-linearità intrinseca del problema trascurabile. Per quanto riguarda le immagini DEXP, gli effetti non-lineari a causa della interferenza delle due-sorgenti dell'anomalie sono evidenti quando si usa $\Re_{43}$, dove un ghost ad alta intensità appare a profondità maggiori di 25 m (Fig. 1d). Così la profondità al top del dicco è ben stimata (10 m), ma la profondità al centro del cilindro orizzontale è poco definita a causa dell'effetto di interferenza. Tuttavia, quando si utilizza la DEXP del rapporto $\Re_{43}$, il ghost scompare (Fig. 1g) ed entrambe le stime della profondità sono corrette. Si noti che questo risultato è stato possibile grazie alle proprietà ad alta risoluzione della trasformazione DEXP, che è stabile, indipendentemente dall'ordine di differenziazione (Cella *et al*., 2009;. Florio *et al*., 2009).

Conclusioni. In questo lavoro, abbiamo sviluppato un nuovo metodo di imaging DEXP che è completamente automatico e indipendente dall'indice strutturale. Queste proprietà sono ottenute applicando la trasformazione DEXP al rapporto tra una coppia di derivate di ordini differenti del campo e/o alle derivate parziali di questo rapporto. Questa versione automatica della trasformazione DEXP rende il metodo ancora più veloce e garantisce una stima precisa della profondità anche per grandi dataset.

Bibliografia

Cella, F., Fedi, M., and Florio, G., 2009. Toward a full multiscale approach to interpret potential fields. Geophysical Prospecting, 57 (4), 543–557.

Fedi, M., 2007. DEXP: A fast method to determine the depth and the structural index of potential fields sources. Geophysics, 72 (1), I1–I11.

Fedi, M., e Abbas, M. A., 2013. A fast interpretation of self-potential data using the depth from extreme points method. Geophysics, 78 (2), 1-10.

Fedi, M., Florio, G., e Quarta, T., 2009. Multiridge analysis of potential fields: geometrical method and reduced Euler deconvolution. Geophysics, 74, L53–L65.

Fedi, M., e Pilkington, M., 2012. Understanding imaging methods for potential field data. Geophysics, **77** (1), G13-G24.

Florio G., Fedi M. e Rapolla A., 2009. Interpretation of regional aeromagnetic data by multiscale methods: the case of Southern Apennines (Italy). Geophysical Prospecting, 57, 479-489.

INTEGRATED MARINE MAGNETICS OF THE NAPLES BAY – FROM OLD TO NEW DATA: EXAMPLES FROM NAPLES AND POZZUOLI GULFS (SOUTHERN ITALY)

G. Aiello, E. Marsella
Istituto per l'Ambiente Marino Costiero (IAMC), Consiglio Nazionale delle Ricerche (CNR), Napoli, Italy

Introduction. The integrated marine magnetics of the Naples Bay, coming from the old to the new data is here tentatively resumed and discussed, focussing on some examples from Naples and Pozzuoli Gulfs (Southern Italy).

Significant correlations between geophysical data come from the comparative analysis of seismic and magnetometric datasets. A magnetometer usually measures the strength or direction of the Earth's magnetic field. This last can vary both temporally and spatially for various reasons, including discontinuities between rocks and interaction among charged particles from the sun and the magnetosphere. Most technological advances dedicated to measure the Earth's magnetic field have taken place during World War II. The most common are: the fluxgate, the proton precession, Zeeman-effect, sensor-suspended magnet and satellite magnetometers. The fluxgate and the proton precession magnetometers are effectively the most used for marine surveys, they are both cable drown. The fluxgate magnetometer was the first ship-towed instrument, and it can measure vector components of the magnetic field. Its sensor consists of two magnetic alloy cores that are mounted in parallel configuration with the windings in opposition. The proton precession magnetometer consists of a sensor containing a liquid rich in protons surrounded by a coil conductor. The sensor is towed from the vessel through an armoured coaxial cable whose length depends on vessel length and seafloor depth. Circulating current within the coil generates a magnetic field of approximately two orders of magnitude the Earth's field. In this way, one proton each ten will follow the coil positioning. Stopping the induced magnetic field, the protons will align according to the Earth's magnetic field through a movement of precession.

The proton precession magnetometer is one of the most used for offshore surveys and it records the strength of the total field by determining the precessional frequency (f) of protons spinning about the total field vector ($\mathbf{F}$) as follows:

$$f=\gamma_p \mathbf{F}/2\pi \quad (1)$$

where γ_p is the gyromagnetic ratio of the proton uncorrected for the diamagnetic effect, so that knowing it from laboratory measurements, the total field in nanotesla can be calculated as:

$$\mathbf{F}=23.4866 \times f \quad (2)$$

The total magnetic field calculated through the Eq. (2) is stored by magnetometer into a string of data containing position data that is displayed as an x,y chart. The signal frequency is measured on a time span of 0.5 seconds when the signal-noise ratio is highest. To ensure a maximum value of initial value of proton precession the angle between the axis of the coil and the Earth's field it is necessary to use two orthogonal coils. The measured field must be corrected with respect to the regional field in order to evaluate the anomalies.

The proton precession magnetometer was largely used to explore magnetic anomalies in the Bay of Naples. Interesting examples of magnetic data acquisition related in the Naples and Pozzuoli bays are reported in Galdi *et al.* (1988), Secomandi *et al.* (2003), Aiello *et al.* (2004) and will be discussed in the following paragraphs.

Geologic and geophysical setting. In the Gulf of Naples one of the most important lineaments is the Somma-Vesuvius volcano. The Vesuvius volcano has been intensively studied with respect to the eruptive events, the recent seismicity, the geochemistry and the ground movements of the volcano and the related volcanic hazard (Cassano and La Torre, 1987; Santacroce *et al.*, 1987; Castellano *et al.*, 2002; Esposti Ongaro *et al.*, 2002; Mastrolorenzo *et al.*, 2002; Saccorotti *et al.*, 2002; Scarpa *et al.*, 2002; Todesco *et al.*, 2002). The Somma edifice started to grow after the eruption of the Campanian Ignimbrite deposits. Its eruptive

activity ranges from the "Pomici di Base" (18 ky) and the "Pomici Verdoline" plinian eruptions, enabling the collapse of the Somma edifice and the consequent calderization. Three main plinian eruptions ("Mercato", "Avellino" and "Pompei") followed among 7900 B.C. and 79 A.D. The total magnetic field map of the Somma-Vesuvius volcano (Fig. 1) shows interpretative elements that have an indicated value for the trend of volcanites in the volcanic complex's peripheral areas (Cassano and La Torre, 1987). A main sub-circular anomaly is centred on the volcano; two positive appendages diverge towards SE and SW. They might correspond to a great thickness of lava products, possibly in pre-existing depressions of the sedimentary basement of the graben of the Campania Plain. These products should have enhanced the occurrence of an elongated magnetized body, which tends to move towards the Naples Bay from the Vesuvius volcano towards Torre del Greco; an alternative explanation would be the presence of a strip of eruptive vents, settled on a system of NE-SW normal faults (Bernabini *et al.*, 1971; Finetti and Morelli, 1973). A new aeromagnetic map of the Vesuvius area has been produced (Paoletti *et al.*, 2005). It is dominated by a large dipolar anomaly related to the volcano, showing a southwards trending elliptical shape. A narrow anomaly is located on the western flank of the edifice and small anomalies are located on the south-eastern slope of the volcano. High frequency anomalies occur in the area surrounding the edifice, related to the high cultural noise of this densely inhabitated area.

The Phlegrean Fields are a volcanic district surrounding the western part of the Gulf of Naples, where volcanism has been active since at least 50 kyr (Rosi and Sbrana, 1987), corresponding to a resurgent caldera having a diameter of 12 km and erupting the Campanian Ignimbrite (37 ky B.P.) and the Neapolitan Yellow Tuff (12 ky B.P.) deposits. A volcano-tectonic uplift of the caldera center is indicated by coastal sediments ranging in age from 10 to 5.3 ky B.P., cropping out in correspondence to the marine terrace of La Starza (Gulf of Pozzuoli). Gravimetric and magnetometric informations available for the Phlegrean Fields have been summarized (Cassano and La Torre, 1987), focussing on volcanological and structural reconstruction of the area. From north to south, the most important gravimetric elements are the positive anomaly related to the carbonatic horst of the Massico Mount, the negative anomaly of the Volturno graben, the positive gravimetric anomalies of Villa Literno and Parete. The total magnetic field map (Cassano and La Torre, 1987; Fig. 1) has evidenced a strong positive anomaly in the area of Monte di Procida, related to the weaker anomalies of the Procida Channel, Procida and Ischia. It may be related to considerable volumes of lavas, confirmed by the presence of trachybasaltic and latitic eruptive centres at Procida. Another large

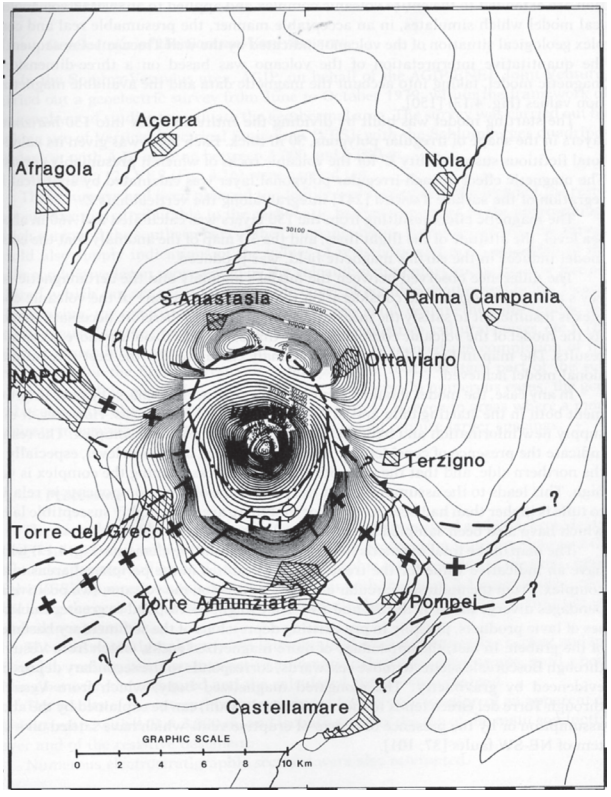

Fig. 1 – Total magnetic field map of the Somma-Vesuvius volcanic complex with sketch structural interpretation (modified after Cassano and La Torre, 1987).

magnetic anomaly characterizes the Astroni-Agnano volcanic area, probably the result of the overlapping of several lava bodies. A new aeromagnetic map supplement the northern sector of the Phlegrean Fields (Paoletti *et al*., 2004), allowing for a better geological interpretation of the structural patterns and morpho-structural features of the Volturno Plain and the Gulf of Pozzuoli and its offshore areas. The main magneto-structural features are the caldera rims of the Neapolitan Yellow Tuff and the Torregaveta anomaly. The Patria lake anomaly has a sub-circular shape and a diameter of about 10 km. A complex pattern of magnetic anomalies coincides with the Parete volcanic complex (Aiello *et al*., 2011), while another isolated anomaly corresponds to the Volturno river.

Data and methods. A Total Earth Magnetic Field (EMF) survey was performed in the Naples Bay during the oceanographic cruise GMS00-05 (Leg II – October November 2000) carried out by the CNR-IAMC of Naples, Italy onboard of the R/V Urania, resulting in a high resolution magnetic anomaly map of the Naples Bay (Aiello *et al*., 2004). The collected data have a densely-spaced coverage if compared to previous measurements, such as the airborne magnetic survey (Agip, 1981; Caratori Tontini *et al*., 2003). The acquisition of magnetic data at a shorter distance from the source and at a lower velocity has given more precise sampling and an improved field restoration. The magnetic data have been recorded using a G811 proton magnetometer; the sensor was placed in a fish towed at about 200 m from the ship and at an average depth of 15 m below the sea level. The magnetometer position was regularly controlled and recorded and the data were sampled at 3 sec, corresponding to an average spatial sampling of about 6.25 m. The magnetic anomaly map was compiled with a grid cell size of 200 m. A colorimetric scale expressed in nT is shown on the right side of the maps to quantify the intensity of measured magnetic anomalies. An accurate inspection of the magnetic lines recorded contemporaneously to the seismic lines has been preliminary carried out, since they showed spikes regular to the shot frequency. A non-linear filter has been used to remove the peaks due to non-geological sources. A repositioning of the marine lines has been carried out, taking into the account the offset among the fish and the GPS. The elimination of the variation for the diurnal component has been carried out using as reference magnetic station the geomagnetic observatory of L'Aquila. In order to recognize the total field anomaly linked to the geological structures, the values of the main magnetic field must be subtracted to the measured values corrected according to the Italian Geomagnetic Reference Field (Coticchia *et al*., 2001). Some factors contribute to explain the shifts in the magnetic field among adjacent navigation lines. They include the differences in height among the navigation lines and the inadequate removal of the variations of magnetic field due to the diurnal component. The elaboration of the magnetic data has been carried out according to a procedure of levelling, consisting in the removal of the short period magnetic variations.

The high resolution magnetic anomaly map of the Naples Bay. The main magnetic anomaly fields recognized on the high resolution magnetic anomaly map of the Naples Bay have been constrained by geological features based on the geologic interpretation and on the correlation with high resolution Multibeam bathymetry (Fig. 2; Aiello *et al*., 2004). The magnetic anomaly fields have been also correlated with morpho-structural features and volcanic edifices, recognized on high resolution seismic profiles recorded along the same navigation lines. Two main belts of sharp magnetic anomalies have been identified, the first located offshore the Somma-Vesuvius volcanic complex and the second offshore the Phlegrean Fields volcanic complex. The latter one is interpreted as the seaward boundary of the Phlegrean caldera (Pescatore *et al*., 1984; Orsi *et al*., 2002). The detailed interpretation of the magnetic anomaly field and related seismic structures offshore the Somma-Vesuvius volcanic complex suggests a NNW-SSE structural alignment, while in the Pozzuoli Gulf several complex E-W and NE-SW trending anomalies have been identified, whose values are related to small buried volcanic structures. The shape of magnetic anomalies is not directly related to the submarine topography of large volcanic banks, revealed by Multibeam bathymetry. Main fields are also

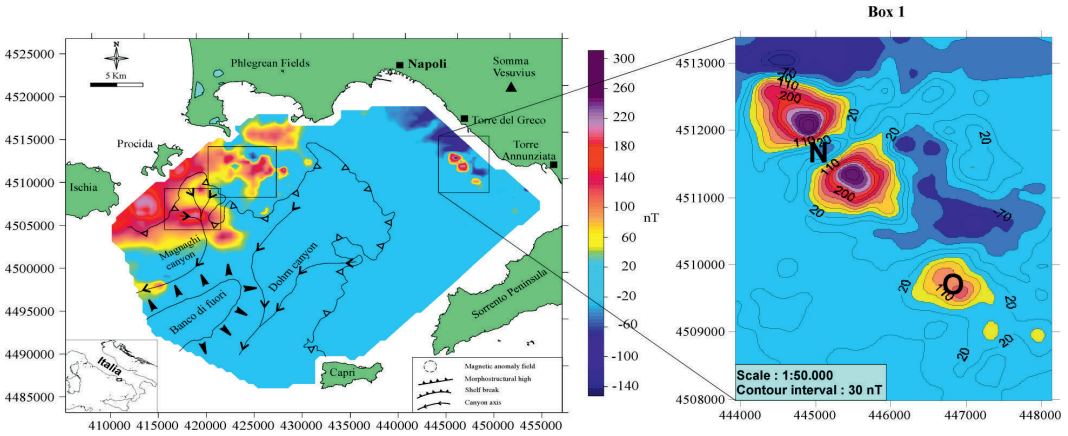

Fig. 2 – High resolution magnetic anomaly map of the Naples Bay (on the left in the figure; modified after Aiello *et al.*, 2004). The inset shows a detail of the magnetic map offshore the Somma-Vesuvius volcanic complex.

related to the Procida continental shelf, to the Gaia bank, to the head of the Magnaghi canyon, to an edifice located among the Dohrn and Magnaghi canyons, to the Magnaghi canyon and to the Ischia bank.

Magnetic anomaly measurements in the Gulf of Pozzuoli. The magnetic field anomalies in the Gulf of Pozzuoli (modified after Galdi *et al.*, 1988), have shown both positive and negative anomalies (Fig. 3). The area shows an interruption of the regional trend from NE to SW, where circular anomalies are probably connected to a post-calderic activity of the Phlegrean Fields. Moreover, the internal area of the Pozzuoli Bay is characterized by a negative anomaly, increasing towards the south. Conversely, in the external area there is mainly an alternance of positive and negative anomalies, with a dominance of positive values near the area of Bagnoli. The inner continental shelf of the Gulf of Pozzuoli is regarded as negative magnetic anomalies. In particular, the area surrounding the Pozzuoli harbour does not show significant magnetic anomalies. On the contrary, the area adjacent the resort Lucrino-Punta Pennata owns a negative anomaly increasing southwards up to the magnetic minimum at 600-700 m in correspondence to the Baia Castle. On the outer shelf of the Gulf of Pozzuoli it is possible to observe magnetic maxima and minima. In particular, an area of magnetic maximum is located on a belt long about 1.7 km, NE-SW oriented. At the same time, the inner continental shelf of the Gulf of Pozzuoli, from Bagnoli to the Rione Terra of Pozzuoli shows two strong magnetic anomalies, separated by a thin belt having a normal magnetic value. Proceeding seawards, in the offshore surrounding Bagnoli, two magnetic minima (40 nT and 60 nT) are positioned, which result slightly

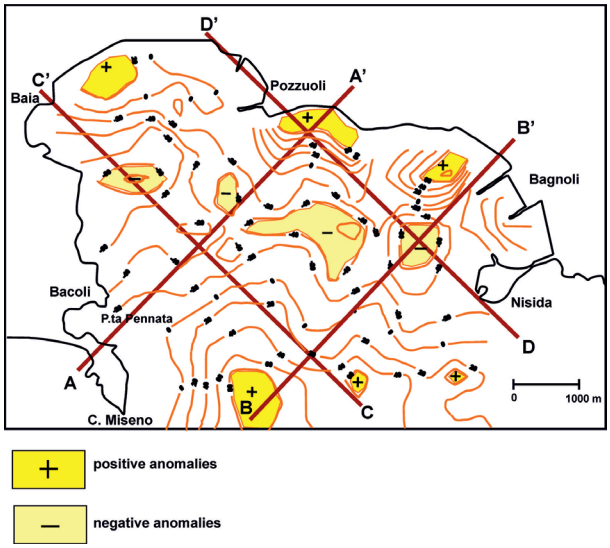

Fig. 3 – Interpreted map of the magnetic anomalies of the Gulf of Pozzuoli (modified after Galdi *et al.*, 1988). The positive anomalies are represented in yellow and the negative anomalies in light yellow.

E-W elongated, culminating with the absolute magnetic minimum (-100 nT) in correspondence to the Baia Castle. Four magnetic sections have also been constructed (Aiello *et al.*, 2012). The first one runs from Punta Pennata (Gulf of Pozzuoli) to the Pozzuoli town (Via Napoli). The total magnetic intensity shows a trending with a magnetic minimum of – 80 nT in the central area (corresponding to a depth of the sea bottom of – 90 m) and a magnetic maximum of 70 nT in correspondence to the Pozzuoli shoreline. The section section runs from Bagnoli to Capo Miseno and shows, starting from south-west a monotonous magnetic trend up to the offshore surrounding Nisida, where a strong increase to the gradient occurs. The magnetic highs occurring nearshore appear to be related not to the geology, but to the occurrence of the industrial systems of Bagnoli.

Conclusions. The Naples Bay is characterized by two main magnetic fields, offshore of Somma-Vesuvius and offshore the Phlegrean Fields volcanic complexes. Three magnetic maxima, dipolar in shape, are related to the Torre del Greco volcanic structure, already observed based on seismic interpretation (Aiello *et al.*, 2010). The rising of the Torre del Greco volcanic structure corresponds to the occurrence of topographic undulations of the sea bottom of up to ten metres. This is confirmed by the interpretation of seismic profiles, showing three main vertical culminations of the volcanic structure, linked to significant magnetic anomaly extremes. Significant anomalies have been identified offshore the Phlegrean Fields volcanic complex, in correspondence to the outer belt of the Gulf of Pozzuoli. They are related to volcanic bodies buried by sediments and to small volcanic edifices. Significant anomalies also occur in correspondence to the Magnaghi canyon, which is completely incised in volcanic deposits. The interpreted map of the magnetic anomalies in the Gulf of Pozzuoli has allowed to distinguish positive and negative magnetic anomaly areas. The inner continental shelf of the Gulf of Pozzuoli is characterized by negative magnetic anomalies and the correlation with the volcanic structures evidenced by the Sparker data is not clear. The volcaniclastic units identified on seismic profiles does not seem to produce significant magnetic signatures, probably due to its composition (tuffs and lavas).

References

Agip; (1981): *Carta magnetica – Anomalie del campo magnetico residuo – scala 1:500.000.* S. Donato Milanese, Italy.

Aiello G., Angelino A., Marsella E., Ruggieri S. & Siniscalchi A.; (2004): *Carta magnetica di alta risoluzione del Golfo di Napoli.* Bollettino della Società Geologica Italiana, **123:** pp. 333-342.

Aiello G., Marsella E. & Ruggieri S. (2010): *Three-dimensional magneto-seismic reconstruction of the "Torre del Greco" submerged volcanic structure (Naples Bay, Southern Tyrrhenian sea, Italy): Implications for the Vesuvius' marine geophysics and volcanology.* Near Surface Geophysics, **8 (1)**: pp. 17-31.

Aiello G., Cicchella A.G., Di Fiore V. & Marsella E.; (2011): *New seismo-stratigraphic data of the Volturno Basin (northern Campania, Tyrrhenian margin, southetn Italy): implications for tectono-stratigraphy of the Campania and Latium sedimentary basins.* Annals of Geophysics, **54 (3)**: pp. 265-283.

Aiello G., Giordano L., Marsella E. & Passaro S.; (2012): *Seismic stratigraphy and marine magnetics of the Naples Bay (southern Tyrrhenian sea, Italy): the onset of new technologies in marine data acquisition, processing and interpretation.* In: Elitok O. (Ed.) *Stratigraphic Analysis of Layered Deposits.* Intech Ed., Chapter 2; pp. 21-60.

Bernabini M., Latmiral G., Mirabile L. & Segre A.G.; (1971): *Alcune prospezioni sismiche per riflessione nei Golfi di Napoli e Pozzuoli.* Rapp. Com. Inter. Mer. Medit., **21**: pp. 929-934.

Caratori Tontini F., Faggioni O., Giori I. & Stefanelli P:, (2003): *La nuova carta aeromagnetica d'Italia. Confronto con i principali lineamenti tettonico-strutturali.* Atti 22° Cong. Naz. GNGTS, 3° Cong. Naz. EAGE-SEG, Rome (Italy), CNR, 19-21 November 2003.

Cassano E. and La Torre P.; (1987): *Geophysics.* In: Santacroce R. (Ed.) *Somma-Vesuvius.* CNR, Quaderni De La Ricerca Scientifica, Rome, Italy.

Castellano M., Buonocunto C., Capello M. & La Rocca M.; (2002): *Seismic surveillance of active volcanoes: the Osservatorio Vesuviano seismic network (OVSN-Southern Italy).* Seismology Research Letters, **73:** pp. 177-184.

Coticchia A., De Santis A., Di Ponzio A., Dominici G., Meloni A., Pierozzi M. & Sperti M.; (2001): *La Rete Magnetica Italiana e la Carta Magnetica d'Italia al 20000.* Boll. Geod. e Sc. Affini, Rivista dell'Istituto Geografico Militare, **4.**

Finetti I. and Morelli C.; (1973): *Esplorazione sismica per riflessione dei Golfi di Napoli e Pozzuoli.* Boll. Geof. Teor. Appl., **16 (62-63)**, pp. 175-222.

Galdi A., Giordano F., Sposito A. & Voltaggio M.; (1988) *Misure geomagnetiche nel Golfo di Pozzuoli: Metodologia e risultati.* Atti del 7° Convegno GNGTS-CNR, **3**: pp. 1647-1658.

Mastrolorenzo G., Palladino D., Vecchio G. & Taddeucci J.; (2002): *The 472 AD Pollena eruption at Somma-Vesuvius, Italy and its environmental impact at the end of Roman Empire.* Journ. of Volcanol. and Geoth. Res., **113**: pp. 19-36.

Orsi G., De Vita S., Di Vito M., Isaia R., Nave R. & Heiken G.; (2002): *Facing volcanic and related hazard in the Neapolitain area.* In: Heiken G., Fakundiny R. and Sutter J. (Eds.) *Earth Sciences in the city.* American Geophysical Union Spec. Publ., Washington, pp. 121-170.

Paoletti V., Fedi M., Florio G., Supper R. & Rapolla A.; (2004): *The new integrated aeromagnetic map of the Phlegrean Fields volcano and surrounding areas.* Annals of Geophysics, **47 (5)**, pp. 1569-1580.

Paoletti V., Secomandi M., Fedi M., Florio G. & Rapolla A.; (2005): *The integration of magnetic data in the Neapolitain volcanic district.* Geosphere, **1 (2)**: pp. 85-96.

Pescatore T., Diplomatico G., Senatore M.R., Tramutoli M., Mirabile L.; (1984): *Contributi allo studio del Golfo di Pozzuoli: aspetti stratigrafici e strutturali.* Memorie della Società Geologica Italiana, **27**: 133-149.

Rosi M. and Sbrana A.; (1987): *Phlegrean Fields.* Quaderni De La Ricerca Scientifica, CNR, Italy.

Saccorotti G., Ventura G. & Vilardo G.; (2002): *Seismic swarms related to diffusive processes: the case of Somma-Vesuvius volcano, Italy.* Geophysics, **67**: pp. 199-203.

Santacroce R:, (1987): *Somma-Vesuvius.* Quaderni De La Ricerca Scientifica, CNR, Italy.

Secomandi M., Paoletti V., Aiello G., Fedi M., Marsella E., Ruggieri S., D'Argenio B. & Rapolla A.; (2003): *Analysis of the magnetic anomaly field of the volcanic district of the Naples Bay.* Marine Geophysical Researches, **24**: pp. 207-221.

Scarpa R., Tronca R., Bianco F. & Del Pezzo E. (2002): *High resolution velocity structure beneath Mount Vesuvius from seismic array data.* Geophysical Research Letters, **29:** pp. 204-219.

Todesco M., Neri A., Esposti Ongaro T., Papale P., Macedonio G. & Santacroce R. (2002): *Pyroclastic flow hazard at Vesuvius from numerical modelling I. Large scale dynamics.* Bulletin of Volcanology, **64**: pp. 155-177.

TIME LAPSE 3D ELECTRICAL TOMOGRAPHY FOR SOIL-PLANT DYNAMICS INTERACTIONS

J. Boaga, M. Rossi, G. Cassiani
Dipartimento di Geoscienze, Università degli Studi di Padova, Italy

Introduction. We are fronting an increasing global demand of optimization in terms of land use and water management, both for civil exploitation and agriculture. This means a growing demanding in quality and quantity calls for sustainable management of water catchments and better understanding of water and solute movement in the critical vadose zone. Non invasive geophysical techniques can play a key role in the hydrological investigation of the near surface, as they provide spatially extensive imaging that complement the more traditional hydrological point measurements (e.g. Vereecken *et al.*, 2006). Between geophysical techniques, time-lapse Electrical Resistivity Tomography (ERT) was recently adopted in several studies to estimate, albeit indirectly, changes in moisture content (e.g. Binley *et al.* 2002, Strobbia and Cassiani, 2007) and solute concentration (Cassiani *et al.*, 2006). In the framework of plants/subsoil interactions ERT techniques were recently downscaled to image the root zone geometry (Jayawickreme *et al.*, 2008; Muller *et al.*, 2003; Werban *et al.*, 2008; al Hagrey and Petersen, 2011; Jarvaux *et al.*, 2008). These applications pose new interdisciplinary high demanding challenges from ecohydrology to geoecohydrology (Eagleson, 2002). In this framework we are applying hydrogeophysical methodologies to several sites of different climatic zones in terms of upper soil hydrology, downscaling non invasive geophysical techniques to the upper subsoil biosphere interactions.

The aim of this work was to apply ERT techniques to the monitoring of plant root zone for 2 field cases. For this specific purpose it is necessary a 3D ERT apparatus with very detailed resolution capabilities and, due to the small target, extremely attention to be non invasive. In order to get a 3D resistivity imaging under a plant, we need small inter-electrodes spacing both in depth buried electrodes and surface ones. We need also the lowest possible resistance contact with soil and the minimum site disturbance together with reasonable efficiency in time to perform time-lapse measurements. For all these reasons we designed 1 inch PVC boreholes totally internal wired, equipped with 12 round steel electrodes each with 0.1m spacing.

We present on the results of experiments of 3D and 2D Micro-ERT, supported by Time Domain Reflectometer (TDR) measurements and tensiometers measurements in a very well monitored fruit garden of Val di Non, Trentino Region and for the Venice lagoon salt marsh environment (Italy). In the specific we performed 3 controlled irrigation tests for the apple tree and 1 field experiment in the Venice lagoon during marsh flooding. Very different seasonal and environmental conditions are highlighted with interesting behaviors. In order to quantify soil moisture content in the first case study, we performed laboratory analysis on earth samples to evaluate the electrical response at different saturation steps and to calibrate petro-physical relationships. This allows transforming geophysical quantities into hydrological quantities, which represents a key point to clearly understand the groundwater dynamics and soil-plant interactions.

Test sites. Test site 1 is located in Cles (650 m amsl), in the Val di Non valley of Trentino Region, North Italy. We installed our micro ERT 72 channels (48 buried electrodes + 24 surface electrodes) and 2 TDR antennas around a single tree in an apple culture, already monitored in the framework of the FP7 CLIMB project, with controlled irrigation system and monitored weather-stations. The site is located on a moraine versant of an ancient Wurmian glacier valley and presents an heterogeneous glacial deposit (presence of blocks and pebbles in a sandy-silty matrix). We conducted monitoring of both long term natural changes and controlled irrigation experiments around a single apple tree, in order to assess value, strengths and limitations of the non invasive techniques for root/vadose zone monitoring.

Test site 2 is located in the northern part of the Venice Lagoon (Italy), in a periodically flooded salt marsh. In this case the ERT apparatus had 24 buried electrodes plus 24 surface

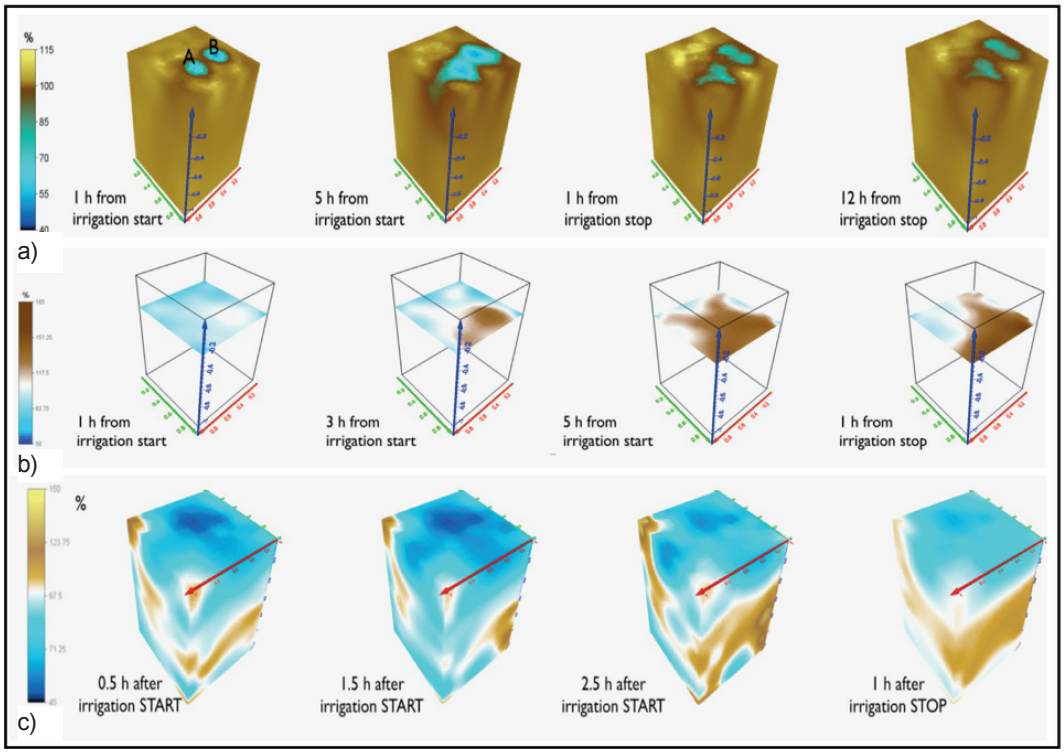

Fig. 1 – a) August 2011 experiment: resistivity ratio with respect to background at four time steps. In (a), A and B indicate the locations of the two drippers. b) May 2012 experiment: resistivity ratio with respect to background at four time steps. Surface at 30 cm depth. c) November 2012 experiment: resistivity ratio with respect to background at four time steps, (from Boaga *et al.*, 2013, modified).

electrodes. 3 tensiometers with log recorder were installed at 20, 30 and 40 cm depth in the subsoil.

Methods. Our 3D micro ERT configuration consists of 24 or 48 electrodes buried in depth, installed on boreholes, plus 24 steel electrodes on the surface, Electrodes are round steel electrodes spaced 0.1 m, with all wire connection sited inside the PVC casing. This allows their installation by percussion avoiding invasive pre-drill with a very efficient contact resistance between electrodes and soil.

For all the measurements we adopted a dipole-dipole skip-zero acquisition. For the inversion process we adopted a 3D mesh with detailed triangular prisms elements of 0.025 m side for the root zone box, while larger mesh cells were used for the background. All reciprocal measures, that show the statistical operator RSD (Relative Standard Deviation) exceeding the 5%, were removed from the dataset. The reciprocal procedure leads to different datasets, so to have comparable results the inversions are performed only on the same quadripoles that are present in all datasets. For the inversion we adopted the codes R3T (Binley *et al.*, 2011), a 3D current flows solution for finite element triangular prisms mesh.

In order to enhance the time-lapse monitoring we inverted the data as a ratio of electrical resistances at a specific time respect to the resistance values at the background measurement (in our case the time step before the irrigation):

$$R = \left(R_i / R_0\right) R_{\text{hom}} \qquad (1)$$

where R_i is the electrical resistance at the *i-th* time-step, R_0 is the electrical resistance at the background measure and R_{hom} is the electrical resistance for an homogenous space of 100 Ω·m. The inversion of resistance values can clearly enhances the variation of electrical resistivity during the time-lapse experiment. The results of the inversion is a map of the percentage variation of resistivity respect to the background values: values equal to 100 Ω·m show unchanged resistivity during time, while values less or more than 100 Ω·m show a decreasing or an increasing resistivity, respectively.

Results.

The Val di Non case studies. We performed 3 irrigation tests in 3 different seasonal conditions and with different type of irrigation. In August 2011 we performed a drip irrigation (2.4 lt/h) experiment under the dry conditions of the summer season. In May 2012 we performed a widespread irrigation experiment (198 lt/h) in a wet conditions during the highest spring dynamic growing season period of the plants, and in November 2012 we repeated the experiment in very wet condition. For the first experiment micro enhanced the conductive areas are restricted on the 2 drip irrigation points. The wet areas progressively expand during irrigation; after the end of the irrigation the shallow wet areas slowly start to dry (Fig. 1a). The second and third irrigation experiments were conducted in different climatic conditions, during the top of the growing season plant. The site soil this time was very wet due to huge amount of rain during the previous month. The hot sunny days of the experiment (26°), assured a large amount of evapotranspiration. We used an irrigation sprinkler system in order to obtain a more uniform and widespread irrigation as possible. We performed also Time Domain Reflectometer (TDR) measurements during and after the irrigation to estimate soil-water content (θ).

Results (Fig. 1b) show how, at the depth where are expected the main suction zone linked to root plant activity (De Silva, 1999), there is a clear increasing of resistivity due to the root uptake. Extremely interesting is the shape of the drier zone since position of the root activity is not uniformly widespread on the horizontal plane, but it is confined in the area of the parallelepiped that is directly linked with the location of the drip irrigation system. Results of the 3d experiment (Fig. 1c) show also an higher resistivity zone at greater depth after 3 h from irrigation start. Since resistivity properties are not effect only of water saturation but also of salinity, we believe the observed phenomenon can be related to the replacement of the resident

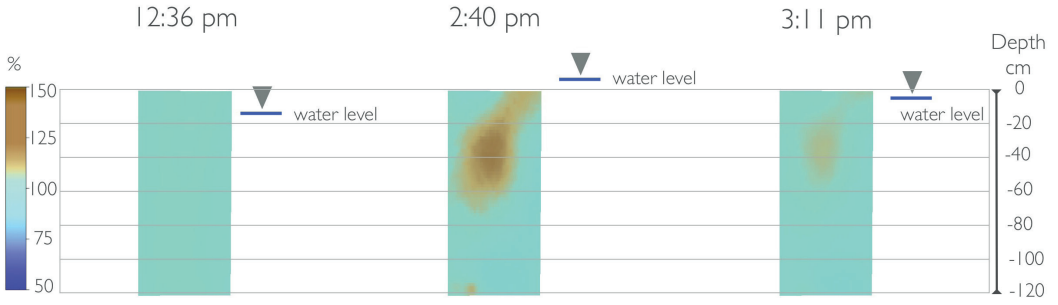

Fig. 2 – Time-lapse ERT results: resistivity ratio with respect to background at three time steps before (left panel), during (central panel) and after (right panel) marsh flooding by tide. Note the 140% value zone (drier zone) located at a depth of 20-40 cm below the marsh surface around 2.40 pm (central panel), when the marsh is completely flooded, (from Boaga *et al.*, 2013, modified).

water with the new low salinity irrigation water (piston effect). This vey interesting aspect will be examined by the use of theoretical modeling.

Venice Lagoon case studies. Venice salt marsh location was chosen to test the capability of tidal plants to generate a persisting aerated layer in the subsoil when flooded, due to root uptake (Marani *et al.*, 2006). We planned time lapse ERT measurements and tensiometers measurements before, during and after sea flooding of the marsh in a hot summer day (33°) of July 2012, with slow wind. This was expected to be the best conditions for salt marsh uptake process (potential evapotranspiration estimated to be approximately 8 mm/day, based on Penman-Monteith equation). Fig. 2 shows the inversion results at three time steps during the flooding of the marsh by seawater. Here we consider only the portion of subsoil between the instrumented boreholes, which presents the highest sensitivity. The three time steps are before the marsh is flooded (12:36 pm), when the marsh is flooded (2:40 pm), and after the marsh surface has been flooded and has started drying (3:11 pm) during ebb, the highest tidal level being of 0.34 m above MSL, at 1:52 pm.

These ERT ratio images clearly show the development of a zone of increased electrical resistivity near a depth of 30-40 cm below soil surface. Note that the tide starts flooding the marsh shortly after noon (that corresponds to the reference time instant) but is not visible *per se* in the ERT images, confirming that the high pore water salinity makes the system poorly sensitive to the modest change in water saturation due to water level rise. The area which is getting dryer during marsh flooding is the expected root zone for the typical wetlands vegetation (Sarcocornia fruticosa, Juncus, and Limoniumn narbonense, etc.).

Tensiometers measurements, installed at 20, 30 and 40 cm depth confirmed the micro ERT results (Fig. 3). Surface tensiometers shows in fact a wetter condition when sea flooded the marsh but tensiometer installed at root depth (30-40 cm) show a surprising dryer condition during the flooding. ERT and tensiometers results are summarized in Fig. 3. The geophysical techniques were able enhance the dynamics interaction within marsh plants and first subsoil.

Discussion and Conclusion. We performed 3D and 2D micro-ERT measurements of root plant during controlled irrigation tests and natural flooding, in order to verify the potential of these non-invasive techniques to monitor the dynamic root zone activities.

The advanced 3D micro-ERT methodology exposed proved to be able to monitor suction zones, in good agreement to the expected root positions. In dryer conditions micro 3D-Ert image the penetrating water plumes injected, while in wetter high growing seasons of the plants micro 3D-ERT points out how certain subsoil zones are interested by quick drying conditions. These drying suction areas are in good agreement with the expected depth of the apple tree root activities. 3D micro ERT through indirect estimations enhanced the root zone

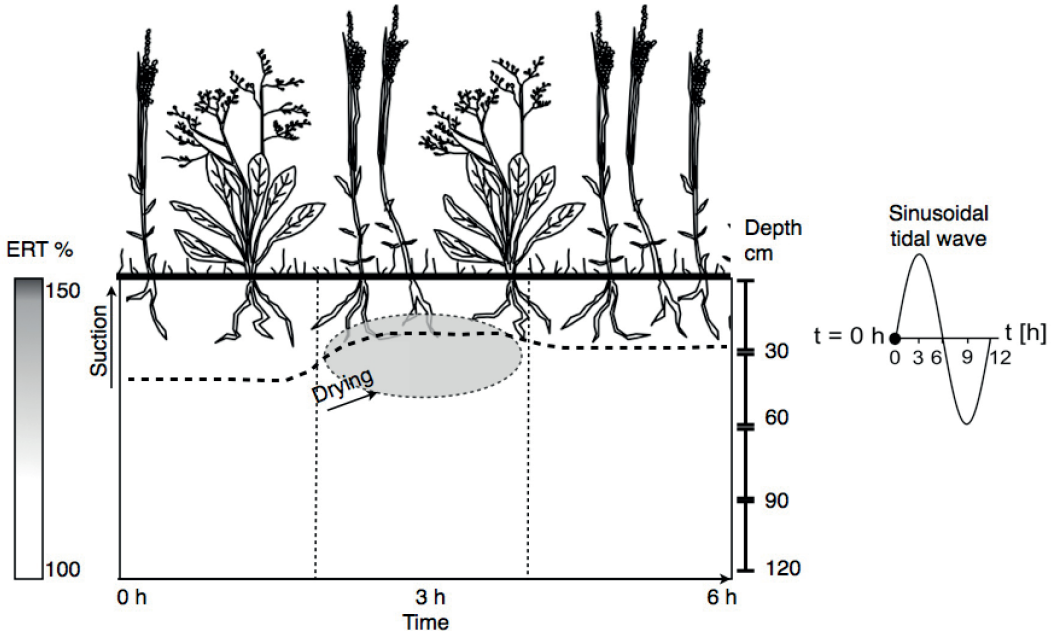

Fig. 3 – Schematic representation of time-lapse resistivity ratio imaging and tensiometer suction as observed during the flood phase in the San Felice marsh (half of the semidiurnal tidal period). The grey area at a depth of 20cm - 40cm (the root zone) represents the ERT resistivity ratio values greater than 100%. The dashed line shows the 40 cm deep tensiometer suction as a function of time, emphasizing drying conditions, (from Boaga *et al.*, 2013, modified).

depth at which water content decay during the irrigation experiment, quantifying difference in water content zone by zone.

2D Time-lapse ERT in Venice lagoon enhanced how salt marsh plants are able to generate a persisting aerated layer in subsoil, even when flooded. In particular the large hyper-saline plants root uptake seems to be able to determine the persistence of an aerated layer, as previously observed (Marani *et al.*, 2007, 2006; Ursino *et al.*, 2004). It is authors' opinion these analyses may help refine the understanding of the central importance of plant-soil interactions in coupling biological and geomorphological processes (via organic soil production and inorganic sediment trapping). The ERT methodology coupled with the tensiometer data can be used to quantify the dynamics of the soil water content, thus contributing to determine the state and evolutionary trends of tidal landforms forced by anthropogenic pressures and sea level rise.

In conclusion the non-invasive Micro-ERT techniques are promising tools for critical soil-plants interaction study, especially if they will support by advanced and accurate hydrological modelling. Suitable modelling techniques will be in fact necessary to exploit the information content of geophysical field data and answer critical questions about basic mechanisms, e.g. the soil moisture balance equations at the scale of the representative elementary volume (Bear, 1971; Richards, 1931).

Acknowledgements. We thanks Mario Putti, Giuseppe Fadda, Andrea D'Alpaos and Marco Marani for their invaluable supports for the modeling and interpretation of the results. We thank also Alberto Bellin and Bruno Majone for the Val di Non experiment. Funding for this work is acknowledged from the EU FP7 project CLIMB "Climate Induced Changes on the Hydrology of Mediterranean Basins" and from the Excellence Project "Transport phenomena in hydrological catchments: hydrological and geophysical experiments and modeling" funded by the CARIPARO Foundation.

References

al Hagrey, S.A. and T. Petersen, 2011, Numerical and experimental mapping of small root zones using optimized surface and borehole resistivity tomography, Geophysics, 76(2) DOI: 10.1190/1.3545067.671

Binley, A.M., Cassiani, G., Middleton, R. and P., Winship, 2002, Vadose zone flow model parameterisation using cross-borehole radar and resistivity imaging, Journal of Hydrology, 267, 147-159

Binley,A.,2011,http://www.es.lancs.ac.uk/people/amb/Freeware/freeware.htm (accessed June 4, 2012)

Boaga, J., M. Rossi, G. Cassiani, 2013, Monitoring soil-plant interactions in an apple orchard using 3D electrical resistivity tomography, Proceeding of 'Four Decades of Progress in Monitoring and Modeling of Processes in the Soil-Plant-Atmosphere System: Applications and Challenges', Naples 2013, Procedia Environmental Sciences 19, 394 – 402, doi: 10.1016/j.proenv.2013.06.045.

Boaga J., D'Alpaos A., Cassiani G., Marani M., Putti M. 2013 Plant-soil interactions in salt-marsh environments: experimental evidence from electrical resistivity tomography (ERT) in the Venice lagoon, submitted to Geophysical Research Letter,

Cassiani G., N. Ursino, R. Deiana, G. Vignoli, J. Boaga, M. Rossi, M. T. Perri, M. Blaschek, R. Duttmann, S. Meyer, R. Ludwig, A. Soddu, P. Dietrich and U. Werban, (2012), Non-invasive monitoring of soil static characteristics and dynamic states: a case study highlighting vegetation effects, Vadose Zone Journal, 11, doi: 10.2136/2011.0195.

Cassiani G., Ursino N., Deiana R., Vignoli G., Boaga J., Rossi M., Perri M.T., Blaschek M., Duttmann R., Meyer S.,Ludwig R., Soddu A., Dietrich P. and Werban U. Non-invasive monitoringof soil static characteristics and dynamic states: a case study highlighting vegetation effects. *in press* Vadose Zone Journal Special Issue on SPAC- Soil-plant interactions from local to landscape scale

Cassiani, G., A. Kemna, A.Villa, and E. Zimmermann, 2009, Spectral induced polarization for the characterization of free-phase hydrocarbon contamination in sediments with low clay content, Near Surface Geophysics, special issue on Hydrogeophysics, p. 547-562.

De Silva H.N., Hall A.J.,Tustin D.S., Gandar P.W., 1999, Analysis of Distribution of Root Length Density of Apple Trees on Different Dwarfing Rootstocks, Annals of Botany, Volume 83, Issue 4, Pages 335–345

Jayawickreme H., Van Dam R., Hyndman D.W. Subsurface imaging of vegetation, climate, and root-zone moisture interactions GEOPHYSICAL RESEARCH LETTERS, VOL. 35, L18404, doi:10.1029/2008GL034690, 2008

Javaux M., T. Schroder, J. Vanderborght, and H. Vereecken. 2008, Use of a Three-Dimensional Detailed Modeling Approach for Predicting Root Water Uptake Vadose Zone J.. Vadose Zone J. 7(3), 1079 - 1088

Eagleson P.S., , Ecohydrology: Darwinian expression of vegetation form and function, Cambridge University Press, Cambridge, UK, 2002

Marani, M., S. Silvestri, E. Belluco, N. Ursino, A. Comerlati, O. Tosatto, and M. Putti (2006), Spatial organization and ecohydrological interactions in oxygen-limited vegetation ecosystems, Water Resour. Res., 42, W06D06,

Marani, M., A. D'Alpaos, S. Lanzoni, L. Carniello, and A. Rinaldo (2007), Biologically-controlled multiple equilibria of tidal landforms and the fate of the Venice lagoon, Geophys. Res. Lett., 34, L11402.

Strobbia C. and G. Cassiani, 2007, Multi-layer GPR guided waves in shallow soil layers for the estimation of soil water content, Geophysics, Vol. 72, No. 4; p. J17–J29, 10.1190/1.2716374

Tosatto, O., E. Belluco, S. Silvestri, N. Ursino, A. Comerlati, M. Putti, and M. Marani (2009), Reply to comment by L. R. Gardner on ''Spatial organization and ecohydrological interactions in oxygen-limited vegetation ecosystems,'' Water Resour. Res., 45, W05604, doi:10.1029/2007WR006345

Ursino, N., S. Silvestri, and M. Marani (2004), Subsurface flow and vegetation patterns in tidal environments, Water Resour. Res., 40, W05115.

Ursino N., G. Cassiani, R. Deiana, G. Vignoli, J. Boaga, 2013, Measuring and Modelling water related soil – vegetation feedbacks in a fallow, Hydrol. Earth Syst. Sci. Discuss., 10, 11151-11184, 2013

Vignoli G., Cassiani G., Rossi M., Deiana R., Boaga J. Fabbri P. An integrated geophysical approach for the characterization of a small pre-alpine catchment. Journal of Applied Geophysics *80 (2012) 32–42 doi:10.1016/j.jappgeo.2012.01.007*

Vereecken H., A. Binley, G. Cassiani, I. Kharkhordin, A. Revil, K. Titov (eds), 2006, Applied Hydrogeophysics, Springer-Verlag, Berlin.

Waxman, M.H. and Thomas, E.C.: "Electrical Conductivities in Shaly Sands Sands – I. The Relation Between Hydrocarbon Saturation and Resistivity Index: II. The Temperature Coefficient of Electrical Conductivity", JPT. pp213-250, Feb., (1974), or Trans., AIME, Vol. 257. (1974)

Werban, U., S. A. al Hagrey, and W. Rabbel, 2008, Monitoring of root-zone water content in the laboratory by 2D geoelectrical tomography, Journal of Plant Nutrition and Soil Science, 171(6), 927–935. Doi: 10.1002/jpln.200700145. 781

Wiley, MJ, DW Hyndman, BC Pijanowski, AD Kendall, C Riseng, ES Rutherford, ST Cheng, ML Carlson, JA Tyler, RJ Stevenson, PJ Steen, PW Seelbach, JM Koches, and RR Rediske, 2010, A multi-modeling approach to evaluating climate and land use change impacts in a Great Lakes River Basin. Hydrobiologia. doi: 10.1007/s10750-010-0239-2

APPLICATION OF ELECTRICAL RESISTIVITY TOMOGRAPHIES FOR THE GEOELECTRIC CHARACTERIZATION OF MONTAGUTO LANDSLIDE (SOUTHERN ITALY)

G. Calamita[1], A. Perrone[1], J. Bellanova[1], A. Giocoli[2], V. Lapenna[1], R. Luongo[1], S. Piscitelli[1]
[1]Institute of Methodologies for Environmental Analysis (IMAA-CNR), Tito Scalo (PZ), Italy
[2]Italian National Agency for New Technologies, Energy and Sustainable Economic Development (ENEA), Rome, Italy

Introduction. This paper reports the results of a geoelectrical survey carried out on the Montaguto landslide, located in the Apennine Chain (Campania Region, Southern Italy) (Fig. 1).

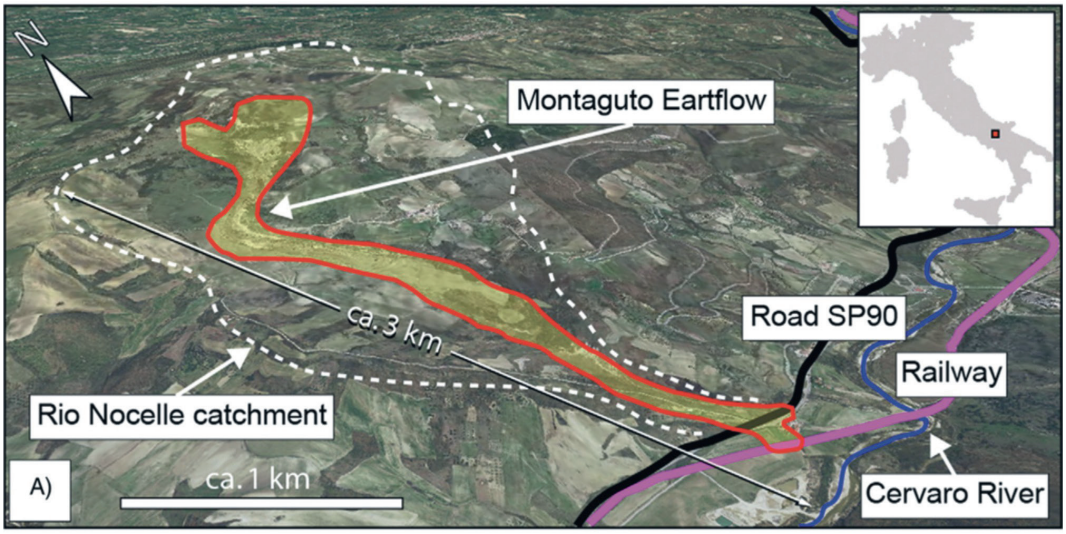

Fig. 1 – Location of the Montaguto earthflow, Campania, southern Italy. (A) 3D view. Red line: landslide boundary. White dashed line: Rio Nocelle catchment divide. Black line: SP90 provincial road. Violet line: railroad. Blue line: Cervaro River (from Giordan *et al.*, 2013).

Montaguto landslide is an earthflow and it is considered one of the larger and complex mass movements in Europe, with a length of about 3 x 10^3 m, an estimated volume of displaced material of about 4-6 x 10^6 m^3 and a sliding surface depth varying from 5 m, near the center, to 20-30 m, at the toe. Its areal extension is about 6.6 x 10^5 m^2 (~66 ha), whereas its width ranges between 45 and 420 m (Ventura et. al., 2011; Giordan *et al.*, 2013; Guerriero *et al.*, 2013). As stated by Ventura *et al.*, (2011), the depth of the water table roughly corresponds to the thickness of sliding material with sag ponds occurring in the upper and central zone. The altitude gap between the head scarp, 830 m a.s.l., and the toe, 420 a.s.l., is about 420 m (Giordan *et al.*, 2013).

The earth-flow has been active for almost 60 years starting from, at least, 1954. Long periods of relatively slow movement and shorter periods of relatively rapid movement periodically follow one another in the earth-flow activity (Guerriero *et al.*, 2013).

In the mid spring season 2006 began the most extensive reported slope failure, when an estimated volume of 6 x 10^6 m^3 earthflow activated. Four years later, in the spring of 2010, the earth-flow reached the Cervaro River valley, obstructed and strongly damaged the strategic rail corridor infrastructure connecting the Tyrrhenian and Adriatic coasts of Italy and the National Road SS90, that connects Naples to Foggia (Ventura *et al.*, 2011; Guerriero *et al.*, 2013).

The reported velocities of most movement, from 1954 to 2010, ranged from 1 – 2 mm/month to 2 – 5 cm/day. A sharp increase was registered during the large mobilization in both 2006 and 2010, from 1 m/day to 1 m/hour, as reported by Guerriero *et al.* (2013), or 5 m/day, as reported by Giordan *et al.* (2013).

Fig. 2 – Electrical resistivity tomography surveys carried out on the Montaguto landslide on July 2011 (A) and October 2012 (B).

Mostly because of the road and rail interruption and the resulting closure, the event caused severe damages not only to the local community, but also to the national railway system, especially on Southern and Central Italy.

Considerable efforts were carried by the Italian national Civil Protection Department (DPC) to tackle the emergency. Moreover, a series of actions (artificial drainages, removal of slide material from the toe, etc.) has been taking place since then, in order to mitigate the effects of the moving landslide. Notwithstanding the resulting slowdown of the earth-flow obtained, further coordinate actions are yet ongoing, in order to ensure safer conditions to the rail and road infrastructures.

In this context arose the collaboration between Italian national DPC and the Institute of Methodologies for Environmental Analysis (IMAA) of the National Research Council (CNR). In the framework of the agreement between DPC and IMAA-CNR, two field surveys were carried out in the area, one in July 2011 and one in October 2012.

The Electrical Resistivity Tomography (ERT) technique was adopted, in order to collect indirect information about the features of the landslide geometry. Data were acquired through a multi-electrode system using a Syscal R2 (Iris Instruments) device. The apparent resistivity data were inverted by the RES2DINV software (Loke, 2001) to obtain a subsurface image of the electrical resistivity pattern. All the ERT were placed perpendicularly to the landslide body and realized with a 5 m electrode spacing array that allowed to explore up 40 m in depth.

During the first field survey, on 5th-6th of July 2011, 4 ERT were carried out in the upper-zone, whereas the 5th in the lower part, at about 530 m a.s.l. (Fig. 2).

More than one year later, on 23rd-25th of October 2012, 11 ERT were realized at almost regular intervals of about 50-60 m. As explicitly required by the DPC, the attention was focused on the central part of the landslide, despite the drainage interventions, continues to move downward of some mm per day (Fig. 2).

Geological setting. In the area Miocene sedimentary rocks crop out (Guadagno *et al.*, 2005), including:

- layered limestone, calcarenite, marly limestone, marl and argillaceous marl pertaining to the Faeto Flysch Formation, Langhian to Tortonian in age (Crostella and Vezzani, 1964),
- clay, argillaceous marl and fine sand pertaining to the Villamaina Unit, Messinian in age (D'Argenio *et al.*, 1975).

The Faeto Flysch crops out in the upper and middle parts of the Rio Nocelle catchment, and the Villamaina Unit crops out in the lower part of the catchment. Quaternary alluvial sediments are present in the Cervaro River valley. In the study area, rocks exhibit a composite structural setting, reflecting a complex tectonic history (Pescatore *et al.*, 1996; Amore *et al.*, 1998; Di Nocera *et al.*, 2011).

Results. Here we discuss only two of the sixteen ERT carried out on Montaguto landslide: the ERT 1 of both the first (July 2011) and second field surveys (October 2012) (Fig. 3).

For all the ERT carried out, the spatial variability of the electrical resistivity was quite limited. Resistivity values ranged between 3 and 40 Ω·m, that are typical values for clayey soils.

The ERT 1 carried out during the first field survey was placed in parallel to the drainage trench at a quote of 675 m a.s.l. and showed both vertical and horizontal varying resistivity (Fig. 3). More in detail, between 100 and 160 m a superficial sector relatively more resistive, about 10 m thick, likely due to the drainage trench and landslide material, was clearly identifiable. Underlying that, there was a conductive layer limited laterally by more resistive zones, probably constituted by bedrock. Finally, in the NW sector, a low resistivity zone is evident that can be interpreted as clayey or water-rich material.

The ERT 1 carried out during the second field survey (Fig. 3) was realized at about 616 m a.s.l.. The electrical image showed both vertical and horizontal varying resistivity. In particular,

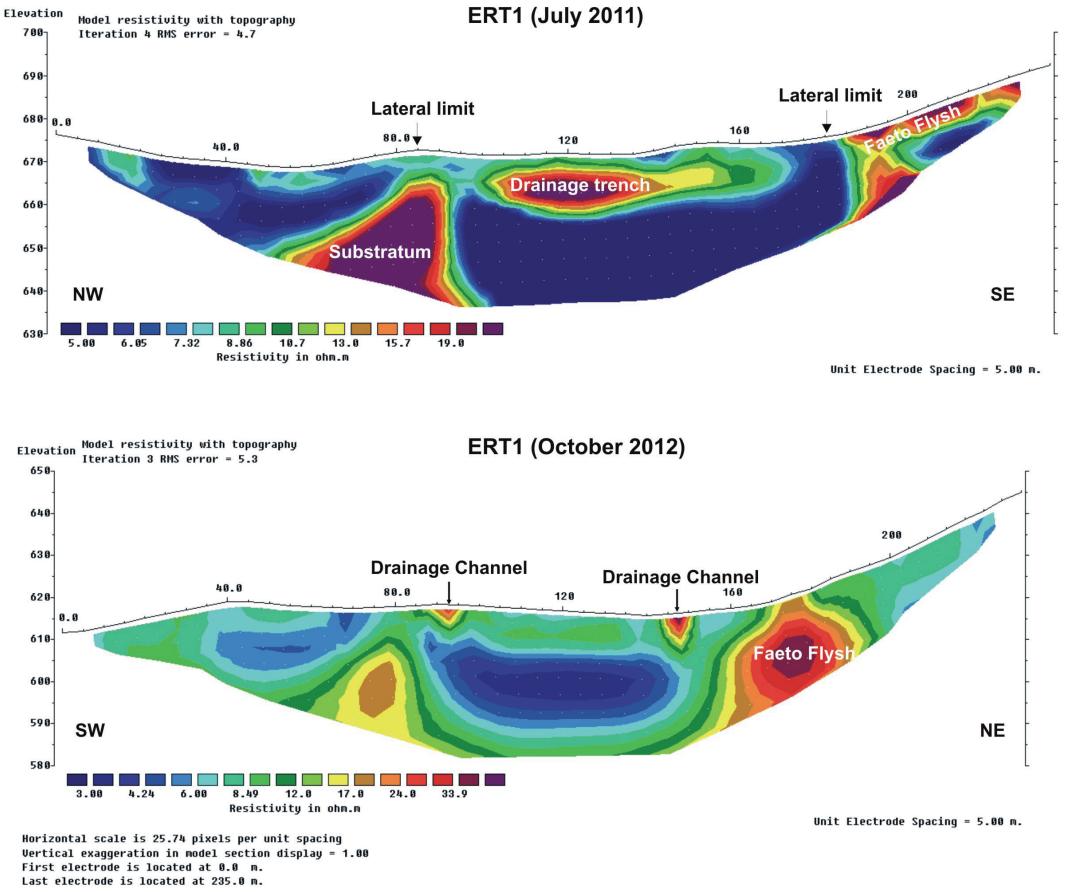

Fig. 3 – Resistivity models of ERT 1 carried out on the Montaguto landslide in July 2011 (top) and October 2012 (bottom).

between about 90 and 150 m two shallow highly resistive nuclei were present due to drainage channels. In between the two draining channels there is an almost 10 m thick layer, probably constituted by the landslide body. Underlying there is a conductive layer limited on laterally by more resistive zones, probably constituted by bedrock. Finally, both lateral sectors of the ERT showed low resistivity zones that can be interpreted as clayey or water-rich material. The lateral limit of the landslide in the NE sector could be indicated by the change between conductive and resistive material close to 165-170 m. However, this change of electrical properties could also be related with a changing lithology.

Piezometric data confirmed that the central and deeper part of the ERT can be related to a water-rich material.

Conclusions. Although contrasts of electrical resistivity in the ERT images were not pronounced, it was possible to observe the presence of both lateral and vertical discontinuities, that could be ascribed to lithological limits and/or to physical variation of the same material with varying water content.

In some instances, discontinuities allowed to better define the landslide geometry of deep zones, whereas this was not possible for all the ERT. Furthermore, ERT images highlighted the presence of very conductive areas, which can be an evidence of old landslide bodies and/or relatively more water saturated zones.

A synoptic view on all the ERT carried out in the area showed high conductivity properties of the deeper material between the drains and lower conductivity in the shallower part (up to 10 m). Piezometric data showed that the higher conductivity values of deeper part can be related to the higher water presence. On the other hand, the more resistive shallow part is likely to be moving material, continuously drained and thus dryer.

Is worth to underlie that the analysis of the ERT here presented is preliminary, because it is only based on electrical and geo-morphological features. Future steps will focus on the analysis of direct or indirect data collected in boreholes, in order to have a better interpretation of the ERT here presented.

References

Amore O., Basso C., Ciampo G., Ciarcia S., Di Donato V., Di Nocera S., Esposito P., Matano F., Staiti D. and Torre M., 1998. *Nuovi dati stratigrafici sul Pliocene affiorante tra il fiume Ufita ed il torrente Cervaro (Irpinia, Appennino meridionale)*. Bollettino della Societa Geologica Italiana **117**, 455–466 r indirect data

Crostella A., Vezzani L., 1964. *La geologia dell'Appennino Foggiano*. Bollettino della Societa Geologica Italiana **83**, 121–141.

Di Nocera S., Matano F., Pescatore T., Pinto F. and Torre M., 2011. *Caratteri geologici del settore esterno dell'Appennino campano-lucano nei Fogli CARG*. Rendiconti Online Società Geologica Italiana (Suppl. 12), 39–43.

D'Argenio B., Pescatore T. and Scandone P., 1975. *Structural pattern of the Campania–Lucania Apennines*. In: Ogniben, L., Parotto, M., Praturlon, A. (Eds.), Structural Model of Italy.Quaderni de "La Ricerca Scientifica", 90. Consiglio Nazionale delle Ricerche, Roma, pp. 313–327.

Giordan D., Allasia P., Manconi A., Baldo M., Santangelo M., Cardinali M., Corazza A., Albanese V., Lollino G. and Guzzetti F.; 2013. *Morphological and kinematic evolution of a large earthflow: The Montaguto landslide, southern Italy*. Geomorphology, 187, 61–79, DOI:.10.1016/j.geomorph.2012.12.035.

Guadagno F.M., Forte R., Revellino P., Fiorillo F. and Focareta M., 2005. *Some aspects of theinitiation of debris avalanches in the Campania Region: the role of morphological slope discontinuities and the development of failure*. Geomorphology **66**, 237–254.

Guerriero L., Revellino P., Coe J.A., Focareta M., Grelle G., Albanese V., Corazza A. and Guadagno F.M., 2013. *Multi-temporal Maps of the Montaguto Earth Flow in Southern Italy from 1954 to 2010.* Journal of Maps, 9:1, 135-145, DOI: 10.1080/17445647.2013.765812.

Ventura G., Vilardo G., Terranova C. and Bellucci Sessa E., 2011. *Tracking and evolution of complex active landslides by multi-temporal airborne LiDAR data: The Montaguto landslide (Southern Italy)*. Remote Sensing of Environment, 115:12, 3237–3248.

Pescatore T., Russo B., Senatore M.R., Ciampo G., Esposito P., Pinto F., Staiti D., 1996. *La successione messiniana della valle del Torrente Cervaro (Appennino Dauno, Italia Meridionale).* Bollettino della Societa Geologica Italiana **115**, 369–378.

DYNAMIC CONTROL OF HISTORICAL BUILDINGS THROUGH INTERFEROMETRIC RADAR TECHNIQUE: AN USEFUL APPROACH FOR STRUCTURAL HEALTH MONITORING ON EARTHQUAKE DAMAGED STRUCTURES

S. V. Calcina, L. Piroddi, G. Ranieri
Dpt of Civil Engineering, Environmental Engineering and Architecture (DICAAR), University of Cagliari, Italy

Introduction. Structural damage identification is a fundamental element following an earthquake. A correct definition of the damage state of buildings allows us to establish technical procedures and operational standards for safeguarding the structures, aimed at restoring their original conditions.

Structural Health Monitoring techniques (SHM) make it possible to deduce the presence of lesions and estimate the severity of the damage to the structures by measuring the mode of vibration of the buildings. This is possible because the dynamic response of structures is strongly influenced by the conservation state of materials and by structural lesions. The scientific literature includes many methods of structural dynamic response evaluation and algorithms for the extraction of main modal parameters (Ivanovic *et al.*, 2000; Sohn *et al.*, 2004). Several experimental configurations are classified in function of the number of measured output signals (number of sensors) and of the type of sources used to energize the structures. In this context there are several experimental layouts to modal parameters identification. Specifically, it is possible to differentiate in forced vibration tests (i.e. using mechanical shaker or vibrodines), free vibration tests (i.e. by means of falling objects inside or outside the buildings – impulsive signals) and ambient vibration tests (i.e. using random sources as wind and artificial noise) (Maia *et al.*, 1997). The last methods are very useful for assessing dynamic behaviour and for a rapid evaluation of the true conditions of existing damaged structures after an earthquake. However, the most common data acquisition techniques use in-contact sensors. Velocimeters or accelerometers arrays are placed inside the building and are used to record time series of ambient vibration. In the last decade, advances in the field of Ground Based Remote Sensing assure remote data acquisition and real-time monitoring of vibrations in critical conditions, as well as dynamic control of severely damaged structures after earthquakes. In this paper the authors propose a procedure for assessing the state of damage to structures in areas affected by earthquakes. This approach is founded on remote monitoring techniques of mechanical vibrations by means of interferometric surveys. This method allows us to ensure maximum safety conditions during the monitoring of potentially damaged structures. In fact, the assessment of the structural damages during the next phase is extremely delicate due to precarious stability conditions of structures and due to possible further aftershocks during technical inspections by specialists. For this reason a new application of this proposed operational approach will be discussed in the case of the Emilia earthquake (Italy) for the stability control of the bell tower of San Giacomo Roncole using IBIS-S ground-based microwave interferometer.

Instrumental features of the IBIS-S technology. Microwave interferometry has recently emerged as a new technology, specifically suitable to remotely measuring the vibration response of structures. Several authors observe that the interferometric technique has proven to be a useful remote sensing tool for vibration measurements of structures, such as architectural heritage structures (Pieraccini *et al.*, 2005, 2009; Atzeni *et al.*, 2010), engineering infrastructures (Gentile and Bernardini, 2008 and 2009) and vibrating stay cables (Gentile, 2010 a, b). This radar technology is founded on the combined use of high-resolution waveforms (Wehner, 1995) and interferometric technique (Henderson, 1998). This technique is implemented to compute the displacement of each target through the phase shift $\Delta\vartheta$ of the back-scattered microwave signals collected at different time intervals. The displacement along the radar line of sight d_r is computed from the phase-shift with the following simple Eq. (1):

$$d_r = -\frac{\lambda}{4\pi}\Delta\vartheta \qquad (1)$$

where λ is the wavelength of the signal (Taylor, 2001). The main advantages of the interferometric radar for structural health monitoring of civil infrastructures are high accuracy of measurements (sensitivity of 0.01-0.02 mm) and high spatial resolution, simultaneous monitoring of several targets within the sensor applicable distance, independence from daylight and weather conditions for short recordings, portability, and quick set-up time. The sensor module is provided with two horn antennas (-3dB beamwidth of 17° and 15° in the horizontal and vertical plane) and transmits the electromagnetic signals in Ku frequency band from 17.1 to 17.3 GHz, receiving the echoes from several targets placed inside the radar scenario.

The acquired time history s(t) is the displacement of the target projected along the sensor-target line of sight (LOS). The LOS displacement s(t) is linked to the displacements component *V(t)* and *H(t)*, in vertical and in horizontal plane respectively, through the following Eq. (2):

$$s(t) = V(t)\sin(\beta) + H(t)\cos(\beta) \qquad (2)$$

with β being the LOS angle computed from the horizontal axis. The interferometric survey may thus be considered a powerful tool to evaluate the deformation related to dynamic applied loads and to evaluate the stiffness of structures.

Description and method. The test site was chosen in order to analyze a strongly damaged but not totally crushed bell tower, for which remote sensing approach was the only compatible one with safety conditions. The experimental settings were designed with the task to have comparable results from two main acquisition distances from the target and two different direction projection of measured displacement.

The tower: a brief historical overview and description of the damage. The Emilia earthquake has caused numerous damages to the structures. The buildings most affected by the earthquake are industrial structures (factories and storage magazines) and cultural heritage buildings (churches, bell towers, civic towers, etc..), whose geometric and constructive features have contributed to increasing their vulnerability in case of earthquakes. In this work we present the study performed for the bell tower of San Giacomo Roncole. The actual structure was built from 1771 to 1774 with the same materials of the previous Carmelite Convent of *Santa Maria delle Grazie della Galeazza* (Andreoli, 1987). The building is located few metres away from the singular nave of the church. The structure replaced an earlier tower, adjacent to the body of the church and demolished by the damage caused by the vibrations of the bells. The new tower is a masonry structure located at South-west of the church. The tower reaches a height of about 36 metres with a square base (5 metres per side). After the earthquakes of 20th and 29th May 2012 (magnitude M_l=5.9 and M_l=5.8, respectively) the building sustained serious damage to the base, highlighted by displacements of about 2 cm toward the South-West side and of 1 cm on the South-East side. In other words, after the earthquake the structure was shifted at the base, assuming an eccentric position. Also there are various fractures on the first section of the tower horizontally and diagonally crossing its perimeter walls, where a rigid motion on the order of centimetres was measured. The top of the structure collapsed at about 9 metres from the base toward the South-West side.

Sensor installation and data processing. The tower of San Giacomo Roncole is a slim structure with a shape characterized by several natural corners (see Fig. 1). Consequently, the measurements are performed without artificial corner reflectors installed on the body surface of the structure. This is an essential condition because the structure is seriously damaged. Dynamic surveys are carried out using three different configurations. In the first one, the IBIS-S system was placed in front of the tower in the South-East direction in order to monitor the dynamic behaviour of the full body of the structure with 30° LOS angle. The second radar

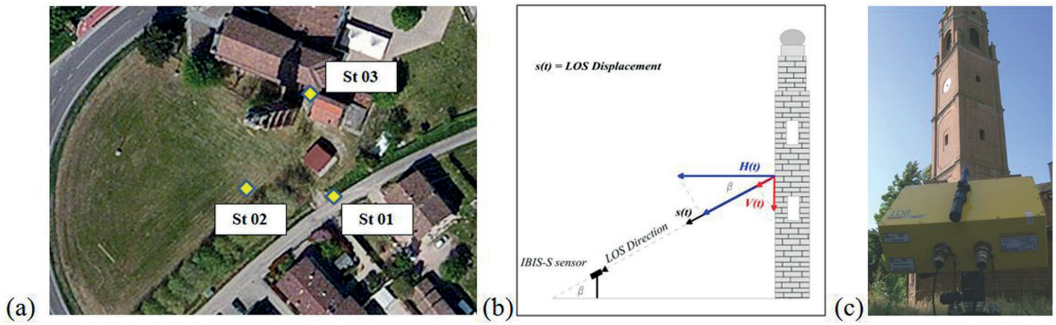

Fig. 1 – **a)** Installation of the IBIS-S system in several acquisition stations placed at 25 m (St 01) and 23 m (St 02) from the base of the tower with LOS angle of 30° (central beam) and at 8 m (St 03) with LOS angle of 70°. **b)** Radar line of sight displacement and true displacement vector. **c)** Image of the IBIS-S system used during the experiments.

station was placed in the SW direction (30° LOS angle). The last acquisition was performed with the IBIS-S system located under the tower (70° LOS angle). The acquisition geometry was selected in order to reduce the effects of all possible noise sources, such as suspended cables and other metal structures, or trees and vegetation inside the radar profile. Each acquisition had a duration of about 10 min with a sampling frequency of 200 Hz. The vibrations of the building were monitored in real time during field operations. The Fourier spectra of signals were provided by processing the acquired data with IBIS Dataviewer and Matlab software in order to assess the main frequencies of the structure. Before of the spectral analysis, the displacement data were detrended and tapered with Hamming function to reduce leakage effects. The knowledge of the deformation kinematics allows to evaluate main vibration properties of the structure by means of the Frequency Domain Decomposition technique FDD (Brincker *et al.*, 2001). This method is based on the Singular Values Decomposition of the output Power Spectral Density matrix G_{yy} through the following Eq. (3):

$$[\mathbf{G}_{\mathbf{yy}}(j\omega_i)] = [\mathbf{U}]_i [\mathbf{S}]_i [\mathbf{U}]_i^H \qquad (3)$$

where $[\mathbf{U}]_i$ is a unitary matrix of the singular vectors $\mathbf{u}_{ij}$, **S** is a diagonal matrix of the scalar singular values $\mathbf{s}_{ij}$ and $[\mathbf{U}]^H$ is the hermitian matrix of **[U]** (complex conjugate transposed matrix). Assuming that each mode will be dominant around its corresponding frequency, the first singular vector represents an estimation of the mode shape and the corresponding singular value belongs to the auto-power spectral density function of the corresponding Single Degree Of Freedom system. By using this decomposition method, main modal parameters can be identified with high accuracy even in the case of strong noise contamination of the signals.

Results and discussion. The range-bins with high signal-to-noise ratio (SNR) along the radar power profile are associated with different natural back-scatterers located inside the radar scenario. However, the signal-to-noise ratio of the radar response from this structure is high and the structure is isolated inside the radar scenario. Thus several range-bins may be selected to be analyzed. Five range-bins of the radar power profile are selected to estimate fundamental vibration properties of the structure by means of the FDD decomposition technique. The radar-bins are selected in function of the distance along the radar line of sight between each radar-bin and the IBIS-S sensor. These range-bins correspond to five reflective points placed on the bell tower facade. This operation is easily performed knowing the geometric characteristics of the tower (the height of several architectonic elements such as windows and other ledges), the horizontal distance of the radar station, and the inclination of the IBIS-S head. The displacements retrieved from radar data are shown in Fig. 2. These time series have been obtained observing the tower from a position to the base of the tower, at a distance of 23 metres

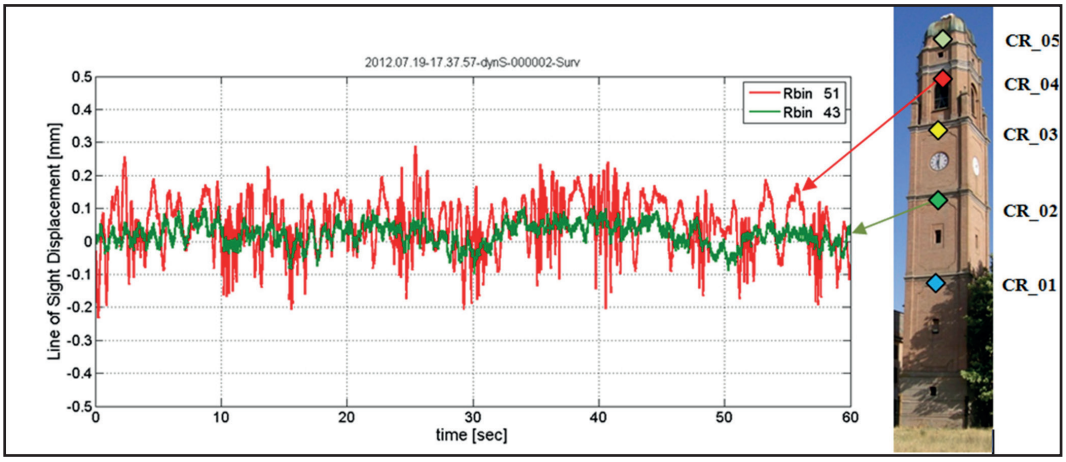

Fig. 2 – One minute record acquired with the second configuration: LOS displacement retrieved from radar data as a function of the time. The time histories refer to two range-bins selected from the radar power profile and correspond to different heights of the tower.

(configuration 2). During all measurements a regular wind with moderate speed of 5.5 m/s blew.

The displacement spectra are obtained over the whole recorded ten minutes signal. A band-pass filter (0.3Hz-10Hz) was applied to reduce the presence of disturbances linked to atmospheric effects and to vibration of the sensor itself. The influence of the first effect is prevalent on the measured phases and, as a consequence, on the estimated displacements with long period (0.1-0.2Hz). Another effect is caused by the vibration of the measurement tool. Luzi *et al.* (2012) observe that the measured resonant frequency of the system ranges within

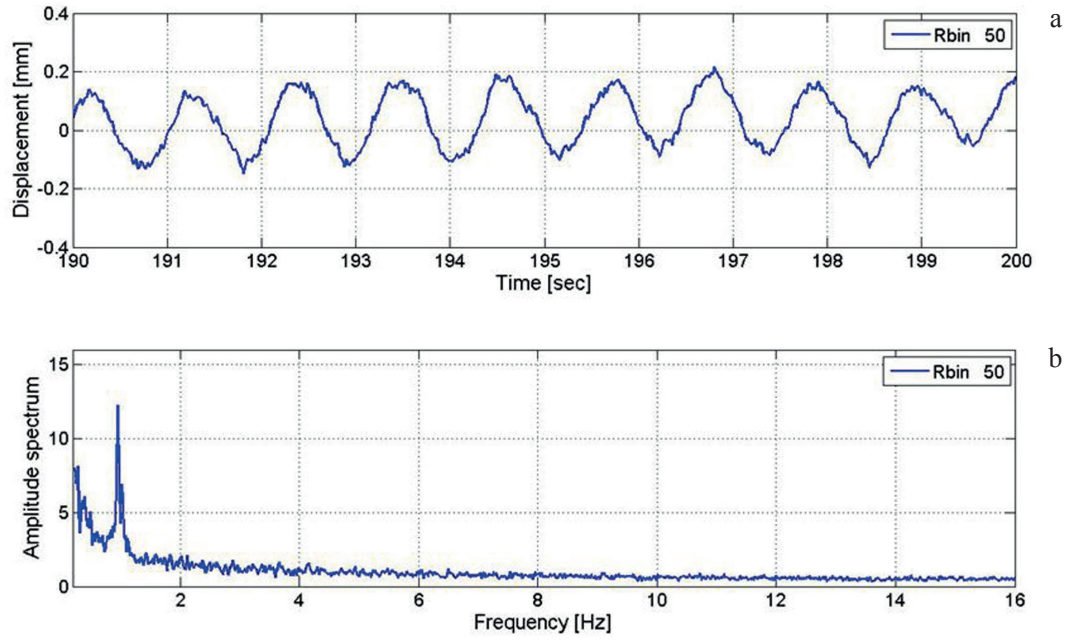

Fig. 3 – **a)** Sinusoidal trend of the displacement record obtained for the 50th range-bin (30 metres height). **b)** Frequency analysis of the same time-history.

10 Hz±2 Hz for typical working conditions. Then a low-pass filtering may be applied in order to assure that the measured vibrations are not imputable to the natural response of the tripod-head sensor system. All amplitude spectra are characterized by a clear harmonic component at 0.96 Hz (corresponding period of 1.04 s) whose amplitude increases with the height of the analyzed range-bin. This behaviour agrees with the expected amplitude variation associated at the first natural mode (simple bending). This periodicity cannot be directly retrieved from all displacement time series but only for the 50th range-bin corresponding to the reflection from the height of 30 metres on the tower (see Fig. 3).

The obtained value of 0.96 Hz could be influenced by the presence of structural damage caused by the earthquake. This value could be compared with the theoretical one achieved through numerical modelling of the building before the damage. However, even without a direct model, several empirical relationships available for masonry structures, like those proposed by the Italian Building Code NTC-2008, the Spanish National Code NSCE-02 and by literature studies (Rainieri and Fabbrocino, 2012), are used to assess the fundamental frequency of vibration. The obtained results range between 1.4 and 1.5 Hz. The significant difference (31-36%) between the experimental value and the estimated values could be imputed to the damage caused by the earthquake. It is generally recognised that the period of vibration grows while increasing the mass of the vibrating system and while reducing the stiffness.

The radar measurements allows the evaluation of the dynamic behaviour (amplitude of vibration) of several parts of the building located at different heights. In this case we have monitored the structure from different perspectives and we have compared the experimental mode shapes obtained for the IBIS-S configurations 1 and 2. The mode shape retrieved by the configuration 3 was not used for this analysis because the displacements measured in LOS direction are not comparable with the others. In fact, in this configuration the microwave sensor is more inclined (70°) and is placed at short distance from the tower (8 metres). Measured displacements along two directions are projected along the horizontal plane. The experimental mode shapes show a similar trend. We observe that maximum values are measured from St 02 IBIS-S station and are characterized by amplitude ranges from 0.05 to 0.2 mm. The fundamental mode of vibration is a bending mode with the same frequency of 0.96 Hz in both directions of measurement. Anomalous behaviour is detected at the point placed at 17 metres height with experimental measured displacements greater than those expected. This trend could be correlated with the structural damages of the building at the middle level. Moreover, the larger displacements obtained in the second acquisition are justified by the major shift recorded in this direction (about 2 cm) due to seismic action.

Conclusions. This paper proposes the use of the ground-based microwave interferometry for remote sensing of vibrations of structures aimed at providing useful information for specialists about the damage state of structures in areas affected by earthquakes. For this reason, this work is the first application of ground-based radar interferometry to the study of an inaccessible damaged building. The authors report the results of the experimental dynamic test aimed at estimating the vibrations of an historical bell tower in an urban environment, performed through ambient vibration testing. Also, the basic principle of the interferometric technique has been briefly resumed and the main experimental data obtained for the vibration features of the structure have been critically discussed to identify anomalous dynamic behaviours linked to structural damages. In general, the proposed method can estimate displacements ranging from a few microns up to several millimetres for large structures, ranging from thin and tall structures to other types of buildings (towers, skyscrapers and bridges). The possibility of working remotely makes this approach suitable for the dynamic control of buildings that have reported structural damage after an earthquake, especially for civil structures of strategic interest during the emergency and for cultural heritage buildings which represent the history and the social identity of a community.

Acknowledgements. Sergio Vincenzo Calcina gratefully acknowledges Sardinia Regional Government for the financial support of her PhD scholarship (P.O.R. Sardegna F.S.E. Operational Programme of the Autonomous Region of Sardinia, European Social Fund 2007-2013 - Axis IV Human Resources, Objective l.3, Line of Activity l.3.1.)".
Luca Piroddi gratefully acknowledges Sardinia Regional Government for the financial support (P.O.R. Sardegna F.S.E. Operational Programme of the Autonomous Region of Sardinia, European Social Fund 2007-2013 - Axis IV Human Resources, Objective l.3, Line of Activity l.3.1 "Avviso di chiamata per il finanziamento di Assegni di Ricerca").

References

Andreoli E.; 1987: *San Giacomo Roncole: raccolta di notizie storiografiche popolari*, Mirandola edizioni, Mirandola, Italy.

Atzeni C., Bicci A., Dei D., Fratini M., Pieraccini M.; 2010: *Remote Survey of the Leaning Tower of Pisa by Interferometric Sensing*, IEEE Geoscience and Remote Sensing Letters, no. 7, pp. 185-189.

Brincker R., Zhang L., Andersen P.; 2001: *Modal identification of output-only systems using frequency domain decomposition*, Smart Materials and Structures, no. 10, pp. 441-445.

Gentile C., Bernardini G.; 2008: *Output-only modal identification of a reinforced concrete bridge from radar-based measurements*, NDT & E International, no. 41, pp. 544-553.

Gentile C., Bernardini G.; 2009: *An interferometric radar for non-contact measurement of deflections on civil engineering structures: Laboratory and full-scale tests*, Structure and Infrastructure Engineering, vol 6, no. 5, pp. 521–534.

Gentile C.; 2010a: *Application of microwave remote sensing to dynamic testing of stay-cables*, Remote Sensing, no. 2, pp. 36-51.

Gentile C.; 2010b: *Deflection measurement on vibrating stay cables by non-contact microwave interferometer*, NDT & E International, vol. 43, no. 3, pp. 231-240.

Henderson F.M., Lewis A.J.; 1998: *Manual of Remote Sensing. Principles and Applications of Imaging Radar*, Wiley: New York, USA.

Ivanovic S.S., Trifunac M.D., Todorovska M.I.; 2000: *Ambient vibration tests of structures – A review*, Bulletin of Indian Society of Earthquake Technology: Special Issue on experimental methods, pp. 1-49.

Luzi G., Monserrat O., Crosetto M.; 2012: *Real Aperture Radar interferometry as a tool for buildings vibration monitoring: limits and potentials from an experimental study,* Proceedings of the 10th International Conference on Vibration Measurements by Laser and Non-contact Techniques — AIVELA 2012, pp. 309-317, Ancona, Italy.

Maia N.M.M., Silva J.M.M., He J., Lieven N.A., Lin R.M., Skingle G.W., To W.M.; 1997: *Theoretical and Experimental Modal Analysis*, Research Studies Press: New York, USA.

Pieraccini M., Fratini M., Parrini F., Pinelli G., Atzeni C.; 2005: *Dynamic survey of architectural heritage by high speed-microwave interferometry*, IEEE Geoscience and Remote Sensing Letters, no. 2, pp. 28-30.

Pieraccini M., Fratini M., Dei D., Atzeni C.; 2009: *Structural testing of historical heritage site towers by microwave remote sensing*, Journal of Cultural Heritage, no. 10, pp. 174-182.

Rainieri C., Fabbrocino G.; 2012: *Estimating the elastic period of masonry towers,* Proceedings of the SEM IMAC 30th Conference, Society for Experimental Mechanics Inc., Jacksonville, FL, USA.

Sohn H., Farrar C.R., Hemez F.M., Shunk D.D., Stinemates D.W., Nadler B.R., Czarnecki J.J.; 2004: *A Review of structural health monitoring literature: 1996–2001*, Los Alamos National Laboratory Report, LA-13976-MS, USA.

Taylor J.D.; 2001: *Ultra-Wideband Radar Technology*, Boca Raton, CRC Press, USA.

Wehner D.R.; 1995: *High-resolution radar*, 2nd Ed. Artech House, Boston, London.

NEW DATA ABOUT THE SINKHOLE HAZARD AT CASALABATE (LECCE PROVINCE)

M. Delle Rose[1], L. De Giorgi[2], G. Leucci[2]
[1]Istituto di Scienze dell'Atmosfera e del Clima – CNR, Lecce, Italy
[2]Istituto per i Beni Archeologici e Monumentali – CNR, Lecce, Italy

Introduction. Casalabate is a coastal small town frequently affected by sinkhole events. The first noticed event occurred on 1993 and caused several destructions of buildings. In the same year, a sinking of a small portion of emerged beach happened (Delle Rose and Federico, 2002). Four years later a collapse affected the submerged portion of beach and allowed the formations of a submarine spring, since then the bathing was forbidden for some weeks. Two episodes of sinkhole on the emerged beach occurred during 2000 and 2004, along a strike no longer than 30 meters. Each of they caused on surface short-lived elliptical depression quickly filled by sand. All the aforementioned episodes occurred inside a narrow area (about 250 m long and 100 m wide) close to the coast and oriented according to a north-north-east - south-south-west tectonic structures system (Delle Rose and Leucci, 2010). Further episodes occurred on March 2010, November 2010 and March 2011. The last noticed sinkhole happened on 7 January 2012. Usually the sinkholes occurred during or after rains or sea storms and each episode lasts some minutes at least. Due to geological and geotechnical uncertainties, Casalabate became an intriguing case study of sinkhole hazard in urban areas and three geological-geophysical models were recently proposed to explain the ground-instability and to asses the related hazard (Delle Rose and Leucci, 2010; Calò *et al.*, 2011; Margiotta *et al.*, 2012). 3D geological model and new geophysical data here shown can contribute to an efficient predictive model taking into account the hydrogeology context. Moreover, some epistemological considerations had performed to improve the interdisciplinary exchange between geologists and geophysicists.

Geological setting. Casalabate is located on the Adriatic side of the Salento Peninsula (Southern Italy) on a coastal plain elevated a few meters above sea level (Fig. 1). The Salento Peninsula is the emerged southeastern portion of the Adriatic Carbonatic Plate (Auct.) which is formed by Jurassic-Cretaceous limestones and dolostones covered by Tertiary and Quaternary carbonates and marls. The bedrock of Casalabate is build up by Quaternary carbonate deposits, some ten of meters thick, lie on Cretaceous limestone (Rossi, 1969). Nevertheless, geological and geotechnical data suitable to civil engineering lacked until few years ago. As a consequence, to face the sinkhole hazard the municipal authority performed a extensive bedrock survey by means of boreholes and geophysical measures. The results of such a survey was used in Delle Rose and Leucci (2010) and in Calò *et al.* (2011). Casalabate bedrock resulted built up by "two overlap units the lower of which is a moderately cemented massive calcarenite made up mainly of marine bioclasts and medium-large in grain size. The upper units is formed by sets of variableness cemented thinly laminated and cross-stratified calcarenite [ancient dunes] whose grains were terrestrial or marine supplied. The latter is 5-10 m thick, whereas the base of the former are locally unknown but, on the base of the setting surrounding Casalabate, the thickness of the massive calcarenite doesn't excess 20-25 m. Both the calcarenite units show a nearly omogeneous low-angle beds dip, which seems to be due to primary clinostratification as well as tectonic eastward tilting" (Delle Rose and Leucci, 2010). Four tectonic fracture systems (medium strikes N 5°E, N55°E, N100°E and N145°E) probably affect both the stratigraphic units. The shape and orientation of the landforms are clearly due to the spatial arrangement of the tectonic fractures. This structural control is particularly evident concern the shape of the depressions filled by clayey-silt marsh deposits. The calcarenite units were interested by various periods of dissolution karst processes to begin from the Middle Pleistocene. Usually such a process are named as "parakarstic" (Auct.) to emphasize the small dimension of the morphological forms respect those charactering the Jurassic-Cretaceous limestones and dolostones.

A shallow coastal aquifer flows out along the Casalabate coast. The groundwater circulation is influenced by the tectonic fracture systems and is manifested by some submarine springs. Underwater investigations of the sinking of a portion of submerged beach in 1997 revealed the presence of a karst spring (Delle Rose and Federico, 2002) probably joined with the cave that induced the 1993 sinkholes. Such springs are not perennial and can occur suddenly. The last case of new spring formation occurred below an house on the beginning of September 2013 and caused a new warning of the residents.

3D models. Using the software Groundwater Modeling System (GMS) a 3D geological model and a 3D groundwater model are in progress. The scope of building the models is to simplify the field problem and organize the field data so that the system can be analyzed more readily (Anderson and Woessner, 2002). The conceptualization of the models includes synthesis and framing up of data pertaining to geology, hydrogeology, hydrology, and meteorology. The lithologic data were collected from 23 core lithologs data (kindly provided by the technical office of Lecce municipality). Such a borehole survey was performed on 2008 and was related to the project "actions to protect the soil in the hydrogeological risk areas of the municipality of Lecce" funded by the Ministry of Environment and Protection of Land.

The geological model was created using a block-centric finite-difference grid. The gridding was performed through the eight nearest-neighbor methodology with 3-D interpolation by average minimum distance. The solid model was developed to a depth of about 10 m below the ground level. The sensitivity of the model was tested by varying the horizontal and vertical spacing of the nodes, and an optimized final model, least sensitive to changes in spatial resolution (i.e., smaller grid sizes), was built. The resolution of the final model was 100m×100m×2m. The resulting discretization consisted of 250nodes×250nodes×100nodes, obtaining 6,250,000 solid model nodes, each with a voxel volume of 20,000 m^3. It should be noticed that the results of the modeling are not free from uncertainties, which could be reduced by increasing datapoints, but they illustrate one of the most probable scenarios. The smallest scale of variation that the model is able to depict is equal to the resolution of one voxel. The 3D geological model (Fig. 2a) with the cross-sections in Fig. 2b provides a depictions of the bedrock of the studied area. Such model was vertically discretized in 8 layers (paving; artificial landfills; sands of beach; organic soils; residual soils; marsh deposits; cemented thinly laminated and cross-stratified calcarenites; moderately cemented massive calcarenites). The layers were allowed to have seepage from the top and leakage through the base, making them hydraulically connected. The top-most layer and the second layer were defined as unconfined. The rest of the layers were defined as confined, as the water table was not expected to fall > 10 m. Such a model has reached a first level of advancement and needs several new data to be fully efficient, to start from the boundary conditions as well as the real physical characters of the higher layers.

Given the heterogeneity and complexity associated with the study area (e.g. local-scale variations of aquifer properties), some generalizations, simplifications and assumptions will be made to construct the groundwater flow model. The modeling area is limited in the east by the Adriatic sea, and it accounts for about 1,5 km in length and 0,5 km in width. The 3-D constant-density groundwater flow will be simulated by a block-centric, finite-difference grid model, using MODFLOW code inside GSM software. Furthermore MODAEM code, which allows the analysis to the analytical elements (polygons, lines and points), will be used.

New geophysical measures. In our previous work, we have proposed a method to integrate geophysical survey and geological knowledge to characterize the sinkhole hazard at Casalabate. As regards geophysics job, the performed 3D GPR and 3D ERT allowed us to reveal a complex hypogean cavity system inside the urban area affected by sinkhole since the 1993 (Delle Rose and Leucci, 2010). Here we propose an ERT survey carried out in an area (Fig. 3a) next to the 1993 sinkhole collapsed that caused the collapsing of three buildings and irreparable damage to various others, which were demolished later. A 48-channel Syscal-Pro Resistivity-meter in a multielectrode configuration using a Wenner–Schlumberger array (Loke 2009) was used. This

is a hybrid between the Wenner and Schlumberger arrays (Pazdirek and Blaha, 1996) arising out of more recent work with electrical imaging surveys. This array is moderately sensitive to both horizontal and vertical structures. In areas where both types of structures are expected, this array might be a good compromise between the Wenner and the dipole–dipole array (Loke, 2009).

The electrode spacing was of 5 m. The line were oriented predominantly in a W-E direction. The measurements were stacked at least three times for each point along the profile to enhance data quality. Standard deviation was used for evaluating the statistical dispersion of recorded resistivity data from their arithmetic mean. The chosen electrode array and spacing made it possible to investigate about 30 m of subsoil with a good resolution. Resistivity data were inverted with the ErtLab software (Geostudi Astier, 2010). The 2D resistivity model is shown in figure 3b. It shows the resistivity distribution of the upper 30 m, in which it is possible to note the following: (i) a layer of relatively low resistivity (about 5–50 ohm m), from the surface to about 2 m in depth (labelled A); (ii) a layer (labelled B) in which resistivity values range between 100 and 150 ohm m; (iii) the area of highest resistivity (ρ = 200 ohm m), inside the layer B; iv) a deeper layer (labeled C) in which resistivity values range between 100 and 130 Ω·m. The model established by means of 2D resistivity imaging profiles thus allows three different zones to be detected and analysed. The first one (A) may correspond to the anthropogenic layer (paving; artificial landfills) in which a groundwater with salt water intrusion is present. The second one (B) corresponds to lamp strata of the laminated and cross-stratified calcarenites and the third one (C) to the moderately cemented massive calcarenites.

The area of highest resistivity inside the layer B could be related to karstic forms. The location of such a forms well fits a complex marsh depression (probably a group of coalescent dolines or sinkholes) buried below the anthropogenic layer, that was detected by means of photo analysis of aerial photo taken before urbanization (Delle Rose and Fiorito, 2000, Fig. 1 of p. 76).

How geological uncertainties worsen the hazard assessment. How previous said, three geological-geophysical models were proposed to explain the instability of the underground of Casalabate (Delle Rose and Leucci, 2010; Calò *et al.*, 2011; Margiotta *et al.*, 2012). The first of these considers a shallow karst cavities system in carbonate rocks filled by different kind of deposits (marsh deposits; residual soils; organic soils; sands of beach) suitable to be removed by water flows. In such a context, sinkholes could be due to both the break of cavities' vault (i.e. collapse sinkhole, cf. Waltham *et al.* 2005) and the down-washing of the filling deposits inside the cavities system (i.e. suffosion sinkhole, cf. Waltham *et al.* 2005). This latter phenomena "is particularly probable taking into account both the sea level changes and the variations of the piezometric level of the groundwater inside the hypogean system, that can lead high energy water flows that are able to remove and wash away the sediment filling" (Delle Rose and Leucci, 2010, p. 153). According to Calò *et al.* (2011) the sinkhole "phenomena cannot be due to the collapse of the underground cavities vault, but because of the incidence and combination of the following factors: poor, and in some cases, very poor geotechnical characteristics of foundation grounds; the lack of a preliminary geotechnical characterization of buildings leading to the choice of improper practice in laying down foundations; the letting of rainwater into the subsoil which caused the leaching and the removal of the fine fraction of the foundation

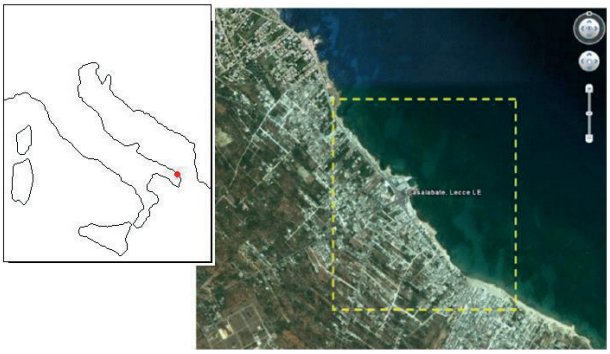

Fig. 1 – Surveyed area (photo by Google Earth).

grounds". Finally, Margiotta *et al.* (2012) claim the occurrence of collapse sinkholes inside the marsh deposits and suffosion sinkholes moving down sandy beach deposits. Such last Authors emphasize how their "data" with "particular regard to the stratigraphical succession, are in strong disagreement" with the model of Delle Rose and Leucci (2010) whereas in the same time they are suitable to "mapping the susceptibility to sinkhole" at Casalabate. So, apparently these three models are incompatible each with an other one. Really the divergence are mainly due to the different methods to achieve the scientific knowledge or, in other words, they concern epistemological aspects of the research.

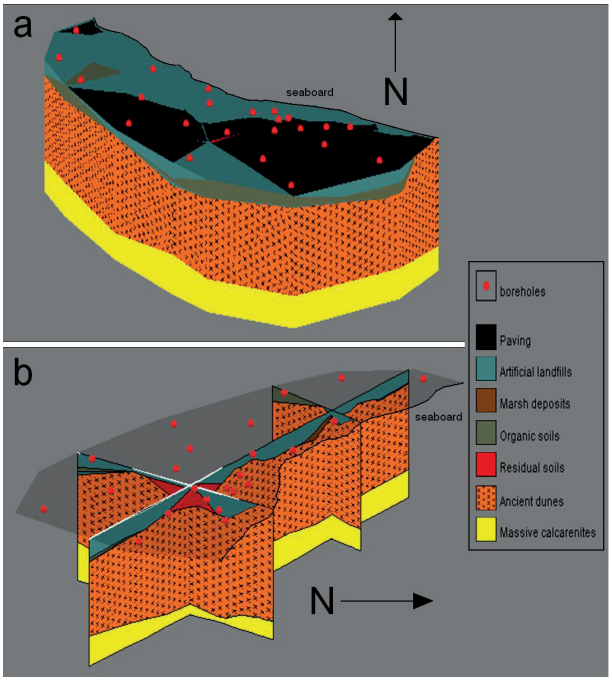

Fig. 2 – Geological 3D model (a) and cross sections of Casalabate urban area (b).

Both the models proposed by Delle Rose and Leucci (2010) and Calò *et al.* (2012) used a stratigraphy reconstruction based the boreholes drilled in the aforementioned project "actions to protect the soil in the hydrogeological risk areas". However, "outcrops available to geological observations are scarce in the Casalabate area, so a borehole survey and sampling had been the key tools to reconstruct the main features of the local geological substratum" (Delle Rose and Leucci, 2010). The subsoil detection performed let us to recognize in the first ten meters of the bedrock two overlap units, the lower of which is a moderately cemented massive calcarenite and the upper unit is formed by sets of variably cemented thinly laminated and cross-stratified calcarenite. As regard the differences between the model proposed by Delle Rose and Leucci (2010) and Calò *et al.* (2012), these last Authors stressed how "the integrated analysis of information obtained from logs and georadar investigation evidences that […] no cavities and/or channels referable to parakarstic dissolution phenomena have been detected". We point out that only 2 out of 23 boreholes performed on 2008 were performed within the area really affected by sinkholes (the "collapsed area" evidenced in Fig. 3a). Moreover, one of the such two boreholes crossed red residual soils that are a typical filling of dolines. So, in our opinion, the conclusion of Calò *et al.* (2011) can be relevant at the entire urban scale but is inconsistent with the scale of the dangerous area. As before said, such an area where sinkholes occurred is narrow (about 250 m long and 100 m wide) and close to the coast. However we have to observe that Calò *et al.* (2011)

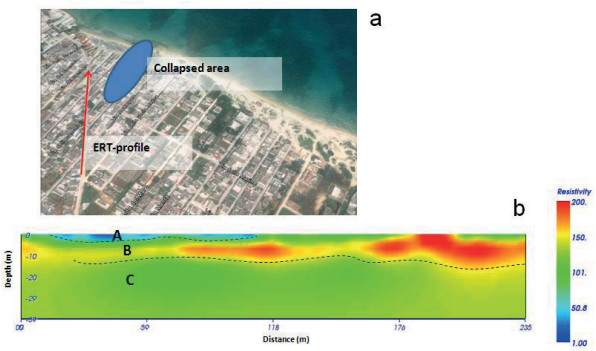

Fig. 3 – ERT survey: location (a) and 2D resistivity model (b).

do not show the profiles of their georadar investigation and therefore don't allow a critical evaluation of their measures and data.

The divergences between the models of Delle Rose and Leucci (2010) and Margiotta *et al.* (2012) might be explained from the different results of the respective stratigraphy and geophysical surveys. It must be observed that Margiotta *et al.* (2012) ignored both the aforementioned borehole survey performed on 2008 and the paper of Calò *et al.* (2011). However they misunderstand the model of Delle Rose and Leucci (2010) especially when assert that such a model "is based on a stratigraphy consisting exclusively of carbonate deposits, without taking into the due account the crucial presence of cover deposits above the calcarenite bedrock, and primarily that of the organic-rich clays [i.e. marsh deposits]" (Margiotta *et al.*, 2012, p. 667).

Margiotta *et al.* (2012) described the marsh deposits with a thickness up to of 11 m and overlying (without interruptions) the calcarenites along the coast for an outcropping area wide from 100 to 250 meters. This stratigraphy setting does not fit the boreholes data of the aforementioned project funded by the Ministry of Environment and Protection of Land: in fact only 6 perforations out of 23 crossed palustrine deposits of thicknesses ranging from 0.3 to 1.4 m. Moreover, the whole stratigraphical model proposed in Margiotta *et al.* (2012) appears based on subjective considerations. Such Authors affirmed that their "research involved […] the critical revision of more than 40 well-core stratigraphies", without describing what is such a "critical revision". Their subsoil model seems mainly based on interpretation of geophysical measures. Consequently the controversy between the models embraced also methodological aspects regarding data processing and interpretation. We have to observe that for geophysical data Margiotta *et al.* (2012) associate individual radar signal reflections to specific geological boundaries and even associate a radar signal reflection to a prediction of subsidence. However, it is common practice to perform the radar profiles in correspondence of stratigraphical columns or trenches to be able to associate a specific radar reflections to geological stratigraphy (Conyers and Goodman, 1997; Conyers, 2004). A confrontation with the geophysical data of Margiotta *et al.* (2012) is really difficult because the figures were not possible to read the metric scales, time scales, and resistivity scales. Their radar sections are surely affected by ringing (Conyers and Goodman, 1997; Conyers, 2004) probably related to low penetration of radar signal. Seems that the radar signal do not propagate below 20ns. This is due to the high conductive materials presents in the subsoil as confirmed by ERT results presented by the same Authors. In fact in the surveyed area electrical resistivity seems to ranging from 0.5 to 20 Ω·m, index of highly conductive subsurface. Therefore the anomalous zones below 20 ns could probably be an artifact due to the application of the back ground removal filter. For ERT profiles Margiotta *et al.* (2012) associate resistivity values to specific geological formations. For example 0.5–2 ohm m were related to clay sediments without any reference to a nearby stratigraphycal core or a bibliography. In fact Reynolds (2011) at page 291 done table in which correlates various types of geological materials with a range of values of electrical resistivity (for clay materials resistivity value ranging from 1 to 150 Ω·m). Also in Loke (2011, page 6) for clay materials, resistivity value ranging from 1 to 100 Ω·m, while for the sea water resistivity value is about 0.2 Ω·m (due to the relatively high salt content). Given the above, the stratigraphical features of the marsh deposits described by Margiotta *et al.* (2012) appear inconsistent and the result of a wrong interpretation of geophysical data. Consequently, their model of sinkhole susceptibility is questionable.

Conclusions. The case of Casalabate is a good example of how geological uncertainties can worse the hazard assessment. In consideration of the complexity of the problem and the concerns of the collectivity, an efficient predictive model of the hazard should be defined. In order to select the most appropriate geological-geophysical model, confrontations among all the researchers working on this issue would be desirable. Especially the knowledge exchange between geologists and geophysicists must be improved. As revealed the ERT survey exposed in this report, dangerous cavities could be placed also out of the area repeatedly interested

by sinkholes since 1993. Consequently an efficient predictive model taking into account the hydrogeology and hydraulic context, especially the occurrence of rains and sea storms, must be produced.

References

Anderson, M.P. and Woessner W.W.; 1992: Applied Groundwater Modeling. Academic Press, Inc., San Diego, 381 pp.

Calò P., Macrì F., Piccinni F. and Tinelli R.; 2011: Instabilità del centro urbano di Casalabate (Lecce, italia): analisi delle condizioni di rischio - Instability of Casalabate village (Lecce, Italy): analisys of risk conditions. Italian Journal of Engineering Geology and Environment, 11(1), 55-64.

Conyers L.B. and Goodman D.; 1997: Ground-penetrating radar – an introduction for archaeologists. Alta Mira Press.

Conyers L.B.; 2004: Ground-Penetrating Radar for Archaeology. (Walnut Creek, CA: Alta Mira).

Delle Rose M. and Fiorito F.; 2000: Ipotesi di recupero del territorio di Casalabate. Economia e Società, 2, 71-81.

Delle Rose M. and Federico A.; 2002: Karstic phenomena and environmental hazard is Salento costal plains. Proc. IX IAEG Congress, J.L. van Rooy and C.A. Jermy editors, Durban, 1297-1305.

Delle Rose M. and Leucci G.; 2010: Towards an integrated approach for characterisation of sinkhole hazards in urban environments: the unstable coast site of Casalabate, (Lecce, Italy). Journal of Geophysics and Engineering, 7, 143-154.

Geostudi Astier; 2010: ErtLab Solver – Release 1.3.1.

Loke M.H.; 2011: Tutorial: 2-D and 3-D electrical imaging surveys. www.geoelectrical.com

Margiotta S., Negri S., Parise M. and Valloni R.; 2012: Mapping the susceptibility to sinkholes in coastal areas, based on stratigraphy, geomorphology and geophysics. Nat. Hazards, 62, 657–676.

Pazdirek O. and Blaha V.; 1996: Examples of resistivity imaging using ME-100 resistivity field acquisition system. EAGE 58th Conf. and Technical Exhibition Extended Abstracts, Amsterdam.

Reynolds J.M.; 2011: An Introduction to Applied and Environmental Geophysics, John Wiley & Sons Ltd., Baffins Lane, Chichester, second edition.

Rossi D.; 1969: Note illustrative della Carta Geologica d'Italia. Fogli 203, 204, 213 – Brindisi, Lecce, Maruggio. Servizio Geol. It., 42 pp.

A NEW METHODOLOGY TO ESTIMATE THE EM VELOCITY FROM COMMON OFFSET GPR: THEORY AND APPLICATION ON SYNTHETIC AND REAL DATA

M. Dossi[1], E. Forte[1], M. Pipan[1], R.R. Colucci[2]

[1] Department of Mathematics and Geosciences (DMG), University of Trieste, Italy

[2] Institute of Marine Sciences (ISMAR), National Research Council (CNR), Trieste, Italy

Introduction. A good EM wave velocity model is an important parameter in various GPR processing and analysis steps, such as depth conversion, data imaging and extraction of qualitative/quantitative information about subsurface lithology and fluid content. Unlike the seismic reflection case, where the velocity model is estimated from data collected with multiple source-receiver offsets, most GPR data acquisitions are performed with a single receiver antenna, so that the acquisition of multi-offset datasets is extremely demanding (Pipan *et al.*, 1999). Therefore the velocity field used for radar imaging is most often a constant value or, less frequently, a single approximated velocity function of depth [v(z)], obtained by analyzing single common midpoint (CMP) gathers. In most subsurface conditions, such model is inadequate to produce correct images even for qualitative studies.

Multi-channel GPR systems present numerous advantages, such as significantly reduced 3-D survey times by simultaneously collecting multiple profiles, or full multi-offset data measurement through multiple receiver antennas at different offsets. By processing such continuous multi-offset data gathering, it is possible to obtain an EM velocity model over the whole survey area (e.g. Moysey, 2011) with high horizontal resolution, while traditional single-channel GPR systems normally limit CMP data acquisition to only a few locations.

Besides such advantages, multi-channel GPR systems have some logistical limitations related to their size, which prevent their application in indoor surveys, in remote areas unreachable by motorized vehicles (such as mountains or glaciers), or in areas with rough topography. Moreover, the velocity analysis, which can be performed on multi-offset GPR

data, does not generally provide very accurate estimates, mainly because GPR velocity often decreases with depth, unlike seismic velocity. Therefore some assumptions used in standard velocity analysis, such as assimilating RMS velocity to stack velocity, produce inaccurate results when applied to GPR data analysis (Becht *et al.*, 2006).

We developed and tested a new procedure to estimate the EM velocity field from Common Offset (CO) GPR data, which is still the most common and less demanding acquisition scheme.

Current velocity analysis methods on CO GPR data. There are various techniques to estimate the EM velocity distribution from CO GPR data by taking into account the diffractions recorded on the GPR sections, which are caused by objects having dimensions comparable with the mean wavelength of the radar signal incident on them. The most common are: 1) the Diffraction Hyperbola Fitting and 2) the Migration Velocity Scan.

1) The diffractions in a GPR section have a hyperbolic shape, whose convexity depends on the RMS velocity of the radar wave between the ground surface and the scattering object. Therefore the velocity distribution can be estimated by fitting the diffraction hyperbolas at different depths. This method is very simple and can be applied to any hyperbolic event within a GPR section. Moreover, in situations where there are no reflection events, such as in some urban environments, this is the only available method.

However, the hyperbola fitting method has different problems, which limit the accuracy of the final results. In order to have truly hyperbolic diffraction events, the analyzed system must have plane, parallel and homogeneous layers. In a real system, lateral variations of the velocity distribution cause distortions of the hyperbolic shape and consequent errors in velocity estimation. Another cause of distortions is the shape of the scatterer since, if it has one dimension longer than the others, it does not behave as a point source and the recorded event results from a combination of reflection and diffraction.

Further limitations to such procedure depend on the actual presence and regular distribution of scatterers in the GPR section, able to produce well-defined diffraction hyperbolas, free from interferences with other reflection or diffraction events. The lower the number of diffractions is, the lower will be the resolution of the velocity field, both vertically and horizontally.

Finally, in a GPR section the diffraction hyperbolas are often spatially limited to an interval around their vertex. This fact, together with the non-impulsivity of the radar signal, adds further uncertainty to velocity estimation because hyperbolas with very different curvatures can fit the same data.

2) Migration is used to collapse diffractions and to move dipping reflectors to their correct position in a GPR section, and it requires an accurate velocity distribution as input parameters. Therefore, by iteratively applying the process of migration and by analyzing the results, it is possible to estimate the actual velocity distribution. If the distribution is accurate, all the diffraction hyperbolas will collapse around their apexes, otherwise there will be either an under-migration for lower velocities or an over-migration for higher velocities. Theoretically, dipping reflectors can also be used to analyze the results of the migration, if independent information on their real position is available.

However, also such method depends heavily on the actual presence, abundance and regular distribution of clearly visible diffraction hyperbolas in the entire GPR dataset.

New method. The new proposed procedure is a generalization of the one developed by Forte *et al.* (2013) and estimates the EM velocity distribution from each recorded trace, in a 2-D bistatic CO GPR profile, using the principles of geometrical ray theory. The method makes four assumptions:

1. In the proximity of each trace position the system is horizontally layered.
2. Each layer is lossless, non-dispersive, homogeneous, and isotropic. Such conditions are not generally respected by earth materials, but they are good approximations for many media in which the GPR signal propagates efficiently (Davis and Annan, 1989).
3. The radar propagates a plane EM wave.

4. The amplitudes of the reflected signals depend only on the partial reflections at each interface, having removed the effect of geometrical spreading and disregarding variations in antenna coupling and intrinsic and scattering attenuation effects.

In such a system, at a given offset, the ray paths of the recorded signals are fixed by geometrical constraints, and are symmetrical with respect to the mid-axis. The method estimates the velocity distribution by reconstructing the travel paths through an iterative process, requiring as input the value of the offset (x), the velocity (v_1) of the radar signal in the first layer, the peak amplitude (Ai_1) of the wavelet incident on the first interface and the peak amplitudes (As_i) and traveltimes (twt_i) of the reflected waves.

By knowing the thicknesses of the first n-1 layers and the velocities of the radar signal in the first n layers, each cycle calculates the thickness of the n-th layers and the velocity of the radar wave in the (n+1)-th layer, using the amplitude of the wavelet incident on the first interface and the amplitude and twt of the wave reflected by the n-th reflector.

The thickness h_n of the n-th layer is obtained by rearranging the reflection traveltime equation for the n-th interface:

$$twt_n = \sqrt{\frac{x^2}{\overline{v}_n^2} + 4\left(\sum_{i=1}^{n}\frac{h_i}{v_i}\right)^2} \quad \text{with} \quad \overline{v}_n^2 = \sum_{i=1}^{n} v_i h_i \Big/ \sum_{i=1}^{n}\frac{h_i}{v_i}$$

which reduces to the single reflection equation when n is equal to 1.

In a 1-D system the travel paths are fixed at a given offset, and the incident angle for the k-th interface is equal to the transmission angle at the (k-1)-th interface. Considering the propagation path of the wave reflected by the n-th interface and taking into account the small spread approximation (offset much smaller than depth), the angle of incidence ϑ_k on the k-th interface can be approximated by:

$$\vartheta_k = Arctg\frac{xv_k}{2\sum_{i=1}^{n} v_i h_i} \quad \text{with} \quad k \le n$$

From such angles, the reflection and transmission coefficients of the first n-1 interfaces are obtained from the Fresnel equations of TE (or TM) antenna configuration, while the n-th reflection coefficient is obtained by reconstructing the incident and reflected amplitudes at the n-th interface:

$$R_n = \frac{Ar_n}{Ai_n} \qquad \text{with} \qquad Ai_n = Ai_1\prod_{i=1}^{n-1} T_k \qquad Ar_n = \frac{As_n}{\prod_{i=1}^{n-1}(2-T_k)}$$

The EM velocity in the (n+1)-th layer is given by the Snell equation:

$$v_{n+1} = \frac{\sin(\vartheta_{n+1})}{\sin(\vartheta_n)} v_n \quad \text{with} \quad \vartheta_{n+1} = Arctg\left(\frac{1+R_n}{1-R_n}\tan\vartheta_n\right)$$

where ϑ_{n+1} is calculated in the TE antenna configuration.

By iterating the procedure for all the reflected ray paths, it is possible to obtain thicknesses and velocities in all the imaged layers. Input parameters are a) velocity of the shallow layer; b) amplitude of the wave incident on the first interface; c) amplitude and twts of all the recorded reflections.

Results and discussion. We first tested the new methodology on 1-D velocity models, from which synthetic GPR traces were calculated by using a known wavelet, taking into account only the partial reflection and transmission from each interface, both downward and upward, while disregarding dissipations and geometrical spreading as requested by the inversion algorithm. The shape of the wavelet used in the forward modeling is not important, since the only trace data requested by the inversion process are just the peak reflected amplitudes and the traveltimes associated with such reflections. The new procedure was then applied to the simulated traces to reconstruct the models' velocity distributions.

Tab. 1 shows two different velocity distribution models, one with decreasing velocities and the other with a deep high velocity layer. Both models have small and large velocity contrasts, to further test the accuracy of the inversion. The layer thicknesses are also different, with values generally increasing with depth. In both forward modeling and inversion, only the TE case is simulated (with a 70 cm constant offset) since it is the usual acquisition configuration for GPR surveys.

This is another test for the method, since with such GPR system the two models have different travel paths and reflection coefficients. In particular, the different thicknesses of the shallow layer in the two models give 19.3° and 9.9° incident angles at the first interface, respectively.

Tab. 1 – Parameters of the two 1-D velocity models used in forward modeling.

	Model 1		**Model 2**	
Layer	h_i [m]	v_i [cm/ns]	h_i [m]	v_i [cm/ns]
1	1.0	25.0	2.0	16.0
2	3.0	24.0	5.0	17.0
3	5.0	19.0	1.0	24.5
4	2.0	18.5	3.0	25.0
5	6.0	17.0	6.0	15.5
6	9.0	16.0	9.0	15.0

The forward and inverse processes are completely independent. The peak amplitudes, including their polarity, and the traveltimes required as input for the inversion, were taken from the synthetic GPR traces, while the velocities of the shallow layer of each model, the peak value of the initial wavelet and the offset are supposed to be known. Typical measurement uncertainties were added to each input parameter to estimate the error propagation, with the confidence of the velocity in the first layer being the most important factor in determining the uncertainties of the results.

The results of the inversion are consistent with the initial models parameters, as shown in Tab. 2. One important aspect is the general increase of the estimated error with depth, which is due to the iterative nature of the inversion program. Nevertheless, while the estimated errors can grow quite large, especially in the deeper layers and depending mainly on the initial measurement uncertainties used, the mean values are nonetheless very close to the initial values used in the forward modeling (Tab. 1).

Tab. 2 – Results of the inversion of the traces obtained from the models in Tab. 1, with the EM wave velocities in the shallow layer of the two models fixed as input parameters of the inversion procedure. The mean values in each layer are consistent with the initial models, while the main influence on the errors estimation is the uncertainty related to the velocities in the first layer.

	Model 1		**Model 2**	
Layer	h_i [m]	v_i [cm/ns]	h_i [m]	v_i [cm/ns]
1	1.00 ± 0.05	25.00 ± 0.20	2.00 ± 0.05	16.00 ± 0.20
2	3.00 ± 0.16	24.01 ± 0.20	5.00 ± 0.20	17.01 ± 0.21
3	5.00 ± 0.39	18.98 ± 0.24	1.01 ± 0.58	24.56 ± 0.55
4	2.00 ± 0.69	18.47 ± 0.25	3.00 ± 1.26	25.06 ± 0.59
5	5.99 ± 1.41	16.96 ± 0.32	5.98 ± 2.25	15.44 ± 1.19
6	8.98 ± 2.91	15.97 ± 0.40	8.96 ± 5.63	14.93 ± 1.25

We then applied the method on a real dataset acquired on a glacier (Eastern Glacier of Mt. Canin (UD), Italy) with a ProEx Malå Geoscience system equipped with 250 MHz shielded antennas. A proper processing flow must be applied to the GPR data before amplitude picking, in order to satisfy the assumptions of the method and to avoid artifacts as much as possible. A bandpass filtering and a true amplitude recovery are the basic operations required before amplitude picking. In fact, most of coherent and random noise is often either outside or at the low end of the useful frequency spectrum, and can be effectively removed by means of bandpass filters.

A glacier represents a particularly favorable system for GPR studies, given the low intrinsic dissipation of the frozen materials. In such a system, the signal attenuation is mainly caused by geometrical spreading, scattering and partial reflections. After the data processing, the signal attenuation is assumed to be exclusively due to partial reflections from the interfaces between the glacier's layers.

The required approximation of a multilayered model with plane parallel interfaces in the proximity of each trace position is acceptable for most real cases, particularly in a glacier were stratification is often sub-parallel except possibly in the proximity of the rock basement. Moreover the actual slopes of the layers often do not have a major influence on the reflection coefficients and, therefore, on the results. In fact, for most real situations, the incident angles are small and, in such situations, the reflection coefficient does not vary much, according to the Fresnel equations, for most real velocity contrasts. This is a very important fact, since the actual subsurface geometry is unknown, being it the ultimate outcome of any geophysical survey, and it is an essential information in calculating the actual ray paths. Therefore, this geometrical assumption can be considered a good approximation of real conditions except in some uncommon and very peculiar situations.

The results of the inversion program are shown in Fig. 1. On such GPR section six layers were identified and the peak amplitudes, including their polarity, and the traveltimes were taken from the interpreted interfaces. The peak value of the initial wavelet can be easily estimated by placing the GPR system above the ground, in order to separate the airwave from the groundwave; the recorded airwave values can be in fact considered equal to the actual transmitted wave and used as reference amplitude.

The velocity values of the shallow layer were obtained from single CMP gathers acquired on selected locations; a constant mean value of 24.1 cm/ns was used for the entire dataset. Other possible independent methods to estimate the velocity include direct density measures or trans-illumination experiments.

It is important to note that the proposed inversion process could give unrealistic results if the used velocity values are considerably higher of lower than the real ones, because in both cases such erroneous values could interact with the picked traveltimes and amplitudes, giving in the various layers negative or imaginary values for the thickness, or clearly unrealistic velocities. On the other hand, a slightly wrong velocity input does not severely impact the results, which would be simply normalized with respect to a reference velocity, preserving the velocity contrasts at the interfaces. Moreover, the errors associated with the calculated velocity field constitute valuable information on the effect of the uncertainty of the used reference velocity.

Conclusions. We implemented and validated a new method to estimate the velocity distribution from CO GPR data by using the reflection amplitudes and traveltimes picked on the interpreted interfaces in a GPR profiles. Since the method assumes the picked amplitudes to be related only to the reflection coefficients, an accurate data processing is essential before any amplitude picking, the most important steps being the amplitude recovery and the removal of scattering effects.

The method also requires as input: 1) the value of the offset, 2) the velocity of the EM wave in the shallow layer, 3) the peak amplitude of the wavelet incident at the first interface. The

error associated to the velocities in the first layer has the major influence on the uncertainties of the final results. Nevertheless, this error can be reduced by combining different independent measurements, like CMP gathers, TDR measurements, or dedicated trans-illumination experiments.

The assumption of 1-D model in the proximity of each trace position, as well as the small spread approximation used in the algorithm, are acceptable for most of the real GPR

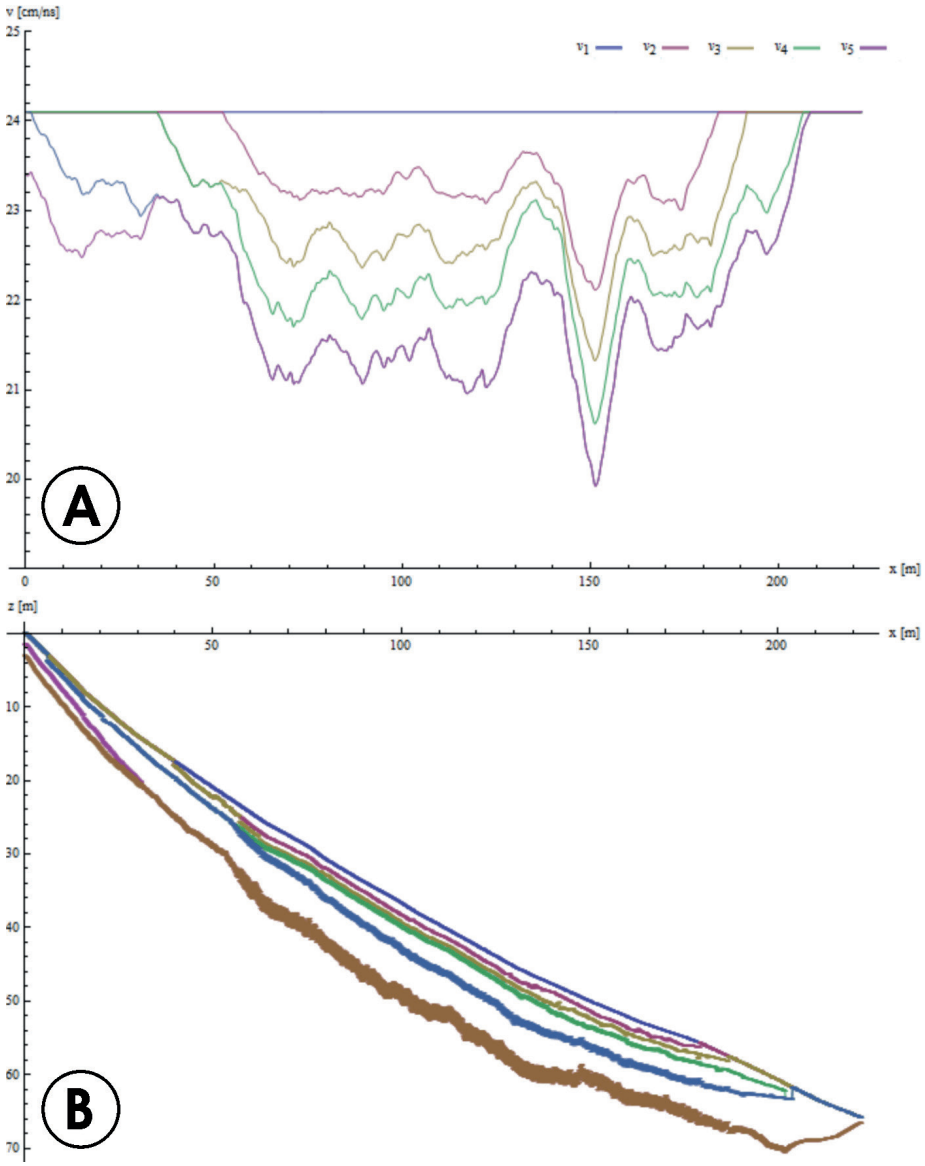

Fig. 1.– Results of the inversion program. A) Velocity distribution in the six layers, with the mean uncertainties in each layer equal to 0.20, 0.19, 0.20, 0.21, 0.20 and 0.20 cm/ns, for increasing depths. The value and uncertainty in the first layer are constant and defined by the operator, as required by the inversion program. Where layers are not defined, their graph merges with the nearest ones. For clarity, the velocity values were smoothed with a 101 trace window, and the error bars were not shown. B) Geometrical location and shape of the six picked layers; with the mean uncertainties in each underground interface equal to 0.01, 0.03, 0.08, 0.19, 0.51 and 0.52 m, for increasing depths.

applications. In fact, given the small offsets normally used for CO GPR surveys, the incident angles on the various interfaces are small even for shallow targets.

The method assumes the subsurface material as lossless and non-dispersive. The latter assumption is satisfied for most practical applications, but most geological media are characterized by high intrinsic attenuation. In such conditions, the procedure could be still valid if applied on data properly corrected for dissipation effects. Further research must address this topic for a better understanding not only of the kinematic, but also of the dynamic behavior of the EM waves in real media at practical field conditions.

Acknowledgements. This research is partially funded by the "Finanziamento di Ateneo per progetti di ricerca scientifica – FRA 2012" of the University of Trieste. Several other institutions financially or logistically supported this project: Unione Meteorologica del Friuli Venezia Giulia, Comunità Montana del Gemonese, Canal del Ferro e Valcanale, Direzione Centrale Risorse Rurali, Agroalimentari e Forestali - Servizio neve e valanghe, Ente Parco Naturale delle Prealpi Giulie, Protezione Civile Regione Friuli Venezia Giulia, Osservatorio Meteorologico Regionale ARPA-FVG, V Rgt. Cavalleria dell'aria "Rigel" – Casarsa (PN), Promotur Sella Nevea-Canin.

References

Becht A., Appel E., Dietrich P., 2006. Analysis of multi-offset GPR data: A case study in a coarse grained gravel aquifer, Near Surface Geophysics, 4, 227–240.

Davis J.L., Annan A.P., 1989. Ground-Penetrating-Radar for high-resolution mapping of soil and rock stratigraphy, Geophysical Prospecting, 37, 531-551.

Forte E., Dossi M., Colucci R.R., Pipan M., 2013. A new fast methodology to estimate the density of frozen materials by means of common offset GPR data, J. of Applied Geophysics, DOI: 10.1016/j.jappgeo.2013.08.013, available on-line.

Moysey S.M., 2011. Advances in 3D soil mapping and water content estimation using multi-channel ground-penetrating radar, American Geophysical Union, Fall Meeting 2011, abstract #H44B-01.

Pipan M., Baradello L., Forte E., Prizzon A., Finetti I., 1999. 2-D and 3-D processing and interpretation of multi-fold Ground Penetrating Radar data: a case history from an archaeological site, Journal of Applied Geophysics, Vol. 41/2-3, 271-292.

THE ROLE OF THE IMPEDIVITY IN THE MAGNETOTELLURIC RESPONSE OF 1D AND 2D STRUCTURES

R. Esposito[1], M.G. Di Giuseppe[2], A. Troiano[2], D. Patella[3], R.M. Castelo Branco[1]

[1] Federal University of Ceará, Fortaleza, Brazil

[2] Istituto Nazionale di Geofisica e Vulcanologia, Osservatorio Vesuviano, Napoli, Italy

[3] Department of Physical Sciences University Federico II, Naples, Italy

Introduction. In this work we study the influence of the resistivity dispersion on the magnetotelluric (MT) response. The dispersion consists in a variation of the resistivity according to the frequency of the telluric currents.

The MT method uses the natural electromagnetic (EM) field to determine the electrical resistivity values of the subsoil. The purpose is to retrieve the geometry of lithospheric structures through the spatial variations of the resistivity, and reveal the presence of bodies with potential economic interest, as metallic deposits, hydrocarbons reservoirs, geothermal fluids.

The frequency range of the EM field used in MT vary from 10^{-4} to 10^{4} Hz. Specifically into this range, if the soil is polarizable, the dispersion of the resistivity, whose characteristic frequency interval is between 10^{-2} and 10^{2} Hz, may affect MT responses (Patella, 1987).

Resistivity dispersion is a known phenomenology, which in geophysics constitutes the basis of the Induced Polarization (IP) prospecting method. In the frequency domain (FD), the dispersion consists in a variation of the resistivity parameter as the frequency of the exciting current is changed. The dispersive resistivity, called impedivity (Patella, 1993), is a complex function of the frequency. At vanishing frequency, however, the impedivity is real and coincides with the classical resistivity parameter used in DC geoelectrical methods. A real asymptote is also approached by the impedivity as the frequency tends to infinity. Geothermal and hydrocarbon research are application fields where MT can be affected by this phenomenon.

The complex physical and chemical fluid-metal-rock interactions may produce induced polarization effects, which are related to the dispersion in rocks. This is manifested on the MT response either in recognizable or in subtle forms, in both cases creating a distortion on the experimental curves. Disregarding the distortion effect may lead to misleading interpretation of the surveyed structures. We performed MT synthetic responses adopting 1D and 2D models in order to illustrate the dispersion effect on a geometrical structure typical of a volcano-geothermal environment.

The dispersion model. A generalized physical model was examined by Patella (2003), by solving in the FD the following electrodynamic equation of a charge carrier subject to an external electrical field **e**(ω)

$$\sum_{p=0}^{2} m_p (i\omega)^p \mathbf{r}(\omega) = q\mathbf{e}(\omega) \qquad (1)$$

In Eq. (1), q and m_2 are the electrical charge and mass of the carrier, m_0 is an elastic-like parameter explaining recall effects, m_1 is a friction-like parameter accounting for dissipative losses due to collisions and $\mathbf{r}(\omega)$ is the Fourier transform of the trajectory of the charge. Assuming, for simplicity, only one species of charge carriers and putting with K their number per unit of volume, the following elementary expression was derived for the impedivity $\rho(\omega)$ (Patella, 2003),

$$\rho(\omega) = \frac{m_0 + i\omega m_1 - \omega^2 m_2}{i\omega K q^2} \qquad (2)$$

Eq. (2) is a simple physical model, describing the behavior of a tuned circuit-like cell, i.e., a resistor–inductor–capacitor (RLC) series link. It is the equivalent of Lorentz's solution to the 2nd-order differential equation of harmonic oscillation (Balanis, 1989). We can distinguish different type of models, the positive non-resonant model, the negative non-resonant model and the resonant model, both positive and negative.

For the purpose of this work we will consider the positive non-resonant model since positive dispersion effects in MT were experimentally recognized in volcanic and geothermal areas (Coppola *et al*., 1993, Di Maio *et al*., 1997, 2000; Giammetti *et al*., 1996; Mauriello *et al*, 2000, 2004; Patella *et al*., 1991).

The positive model. By the generalized scheme reported above, a positive dispersion model was derived, assuming a dispersive rock equivalent to a serial chain of N two-branch parallel circuits. Each two-branch parallel circuit simulates the behavior of two different ionic species, which are both assumed to have negligible inertia, i.e., $m_2, j\omega_2 \approx 0$, where the index j = 1, 2 indicates the ionic species. One species (j = 1) is also assumed unbound, i.e., with $m_{0,1}$ negligible, and the other (j = 2) bound. In other words, one branch is a single R, in order to represent the path the unbound light ions can run through, with constant speed, under the action of an external exciting field. The other branch is, instead, an RC series link, in order to represent the path the bound light ions can move through, under the action of the same external field and against the decelerating recall forces (Patella, 2003). This assumption was proved to lead to the following dispersion formula (Patella, 2003, 2008)

$$\rho_+^{CC}(\omega) = \rho_{+,0}\left(1 - m_+ \frac{(i\omega\tau_+)^{C_+}}{1 + (i\omega\tau_+)^{C_+}}\right) \qquad (3)$$

which describes a typical positive dispersion model. In Eq. (3), $i = \sqrt{-1}$, ω is the angular frequency, ρ_0 is the DC resistivity and m $\in$[0, 1], known in mining geophysics as chargeability, is the dispersion amplitude defined as $m=(\rho_0 - \rho_\infty)/\rho_0$, where $\rho_\infty \in [0, \rho_0]$ is the real impedivity at infinite frequency. Moreover, c $\in$[0, 1] is the decay spectrum flatting factor and $\tau \geq 0$ is the main time constant.

The Cole-Cole model was used to study the distortion on 1D (Di Maio *et al*., 1991) and 2D (Mauriello *et al*., 1996) MT models created by the dispersion of the resistivity.

The formula used to extract modulus and phase of the MT complex response at the Earth's surface, i.e., the apparent impedivity function $\rho_a^d(\omega)$, for the three-layer Earth with a dispersive intermediate layer is given as (Patella, 1993)

$$\rho_a^d(\omega) = \rho_1 th^2 \left\{ k_1 t_1 + th^{-1} \left[\sqrt{\frac{\rho_2(\omega)}{\rho_1}} th\left(k_2 t_2 + th^{-1} \sqrt{\frac{\rho_3}{\rho_2(\omega)}} \right) \right] \right\} \qquad (4)$$

where t_1 and t_2 are the thickness of the 1st and 2nd layer, respectively, ρ_1 is the DC resistivity of the 1st layer and ρ_3 that of the substratum, and *th* stands for hyperbolic tangent. Moreover k_1 and k_2 are the wavenumbers in the 1st and the 2nd layer.

New examples of 1D and 2D synthetic dispersive MT responses. We show the results from a simulation of the MT responses, when dispersion is assumed to characterize the electrical properties of a region of the explored half-space. A 1D three-layered earth, with its four A, Q, H, K type sections (Kaufman and Keller, 1981), is considered, with only the intermediate layer assumed to be dispersive. A fixed sequence of DC resistivities and thickness is attributed as in Fig. 1.

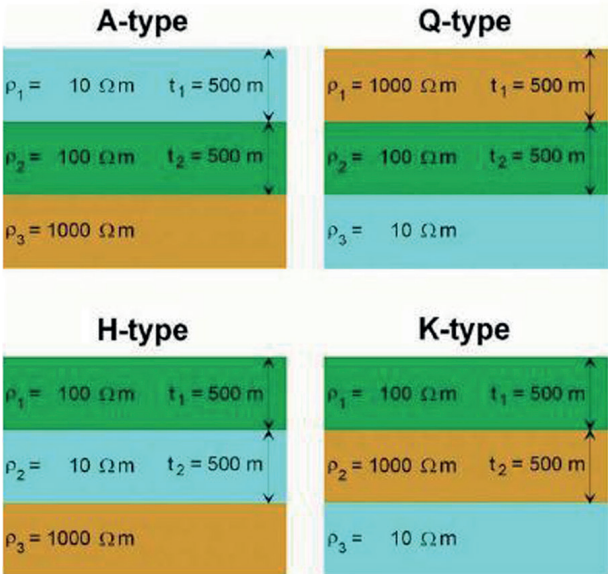

Fig. 1 – The three-layer A, Q, H and K type sections used for the 1D dispersive MT simulations.

Fig. 2 shows how large is the influence of the dispersion amplitude m on the shape of the MT responses. A large spread appears from the red curves, corresponding with the lowest value of m, which nearly coincide with the dispersion-free curves, to the blue curves, corresponding with the highest value of m.

These simulations show that the dispersion alters the shape of the curves in the same way as a lowering of the DC resistivity of the second layer does in a not dispersive situation. Such equivalence, without any external constraints, may make the interpretation of the curves quite ambiguous, as far as the maximum permitted slopes for 1D dispersion-free curves are not surpassed.

It is worth stressing that the H-type layer sequence has been shown to be the most recurrent model, fitting the MT spectrum in oil and geothermal exploration (Pellerin, 1996; Zhdanov, 1994). In fact, strong dispersion phenomena may occur in a permeable rock, underlying a cover layer, because of the diffuse presence of mineral and clay particles formed by the aggressive action of uprising fluids from a subjacent reservoir.

For the 2D case a model of magma chamber (10 Ω/m) at a depth of 1 km was considered, buried into a soil of 200 Ω/m.

The synthetic responses, as the 1D model, were performed considering both the non-dispersive and the dispersive case.

In Fig. 3 we show the differences of the 2D modelled MT responses compared with the true position and the dimensions of the body. As for the 1D case, the dispersion alters the resistivity values, particularly at the boundary of the buried body, leading to an ambiguous interpretation.

The magnetotelluric method, as previously mentioned, may recognize induced polarization phenomena when the soil is polarizable; unless we have the certainty to perform surveys of polarizable media, magnetotelluric responses can be interpreted as corresponding to non-

dispersive soils, while in reality it may refer to dispersive situations. When the dispersion effects on the MT curves do not cause any apparent incompatibility with the MT theory over layered structures, a dispersive MT response can as well be interpreted as a non-dispersive one and erroneously be modeled by a section, where the dispersive layer is totally suppressed (Esposito and Patella, 2009). MT data alone are not sufficient to distinguish polarization effects or can induce to see dispersion where is not present. An approach to solve this problem consists of the combinated interpretation of direct-current geoelectrical (d.c.) and MT data collected at the same site.

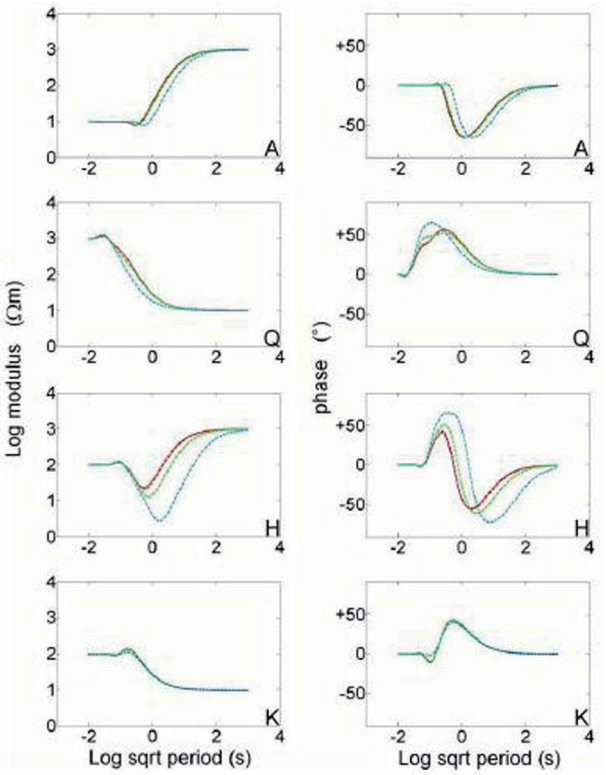

Fig. 2 – MT apparent impedivity modulus and phase simulated responses for the A, Q, H and K three-layer sequences of Fig. 1, with the second layer affected by a Cole-Cole type dispersion. The black lines are the reference not dispersive MT responses. The flatting factor and principal time constant are fixed, c=0.75 and τ=100s, respectively, while the positive dispersion amplitude is variable with values m=0.1 (red lines), m=0.5 (green lines) and m=0.9 (blue lines).

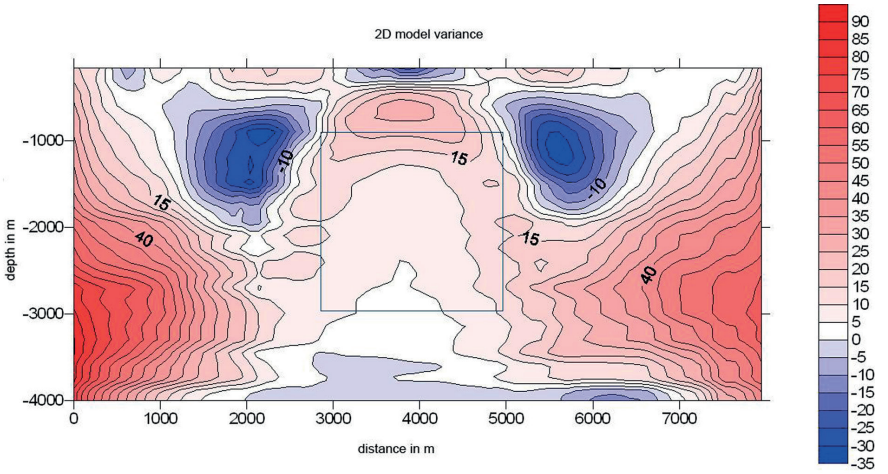

Fig. 3 – Variance of 2D models. The box at the center of the figure represents the position and the dimension of the buried body.

References

Balanis, C. A. *Advanced Engineering Electromagnetics*, J. Wiley & Sons, New York, 1989.

Cole, K. S. and R. H. Cole, "Dispersion and absorption in dielectrics," J. Chem. Phys., Vol. 9, 341–351, 1941.

Coppola, B., R. Di Maio, I. Marini, A. Merla, D. Patella, G. Pulelli, F. M. Rossi, and A. Siniscalchi, "Study of the Simplon area geothermal anomaly in the frame of a transalpine deep railway tunnel feasibility project," Underground Transportation Infrastructures, 93–102, ed. J. L. Reith, Balkema, Rotterdam, 1993.

Di Maio, R., Patella, D., e Siniscalchi, A., "Sul problema del riconoscimento di uno

strato elettricamente polarizzabile mediante misure magnetotelluriche," Atti del II Convegno di Geomagnetismo ed Aeronomia, a cura di A. Meloni e B. Zolesi, ING, Roma, 239-250, 1991.
Di Maio, R., P. Mauriello, D. Patella, Z. Petrillo, S. Piscitelli, A. Siniscalchi, and M. Veneruso, "Self-potential, geoelectric and magnetotelluric studies in Italian active volcanic areas," Ann. Geofis., Vol. 40, 519–537, 1997.
Di Maio, R., D. Patella, Z. Petrillo, A. Siniscalchi, G. Cecere, and P. de Martino, "Application of electric and electromagnetic methods to the study of the Phlegrean Fields caldera," Ann. Geofis., Vol. 43, 375-390, 2000.
Esposito, R., D. Patella, "The role of the impedivity in the magnetotelluric response" PIER, 89, 225-253, 2009.
Giammetti, S., D. Patella, A. Siniscalchi, and A. Tramacere, "The Siena Graben: Combined interpretation of DES and MT soundings," Ann. Geofis., Vol. 39, 189–200, 1996.
Kaufman, A. A. and G. V. Keller, The Magnetotelluric Sounding Method, Elsevier, Amsterdam, 1981.
Mauriello, P., D. Patella, Z. Petrillo, and A. Siniscalchi, "An integrated magnetotelluric study of the Mt. Etna volcanic structur," Ann. Geofis., Vol. 43, 325–342, 2000.
Mauriello, P., D. Patella, Z. Petrillo, A. Siniscalchi, T. Iuliano, and C. Del Negro, "A geophysical study of the Mount Etna volcanic area," Mt. Etna: Volcano Laboratory, Vol. 143, 273–291, ed. A. Bonaccorso, S. Calvari, M. Coltelli, C. Del Negro, S. Falsaperla, American Geophysical Union, Geophysical Monograph Series, 2004.
Mauriello, P., D. Patella, A. Siniscalchi, "The magnetotelluric response over 2D media with resistivity frequency dispersion," Geophysical Prospecting, Vol. 44, 789-818, 1996
Patella, D., A. Tramacere, R. Di Maio, and A. Siniscalchi, "Experimental evidence of resistivity frequency-dispersion in magnetotellurics in the Newberry (Oregon), Snake River Plain (Idaho) and Campi Flegrei (Italy) volcano-geothermal areas," J. Volcanol. Geoth. Res., Vol. 48, 61–75, 1991.
Patella, D., "Tutorial: Interpretation of magnetotelluric measurements over an electrically dispersive one-dimensional earth," Geophysical Prospecting, Vol. 35, 1-11, 1987.
Patella, D., "I principi metodologici della magnetotellurica su mezzi generalmente dispersivi," Annali di Geofisica, Vol. 36, 147-160, 1993.
Patella, D., "On the role of the J-E constitutive relationship in applied geoelectromagnetism," Ann.Geophys., Vol. 46, 589-597, 2003.
Patella, D., "Modelling electrical dispersion phenomena in earth materials," Ann. Geophys., Vol. 51, 2008.
Pellerin, L., J. M. Johnston, and G. W. Hohmann, "A numerical evaluation of electromagnetic methods in geothermal exploration," Geophysics, Vol. 61, 121–137, 1996.
Zhdanov, M. S. and G. V. Keller, *The Geoelectrical Methods in Geophysical Exploration*, Elsevier, Amsterdam, 1994.

LABORATORY SCALE ELECTRICAL RESISTIVITY MEASUREMENTS TO MONITOR THE HEAT PROPAGATION WITHIN POROUS MEDIA FOR LOW ENTHALPY GEOTHERMAL APPLICATIONS

N. Giordano[1], L. Firmbach[2], C. Comina[1], P. Dietrich[2,3], G. Mandrone[1], T. Vienken[2]
[1] Department Earth Science - University of Torino, Italy
[2] Department Monitoring & Exploration Technology - UFZ Leipzig, Deutschland
[3] Centre for Applied Geoscience, Institute for Geosciences - University of Tubingen, Deutschland

Introduction. In the context of energy transition, the utilization of the underground as a heat source and a volume for storing the thermal energy has gained increasing importance in recent years. Several kind of low enthalpy geothermal applications were developed and most of them are emerging in various European countries (in particular Northern Europe). Nevertheless, at present no homogenous legislation exists for economical, ecological or political control of these systems. It is common to find different temperature limits for groundwater reinjection and, additionally, various legal constraints for heat transfer (Hähnlein *et al.*, 2011). Within each country it is also not so rare that local governments allow what other administrations forbid. This confusion contribute to obstruct this growing market and does not guarantee a correct design and monitoring of these applications, which are fundamental for a valuable system's efficiency and safety. The design of these applications is indeed mostly based on literature extracted values of the thermal properties and on numerical simulation of the heat propagation within soils. These assumptions are often inadequate for real applications and they could lead to system's efficiency problems. According to Leong *et al.* (1998), coupling of ground data and detailed mathematical model of heat and moisture flow (i.e. numerical simulation) should be the starting point of a reliable design. Conversely there is not still any protocol for a large scale

correct monitoring of these systems besides local temperature measurements carried out in the thermal exchangers themselves.

Basically, two types of geothermal systems use the ground as a heat source - open and closed loop systems. Both open and closed loop systems are generally coupled with electric heat pumps which arise the achieved temperature with a thermodynamic cycle. On the one hand, the open loop systems (aquifer thermal systems) use the shallow groundwater as warm or cold source directly. The groundwater circulates within one or more extraction and injection wells. In summer periods, the groundwater is used to cool down the building and the heat is transferred into the ground, with an increasing groundwater temperature approximately from 6 to 8 °C (Bonte *et al.*, 2011). In winter periods, the groundwater gives the heat necessary to warm up the building, with a consequent cooling effect on the groundwater temperature of approximately 5 to 10 °C being observed (Bonte *et al.*, 2011). On the other hand, the closed loop systems exploit the ground as a heat source. The borehole heat exchangers (BHEs) used by these applications are conductor pipes filled with different heat transfer fluid. The circulating fluid within these pipes extracts the heat from the ground and thereby it influences the ground temperature indirectly. Similarly, other shallow geothermal applications exploit the ground as a storage volume for the thermal energy. These systems are generally called Seasonal Thermal Energy Storage (STES), because they transfer the heat in the ground in the summer periods and they extract it when the heating demand arises, in the cold periods (Xu *et al.*, 2013). The STES systems include several methodologies for storing the heat: for instance the ground is used as storing medium and the connection with the ground is provided by a series of BHEs (Reuss *et al.*, 2006).

In all of the mentioned applications a wide knowledge of the thermal properties of the ground and their influencing factors is needed towards a reliable design, which should be efficient, cost-effective and environmentally sustainable. Moreover, some correct monitoring protocols are required to evaluate the efficiency of the system and prevent environmental problems.

This study aimed at evaluate at laboratory scale the use of non-invasive electrical measurements for the characterization and monitoring of shallow geothermal applications. Electrical measurements could be indeed considered as a time and cost efficient method for the characterization and long-term monitoring of shallow geothermal systems. We have evaluated their potentiality in monitoring groundwater and soil changes under temperature variations by performing laboratory measurements under known boundary conditions in an *ad hoc* designed thermal box and to analyze the correlation between electrical and thermal properties for different media, taking their influencing parameters into account. This can be viewed as a fundamental calibration step for a further application of the methodology to a real case study.

Theoretical background.

State of the art. So far, there is limited specific knowledge about the long-term effects of unsuitable system design or the effects of groundwater temperature changes and chemical changes within the subsurface and the resulting consequences. A few studies have already measured the thermal effects of geothermal plants within field sites, for instance Huber and Arslan (2012). They also compared their field results with numerical simulations and laboratory measurements with a forced groundwater flow (Arslan and Huber 2013). Nevertheless, these studies do not fill the criteria of being rapid, non-invasive and in-expansive monitoring technologies for efficient applications and environmental protection.

Geophysical methods can conversely provide information over large areas at relatively inexpensive costs compared to other general methods or applications. For example the surface electrical resistivity tomography (ERT) has many practical applications for studying soil properties and processes in the subsurface (Ramirez *et al.*, 1993). In the context of geothermal reservoirs, ERT has already been extensively applied for hydrothermal fluids. For temperatures up to 150 °C, it reveals characteristic specific resistivity values in contrast to their corresponding soil resistivity values. Therefore, with the ERT method, the geothermal

reservoir itself and the flow path can be mapped (e.g. Bruno *et al*., 2000; Garg *et al*., 2007). Hermans *et al*. (2012) demonstrated the ability of ERT to study heat flow and heat storage within a small field experiment in a shallow aquifer. They injected heated water and monitored the electrical values with cross-borehole time-lapse ERT but did not measure the temperature changes. Fragogiannis *et al*. (2008) also used ERT for monitoring the thermal performance of the ground at the University of Athens with an installed ground-source heat pump system consisting of 12 borehole heat exchangers.

Electrical resistivity effecting parameters. The electrical resistivity ρ (or its inverse conductivity σ) depends on different soil and environmental attributes. Friedman (2005) gave an overview of these parameters and their impact. He stated three categories: 1) parameters describing the bulk soil, such as porosity (n), water content (θ) and structure, 2) the time-invariable solid particle quantifiers such as particle shape and orientation, particle-size distribution, wettability or cation exchange capacity (CEC) and 3) fast-changing environmental factors, such as ionic strength, cation composition and temperature. However, these factors do not act separately. For unsaturated soils, porosity (n) especially influences the attributes of the second group. So with the main influencing factors of water content and therefore the electrical conductivity of the water/fluid within the soils pores (σ_w) (Friedman, 2005; Dietrich, 1999), the differentiation of soils as a two-phase system (saturated soils) and as a tri-phase system (unsaturated soils) must be considered.

For the electrical resistivity of soils, as a two-phase systems with negligible matrix conductivity of clay-free porous media, the most important attribute is the conductivity of the fluid within the pores. Therefore, the Archie's empirical law is the most widely used application:

$$\frac{\rho_w}{\rho_a} = \frac{\sigma_a}{\sigma_w} = \frac{1}{F} = n^m \qquad (1)$$

whereby ρ_a and ρ_w are the resistivities of the mixture and of the saturating water respectively (and σ their inverse conductivities), F is a formation factor and m a material-depending exponent (cementation index) of the porosity n (Archie, 1942). Further applications are shown in Friedman (2005) or Sihvola and Kong (1988).

For unsaturated soils as part of a three-phase-system, the ρ_a is a mixture of the soil properties, especially porosity, saturation degree with the fluid composition (ions) and the air content. In this case, Archie's law can be rewritten as:

$$\rho_a = \frac{\rho_S}{\theta^x} \qquad (2)$$

here, the saturation degree (θ) has to be considered, ρ_s is the resistivity of the solid phase and the coefficient x is the saturation coefficient, that takes different values depending on the saturation level (Dietrich, 1999).

Under laboratory conditions some of the electrical resistivity-influencing soil parameters can be a-priori known (e.g. medium porosity and composition, saturation degree) so that the temperature is the part which can be analyzed to understand the correlation with electrical resistivity. As these are the same influencing parameters for thermal conductivity (Singh and Konchenapalli, 2000; Singh *et al*., 2001), a general relationship between the electrical (ρE) and the thermal resistivities (ρT) can be expected:

$$\log(\rho E) = C_R \log(\rho T) \qquad (3)$$

C_R is a multiplier dependent upon the gravel and sand size fraction of the soil (Singh *et al*., 2001). Different authors (e.g. Singh *et al*., 2001; Sreedeep *et al*., 2005; Fragogiannis *et al*., 2010) showed this correlation of thermal and electrical conductivities within laboratory measurements for different soils in dependence of the water content.

Materials and methods. A common box, sized 1.0 m x 0.4 m x 0.4 m, was prepared for the experimental tests. Within this box, the correlation of the thermal and electrical measurements

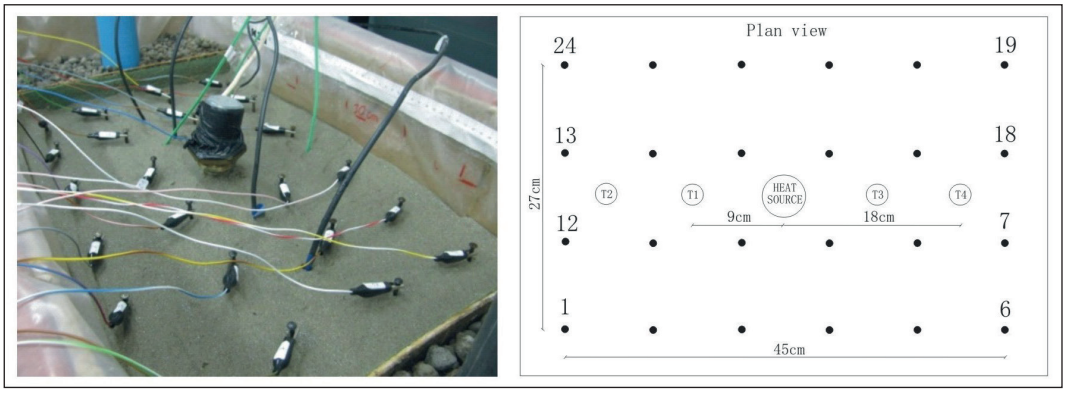

Fig. 1 – Laboratory device built for temperature and resistivity monitoring. A picture on the left and an explanatory sketch on the right, with the progressive electrode number and the position of the heat source and temperature sensors (T).

can be analyzed for a known porous medium to validate the influences that material characteristics and water content have on them. Within the box, three parts were separated by permeable membranes. For the analyses, the central part, approximately 0.6 m in length, was filled by the porous medium for a thickness of about 0.3 m. In the outer sectors, two PVC pipes were placed surrounded by high porosity material for adjusting the water level and establishing a water flux if needed. In the central sector within the analyzing medium, a thermal resistor, controlled by a thermometer and rheostat to ensure a constant temperature, served as a heat source. Four resistance thermometers (Pt-100) were placed at specified distances from the heat source, while four watermark sensors continuously monitored the soil moisture, assuring a constant water content. A total of more than 50 experiments were carried out. They differ in time of heat up, static or dynamic conditions of water fluxes, number, position, temperature and geometric configuration of the heat sources, position of the T-sensors. During some of these temperature-recording tests, electrical surveys were carried out with different configurations.

Fig. 1 reports the configuration adopted during the tests presented in this paper. The heat source was placed in the center of the box and the T-sensors were aligned, aside of the heat source, along the major axis of the box. For monitoring the electrical resistivity changes in two perpendicular directions, 24 electrodes were placed in a network mode all around the source with a 9 cm spacing. The variation of the apparent resistivity as a function of temperature and time was therefore recorded in different locations. This kind of configuration was useful for checking the heat spreading in a plan view located at about 10 cm depth, which is also the depth of the temperature sensors. The tested porous medium presented in this paper has 91% vol. of sand and 9% vol. of silt, compacted to a porosity of 0.46 and at complete saturation.

Results and discussions. The results of the electrical surveys showed the expected correlation of decreasing electrical resistivity values with the increasing temperature induced by the heat source, the opposite is true after the source's turn off. The electrical resistivity decreases more slowly with increasing distance from the heat source, as temperature does, and is dependent upon the heat flux within the material.

Fig. 2 shows the comparison between the temperature recorded by each sensor and the apparent resistivity measured close to it. The resistivity changes achieved show an inverse trend with the temperature data. More specifically, a good agreement is clear in the heating period, while a less marked increase in resistivity is noticeable when the source was turned off. The electrical resistivity shows also a slower return to the initial conditions than temperature. As an average, it has been observed that a 10% positive variation in temperature generates a 2.5% negative change in electrical resistivity. Fig. 3 presents the time-lapse sequence of the apparent resistivity during the heating and the cooling period imaged in the plan view

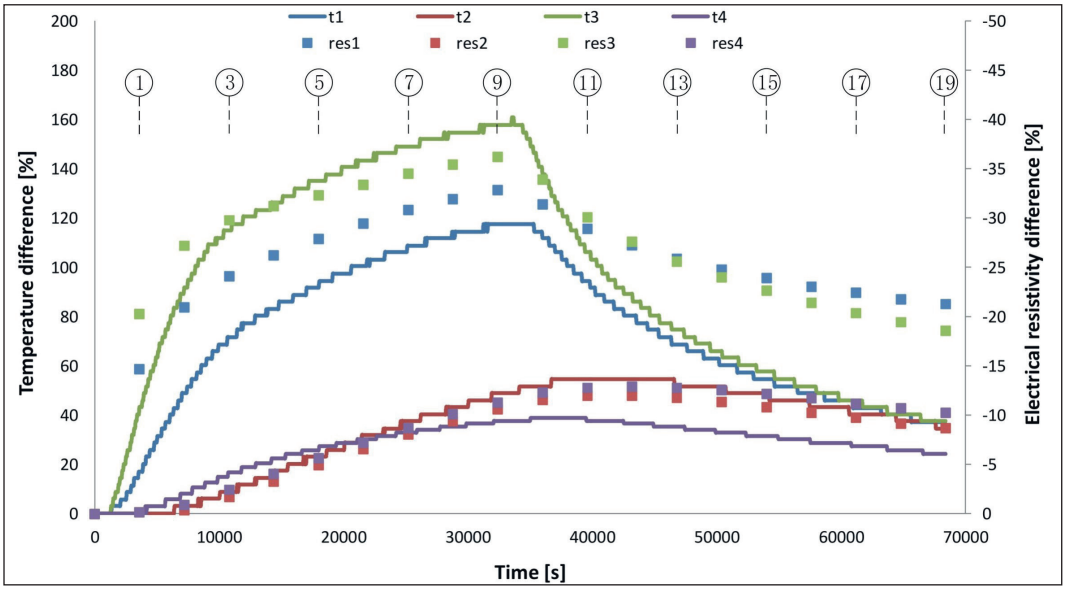

Fig. 2 – Temperature and electrical resistivity differences plotted as a function of time. The lines and the dots show the temperature and resistivity trend respectively. The rounded numbers indicate the steps of the electrical measurements imaged in Fig. 3.

within the whole central sector. The radial heat propagation is well described by the changes in electrical resistivity, showing an homogeneous radial distribution in the heat up. The more heterogeneously distributed resistivity during the cool down is probably influenced by some evaporation occurred within the medium throughout the test that could have influenced the propagation patterns. This can also partially explain the difference observed with temperature in the cool down period.

The network configuration allowed us to describe the heat propagation in two dimensions around the source. The outcomes highlighted that the heat flows quite homogenously in a radial mode from the source, if no advective flux occurs. The possible differences within the medium, noted in particular in the cooling period, are caused by different water contents due to evaporation phenomenon which influences the local thermal properties. The electrical method was therefore useful to highlight heterogeneous water contents within the medium, key factor in the lab experiments performed for understanding the differences in the heat distribution at different saturation degrees (Comina *et al.*, 2013).

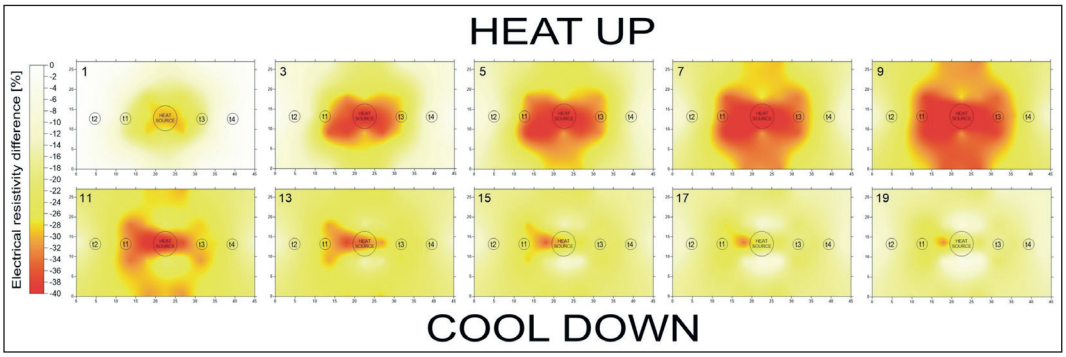

Fig. 3 – Electrical resistivity difference map; plan view 10 cm. deep. The heat source is in the center and each step takes 2 hours. The upper row shows the heating period, while the lower row shows the cool down, after the source was turned off. The position of the heat source and the T-sensors are indicated.

Additionally, the thermal properties of the medium can be achieved by means of the electrical surveys results. Applying Eq. (3), we obtained the thermal resistivities of the medium at each of the 19 steps, starting from the recorded electrical resistivities. We calculated the multiplier C_R with the equations proposed by Sreedeep *et al.* (2005), founding a value of C_R = 2.01. The results, ρT ranging between 6.56 and 4.56 °C m W^{-1}, are reported in Tab. 1. The outcomes are rather high for a fine sand but in general accordance with many studies on this topic (Sreedeep *et al.*, 2005; Singh and Konchenapalli, 2000).

Tab. 1 – Thermal resistivities close to sensors t1 and t3, calculated with Eq. (3).

steps	sensor t1			sensor t3		
	ρE	temperature	ρT	ρE	temperature	ρT
	[Ω m]	[°C]	[°C m W^{-1}]	[Ω m]	[°C]	[°C m W^{-1}]
0	33.96	19.40	5.54	48.16	19.40	6.56
1	28.98	22.70	5.13	38.39	27.80	5.88
2	26.85	28.90	4.94	35.06	37.20	5.62
3	25.78	33.30	4.84	33.82	41.70	5.53
4	25.05	35.50	4.78	33.11	43.90	5.47
5	24.48	37.20	4.72	32.59	45.60	5.43
6	23.97	38.90	4.68	32.08	47.20	5.39
7	23.49	40.50	4.63	31.52	48.30	5.34
8	23.12	41.10	4.59	31.09	49.40	5.31
9	22.81	42.20	4.56	30.71	50.00	5.27
10	23.29	41.10	4.61	31.83	46.10	5.37
11	24.14	37.70	4.69	33.65	40.00	5.51
12	24.71	35.00	4.75	34.86	36.70	5.61
13	25.17	32.70	4.79	35.83	33.90	5.68
14	25.54	31.10	4.82	36.59	32.20	5.74
15	25.84	30.00	4.85	37.25	30.60	5.79
16	26.13	28.90	4.88	37.83	29.40	5.84
17	26.35	27.70	4.90	38.35	28.30	5.87
18	26.56	27.20	4.92	38.79	27.20	5.91
19	26.73	26.10	4.93	39.20	26.70	5.94

Conclusions. The first experimental results of this study confirmed the expected correlation of decreasing electrical resistivity with an increasing temperature induced by the heat source. A general negative variation of around 2.5% of resistivity was recorded when a temperature increase of 10% occurs. Moreover, the correlation between electrical and thermal resistivities was tested. Our electrical surveys on the lab device highlighted therefore their potential for monitoring and quantifying the increase in temperature at the respective measuring points and the differences in heat propagation through the medium.

A possible future work that could be carried out includes further testing of different materials under the same conditions, to ensure comparability of the different media and their influencing soil parameters for the thermal and electrical conductivities.

Further, a numerical simulation of electrical resistivity values for different porous media within the box should be carried out, to evaluate the reliability of frequently-used numerical models for the dimensioning of near surface geothermal systems. Comparisons between the experimental results and the numerical model should be verified. Moreover, the same methodology will also be applied at field scale by performing electrical surveys on a test site of STES system, which is being built at the University Campus of Torino (Grugliasco, TO, Italy). In particular, the network configuration shall be applied with more than 24 electrodes (48 or 72) in order to acquire data for a useful 3D imaging of the subsoil. The periodical geophysical surveys will be coupled with a continuous temperature recording data within the BHEs and the solar panels. A numerical modeling of the site and some direct measurements of the thermal properties will be compared to the geophysical outcomes within a multidisciplinary approach able to achieve reliable and valuable results.

References

Archie G. E.; 1942: *The electrical resistivity log as an aid in determining some reservoir characteristics*. Transactions of the American Institute of Mining, Metallurgical, and Petroleum Engineers Inc. E, **146** (1), 54 - 62.

Arslan U. and Huber H.; 2013: *Numerical back-analyses of laboratory tests with forced groundwater flow*. Proceedings of the Thirty-Eighth Workshop on Geothermal Reservoir Engineering, 1 - 5.

Bonte M., Stuyfzand P. J., Hulsmann A. and Van Beelen P.; 2011: *Underground Thermal Energy Storage: Environmental Risks and Policy Developments in the Netherlands and European Union*. Ecology and Society, **16**(1), 22.

Bruno P. P. G., Paoletti V., Grimaldi M. and Rapolla A.; 2000: *Geophysical exploration for geothermal low enthalpy resources in Lipari Island, Italy*. Journal of Volcanology and Geothermal Research, **98**, 173 – 188.

Comina C., Dietrich P., Firmbach L., Giordano N., Kolditz O., Mandrone G., Vienken T. and Watanabe N.; 2013: *Heat flow's propagation within a porous medium: analogical and numerical modelling*. In: Proceedings of the European Geothermal Congress, June 3rd-7th, Pisa, Italy.

Dietrich P.; 1999: *Konzeption und Auswertung gleichstromgeoelektrischer Tracerversuche unter Verwendung von Sensitivitätskoeffizienten*. University Tübingen, Germany.

Fragogiannis G., Papatheodorou N. and Stamataki S.; 2008: *Evaluation of Thermal Performance of Ground - Source Energy Systems. A geophysics supported approach*. World Renewable Energy Congress X and Exhibition, July 19th-25th, Glasgow, Scotland.

Fragogiannis G., Apostolopoulos G. and Stamataki S.; 2010: *Correlation of Thermal and Electrical Resistivity of Soil, for Near Surface Geothermal Applications*. 72nd EAGE Conference and Exhibition incorporating SPE EUROPEC, June 14th-17th, Barcelona, Spain.

Friedman S. P.; 2005: *Soil properties influencing apparent electrical conductivity: a review*. Computers and Electronics in Agriculture, **46**, 45 – 70.

Garg S. K., Pritchett J. W., Wannamaker P. E. and Combs J.; 2007: *Characterization of geothermal reservoirs with electrical surveys: Beowave geothermal field*. Geothermics, **36**, 487 – 517.

Hähnlein S., Blum P. and Bayer P.; 2011: *Shallow geothermal energy - current legal situation*. Grundwasser - Zeitschrift der Fachsektion Hydrogeologie, **16**, 69 – 75.

Hermans T., Vandenbohede A., Lebbe L. and Nguyen F.; 2012: *A shallow geothermal experiment in a sandy aquifer monitored using electric resistivity tomography*. Geophysics, **77**(1), B11 - B21.

Huber H. and Arslan U.; 2012: *Geothermal field tests with forced groundwater flow*. Proceedings of the Thirty-Seventh Workshop on Geothermal Reservoir Engineering, 1 – 5.

Leong W. H., Tarnawski V. R. and Aittomäki A.; 1998: *Effect of soil type and moisture content on ground heat pump performance*. International Journal of Refrigeration, **21,** 595 – 606.

Ramirez A. and Daily W.; 1993: *Monitoring an Underground Steam Injection Process Using Electrical Resistance Tomography*. Water Resources Research, **29**(1), 73 – 87.

Reuss M., Beuth W., Schmidt M. and Schoelkopf W.; 2006: *Solar district heating with seasonal storage in Attenkirchen. ECOSTOCK 2006*. In: 10th International Conference on Thermal Energy Storage, Stockton, USA.

Singh D. N. and Konchenapalli D.; 2000: *Generalized relationship for estimating soil thermal resistivity*. Experimental Thermal and Fluid Science, **22**, 133 – 143.

Singh D. N., Kuriyan S. J. and Manthena K. C.; 2001: *A generalized relationship between soil electrical and thermal resistivities*. Experimental Thermal and Fluid Science, **24**, 175 – 181.

Sreedeep S., Reshma A. C. and Singh D.N.; 2005: *Generalized relationship for determining soil electrical resistivity from its thermal resistivity*. Experimental Thermal and Fluid Science, **29**, 217 – 226.

Xu J., Wang R. Z. and Li Y.; 2013: *A review of available technologies for seasonal thermal energy storage*. Solar Energy, http://dx.doi.org/10.1016/j.solener.2013.06.006.

INDAGINE GEORADAR ALL'INTERNO DELLA BASILICA DI SANTA MARIA MAGGIORE DI ISPICA (SICILIA)

S. Imposa, S. Grassi
Dipartimento di Scienze Biologiche, Geologiche e Ambientali, Sezione di Scienze della Terra, Università di Catania

Introduzione. Le indagini effettuate con metodologie non invasive hanno assunto, negli ultimi anni, un ruolo chiave nella diagnosi e controllo delle strutture di interesse artistico - storico – architettonico. Tali strutture sono soggette a particolari fenomeni di degrado causato, molto spesso, dalla presenza di vuoti e materiale dissestato, soprattutto al di sotto della pavimentazione.

In questo lavoro vengono presentati i risultati di una indagine GPR eseguita sulla pavimentazione della chiesa di Santa Maria Maggiore di Ispica (RG), allo scopo di evidenziare la presenza di cripte e/o cavità presenti nel sottosuolo. L'area d'indagine è stata interessata dalla esecuzione di numerosi profili sia longitudinali (29), che trasversali (9), ubicati in modo tale da formare una griglia e la cui spaziatura è minima tra i profili longitudinali eseguiti lungo le tre navate mentre aumenta tra i profili trasversali.

La costruzione della Basilica, iniziata dopo il terremoto del 1693 per accogliere la statua del Cristo alla Colonna, fu completata nel 1725 su progetto di Rosario Gagliardi; solo due anni dopo, un secondo terremoto ne fece crollare gran parte, che fu ricostruita nell'arco del trentennio successivo. Il tempio è a croce latina, la navata centrale è lunga 43 m ed ha la stessa altezza del transetto che misura 32 m e le tre navate sono larghe 20 m (Trigilia, 2007). La Basilica fu eretta a monumento nazionale data la sua importanza per la storia della pittura in Sicilia, essendo decorata da pitture di Olivio Sozzi e Vito D'Anna, i più illustri pittori del Settecento siciliano. Infine, il loggiato esterno, progettato dal Sinagra sul modello del colonnato del Bernini di Piazza S. Pietro a Roma, venne realizzato nella metà del sec. XVIII, presenta una forma semiellittica e comprende tre arcate centrali e altre dieci per lato.

Le caratteristiche geolitologiche dell'area su cui è ubicata la Chiesa sono tipiche del settore sud-orientale dell'altopiano ibleo con una morfologia tabulare e collinare, degradante verso il mare; questo tipo di morfologia può essere connessa alla natura geologica dei litotipi affioranti, quali calcari con livelli marnosi, fratturati e carsificati, con grado di cementazione crescente man mano che si va in profondità ed appartenenti alla F.ne Ragusa-membro Irminio (Lentini *et al.*, 1987); tale litotipo è il più diffuso nell'area è può presentare spessori fino ad oltre 40 metri, così come è visibile dalla stratigrafia associata al sondaggio meccanico eseguito nei pressi del nostro sito di interesse. Nella successione stratigrafica che caratterizza l'area, sono presenti anche marne argillose grigio-azzurre a frattura sub-concoide della formazione Tellaro, che affiorano estesamente ad est e a sud di Ispica; la successione stratigrafica è completata verso l'alto da depositi pleistocenici-olocenici, costituiti per lo più da ghiaie a elementi carbonatici e sabbie carbonatiche (Grasso *et al.*, 1992, 2000).

Sotto il profilo morfologico, l'area di interesse va inquadrata in quello che viene chiamato paesaggio fluvio-carsico, in cui si distinguono morfologie legate alla capacità di erosione meccanica e di corrosione chimica dell'acqua meteorica, nei confronti di rocce carbonatiche ivi affioranti. Infatti, nell'area dei monti Iblei la diffusa carsificazione, soprattutto nel settore orientale dell'area, si manifesta sia con morfologie superficiali, sia con vaschette di dissoluzione e solchi di vario tipo, sia con grotte carsiche.

Dal punto di vista strutturale l'area presenta delle caratteristiche strettamente legate ad un insieme di eventi di origine tettonica (Ghisetti e Vezzani, 1980; Monaco e Tortorici, 1995). Essa è infatti caratterizzata dalla presenza di una serie di horst e graben con orientazione principale NE-SW e una secondaria NW-SE (Grasso *et al.*, 1992). Questa struttura è interrotta a sud-est dalla faglia di Ispica (Carbone *et al.*, 1982) avente un rigetto sub-verticale di circa 80 – 100 m. La presenza di tale faglia, forma più a est l'ampia depressione di Ispica-Capo Passero (Ghisetti e Vezzani, 1980; Patanè e Imposa, 1987). In un territorio così pesantemente interessato da

fratture e discontinuità tettoniche, le successioni carbonatiche sono state profondamente modificate dalle acque meteoriche e di dilavamento ricche in CO_2.

Metodologia utilizzata. Il GPR (Ground Penetrating Radar) utilizza la propagazione di onde elettromagnetiche per indagare le condizioni del sottosuolo e individuare la presenza di oggetti e/o strutture sepolte. La strumentazione è costituita da una unità di controllo che genera un impulso elettromagnetico di pochi nanosecondi (ns) e lo invia ad un'antenna che a sua volta lo trasforma in un impulso di ampiezza superiore che viene irradiato nel terreno. La frequenza dell'antenna può variare da pochi MHz fino ai GHz e si sceglie in funzione della profondità di investigazione che si vuole raggiungere e della risoluzione desiderata; questi due parametri sono tra loro inversamente proporzionali, infatti dal punto di vista metodologico all'utilizzo di basse frequenze corrisponde un aumento della profondità di penetrazione del segnale con conseguente diminuzione della risoluzione (Barone *et al*., 2004; Imposa *et al*., 2004, 2006, 2009; Coco e Corrao, 2009).

Qualsiasi passaggio tra materiali con proprietà elettriche e magnetiche differenti provoca la riflessione di una parte dell'energia. Anche le cavità sotterranee piene d'aria, sono buoni riflettori e la tecnica georadar ha dimostrato di essere idonea al loro rilevamento (El-Qady *et al*., 2005; Anchuela *et al*., 2009; Imposa *et al*., 2009; Barilaro *et al*., 2006, 2007). La quantità residua di energia che non è stata riflessa, continua ad attraversare il mezzo fino a colpire un'altra superficie di separazione tra mezzi con costante dielettrica diversa provocando a sua volta ulteriori riflessioni.

In presenza di superfici piane come ad esempio un orizzonte stratigrafico e nel caso in cui la scansione venga effettuata parallelamente alla sua estensione otterremo un radargramma tendenzialmente piano; contrariamente, se la scansione viene effettuata ortogonalmente ad elementi lineari sepolti o oggetti isolati essi provocano riflessioni puntuali. Dall'inviluppo di tutti i primi arrivi dell'onda e.m. che colpisce il bersaglio, si ha la formazione della caratteristica iperbole di riflessione che ci permette di ottenere una "immagine" dell'oggetto sepolto (Barone *et al*., 2004; Castellaro *et al*., 2008; Imposa, 2010). Tali iperboli sono dovute alla trasmissione in forma conica del fascio radar che fa si che l'energia venga riflessa anche quando gli oggetti non si trovano direttamente sotto l'antenna ma nelle vicinanze.

Un rilievo GPR, fornisce come risultato una sezione bidimensionale dove sono visibili una serie di segnali che rappresentano le riflessioni delle onde causate dalle discontinuità elettriche del mezzo attraversato. L'asse x mostra la distanza percorsa dall'antenna sulla superficie mentre l'asse y rappresenta il tempo trascorso tra l'emissione e la ricezione dell'impulso; per poter convertire il tempo di acquisizione in profondità è necessario conoscere il valore della velocità media del mezzo interessato dalla prospezione. La valutazione della velocità dell'onda ai fini della conversione tempo-profondità dei radargrammi, rappresenta una delle maggiori difficoltà nell'applicazione della tecnica GPR (Tillard e Dubois, 1995).

$$V_m = \frac{1}{\sqrt{\mu_0 \mu_r \varepsilon_0 \varepsilon_r}} = \frac{C}{\sqrt{\mu_r \varepsilon_r}} = \frac{C}{\sqrt{\varepsilon_r}}$$

dove:

$$C = \frac{1}{\sqrt{\mu_0 \varepsilon_0}}$$

μ (permeabilità magnetica) = $\mu_0 \cdot \mu_r$; con μ_0 permeabilità magnetica in aria e μ_r permeabilità magnetica relativa al mezzo attraversato;
ε (costante dielettrica)= $\varepsilon_0 \cdot \varepsilon_r$; con ε_0 costante dielettrica in aria e ε_r costante dielettrica relativa al mezzo attraversato.

La velocità dell'impulso, infatti, varia a seconda del tipo di materiale attraversato, in generale tra 10 e 80 cm/ns; conoscendo la velocità, si possono facilmente trasformare i tempi di tragitto dell'impulso in profondità. La profondità può essere ricavata dalla seguente formula:

$$h = \frac{V_m T}{2}$$

Acquisizione ed elaborazione dati. L'indagine GPR che ha interessato l'intera Basilica ha coperto un area approssimativa di circa 800 m^2. Per l'esecuzione dei rilievi è stato impiegato il sistema radar "GPR/RAMAC della MALA GEOSCIENCES (SWEDEN)" corredato da due antenne con frequenze centrali di 250 MHZ e di 500 MHZ rispettivamente. La trasmissione dei dati avviene a 4 Mbit/s attraverso cavi a fibre ottiche; lo strumento riesce ad eseguire fino a 200 scansioni al secondo con un range dinamico di 150 dB ed un tempo di scansione 4-6.000 ns.

I rilievi georadar sono stati eseguiti lungo direttrici progettate per indagare al meglio il sottosuolo all'interno della chiesa: n° 6 profili longitudinali lungo la navata centrale e n° 5 lungo ogni navata laterale e trasversalmente ai precedenti n° 6 profili; sono stati eseguiti profili GPR anche in corrispondenza degli altari e della sagrestia. La lunghezza dei singoli profili varia da 2 a 33 m, con una spaziatura massima tra profili adiacenti di 1,5 m circa per quelli longitudinali e 5,5 m per quelli ortogonali.

I tempi di analisi dei segnali radar (durata della registrazione di ogni singolo segnale) sono stati impostati generalmente a valori pari a 90 ns per l'antenna 500 MHZ e 120 ns per l'antenna da 250 MHZ, corrispondenti a circa 4 e 5 m di profondità considerando una velocità di propagazione delle onde elettromagnetiche nei materiali investigati (calcarenite) nell'ordine di 12 cm/ns.

I dati sono stati registrati su un notebook tramite un software dedicato (GROUND VISION VER 1.3.1) e successivamente elaborati utilizzando il programma REFLEXW © version 2.1. Le principali operazioni di elaborazione sono consistite nell'applicazione di un algoritmo di guadagno lineare, nell' applicazioni di filtri verticali (nel dominio del tempo) e orizzontali (nel dominio dello spazio) per eliminare i vari disturbi presenti nei dati rilevati, nella riproduzione dei segnali con opportune scale di intensità del grigio per esaltare le riflessioni di interesse (Davis e Annan, 1989; Tillard e Dubois, 1995); nella rappresentazione delle sezioni georadar rilevate con preciso riferimento delle caratteristiche planimetriche.

Analisi dei dati. I radargrammi rappresentano una sezione dielettrica del sottosuolo ad alta risoluzione ed in questo paragrafo, sono riportati e descritti alcuni esempi che mettono in luce quanto emerso dall'indagine effettuata in superficie e dalla loro interpretazione. Le sezioni sono state rappresentate ad intensità variabile di grigio; il bianco corrisponde alla massima ampiezza positiva invece il nero alla massima ampiezza negativa del segnale radar.

Dall'elaborazione dei 48 profili radar eseguiti all'interno della Basilica è emersa la presenza di differenti tipologie di anomalie, ubicate a diverse profondità, riconducibili alla probabile presenza di strutture quali cavità superficiali e/o profonde, cripte e/o materiale fratturato.

I profili longitudinali sono stati acquisiti spostandoci dall'entrata della Basilica verso l'altare maggiore, quelli trasversali muovendoci dalla navata laterale sinistra in direzione di quella destra. La Fig. 1 mostra quattro sezioni radar: le prime tre effettuate lungo la navata centrale di cui una longitudinale (n.11) e due ortogonali (n. 30, 34) e la quarta eseguita in corrispondenza della sagrestia (n. 44). Nel profilo 11 è stato possibile individuare la presenza di tre anomalie, una a circa 3,5 m dall'ingresso, osservabile anche nella sezione radar relativa al profilo 30 e la seconda nell'area centrale, entrambe dovute probabilmente alla presenza di roccia fratturata o all'esistenza di una cavità riempita da materiale di riporto; tra i 28 e i 32 m è visibile una terza anomalia estesa in profondità tra i 60 cm ed i 2 m, forse legata alla presenza di una cripta. Il radiogramma relativo al profilo ortogonale 34, conferma tale anomalia e infatti sono ben visibili le iperboli di riflessione che interessano quasi interamente la sezione radar; in essa si osserva una ulteriore anomalia imputabile, anche in questo caso, alla probabile presenza di una cripta. Nella sezione radar relativa al profilo 44, eseguito nella sagrestia, sono chiaramente visibili i segnali causati dalla riflessione dell'onda sul tetto a volta dell'ambiente

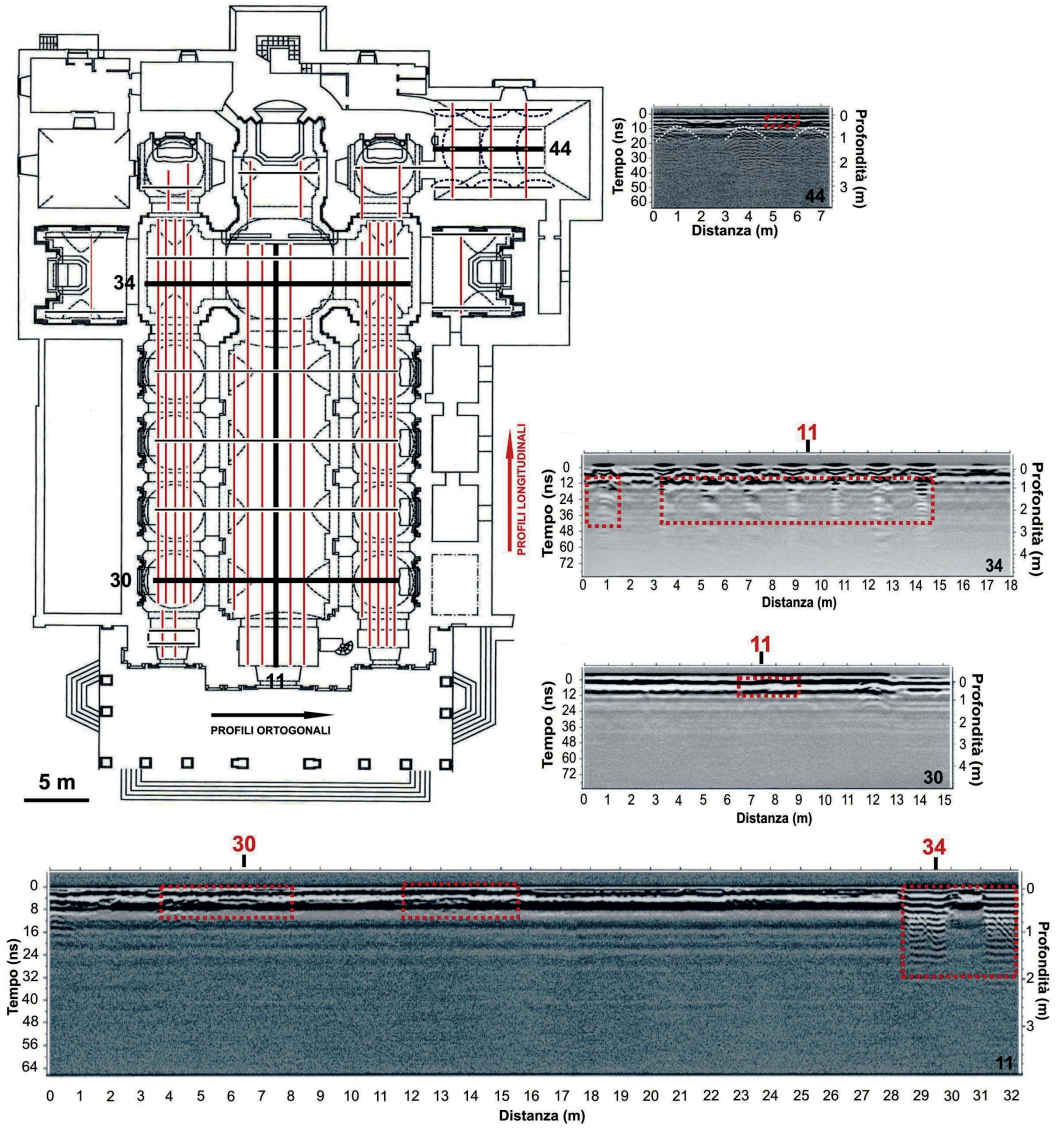

Fig. 1 – Ubicazione dei profili GPR (osservabili in pianta evidenziati con linee di maggior spessore) e radargrammi relativi al profilo n. 11 eseguito lungo la navata centrale, ai profili n. 30 e 34 ad esso ortogonali e al profilo n. 44 eseguito all'interno della sagrestia. I rettangoli rossi evidenziano le anomalie riscontrate all'interno delle sezioni radar; nel radargramma 44, eseguito all'interno della sagrestia, in bianco sono evidenziate le iperboli di riflessione causate dalla presenza di volte nell'ambiente sottostante. Su ciascun radargramma sono segnati i punti di intersezione con gli altri profili GPR.

sottostante; è individuabile anche una ulteriore anomalia a circa 4,7 m dall'origine, che si estende in profondità tra i 20 e i 40 cm, attribuibile alla presenza di aree di roccia degradate superficialmente.

Nella Fig. 2 sono riportate quattro sezioni radar, di cui due eseguite lungo le navate laterali (n.14 e n.4) ed altre due ortogonali a queste (n.32 e n.33). Nel radargramma relativo al profilo 14, eseguito lungo la navata laterale destra si osservano due anomalie, probabilmente causate dalla presenza di materiale poco addensato a profondità compresa tra i 30 e gli 80 cm; una di queste anomalie è individuabile nella parte finale del radargramma relativo al profilo 33

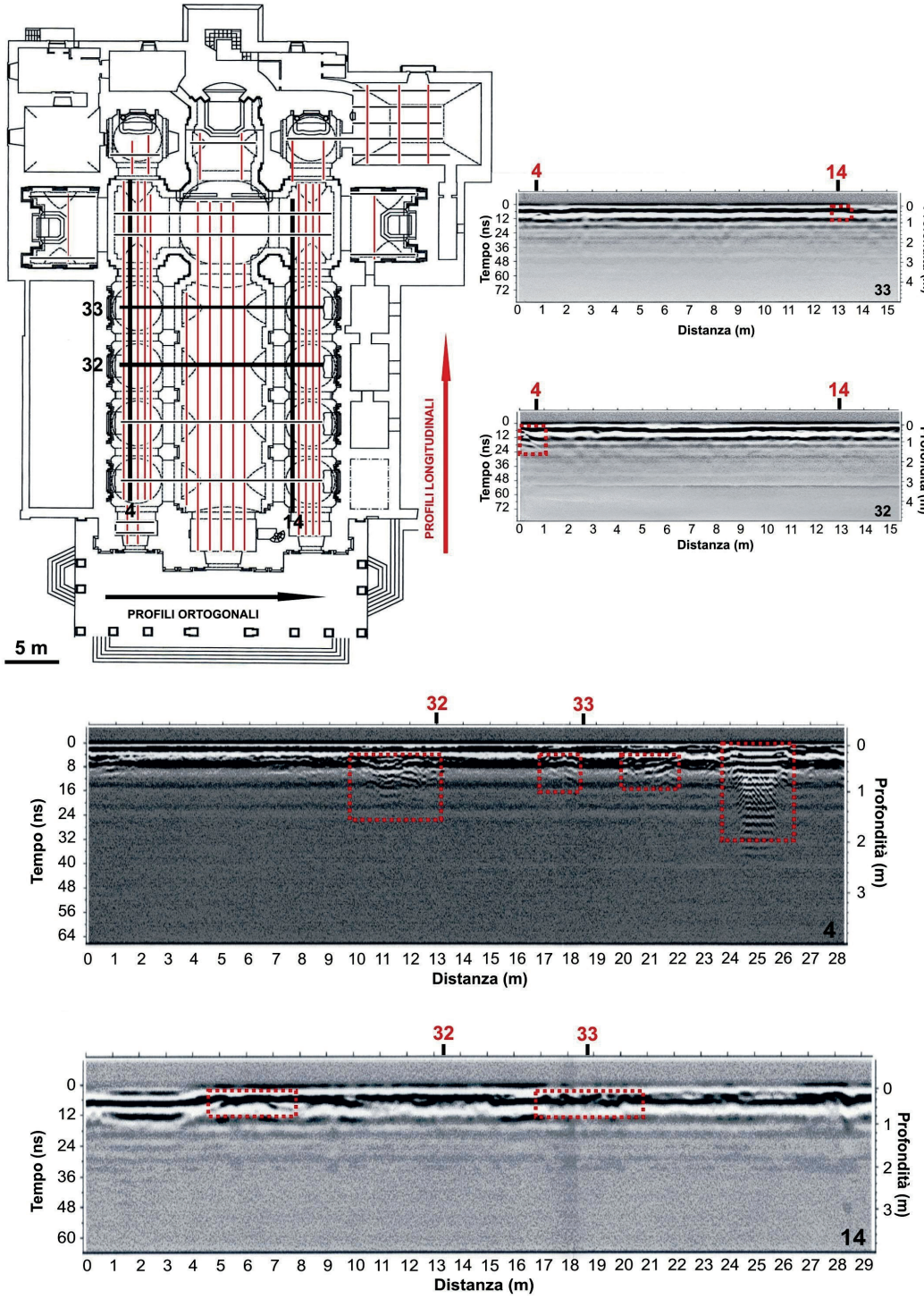

Fig. 2 – Ubicazione dei profili GPR (osservabili in pianta evidenziati con linee di maggior spessore) e radargrammi relativi ai profili n. 4 e 14, eseguiti rispettivamente lungo la navata laterale sinistra e destra, e dei profili n. 32 e 33 ad essi ortogonali. I rettangoli rossi evidenziano le anomalie riscontrate nel corso dell'indagine. In ciascuna sezione radar vengono anche mostrati i punti di intersezione tra i vari profili.

ad esso ortogonale. Nella sezione radar relativa al profilo 4, eseguito lungo la navata laterale sinistra, sono visibili diverse anomalie riconducibili a differenti tipi di strutture; la prima tra i 10 e i 13 m dall'origine del profilo si estende da una profondità di 40 cm fino ad 1,5 m ed è imputabile probabilmente alla presenza di una cavità sotterranea, trasversalmente la sua estensione può essere ricavata dall'osservazione del radargramma relativo al profilo 32, ad esso ortogonale, dove tale anomalia è ben visibile nella parte iniziale. Nella sezione radar del profilo 4 si osservano altre anomalie tra 17 e 18 m e tra 20 e 22 m, con un estensione in profondità che va da i 40 cm fino ad un massimo di 1 m, riconducibili probabilmente a cavità superficiali; è chiaramente visibile anche un ulteriore anomalia, in corrispondenza della parte finale del profilo, tra 23,5 e 27,5 m e che si estende fino ad una profondità di 2 m probabilmente legata alla presenza di una cripta.

I risultati complessivi sono rappresentati nella Fig. 3 dove sono state evidenziate tutte le aree con presenza di anomalie radar; ad ogni area con caratteristiche elettromagnetiche diverse è stato assegnato un colore: VERDE - per le zone dove il segnale indica la presenza di una cripta; GIALLO - per le zone dove sono stati osservati dei fenomeni di ringing dell'onda elettromagnetica dovuti ad una densità minore del mezzo per cause imputabili o al riempimento di cavità o alla fratturazione della roccia in posto; ROSSO - dove sono state individuate cavità superficiali (da -40 cm fino ad un massimo di -1m); GRIGIO - dove sono state individuate cavità profonde (oltre il metro); BEIGE - dove è stata individuata un'anomalia concentrata solo al di sotto della pavimentazione della chiesa stessa probabilmente dovuta a difetti (scollamenti o presenza di corpi estranei); ARANCIONE - l'area sotto la pavimentazione dove è stata individuata un'anomalia dovuta alla presenza di ambienti sottostanti (cunicolo di comunicazione tra la sagrestia e l'altare destro); BLU - dove sono state riscontrate delle discontinuità nel tetto a volta dell'ambiente sottostante la sagrestia.

Discussioni. L'analisi dei dati ha portato a concentrare l'attenzione sul dataset ottenuto con l'antenna da 500 MHz perché ha consentito di individuare distintamente le strutture sepolte, mentre il dataset acquisito con l'antenna da 250 MHz è stato un'utile conferma delle anomalie rilevate nei profili con antenna a più alta frequenza. Il sottosuolo, prevalentemente costituito da terreni rocciosi misti a materiali eterogenei dal medio coefficiente di assorbimento (granulometria da media a fine in parziale stato di imbibizione) ha causato un'attenuazione nella trasmissione dell'energia elettromagnetica.

I radargrammi mostrano delle geometrie abbastanza definite relative alla presenza di strutture sepolte anche se diverse sezioni sono caratterizzate da riverberi laterali e diffusi fenomeni di scattering dell'energia, attribuibili alla presenza di corpi singoli riflettenti immersi in un terreno di sedime localmente rimaneggiato (Imposa e Mele, 2011). L'intensità dello scattering è determinata dal rapporto tra dimensioni medie delle eterogeneità e lunghezza d'onda principale dell'impulso elettromagnetico; se si ha equivalenza tra queste due grandezze si determina un fenomeno noto come "clutter" (Kazunori *et al*., 2012). Esaminando singolarmente le aree oggetto dell'indagine (Fig. 3) si ha:

Navata centrale. I dati hanno evidenziato la presenza di due zone, la prima a circa 3,5 m dall'ingresso e la seconda nell'area centrale a minore densità dovute o alla fatturazione della roccia in piccoli elementi o alla presenza di cavità riempite con materiale di riporto. La presenza di aria provoca il fenomeno di "ringing" riscontrato (Jung-Ho-Kim *et al*., 2007). Tra la seconda e la terza colonna di sinistra è stata individuata un'area che denuncia un degrado dello strato superficiale del terreno compreso tra i -20 e i -80 cm. In corrispondenza della quarta colonna è stata individuata una cavità tra i -60 cm ed i -2 m, dovuta probabilmente alla presenza di una cavità profonda. Infine, è stata rilevata la presenza di una cripta poco prima dell'altare maggiore che si estende trasversalmente rispetto alla navata e che in profondità arriva fino a circa 2 m.

Navata laterale sinistra. Nella parte iniziale è stata individuata una porzione degradata di terreno fino ad 1 metro di profondità; in corrispondenza del terzo altare è presente tra i 40

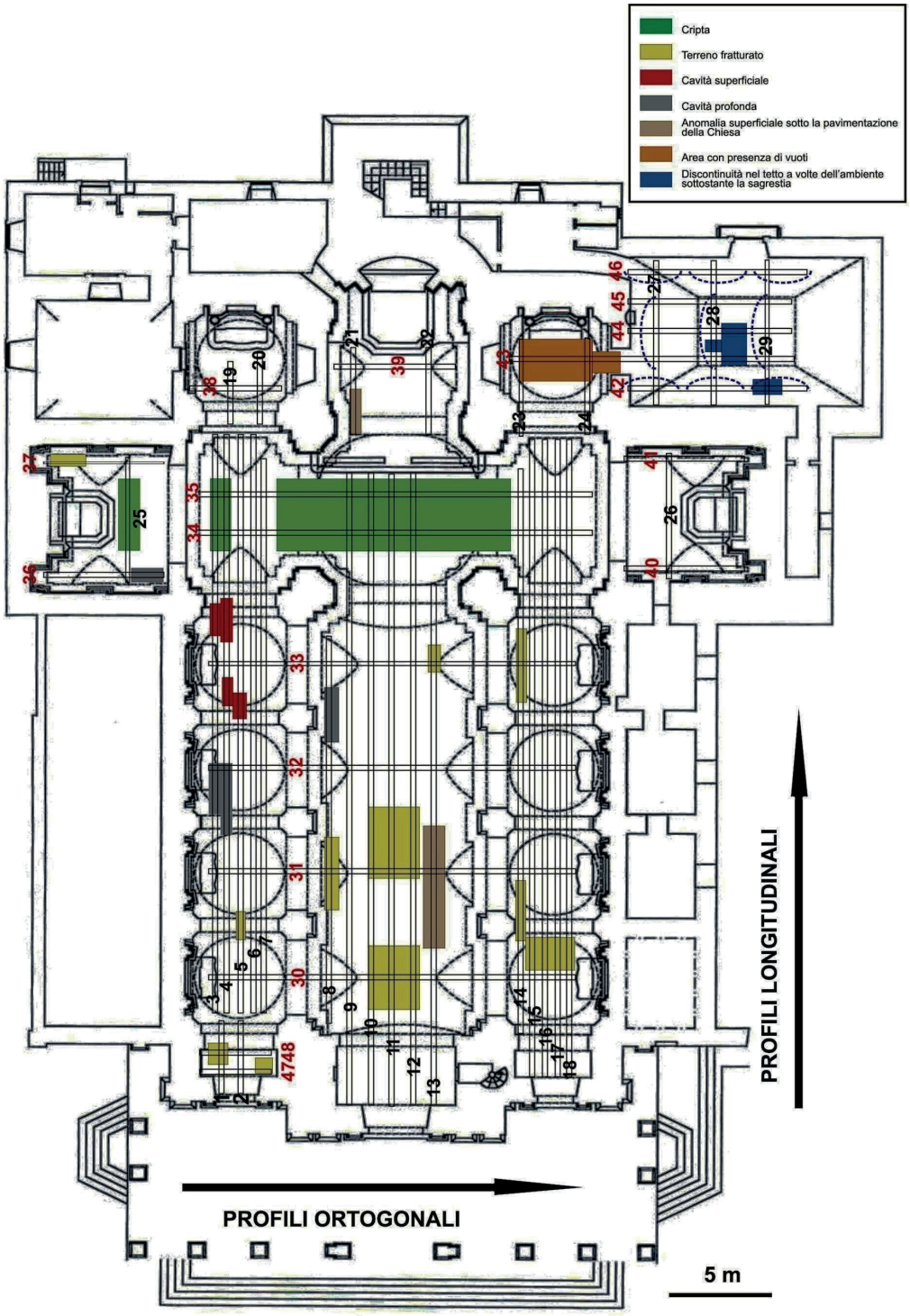

Fig. 3 – Pianta della Chiesa di Santa Maria Maggiore, con ubicazione ed interpretazione delle anomalie riscontrate nei vari profili GPR eseguiti nel corso dell'indagine; ad ogni area con caratteristiche elettromagnetiche diverse è stato assegnato un colore (vedi legenda).

cm ed 1,5 m di profondità una cavità che si estende fino a metà dell'altare stesso. Altre cavità superficiali sono state riscontrate davanti il quarto altare. Infine, è stata riscontrata la presenza di una cripta ad una profondità compresa tra 60 cm e 2 m nella parte finale della navata.

Navata laterale destra. Sono presenti due anomalie, una è davanti il primo altare in prossimità della seconda colonna ad una profondità compresa tra i 30 e gli 80 cm, mentre la seconda si trova in una ristretta fascia davanti il quarto altare. In entrambi i casi il segnale radar ha evidenziato la presenza di materiale poco addensato.

Altare laterale sinistro. Oltre alla cripta centrale sono presenti due cavità, una alla sinistra della cancellata ed un'altra alla destra dell'altare, probabilmente riempite da materiale di riporto.

Altare maggiore. Presenza di una anomalia abbastanza regolare al di sotto della pavimentazione dovuta probabilmente ad un rinforzo strutturale della pavimentazione stessa sulla parte anteriore sinistra.

Altare destro e sagrestia. Sono stati considerati insieme perché co-interessati dalla presenza di cavità in comunicazione tra loro. In corrispondenza della porta che immette all'interno della sagrestia è stata individuata un'area con presenza di terreno di riporto. Al di sotto della sagrestia è presente un ambiente sormontato da tetti a volta, ben visibili nel segnale radar, che evidenzia un area con presenza di roccia degradata (20-40 cm).

Conclusioni. Vengono presentati i risultati di una campagna di prospezioni georadar effettuata all'interno della chiesa di S. Maria Maggiore, ubicata nel Comune di Ispica, Sicilia, utilizzando antenne di 250 e 500 MHz; la tecnica di acquisizione è stata del tipo continuos profiling eseguendo scansioni sia longitudinali che trasversali.

Le indagini hanno consentito di differenziare nell'area in esame zone caratterizzate dalla presenza di anomalie di propagazione dell'energia elettromagnetica, fornendo una notevole quantità di informazioni, tra cui anche la forma delle anomalie, e permettendo la ricostruzione della geometria delle strutture sepolte sotto la pavimentazione della chiesa (Fig. 3).

Tenuto conto delle finalità dell'indagine e dell'importanza storico-architettonica della Basilica, si è ritenuto opportuno differenziare le riflessioni radar rilevate, per mettere meglio in risalto le zone anomale più significative, al fine di poter pianificare interventi di recupero successivi. In questo scenario, è stato possibile ricostruire la geometria delle cripte, specialmente dove il segnale evidenziava delle strutture ben delineate, delle aree più degradate e delle cavità non segnalate in superficie. Le cripte sono state rinvenute ad una profondità di circa 80 cm e si sviluppano fino a circa 2 metri (Figg. 1, 2). Analizzando i radargrammi sono state individuate delle anomalie superficiali dovute al parziale scollamento di porzioni della pavimentazione che non sono state segnalate sulla carta perché di scarso interesse. Di notevole interesse, invece, sono i dati acquisiti al di sotto della sagrestia, che permettono di delineare la presenza di un tetto a volta con ambiente sottostante e con un'area di debolezza strutturale concentrata quasi al centro dell'ambiente stesso e segnalato con il colore blu (Fig. 3).

Infine, è possibile affermare che l'interpretazione dei radargrammi ha permesso di ricostruire l'andamento del sottosuolo evidenziando diverse tipologie di anomalie legate alla storia del sito, che risulta completamente rimaneggiato in quanto è stato oggetto di scavi, seppellimento di defunti e riempimento per la costruzione della chiesa stessa.

È evidente che i risultati ottenuti con la tecnica georadar si sono dimostrati utili per l' individuazione, la localizzazione di cavità e/o cripte e la caratterizzazione dei materiali che le costituiscono e che le riempiono parzialmente o totalmente, ai fini della pianificazione di ulteriori interventi volti al restauro e conservazione della Basilica.

Riconoscimenti: Questo articolo é stato eseguito con il supporto finanziario dell'università di Catania (PRA n 20104001082, Responsabile Scientifico: Imposa S.).

Bibliografia

Anchuela Pueyo Ó.,Casas-Sainz A.M.,Soriano M.A., Pocoví-Juan A.2009. Mapping subsurface karst features with GPR: results and limitations. Environmental Geology 58, 391–399.

Barilaro D., Majolino D., Gresta S., Imposa S., Schillaci A., Leone A. 2006. Geophysics and thermographic investigations addressed to the study of the church of "S. Maria del Rosario" in Sicily (Italy). Contribution to Geophysics & Geodesy 36, 239-253, ISSN: 1335-2806.

Barilaro D., Branca C., Gresta S., Imposa S., Leone A., Majolino D. 2007. Ground Penetrating radar (G.P.R.) surveys applied to the research of crypts in San Sebastiano's church in Catania (Sicily-Italy). Journal of Cultural Heritage 8/1, 73-76, ISSN: 1296-2074

Barone G., Branca C., Gresta S., Imposa S., Leone A., Majolino D. 2004. Geoarcheometric and Geophysical methodologies applied to the study of cultural heritage: "S. Agata la Vetere" in Catania(SICILY-ITALY). Journal of Cultural Heritage 5, 263-271, ISSN: 1296-2074

Carbone S., Grasso M., Lentini F. 1982. Considerazioni sull'evoluzione geodinamica della sicilia sud-orientale dal cretaceo al quaternario. Memorie della Società Geologica Italiana 24, 367-386, 9 fig.

Castellaro S., Imposa S., Barone F., Chiavetta F., Gresta S., Mulargia F. 2008. Georadar and Passive Seismic Survey in the Roman Amphitheatre of Catania (Sicily). Journal of Cultural Heritage 9, 357-366, ISSN: 1296-2074.

Coco G., Corrao M. 2009.Geofisica applicata. Flaccovio editore, 198-226.

Davis J.L.,, Annan A.P. 1989. Ground penetrating Radar for High-Resolution Mapping of Soil and Rock Stratigraphy. Geophysical Prospecting 37, 531-551.

Gad E.-Q., Mahfooz H., Mohamed A. A., Keisuke U. 2005.Imaging subsurface cavities using geoelectric tomography and Ground-Penetrating Radar. Journal of Cave and Karst Studies 67, no. 3, 174–181.

Grasso M., Reuther C.D., Tortorici L. 1992. Neotectonic deformation in S.E Sicily: the Ispica fault, evidence of late Miocene-Pleistocene decoupled wrenching within the central Mediterranean stress regime. Journal Geodynamics 16, no. 1/2, 135-146, Great Britain.

Grasso M., Pedley H.M., Maniscalco R., Ruggieri R. 2000. Geological context and explanatory notes of the "Geologica Map of central-southern sector of the Hyblean Plateau. Memorie della Società Geologica Italiana 55, 45-52.

Ghisetti F.,Vezzani L. 1980. The structural features of the Hyblean Plateau and of the Mount Judica area(South-Eastern Sicily): a microtectonic contribution to the deformation history of the Calabrian Arc. Bollettino, Società Geolologica, Italiana, 99,57-102.

Imposa S., Barone G., Coco G., Corrao M., Dell'ali P., Puglia A., Nicotra A., Vinci S. 2004. Ground penetrating radar and electrical survey of the roman "Terme Achelliane" in Catania (Sicily): a case history. Contributions to Geophysics & Geodesy 34/4, 387-403, ISSN: 1335-2806.

Imposa S. 2006. Site response and G.P.R. investigation: a case study applied to the Minoritelli church (Catania – Italy). In: Proceedings XVIIIth Congress of the Carpatian-Balkan Geological Association. Belgrade–Serbia, September 3-6, 1, 233-235.

Imposa S., Barone F., Gresta S., Leone A. 2009. Ground penetrating radar survey finalized to the recovery of the "S. Agata alla Badia" church in Catania (eastern Sicily, Italy). Enviromental Geology 58, 889-896, ISSN: 0943-0105.

Imposa S. 2010. Infrared thermography and Georadar techniques applied to the "Sala delle Nicchie" (Niches Hall) of Palazzo Pitti, Florence (Italy). Journal of Cultural Heritage 11, 259-264, ISSN: 1296-2074.

Imposa S., Mele G. 2011. Ground penetrating radar survey inside the S. Agata cathedral of Catania (Eastern Sicily). International Journal of Architectural Heritage 5, 188-197.

Jung-Ho-Kim, Seong-Jun Cho, Myeong-Jong Yi 2007. Removal of ringing noise in GPR data by signal processing. Geoscences Journal, 11, no. 1, 75-81.

Takahashi K., Igel J., Preetz H. 2012. Modeling of GPR clutter caused by soil heterogeneity. International Journal of antennas and propagation. Artiche Id 643430, 7 pages. http://dx.doi.org/10.1155/2012/643430.

Monaco C., Tortorici L. 1995. Tettonica estensionale quaternaria nell'arco Calabro e in Sicilia sud-orientale. Studi geologici Camerti, Volume speciale 1995/2, 351-362.

Patanè' G., Imposa S. 1987. Tentativo di applicazione di un modello reologico per l'Avampaese ibleo ed aree limitrofe. Memorie della Società Geologica Italiana 38, 341-359, ISSN: 0375-9857

Tillard S.,Dubois J.C. 1995. Analysis of GPR data: wave propagation velocity determination. Journal of Applied Geophysics 33, 77-91.

Trigilia M. 2007. La basilica di Santa Maria Maggiore. (Editrice SO.GE.ME) Pag. 1- 10; 2- 15.

PORTABLE LOW-COST MEASUREMENT SYSTEM DEVELOPMENT FOR SELF-POTENTIAL (SP) MONITORING IN SEVERE ENVIRONMENTAL CONDITIONS

M. Masi[1], V. Pazzi[2]
[1] *Department of Information Engineering, University of Firenze, Italy*
[2] *Department of Earth Sciences, University of Firenze, Italy*

Introduction. In the field of environmental sciences self-potential (SP) data are generally considered as promising and reliable to investigate subsurface properties, especially for their ease of acquisition and simplicity in making qualitative interpretations (Revil and Jardani, 2013). Although it is one of the oldest geophysical method, the self-potential technique is currently adopted in a broad range of both qualitative and quantitative applications such as localizing and quantifying groundwater flows (Revil *et al.*, 2006; Jardani *et al.*, 2007; Jouniaux *et al.*, 2009), characterizing volcanic areas (Fournier, 1989; Di Maio *et al.*, 1996; Zhang and Aubert, 2003), monitoring contaminant plumes (Weigel, 1979; Naudet *et al.*, 2003), studying landslides (Perrone *et al.*, 2004; Naudet *et al.*, 2008) and geothermal exploration (Corwin and Hoover, 1976).

Self-potential is a passive method consisting in the measurement of the electric potential at a set of measurements stations. SP anomalies usually indicate the presence of a source of current in the ground due to subsurface disturbances (e.g. ground waters, geochemical phenomena). Three main contributions are widely recognized as a source of occurrence of SP signal (Revil and Jardani, 2013): the reduction-oxidation (redox) potentials, the diffusion potentials and the electrokinetic effect. The presence of an electronically conductive body creates an oxidizing area acting like an anode, and a reducing area acts like a cathode. This source of electrical potentials is referred to as the redox potential. Besides, the diffusion potential is related to the concentration gradients of ionic species in pore water. The electrokinetic effect (or streaming potential) is associated with the drag of excessive charge by the flow of water in porous rocks, causing a net source current density.

The SP method can also be applied as a monitoring method (Perrier *et al.*, 1998; Trique *et al.*, 2002) where a multi-electrode array is used to track the changes of the subsurface variables with time.

Monitoring strategies are generally required to evaluate the performance of engineered environmental control systems (e.g. remediation systems, leachate in landfills), to assess potential environmental impacts and public health risks from contaminant releases or to characterize environmental processes including chemical transformations, diffusion and advection phenomena or biological reactions, occurring in natural or engineered systems. Measuring the temporal variations of the electric potential is an effective tool to characterize and monitor these phenomena especially with regard to hydrogeological fluxes and electrochemical processes in the subsoil.

In several occasions the monitoring instrumentation is required to operate unattended or is exposed to environmental condition in which a degradation/oxidation of electromechanical parts is expected. In such situations the investment for the equipment could be economically unfeasible. In order to fulfill such requirements we developed a measurement setup with the main advantages of being portable, low cost, rugged, sufficiently accurate and optimized for low power consumption.

The measurement setup was first checked in laboratory for reliability and accuracy then was evaluated during a data acquisition campaign in Kenya to measure the SP variation linked to the fluctuations of the sea level during tidal events.

Apparatus.

Measurement system. The measurement system (Fig. 1a) was designed to monitor electrical potential in soil and sediments in locations where rugged instrumentation is required because of the harsh environmental conditions or when instrumentation security is critical.

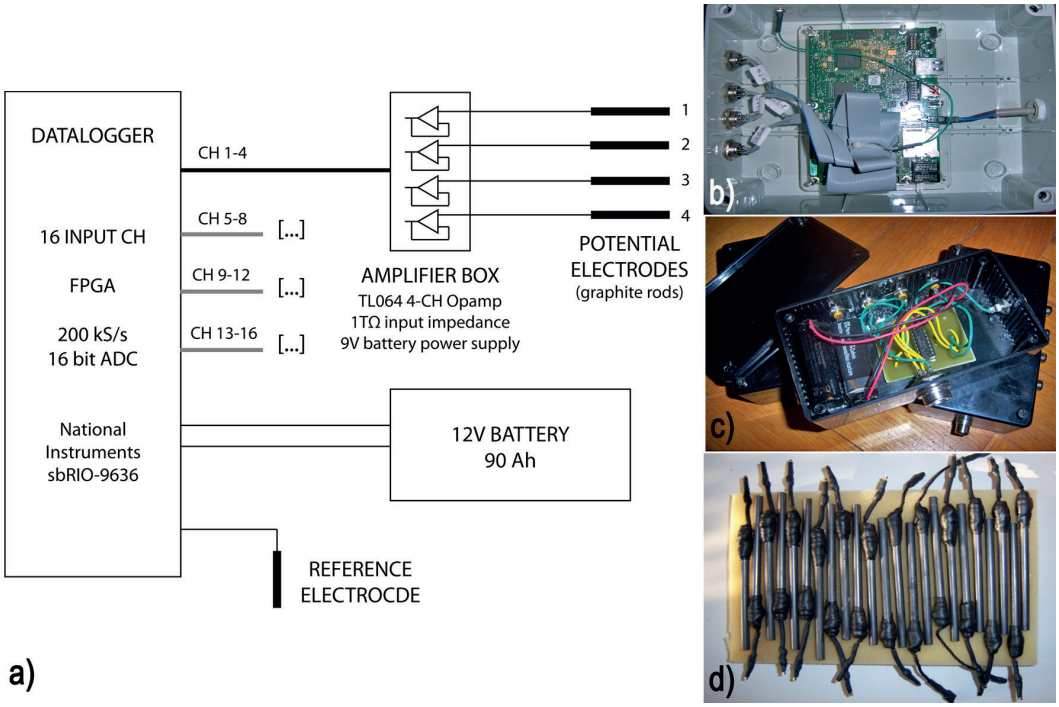

Fig. 1 – a) Block diagram of the measurement system designed for the self-potential monitoring; b) the data acquisition device NI-sbRIO-9636 by National Instruments; c) the amplifier boxes with the four-channel JFET-input operational amplifier (Texas Instruments TL064); d) the graphite electrodes.

The system consists of up to 16 channels to measure the voltages between the potential electrodes and a reference electrode connected to the system ground. The potential electrodes (Fig. 1d) are connected to 4 amplifier boxes (Fig. 1c) with a 4-channel buffer amplifier within each box and then the signals are fed to the acquisition device (Fig. 1b), powered by an external battery.

The data acquisition device is a NI-sbRIO-9636 by National Instruments. It features 16 single-ended (8 differential) 16-bit analog inputs at 200 kS/s, +/- 10V maximum input range, a real-time processor, a user-reconfigurable FPGA, 256 MB of DRAM for embedded operation and 512 MB of nonvolatile memory for storing programs and data logging. The 16-bit analog-to-digital converter allows to obtain a sensitivity (LSB) of 32 μV when the +/- 1V input range is selected, much higher than the minimum required of 0.1 mV (Revil and Jardani, 2013).

The sbRIO-9636 is hereby used as a standalone device and it is programmed for data logging and real-time data processing in LabVIEW programming environment. The acquisition is controlled by the FPGA and a sampling frequency of 1 kHz for each channel is chosen. The signals are then filtered and downsampled to 1 Hz by the real-time processor and data is stored on the internal nonvolatile memory.

Measurements of self-potential are subject to a number of errors such as the instability of the measuring electrodes and near surface noise due to anthropogenic activities (e.g. power lines, electromagnetic interference), telluric currents, meteorological effects or natural processes associated with soil electrochemical reactions or root activities (Perrier and Pant, 2005).

Other common sources of error are related to the measurement of voltage sources with high internal impedance (i.e. high contact impedance between electrode and soil). In this case the measurements are subject to loading errors and offset current errors occurring at the input of

the acquisition device. In order to avoid these errors the input impedance of the acquisition device should be much higher than the source impedance (Keithley, 1998).

A four-channel JFET-input operational amplifier (Texas Instruments TL064) is used for this purpose, configured as a buffer amplifier (Jung, 2004). The JFET-input stage has an extremely high input impedance (1TΩ), much higher than the maximum expected contact resistance (in the MΩ range) typically measured in the field (Corry *et al.*, 1983). Moreover the low output impedance of the operational amplifier significantly reduces the error relative to the input offset current of the acquisition device. The TL064 features low input offset and input bias current thus further reducing the measurement errors. Furthermore, the TL064 is a low-power consumption device with a typical supply current of 200 μA per channel which makes it particularly suitable for a battery-powered system.

Printed circuit boards, amplifier boxes, cables and data logger chassis were self-made and all parts were assembled in laboratory. The connections between devices were made by means of shielded multicore cables with multipole connectors. Two 6LR61 9 V batteries (550 mAh capacity) were used to power each TL064 with a current drawing of 0.8 mA and a runtime of about 28 days. One 12 V, 90 Ah battery was used to power the data logger. The current drawing of the data logger was about 200 mA and the battery life of about 18 days.

The devices were tested in laboratory feeding a signal through each channel with a HP 33120A signal generator and verifying their performance (gain, distortion, frequency response and noise) with test equipment.

The key benefits of the proposed system design are: i) the low bias currents at input stage which prevent the polarization of the electrodes, ii) the low-impedance output of the operational amplifier which decreases the time required for settling of the multiplexed acquisition device, reducing ghosting and crosstalk between channels, iii) the high-impedance input of the amplifier which prevents the source impedance act as a voltage divider across the input of the acquisition device (loading error).

Electrodes. The measurements were performed with non-commercial electrodes (Fig. 1d): they were designed and realized in order to be cheap, resistant, high conductivity and easily portable. The basic requirements for the electrodes were durability, long-term stability, and low noise level. Usually non-polarizing porous-pot electrodes (typically Ag-AgCl, Cu-$CuSO_4$, or Pb-$PbCl_2$) are used to perform self-potential measurements. Numerous authors have investigated electrode designs that reduce measurement errors and are stable over long periods of time (Perrier *et al.*, 1997; Clerc *et al.*, 1998; Petiau, 2000). Measurement errors on the order of several (~5) millivolts should be expected with modern surveying equipment, and this can be significantly reduced by installing the electrodes (semi) permanently (Perrier *et al.*, 1997; Perrier and Pant, 2005).

Since graphite is an excellent electrical conductor and it is not affected by corrosion or electro-chemical effects, graphite electrodes are commonly employed for the application of electric fields such in electrokinetic remediation (Pazzi *et al.*, 2012). Electrodes made of graphite are also found commercially and used for geophysical monitoring purposes, to eliminate the damaging effects of corrosion and electrochemical degradation with time (Patent US 6,674,286).

The electrodes were made of carbon rod 100 mm long with a diameter of 6 mm; at the top a 5 cm carbon rope (®Sigrafil D2-3K Cord, Ø = 19 mm) was fixed with a self-fusing silicon rubber tape and a stainless steel male-connection was protected with heat shrinks. The connection with the amplifier boxes were carried out by means of wires with a stainless steel female-connection on one end. Furthermore, to avoid chemical oxidation all the connections were isolated by means of heat shrinks.

Graphite electrodes have been tested in laboratory in a 7-days experiment. The electrodes were placed in an experimental cell (Masi *et al.*, 2013) filled with quartz sand. The sand was saturated with tap water and the saturation was ensured by recirculating water inside

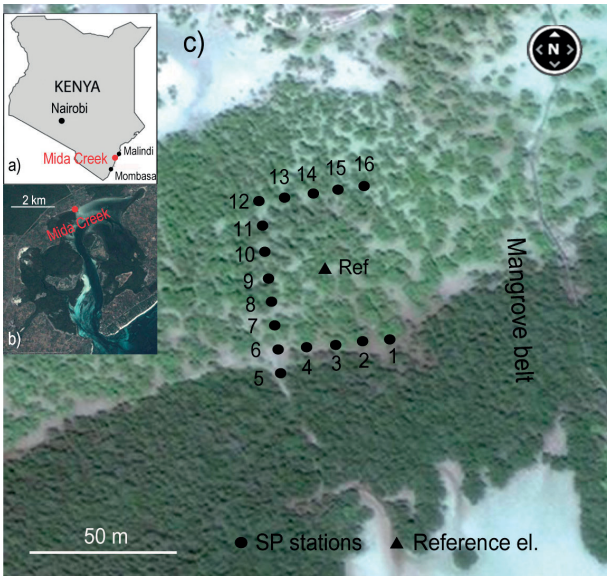

Fig. 2 – The test area in Kenya, about 25 km south of Malindi (a) in the north-western margin of Mida Creek (b); c) the C-shaped self-potential array.

the electrolytic compartments. The electrodes have proved to be sufficiently stable with a maximum drift of 0.8 mV over the entire period.

Field tests. The instrumental apparatus has been tested during a scientific expedition in the north-western margin of Mida Creek (03°20'S, 40°5'E), a wide swamp about 25 km south of Malindi (Kenya) (Fig. 2a, b). Mida Creek is bordered by a mangrove belt consisting of three different species: *Avicennia marina* at the landward level and *Rhizophora mucronata* and *Ceriops tagal* at the seaward level. In the test area the whole belt is about 300 m wide: the area dominated by *Avicennia marina* is nearly the half and it is comprised between the average high water spring tide and the average high water neap tide. Within the creek the tidal range is at least 2 m, while on the surrounding coast is about 4.2 m (Vannini *et al.*, 2008).

Sixteen electrodes have been placed to obtain a C-shaped array (Fig. 2c): this configuration was selected in order to measure the self-potential variation along the sea-land direction (NS direction, electrodes 5-12) and along two profiles perpendicular to this direction (EW direction, electrodes 1-6 the southern and electrodes 12-16 the northern). The distance between two adjacent electrodes was 10 m. The reference electrode was located at the centre of the array as shown in Fig. 2c. The acquisition run for about 10 days (245 hours). The sampling interval was 1 s.

As an example, sample data corresponding to a semidiurnal cycle of the tide (12 hours duration) were selected from the whole time-series. The data have been pre-processed with a low-pass filter in order to remove the high-frequency content from the signals. Time-lapse mapping of the SP anomalies was obtained from the data at five different time instants (Fig. 3). The tide data were obtained by reconstruction from the tide heights recorded in Mombasa harbour. The data then were shifted in time to match the delayed arrival of the tide in Mida Creek, calibrated with on-site sea level measurements. The results are shown in Fig. 3. Negative SP anomalies are observed throughout the selected period and they were of the order of magnitude of hundreds millivolts with respect to the voltage at the reference electrode. The changes in the sea level clearly affect the SP response. This effect is most likely due to both the electrokinetic effect of the tidal volume flowing through the subsurface and the change in the ionic concentration and species of the pore water (Martínez-Pagán, 2010).

Conclusions. The design and implementation of a low-cost setup for SP monitoring in the field was discussed. The main advantages of such setup are the portability, the ruggedness and the low power consumption while ensuring a good measurement reliability. The system is capable of measuring the electric potential from up to 16 electrodes referenced to a common ground (reference electrode). The maximum acquisition rate in 200 kS/s per channel and the analog-to-digital converters resolution in 16 bits, allowing for a sensitivity of 32 μV. The recorded data is stored in an internal non-volatile memory for standalone operation. The measurement errors due to source loading and offset currents are minimized through the use of

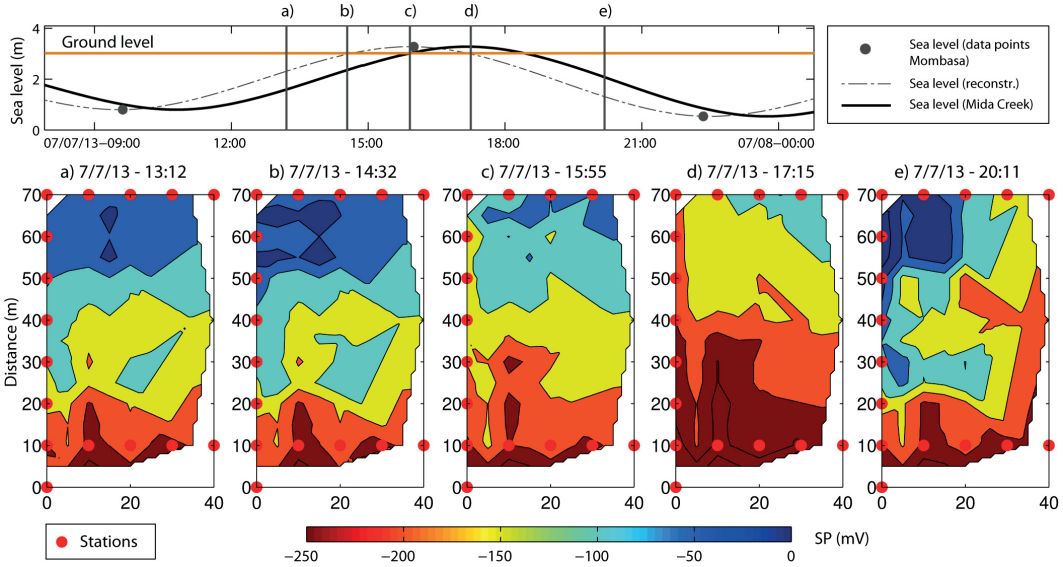

Fig. 3 – On the top the tide data (black dots) obtained from the Tide Table of Mombasa harbour, the reconstructed sea level (dashed black line) and the sea level in Mida Creek (solid black line) obtained shifting in time the reconstructed sea level to match the delayed arrival of the tide in Mida Creek recorded by on-site sea level measurements. On the bottom the time-lapse mapping of the SP anomalies obtained from the data at five different time instants (a-e).

high input impedance (1TΩ) buffer amplifiers. The system was tested in the field to monitor the SP anomalies due to the fluctuations of the sea level during tides. It is seen that the combination of various sources of SP due to the tides can affect the SP response with time. These effects are most likely due to the electrokinetic effect and diffusion potentials induced by the tidal fluctuations. The graphite electrodes used in this work for SP acquisition are proven to be stable in laboratory. In the field they were not subjected to relevant drifts over the entire duration of acquisition (10 days), as well.

Acknowledgements. Many thanks to professor Marco Vannini (University of Firenze) for getting us involved in this project and to professor Nicola Casagli (University of Firenze) for letting us take part in the summer scientific expedition. We are grateful to professor Gabriella Losito (University of Firenze) and professor Stefano Mancuso (University of Firenze) for discussing with us about several aspects of the instrumentation. Special thanks also to Eng. Riccardo Susini (National Instrument) for his technical assistance. The assembly work could not have been done without the collaboration of Nadia Bazihizina, Alessandro Anastassopoulos and Francesco Spennati. We also wish to express gratitude to the people who contributed to the field work in Kenya: Giorgia Campiero, Stefano Giannotti, Giulia Giberti, Veronica Lisini Baldi, Alessia Lotti, Alessio Raspanti, Leonardo Terreni, and the Kenyan guides of Mida Creek.

References

Clerc, G., Petiau G., Perrier F.; 1998: The Garchy 1995-1996 electrode experiment technical report. INSU-CNRS/CEA, Paris.

Corry C.E., De Moully G.T., Gerety M.T.; 1983: Field Procedure Manual for Self-Potential Surveys. Z.E.R.O. Publishing, Arizona, USA.

Corwin R. F., Hoover D.B.; 1979: The self-potential method in geothermal exploration. Geophysics, **44**, 226 – 245, doi: 10.1190/1.1440964.

Di Maio R., Di Sevo V., Giammetti S., Patella D., Piscitelli S., Silenziario C.; 1996: Self-potential anomalies in some Italian volcanic areas. Annals of Geophysics, **39 (1)**, 179-188, doi: 10.4401/ag-3960.

Fournier C.; 1989: Spontaneous potentials and resistivity surveys applied to hydrogeology in a volcanic area: case history of the Chaı̂nedes Puys (Puy-de-Doˆme,France). Geophys. Prosp., **37 (6)**, 647–668, doi: 10.1111/j.1365-2478.1989.tb02228.x.

Jardani A., Revil A., Bolève A., Dupont J.P., Barrash W., Malama B.; 2007: Tomography of groundwater flow from self-potential SP data. Geophysical Research Letters, **34**, L24403, doi: 10.1029/2007GL031907.

Jouniaux L., Maineult A., Naudet V., Pessel M., Sailhac P.; 2009: Review of self-potential methods in hydrogeophysics. C.R. Geoscience, **341 (10-11)**, 928-936, doi: 10.1016/j.crte.2009.08.008.

Jung W.; 2004: Op Amp Applications Handbook (Analog Devices Series). Paperback, 896 pp.

Keithley L.E.; 1998: Low Level Measurements. Application Notes. Keithley Instruments, Inc. - Aurora Road, Cleveland, Ohio, USA, (5th Edition).

Martinez-Pagan P., Jardani A., Revil A., Haas A.; 2010: Self-potential monitoring of a salt plume. Geophysics, **75 (4)**, WA17-WA25, doi: 10.1190/1.3475533.

Masi M., Pazzi V., Losito G.; 2013: Laboratory scale electrokinetic remediation and geophysical monitoring of metal-contaminated marine sediments. Geophysical Research Abstract, **15**, EGU2013-11277-1, EGU General Assembly 2013.

Naudet V., Revil A., Bottero J.Y., Be´gassat P.; 2003: Relationship between self-potential (SP) signals and redox conditions in contaminated groundwater. Geophys. Res. Lett., **30 (21)**, 2091, doi:10.1029/2003GL018096.

Naudet V., Lazzari M., Perrone A., Loperte A., Piscitelli A., Lapenna V.; 2008: Integrated geophysical and geomorphological approach to investigate the snow melt-triggered landslide of Bosco Piccolo village (Basilicata, southern Italy). Eng. Geol., **98**, 156–167, doi: 10.1016/j.enggeo.2008.02008.

Pazzi V., Losito G.M.S., Mazzarelli R., Trova A., Lapenna V., Rizzo E.; 2012: Electrokinetic remediation (EKR) effects under linear and radial electric field at laboratory scale. BGTA, **53 (3)**, 347-365, doi: 10.4430/bgta0061.

Patent US 6,674,286 B2; 2004: Methods and apparatus for measuring electrical properties of a ground using a graphite electrode. Unites States Patent.

Perrier F., Trique M., Lorne B., Avouac J.P.; 1998: Electric potential variations associated with yearly lake level variations. Geophysical Research Letters, **25 (11)**, 1955-1958, doi: 10.1029/98gl01193.

Perrier F., Pant S.R.; 2005: Noise reduction in long-term self-potential monitoring with travelling electrode referencing. Pure appl. geophys., **162**, 165-17, doi: 10.1007/s00024-004-2585-3.

Perrier F., Pant S.R.; 2005: Noise reduction in long-term self-potential monitoring with travelling electrode referencing. Pure Appl. Geophys., **162 (1)**, 165-179, doi: 10.1007/s00024-004-2585-3.

Perrier F.E., Petieu G., Clerc G.; 1997: A one-year systematic study of electrodes for long period measurements of the electric field in geophysical environments. J. Geomagn. Geoelectr., **49 (11-12)**, 1677-1696.

Perrone A., Iannuzzi A., Lapenna V., Lorenzo P., Piscitelli S., Rizzo E., Sdao F.; 2004: High-resolution electrical imaging of the Varco d'Izzo earthflow (southern Italy). J. Appl. Geophys., **56**, 17–29, doi: 10.1016/j.jappgeo.2004.03.004.

Petiau G.; 2000: Second generation of lead-lead chloride electrodes for geophysical applications. Pure Appl. Geophys., **157 (3)**, 357-382, doi: 0033-4553/00/030357-26.

Revil A., Titov K., Doussan C., Lapenna V.; 2006: Applications of the self-potential method to hydrological problems. In: Applied Hydrogeophysics, Springer Netherlands, NATO Ser. IV, **71**, 255–292.

Revil A., Jardani A.; 2013: The Self-Potential Method: Theory and Applications in Environmental Geosciences. Cambridge University Press, 383 pp.

Trique M., Perrier F., Froidefond T., Avouac J., Hautot S.; 2002: Fluid flow near reservoir lakes inferred from the spatial and temporal analysis of the electric potential. Journal of Geophysical Research, **107**, 1978-2012, doi: 10.1029/2001JB000482.

Vannini M., Mrabu E., Cannicci S., Rorandelli R. and Fratini S.; 2008: Rhythmic vertical migration of the gastropod Cerithidea decollata in a Kenyan mangrove forest. Mar. Biol., **153**, 1047-1053, doi: 10.1007/s00227-007-0877-8.

Weigel M.; 1989: Self-potential surveys on waste dumps: Theory and practice. in Merkler G.P., Militzer H., Hötzl H., Armbruster H., and Brauns J., eds., Detection of subsurface flow phenomena: Lecture Notes in Earth Science, **27**, 109–120, doi: 10.1007/BFb0011626.

Zhang G.B., Aubert M.; 2003: Quantitative interpretation of self-potential anomalies in hydrogeological exploration of volcanic areas: a new approach. Near Surf. Geophys., **1 (2)**, 69–75, doi: 10.3997/1873-0604.2002008.

ACCURATE EVALUATION OF EDGES AND DIP OF FAULTS AND CONTACTS THROUGH THE VOLUME UPWARD CONTINUATION (VUC) OF GRAVITY DATA

D. Mastellone, M. Fedi, V. Paoletti
DISTAR, Department of Earth Sciences, Environment and Resources, University of Naples Federico II, Italy

Introduction. Several methods have been used to retrieve values of dip of faults by using lateral offsets of the zero-crossover point of the second horizontal derivative of upward-continued gravity profiles. The use of derivatives of potential fields represents a signal enhancement technique experimented since a long time. It allows the information content of the signal to be enhanced without implying any arbitrary assumption. Often, such methods are coupled with upward continuation, which is used to transform anomalies measured on one surface into those that would have been measured on some higher altitude surface.

In this paper we demonstrate the efficiency of a new approach to upward continue potential field data, the Volume Upward Continuation (VUC), coupled with traditional horizontal derivative techniques. By using VUC it is immediate showing that upward continuation of the signal to higher altitudes yield information about progressively deeper sectors of the discontinuity. In particular, looking at the position of the maxima of the horizontal derivative of the continued field, we can observe that they will be laterally shifted toward the dipping direction of the discontinuity, in a way proportional to the continuation height.

We applied VUC followed by horizontal derivative to a gravity profile extracted from a gravity survey on the Venelin-Aksakov fault in Bulgaria, in order to get further information on the dipping direction of this structure.

Upward continuation and horizontal derivatives. Upward continuation operator uses measurements of a field at one elevation, level or surface to determine the values of the field at a higher level.

Upward continued data can be calculated by convolution in either the space domain or the Fourier domain. In this last domain the Fourier transform of the data is simply multiplied by the frequency filter:

$$e^{-|\mathbf{k}|\Delta z} \qquad \Delta z > 0 \qquad (1)$$

where **k** is the wavenumber vector and Δz is the distance between the original surface and the final one. Real data are discrete and refer to a finite survey area; so, when using circular convolution to calculate upward continuation in the frequency domain, aliasing errors can affect the low frequency content of upward continued data. These errors can be reduced by performing the Fourier transform on a larger dataset, which spreads outside the survey area (Oppenheim and Schafer, 1975; Fedi *et al*., 2012), built with other surveys data or, through extrapolation algorithms (zero-padding, maximum entropy extension, symmetric extension).

Upward continuation is mostly helpful to enhance the effects of deep sources, as it attenuates the highest frequency content of the signal, which is usually associated to shallow sources; or to trace the dipping direction of oblique discontinuities (e.g. faults) (Rapolla *et al*., 2002; Cella *et al*., 2000; Tatchum *et al*., 2011).

The horizontal derivative method (Cordell and Grauch, 1985) represents one of the most used derivative approaches of potential fields, as it allows locating the horizontal position of the density or magnetization boundaries (Paul and Goodacre, 1984; McGrath, 1991; Rapolla *et al*., 2002; Cella *et al*., 2010; Stavred and Reid, 2010; Tatchum *et al*., 2011).

The expression for the horizontal derivative of a potential field M, in the space domain (x,y) is

$$h(x,y) = \sqrt{\left(\frac{\partial M}{\partial x}\right)^2 + \left(\frac{\partial M}{\partial y}\right)^2} \qquad (2)$$

The horizontal derivative has its maxima in correspondence of the lateral boundaries of the source anomaly. This supplementary information cannot be, of course, straightaway

recognized from the original signal and can be really helpful to constrain geological models and guide the geological interpretation.

However, as suggested by Grauch and Cordell (1987) and Rapolla *et al.* (2002), the maxima of the horizontal gradient magnitude can be offset from a position directly above the geologic contacts, especially when contacts are not steep or when several contacts are close together; so this link between maximum points and edges position is consistent only in the case of vertical or sub-vertical discontinuities. For example Khattach *et al.* (2004) associated the horizontal gradient magnitude of the Bouguer gravity anomaly to the upward continuation of the field to characterize the faults of the Triffa basin in North Morocco.

However, in the presence of oblique surfaces, the maxima of the horizontal derivative are located in correspondence with the discontinuity at an intermediate depth (Grauch and Cordell, 1987), without any information about the dipping direction.

Therefore, the efficacy of this simple method is good in the case of structural features typical of an extensional regime (normal faults, transform faults) or in the presence of dykes, volcanic conduits, plutonites, etc. On the contrary, the method is hardly usable when the structural setting is characterised by a compressive tectonic style (presence of inverse faults, transpressive faults, multiple thrust systems, etc.).

To overcome this issue many authors (i.e. Cella *et al*., 2000; Martelet *et al*; 2001; Rapolla *et al*., 2002; Tatchum *et al*., 2011; Fedi and Pilkington, 2012) propose to couple upward continuation with gradient: first upward continuing the data and then computing its horizontal derivative to see how its maxima shift with respect to the subsurface structure. In fact, the position of the maxima of the horizontal derivative of the continued field will be laterally shifted toward the dipping direction of the discontinuity, proportionally to the continuation level.

The DEXP method adds a third step to this procedure consisting in multiply the derived field with a scaling function (Fedi, 2007; Fedi and Pilkington, 2012).

The maxima of the horizontal derivative of the field continued at different levels can also be localized automatically (see for example Blakely and Simpson, 1986) to speed up the data analysis.

In this work we propose to follow this procedure, but taking in account the VUC method for upward continuation. One of the first advantages of using VUC instead of standard upward continuation algorithms is that edge effects are automatically encountered as long as the final result is built. Another important advantage occurs especially in the gravity case, where the VUC has an intrinsic connection also with the vertical derivative of the field. These two topics will be better clarified in the paragraph on VUC method.

Volume Upward Continuation. We propose a new approach to upward continue potential field data, based on the *minimum-length* solution of the inverse potential field problem. The method yields a volume upward continuation, and reveals to be advantageous over the classical techniques based on the Fast Fourier transform (Cordell, 1985; Pilkington and Roest, 1992; Blakely, 1996; Fedi *et al*., 1999; and Ridsdill-Smith, 2000) especially when dealing with truncated anomalies and when draped-to-level upward continuation is needed.

This approach has the advantage of generating the field in the upward continuation domain (i.e., at many altitudes) as a unique solution in a 3D volume. Within this volume, all the three types of continuation (level-to-level, level-to-draped and draped-to-level) are naturally defined. In fact, the upward continued data volume can be immediately visualized and used to obtain the field on several surfaces of whatever kind (draped or level).

Due to this feature we will call this method Volume Upward Continuation (VUC). In the VUC the border effects, typical of upward continuation, are controlled in an optimal way: the upward continued data are in fact proportional to a least-square solution of the inverse problem.

Starting from the continuous inverse geomagnetic problem (e.g., Fedi *et al*., 2005) discretized over a volume Ω of N cells, each of them with constant magnetization m_j, we can write a linear system of equations:

$$\mathbf{Km}=\mathbf{d} \qquad (3)$$

where **K** is the kernel coefficients matrix and **d** is the measured data vector. This inverse problem is under-determined, as the unknowns are more than data, so it has infinite solutions. The simplest solution is that minimizing the Euclidean norm of the solution **m**:

$$\mathbf{m} = \mathbf{K}^T(\mathbf{K}\mathbf{K}^T)^{-1}\mathbf{d} \qquad (4)$$

Cribb (1976) showed, for this solution, this remarkable equation in the frequency domain:

$$e^{-|\mathbf{k}|h_i}F[\mathbf{d}] = F[\mathbf{m}_i]\frac{V(\mathbf{k})}{4} \qquad i=1, \ldots, L \quad (5)$$

where F denotes the Fourier transformation, L is the number of layers, $\mathbf{m}_i$ is the magnetization intensity vector of the i^{th} layer, $\mathbf{h}_i$ is its depth, $\mathbf{k}$ is the wavevector with components k_x, k_y and $(k_x^2+k_y^2)^{1/2}$, $V(\mathbf{k})=(\mathbf{t}.\mathbf{k})(\mathbf{n}.\mathbf{k})/|\mathbf{k}|^2$, with **t** and **n** unit-vectors along the inducing field and magnetization vectors. Therefore the i^{th} layer of the magnetization distribution $\mathbf{m}_i$ is directly related to the upward continued field of the data **d**, to a distance equal to the opposite of the layer depth: $z=-h_i$. Anti-transforming the second member of Eq. (5) and assuming, for simplicity, magnetization and inducing field both vertical, we find:

$$\frac{\mathbf{m}_{z_i}}{4} = \mathbf{d}_{h_i} \qquad i=1,\ldots,L \qquad (6)$$

showing that $\mathbf{d}_{h_i}$ and $\mathbf{m}_{z_i}$ differ only for a numeric constant.

Based on Eqs. (5) and (6) we therefore may use the *minimum length* solution as an effective alternative to common upward continuation techniques.

In Fig. 1 we tested the VUC approach in two simple cases: level-to-level and level-to-draped upward continuation of the magnetic anomaly due to a horizontal dipole line located at 30 m depth. We observe that the field obtained from the *minimum-length* solution well reproduces the computed anomaly at the same altitude.

The result has been achieved following these steps:

- inverting the magnetic anomaly to obtain the *minimum-length* solution;
- converting the magnetization volume to an upward continued field volume through Eq. (6);
- extracting the i^{th} layer corresponding to the desired continuation altitude $z=-h_i$ (level-to-level);
- or extracting the field corresponding to the desired draped surface (level-to-draped).

The most valuable advantage of the VUC method occurs when the field data are on a draped surface (e.g., a topographic surface) and are continued to a constant level. Some synthetic tests (Mastellone *et al.*, 2013) shows that the VUC result, compared with that produced by using other continuation algorithms, can better avoid topographic effects in the continued data.

VUC is helpful also if the profile is severely truncated, and extrapolation is needed before performing upward continuation. In this case, one could obtain very different results, from several extrapolation algorithms. In this case VUC helps to circumvent the border effects by extending the source-volume with additional blocks at its borders. The border effects are better controlled, because of the constraint, inherent in the inversion process, that the predicted data must fit the measured data..

VUC in the gravity case: the role of the vertical derivative. In the gravity case the anomalous density distribution coming from a *minimum-length* inversion is proportional to the upward continuation of the vertical derivative of the observed data:

$$F[\mathbf{d}] = \frac{\mathbf{k}e^{-|\mathbf{k}|h_i}}{\pi G}F[\mathbf{m}_i] \qquad i=1, \ldots, L \quad (7)$$

where G is the gravitational constant, F denotes the Fourier transformation, L is the number of layers, $\mathbf{m}_i$ is the density vector of the i^{th} layer, $\mathbf{h}_i$ is its depth, $\mathbf{k}$ is the wavevector with components k_x, k_y and $(k_x^2+k_y^2)^{1/2}$. Therefore the i^{th} layer of the density distribution $\mathbf{m}_i$ is directly

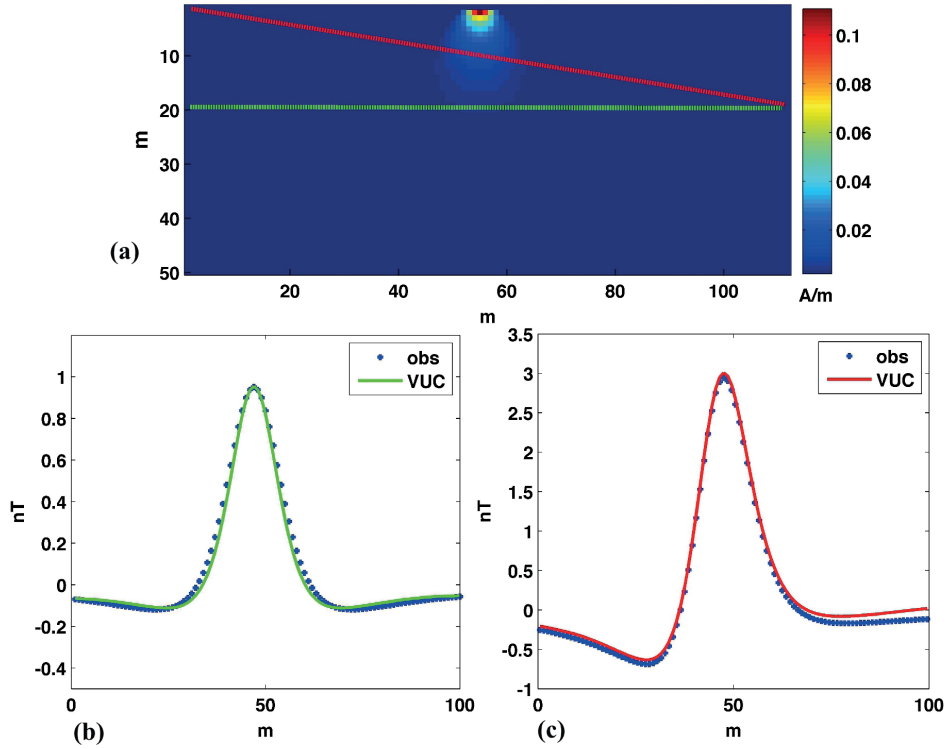

Figure 1 - VUC continuation workflow: synthetic test on a magnetic anomaly due to a horizontal dipole line located at 30 m depth. **a**) *minimum-length* solution section; **b**) *level-to-level* VUC profile (green line) converted, in agreement with equation **(6)**, from the *minimum-length* solution (green line at z= -20 m in (**a**)); **c**) *level-to-draped* VUC profile (red line) converted from the *minimum-length* solution (inclined red line in (**a**) rising from 0 to 20 m). We note a good agreement of VUC field with the true data (blue lines in (**b**) and (**c**)).

related to the upward continued field of the vertical derivative of the data **d**, to a distance equal to the opposite of the layer depth: $z=-h_i$.

So the resulting signal is a combination of a vertical derivative filter, which amplifies the high-frequency components of the data, and an upward continuation, which is, on the contrary, a low pass filter for definition.

This feature is interesting and has been investigated by many authors who tested the coupling of upward continuation and field derivatives.

The benefits of using the vertical derivative were documented by Fedi and Florio (2001): they showed that when the gravity fields of several sources interfere, it is more accurate to use the vertical derivative of the field rather than the field itself to determine the location of contacts of the sources. This is in part due to the vertical derivative being able to isolate the gravity effects of individual sources better than the Bouguer anomaly. Hence, the signatures of small-scale features that are not easily identified in Bouguer anomaly maps can be identified and mapped using the vertical derivative response.

So from the horizontal derivative magnitude of the VUC response, it is possible to outline and differentiate vertical and dipping geological contacts as well as the direction of the dip; and also to separate multiple anomalies.

The higher frequencies will be enhanced at the expense of lower frequencies; however, if the data contain noise or small errors, the coupled filter already inbuilt in Cribb's relationship

[Eq. (7)] for gravity fields, by first suppressing the highest frequencies, (upward continuation), can help to remove that noise.

Case history: the Venelin-Aksakov fault (Bulgaria). The VUC method combined with horizontal derivative was applied to an anomalous gravity profile (Stavrev and Reid, 2010) in the area of the Dolna Kamchia depression (Bulgaria), across the Venelin-Aksakov fault, at the western bound of the depression.

The Dolna (lower) Kamchia depression lies in Eastern Bulgaria along the lower course of the Kamchia river. This depression is elongated west to east and runs into the adjoining Black Sea shelf, according also to geophysical data. It belongs geologically to the most northeastern part of the Balkan orogenic system. The Venelin-Aksakov fault is the western bound of the depression.

An intense gravity gradient zone (see Figs. 5 and 6 in Stevrev and Reid, 2010) indicates a steep contact structure with north-to-south orientation. Exploratory wells west and east of the line of the gravity gradient zone indicate a considerable difference in the depth to the boundary between the low-density tertiary-upper Cretaceous layers and the denser lower Cretaceous and deeper sediment layers, the depth to high-density strata increases by a factor of 10, going from the western elevated horst structure to the eastern depression.

Core samples from wells in the Dolna Kamchia depression show also a significant difference in the density of tertiary-upper Cretaceous layers and lower Cretaceous-Jurassic-Triassic layers.

The analysed Bouguer gravity profile was extracted across the gradient axis of the gravity anomaly map shown in Fig. 2a and the geologic data available for the area strongly suggest that this is a contact of considerable depth extent.

We performed VUC on the anomaly gravity profile in Fig. 2b obtaining the vertical section showed in Fig. 2c. Then we calculated the horizontal derivative of the VUC result, following Eq. (2), and we extracted from the section profiles corresponding to increasing continuation heights (see Fig. 2d and the related key table).

For a vertical contact, the derivative maximum values, related to different continuation heights, are along the same vertical line, whereas for dipping contacts, the maxima gradually move in the direction of dip.

Furthermore the absolute values of the horizontal derivative maxima decrease as the height continuation height increases, as one could obviously expect. In fact the resulting signal is related to progressively deeper sectors of the discontinuity, if increasing continuation heights are analysed.

In the case shown in Fig. 2c the position of the maxima slightly shifts in the direction of dipping, but the shape of the derivative function is skewed in the direction of dipping. This is in agreement with other geophysical and geological data, suggesting a steep and abrupt contact between tertiary-upper Cretaceous layers and lower Cretaceous-Jurassic-Triassic layers.

Conclusions. In this paper we introduce a new tool, the VUC (Volume Upward Continuation), for the well-known procedure of combining upward continuation and vertical and horizontal derivatives of potential field data.

The VUC by itself yields good results especially in case of draped-to-level upward continuation and when dealing with the continuation of severely truncated anomalies. One advantage of the VUC tool is that it yields a volume upward continuation, and thus it may be used to extract in a simple way the continuation on any kind of surface and also to multiple levels. We may in fact define all the three kinds of continuation problems (*level-to-level, level-to-draped and draped-to-level*) by simply picking up the sought surface on the inverted 3D magnetization model and then transforming the corresponding magnetization data into upward continued data, through Eqs. (5) and (6). So it can be usefully placed side by side to common upward continuation techniques.

In the gravity case, moreover, the VUC absorbs also the vertical derivative in its result, fulfilling a remarkable feature, already examined by many authors who tested its efficiency if

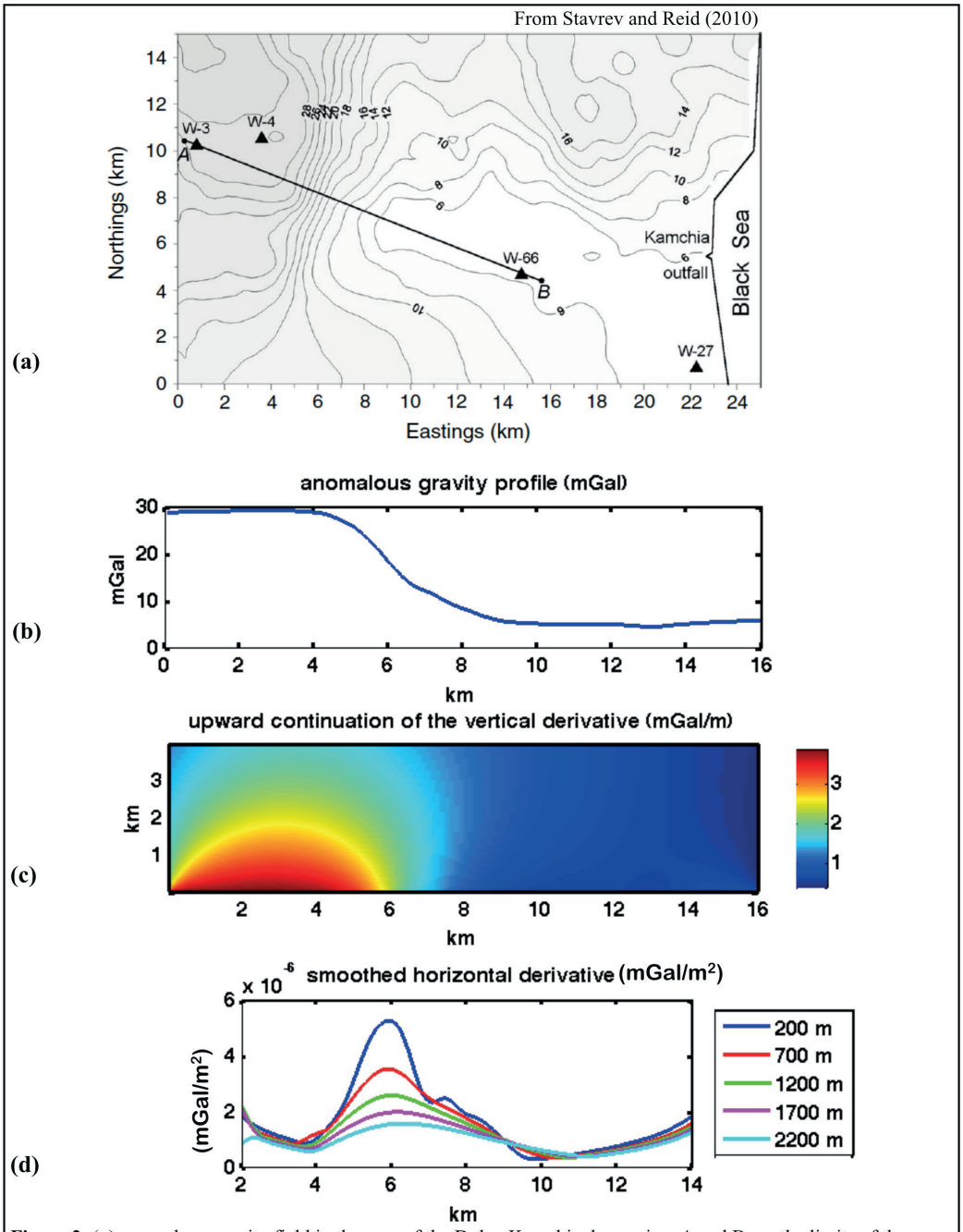

Figure 2: (**a**) anomalous gravity field in the area of the Dolna Kamchia depression, A and B are the limits of the gravity profile across the Venelin-Aksakov fault shown in (**b**); (**c**) VUC of the first vertical derivative of the gravity profile in (**b**); (**d**) horizontal gradient of the VUC for different continuation heights listed in the box at the right side).

combined with horizontal derivatives also (Fedi and Florio, 2001; Florio *et al.*, 2006; Tatchum *et al.*, 2011). The VUC, when applied to a real field data example from the Venelin-Aksakov fault in Bulgaria, to locate fault edge and dipping direction, provides results in agreement with geological and geophysical studies already performed in the same area.

References

Blakely R.J., 1996: *Potential theory in gravity and magnetic applications*. Cambridge University Press.

Blakely R.J. and Simpson R.W., 1986: *Approximating edges of source bodies from magnetic or gravity anomalies*. Geophysics, **51** (7), 1494-1498.

Cella F., Fedi M., Florio G. and Rapolla A., 2000: *Boundary analysis del campo 3D di anomalie gravimetriche*. XIX Convegno del Gruppo Nazionale di Geofisica della Terra Solida – Riassunti delle Comunicazioni, Novembre 2000, CNR, p. 131.

Cordell L., 1985, *Techniques, applications and problems of analytical continuation of New Mexico aeromagnetic data between arbitrary surfaces of very high relief*. International Meeting on Potential Fields in Rugged Topography, **7**, 96–99.

Cordell L. and Grauch V.J.S., 1985: *Mapping basement magnetization zones from aeromagnetic data in the San Juan basin, New Mexico*. Hinze, W.J., (Ed.), The utility of regional gravity and magnetic anomaly Maps: Society of Exploration Geophysicists, 181–197.

Cribb J. B., 1976: *Application of the generalized linear inverse to the inversion of static potential data*. Geophysics, **41**, no. 6, 1365-1369.

Fedi M., Rapolla A., and Russo G., 1999: *Upward continuation of scattered potential field data*. Geophysics, **64**, no. 2, 443-451, doi: 10.1190/1.1444549.

Fedi M. and Florio G., 2001: *Detection of potential fields source boundaries by enhanced horizontal derivative method*. Geophysical Prospecting, **49**, 40–58.

Fedi M., Hansen P. C., and Paoletti V., 2005: *Analysis of depth resolution in potential-field inversion*. Geophysics, **70**, no. 6; P. A1–A11; doi: 10.1190/1.2122408

Fedi M. and Pilkington M., 2012: *Understanding imaging methods for potential field data*. Geophysics, **77**, 1, G13-G24

Fedi, M., 2007: *DEXP: a fast method to determine the depth and the structural index of potential fields sources*. GEOPHYSICS, **72**, I1.

Fedi, M., Florio G. and Cascone L., 2012: *Multiscale analysis of potential fields by a ridge consistency criterion: the reconstruction of the Bishop basement*. Geophysical Journal International, **188**, 103-114.

Florio G., Fedi M. and Pasteka R., 2006: *On the application of Euler deconvolution to the analytic signal*. Geophysics, **71**, L87–L93.

Grauch V.J.S. and Cordell L., 1987: *Limitations of determining density or magnetic boundaries from the horizontal gradient of gravity or pseudogravity data*. Geophysics, **52**, 118–121.

Khattach D., Keating P., Mostafa M.L., Chennouf T., Andrieux P. and Milhi A., 2004: *Apport de la gravimétrie à l'étude de la structure du bassin des Triffa (Maroc nord-oriental): implications hydrogéologiques*. C. R. Geosciences **336**, 1427–1432.

Martelet G., Sailhac P., Moreau F. and Diament M., 2001: *Characterization of geological boundaries using 1-D wavelet transform on gravity data: Theory and application to the Himalayas*. Geophysics, **66**(4), 1116.

Mastellone D., Fedi M., Ialongo S. and Paoletti V., 2013: *Volume upward continuation of potential fields from the minimum-length solution: An optimal tool for continuation through general surfaces*. SEG Technical Program Expanded Abstracts 2013: pp. 1200-1205. doi: 10.1190/segam2013-0593.1

McGrath P.H., 1991: *Dip and depth extent of density boundaries using horizontal derivatives of upward continued gravity data*. Geophysics, **56** (10), 1533-1541

Oppenheim A. V. and Schafer R. W., 1975: *Digital Signal processing*: Prentice-Hall.

Paul M.K. and Goodacre A.K., 1984: *The gravity profile and its role in positioning the edge of a two-dimensional faulted structure having an arbitrary vertical variation of density*. Geophysics, **49**, 1097-1104.

Pilkington M., and Roest W., 1992: *Draping aeromagnetic data in areas of rugged topography*. Journal of Applied Geophysics, **29**, no. 2, 135–142.

Rapolla A., Cella F., Fedi M. and Florio G., 2002: *Improved techniques in data analysis and interpretation of potential fields: examples of application in volcanic and seismically active areas*. Annals of geophysics, **45**, 6; and references therein.

Ridsdill-Smith T. A., 2000: *The Application of the Wavelet Transform to the Processing of Aeromagnetic Data*. PhD thesis, University of Western Australia.

Stavrev P. and Reid A., 2010: *Euler deconvolution of gravity anomalies from thick contact/fault structures with extended negative structural index*. Geophysics, **75**, 6; p. i51–i58, 6 figs., 2 tables.

Tatchum, C. N., Tabod T. C., Koumetio F. and Manguelle-Dicoum E., 2011: *A gravity model study for differentiating vertical and dipping geological contacts*. Geophysica, **47** (1-2), 43-55.

MISURE CURLOMETRICHE NEI FONDALI MARINI

P. Palangio[1], C. Carmisciano[2], C. Di Lorenzo[1], M. Pietrolungo[1]

[1] Ist. Naz. di Geofisica e Vulcanologia, Sezione Roma II - UF Osservatorio Geofisico di L'Aquila

[2] Ist. Naz. di Geofisica e Vulcanologia, Sezione Roma II - UP Geofisica e Tecnologie Marine - Portovenere (La Spezia)

Premessa. Nei fondali marini in cui sono presenti discontinuità nelle proprietà fisico-chimiche quali ad esempio giacimenti minerari o di combustibili naturali (Christensen e Rajagopalan, 2000) oppure discontinuità tettoniche si possono generare correnti elettriche che si chiudono in parte attraverso l'acqua del mare elettricamente molto conduttiva e in parte nel sottosuolo marino. Inoltre sono presenti anche correnti elettriche indotte dalle variazioni del campo magnetico e correnti generate per effetto MHD dal moto dell'acqua. In generale il campo magnetico misurato al di fuori del sistema di correnti che lo generano gode di due fondamentali proprietà: è indivergente e irrotazionale (Schmidt e Clark, 2000). All'interno delle sorgenti il rotore del campo magnetico è legato alle correnti e quindi al campo elettrico, mentre la divergenza è legata alla presenza di pozzi o sorgenti di corrente o a gradienti non lineari del campo magnetico. In questo lavoro si propone il rilevamento del campo magnetico e delle correnti nei fondali marini mediante misure dirette della divergenza e del rotore del campo magnetico locale.

Introduzione. La gradiometria tensoriale vettoriale consente di misurare direttamente la divergenza e il rotore del campo magnetico, la conoscenza di questi due operatori consente la rappresentazione integrale del campo elettromagnetico nel dominio spaziale mediante l'applicazione del teorema di Stokes e del teorema di Gauss. Questo tipo di rappresentazione ricade nell'ambito del metodo degli elementi al contorno (Boundary Element Method). Questo approccio riduce la determinazione delle grandezze elettromagnetiche in un dato dominio tridimensionale o bidimensionale a quelle delle medesime sulla frontiera bidimensionale o monodimensionale del dominio stesso e si presta all'analisi di strutture composte da più regioni omogenee occupate da materiali conduttori con diverse caratteristiche.

Le incognite delle equazioni integrali al contorno sono le correnti equivalenti elettriche e magnetiche definite sulle superfici di interfaccia fra mezzi diversi. Tali correnti sono legate alle componenti tangenziali e normali dei campi magnetici ed elettrici sulle superfici di discontinuità. Le misure curlometriche consentono di determinare le correnti equivalenti elettriche e magnetiche mediante l'analisi del tensore gradiometrico.

Fig. 1 – Gradiometro tensoriale a 12 componenti costituito da 4 terne magnetometriche triassiali.

Poichè l'oggetto di queste indagini è la misura di campi magnetici a divergenza e a rotore non nulli, le misure curlometriche implicano che le variazioni spaziali del campo magnetico debbano essere non lineari all'interno del volume occupato dallo strumento di misura. La presenza di gradienti non lineari si riflette sulla somma degli elementi della diagonale principale del tensore gradiometrico ovvero sulla divergenza del vettore B e sugli elementi non diagonali del tensore T ovvero sul rotore di B.

Gradiometro tersoriale. Lo strumento è costituito da 4 terne triassiali di sensori magnetici di tipo flux-gate, assemblati in una piramide equilatera triangolare (Fig. 1), i sensori sono quattro a quattro paralleli tra di loro. Questa configurazione di sensori consente di misurare direttamente i nove elementi del tensore gradiometrico. Ciascuna terna misura le 3 componenti del campo magnetico con una dinamica di +/- 100 μT e una banda passante che si estende dal continuo fino a 1 Hz. La sensibilità massima del gradiometro è di 4 pT/m.

Il sensore magnetico è costituito da 6 bobine quadrate e 6 bobine toroidali. Le prime 6 bobine sono avvolte sulla superficie di un cubo di vetroresina e formano 3 bobine di Helmholtz quadrate ortogonali tra di loro. Queste bobine servono sia per raccogliere il segnale sia per creare un campo esattamente uguale e opposto a quello da misurare. Le 6 bobine toroidali sono avvolte intorno a 6 anelli di metglass 2914 con elevata permeabilità magnetica, servono per eccitare i nuclei ferromagnetici.

La simmetria cubica del sensore (Fig. 2) consente di eliminare soprattutto l'effetto dei campi trasversali sui nuclei ferromagnetici perchè il campo prodotto dalle 3 bobine di Helmholtz è tale da annullare quasi del tutto il campo magnetico esterno nello spazio occupato dai 6 anelli, pertanto i 6 nuclei si trovano costantemente in campo nullo, ciò che si misura è la corrente necessaria per mantenere il campo interno approssimativamente intorno allo zero[4].

I sensori sono assemblati ai vertici di una piramide equilatera triangolare (Fig. 1). Nella Fig. 3 è illustrata la struttura che verrà depositata sul fondo del mare, è costituita da 4 sfere di titanio in cui sono alloggiate le terne magnetometriche, il sistema di condizionamento dei segnali analogici, il convertitore AD a 24 bit e il sistema di gestione dei dati digitali che verranno trasmessi in superficie. Le misure effettuate nel

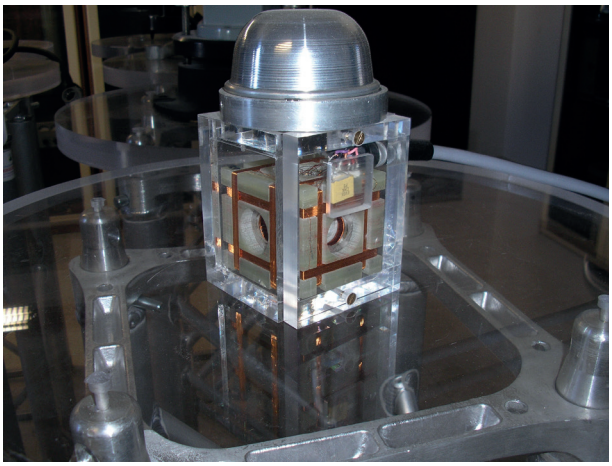

Fig. 2 – Sensore magnetico triassiale impiegato nel gradiometro tensoriale.

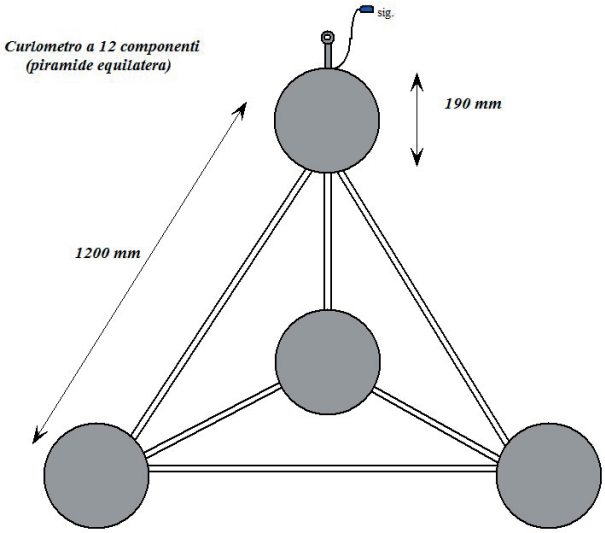

Fig. 3 – Struttura sottomarina del curlometro tensoriale realizzata in titanio.

sistema di riferimento piramidale vengono traslate in un sistema di riferimento cartesiano ortogonale, mediante una matrice di trasformazione.

Le misure traslate nel riferimento ortogonale generano il tensore gradiometrico completo:

$$\boldsymbol{T} = \begin{pmatrix} \frac{\partial \boldsymbol{B}_x}{\partial \boldsymbol{x}} & \frac{\partial \boldsymbol{B}_x}{\partial \boldsymbol{y}} & \frac{\partial \boldsymbol{B}_x}{\partial \boldsymbol{z}} \\ \frac{\partial \boldsymbol{B}_y}{\partial \boldsymbol{x}} & \frac{\partial \boldsymbol{B}_y}{\partial \boldsymbol{y}} & \frac{\partial \boldsymbol{B}_y}{\partial \boldsymbol{z}} \\ \frac{\partial \boldsymbol{B}_z}{\partial \boldsymbol{x}} & \frac{\partial \boldsymbol{B}_z}{\partial \boldsymbol{y}} & \frac{\partial \boldsymbol{B}_z}{\partial \boldsymbol{z}} \end{pmatrix} \quad (1)$$

Dove $\frac{\partial \boldsymbol{B}_i}{\partial \boldsymbol{k}} = \boldsymbol{T}_{ik}$. Il sistema genera un tensore ogni secondo. Poichè le misure vengono effettuate all'interno delle sorgenti del campo magnetico, questo tensore non è hermitiano, pertanto gli autovalori possono essere anche complessi (Schmidt e Clark, 2000).

Teoria. La divergenza di B è legata agli elementi diagonali del tensore T:

$$\nabla \cdot \boldsymbol{B} = \frac{\partial \boldsymbol{B}_x}{\partial \boldsymbol{x}} + \frac{\partial \boldsymbol{B}_y}{\partial \boldsymbol{y}} + \frac{\partial \boldsymbol{B}_z}{\partial \boldsymbol{z}} = \boldsymbol{T}_{xx} + \boldsymbol{T}_{yy} + \boldsymbol{T}_{zz} \quad (2)$$

Nella forma integrale la divergenza è legata al flusso del campo magnetico attraverso la superficie S che delimita il volume V del sensore gradiometrico:

$$\iiint_V (\boldsymbol{T}_{xx} d\boldsymbol{x}) d\boldsymbol{y} d\boldsymbol{z} + (\boldsymbol{T}_{yy} d\boldsymbol{y}) d\boldsymbol{x} d\boldsymbol{z} + (\boldsymbol{T}_{zz} d\boldsymbol{z}) d\boldsymbol{x} d\boldsymbol{y} = \boldsymbol{\Phi}_{yz} + \boldsymbol{\Phi}_{xz} + \boldsymbol{\Phi}_{xy} \quad (3)$$

Possiamo calcolare le tre componenti del flusso del campo magnetico attraverso i 3 piani che delimitano il volume del sensore, direttamente tramite gli elementi diagonali del tensore T. T_{xx} è legato al flusso del campo attraverso il piano ortogonale yz, T_{yy} è legato al flusso nel piano xz e T_{zz} è legato al flusso nel piano xy. In generale la divergenza del campo magnetico è sempre nulla al di fuori delle sorgenti del campo magnetico misurato (Heath *et al*., 2003). In un contesto conduttivo in cui le correnti possono fluire nello spazio che delimita i sensori del gradiometro la divergenza di B può essere diversa da zero. Ad esempio la presenza di sorgenti geotermiche o in ogni caso la presenza di gradienti termici genera gradienti non lineari della conducibilità elettrica del mezzo. In generale se il legame tra la densità di corrente e il campo elettrico coinvolge un tensore di rango 2, la divergenza del campo magnetico prodotto dalle correnti è proporzionale ai gradienti della conducibilità elettrica del mezzo conduttore oppure alla presenza di strutture assimilabili a pozzi o sorgenti di J. Il rotore di B è legato ai gradienti trasversali del campo magnetico B:

$$\nabla \times \boldsymbol{B} = (\boldsymbol{T}_{xy} - \boldsymbol{T}_{yz}) \boldsymbol{i}_x + (\boldsymbol{T}_{xz} - \boldsymbol{T}_{zx}) \boldsymbol{i}_y + (\boldsymbol{T}_{yx} - \boldsymbol{T}_{xy}) \boldsymbol{i}_z \quad (4)$$

Nella forma integrale il rotore è legato alla circuitazione del campo integrando sul perimetro dei 3 piani xy, xz e yz:

$$\begin{aligned} &\oiint \left(\frac{\partial \boldsymbol{B}_z}{\partial \boldsymbol{y}} - \frac{\partial \boldsymbol{B}_y}{\partial \boldsymbol{z}} \right) + \left(\frac{\partial \boldsymbol{B}_x}{\partial \boldsymbol{z}} - \frac{\partial \boldsymbol{B}_z}{\partial \boldsymbol{x}} \right) + \left(\frac{\partial \boldsymbol{B}_y}{\partial \boldsymbol{x}} - \frac{\partial \boldsymbol{B}_x}{\partial \boldsymbol{y}} \right) d\boldsymbol{x} d\boldsymbol{y} d\boldsymbol{z} = \\ &\oint (\boldsymbol{T}_{xz} d\boldsymbol{z} + \boldsymbol{T}_{xy} d\boldsymbol{y}) d\boldsymbol{x} + (\boldsymbol{T}_{yx} d\boldsymbol{x} + \boldsymbol{T}_{yz} d\boldsymbol{z}) d\boldsymbol{y} + (\boldsymbol{T}_{zy} d\boldsymbol{y} + \boldsymbol{T}_{zx} d\boldsymbol{x}) d\boldsymbol{z} \end{aligned} \quad (5)$$

Il vettore B può essere rappresentato mediante la somma di due vettori indipendenti, un campo vettoriale conservativo e un campo vettoriale solenoidale:

$$\boldsymbol{B}_{tot} = \boldsymbol{B}_c + \boldsymbol{B}_s \quad (6)$$

che soddisfano le seguenti condizioni:

$$\nabla \times \boldsymbol{B}_c = 0, \nabla \cdot \boldsymbol{B}_s = 0, \nabla \times \boldsymbol{B}_s \neq 0, \nabla \cdot \boldsymbol{B}_c \neq 0 \quad (7)$$

La componente conservativa di B_c è legata alle sorgenti di tipo dipolare (Frahm, 1972) che generano gradienti trasversali che soddisfano le seguenti condizioni $(\nabla \times \boldsymbol{B}_c = 0)$:

$$\begin{aligned}\left(T_{yz}-T_{zy}\right)&=0\\ \left(T_{xz}-T_{zx}\right)&=0\\ \left(T_{xy}-T_{yx}\right)&=0\end{aligned} \qquad (8)$$

mentre la componente solenoidale B_s genera gradienti longitudinali tali che la loro somma è nulla $\left(\nabla \cdot \boldsymbol{B_s}=0\right)$:

$$T_{xx}+T_{yy}+T_{zz}=0 \qquad (9)$$

La componente non conservativa B_s, all'interno delle sorgenti, è legata direttamente alle correnti tramite il rotore del campo magnetico. Possiamo calcolare le componenti della corrente J direttamente mediante gli elementi non diagonali del tensore T associato ai gradienti trasversali del campo magnetico generato dalla corrente J:

$$\begin{aligned}J_x&=\frac{1}{\mu_0}\left(T_{yz}-T_{zy}\right)\\ J_y&=\frac{1}{\mu_0}\left(T_{xz}-T_{zx}\right)\\ J_z&=\frac{1}{\mu_0}\left(T_{xy}-T_{yx}\right)\end{aligned} \qquad (10)$$

Il campo magnetico prodotto dalle correnti volumetriche è:

$$B=\frac{\mu_o}{4\pi}\iiint_V \frac{J\times r}{r^3}dV \qquad (11)$$

dove V è il volume della sfera la cui superficie interseca i 4 sensori gradiometrici.

Il tensore conducibilità σ_{ij} lega le componenti della densità di corrente alle componenti del campo elettrico mediante la relazione:

$$\begin{pmatrix}J_x\\ J_y\\ J_z\end{pmatrix}=\begin{pmatrix}\sigma_{xx} & \sigma_{xy} & \sigma_{xz}\\ \sigma_{yx} & \sigma_{yy} & \sigma_{yz}\\ \sigma_{zx} & \sigma_{zy} & \sigma_{zz}\end{pmatrix}\cdot\begin{pmatrix}E_x\\ E_y\\ E_z\end{pmatrix} \qquad (12)$$

La componente non lineare del gradiente di B è proprio legata al tensore σ_{ij}.

Conclusioni. Il tensore σ_{ij} è legato alla divergenza della componente conservativa di B mentre le componenti di J sono legate al rotore della componente solenoidale di B.

Le tre componenti Jx,Jy e Jz della densità di corrente J che fluisce nei fondali marini sono associate a tutta una serie di sorgenti di varia natura.

Queste sorgenti possono essere legate a fenomeni tellurici o vulcanici oppure alla presenza di giacimenti di combustibili quali gas, petrolio ecc., oppure alla presenza di sorgenti geotermiche. Le misure curlometriche consentono, mediante l'analisi del tensore gradiometrico (Wilson, 1985), di definire il sistema di correnti che fluiscono nell'acqua del fondo marino, consentono di dedurre la dimensionalità della struttura di conducibilità locale e consentono anche di caratterizzare le strutture assimilabili a pozzi o sorgenti di correnti

Riconoscimenti. Questo sistema è stato sviluppato presso i laboratori dell'Osservatorio Geomagnetico di Duronia dell'INGV nell'ambito del progetto FIRB-Abruzzo. Si ringrazia il Sindaco del Comune di Duronia per aver concesso i locali che ospitano i laboratori di Duronia. Mentre la progettazione e la realizzazione del sistema subacqueo verrà effettuata presso la UP Geofisica e Tecnologie Marine - Portovenere (La Spezia)

Bibliografia

C. Christensen, S. Rajagopalan (2000): *The magnetic vector and gradient tensor in mineral and oil exploration,* Preview, **84**, 77.

P. Frahm (1972): *Inversion of the magnetic field gradient equation for a magnetic dipole field,* NCSL Informal Report, 135–72.

P. Heath, G. Heinson, S. Greenhalgh: (2003): *Some comments on potential field tensor data*, Exploration Geophysics, **34**, 57–62.
P. Palangio (1998): *A broad band two axis flux-gate magnetometer*, Annali di Geofisica, Vol. 41, N. 3, August.
P. Schmidt, D.A. Clark (2000): *Advantages of measuring the magnetic gradient tensor*, Preview, **85**, 26–30.
H. Wilson (1985): *Analysis of the magnetic gradient tensor,* Defence Research Establishment Pacific, Canada Technical Memorandum, **85-13**, 47.

ELECTRICAL RESISTIVITY TOMOGRAPHY SURVEYS TO INVESTIGATE THE IVANCHIC LANDSLIDE (ASSISI, UMBRIA REGION, ITALY)

A. Perrone[1], J. Bellanova[1], G. Calamita[1], F. Ardizzone[2], S. Piscitelli[1]
[1] *Istituto di Metodologie per l'Analisi Ambientale – CNR, Tito (PZ), Italy*
[2] *Istituto di Ricerca per la Protezione Idrogeologica – CNR, Perugia, Italy*

Introduction. This paper reports the in-situ geophysical results obtained in the Ivanchic landslide (Assisi, Umbria region), one of the DORIS project test sites (under FP7 grant agreement No. 242212). DORIS (www.doris-project.eu) is an advanced downstream service for the detection, mapping, monitoring, and forecasting of ground deformations (landslides and ground subsidence), which operates in different study areas (Hungary, Italy, Poland, Spain, and Switzerland). The project aims to integrate traditional and innovative Earth Observation (EO) and ground based (non-EO) data and technologies to improve the understanding of the complex deformation phenomena. The Ivanchic landslide, affecting the eastern part of the Assisi town, was investigated by applying satellite and in-situ geophysical methods. Satellite method allowed the definition of the dynamics occurring on the slope (Ardizzone *et al.*, 2011). In-situ geophysical measurements, compared with geological and stratigraphical data from previous direct investigations (Angeli and Pontoni, 1999), provided information on subsoil geometrical setting and landslide body characteristics.

Geological and geomorphological setting. The Assisi town is located along the NW sector of the Monte Subasio, a distinct physiographical feature in central Umbria, and is bounded to

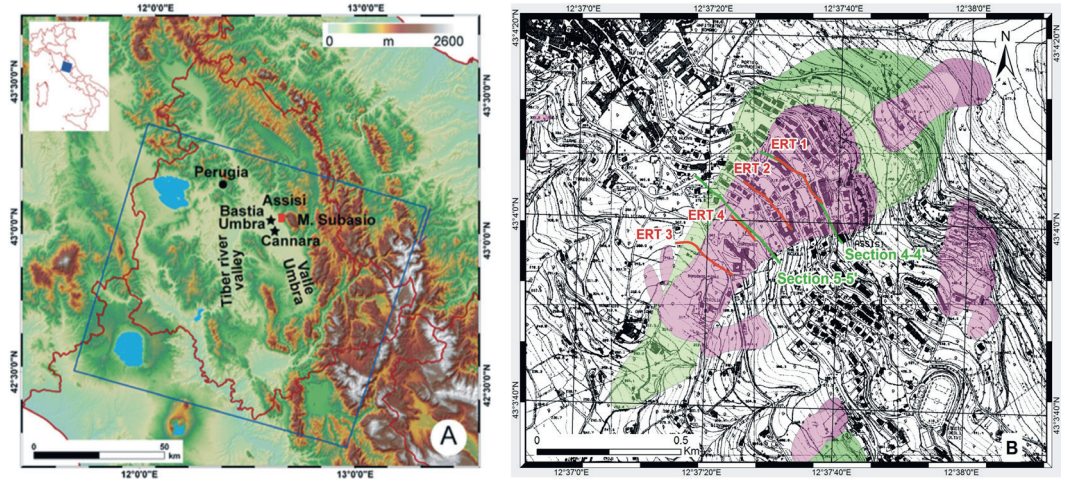

Fig. 1 – A) Map showing terrain in Umbria, Italy. The study area, shown by the red polygon, is located in the Assisi municipality. The blue line shows the area covered by the ERS-1/2 and the ASAR radar images and stars indicate the location of two rain gauges used in a study carried out by Ardizzone *et al.* (2011). B) Map showing landslides in the Ivancich area. Green polygons are old landslides and purple polygons are recent landslides. Landslide crown areas (darker colors) are shown separately from landslide deposits (lighter colors). Red lines are ERT profiles; green lines are geological sections.

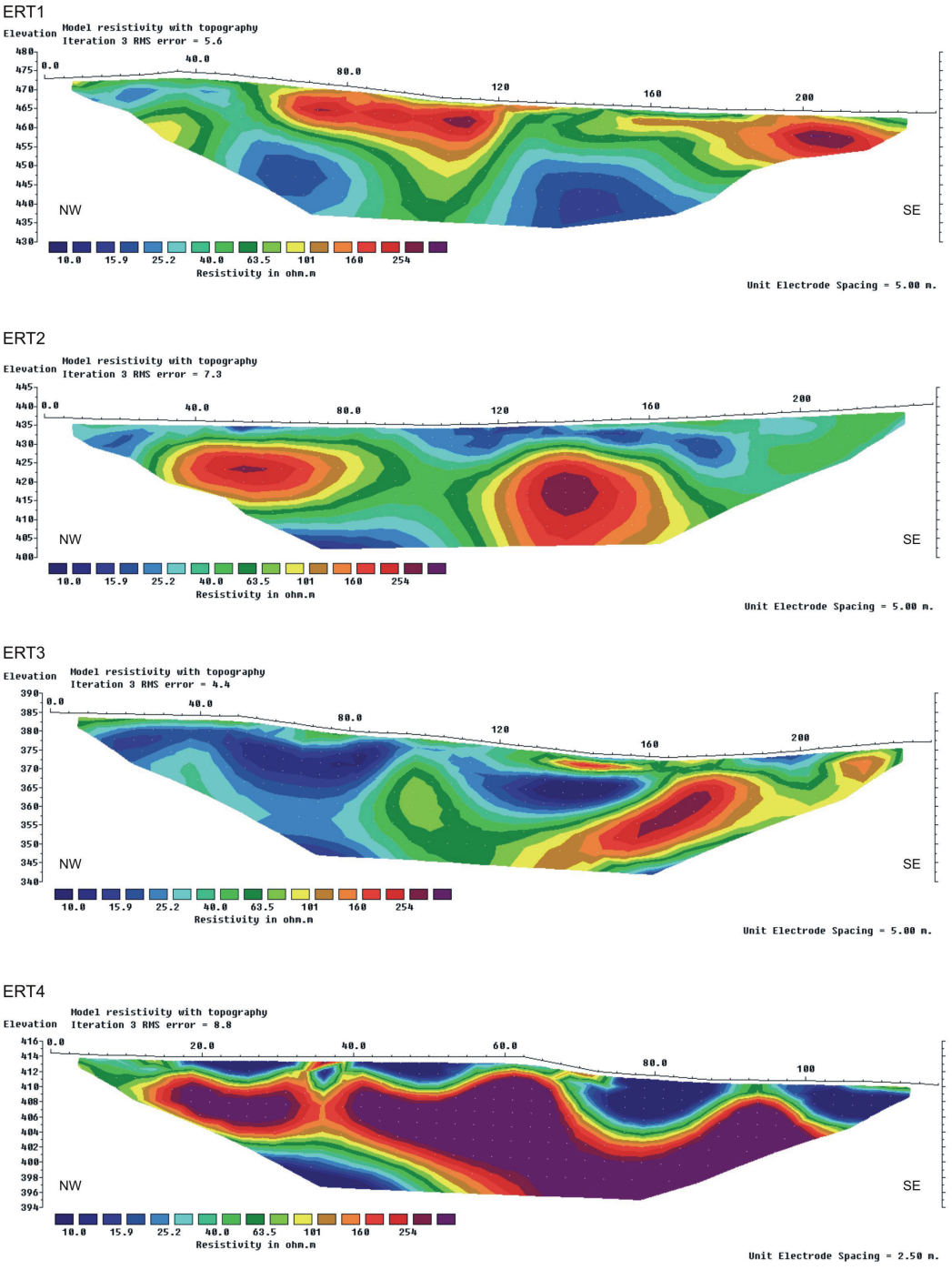

Fig. 2 - Electrical resistivity tomographies carried out on the Ivanchic landslide.

the SW by the Valle Umbra plain (Fig.1a). Sedimentary rocks crop out in the area, where layered and massive limestone, marl and clay pertaining to the Umbria-Marche stratigraphic sequence (Lias-Eocene), are overlaid by lake deposits (lower Pliocene-Quaternary) and by fluvial deposits of Recent age. Ivancich is a neighborhood in the Assisi municipality, located at

SE of the mediaeval part of the town. Built mainly in the period 1960 – 1970, the neighborhood is a residential area of one-to- three-storied private homes, and hosts the Assisi hospital and a Franciscan convent. This area is affected by an active deep-seated landslide (Fig. 1b). Geomorphological, geotechnical and topographical investigations have revealed that the Ivancich landslide is an old (ancient) translational slide involving the debris deposits. The slope debris (Middle-Upper Pleistocene) are usually stratified according to the slope, and consist of limestone fragments with sharp edges. The source rocks of these debris are mainly represented by the "Scaglia rossa" and "Maiolica" limestones. The bedrock, in this area, is characterized by a pelitic-sandstone unit and consists mainly of marl, clayey marl and calcareous marl, interbedded with sandstone layer with thickness from a few centimeters to a few meters. The upper part of this formation, at the contact with the debris, is strongly altered.

Geological and in-situ geophysical survey. Damages caused by the Ivanchic landslide are well visible on the structures and infrastructures located in the area. For many years, the slope has been exposed to geological investigations and monitoring activities planned by the local administration office. In particular, the "Provveditorato Regionale alle opere pubbliche dell'Umbria" (Ministero dei Lavori Pubblici), in charge to carry out activities necessary to stabilize the slope, has ordered the execution of many geognostic soundings (Angeli and Pontoni, 1999), in order to obtain information on the dynamics of the slope, by means of inclinometric probes, and its hydrogeological characteristics, by using piezometers. The inclinometric data, reported in the technical reports provided by the Provveditorato, have confirmed that the landslide is in constant slow movement with an average displacement velocity of 2.5 mm/y at a depth of about 50 m in the upstream zone, 12 mm/y at a depth of about 33 m in the intermediate zone and of 8 mm/y in the downstream zone (close to the Civil Hospital) at a depth of about 24 m. The piezometric levels have denoted that the maximum excursions of about 6-8 m occur in the upstream and downstream areas of the landslide. To increase the information useful to better characterize the slope involved in the movement, in the frame of DORIS project, a geophysical survey has been planned. In particular, four electrical resistivity tomographies (ERT) were carried out along profiles with transversal direction to the landslide body (Fig. 1b). The profiles were located in the high portion of the slope where many buildings are present and the satellite results, obtained by applying the differential interferometric synthetic aperture radar technique (Ardizzone *et al.*, 2011), indicate greater dynamics. The ERT were carried out by using a georesistivimeter Syscal Junior connected to a multielectrode cable with 48 electrodes. For the ERT1, ERT2 and ERT3 an electrode spacing of 5 m was chosen, reaching an investigation depth of about 35-40 m; while for the ERT4 the electrodes were spaced 2.5 m and an investigation depth of about 20 m was reached.

Results and discussion. All the ERT show a heterogeneous distribution of resistivity values varying in a relatively low range ($10 < \rho < 300\ \Omega \cdot m$) (Fig. 2). This is due to both the lithological nature of the outcropping and investigated material (debris) and the weather conditions of the acquisition period (June 2013), characterized by intense rainfall events. The first 25 meters of the ERT1 are characterized by relatively high resistive material. This material, with a lenticular shape and overlying a conductive bedrock, could be associated with reworked and more aerated slide material. The ERT2 shows a shallow layer of conductive material which rests upon a more resistive layer characterized by two well-defined nuclei. The low resistivity values of the first few meters could be due to the rainwater infiltration following the precipitations of previous days. ERT3 is characterized by low resistivity values in the NW portion, whereas by more resistive values in the SE sector. Observing the location of the profile along which ERT3 was carried out in figure 1b, it is possible to verify that the NW part is located outside of the recent landslide body. This could explain the sub-vertical resistivity contrast between the two different portions of the ERT. Indeed, the slide material should be reworked, therefore more aerated, and characterized by relatively high resistivity values respect to the material not involved in the movement. Finally, ERT4 is the shortest and the shallowest of those realized. It is characterized

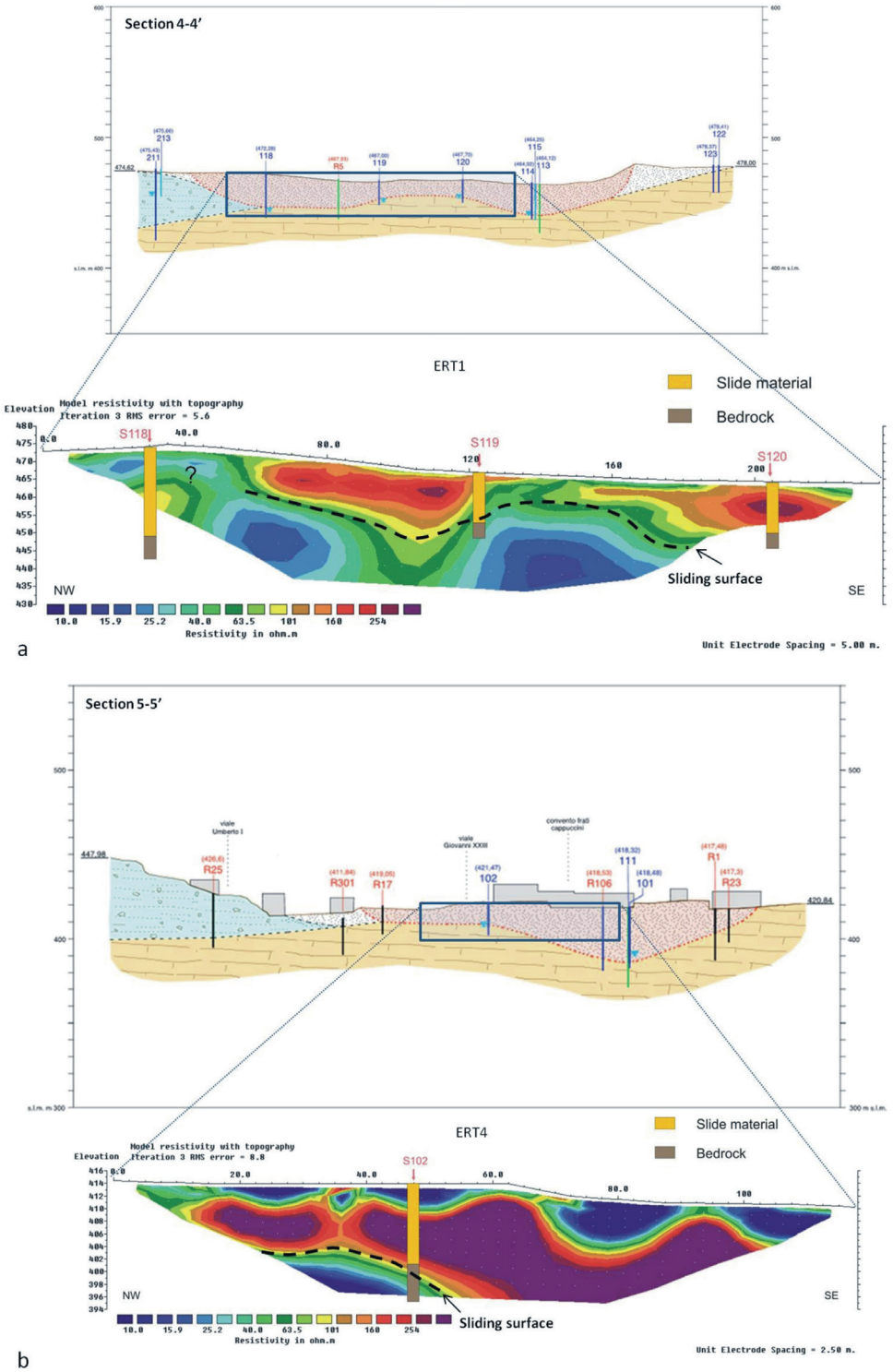

Fig. 3 - a) Comparison between ERT1, geological section 4-4' and stratigraphical data; b) comparison between ERT4, geological section 5-5' and stratigraphical data.

by shallow lenticular shapes of conductive material overlying resistive material. The shallow conductive values could be associated to an increase of water content due to the rainwater infiltration, while resistive values to the reworked slide material.

Where possible, the ERT were compared with geological sections and stratigraphies from boreholes previously carried out by the technicians of "Provveditorato Regionale alle opera pubbliche dell'Umbria". Fig. 3a shows the comparison between ERT1 and direct data. Both the geological section 4-4' and the stratigraphies from boreholes 118, 119 and 120 report slide material up to a maximum depth of about 25 m. The comparison between the geological section and the ERT highlights the correspondence between slide material and more resistive values. The sliding surface, indicated with red dashed line on the geological section, corresponds to the horizontal resistivity contrast in the ERT indicated with black dashed line.

Fig. 3b reports the comparison between the ERT4, the geological section 5-5' and the stratigraphy from borehole 102. Geological section highlights that the maximum thickness reached by the landslide is about 30 m, whereas the ERT reaches an investigation depth of only about 20 m. Despite that, also in this case, the comparison allows us to associate the resistive material to the landslide body and locate the sliding surface on the ERT (black dashed line). The conductive material, which characterized the shallow portion of the ERT, could be due to the rainwater infiltration.

Acknowledgements. The research leading to this paper has received funding from the European Community's (EC) Seventh Framework Programme (FP7/2007-2013) under Grant Agreement n. 242212. The authors wish to thank Ing. Renzo Tascini of the Provveditorato Regionale alle opere pubbliche dell'Umbria (Ministero dei Lavori Pubblici) for providing technical material and for the availabilty during the field activities.

References

Angeli M.G., Pontoni F.; 1999: Progetto degli interventi relativi alla sistemazione idrogeologica del versante in frana in località Ivancich di Assisi (Ordinanza Min. Int. n. 2793 del 27/06/98 - G.U. 03/07/98) - Relazione Geologica. Pratica n.1299NO, Elaborato B.

Ardizzone F., Rossi M., Calò F., Paglia L., Manunta M., Mondinia A.C., Zeni G., Reichenbach P., Lanari R., Guzzetti F.; 2011: Preliminary analysis of a correlation between ground deformationsand rainfall: the Ivancich landslide, central Italy. Proceedings of SPIE - The International Society for Optical Engineering 8179, art. no. 81790L.

PROSPEZIONI GPR AD ALTA RISOLUZIONE IN AMBIENTE URBANO: IL CASO DI P.ZZA DELLE CARCERI A PRATO

S. Piro[1], C. Marcotulli[2], D. Zamuner[1], G. Vannini[2]

[1] Istituto per le Tecnologie Applicate ai Beni Culturali, ITABC-CNR

[2] Dipartimento Archeologia Medievale, Università di Firenze

Introduzione. I lavori per la riqualificazione ed il recupero urbano di Piazza delle Carceri a Prato interessano uno dei principali nuclei storici di questa città fra i secc. X – XIII. Qui infatti erano ubicati sia alcuni degli edifici più importanti del primo insediamento urbano medievale, come la *curtis* ed il *palatium* dei conti Alberti, sia il monumento più significativo e simbolico del periodo successivo, il *castrum/castellum* dell'Imperatore Federico II. Sempre in questo punto strategico si interseca anche una delle principali fasi evolutive dell'impianto difensivo urbano: la seconda cinta muraria.

Queste indagini, che si sono in parte svolte e si svolgeranno ancora nel cuore del nucleo urbano, si correlano con quelle già portate a termine in altre aree storicamente significative della città sotto la cura della Cattedra di Archeologia Medievale dell'Università di Firenze.

In accordo con la strategia operativa proposta dall'Università di Firenze, la prima fase di indagini si è svolta nel periodo da metà settembre 2012 a fine novembre 2012, precedendo i lavori di rimozione della pavimentazione.

La determinazione dell'areale delle indagini aveva due principali motivazioni, trattandosi di una zona "strategica" della piazza, a diretto contatto con il castello dell'Imperatore e

prospiciente un'area che, dalle prime indagini archeologiche (Vannini, 1975), si sapeva essere "fertile". Qui era stato aperto anche uno scavo non stratigrafico negli anni settanta del Novecento che aveva messo in luce le strutture di una porta monumentale: la *posterula* (Guerrieri, 1975), di cui andavano recuperate le informazioni e aggiornati i rilievi e, inoltre, l'essere a margine della piazza, consentiva di utilizzare questa zona come test diagnostico sulle potenzialità del deposito al di sotto del piano attuale di calpestio della piazza.

Obiettivo primario delle indagini archeologiche, quindi era quello di verificare ed ampliare le conoscenze sulle strutture rinvenute nel vecchio scavo, sia superandone il deposito stratigraficamente sia triplicando, di fatto, anche la cubatura dell'intervento.

Un secondo obiettivo era quello di elaborare una prima valutazione diagnostica delle potenzialità del deposito di piazza delle Carceri, necessaria per la pianificazione degli interventi archeologici previsti nelle due fasi successive del progetto. Questa operazione è stata portata avanti, nell'ambito della collaborazione tra la Cattedra di Archeologia Medievale dell'Università di Firenze e l'ITABC CNR (Gruppo di Geofisica), programmando una indagine estensiva su tutta l'area interessata dal progetto di riqualificazione, impiegando il GPR ad alta risoluzione con diverse frequenze di acquisizione.

La programmazione di una indagine geofisica su tutta l'area della piazza delle Carceri si è resa necessaria per una conoscenza e valutazione preliminari delle emergenze archeologiche eventualmente presenti al di sotto della superficie e, di conseguenza, per una pianificazione e programmazione delle successive fasi dell'indagine di Archeologia Preventiva.

La scelta dell'area è ricaduta su tutta quella porzione di suolo urbano sulla quale non era a disposizione alcun tipo di informazione su eventuali preesistenze e che, invece, si ipotizzava potenzialmente molto fertile, perché in stretta connessione topografica con le evidenze archeologiche di fronte al Castello (come la *posterula*) e quelle emerse durante gli scavi nel vicino Palazzo Banci-Buonamici (Fig. 1).

La collaborazione fra l'ITABC CNR e la Cattedra di Archeologia Medievale dell'Università di Firenze con i Laboratori Archeologici San Gallo (*spin-off* dell'Università di Firenze) ha permesso di condividere, quindi, gli obiettivi e le aspettative su questo tipo di intervento, e di individuare, di conseguenza, una strategia di azione che potesse integrare al meglio il lavoro dei geofisici e degli archeologi.

Indagine GPR presso l'area di P.zza delle Carceri (Prato). L'area in studio è stata investigata con il metodo GPR (Ground Penetrating Radar) ad alta risoluzione nel corso della campagna di settembre 2012. L'obiettivo delle indagini è stato quello di verificare l'esistenza di strutture archeologiche tuttora sepolte a diverse quote in profondità. Per ragioni logistiche la superficie da investigare è stata suddivisa in tre settori, come indicato in Fig. 1.

Le sezioni radar sono state acquisite impiegando il sistema: *SIR3000 (GSSI)*, equipaggiato con una antenna bistatica ad offset costante e frequenza nominale di 400 MHz (alta

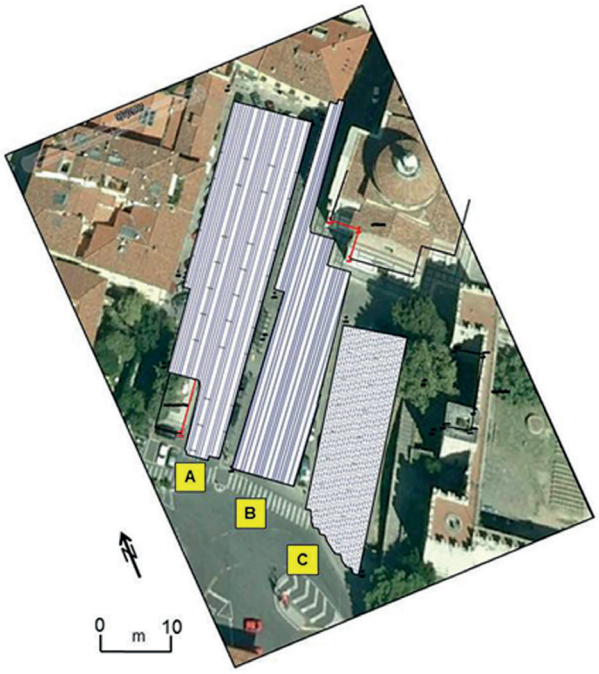

Fig. 1 – Prato, P.zza delle Carceri. Localizzazione delle aree A, B e C investigate con il Georadar ad alta risoluzione.

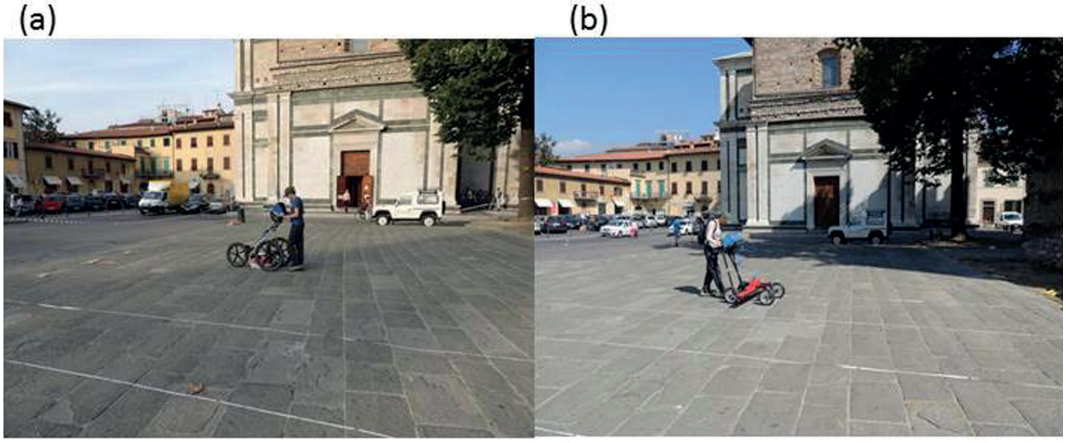

Fig. 2 – GPR Sir3000 con antenna da 400 MHz (a) e 70 MHz (b).

frequenza) (Fig. 2a) ed una antenna monostatica con frequenza di 70 MHz (bassa frequenza), (Fig. 2b).

Nel corso dell'indagine sono stati acquisiti un totale di 303 profili paralleli, di diversa lunghezza, equispaziati di 0.5 m.

Dopo gli usuali test preventivi e considerando sia la situazione geoambientale che il tipo di strutture ipotizzate è stata adottata la seguente configurazione strumentale: fondo scala dei tempi 105 ns (nanosecondi) per l'antenna da 400 MHz e 185 ns per l'antenna da 70 MHz, range dinamico di 16 bit, 512 campioni per traccia e 60 scan s^{-1} per la 400 MHz e 30 scan s^{-1} per la 70 MHz.

La superficie totale che viene rappresentata nelle immagini planimetriche del GPR si riferisce esclusivamente ai percorsi effettuati dall'antenna (profili di diversa lunghezza) ed è contenuta all'interno dei limiti delle aree investigate. Questi limiti sono stati rilevati topograficamente dal team dei Laboratori Archeologici San Gallo dell'Università di Firenze, presente sul posto durante le indagini geofisiche.

Il posizionamento lungo ogni profilo, per stabilire la disposizione geometrica di superficie dell'antenna e di conseguenza attribuire la localizzazione delle anomalie rilevate, è stato effettuato mediante un *odometro* di cui sono equipaggiati entrambe i carrelli impiegati. Le tracce radar sono state acquisite in modalità *line scan*, che consiste nel movimentare l'antenna lungo la direzione prefissata (profilo) in registrazione continua.

Per recuperare tutte le informazioni contenute nei profili paralleli ottenendo una visione d'insieme del volume di sottosuolo investigato, è stata applicata durante il processing la tecnica di elaborazione e rappresentazione nota come *time-slices*, (Goodman and Piro, 2013).

Le *time-slices* sono state calcolate con opportuni intervalli di tempi (4 ns per la 400 MHz e 6 ns per la 70 MHz) e successivamente rappresentate come mappe bidimensionali 2D, corrispondenti a diverse profondità di investigazione. Al fine di eliminare il contributo in termini di rumore che è stato registrato nel corso delle misure e che va attribuito alle particolari condizioni ambientali e del terreno o a fenomeni di accoppiamento antenna - superficie, sono stati impiegati alcuni filtri sui segnali registrati: rimozione effetto DC-drift, ricampionamento dei profili, filtro passa-banda, migrazione e filtro back-ground-removal (sottrazione della traccia media) (Goodman *et al.*, 2008, 2013; Piro *et al.*, 2008; Piscitelli *et al.,* 2007).

I risultati ottenuti nelle fasi delle indagini, impiegando il metodo GPR, sono relativi a diversi livelli di profondità (superfici) per uno spessore di sottosuolo (profondità) pari a circa 3.5 m con l'antenna da 400 MHz e 5 m con l'antenna da 70 MHz.

Nel caso dell'indagine in questione, non disponendo di sezioni CMP acquisite per la valutazione della velocità e dopo una prima stima orientativa delle profondità investigate, la

velocità media è stata ottenuta attraverso il riconoscimento delle iperboli di diffrazione, a diversi tempi, direttamente sui radargrammi sperimentali. In tal modo è stato possibile valutare che la velocità media di propagazione dell'onda elettromagnetica nel terreno è pari a circa 10 cm/ns, nel caso dell'antenna da 400 MHz e 8 cm/ns nel caso dell'antenna da 70 MHz.

Tutte le fasi di processing sono state effettuate impiegando il software GPR-Slice (Goodman, 2011).

L'analisi delle *time-slices* ottenute per le tre zone A, B e C ha permesso l'individuazione di diversi corpi riflettenti. Le profondità stimate, a cui si riferiscono le time-slices calcolate per la 400 MHz sono: 0.30 m, 0.60 m, 0.90 m, 1.20 m, 1.40 m, 1.90 m, 2.30 m, 2.50 m, 3.0 m e 3.40 m.

Fig. 3 – GPR 400 MHz, time-slices alla profondità stimata di 0.40-0.60 m.Primi risultati dei saggi D e E.

Nella Fig. 3 sono riportate le time slices, per le tre zone investigate, relative all'intervallo di profondità stimato di 0.40 - 0.60 m.

Risultati preliminari. A marzo 2013 è iniziata la seconda fase del progetto di analisi archeologiche in piazza delle Carceri, che aveva lo scopo principale di sondare, tramite la realizzazione di saggi diagnostici mirati, le anomalie evidenziate dalle prospezioni geofisiche (interpretate e valutate congiuntamente fra la Cattedra di Archeologia Medievale dell'Università di Firenze, gli archeologi dei Laboratori Archeologici San Gallo ed il Gruppo di Geofisica del CNR-ITABC di Montelibretti)

Nella Fig. 3 sono indicate due aree oggetto di scavo di verifica indicate come saggio D e saggio E.

*SAGGIO D***.** Aperto per sondare l'anomalia "a1". Lo scavo conferma la presenza di una struttura, evidenziata dall'indagine GPR, di forma quadrangolare con 6.40 m di lato e posizionata a 0.30-0.40 m di profondità rispetto al piano stradale. La struttura, in muratura piena di ciottoli e malta, ha in appoggio strati con tracce di frequentazione antropica ricchi di ceramica acroma ed un piano di calpestio. L'area è di interesse archeologico anche in considerazione di possibili confronti con una struttura simile rinvenuta in un'altra area archeologica.

*SAGGIO E***.** Aperto per sondare l'anomalia "a2", di forma irregolare. L'apertura del saggio conferma la presenza, sotto una canaletta ormai ostruita di epoca recente, di un setto murario ad "L", evidenziato dall'indagine GPR, affiancato da una porzione di lastricato, forse residuo di un piano stradale, posizionato a 1.75 m di profondità e avente la stessa direttrice del vicolo de' Bardi, apparentemente direzionato verso il Castello. La strada ed il setto murario sono sigillati da strati estremamente ricchi di ceramica aventi un orizzonte cronologico piuttosto definito che non sembra andare, ad una prima osservazione autoptica, oltre la prima metà del XV secolo. L'area è dunque di primaria importanza per comprendere lo sviluppo urbanistico della città in questo nodo nevralgico fra il Castello e il vicino Palazzo Banci, contenente le strutture Albertesche già scavate in precedenza.

Il progetto tuttora in corso, procede con l'analisi integrata tra i risultati ottenuti con il GPR e le strutture individuate con altri saggi di scavo che hanno interessato altri settori dell'area investigata.

Riconoscimenti. Gli autori ringraziano gli archeologi dei Laboratori San Gallo dell'Università di Firenze per il supporto durante le acquisizioni sul campo ed il Comune di Prato per il supporto finanziario a tutte le indagini.

Bibliografia

Goodman D., Piro S., Nishimura Y., Schneider K., Hongo H., Higashi N., Steinberg J., Damiata B., 2008. GPR Archeometry. In "Ground Penetrating Radar Theory and Applications**",** Edited by: Harry M. Jol. Elsevier (Ed.), pp. 479 – 508.

Goodman D.,2011. GPR-Slice 7.0, Manual. (http://www.gpr-survey.com,January/2011.)

Goodman D., Piro S., 2013. GPR Remote sensing in Archaeology. Springer (Ed), ISBN 978-3-642-31856-6, ISBN 978-3-642-31857-3 (eBook), DOI 10.1007/978-3-642-31857-3. Springer, Berlin, (Germany).

Guerrieri F., 1975 (a cura di), Il Castello dell'Imperatore a Prato, Centro Di, Firenze.

Piro S., Goodman D., 2008. Integrated GPR data processing for archaeological surveys in urban area. The case of Forum (Roma, Italy). 12th International Conference on Ground Penetrating Radar, June 16-19, 2008, Birmingham, UK. Proceedings Extanded Abstract Volume.

Piscitelli S., Rizzo E., Cristallo F., La penna V., Crocco L., Persico R., Soldovieri F., 2007. GPR and Microwave Tomography for Detecting shallow Cavities in the Historical Area of Sassi of Matera (Southern Italy), Near Surface Geophysics, vol. 5, pp. 275-285,.

Vannini G., 1975. Scavi nell'area antistante il Castello dell'Imperatore. Notizia preliminare, in F. Gurrieri (a cura di),Il Castello dell'Imperatore a Prato, Centro Di, Firenze, pp. 26-29.

REGIONAL MODELING OF THE GEOMAGNETIC FIELD IN EUROPE USING SATELLITE AND GROUND DATA: GEOLOGICAL APPLICATIONS

E. Qamili[1], F.J. Pavón-Carrasco[1], A. De Santis[1,2], M. Fedi[3], M. Milano[3]
[1] Istituto Nazionale di Geofisica e Vulcanologia, Roma, Italy
[2] Università G. D'Annunzio, Chieti, Italy
[3] Università Federico II, Napoli, Italy

Introduction. The geomagnetic field varies in time and space. In order to describe these spatial and temporal variations, systematic surveys are necessary. Before the satellite era, continuous records at magnetic observatories and repeat station measurements were the principal resources of the geomagnetic field studies. But the Earth's surface is not uniformly covered by these ground magnetic measurements (especially over the seas). If we want to model properly the geomagnetic field, more data are necessary to cover the area under study and these data should be also distributed at different heights, in order to better sample the entire space of interest. For this reason, satellites play an outstanding role for geomagnetic field measurements and modeling. Different satellite missions (i.e. Magsat, Ørsted, Champ, SAC-C etc.) have produced high quality geomagnetic data with global coverage and high spatial resolution (Matzka *et al*., 2010). Taking advantages of the high quality of the satellite data, in this work, we want to see if it is possible to model both main and anomaly Earth's magnetic fields using an appropriate satellite dataset, with a particular objective in mind: to construct a reliable European model of the geomagnetic anomaly field. To do this, we have here selected a set of 6 years (1999-2005) of data (vector and total intensity) from the Ørsted, CHAMP and SAC-C satellites, which is the same dataset used for deriving the CHAOS-4 model (Olsen *et al*., 2010). In order to properly model the above-mentioned contributions of the geomagnetic field, appropriate selection criteria should be applied to these satellite data. Data selection based on geomagnetic indices and local time minimizes the influence of the external fields. When considering the data selection procedure, it is necessary to take into account also the characteristics of the region under study.

Considering what said above, we considered data that satisfy the following stringent criteria:

1. at the European latitudes it is required that the *Dst* index (that measures the strength of the magnetospheric ring-current) does not change by more than 2 nT/hr,
2. at non-polar latitudes is required that the geomagnetic activity index should be Kp $\leq$ 2o,
3. data sampling interval applied is 60 sec,
4. only data from dark regions (sun 10° below horizon) were considered;
5. for the polar region, data are selected satisfying $E_m < 0.8$mV/m.

Here we have tried to model the main and crustal fields by means of the Spherical Cap Harmonic Analysis (SCHA) in space. The crustal field is time invariant so it does not need to be modeled in time, while the changes in time of the main field are modeled by means of the classical penalized cubic B-splines, covering the indicated time interval. We will see below that these techniques provide optimal representation of the internal field over the area of investigation.

Methodology. Modeling the global geomagnetic field at the Earth's surface and above is usually approached using the well-known *Spherical Harmonic Analysis* (SHA). However, global techniques do not provide in general higher resolution when the study is carried out in a restricted part of our planet, and then, a regional approach is usually the most plausible mathematical technique. A useful contribution for such a regional analysis is given by the *Spherical Cap Harmonic Analysis* (SCHA) introduced for the first time by Haines (1985). The SCHA is a powerful analytical technique for modeling the Laplacian potential and the corresponding field components over a spherical cap. The solution of Laplace's equation in spherical coordinated (r,θ,ϕ) for the magnetic potential V due to internal and external sources over a spherical cap can be written as an expansion of non-integer degree spherical harmonics (Haines, 1985):

$$V(r,\theta,\lambda) = a\sum_{k=0}^{K_{INT}}\sum_{m=0}^{k}\left(\frac{a}{r}\right)^{n_k+1}\left[g_{n_k}^{m,\mathrm{int}}(t)\cdot\cos(m\cdot\lambda)+h_{n_k}^{m,\mathrm{int}}(t)\cdot\sin(m\cdot\lambda)\right]P_{n_k}^{m}(\cos\theta) + \\ + \quad a\sum_{k=1}^{K_{EXT}}\sum_{m=0}^{k}\left(\frac{r}{a}\right)^{n_k}\left[g_{n_k}^{m,ext}(t)\cdot\cos(m\cdot\lambda)+h_{n_k}^{m,ext}(t)\cdot\sin(m\cdot\lambda)\right]P_{n_k(m)}^{m}(\cos\theta) \tag{1}$$

where $g_{n_k}^{m}$ and $h_{n_k}^{m}$ are the spherical cap harmonic coefficients that determine the model (*INT*/*EXT* stand for internal and external contributions, respectively), $P_{n_k}^{m}(\cos\theta)$ are associated Legendre functions that satisfy the appropriate boundary conditions (null potential or co-latitudinal derivative at the border of the cap) and have integer order *m* and real, but not necessary integer, degree n_k (*k* is an integer index selected to arrange, in increasing order, the different roots *n* for a given *m*). The number of the coefficients depends on the maximum spatial indexes of expansion K_{INT} *and* K_{EXT}. This technique was introduced by Haines (1985) for geomagnetism but it has been successfully applied also in gravity and crustal field studies. In this study, we will try to apply this technique to model the crustal field of the European area using only magnetic satellite data.

First, we have to model both vector and total intensity data. For this reason, we apply an iterative approach to establish a linear relation between the model coefficients and the intensity data. The geomagnetic field elements are defined as a non-linear function which depends on the model coefficients as:

$$d = f(\vec{m}) + \varepsilon \tag{2}$$

where the vector $\vec{m}$ contains all the model coefficients and ε is the error which is assumed as Gaussian. To find the optimal set of the model coefficients, we chose the regularized weighted least square inversion applying the Newton-Raphson iterative approach (Gubbins and Bloxham, 1985):

$$\vec{m}_{i+1} = \vec{m}_i + \left(\hat{A}_i{}'\cdot\hat{C}_e^{-1}\cdot\hat{A}_i + \alpha\cdot\hat{\Psi} + \tau\cdot\hat{\Phi}\right)^{-1}\left(\hat{A}_i{}'\cdot\hat{C}_e^{-1}\cdot\vec{\gamma}_i - \alpha\cdot\hat{\Psi}\cdot\vec{m}_i - \tau\cdot\hat{\Phi}\cdot\vec{m}_i\right) \tag{3}$$

where $\hat{A}$ is the matrix of parameters which depends on the spherical cap harmonic functions in space and time (the so-called Frechet matrix). $\hat{C}_e$ is the data error covariance matrix (the inverse matrix of weights) and $\vec{\gamma}$ is the vector of differences between the input data and modeled data for the *i*-th iteration. The $\hat{\Psi}$ and $\hat{\Phi}$ matrices are the spatial and temporal regularization matrices, respectively, with damping parameters α and τ. The index *i* indicates the number of the iteration, which requires a first initial solution $\vec{m}_0$.

Then, we define a spatial roughness that depends on the norm of the geomagnetic field B^2 in terms of the model coefficients (see Korte and Holme, 2003):

$$N_S = \alpha\cdot\Psi = \frac{\alpha}{t_e - t_s}\iint_{\Omega}\int_{t_s}^{t_e} B^2\Big|_{r=a}\, d\Omega dt \tag{4}$$

where t_s and t_e are the initial and final epoch respectively, and $d\Omega$ is the differential solid angle over the spherical cap Ω at the Earth's surface (radius *a*). The temporal roughness is defined in terms of the second derivative of the geomagnetic field as:

$$N_T = \tau\cdot\Phi = \frac{\tau}{t_e - t_s}\iint_{\Omega}\int_{t_s}^{t_e}\left(\frac{\partial^2 B}{\partial t^2}\Big|_{r=a}\right)^2 d\Omega dt \tag{5}$$

Both matrices, $\hat{\Psi}$ and $\hat{\Phi}$, are diagonal in the global case due to the orthogonality of the basis functions over the sphere. However, for spherical caps the two sets of basis functions involved in the SCHA technique (with indices $k - m$ = odd and $k - m$ = even, respectively) are not orthogonal among themselves (Haines, 1985) and both matrices have non-diagonal elements (see Korte and Holme, 2003 for a review).

Finally, to model in time, we use the penalized cubic b-splines (de Bor, 2001). This kind of temporal functions provide more realistic temporal variation than the classical polynomial or sinusoidal functions.

Modeling process. In order to know if the present temporal and spatial distribution of the magnetic satellite data allows us to obtain a robust geomagnetic main field model for the European region, we first carried out a test using synthetic data. The synthetic data were obtained from the global model "Comprehensive Model ver. 4", CM4 (Sabaka *et al.*, 2004) which was developed by using all the different magnetic sources which characterize the present geomagnetic field, and has a temporal validity from 1960 to 2002. The CM4 model gives information about the internal field (global degree $n \leq 13$), crustal field (global degree $n > 13$) and the external field, and was obtained simultaneously modeling all these contributions at the same time, from this the term "comprehensive" model.

As indicated in Eq. (3), we need an initial set of the time-dependent model coefficients. We have fixed the initial values as g_0^0 = -15000 nT and $g_k^m = 0$ nT for $k>0$. The spatial resolution of the model is given by the selection of the degree n_k and the size of the spherical cap θ_0. In order to test the influence of these two parameters in the modeling process, we have used different values of them. According to the selection area, i.e. the European continent, the cap was centered at 45ºN, 15ºE choosing different half angles of 36º, 43º, 50º and 56º. The degree k in Eq. (1) was fixed between 5 and 8, providing a more or less constant global degree n_k of 13 (see Table 1). We have performed different tests changing the spatial parameters but keeping constant the influence of the external field up to degree $K_{EXT} = 1$. The cubic B-splines control the temporal resolution of the modeling approach. In our work, a set of knot points every 0.5 yr for the temporal interval from 1999.0 to 2005.0 was used.

Tab. 1 – Tests with different index K_{INT} and half-angle θ_0 (K_{EXT} is maintained equal to 1) and corresponding residuals given as root mean squares (RMS) in nT for the different main field (SCHA and CM4) models; n_k is automatically determined by K_{INT}, θ_0 and the boundary conditions and is comparable with the maximum degree of a typical global model of the main field.

K_{INT}	K_{EXT}	θ_0	n_k	RMS_X	RMS_Y	RMS_Z	RMS_F	RMS_{XYZF}
5	1	36	13.3	58,265	36,033	62,901	75,889	60,018
6	1	43	13.1	6,748	5,055	7,232	8,255	6,920
7	1	50	13	0,713	0,573	0,836	0,996	0,795
8	1	56	13.1	0,271	0,239	0,248	0,334	0,275

After synthesizing all the vector and total intensity data at the same location and time of the real satellite data, we have applied the Eq. (3) to obtain the time-dependent model coefficients. In this case, the synthetic data include both main and crustal fields. The results, not shown here, were extremely good: our models were able to reproduce very well the characteristics of the crustal field provided by the CM4 model in this region. Moreover, these tests also indicated that the best pair of spatial parameters (K_{INT}, θ_0) was 7 and 50º respectively. These values were selected taking into account the final root mean square (rms) of the models and the different trade-off curves of the spatial and temporal norms of the geomagnetic field given in Eqs. (4) and (5).

After the validation of the method, our next step was to apply it to the real satellite data. In this case, we have to pay a special attention for modeling both internal fields, i.e. the main and the crustal field.

In order to model the main and crustal fields two different subsequent inversions have been carried out. We first used a $K_{INT} = 7$ (with θ_0= 50º, n_k is approximately 13) to model the main field and K_{EXT} =1 to discriminate an eventual external field. After generating the time-dependent model of the main field using eq. 3, we subtracted the model predictions at the real

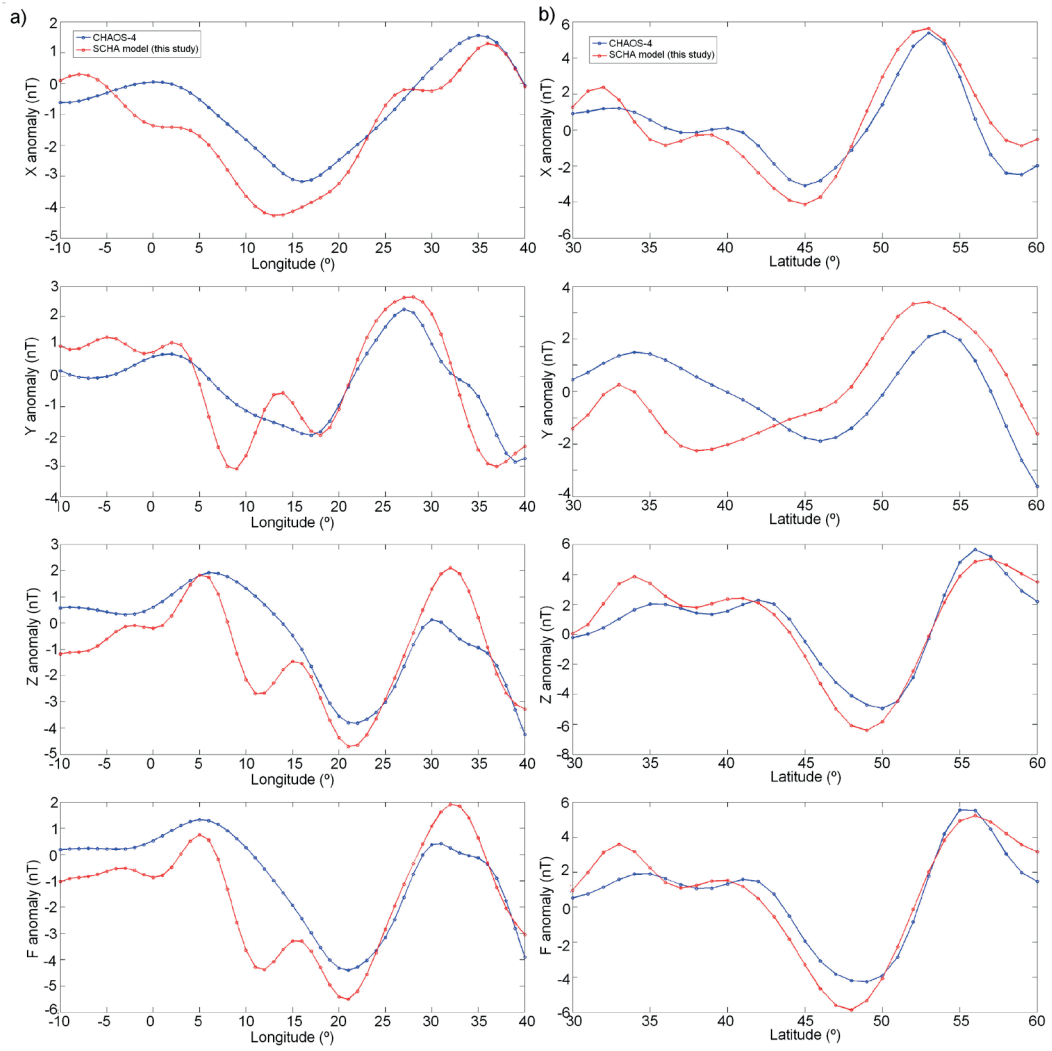

Fig. 1 – Model prediction (red) at 450 km from Earth's surface at 45°N (a) and 15°E (b) compared with CHAOS-4 model (in blue).

input data to obtain in this way the crustal field. This crustal field represents the magnetization content in the continental and oceanic lithosphere at satellite altitude and its values do not reach absolute values higher than 20 nT.

Then, we used these residual values to model the crustal field using a *no-time-dependent* model with $K_{INT} = 35$ (n_k is approximately 65). In this model we apply the spatial regularization norm with damping parameter equal to 10^{-5} nT^{-2} and the approach is not iterative. The penalized B-cube splines are not used in this part of the work as well as the constraint of the temporal norm of the geomagnetic field.

The results are plotted in Figs. 1 and 2. The Fig. 1 shows two different profiles at 450 km of altitude in the north-south and west-east directions centered at 45°N, 43°E. We have chosen this value of altitude because is approximately the mean altitude of the different satellite orbits. For comparison we also show the model prediction of the CHAOS-4 model (Olsen *et al.*, 2010). This global model was developed by using the same set of satellite data including ground data

and covering the time interval 1997 – 2011. As we can see, our regional model presents a higher spatial variability than the global CHAOS-4 model due to the regional characteristic of our model. This characteristic is presented for all the geomagnetic field components and for the total field intensity.

In order to see the spatial prediction of the model, we plot different crustal field maps in Fig. 2. The crustal field model was also calculated at 450 km of altitude and was compared with the prediction given by the CHAOS-4 model. Our results show a clear agreement with the global model, but present more details in terms of the spatial wavelength.

Upward continuation transforms anomalies measured at one surface into those that would have been measured at a higher altitude surface. In the simplest case, i.e., level-to-level, upward continuation is merely a convolution of the original data, performed in either the space or Fourier domain. We made a level-to-level continuation of the Earth's surface CM4 data to 450 km. We first transformed the data coordinates from spherical to Cartesian, then used a maximum entropy extrapolator to realize a square map and finally extended the grid by 10% with a periodic extrapolator. The results are shown in Fig. 3.

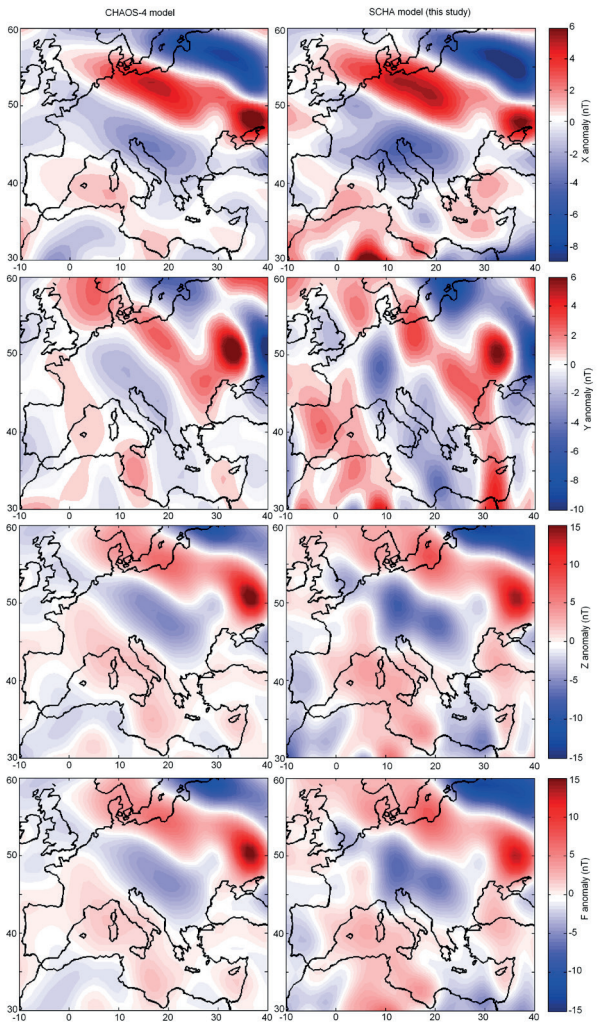

Fig. 2 – Maps of the X, Y, Z and F (from top to bottom) crustal field at 450 km as modeled by a set of real satellite data (right) and the crustal field calculated with CHAOS-4 model (left).

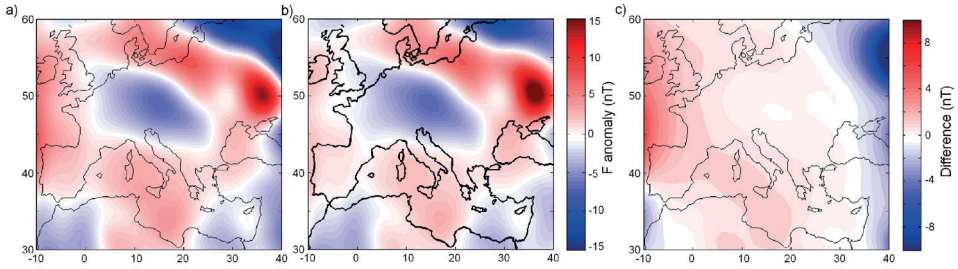

Fig. 3 – Level-to-level upward continuation of total intensity F. The CM4 data at ground level were continued to 450 km (a) with a level-to-level convolution filter. Only little differences (c) among CM4 and continued data occur in a wide central area (within 1 nT), while major differences appear at the edges, i.e., where the edge-effect and the errors for not having taken into account the Earth's curvature are stronger. However, by changing border extrapolator (not shown here) we observed that the edge-effect changes led the continued field to be improved in some areas and to get worse in others. This should demonstrate that most of the error is due to the edge-effect.

Conclusions. The aim of this work was to find a useful technique in order to construct a European model of the main and crustal magnetic fields from real geomagnetic satellite data.

Here, we analyzed different sets of magnetic data, first a set of synthetic data from *CM4* global model in order to validate the analysis procedure, and then a real satellite data set covering a period from 1999 to 2005.

The regional model we present here shows a clear agreement with other global models like CM4 and CHAOS-4, but presents more details in terms of the spatial wavelength. We found that both the datasets allow us to model very well the crustal field, at 450 km height when comparing with the global CHAOS-4 model in the European region. Also, a level-to-level upward continuation to 450 km of the CM4 data at ground level works reasonably well, proving the efficiency of present level-to-level techniques in a satellite-altitude framework.

References

de Boor, C. 2001. A Practical Guide to Splines. Springer, New York, p. 368.

Gubbins, D., and Bloxham J. 1985. Geomagnetic field analysis - III. Magnetic fields on the core-mantle boundary, Geophysical Journal of the Royal Astronomical Society 80, 695-713.

Haines, G. V. 1985. Spherical cap harmonic analysis, *Journal of Geophysical* Research, 90 (B3), 258-2591.

Korte, M., and Holme, R. 2003. Regularization of spherical cap harmonics, Geophysical Journal International 153, 253–262.

Matzka, J., Chulliat, A., Mandea, M., Finlay, C., Qamili, E., 2010. Geomagnetic Observations for Main Field Studies: from Ground to Space. *Space Science Reviews* 155 (1-4), 29-64.

Olsen, N., Luehr, H., Sabaka, T. J., Michaelis, I., Rauberg, J., Tøffner-Clausen, L. 2010. CHAOS-4: A high-resolution geomagnetic field model derived from low-altitude CHAMP data, AGU Fall Meeting.

Sabaka, T.J., Olsen, N., and Purucker, M.E. 2004. Extending comprehensive models of the Earth's magnetic field with Ørsted and CHAMP data. Geophysical Journal International 159, 521–547, 2004.

A PRELIMINARY TEST ON THE FEASIBILITY OF LOCATING AN IRON RESTORATION PIN IN A STATUE BY MEASURING THE TMF ANOMALY WITH A TRIAXIAL MEMS MAGNETOMETER

L. Sambuelli[1], S. Gallinaro[2], M. Grosso[2]

[1] Diati – Politecnico Di Torino, Italy

[2] St-Polito S.c.ar.l., Italy

Foreword. Non-Destructive Testing (NDT) techniques have gained a growing role in Cultural Heritage Conservation. In the last years many scientists and technicians have been testing this increasing role (e.g. Livingston, 2001; Grimberg, 2009; Binda and Siasi, 2009). Recently (Cosentino *et al.*, 2011) the faint border between NDT and Geophysics has been "officially" broken in consideration of the large overlap of the methodologies used in both the disciplines.

With respect to the testing of art artefact such as statues or architectural fragments four types of physical methods are available: sound (mechanical waves), penetrating radiation (X-ray, γ-rays), light (visible, near-visible), electromagnetic (magnetic, electrical impedance, electromagnetic induction, radar).

A particular application of the NDT technique is the location of iron or steel reinforcements or pins.

Many times the purpose of the NDT inspection is to find out not only the presence but also the size and the position of the metal pins to understand if they can properly perform their structural function. Ancient iron pins instead of having a reinforcement function can sometimes contribute to the failure of the restoration work (Jain *et al.*, 1988). This negative effect can derive from different causes: because of rust and/or a wrong positioning of the pins. When the iron rusts the consequent expansion of the oxides generates stresses within the stone and cracks can occur. Sometimes the pins have not been placed in the centre of the volume

that had to be connected, this turns out to be especially dangerous for the moving of statues inasmuch as high stress can be generated and concentrated near the surface with consequent rupture.

Iron or steel pins can be revealed and located with electromagnetic induction techniques even if the location can be sufficiently precise and reliable only when very simple geometries occur: pins parallel to a flat surface (pachometers for concrete rebar detection). On purpose Ground Penetrating radar (GPR) systems and software have been developed to rebar detection and by properly using these systems a 3D reconstruction of the rebar grid is possible. On the other hand, as for the pachometers, single pins of some centimetre length, with a diameter of some millimeter, nearly random oriented in volume with complex geometries such as a statue, cannot be reliably located mainly because of the size of the antennas and the wavelengths of the GPR pulses. Presently the shortest wavelengths that propagate in ornamental stones with GPR are around 5 cm (Vaccaneo *et al*., 2004). This means that even if the presence of a metal pin can be detected, its size and position cannot be reasonably estimated.

Despite the large amount of mathematical tools developed to process potential field data, the analysis of static magnetic field for testing artifacts is, at our knowledge, not used. Very likely one of the main reasons of this lack of application is due to the small volumes that have to be investigated compared to the larger size of traditionally employed magnetometers, such as fluxgate, proton, etc. However, in recent years we assisted to the development and diffusion of a new type of miniaturized sensor and actuator devices based on the semiconductor technology. These devices, known as Micro Electro-Mechanical Systems (MEMS), include accelerometers, gyroscopes, pressure sensors, displays, microfluidic equipment, optical switches, and magnetometers. Miniaturized triaxial MEMS magnetometers are normally used as digital compasses (in combinations with accelerometers) in consumer applications, such as augmented positioning and navigation systems (to facilitate the dead-reckoning navigation) and mobile smart phones.

The magnetometer. MEMS-based magnetic field sensors can offer small-size solution for magnetic field sensing. Smaller devices can be placed closer to the measurement spots, thereby achieving higher spatial resolution. Additionally, MEMS magnetic field sensors do not involve the microfabrication of magnetic material: therefore, the cost of the sensor can be largely reduced. Integration of MEMS sensor and microelectronics can further reduce the size of the entire magnetic field sensing system.

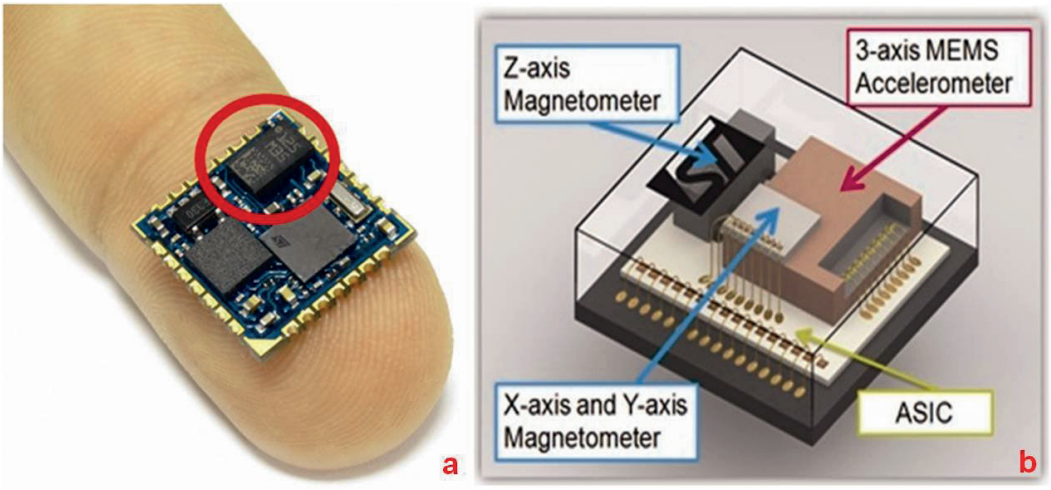

Fig. 1 – The STMircoelectronics iNEMO-M1 board (a) hosting the triaxial magnetometer/accelerometer LSM303DHLC (b, within the red circle in a).

MEMS magnetic field sensors can be based on two different principles: Lorentz-force or Anisotropic Magneto Resistance (AMR) materials. In the former case, the sensor relies on the mechanical motion of the MEMS structure due to the Lorentz force acting on the current-carrying conductor in the magnetic field. The mechanical motion of the micro-structure is sensed either electronically or optically. The mechanical structure is often driven to its resonance in order to obtain the maximum output signal.

In the latter case, AMR effects, which are commonly found in both magnetic and ferromagnetic materials, are enhanced using a specific geometry of the magnetic element, such that a net residual magnetization is induced by the balance among energetic terms (magnetostatic, magnetoelastic, magnetocrystalline). Anisometric thin films exhibit a strong effect and enable the realization of simple, cost-effective sensors where the electrical resistance is a function of the angle between magnetization (function of the external magnetic field) and current density.

The device employed for the experiment is LSM303DHLC, manufactured by STMicroelectronics. It is a system-in-package featuring a triaxial digital linear acceleration sensor and a triaxial digital magnetic sensor based on AMR. The magnetic full-scale is selectable from 130,000 to 810,000 nT, with a maximum sensitivity of 90 nT/digit. The device also includes readout circuitry providing a digital output, easy to be employed in a microprocessor-based system. Its size is 3x5x1mm and its average power consumption is under 400 μW.

The experiment. We made a model of a "restored arm" with a bioclastite cylindrical sample (height= 18 cm; diameter=10 cm) in which an iron pin (length= 9 cm; diameter= 5 mm) was inserted out of the sample axis and obliquely (Fig. 2a). A rotating platform surrounded by a graduated scale allowed us to rotate the sample in step of 10°. A sliding beam was used to move vertically the magnetometer so that, combining the two movements, the sample was scanned along horizontal circles 1 cm apart along its height (Fig. 2b). At each measuring point we recorded 50 times at 50 Sample/s the three magnetic components (Vertical, Radial and Tangent) with the height and the angle. At each point mean, standard deviation and standard deviation of the mean over the 50 readings were calculated and the means were then taken as raw data. With this experimental setup, aimed to perform a preliminary test of the effectiveness of the sensor, the pin rotated within the sample and was always south of the sensor, therefore we did not get the reconstruction of the magnetic field around the sample as it would be in an acquisition, for example, around a statue arm.

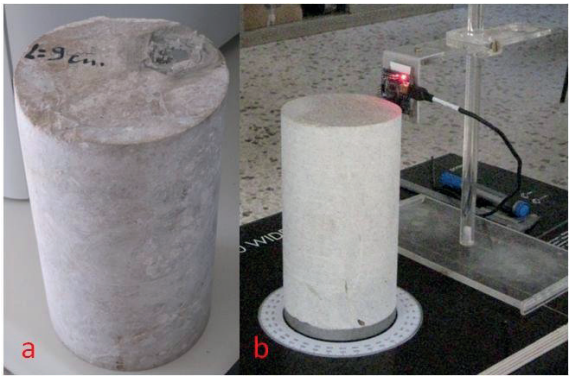

Fig. 2 – The physical model of a limestone statue "restored arm" with the iron pin fitted inside (a). The system, with the vertical sliding arm and the rotating platform, made to realize the cylindrical scanning of the model (b).

Results. With a software developed in Matlab© we plotted on cylindrical surfaces all of the components and the modulus. By subtracting the average value of each component, we estimated the anomaly caused by the iron pin. Among the many representations we made of the results the most meaningful with respect to the question "where and how long is the iron pin" seem to be the plots of the total field TF (Fig. 3a) and the horizontal vector H (Fig. 3b) anomalies onto a cylindrical surface mapping the lateral surface of the sample. The TF vector imaging seems to reasonably describe the magnetic field flux plus some noise. The top view of all the vectors is more suitable to guess the position of the pin with respect to the sample axis.

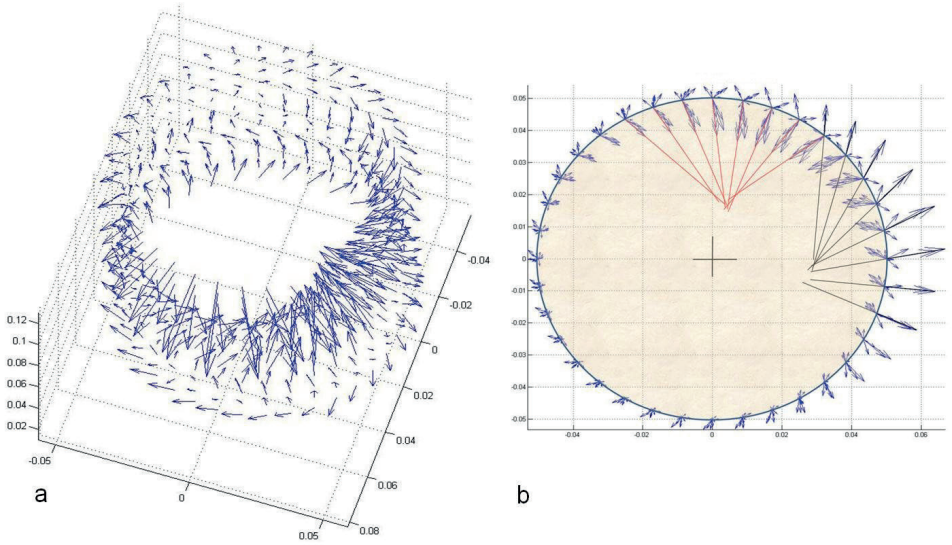

Fig. 3 – Two of the most meaningful representation of the results. The total field vectors (a) and the top side view of all the measured horizontal component (b) plotted at each scanning height and angle.

In Fig. 3b some of the horizontal vector (black segments) taken at the top of the sample, and other horizontal vectors collected to a lower height (red segments), are stretched toward the sample centre. With a fair approximation the intersection areas of the black and red segments match, respectively, the top and the bottom end of the iron pin.

Comments And Conclusions. Some comments on the whole experiment are mandatory. It must be considered that: the test was carried out at the ST-POLITO office in the Politecnico of Turin, a magnetically noisy environment; the results, according to the acquisition procedure we made up, do not represent the magnetic field around the sample. However the intensity of the anomaly and the vicinity of the sensor to the anomalous body concurred to the promising results of the test. On the side of the acquisition, a set of measurements with two triaxial sensors radially separated, in order to acquire a radial gradient, has been already done always with the rotation of the sample and a static sensor. A configuration with four sensor able to measure the gradient tensor is planned as well as measurements with the sensor moved around the sample. On the site of data interpretation we are currently working at finding algorithms for data inversion. Finally it seems reasonable, giving the raw data imaging obtained, to confirm the feasibility of sizing and locating iron restoration pins within statue, with satisfying approximation, by static magnetic field anomaly measurements.

Acknowledgements. The Authors would like to thank Mr. Diego Franco form DIATI for his patient work during data acquisition. ST-Microelectronics is acknowledged for providing the MEMS sensors and the data acquisition circuitry.

References

L. Binda, A. Saisi, 2009, application of NDTs to the diagnosis of historic structures, NDTCE'09, Non Destructive Testing in Civil Engineering, Nantes, 28 pp.

P.L. Cosentino, P. Capizzi, R. Martorana, P. Messina, S. Schiavone, 2011, From geophysics to microgeophysics for engineering and cultural heritage, International Journal of Geophysics, 8pp. doi:10.1155/2011/428412.

R. Grimberg, 2009, Electromagnetic non destructive evaluation: present and future. Keynote lecture at 10th International Conference of the Slovenian Society for Non Destructive Testing, Ljubljana, Slovenia, 267-284

K. Jain, K. Tej Singh, O.P. Agrawal, 1988, Corrosion of iron dowels and clamps in the deterioration of monuments. In Ciabach, J., ed., 6th International Congress on the Deterioration and Conservation of Stone (Torum, Poland: Nicholas Copernicus University), 116–124.

R.A. Livingston, 2001, Nondestructive testing of historic structures. Archives and Museum Informatics, 13, 249-271.

D.Vaccaneo, L. Sambuelli, P. Marini, R. Tascone, R. Orta, 2004, Measurement system of complex permittivity of ornamental rocks in L-frequency band. IEEE Transaction on Geoscience and Remote Sensing, 2490-2498.

sessione 3.3

Metodi integrati

Convenor: L. Sambuelli e A. Vesnaver

co-organizzata con Sezione Italiana Eage-Seg

MARINE GEOLOGICAL MAPPING OF THE CAMPANIA REGION AT THE 1:10,000 SCALE: THE EXAMPLE OF THE GEOLOGICAL MAP N. 465 "ISOLA DI PROCIDA" (NAPLES BAY, SOUTHERN TYRRHENIAN SEA, ITALY)

G. Aiello
Institute of Marine Environmental and Coastal Area (IAMC), National Research Council of Italy (CNR), Naples, Italy

Introduction. Marine geological mapping of the Campania Region at the 1:10.000 scale is herein presented, focussing, in particular, on the geological map n. 465 "Isola di Procida" (Ispra, 2011). The geological map n. 465 "Isola di Procida" covers the Naples Bay from the Sorrento Peninsula up to the Procida island. In this geological map a total amount of 622 km^2 of surface about 10 km^2 are represented by emerged areas and 612 km^2 by marine areas. The bathymetric belt 0/200 extends for 378 km^2 and represents about the 60.8% of the total surface of the map. Sidescan sonar data have been calibrated by numerous sea bottom samples. The geological structures overlying the outcrop of acoustic basement, both carbonate (in correspondence to the Sorrento Peninsula) and volcanic (in correspondence to the Phlegrean Fields) have been investigated using Subbottom Chirp, Sparker and Watergun profiles. The interpretation of seismic data lends support for the reconstruction of the stratigraphic and structural setting of Quaternary continental shelf and slope successions and correlation to outcrops of acoustic basement, Mesozoic carbonate in the Sorrento Peninsula structural high and Quaternary volcanic in the Phlegrean Fields and Procida island. These areas result from the seaward prolongation of the stratigraphic and structural units widely cropping out in the surrounding emerged sector of the Sorrento Peninsula (Cinque *et al.*, 1997), Naples town, Phlegrean Fields and Procida island (Scarpati *et al.*, 1993; Perrotta *et al.*, 2010; Ispra, 2011).

Source data and methods of cartographic representation. Several geological and geophysical surveys on the continental shelf and slope of the Naples Bay have been carried out, particularly referring on the geological map n. 465 "Isola di Procida". In particular, a high resolution Multibeam bathymetry of the Naples Bay allowed for the construction of a marine DEM (Digital Elevation Model) of the area, giving a detailed image of the morpho-structures at the sea bottom (D'Argenio *et al.*, 2004). Moreover, Sidescan Sonar acoustic profiles covering the whole Naples Bay have been acquired for the construction of photomosaics of the sea bottom. The Sidescan Sonar photomosaics and the Multibeam bathymetry represented the base for the marine geological mapping.

The integrated geological interpretation of seismic, bathymetric and Sidescan Sonar data has been tied by sea bottom samples and piston cores. The geological structures and the seismic sequences, both volcanic and sedimentary in nature, which characterize the Naples Bay at a regional scale have been the object of detailed studies carried out using multichannel and single channel seismics of various resolution and penetration, including the Sub-bottom Chirp profiles, often integrated with marine magnetics (Aiello *et al.*, 2001; Secomandi *et al.*, 2003; Aiello *et al.*, 2004, 2005; D'Argenio *et al.*, 2004; Ruggieri *et al.*, 2007).

The interpretation of high resolution seismic reflection profiles (Sub-bottom Chirp, Sparker and Watergun) has supported the reconstruction of stratigraphic and structural framework of the continental shelf and slope successions. The seismo-stratigraphic analysis allowed distinguishing the main volcanic and sedimentary seismic units, separated by regional unconformities, tectonically and eustatically controlled. The Dohrn and Magnaghi canyons, eroding the slope up to 1000 m of water depth, represent in the Naples Bay important morpho-structural lineaments, at the boundary between the sedimentary units of the eastern shelf of the Naples Bay and the volcanic units of the western shelf, in correspondence to the Ischia and Procida islands.

The complex stratigraphic architecture of the Naples Bay has revealed, during the Late Quaternary, a strong control of the volcano-tectonic processes in triggering submarine gravity instabilities. This regional geological framework did not allow a simple application of principles

and techniques of seismic and sequence stratigraphy, as described in the guidelines for the redaction of marine geologic cartography (Catalano *et al.*, 1996; Fabbri *et al.*, 2002). Laterally coeval depositional systems, representing portions of system tracts of Late Quaternary depositional sequence have been recognized and their possible mapping has been taken into account for the cartographic representation.

The seismic units have been later interpreted in terms of depositional sequences and corresponding unconformities have been interpreted as Type 1 or Type 2 sequence boundaries and/or as local unconformities, mainly at the top of relic volcanic edifices or at the top of volcanic seismic units (D'Argenio *et al.*, 2004; Aiello *et al.*, 2005; Ruggieri *et al.*, 2007).

The marine geological maps, realized based on the above mentioned criteria shows the distribution of several lithostratigraphic units cropping out at the sea bottom and of the main morphological lineaments, based on the CARG guidelines for the realization of marine cartography (Catalano *et al.*, 1996; Fabbri *et al.*, 2002).

The main stratigraphic units individuated through the analysis of sea bottom sediments belong to the Late Quaternary Depositional Sequence; in this sequence, it is possible to recognize the space and time evolution and the lateral and vertical migration of marine coastal, continental shelf and slope depositional environments in the Late Pleistocene-Holocene glacio-eustatic cycle. The stratigraphic succession studied by geological survey has recorded the variations of the accommodation space of the Late Quaternary deposits during the last 4th order glacio-eustatic cycle, ranging between 128 ky B.P. (Tyrrhenian stage) and the present (isotopic stage 5e).

One aim of the cartography has been the cartographic representation of the lithofacies associations, whose grouping form the depositional elements (which are portions of system tracts), in relation to the morpho-structural lineaments recognized through the geological interpretation of the geophysical data and the dynamics of depositional environments.

In this way, we tried to realize an integration between classical stratigraphic approach, sequence stratigraphic approach and characterization of actual and recent depositional elements. The volcanic activity, which has mainly controlled the stratigraphic architecture of the Naples Bay prevented a classical stratigraphic approach in the marine geological mapping, which has been realized taking into account both the associations of depositional systems and the interstratified volcanic bodies (volcanites and volcanoclastites).

Moreover, this stratigraphic approach allowed obtaining information comparable with other sectors of the Italian continental margins. The last Quaternary sea level rise, having an excursion of about 120 m and a maximum rate in the order of 10 m/1000 years has left a stratigraphic signature on the morphologic and stratigraphic framework of most continental margins of the world (Chappell and Shackleton, 1986). The deposits associated to this process are strongly different in the various areas, as a function of different sediment supply, morphological framework and oceanographic regimes; to map these deposits allows to correlate the unconformities (erosional and non-depositional) and to compare the facies, the internal geometries and the thickness of the deposits recording the sea level rise in a differential way on the several margins.

The key to the geological maps. The key to the geological map n. 465 "Procida" includes the description of the geologic and morphologic elements. The areal geological elements are represented by two superimposed levels: the textural classes distinguished following the classification of Folk (1954), graphically distinguished with halftone screens; the depositional elements, distinguished with the full colour. The superimposition of the environmental information on the textural one allows for a more complete reading of the cartography, furnishing at the same time geological and environmental information. The morphological elements, both areal and linear represent another level of graphic superimposition to the geological information.

Marine geological units. Several volcanic units of substrate have been distinguished, cropping out between the Procida islands, the promontories of Monte di Procida and Capo Miseno and the coastal cliffs off Nisida and Posillipo (Naples town), of a carbonate unit of substrate, cropping out in the Sorrento Peninsula off Massalubrense and of undifferentiated carbonate and volcanic substrates, distinguished in the offshore area based on geophysics.

The Late Quaternary marine geological units are herein described as it follows (Ispra, 2011). The littoral environment is characterized by different types of deposits, which characterize the high relief coasts and the low relief coasts. The toe of cliff deposits, representative of high relief coasts, represent the terms of passage among the sediments of the volcanic units representing the submerged cliffs and the sands and gravels of inner shelf, sometimes with the interposition of submerged cliff sandy belts. In some cases they represent relict isolated bodies and are not yet linked with the supplying reliefs. For the sectors of low coasts, the deposits of submerged beach are represented mostly by sediments which characterize the deposition of the actual beaches. They represent the natural extension in the submerged sectors of the beach deposits occurring along the emerged coastal belt. These deposits join seawards the inner shelf sediments and sometimes occur in narrow belts interposed among the toe of cliff deposits and the inner shelf ones. The littoral environment is characterized by beach rock deposits (Ispra, 2011) occurring in the Ciraccio Bay (Procida island) and in the Genito Gulf (Vivara, Procida). In the first site they are represented by cemented micro-conglomerates composed of volcanic clasts, in the second one they are represented by coarse-to-middle-grained sandstones (Ispra, 2011; De Muro and Orrù, 1999; Kelletat, 2006; Putignano *et al*., 2009; Putignano and Schiattarella, 2010). The deposits of submerged beach are characterized by different lithologic associations, from gravels to fine-grained sands. The grain variations observed in the sediments are related to the hydrodynamic regimes and the wave motion. The distribution of the beach sediments is strictly connected with the morphological characteristics of the coasts and generally represent pocket beach deposits. They are composed of volcanic gravels and litho-bioclastic sands and middle-to-fine-grained litho-bioclastic sands. The deposits of coastal cliff are often represented by rock fall deposits, composed of heterometric blocks, often tufaceous in nature, mainly at the toe of the coastal cliffs of S. Margherita promontory (Vivara, Procida) and Punta Solchiaro (Procida). Another type is represented by the reworked rock fall deposits, composed of heterometric gravels and lying as isolated bodies on the sea bottom, as at Marina Grande, Ciraccio and Pozzo Vecchio (Procida).

The continental shelf is the depositional area localized between the littoral deposits and the shelf break, localized at variable depths among 130 and 170 m. In the Naples Bay this element is localized in correspondence to the retreating heads of the Dohrn and Magnaghi canyons. Different lithofacies associations occur in this environment, related to the hydrodynamic regimes and sedimentary supply. Sandy belts occur, elongated according to the lines of great steepness of the sea bottom. Wide fields of ripples and mega-ripples are diffused in the bathymetric belt among the 20 and 50 meters of water depth. The continental shelf deposits are mainly litho-bioclastic and characterized by different lithological associations, from the gravels to the sands and the pelites and volcanic grains composed of whole pumices or pumice fragments, tuff fragments and scorias. The bioclasts are composed of fragments of Molluscs shells, Echinoderms or benthic foraminifers. The prevalent lithofacies is represented by gravels, sandy gravels and litho-bioclastic coarse grained sands, often occurring with *Posidonia Oceanica* mattes (Ispra, 2011). These associations characterize wide areas of the continental shelf surrounding the Procida island and the Procida channel. Depositional discontinuities are due to the outcropping of rocky substrates, as in the Pozzo Vecchio and in the Corricella areas. A second shelf lithofacies is represented by the middle-to-fine-grained lithobioclastic sands. The main components are represented by pyroclastic fragments (pumices and lapilli) and bioclasts, often abundant. These deposits individuate wide areas of the remnant part of the inner shelf, characterized by low energy sedimentation in flat sea bottoms. These facies

associations are localized in the Ischia Channel in proximity to the lower boundary of the grasses at *Posidonia Oceanica*. The distal inner shelf and the outer shelf are characterized by sandy pelites and shales, pyroclastic in nature, which characterize the depositional areas of the inner shelf. These deposits represent the passage seawards and occur on flat sea bottoms and characterize areas linked to processes of decantation.

Above the 30 m of water depth the continental shelf is characterized by the occurrence of bioclastic deposits, which grade laterally to lithoclastic gravels. The bioclastic deposits are represented by heterometric gravels, gravel sands and bioclastic gravels, which grade laterally to the coarse-grained lithoclastic deposits. The bioclastic deposits are composed of heterometric gravels, gravelly sands and bioclastic sands in a scarce or absent pelitic matrix. They represent the typical maerl facies (Peres and Picard, 1964), where are mainly abundant fragments of Gastropods, Echinoderms, Bryozoans, Serpulids, benthic foraminifers and Corals (Cladocora coespitosa). These bioclastic deposits are often localized in the surroundings of the Posidonia oceanica mattes and in the inter-mattes areas (Corricella and Punta dei Monaci, Procida).

Marine geomorphology. The Procida and Vivara islands, together with the Ischia Island (Phlegrean islands) bound westwards the Naples Bay. They represent volcanic morpho-structural highs uplifted on the continental shelf, constituting the insular portion of the Phlegrean Fields (Figs. 1 and 2). Wide sectors of continental shelf and slope occur in the Naples Bay, characterized by an articulated morphology for the occurrence of relict volcanic edifices (Aiello *et al.*, 2004, 2005), more than the Dohrn and Magnaghi canyons, representing pathways for sediment transport towards the continental slope (D'Argenio *et al.*, 2004; Ruggieri *et al.*, 2007; Di Fiore *et al.*, 2011). Geological structures due to recent fragile deformation occur, sometimes responsible for the tectonic dislocation of the above mentioned elements. The continental portion of the Phlegrean Fields is bounded seawards by the Monte di Procida and the Posillipo promontories (Naples town), among which the Pozzuoli bay occur. The Phlegrean islands are interposed among sectors of continental shelf having different morpho-structures,

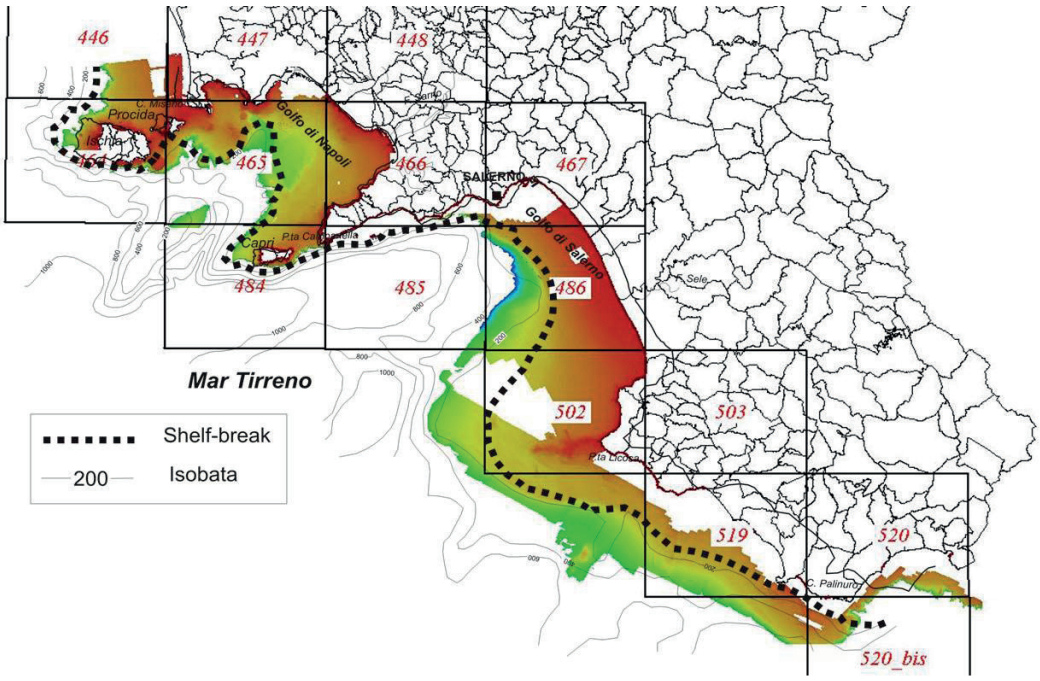

Fig. 1 – Sketch map showing the framework of the geological maps carried out in the Campania region by the CNR-IAMC Institute. Shaded relief bathymetry up to the 200 m isobaths has also been reported.

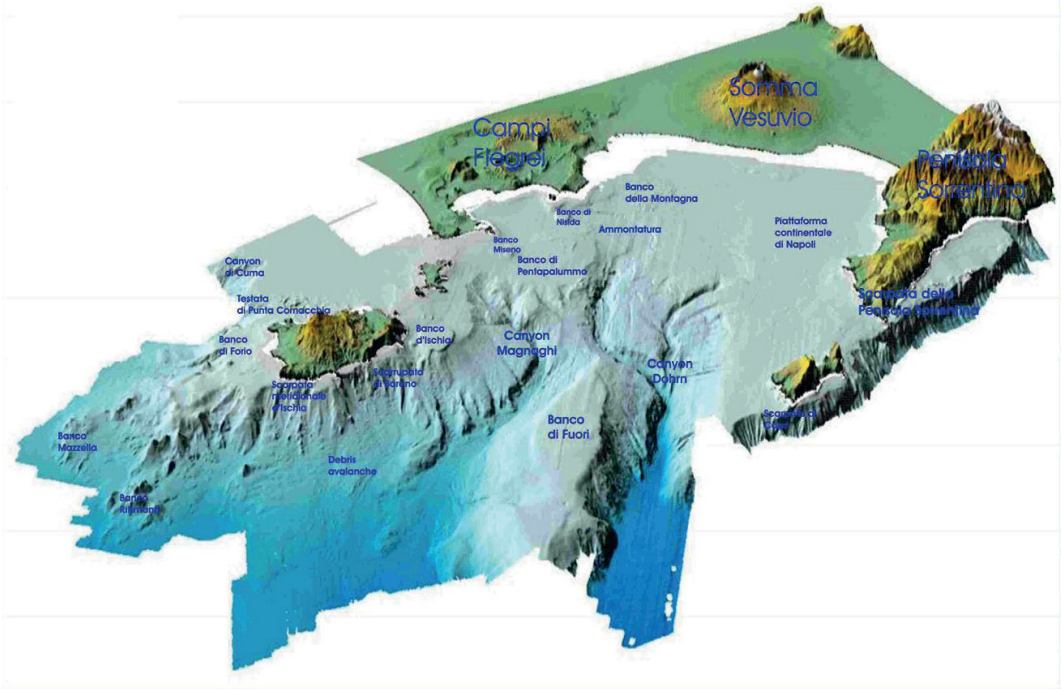

Fig. 2 – Three-dimensional reconstruction of the Naples Bay and Ischia offshore constructed through Multibeam bathymetry. The main morpho-structural lineaments have also been indicated..

separating the sector surrounding the littoral of the southern Latium-northern Campania, characterized by active depositional processes, from the littoral to the south of the Neapolitan area, dominated by the interaction accumulation-erosion.

The sea bottoms ranging among 0 to 30 m of water depth are characterized as the natural geologic and geomorphologic prosecution of the emerged coastal belt. These sectors show morphologic and structural analogies, more than lithologic affinities. The flooding of significant parts of the Italian coasts occurred during recent epochs (post-glacial); moreover, in the Campania area repeated phases of sub-aerial exposure due to tectonic and volcanic setting occurred. A first control on the physiography, structure and evolution of the sea bottoms is due to the coastal typology. It results perhaps evident that a morphologic and morpho-structural reconstruction of these sectors starts from the characteristics related to the sectors of emerged coasts.

The Procida island and the S. Margherita promontory are characterized mainly by high relief coastal cliffs; they represent emerged coastal cliffs, mainly active, extended into the submerged portion with their natural continuity (Ispra, 2011). In particular, the Procida Island is characterized by high sub-vertical coastal cliffs observed along tracts of coasts which, in the north-eastern sector, are the tract among Punta della Lingua and Punta dei Monaci and in the south-eastern sector, the Punta Pizzaco promontory and the Santa Margherita promontory. High coastal cliffs, having gradients ranging between 30° and 40° characterize the coasts of Solchiaro located to the south-east and Punta Pizzaco (Ispra, 2011). The remnant sectors of the shoreline are occupied by narrow sandy belts, surrounded by inactive coastal cliffs, such as in the Chiaia Bay (Procida), where the coastal cliff shows a slightly bent shape, separated by a submerged structural high, which divides the bay into two bays; in the rectilinear coast between Ciraccio and Ciracciello and in the bay from the Punta Serra and Punta Ottimo promontories. The Vivara inlet is distinguished from high coasts directly exposed to the sea erosion. The inner and outer slopes of the crater are very steep, having steepness of more than 40°. The

toe of the submerged cliffs at Vivara is located at a variable depth and is covered by detritic and sandy deposits (Ispra, 2011). Several circular bays rimming the Procida Island give to the island an articulated coastal morphology. These bays coincide with the relicts of the volcanic edifices, whose shapes prolong, in some cases, below the sea level, partially or totally eroded by the wave motion. Their absence in a submarine environment is related also to structural causes, as in the Vivara and Terra Murata cases, where normal faulting has controlled the disarticulation of the volcanic rims or to the sedimentary infill, as in the case of Solchiaro.

Proceeding seawards from the coastal sector of the Chiaiolella beach, starting from a water depth of 40 m up to 20 m, it has been observed the occurrence of steep slopes having a semi-circular trending, related to the volcanic structure of "I Ruommoli" (Aiello *et al*., 2012), whose rim, now completely submerged, is still visible. The general structural setting of the Procida Island is however controlled by numerous volcano-tectonic collapses, also coeval to the formation of several volcanic edifices. NNE-SSW to NE-SW trending structural lineaments seem to prevail at the sea bottom, controlled by the regional tectonic setting of the eastern Tyrrhenian margin.

References

Aiello G., Budillon F., Cristofalo G., D'Argenio B., de Alteriis G., De Lauro M., Ferraro L., Marsella E., Pelosi N., Sacchi M. and Tonielli R.; 2001: *Marine geology and morpho-bathymetry in the Bay of Naples*. In: Faranda F.M., Guglielmo L. and Spezie G. (Eds.) *Structures and Processes of the Mediterranean Ecosystems*, Springer-Verlag Italy, Chapter 1, pp. 1-8.

Aiello G., Angelino A., Marsella E., Ruggieri S. and Siniscalchi A.; (2004): *Carta magnetica di alta risoluzione del Golfo di Napoli (Tirreno meridionale).* Boll. Soc. Geol. Ital., **123**: pp. 333-342.

Aiello G., Angelino A., D'Argenio B., Marsella E., Pelosi N., Ruggieri S. and Siniscalchi A.; (2005): *Buried volcanic structures in the Gulf of Naples (southern Tyrrhenian sea, Italy) resulting from high resolution magnetic survey and seismic profiling.* Annals of Geophysics, **48**: pp. 1-15.

Aiello G., Marsella E. and Passaro S.; (2012): *Stratigraphic and structural setting of the Ischia volcanic complex (Naples Bay, southern Italy) revealed by submarine seismic reflection data.* Rendiconti Lincei, **23 (4)**: pp. 387-408.

Catalano R. *et al.* (1996): *Linee guida alla cartografia geologica marina, scala 1:50.000.* Gruppo di Lavoro del Servizio Geologico Nazionale, Bozza n. 1.

Chappell J. and Shackleton N.J.; (1986): *Oxygen isotopes and sea level.* Nature, **324**: pp. 137-140.

Cinque A., Aucelli P.P.C., Brancaccio L., Mele R., Milia A., Robustelli G., Romano P., Russo F., Russo M., Santangelo N. and Sgambati D. (1997) *Volcanism, tectonics and recent geomorphological change in the Bay of Napoli.* Suppl. Geogr. Fis. Dinam. Quat., III, T2, 123-141.

D'Argenio B., Aiello G. *et al*.; (2004): *Digital elevation model of the Naples Bay and adjacent areas, Eastern Tyrrhenian sea*. In: Atlante di Cartografia Geologica scala 1:50.000 (progetto CARG), Servizio Geologico d'Italia, 32nd International Congress "Firenze 2004", Editore De Agostini, Italy.

De Muro S. and Orrù P.; (1999): *Il contributo delle beach rock nello studio della risalita del mare olocenico. Le beach-rock post-glaciali della Sardegna nord-orientale.* Il Quaternario, **11:** pp. 19-39.

Di Fiore V., Aiello G. and D'Argenio B.; (2011): *Gravity instabilities in the Dohrn canyon (Bay of Naples, southern Tyrrhenian sea): potential wave and tsunami (run-up) reconstruction from a fossil submarine landslide.* Geologica Carpathica, **62 (1):** pp. 55-63.

Fabbri A., Argnani A., Bortoluzzi G., Correggiari A., Gamberi F., Ligi M., Marani M., Penitenti D., Roveri M. and Trincardi F.; (2002): *Carta geologica dei mari italiani alla scala 1:250.000. Guida al rilevamento.* Presidenza del Consiglio dei Ministri, Dipartimento per i Servizi Tecnici Nazionali, Servizio Geologico, Quaderni Serie III, volume 8.

Ispra (2011) *Carta geologica scala 1:10.000 – Isola di Procida.* Regione Campania, Settore Difesa Suolo, Systemcart, Roma, Italy.

Kelletat D. (2006): *Beach rock as sea level indicator? Remarks from a geomorphological point of view.* Journal of Coastal Res., **22 (6):** pp. 1558-1564.

Peres J.M. and Picard J.; (1964): *Noveau manuel de bionomie benthique de la Mer Mediterranee.* Extrait du Recueil des Travaux de la Station Marine d'Endoume, **31 (47)**:, pp. 137.

Perrotta A., Scarpati C., Luongo G. and Morra V.; (2010): *Stratigraphy and volcanological evolution of Campi Flegrei and Procida island, Italy.* In : Stratigraphy and Geology of Volcanic Areas, Geological Society of America Special Papers, **464**: pp. 185-189.

Putignano M.L., Cinque A., Lozej A. and Moccheggiani Carpano C.; (2009) *Late Holocene ground movements in the Phlegrean Volcanic District (Southern Italy): new geoarchaeological evidence from the islands of Vivara and Procida*. Méditerranée, **112**: pp. 43-50.

Putignano M.L. and Schiattarella M.; (2010): *Geomorfologia strutturale e domini di frattura dei fondali marini pericostieri dell'Isola di Procida (Campi Flegrei insulari, Italia meridionale).* Il Quaternario, **23:** pp. 229-242.

Ruggieri S., Aiello G. and Marsella E.; (2007): *Integrated marine geophysical data interpretation of the Naples Bay continental slope.* Boll. Geof. Teor. Appl., **48**: pp. 1-24.

Scarpati C., Cole P. and Perrotta A.; (1993): *The Neapolitan Yellow Tuff: a large volume multiphase eruption from Campi Flegrei, Southern Italy.* Bulletin of Volcanology, **55**: pp. 343-356.

Secomandi M., Paoletti V., Aiello G., Fedi M., Marsella E., Ruggieri S., D'Argenio B. and Rapolla A.; (2003): *Analysis of the magnetic anomaly field of the volcanic district of the Bay of Naples, Italy.* Marine Geophysical Researches, **24**: pp. 207-221.

TOMOGRAFIA SISMICA ED ELETTROMAGNETICA CROSS WELL IN UN ESPERIMENTO SINTETICO DI INIEZIONE DI CO_2 IN ACQUIFERO SALINO

G. Böhm, J. Carcione, D. Gei, S. Picotti
OGS – Istituto Nazionale di Oceanografia e di Geofisica Sperimentale

Introduzione. Il confinamento di CO_2 in strutture geologiche sotterranee è una delle soluzioni che vengono adottate da alcuni anni per ridurre l'effetto serra causato da emissioni di gas inquinanti. La condizione essenziale per poter immettere il gas nel sottosuolo è la presenza di un roccia "serbatoio", permeabile e porosa, che possa contenere il gas e di una roccia "di copertura" impermeabile, che abbia la funzione di sigillo del serbatoio per evitare fuoruscite del gas. Le condizioni migliori per questo scopo si trovano nei giacimenti esauriti di petrolio e gas naturale, nei giacimenti di carbone e negli acquiferi salini. In tutti i casi comunque è necessario, dopo e durante l'immissione del gas, controllare e verificare la presenza di eventuali fuoruscite di anidride carbonica dal giacimento.

Per verificare le potenzialità di monitoraggio del gas nel sottosuolo, in questo lavoro è stato eseguito un esperimento sintetico *cross-well* di propagazione delle onde sismiche ed elettromagnetiche in un modello realistico di acquifero salino parzialmente saturato con CO_2 ed utilizzando la tomografia sismica (velocità ed attenuazione) ed elettromagnetica come strumento di monitoraggio dell'area in esame.

L'esperimento sintetico. È stato eseguito un esperimento sintetico *cross-well* in un modello realistico di acquifero salino confinato da formazioni di scisti (Fig. 1) tra 800 e 1100 m di profondità. I due pozzi distano 160 m tra loro e l'iniezione di CO_2 avviene nel pozzo di destra a 1020 m circa (cerchio nero). Le frecce bianche indicano la migrazione della CO_2 avvenuta dopo l'iniezione e passata attraverso le strutture a destra del pozzo (frecce nere). Sono stati utilizzati 15 punti sorgente sismica ed elettromagnetica inseriti nel pozzo di sinistra ogni 20 m e 29 ricevitori nel pozzo di destra posizionati ad intervalli di 10 m.

Il modello diretto sismico ed elettromagnetico è stato generato in Carcione *et al.* (2012), tenendo conto delle proprietà del mezzo poroso: moduli elastici dei grani, proprietà dei fluidi nello spazio poroso, porosità, contenuto di argilla, permeabilità e conducibilità elettrica. Per mezzo di teorie di fisica delle rocce, sono state calcolate le velocità sismiche, il fattore di qualità, e la conducibilità elettrica delle formazioni prima e dopo l'iniezione di CO_2.

I modelli utilizzati sono quello di White per le proprietà elastiche, e il CRIM (Complex Refractive Index Method), per le proprietà elettromagnetiche. Mettendo insieme le relazioni che descrivono i due modelli, attraverso i parametri comuni (porosità, contenuto d'argilla e saturazione di gas) si ottiene la relazione di *cross-properties* che lega la velocità sismica alla conducibilità elettrica (Carcione *et al*., 2007, 2012).

Algoritmi di simulazione numerica hanno poi permesso di calcolare la risposta sismica ed elettromagnetica ai diversi ricevitori.

Tomografia dei tempi d'arrivo P. Applicando la tomografia dei tempi di arrivo, sono stati invertiti separatamente due gruppi di dati ottenuti dal modello diretto per onde trasmesse P, prima e dopo l'iniezione del gas.

Per entrambe le inversioni è stata applicata la tecnica delle griglie sfalsate utilizzando sia l'algoritmo SIRT che ART, in alternanza, durante le iterazioni. L'utilizzo delle griglie sfalsate (Vesnaver and Böhm, 2000) è un metodo che permette di ottenere un'immagine tomografica finale ad alta risoluzione utilizzando una griglia di base a minor risoluzione ma ben condizionata rispetto al sistema tomografico. La griglia di base viene più volte perturbata nello spazio (nelle due direzioni degli assi) e per ciascuna griglia si applica separatamente l'inversione. I singoli risultati ottenuti dalla tomografia vengono sommati e mediati su un'unica griglia finale ad alta risoluzione che, pur essendo più fine, ha la stessa alta attendibilità delle griglie a minor risoluzione.

In questo esperimento è stata utilizzata una griglia di base di 10x17 pixels. La scelta delle dimensioni della griglia viene fatta dopo un'analisi dello spazio nullo (attendibilità) del sistema tomografico usato (griglia e raggi) per diverse griglie, scegliendo quella che risulta a maggior risoluzione pur mantenendo un'alta attendibilità.

Nelle singole inversioni, inoltre, sono stati utilizzati solo i raggi con angolo minore di 30° dall'orizzontale, escludendo gli arrivi da sorgenti e ricevitori lontani; questo per eliminare parzialmente l'effetto di "*smearing*" presente sui valori di velocità lungo le direzioni dei raggi, che in questo caso viene accentuato e che introduce artefatti sul risultato finale.

Tomografia dell'attenuazione. In questo esperimento sono stati anche presi in considerazione i valori dell'attenuazione intrinseca dell'area investigata, definiti dal fattore di qualità Q associato alle onde P. Dalla teoria mesoscopica della fisica delle rocce (Carcione, 2007) si è calcolato un valore realistico della distribuzione del Q come funzione della porosità, saturazione del gas, contenuto di argilla e permeabilità (Carcione *et al.*, 2012). Nel modello qui simulato l'attenuazione è dovuta alla presenza dell'anidride carbonica immessa dal pozzo; per cui nella fase precedente (pre-iniezione), ipotizzando il mezzo saturo d'acqua, il valore Q è considerato costante su tutta l'area.

Il metodo usato per la stima del Q, è basato sul calcolo dello spostamento delle frequenze dovuto all'attenuazione (Quan-Harris, 1997). Il metodo sfrutta il fatto che, a causa dell'attenuazione, parte delle alte frequenze del segnale iniziale decrescono in ampiezza mentre l'onda si propaga nelle formazioni, spostando il centroide dello spettro verso basse frequenze. Questo spostamento si calcola come differenza tra il centroide dello spettro dell'ondina di riferimento (segnale prodotto dalla sorgente) e il centroide dello spettro dell'ondina del segnale riflesso/trasmesso (segnale d'arrivo). Il modello del fattore di qualità Q dell'area indagata si può determinare con la tomografia d'attenuazione, allo stesso modo con cui si stima il valore di velocità di propagazione dell'onda attraverso l'inversione dei tempi d'arrivo dell'onda stessa (tomografia sismica).

La misura dello spostamento in frequenza è data dall'equazione (1), ottimale per spettri di tipo Gaussiano, dove f_s ed f_r sono rispettivamente i baricentri dello spettro di riferimento (sorgente) e dello spettro da analizzare, mentre σ_s^2 è la varianza dello spettro di riferimento.

$$\xi = (f_s - f_r) / \sigma_s^2 \qquad (1)$$

Questo valore, che rappresenta l'attenuazione $\alpha_0 = \pi/QV$ (dove Q è il fattore di qualità del mezzo attraversato e V è la velocità) può essere calcolato nel modello utilizzando i raggi di propagazione dell'onda all'interno del mezzo indagato. La stima di Q per ciascun pixel del modello può essere ottenuta attraverso la stessa procedura tomografica utilizzata per l'inversione dei tempi d'arrivo dell'onda P (Rossi *et al.*, 2007) considerando i residui come differenza tra $\boldsymbol{\alpha_0}$, misura calcolata, e $\boldsymbol{\zeta}$, misura osseravata (definendo $\boldsymbol{f_r}$ il baricentro dello spettro riferito all'ondina centrata sul tempo di picking considerato per l'inversione).

Tomografia elettromagnetica. Nell'ambito di questo esperimento è stato eseguito anche un test con dati elettromagnetici, diverso dal metodo ERT (Electrical Resistivity Tomography), più comunemente utilizzato. Il modello diretto è stato calcolato generando un impulso elettromagnetico nelle varie posizioni dei punti sorgente e registrando nei singoli ricevitori

il tempo di propagazione del picco massimo della corrispondente onda elettromagnetica che attraversa il campo di diffusività ottenuto dal modello di conducibilità elettrica dalla relazione:

$$\sigma = \frac{1}{\mu D} \qquad (2)$$

dove D è la diffusività del campo elettromagnetico, σ è la conducibilità elettrica e μ è la permeabilità magnetica del vuoto, una costante pari a $4\pi 10^{-7}$.

Anche in questo caso può essere utilizzata una relazione simile a quella che lega il tempo d'arrivo dell'onda sismica con il campo di velocità dell'onda stessa, applicando la teoria dei raggi ed il principio di Fermat (Carcione et. al, 2012). Qui viene considerata la relazione:

$$\sqrt{t_p} = \frac{1}{2}\int_{x_1}^{x_2} \frac{ds}{\sqrt{D}} \qquad (3)$$

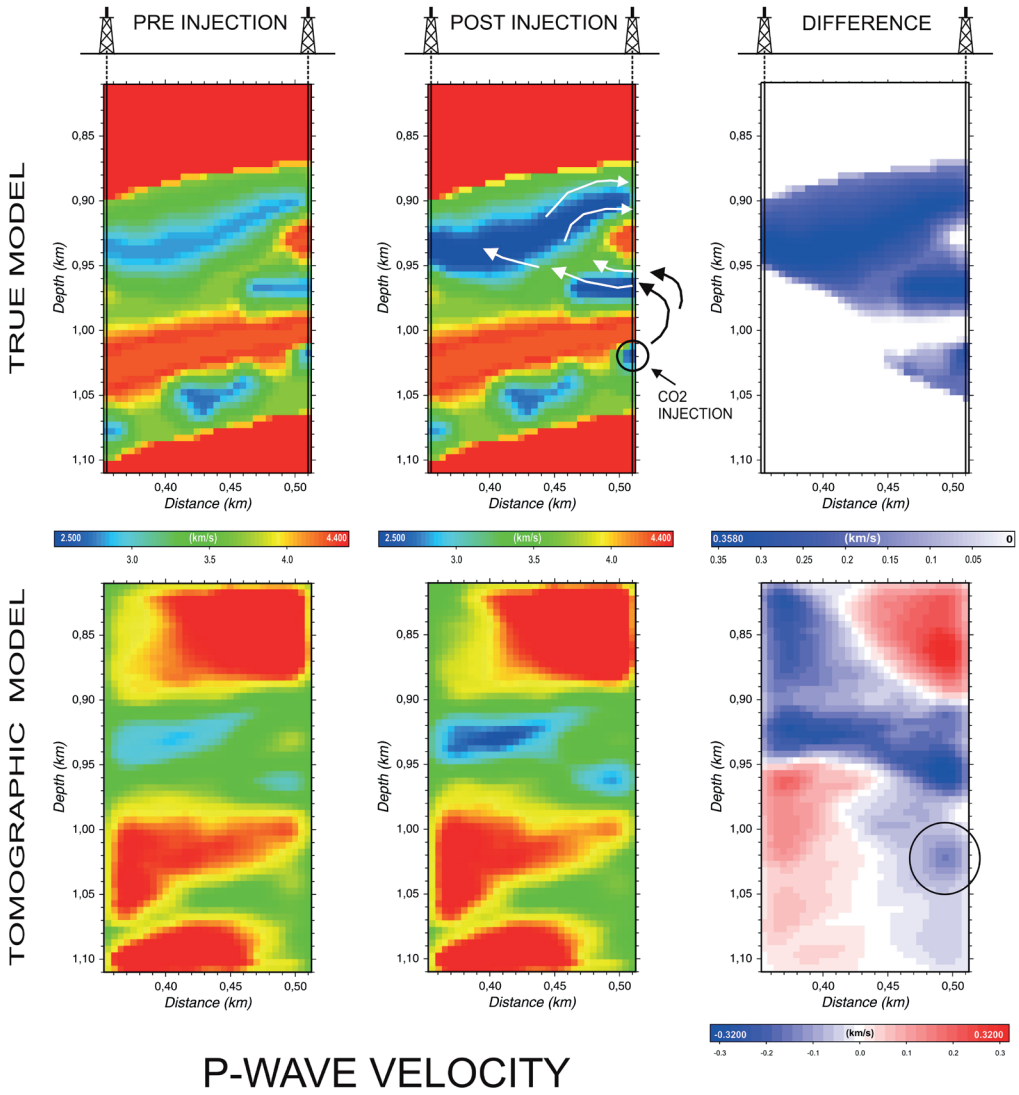

Fig.1 – Rappresentazione del campo di velocità P (prima e dopo l'iniezione del gas) nel modello sintetico utilizzato per l'esperimento. In alto il modello vero, in basso il risultato della tomografia. A destra le rispettive differenze di velocità tra prima e dopo l'iniezione.

dove *tp* è il tempo di propagazione dell'onda elettromagnetica e *D* è il valore della diffusività associato all'area attraversata dall'onda stessa. Dall'inversione di questi tempi si ottiene quindi la diffusività che viene poi convertita in conducibilità elettrica dalla relazione (2).

Risultati. In Fig. 1 viene rappresentato il risultato dell'inversione dei tempi d'arrivo dell'onda sismica trasmessa tra i due pozzi nei due casi, prima e dopo l'iniezione della CO_2. In alto della figura sono visibili i campi di velocità P del modello vero (utilizzato per generare i dati sismici), mentre in basso sono rappresentati i rispettivi campi di velocità ottenuti dalla tomografia. A destra di entrambi sono raffigurati i valori di velocità come differenze tra prima e dopo l'immisione del gas, rispettivamente per il modello vero e per il modello risultato della tomografia. Si può osservare come nel risultato tomografico siano ben rappresentate le zone di anomalia negativa di velocità dovute alla presenza del gas, anche se i valori di velocità sono generalmente sottostimati; ma questa sottostima è una caratteristica intrinseca dell'algoritmo di inversione nel caso di zone a bassa velocità, legato al tracciamento dei raggi (effetto Wielandt: Wielandt, 1987). In particolare l'immagine delle differenze (in basso a destra) tra il risultato dell'inversione prima e dopo l'immissione del gas riproduce bene le effettive differenze calcolate dal modello vero (immagine in alto a destra), anche per la ristretta zona del punto d'immissione (cerchio nero).

Anche l'inversione dell'attenuazione (Fig. 2), calcolata solo per il caso *post*-iniezione, ha messo bene in evidenza le zone a più alta attenuazione (basso valore di *Q*) presenti nel modello vero e corrispondenti alla presenza del gas iniettato.

Il risultato dell'inversione dai dati elettromagnetici è mostrato invece in Fig. 3. Anche qui, come per il caso sismico, il modello vero della distribuzione della conducibilità elettrica è

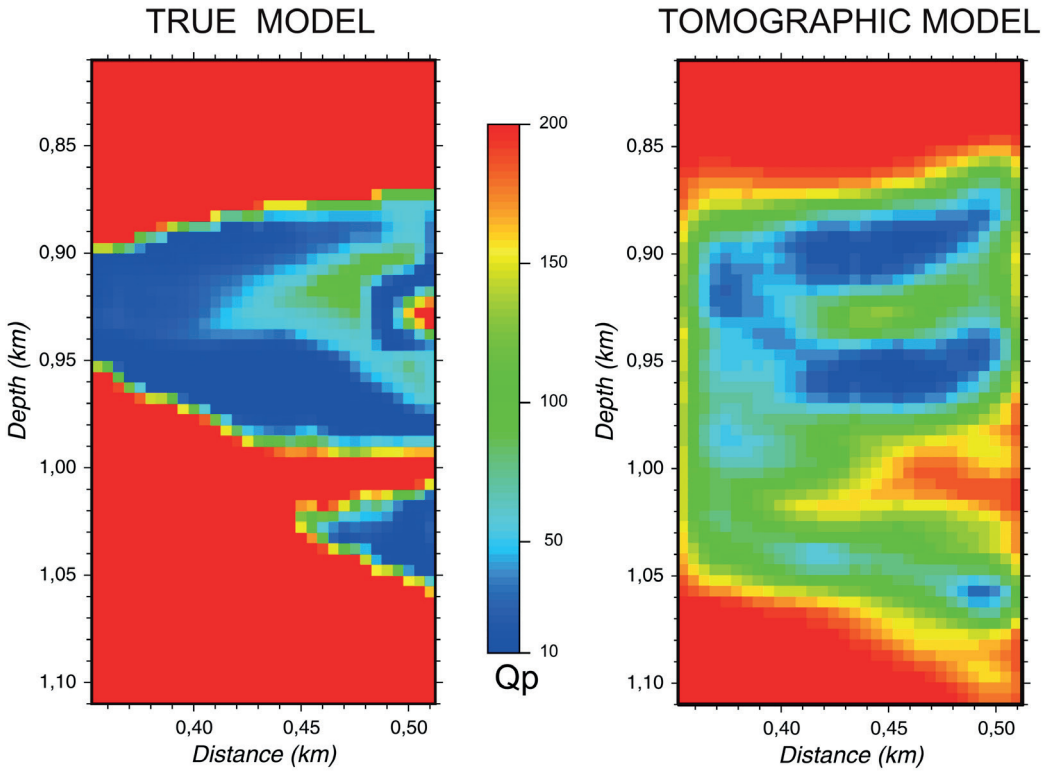

Fig. 2 – Rappresentazione dei valori di *Q* dopo l'iniezione del gas. A sinistra i valori riferiti al modello vero, a destra il risultato della tomografia.

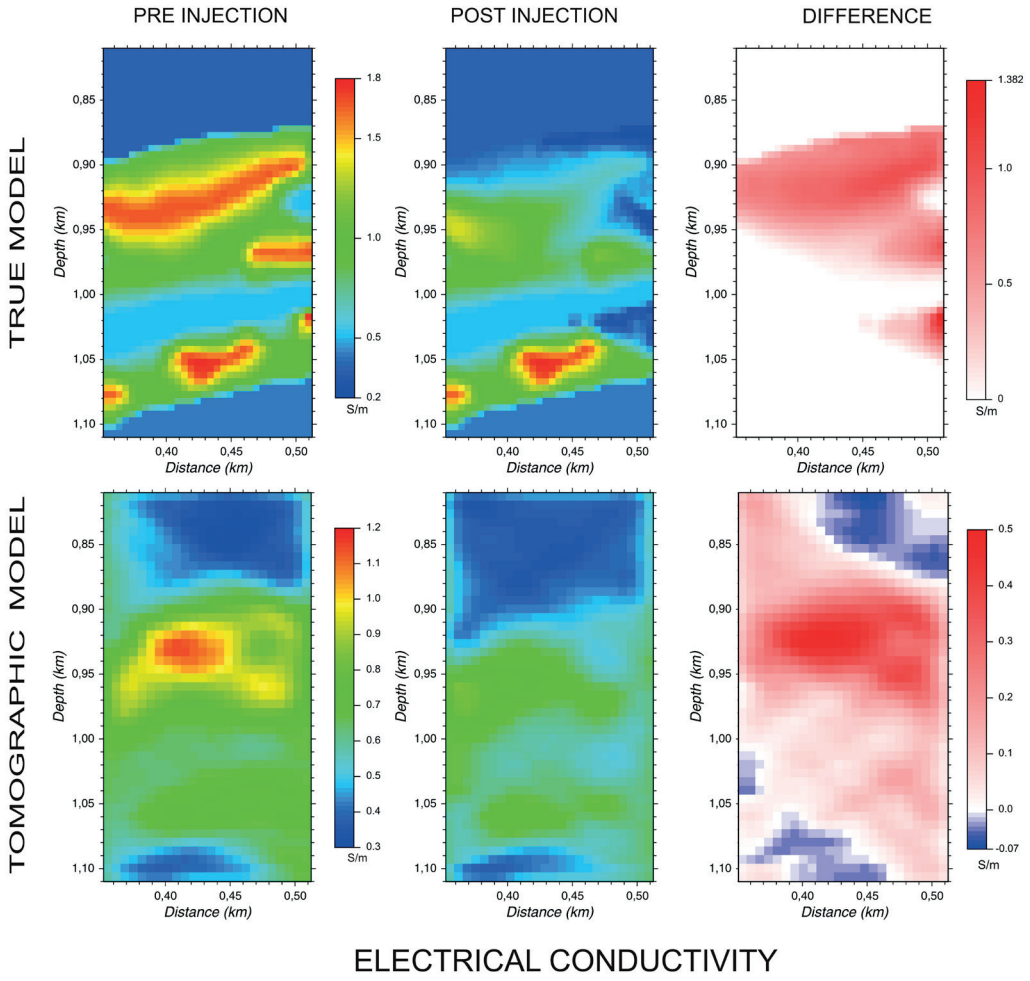

Fig. 3 – Valori della conducibilità elettrica (prima e dopo l'iniezione del gas) nel modello sintetico utilizzato per l'esperimento. In alto il modello vero, in basso i valori di conducibilità ottenuti dalla tomografia dei dati elettromagnetici (vedi testo). A destra le rispettive differenze di conducibilità tra prima e dopo l'iniezione.

rappresentato dalle immagini in alto mentre il risultato della tomografia è visibile nelle figure in basso. Si osserva che l'inversione ha generalmente sottostimato i valori di conducibilità elettrica sia prima che dopo l'iniezione dl gas; l'immagine delle differenze, che rappresenta il dato più interessante dal punto di vista dell'indagine di monitoraggio, identifica invece correttamente le zone caratterizzate dalla presenza del gas, riproducendo abbastanza bene anche la corrispondente immagine riferita al modello vero.

Conclusioni. La tecnica del *"time-lapse"* si basa sull'analisi delle differenze osservate da indagini geofisiche fatte in tempi diversi sulla medesima area e viene utilizzata per monitorare e misurare le proprietà di un giacimento durante la vita del giacimento stesso. In questo lavoro la tecnica tomografica dei tempi d'arrivo è stata applicata a dati sismici ed elettromagnetici *cross-well* generati in un esperimento sintetico di iniezione di CO_2 in un acquifero salino, per individuare la presenza della CO_2 dopo l'iniezione del gas.

Le differenze tra i risultati delle inversioni prima e dopo l'iniezione del gas hanno permesso di individuare le zone parzialmente saturate di CO_2 all'interno dell'area investigata tra i due pozzi. In un ipotetico esperimento reale, i valori di saturazione ottenuti sia dall'approccio sismico

(velocità e *Q*) che da quello elettromagnetico (conducibilità elettrica) potrebbero essere usati per verificare la relazione di *cross-properties* tra le proprietà sismiche ed elettromagnetiche.

Riconoscimenti. Gli autori ringraziano il Dr. Alberto Michelini per le utili discussioni fatte durante questo lavoro. Per tutti i casi d'inversione è stato utilizzato il software tomografico CAT3D.

Bibliografia

Carcione J. M., Ursin B. and Nordskag J. I.; 2007. *Cross-property relations between electrical conductivity and the seismic velocity of rocks*. Geophysics **72**, E193-E204.

Carcione J. M., Gei D., Picotti S. and Michelini, A.; 2012. *Cross-hole electromagnetic and seismic modeling for CO2 detection and monitoring in a saline aquifer.* Journal of Petroleum Science and Engineering, **100**, 162-172.

Quan Y. and Harris J.M.; 1997. *Seismic attenuation tomography using the frequency shift method*. Geophysics **62**, 895–905.

Rossi G., Gei D., Böhm G., Madrussani G. and Carcione J.M.; 2007. *Attenuation tomography: an application to gas-hydrate and free-gas detection*. Geophysical Prospecting, **55**, 655 – 669.

Vesnaver A. and Böhm G.; 2000. *Staggered or adapted grids for seismic tomography?* The Leading Edge, **19**, 944-950.

Wielandt, E.; 1987. *On the validity of the ray approximation for interpreting delay times;* in Seismic Tomography, edited by G. Nolet, pp. 85-98, D. Reidel, Norwell, Mass.

FIRST RESULTS OF WATERBORNE GEOPHYSICAL SURVEYS AROUND THE MALPASSO SITE (TUORO SUL TRASIMENO, ITALY) FOR GEOLOGICAL AND ARCHEOLOGICAL CHARACTERIZATION

L. Borgia[1], C. Colombero[2], C. Comina[2], F. Del Bianco[3], L. Gasperini[3], F. Priore[4], L. Sambuelli[5], G. Stanghellini[3], S. Trippetti[6]

[1] Assessore alla cultura, Comune di Tuoro sul Trasimeno, Italy
[2] DST - Università di Torino, Italy
[3] ISMAR - CNR, Italy
[4] DiFeST - Università di Parma, Italy
[5] DIATI - Politecnico di Torino, Italy
[6] Archeologa, Rotta dei Fenici/Cammino di Annibale, Itinerari Culturali del Consiglio d'Europa, Italy

Introduction. Geological characterization of shallow sediments in water-covered areas is a difficult task with traditional survey techniques. Direct investigations are indeed often neither cost-effective nor reasonably quick and adequate in number to cover the whole surface of a basin and to obtain a reliable correlation of data over a wide area. Geophysical techniques can conversely be very useful to investigate sediments which are entirely located beneath a water-covered area. This could allow for an uniformly spaced, even if indirect, investigation of the interested site. The integration of seismic and non-seismic waterborne surveys can be of great aid in defining related geological properties; the use of non-seismic methods to study shallow inland water is relatively recent but is becoming more and more diffused. Indeed electrical resistivity is very sensitive to fluid phases and clay content, while seismic waves are sensitive to the mechanical properties of the soil skeleton. Therefore a combination and integration of the two methodologies can offer a more complete geological characterization. In this respect we present in this paper preliminary results of waterborne seismic and electrical geophysical surveys on the nothern shore of the Trasimeno Lake in an area around the Malpasso site (Fig. 1).

The Trasimeno lake, located in the Umbria Region of Central Italy, is the broadest lake of the Italian Peninsula, covering about 120 km^2. The extremely low depths, the flat bottom morphology, and the absence of natural outflows and dams along its shorelines caused periodical floods since ancient times, only partially attenuated by creation of an artificial outflows. In contrast to most lakes in Central Italy (Bolsena, Vico, Bracciano, Monterosi, Albano) Trasimeno lake does not fill a volcanic crater, but its origin is related to tectonic processes. In fact, it underwent a complex geological evolution, from a marine gulf in the Early Pliocene, to a subsiding tectonic depression starting in Middle Pleistocene to present (Gasperini *et al*., 2010).

Given this overall interesting geological setting, the area around the Malpasso site (*Fig. 1*) is also particularly characterized by the presence of an emerging sandstone formation protruding towards the lake and is moreover interesting from the archeological point of view. Several historical reconstructions suggest indeed that within this area, and particularly in the Tuoro plain, the Trasimeno battle (217 a.C.) took place. This battle was one of the most important episodes of the II Punic war and it was fought between the army of the Carthaginian general Hannibal and two Roman legions under the command of the consul Caius Flaminius. New evidences related to historical level fluctuations of the lake and more careful reading of the sources and a critical analysis of previous studies have been significant in respect to a positive identification of this site as a most probable location of the battle (Brizzi and Gambini, 2008). The actual shore line leave only a short passage between the lake itself and the Malpasso (Fig. 1), while the same should be wider in ancient times to allow for the passage of huge armies. In this respect the findings of several dated ceramic materials has shown that for long periods in the Etruscan and Roman times lake levels were usually lower than the present (Cattuto *et al.*, 2011).

With the aims of both reconstructing the geological setting of the area around the Malpasso site and to eventually find some localized remains of the battle we carried out several waterborne geophysical surveys on the area. Adopted methodologies were: magnetic surveys, seismic reflection Chirp Sonar surveys and Continuous Vertical Electric Soundings (CVES) profiles. Within this paper we report some preliminary results along an example profile (Fig. 1) for the last two methodologies underlining the main evidences observed and further planned processing on the data and data integration.

Materials And Methods. Seismic reflection profiles were collected using a Benthos Chirp III system with 4 transducers mounted on board of a small catamaran towed by the boat. Data were collected using a pulse length of 5 ms, a frequency sweep from 2 to 7 kHz, and a digitally sampled at 16 kHz rate. Seismic data were stored in SEGY files, after deconvolution and instantaneous amplitudes computation. Data processing was carried out using SeisPrho (Gasperini and Stanghellini, 2009) and included static correction, filtering and automatic gain control. Vertical resolution of acoustic images is <10 cm; maximum penetration reached, about 10 m.

CVES measurements were obtained by the use of an array of nine electrodes fixed on a floating cable dragged by a boat. The array has two current electrodes, in the cable part closest to the boat, followed by seven potential electrodes. The current electrodes were 16 m apart, while the six couples of potential electrodes in dipole-dipole configuration had exponentially increasing spacing from 0.5 to 16 m. The first potential electrode was 0.5 m from the farthest current electrode. This configuration allowed a maximum depth penetration similar to the seismic one. The towed cable floated on the lake surface thanks to appropriate plastic floaters and was kept stretched by a floating anchor fixed at its end. A multichannel georesistivimeter (Syscal-pro by Iris Instruments in Sysmar update) was used to simultaneously acquire the six potential measurements. The acquisitions were treated with a Laterally Constrained Inversion (LCI) process. The LCI approach was developed to invert vertical electrical sounding data acquired along a profile by Auken and Christiansen (2004), using a pseudo-2D layered parameterization of the investigated geological medium and has been implemented in Matlab environment (Sambuelli *et al.*, 2011). The inversion result of LCI is a set of 1D resistivity models, each of which corresponds to a sounding. All the soundings are inverted simultaneously by minimizing a common objective function, which contains the acquired data, the available a priori information and the constraints. Through the lateral constraints, information from one electro-stratigraphic section are then interconnected with the neighboring ones, producing a smoothly varying 2D section.

Both surveys are accurately georeferenced by means of independent GPS acquisition to allow for data integration.

Fig. 1. – Investigated area along the northern shore of the Trasimeno Lake near the Malpasso site. Evidence of the survey line along which the results of geophysical profiles are reported in Fig. 2.

Results and discussions. Both surveys covered the area reported in Fig. 1 in order to obtain a detailed investigation of the surveyed site. We focus here on two almost parallel profiles along a line starting close to the lake northern shore toward the lake center (Fig. 1).

In Fig. 2a the results of the Chirp sonar profile is reported. The lake floor along this profile is almost flat, slightly dipping toward south, and is marked by a weak reflection at about, on average, 3 meter of water depth, partial hidden by the direct wave. We note two main seismic units, a transparent, fine layered upper unit overlaying a lower more reflective unit, showing high-amplitude internal reflectors. The boundary between these units is a dome-shape reflector (U1), which marks a relatively high acoustic impedance contrast. In the first (northern) part of the profile, the presence of gas in the sediment hamper the penetration of the signal down to few decimeters below the lake floor. The observation that the top of gas-bearing deposits is a strong reflector (U0) might indicate early diagenesis due to fluid circulation. The upper unit is punctuated by hyperbolic reflections in the southern, more distal part of the profiles. Observation that these hyperbolas result aligned in correspondence of U0 might suggests a similar origin for such features.

In Fig. 2b the results of the LCI inversion of CVES data approximately acquired along the same profile are reported. The thickness of the low resistivity water layer (average constant resistivity of 7 Ω·m) has been constrained in the inversion thanks to a contemporary acquired bathymetry profile which evidences a lake bottom slightly dipping toward south coherently with the sonar survey. Within the lake sediments it is possible to evidence two low resistivity variations: a reduced increase in resistivity (R1) along an interface which roughly matches the dome-shaped reflector U1 evidenced from the seismic reflection line; this interface can be followed also at the beginning of the profile where the penetration of the seismic signal is hampered by gas bearing sediments. Secondly a slightly more marked decrease in resistivity (R0) is noted towards the lake center with an abrupt change just after the rift of the previous dome. This second resistivity variation appears to be not noted in the seismic reflection line.

Even if these are only preliminary results of the surveys and more accurate and complete comparison over the whole surveyed area, with precise location of each survey line, must be undertaken, it is possible to evidence that both of the surveys have evidenced the presence of a submerged interface within the sediments showing a dome shape that can be related to a more compacted/resistive material probably associable to the ancient shore line. The evidence of lower resistivity sediments in front of this anomaly can support this hypothesis. Moreover electrical surveys mapped this interface for the whole survey area allowing a spatial 2D reconstruction of the this layer; they have also locally evidenced the presence of sandstone formation protruding down the lake bottom near the shore.

Conclusions. Preliminary results of both seismic Chirp Sonar reflection lines and CVES profiles over the survey area have evidenced their potentiality in characterizing the bottom sediments of the area around the Malpasso which is interesting both from the geological and archeological point of views. The results of the two different surveys seem to match in first approximation. However further studies are necessary to allow for an unique reconstruction of the geological setting respectful of both the surveys evidences. In this respect, accurate data

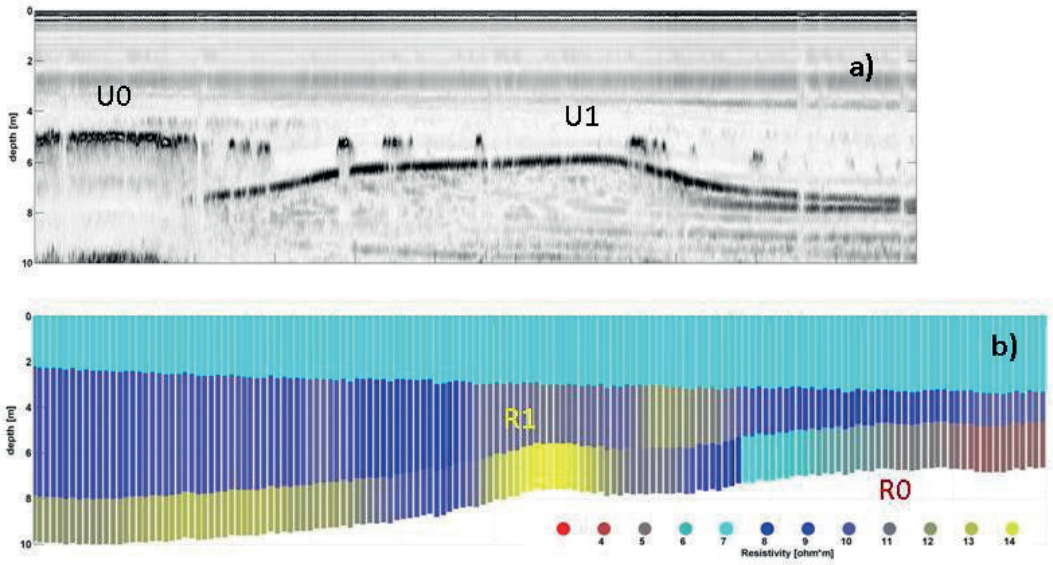

Fig. 2. – Two examples of waterborn geophysical surveys in the investigated area along the survey line of Fig. 1: a) Chirp sonar profile and b) LCI inversion of the CVES survey.

integration must be undertaken; particularly inversions of the CVES data with the a priori constrained interfaces evidenced from the seismic reflection campaigns are planned.

Acknowledgements. The Authors are grateful to the Tuoro sul Trasimeno Municipality, Umbria Region, Perugia county, Soprintendenza per i Beni Archeologici dell'Umbria, Rotta dei Fenici-Cammino di Annibale, Legambiente for their logistic support in field testing.

References

Auken E and Christiansen AV (2004) Layered and laterally constrained 2D inversion of resistivity data. Geophysics, 69, 752-761.

Brizzi G and Gambini E, (2008) Di nuovo sulla battaglia del Trasimeno: qualche ulteriore considerazione, in G. Brizzi, G. Poma (a cura di), «Rivista storica dell'antichità», XXXVII, 2007, Università degli Studi di Bologna –Dipartimento di Storia Antica, Bologna, Pàtron Editore, 77-100.

Cattuto C., Gambini E. and Marinelli C., (2011) Il Trasimeno. La complessa gestione di un lago laminare (con contributi di A. Batinti e O. Fillanti; illustrazioni di G. e M. Agabitini, E. Pasquali e D. Spedaliere), Perugia, EFFE Fabrizio Fabbri Editore, pp. XV, 502.

Gasperini L, Barchi MR, Bellucci LG, Bortoluzzi G, Ligi M and Pauselli C (2010) Tectonostratigraphy of Lake Trasimeno (Italy) and the geological evolution of the Northern Apennines, TECTONOPHYSICS, Volume: 492 Issue: 1-4,164-174.

Gasperini L, Stanghellini G, (2009) SEISPRHO: An interactive computer program for processing and interpretation of high-resolution seismic reflection profiles, COMPUTERS & GEOSCIENCES, 35, 7,1497-1507.

Sambuelli L., Comina C, Bava S and Piatti C (2011) Magnetic, electrical, and GPR waterborne surveys of moraine deposits beneath a lake: a case history from Turin, Italy, Geophysics, 76, 1-12.

3D GEOPHYSICAL MODELLING OF THE VAJONT LANDSLIDE

R. Francese, M. Giorgi, G. Böhm
OGS - Istituto Nazionale di Oceanografia e di Geofisica Sperimentale, Trieste, Italy

Introduction and Motivations. The 1963 Vajont landslide, mostly because of its size and of the catastrophic effects, has been studied for several tens of years by many different authors (Selli and Trevisan, 1964; Rossi and Semenza, 1965; Martinis, 1978; Hendron and Patton, 1985; Semenza and Ghirotti, 2000). The majority of the studies focused on the triggering mechanisms (Kilburn and Petley, 2003) and on the post-failure geology. A comprehensive review is given by Semenza and Ghirotti (2005). Although the collapse has been largely studied some of the factors controlling the dynamic of the movement are still not completely clear. Among the major issues there is the high velocity of the sliding mass itself and the movement almost as a unitary rock block that caused such an unexpected large wave.

A geophysical parameterization of the landslide body could result in a better insight in both in the understanding of the geometry settings and the topology of the collapsed units and in a better estimate of the changes of the elastic properties caused by the collapse. This last information could be used as a vital constrain in the recently developed collapse model. Very few geophysical data are presently available for the landslide body. Some measurements of the P- and S- wave velocity were undertaken on the northern scarp of the *Monte Toc* before the collapse but with conflicting results and no clear indications about the rock quality (Caloi and Spadea, 1960, 1961). After the collapse, on behalf of the Court of Belluno, was carried out a seismic campaign with P-wave velocity and borehole sonic measurements on the landslide body (Morelli and Carabelli, 1965).

A new and comprehensive geophysical investigation, based on 2D and 3D seismic and resistivity imaging was then undertaken since the year 2011 and it's still in progress. This geophysical experiment was designed and conducted integrating the re-interpreted geological (Bistacchi *et al.*, 2013) and structural data (Massironi *et al.*, 2013). A novel series of borehole stratigraphies made recently available by ENEL were also incorporated in the geophysical modelling. Finally some accurate surface models obtained processing aerial and terrestrial laser data were extremely useful to constrain the inversion of resistivity and seismic data and to properly account for the deformation of the electrical field caused by the rough topography.

A geophysical profile collected along the rock wall below Casso on the other side of the Vajont valley was used a reference for the geophysical response of the geological units involved in the landslide. The geophysical images of the landslide body, especially in the near surface, showed a very good correlation with the post-failure geology (Rossi and Semenza, 1965).

An initial correlation between lithology and physical parameters has been proposed for the various geological units embedded in the landslide mass. This 3D physical model of the landslide introduces a series of new constrains for an accurate numerical simulation of the landslide kinematics.

Geological setting. Geology in the Vajont valley is comprised of a Jurassic-Cretaceous carbonate sequence (Carloni and Mazzanti, 1974; Semenza, 1965; Martinis, 1978). The thickness of the various formations, at the landslide scale, could be considered roughly constant. The base of the Jurassic sequence is marked by a massive (Vajont Formation) limestone (350-400 m) overtopped by a layered cherty (10-40 m) limestone (Fonzaso Formation) and followed by the nodular limestone of the Ammonitico Rosso Formation (15 m). The Cretaceous sequence is comprised of the Soccher Limestone (200-250 m) and of the layered marly limestones and marls of the Scaglia Rossa Formation (about 300 m). The upper part of the Fonzaso Formation and the Soccher Limestone Formation were involved in the landslide. Rossi and Semenza (1965), analyzing the post-failure accumulation, mapped six different lithological members indicated with letters from *a* to *f* (from the older to the youngest).

Some very thin clayey interbeds were identified in the upper part of the Fonzaso Formation (unit *a'*) and indicated by Hendron and Patton (1985) as the stratigraphic level where the initial sliding happened. There are just few outcrops of this unit as during the failure the unit was dragged and crunched along the sliding surface. The bottom level of unit *a''* is represented by the Ammonitico Rosso Formation (Rossi and Semenza, 1965) while the body of unit *a''* is comprised of an alternation of layered cherty limestone and marly limestones. Unit *b* is represented by a thin conglomerate layer and it is very important because it represents an isochron surface and it's a marker level within the landslide. Units *c*, *d* and *e* are comprised of massive limestones grading to layered marly and cherty limestones. Finally unit *f* represents the top of the Soccher Formation and it is comprised of layered marly cherty limestones.

A review of available structural data, associated with some new field observations, has been recently completed (Massironi *et al*., 2013). According to these data the E-W trending Erto syncline (Giudici and Semenza, 1960) is further folded by a N-S trending syncline with it's axis elongated along the pre-landslide Massalezza valley. The interference of these two sets is exposed on the sliding surface and in some cases the undulations generated steps that interrupted the continuity of the surface itself.

The ensemble of these structural features appears to be a major constrain in the kinematics of the landslide. In particular the association of the stratigraphy and of the N-trending bedding planes with the curved shape of the sliding surface converging on the Massalezza valley behave as a track for the 1963 failure.

The physical database. The success of the geophysical experiment, in reconstructing the landslide stratigraphy and structure, strongly depends on the possibility of measuring some key properties of the in-situ formations. A reliable and accurate physical reference model of the upper part of the Fonzaso Formation and of the Soccher Limestone Formation was then constructed to reduce the uncertainty in correlating physical properties (e.g. velocity and resistivity) to specific lithological units. This robust tie could be also a constrain while attempting to estimate the degree of fracturing of the landslide mass itself. The first indicator of physical properties is the rock coherency. Hard rocks (HR) will be probably characterized both by high velocity and high resistivity while soft rocks (SR) are generally low velocity and low resistivity. In this simplified approach units *a'*, *a''* and *f* could be classified as moderately soft rocks while units *b*, *c*, *d* and *e* are mostly referable to moderately hard rocks.

Some of the boreholes drilled on the landslide accumulations where also used as major constrains in assisting geophysical data analysis, processing and interpretation. The majority of these boreholes reached the depth of the in-situ bedrock.

The few geophysical data available for the left side of the Vajont valley, before the failure, are represented by four seismic profiles collected immediately after the discovery of the paleolandslide (Caloi and Spadea, 1960, 1961). Results from a first seismic survey indicated how the P-wave velocity in the uppermost layers was higher than 5000 m/s. Some authors (Semenza, 1965; 2001; Selli and Trevisan, 1964) pointed out that these values appear to be too high also for compact limestones. A second seismic survey (Semenza, 2001) carried out after the discovery of the perimetrical crack, showed more realistic P-wave velocities around 2500-3000 m/s. The Court of Belluno to collect new evidences for the trail during the preparation of the case required a new seismic survey. The major purpose of this new survey was to collect data inside and outside the landslide area. Seismic velocities were measured at few locations (Morelli and Carabelli, 2005) inside and outside the landslide area. Unfortunately the measurements on the landslide body were carried out in boreholes mostly below the sliding surface making this new data not directly comparable with the previous surveys. Other measurements carried out on the Cretaceous sequence outside the landslide show P-wave velocities ranging from 2100 m/s to 3000 m/s. These numbers are more and less similar to the values measured during the second seismic survey before the failure.

Under a theoretical point of view (Telford *et al.*, 1990; Dobrin and Savit, 1988) the seismic and electrical properties of a medium mostly depend upon density (also related to lithology and age), porosity and fluid content. Water in the Vajont landslide body is almost absent due to the very high permeability of the collapsed mass. The water table in the accumulation is directly related to the water level in the residual lake located eastern than the landslide body. Several attempts to measure the water level in the boreholes were made but a water table has been never detected. The unknowns are then two: lithology and porosity (or fracturing) and in the equation there is just one parameter (velocity and resistivity). To reduce the uncertainty resistivity and seismic velocities should be measured on the same formations but outside the landslide. For this purpose a reference geophysical profile was then collected along the rock wall below the village of Casso. On this rock wall there is almost a full exposure of the geological sequence involved in the landslide. Unit *a'* is the only missing as it's covered by the talus deposits.

Geophysical data acquisition and processing. Geophysical data acquisition was not straightforward due to the complex morphology of the accumulation and of the associated complications in coupling electrodes and geophones.

The geophysical reference profile, along the rock wall, was comprised of a 24-channel seismic line and of a 48-electrodes electrical line. The spacing was set to 10 m and to 5 m in the seismic line and in the electrical line respectively. Three component geophones were firmly tightened with the rock using special screws while the electrodes were hammered into holes filled with conductive medical gel. Data resulted good quality and the tomographic inversion of both the two datasets was carried out with a misfit lower than 5%.

The landslide body is comprised of three major lobes: the Massalezza lobe and two separate masses (defined as the "eastern lobe" and the "western lobe") probably collapsed just after the washout of the Massalezza lobe (Semenza, 1965, 2001).

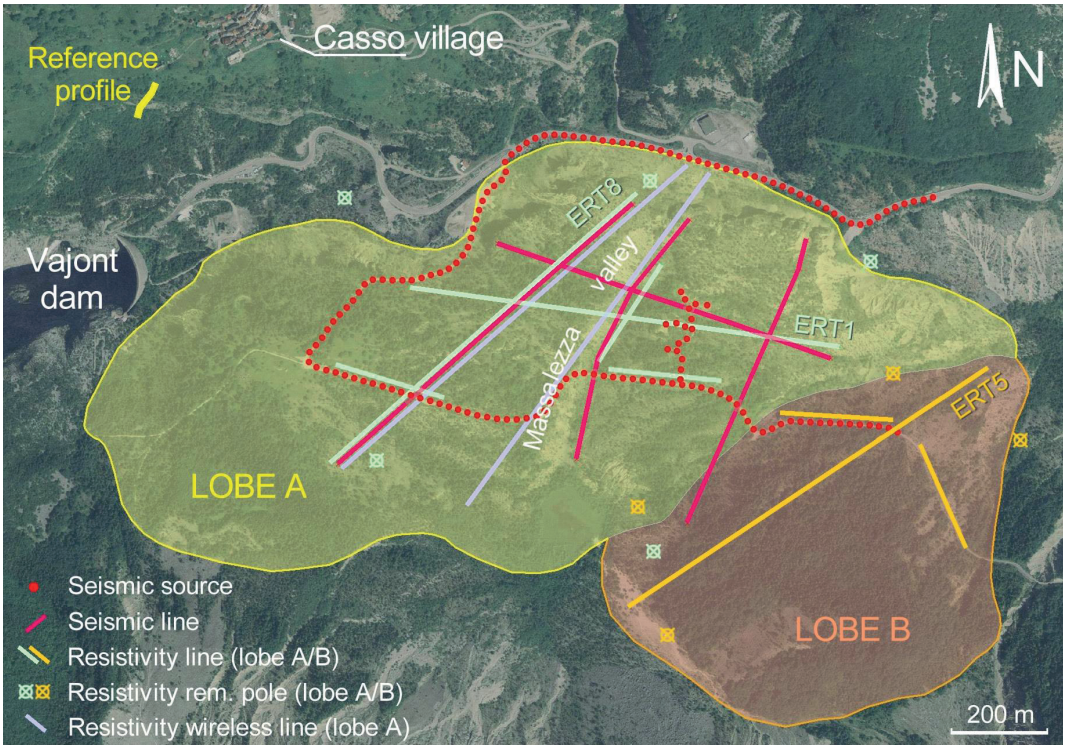

Fig. 1 – Key features of the geophysical campaign on the Vajont landslide.

Seismic data were collected on the Massalezza lobe only (lobe A in Fig. 1) using a DMT Summit modular system with more than 200 double channel A/D conversion units. Each receiving station was equipped with a three component 10-Hz geophone to detect the incoming signal. The three component sensors were laid out along four lines (L100, L200, L300, L400). The average station spacing was 10.0 m for a total of 276*3 live channels. Elastic waves were generated and propagated into the ground using a medium size vibrator (both in P-wave and S-wave modes). The source stations were located along the roads bounding and crossing the Massalezza lobe.

Recorded seismic data were generally of good quality; first breaks, in P-wave mode, were sharp and easy to pick even at offsets larger than 500 m while in S-wave mode the signal was slightly lower amplitude. A total of about 80000 first arrivals were picked and pre-processed and lately inverted using a 3D traveltime tomography. Inversion was carried out with the CAT3D proprietary software. Data resolution was improved using staggered grids (Vesnaver and Bohm, 2000).

Resistivity data were collected on the two landslide lobes (A and B in Fig. 1) using a 48-electrode Syscal R1 system, a 96-electrode Syscal Pro system and an experimental 36-electrode wireless resistivity system manufactured by MultiPhase Technologies LLC. A total of six ERT profiles, in Wenner and in Wenner-Schlumberger configuration, and two ERT volumes, in pole-dipole configuration, were collected on the Massalezza lobe. Three additional ERT profiles and a ERT volume were collected on the eastern lobe. Data were collected in separate sessions during early spring and middle autumn after several days of heavy rain to improve the coupling. The high permeability of the landslide mass allowed for assuming the subsurface layers as homogeneously wet.

Recorded resistivity data also resulted of good quality and just few points needed to be removed from the dataset prior to run the inversions. The inversion was carried out using the package ERTLAB+ that is based on a sophisticated reweight (Morelli and LaBreque, 1996) of the inversion parameters at each iteration.

Results and discussion. Unit *a''* in the reference section appears to be low both in resistivity (0.5-1.0 KΩ·m) and P-wave velocity (2200-2700 m/s). Unit *b*, is very thin and, due to the large sensor spacing, is outside the resolution capability of both the two techniques. Units *c*, *d* and *e* in the middle part of the section are moderately compact limestones and appear show a similar geophysical response. In these units the resistivity is fairly high (2.5-4.5 KΩ·m) as well as the P-wave velocity (3400-3800 m/s). At the top of the rock wall, where unit *f* outcrops, there is a sudden lowering of both the resistivity (0.5-1.0 KΩ·m) and the velocity (2300-2800 m/s).

The terrain resistivity in the landslide accumulation exhibit a large degree of fluctuation. The majority of the values range from 0.15-0.20 KΩ·m to 3.50-4.00 KΩ·m.

The resistivity distribution along the profile ERT1 (Fig. 2) appears to be quite complex and the Average values are slightly lower as compared to the reference profile. This is somewhat related to the fracturing and to the severe changes occurred in the geological layers involved in the landslide. Unfortunately along profile ERT1 there are no borehole data available to constrain the interpretation. The deep conductive unit *a''* was utilized to define the initial geological layout along the profile. The prominent structure is a narrow syncline fold located in the middle portion of the profile. The axis is probably elongated along the old Massalezza valley. The bottom layers are probably belonging to the *a''* unit while in the top layers there are the typical lithologies of the *c* unit. Some resistive bodies could be associated with a partly undifferentiated *c-d-e* lithological sequence while the conductive unit, visible in the distance interval 50-200 m, according to Rossi and Semenza (1965) still belongs to units c, d and e. Possible explanation of this anomaly are the high degree of fracturing in the landslide or the occurrence of lateral changes of lithology moving from the right to the left side of the Vajont valley. These folding with an apparent N-S trend of the lithological units is also visible on the sliding surface (Massironi *et al.*, 2013). The preservation of the structural settings, before and

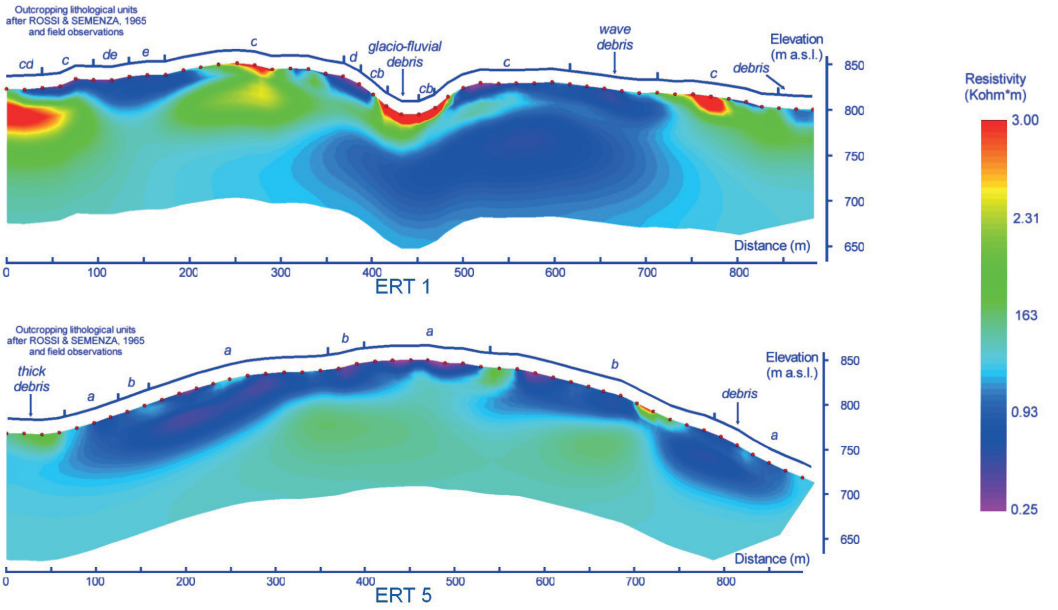

Fig. 2 – 2-D Resistivity inversion images along tomography ERT 1 (top) and ERT 5 (bottom) (see Fig. 1). The investigated landslide mass could be then considered dry.

after the 1963 failure, confirm the hypothesis of a rigid roto-translation of the collapsed mass. The large anomalous thickness of the *c*-*d*-e sequence is probably caused by some detachment phenomena occurred along existing or newly developed high-angle discontinuities (Rossi and Semenza, 1965; Martinis, 1978) during the failure. The profile also show some low angle detachment planes (see for example at the x-coordinate interval 200-300 m) that could explain the anomalous thickness of the *c*, *d* and *e* units in depth.

The resistivity distribution along profile ERT5 (Fig. 2), crossing lobe B, is more homogeneous and it's more and less comparable with the post-failure geological map of Rossi and Semenza (1965). The outcrops are represented by an undifferentiated unit *a* covering almost the entire lobe B (Fig. 1) and by some minor exposures of the unit *b*. The general structure appears to be folded up into an anticline with some major displacements. In this case also the geometry of the bottom layers of lithological unit *a''* was utilized as the prominent geophysical marker to define the settings. In the reference section unit *a'* is not exposed and hence there are no indications about its possible geophysical response. Carloni and Mazzanti (1964) suggest a total thickness of about 80-90 for the undifferentiated unit *a* with a maximum thickness of unit *a''* around 50 m. According to several other authors (Rossi and Semenza, 1965; Martinis, 1978; Hendron and Patton, 1985) unit *a'* is similar to unit *a''* with the sole difference of the presence of the interbedded clays in the base layers. The two units should then exhibit a comparable geophysical signature. The increase of the resistivity in the deeper portion of the profile (where unit *a'* was expected) is rather difficult to explain. There are possible explanations: the upper part of unit *a'* is more resistive than expected; more realistically unit *a''* overthrusts the resistive terrains belonging to the *c*-*d* units in the deeper portion of profile. Several high and low angle discontinuities are also visible in the profile. These planes disrupt the former continuity of the geological layers generating an ensemble of pop-up like structures. Unfortunately on this lobe the sliding surface is not constrained by post-landslide data and also during the failure occurred a partial overlap of lobe B on the Massalezza lobe. The deeper portion of the geophysical image could be then really complex.

The P-wave velocity field in the landslide accumulation range from 700-1000 m/s to 3500-4000 m/s. Seismic data resulted comparable to electrical data with a reasonable degree of confidence.

The correspondence between resistivity and P-wave velocity has been analysed in details along the section of profile ERT1 (Fig. 3). A profile was extracted from the 3D velocity model and compared to the 2D ERT. The syncline structure below the Massalezza ditch is visible also in the seismic data but it is not completely resolved as in the resistivity image probably because the geophone line is located 60 m northern of the electrode line. Right in the middle of the P-wave section there is a high-velocity bottom layer that is not visible in the resistivity section. The high-velocity layer is located at a depth where the signal to noise ratio of the resistivity data is very low. It is known that a deep resistive layer below a conductive layer requires very large AB spacing to be sampled by an electrical field that is forced into the conductor. The seismic data are more reliable because there is a geophone line exactly along the Massalezza ditch (Fig. 1) and the sources are located on the nearby road. This high velocity layer (or high resistivity) below unit *a''* is quite difficult to explain without assuming the presence of a detachment plane that duplicate the sequence.

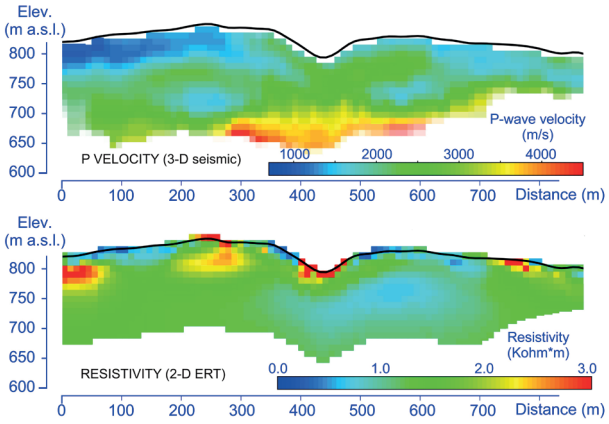

Fig. 3 – Comparison between 3D seismic tomography (top) and 2D electrical resistivity tomography (bottom) response. The profiles are oriented from W to E. The geophysical data are presented as 10m by 10m cell scalars without interpolation. The two sections are computed along the trace of profile ERT1.

Conclusion. The study of a large landslide based on the 2D and 3D geophysical parameterization of the involved geological units is particularly difficult due to the expected complexity of a chaotic accumulation. The Vajont landslide, given its large volume, was even more complicated. The different units involved in the landslide, due to their lithological changes were expected to have a distinct geophysical signature. The reference section collected along the rock wall below the village of Casso confirmed this hypothesis. The pre-slide geological sequence from the bottom to the top is a sort of sandwich of "conductive/low velocity" – "resistive/high velocity" – "conductive/low velocity" layers.

The initial correlation of the geophysical images from the landslide body with the post-failure geology confirmed the observations from the reference section. The conductive unit *a''* is an excellent geophysical marker to guide the interpretation. The pre-landslide stratigraphy appears to be quite well preserved in the shallow layers while in depth the geophysical response is rather complex. Both the resistivity and the seismic images along profile ERT1 highlight a syncline that is fully exposed on the sliding surface. The geophysical images along profile ERT1 also show a series of small-scale folds with north-south axes that are probably pre-landslide as the stress occurred during the failure folded the strata generating east-west axes. This mode of folding is clearly visible in resistivity profile ERT5, collected on lobe B.

These results are satisfactory but further investigations are anyhow required to achieve a reliable reconstruction of the landslide accumulation settings. Unfortunately borehole data collected, before and after the landslide, are of limited use because of the high lateral variability of the physical properties occurring in the collapsed mass. This is somewhat confirmed by the borehole stratigraphy reconstructed by mean of micropalaeontological analysis of drilled

samples. Results of this last analysis suggests the existance of several duplication of the original in-situ sequence.

Further work that will be undertaken in a very near future includes: 1) geophysical parameterization of unit *a'*, 2) inversion of the electrical data into a 3D resistivity volume of the entire landslide, 3) correlation of the seismic and of the resistivity responses to improve interpretation and finally 4) processing of S-wave data in order to estimate the elastic parameters of the landslide body.

Acknowledgements. We acknowledge the Friuli Venezia-Giulia Region for providing the funding for the project (project 35935/2010). A special thank to Alessia Rosolen for her personal support and to Ketty Segatti. A final thank to Giovanni Rigatto and to Nuccio Bucceri for their assistance during topographic measurements.

References

Bistacchi, A., Massironi, M., Superchi, L., Zorzi, L., Francese, R., Giorgi, M., Genevois, R., and Chistolini, F., 2013. A 3D Geological Model of the 1963 Vajont Landslide. Vajont 2013 Conference.

Caloi, P., and Spadea, M., C., 1960. Serie di esperienze geosismiche seguite in sponda sinistra a monte della diga del Vajont (dicembre 1959). SADE Technical Report.

Caloi, P., and Spadea, M., C., 1961. Indagine geosismica condotta nel mese di dicembre 1960 a monte della diga del Vajont in sponda sinistra. SADE Technical Report.

Carloni, G., C., and Mazzanti, R., 1964. Rilevamento geologico della frana del Vajont, In Selli R. *et al*., "La frana del Vajont", Giornale di Geologia, 2, 32/1.

Castellanza, R., Agliardi, F., Bistacchi, A., Massironi, M., Crosta, G.B., and Genevois, R., 2013. 3D finite-element modelling of the Vajont landslide initiation stage. Vajont 2013 Conference.

Dobrin, M.B., and Savit, C.H., 1988. Introduction to Geophysical Prospecting – IV Edition. McGraw-Hill, 867 pp.

Genevois R., and Ghirotti, M., 2005. The 1963 Vaiont Landslide, Giornale di Geologia Applicata 1, 41-52.

Giudici, F., and Semenza, E., 1960. Studio geologico del serbatoio del Vajont. SADE Technical Report.

Hendron A.J., and Patton, F.D., 1985. The Vaiont slide, a geotechnical analysis based on new geological observations of the failure surface. Tech. Rep. GL-85–5, Department of the Army, US Army Cops of Engineers, Washinghton D.C., 2 vols.

Kilburn, C.J., and Petley, D.N., 2003. Forecasting giant, catastrophic slope collapse: lessons from Vajont, Northern Italy. Geomorphology, **54**, 1-2, 21-32.

Martinis B., 1978. Contributo alla stratigrafia dei dintorni di Erto-Casso (Pordenone) ed alla conoscenza delle caratteristiche strutturali e meccaniche della frana del Vajont. Memorie di Scienze Geologiche, Università di Padova, 32, 1-33.

Massironi, M., Superchi, L., Zampieri, D., Bistacchi, A., Ravagnan, R., Bergamo, A., Ghirotti, M., and Genevois, R., 2013. Geological Structures of the Vajont landslide. Vajont 2013 Conference.

Morelli, C., and Carabelli, E., 1965. Misure di velocità delle onde elastiche longitudinali nella roccia del bacino del Vajont. Court of Belluno. Lerici Foundation. Research 410.

Morelli, G., and LaBrecque, D. J., 1996. Robust scheme for ERT inverse modelling. European Journal of Environmental and Engineering Geophysics, 2, 1-14.

Müller, L., 1959. Talsperre Vaiont – 6 Geotechnischer Bericht. SADE Technical Report.

Müller, L., 1964, The rock slide in the Vaiont valley. Felsmechanik und Ingenieur-geologie, 2, 148-212.

Petley, D.N., and Petley, D.J., 2006. On the initiation of large rockslides: perspectives from a new analysis of the Vaiont movement record. In Massive Rock Slope Failure. Mugnozza, G., Strom, A. & Hermanns, R. L. Rotterdam. NATO Science Series, Earth and Environmental Sciences, 49, 77-84.

Rossi, D., and Semenza, E., 1965. Carte Geologiche del versante settentrionale del M. Toc e zone limitrofe prima e dopo il fenomeno di scivolamento del 9 Ottobre 1963. Scala 1:5000. Ist. Geol. Univ. Ferrara, Italy.

Semenza, E., 1960. Nuovi studi tettonici nella valle del Vajont e zone limitrofe. Acc. Naz. Lincei, Rend. Cl. Sc. MMFFNN, 8, 28/2.

Semenza, E., 1965. Sintesi degli studi geologici sulla frana del Vaiont dal 1959 al 1964. Memorie del Museo Tridentino di Scienze Naturali, 16, 1-52.

Semenza, E., 2001. La storia del Vaiont raccontata dal geologo che ha scoperto la frana. Tecomproject Ed., Ferrara, Italy. 279 pp.

Semenza, E., and Ghirotti M., 2000. History of the 1963 Vaiont Slide. The importance of the geological factors to recognise the ancient landslide. Bulletin of Engineering Geology and the Environment, 59, 87-97.

Telford, W., M., Geldart. L., P., and Sheriff, R., E., 1990. Applied Geophysics – II edition. Cambridge University Press, 770 pp.

Vesnaver, A., and Bohm G., 2000. Staggered or adapted grids for seismic tomography?, The Leading Edge, 19, 9, 944-950.

INTEGRATE PROCESSING OF SEISMIC AND INFRASOUND MONITORING IN NORTHEAST ITALY: THE FADALTO CASE

D. Pesaresi[1], M. Ripepe[2]

[1] Centro di Ricerche Sismologiche, OGS (Istituto Nazionale di Oceanografia e di Geofisica Sperimentale), Trieste, Italy

[2] Dipartimento di Scienze della Terra, Università degli Studi di Firenze, Firenze, Italy

Introduction. The Earth Science Department of the Florence University http://www.unifi.it/) in Italy has a long experience in monitoring avalanches, volcano and seismic activities in the infrasound band, also in the framework of several international and EU funded project, and in the Comprehensive Nuclear-Test-Ban Treaty Organization (CTBTO, http://www.ctbto.org/) activities.

The Seismological Research Center (http://www.crs.inogs.it/) of the OGS (Italian National Institute for Oceanography and Experimental Geophysics, http://www.inogs.it/) in Udine (Italy) after the strong earthquake of magnitude M_w=6.4 occurred in 1976 in the Italian Friuli-Venezia Giulia region, started to operate the North-eastern Italy Seismic Network: it currently consists of 17 very sensitive broad band and 18 simpler short period seismic stations, all telemetered to and acquired in real time at the OGS-CRS data centre in Udine. Real time data exchange agreements in place with other Italian, Slovenian, Austrian and Swiss seismological institutes

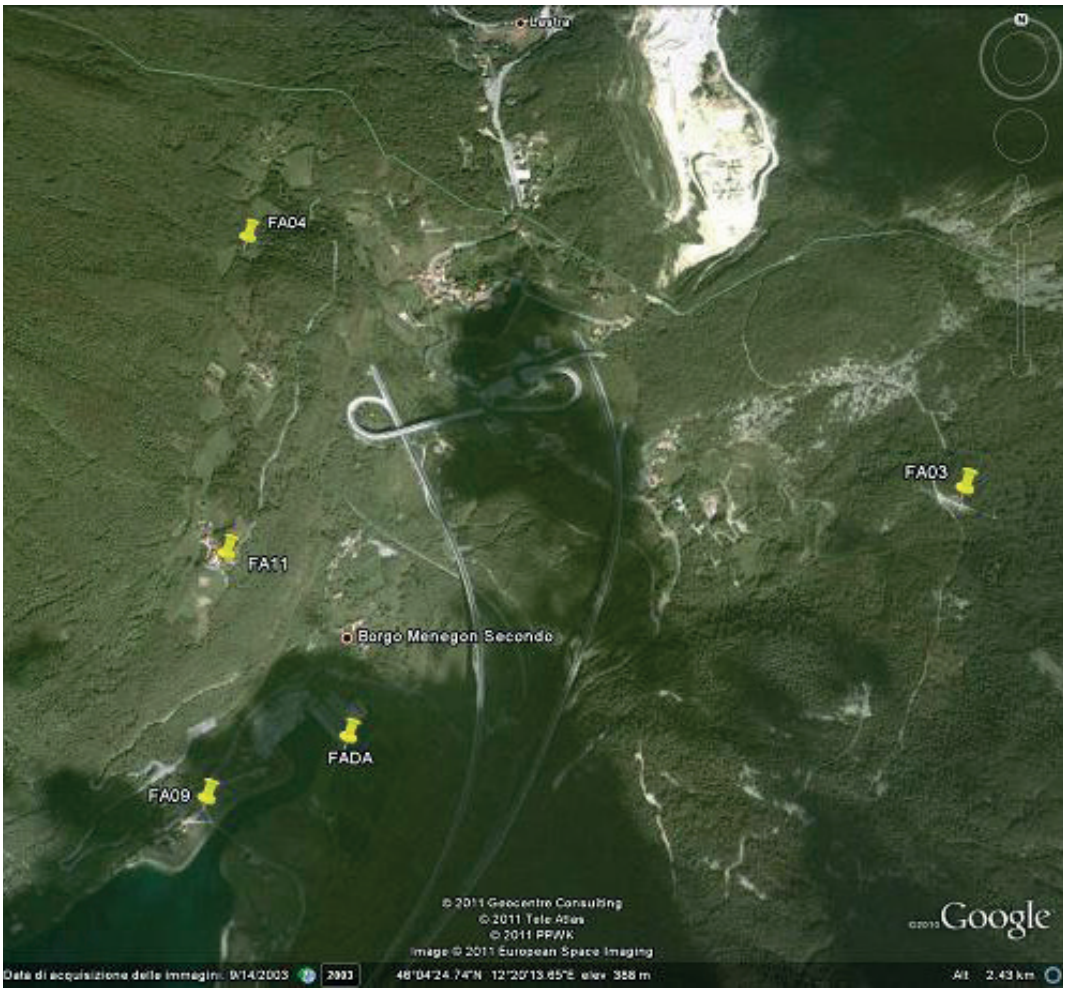

Fig. 1 – Seismic network installed by OGS in Val Lapisina, Fadalto.

lead to a total number of about 100 seismic stations acquired in real time, which makes the OGS the reference institute for seismic monitoring of North-eastern Italy (Bragato *et al.*, 2011).

In 2012 in the Fadalto area in the Belluno province in Northeast Italy several strong rumbles were heard, which eventually scared population and concerned authorities. OGS and University of Firenze installed in cooperation a real time seismic and infrasound monitoring system in the area. A description of the technical system capabilities, together with the preliminary results of the analysis of several months of recordings will be here illustrated.

The area. The Lapisina Valley is located in North-eastern Italy, Venetian Prealps, and separates the Belluno Prealps in the West from the Cansiglio Plateau in the Est. It is a typical glacial valley, with wide bottom, and steep longitudinal profile and represents the original course of the Piave River, abandoned during the Late Glacial epoch for the obstruction of the valley due to the Fadalto landslide, detached from the Costa-Millifret Mount (Pellegrini, 2000).

The pre-Quaternary rock in the Fadalto Valley are all sedimentary (glacial, landslide, talus slope). Fadalto landslide is chaotic and consists of predominantly calcareous debris, in silty-sandy matrix (Autostrade SpA, 1985). The coarse grain decrease in size from North to South. At the edge and bottom of the valley there are Mesozoic formation which are transitional sequence among predominantly pelagic and escarpment faces.

From the tectonic point of view the complex syncline at the bottom of the valley has been dislocated by a system of inverse and transcurrent faults, connected with the line 'Longhene-Fadalto-Cadola', striking almost NNE-SSW (Pellegrini and Surian, 1996).

The Lapisina Valley does not posses a main stream, but from north to south is characterized by four lakes (the main lake of Santa Croce, and the smallest Dead, Restello and Negrisiola lakes, modified for the exploitation of hydroelectric resources, since the beginning of the twentieth century). From the hydro-geological point of view, the Sella of Fadalto represents the watershed between the basin of the Piave and Livenza rivers. Meschio is the only river that collects underground waters from karst relieves of Col Visentin. Farther East, sources give rise to Livenza (Gorgazzo, Santissima, Molinetto), picking up the circulation of karst Group Cansiglio-Cavallo. The position of the water table is heavily influenced by the regime of precipitation and water level of the lakes.

The instrumentation. The seismic network installed by OGS to monitor the Fadalto area is illustrated in Fig. 1. The configuration changed over time according to findings in the actual data, while the initial configuration reflected the population perception of the rumbles (CRS staff, 2011). The seismic stations used were made of Reftek C130 acquisition units and Lennartz LE3D 1 second seismometers. The RefTek 130S-01 Broadband Seismic Recorder (http://www.reftek.com/products/seismic-recorders-130-01.htm) digitizes and stores analog input from a variety of external sensors, including seismometers, accelerometers, tiltmeters and other geophysical sensors. The 130S-01 hardware is optimized for field deployments and is designed to be easy to use: compact, light in weight, low power consumption, and requires few maintenance. The Lennartz LE-3Dlite (http://www.lennartz-electronic.de/index.php?option=com_content&view=article&id=50&Itemid=55) is a 1 Hz to 100 Hz passband, low-power, low-noise, rugged and compact seismometer for applications requiring short-period sensitivity, field worthiness and portability.

The seismic network was completed with the FADA station made of a Quanterra Q330 digital acquisition unit (orange box in Fig. 2, left) with 6 channels, 24 bit digitizer sampled at 200 sps and a Lennartz LE-3D Lite short period seismometer (bronze

Fig. 2 – Seismic (left) and infrasound (right) sensors installed in Fadalto.

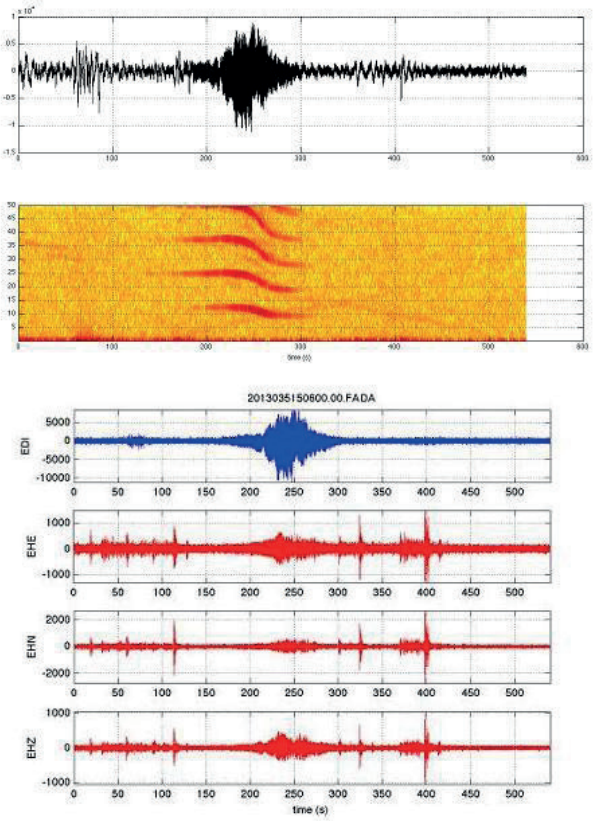

Fig. 3 – Infrasound (black top and blue bottom) and seismic (red bottom) waveforms of observed event with infrasound spectrogram (top).

cylinder up right on the left of Fig. 2) with eigenfrequency 1 Hz, upper corner frequency 100 Hz, and a dynamic range > 136 dB. The Quanterra Q330 (http://www.kinemetrics.com/p-78-Q330.aspx) is a low-power 3-6 channel remote broad-band seismic system: it includes Quanterra's ultra-low-power delta-sigma 24-bit A/D, a DSP/RAM module containing 8Mb, a GPS receiver, power conversion, sensor control, and a telemetry management module. For these characteristics the FADA station was connected via GPRS modem transmitting data in real time to the OGS seismic data centre in Udine. A simple Short Time Average/Long Time Average (STA/LTA) detector after high pass filtering the data at 20 Hz tagged events of interest in real time, automatically sending alarm messages via email and Short Message System (SMS) to OGS and Civil Defence of the Veneto Region personnel.

The FADA station, being the only one in the network sending data in real time, was also equipped with an iTEm infrasonic sensor model "prs 0110a" (right in Fig. 2), with a sensitivity of 25 mV/Pascal @ 1 Hz, ± 100 Pa full scale range, frequency response 0.01 – 100 Hz -3 dB@ 0.02 Hz, and self noise -52 dB relative to 1 Pa. iTEM is a consulting and system design company spin off from Florence University based in Florence (Italy) working in the Earth Sciences and Geophysics (http://www.item-geophysics.it/).

Data analysis. After a first analysis of several months of combined seismic and infrasound recordings in the Fadalto area, after automatically pre-selecting of interesting event time windows based on high pass filter above 20 Hz and STA/LTA detector on vertical component of the seismic signal, we categorized events of interest in several categories, including:

1. Seismic and acoustic recordings of local earthquakes: seismic and acoustic signals share the same high frequency content (10-50 Hz), suggesting that the infrasonic signals is produced by ground-coupled waves.
2. Signals not associated with earthquakes or rumbles generated by the same high frequency and resonant source (Fig. 3): similar signals have been recorded by Florence University with an infrasound sensor in the Valle d'Aosta site during helicopter over flights. MacAyeal *et al.* (2008) however suggested in a personal communication that these signals might express stick and slip of land masses, perhaps premonitory to a large landslide.

Conclusions. No direct evidence in the recordings were found of the rumbles. A deeper seismic analysis of the phenomena however indicated that the rumbles can be associated to variation of underground water levels which in turn causes:

1. micro fractures (change in pressure in the pores);
2. water flow in karst conduits with phenomena type exhaust siphons, water hammer, etc.

The experience of combining Università di Firenze infrasound instrumentation and expertise and OGS seismic instrumentation and expertise proved in the Fadalto case to be very valuable and useful for other Civil Defence and nuclear test explosions monitoring (CTBTO) applications and purposes. Moreover, OGS and Università di Firenze are planning to join forces to star addressing the issue of real time seismic and infrasound monitoring of snow avalanches (Valt *et al.*, 2009).

Acknowledgements. The authors wish to thank all the colleagues at Florence University and OGS who contributed in different ways to this work, including among others Dr. Giacomo Ulivieri from Florence University for his spectrogram analysis of the infrasound recorded data of the suspected rumbles and Dr. Pier Luigi Bragato from OGS for the coordination of the overall multi-disciplinary investigation held in the Fadalto area and for his personal support to this work.

References

Autostrade Spa; 1985: *Progetto Esecutivo Autostrada Meste-V.Veneto-Pian di Vedoia - Relazione Geologica*. Rapporto interno, 41 pp.

Bragato P. L., Di Bartolomeo P., Pesaresi D., Plasencia Linares M. P., Saraò A.; 2011: *Acquiring, archiving, analyzing and exchanging seismic data in real time at the Seismological Research Center of the OGS in Italy*. Annals of Geophysics, **54(1)**, 67-75, doi: 10.4401/ag-4958.

CRS Staff; 2011: *Indagini sismologiche sui fenomeni acustici percepiti in Val Lapisina (Vittorio Veneto) nel 2011*. In: Slejko D. e Rebez A. (eds), Gruppo Nazionale di Geofisica della Terra Solida, 30° Convegno Nazionale, Riassunti estesi delle comunicazioni. Mosetti Tecniche Grafiche, Trieste, pp. 97-100.

MacAyeal D. R., Okal E. A., Aster R. C. and Bassis J. N.; 2008: *Seismic and hydroacoustic tremor generated by colliding icebergs*. J. of Geoph. Research, **113**, F03011, doi:10.1029/2008JF001005.

Pellegrini G. B.; 2000: *Il Vallone Bellunese e la valle Lapisina*. In: Bondesan A., Caniato G., Vallerani F., Zanetti M. (a cura di) Il Piave, Cierre Edizioni, 60-66.

Pellegrini G.B. and Surian N.; 1996: *Geomorphological study of the Fadalto landslide, Venetian Prealps, Italy*. Geomorphology, **15**, 337-350.

Valt M. and Pesaresi D.; 2009: Detecting snow avalanches with seismic stations in North-east Italy: First results of dataset analysis, ISSW 09 - International Snow Science Workshop, Proceedings, 458.

INTEGRATION OF CGPS AND METEOROLOGICAL DATA FOR ATMOSPHERIC PRECIPITABLE WATER RETRIEVAL: SOME CASE HISTORIES CONCERNING THE CAMPANIA REGION

U. Riccardi[1], U. Tammaro[2], P. Capuano[3]

[1] Dipartimento di Scienze della Terra, dell'Ambiente e delle Risorse (DiSTAR) University "Federico II" of Naples, Italy
[2] Istituto Nazionale di Geofisica e Vulcanologia Sezione "Osservatorio Vesuviano" Naples, Italy
[3] Department of Physics "E.R. Caianiello" University of Salerno Fisciano, Italy

Introduction. This research deals with an application of GPS technique in meteorology aimed mainly at weather hazard mitigation. We report on the analysis of the observed tropospheric delay on some continuous GPS (CGPS) stations belonging to the RING (Rete Integrata Nazionale GPS) Italian network (Avallone *et al.*, 2010) and NeVoCGPS (Neapolitan Volcanoes Continuous GPS) network (Bottiglieri *et al.*, 2010). Mainly we focus on the potentialities coming from the integration among meteorological observations (air pressure, temperature, humidity, rain and satellite radio images) and CGPS data in studying the time evolution of the atmospheric precipitable water PW. We report on some selected extreme meteorological events set up on the Campania region.

Since long time ago Global Positioning System (GPS) has acknowledged for other than the classical geodetic positioning even as a tool to study the Earth and other planets atmosphere and namely its water vapor content, if any, with an accuracy comparable to other techniques and means of measurement (Bevis *et al.*, 1992). Most of the ideas in this subject originate from geodesists and geophysicists spending efforts trying to model and removing the atmospheric "noise". Hence the atmospheric effect is going to be time to time transformed from an annoying noise source, degrading the accuracy of positioning, into a valuable meteorological

probe (Champollion *et al.*, 2004). The basic idea behind this topic is that when travelling through the atmosphere to Earth-based antennas or other satellite, microwave radio signals transmitted by GPS satellites experience changes in velocity and deviation (bending) from the Fermat's straight lines depending on the refractive index gradients and related physical conditions of the atmosphere. All these effects increase the travel time of the GPS signals. GPS meteorology is then concerned with inverting this delay time to shed light on the atmospheric conditions. Two main branches of GPS meteorology deal with "radio occultation", which is a satellite-to-satellite technique for limb sounding, and "ground-based GPS" measurements. The propagation problem of the GPS radio waves develops in a different way in the troposphere and ionosphere. Fortunately ionosphere is dispersive (i.e. frequency dependent) for microwave radiation and propagation effects can be reduced by just collecting a linear combination of both L1, L2 frequencies transmitted by the GPS satellites, the so called "LC-ionofree" observable (Hoffman-Wellenhof *et al.*, 2001). On the contrary, the troposphere is non-dispersive, so the consequent delay cannot be directly eliminated from GPS observations. The tropospheric delay in GPS signals is due to the permanent electric dipole moment of the molecule of water so that it is nearly proportional to the quantity of water vapor (WV) integrated along the signal path. Being directly responsible for the unusually large latent energy associated with water's change of phase, WV plays a fundamental role in the transfer of energy through the atmosphere and in the formation and propagation of weather systems and tropospheric fronts (Stephens *et al.*, 1991; IPCC, 1992). Because of its extremely variable distribution both in time and space as well as a poor correlation with surface humidity, the WV is one of the most difficult meteorological parameter to quantify. Routinely WV content in the atmosphere is measured by means of standard synoptic radio soundings (water vapor radiometers –WVR-balloons), but they are too sparsely distributed in space and time to support reliable forecasting. The societal impact of extreme weather events such as floodings and associated effects (rock fall and mud flow) set a claim for an improvement of our skill to monitor moisture-fluxes able to trigger such severe weather.

The nowadays extensive use of geodetic permanent GPS networks offers a powerful tool for a high resolution remote sensing of atmospheric WV and "precipitable water" (PW), which is the total quantity of WV overlying a point on the Earth's surface expressed as the height of an equivalent column of liquid water.

Duan *et al.* (1996) demonstrated that a pure GPS solution was possible for PW retrieval on a regional network by incorporating few remote (distance > 200 km) stations into the geodetic analysis.

Modelling of GPS atmospheric delay. The observed tropospheric delay (TD) of a generic GPS signal is customarily described as resulting from three contributing components according to the equation:

$$TD(\alpha, \phi) = STD_{sym}(\alpha) + STD_{az}(\alpha, \phi) + S \qquad (1)$$

A spherically symmetric component $STD_{sym}(\alpha)$, only depending on the elevation angle (α) of the satellite to the station; a second component allowing to account for the atmosphere anisotropy and dependent on both elevation and azimuth (ϕ) angles and last a generic "residual" term (S), which could be defined as the difference between a model daily solution and the observed one.

Both of the first two terms in the Eq. (1) are customarily implemented in software packages devoted to GPS analysis in the following form:

$$STD_{sym}(\alpha) = \left[ZHD \times M_D(\alpha)\right] + \left[ZWD \times M_W(\alpha)\right] \qquad (2)$$

$$\begin{aligned} STD_{az}(\alpha,\phi) = {} & D_h^{NS} m_{az}(\alpha)\cos(\phi) + D_h^{EW} m_{az}(\alpha)\sin(\phi) \\ & + D_w^{NS} m_{az}(\alpha)\cos(\phi) + D_w^{EW} m_{az}(\alpha)\sin(\phi) \end{aligned} \qquad (3)$$

As described in the previous equations the slant delay (STD) can be split in two zenithal (i.e. vertical) components: an hydrostatic or "dry" part (ZHD), which accounts for nearly 95 % of the observed delay, and a "wet" component (ZWD) due to the WV along the signal path, so that it amounts to zero if there is no WV. The first component represents the delay induced by the troposphere in hydrostatic condition and can be well modelled because once the precise position of the point is known, the delay is only function of the observed surface pressure (Saastamoinen, 1973). On the contrary the "wet" component is poorly predicted by the models. The terms "M_D" and "M_W" represent the "mapping functions" which allows mathematically modelling the elevation dependence of the respective wet and dry delays. The mapping functions (for both the dry and wet terms) amount approximately to the cosecant of elevation. Different mapping functions, implemented as numerical gridded values, are currently available in the geodetic software for GPS data analyses (e.g. Bohem *et al.*, 2006; Niell, 1996).

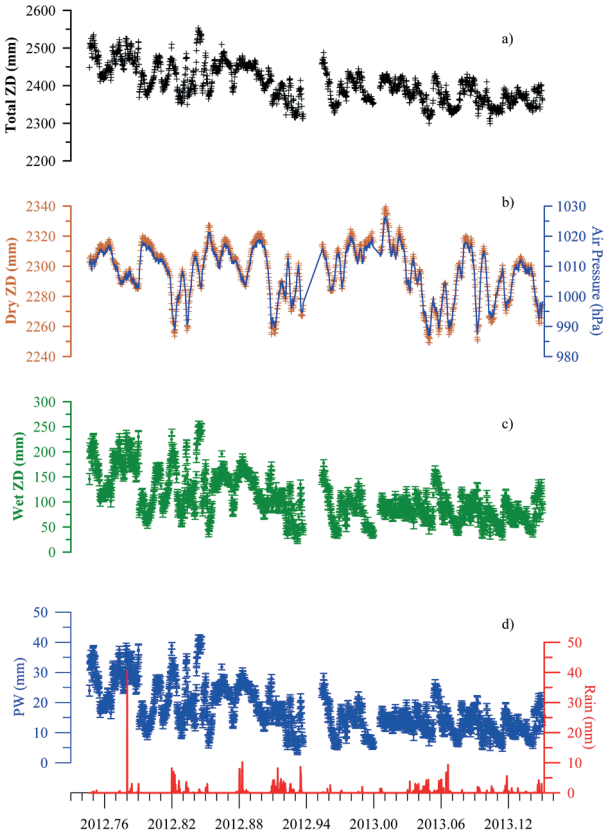

Fig. 1 – Tropospheric parameters and meteorological observations at MAFE CGPS station: (a) total zenith delay, (b) hydrostatic dry and (c) wet components, (d) precipitable water and rain.

D_h^{NS}; D_h^{EW}; D_w^{NS}; D_w^{EW} are NS and EW component of hydrostatic and wet gradients, while $m_{az}(\alpha)$ are the gradient mapping functions having the form:

$$m_{az}(\alpha) = \frac{1}{[\sin(\alpha) * \tan(\alpha) + 0.003]} \qquad (4)$$

Strategy of data processing and analysis. In this study we use CGPS measurements collected at five GPS permanent stations. MAFE, located in Napoli at DiSTAR (University "Federico II" of Napoli), ENAV located at Punta Campanella (Sorrento Peninsula); both stations belong to the GPS network of Neapolitan volcanic area (NeVoCGPS). PACA, located in Palma Campania, and included in the GPS network of Italian Space Agency (ASI). CAGL, located in Cagliari and MATE, installed at ASI headquarters in Matera. The GPS equipments for each station are listed in Tab. 1. In this study MAFE is the reference station because both GPS and meteorological data were available with a suitable continuity. MAFE is equipped with a 12- channels, dual frequency L-band receiver, so that it allows simultaneously assessing the tropospheric delay in GPS signal on up to 12 satellites.

About 7 months of CGPS observations, collected on selected sites spanning an area encompassing Campania Region and surroundings have been analyzed. The ionofree linear combinations were processed by GAMIT v. 10.4 (Herring *et al.*, 2010) in order to have the precise positions of the GPS stations in the ITRF2008 frame (Altamimi *et al.*, 2011). We used

daily sessions (24 hour), a cut-off angle of 10° and IGS final orbits. 11 European IGS stations are used for the frame referencing. The final station coordinates are obtained by constraining the fiducial GPS stations to their ITRF2008 coordinates using the Kalman filter GLOBK (Herring *et al.*, 1990). The final daily solutions resulted to have a repeatability of about 5 mm on horizontal and 10 mm on vertical baseline components. Then a second run have been done with loose constraints of 1 meter on the coordinates to evaluate bi-hourly tropospheric parameters (Haase *et al.*, 2003), i.e., the zenith total delay (ZTD) and the total gradients. Two remote stations (CAGL and MATE, 486 and 208 km far from Napoli respectively) equipped with meteorological sensors have been incorporated into the analysis, in order to overcome the large correlation of the errors among the stations in a small regional network (Duan *et al.*, 1996). This allows retrieving absolute values of the PW even on close stations. The calculated atmospheric parameters are the ZTD and its two constituent components ZHD and ZWD (Fig. 1 a-c). As expected from theory (Saastamoinen, 1973), the hydrostatic delay overlaps the surface pressure time changes (Fig. 1b). Subtracting the hydrostatic delay (ZHD) from the total one (ZTD), we have obtained the wet delay (ZWD) leading us to assess the PW. The PW (Fig. 1d) has been computed with the "sh_metutil" routine available in the GAMIT software package.

Tab. 1 – GPS instruments equipping the network analyzed in this study.

Site	GPS Equipment (Receiver + Antenna)
ENAV	LEICA GRX1200 + LEIAT504 LEIS
CAGL	TRIMBLE 4700 + TRM29659.00 NONE
MAFE	LEICA GRX1200 + LEIAT504 LEIS
MATE	LEICA GRX1200GGPRO + LEIAT504GG NONE
PACA	LEICA RS500 + LEIAT504 NONE

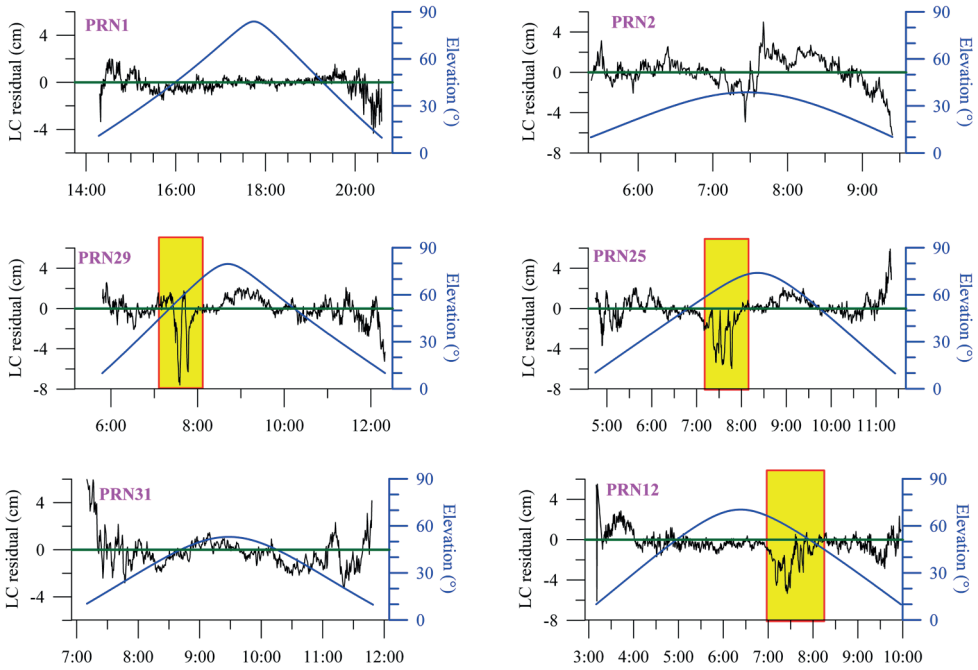

Fig. 2 – Phase residuals (black curve) and elevation angle (blue curve) at MAFE on 2012 October 12th; the largest residuals for the most elevated satellites are highlighted in the yellow box.

Results and conclusions. Although the WV and PW content cannot be directly linked to the precipitation amounts, nevertheless some interesting correlations between the time changes of PW and rainfall can be envisaged (Fig. 1d). We focused on the rainfall event occurred on October 12th 2012 (Julian day: 276), when a cold front coming from Tyrrhenian Sea and moving towards SE has struck the South of Italy. A double thunderstorm cluster enucleates since 07:00 UTC breaking out a heavy event with large rain amount concentrated in a very short time span; about 40 mm of rain in about 50 minutes were detected at MAFE station. Infrared channel of the Meteo satellites (MSG) in the Euro-Atlantic area allowed clearly following the front evolution and migration. Aimed at detecting any traces in the GPS signals, we analysed the phase residuals for each visible GPS satellite at MAFE station above the elevation cut-off angle. In Fig. 2 the time series of the phase residuals around 7:00 UTC are plotted; a "normal" phase plot showing the typical increase of the phase scattering of the radio signal at low elevation is even drawn as a reference (see PRN1 in Fig. 2a). The large phase residuals when the satellites transit at high elevation angles (Fig 2b, …) clearly indicate that the observed delays are likely due to tropospheric effects.

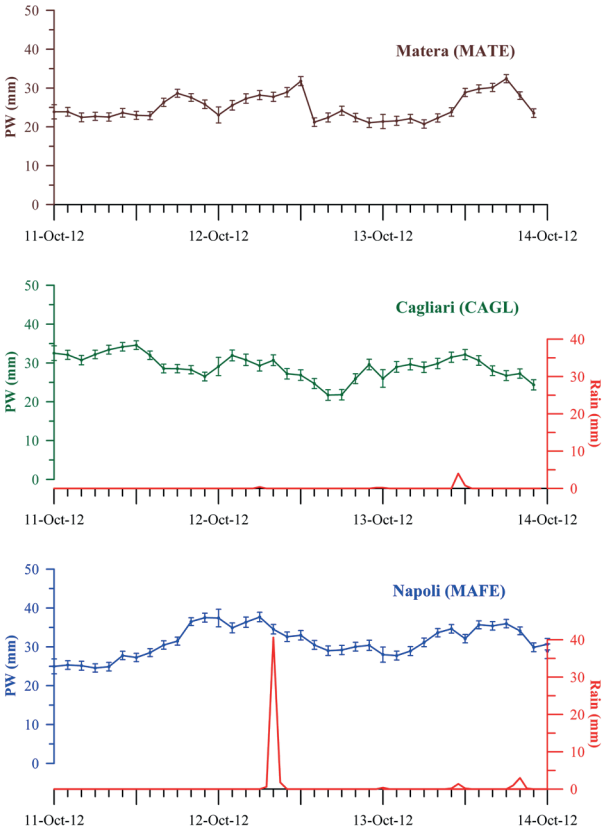

Fig. 3 – Precipitable water (PW) assessed at MAFE and two remote CGPS stations on the occasion of the extreme rainfall event occurred on 2012 October 12th.

To better follow the migration of the cold front and the related WV fluxes, the PW time series were even computed for MATE and CAGL IGS stations (Fig. 3). Unfortunately no rain data were available for MATE station. An increase of about 13 mm peak to peak was observed at MAFE in the PW accumulating during the 24 hours preceding the pouring rain event. Coherently to the evolution shown by the sequence of the satellite radio images, at CAGL station no rainfall was recorded and no significant variation in the PW can be envisaged. On the contrary, in Matera (SE of Napoli) an increase of the PW is observed but it appears to be delayed of about 4 hours in respect to MAFE. The GPS observations in the vicinity of the most intense rainfall area are all consistent with the WV depicted in the satellite meteorological radar observations. Moreover we found that the maximum amplitude of the wet gradients is not correlated with the rain itself but with rapid changes in both the orientation and the amplitude of the wet gradients.

Our study confirms that, thanks to the nowadays dense covering of national networks, the integration of ground based and satellite meteorological data with GPS technique is a useful tool for monitoring atmospheric parameters and for capturing their temporal variability. Actually we acknowledge that raining phenomena are a very complex physical process, hence is naive claiming that PW alone could be enough for rainfall forecast. Nevertheless in a mul-

ti-parametric model PW values, retrieved from dense CGPS networks, can contribute into improving forecast meteorological models.

As a future perspective, a tomographic 3D mapping of the water content in the troposphere could turn useful to better understand the humidity distribution in respect to the topography.

Acknowledgements. We are grateful to Prof A. Mazzarella and Dr. R. Viola who provided us with meteorological data for MAFE station.

References

Altamimi Z., Collilieux X., Métivier L (2011) ITRF2008: an improved solution of the international terrestrial reference frame. J. Geod, 85 (8), 457-473, doi: 10.1007/s00190-011-0444-4.

Avallone A., Selvaggi G., D'Anastasio E., D'Agostino N., Pietrantonio G., Riguzzi F., Serpelloni E., Anzidei M., Casula G., Cecere G., D'Ambrosio C., De Martino P., Devoti R., Falco L., Mattia M., Rossi M., Obrizzo F., Tammaro U., Zarrilli L. (2010). The RING network:improvement of a GPS velocity field in the Central Mediterranean. Annals of Geophysics, vol. 53, 2; p. 39-54, ISSN: 1593-5213, doi: 10.4401/ag-4549.

Bevis, M., S. Businger, T. A. Herring, C. Rocken, A. Anthes, and R. Ware, (1992). GPS meteorology: Remote sensing of atmospheric water vapor using the global positioning system. J. Geophys. Res., 97, 15 787–15 801.

Boehm, J. B. Werl, and H. Schuh (2006). Troposphere mapping functions for GPS and very long baseline interferometry from European Centre for Medium-Range Weather Forecasts operational analysis data, J. Geophys. Res., 111, B02406, doi:10.1029/2005JB003629.

Bottiglieri M., Falanga M., Tammaro U., De Martino P., Obrizzo F., Godano C., Pingue F. (2010). *Characterization of GPS time series at Neapolitan volcanic area by statistical analysis*. Journal of Geophysical Research, vol.115, B10416, doi:10.1029/2009JB006594.

Champollion C., Masson F., Van Baelen J., Walpersdorf A., Chéry J. and E. Doerflinger (2004). GPS monitoring of the tropospheric water vapor distribution and variation during the 9 September 2002 torrential precipitation episode in the Cévennes (southern France). J. Geophys. Res., 109, D24102, doi:10.1029/2004JD004897

Duan J., M. Bevis, Fang P., Bock Y., Chiswell S.R., Businger S., Rocken C., Solheim F. S., Van Hove T., Ware R., McClusky S., Herring T.A. and King R. W. (1996). GPS meteorology: direct estimation of the absolute value of precipitable water, J. Appl. Meteorol., 35, 830-838.

Haase J., Ge M., Vedel H., Calais E. (2003), Accuracy and variability of GPS tropospheric delay measurements of water vapor in the western Mediterranean. J. Appl. Meteorol., 1547–1568.

Herring T.A., King, R. W., McClusky S.C. (2010). Documentation for the GAMIT GPS analysis software, release 10.4, Dep. of Earth Atmos. and Planet. Sci., Mass. Inst. of Technol., Cambridge, Mass.

Hofmann-Wellenhof, B., Lichtenegger, H., Collins, J. (2001). Global Positioning Systen: Theory and Practice (5th Edition). Springer-Wien-New York, 382 pp.

IPCC, 1992. Climate Change (1992): The Intergovernmental Panel on Climate Change (IPCC) Supplementary Report; editors: J.T. Houghton, B.A. Callander and S.K. Varney; Cambridge University Press; 1992.

Niell, A. E. (1996)., Global mapping functions for the atmosphere delay at radio wavelengths, J. Geophys. Res., 101(B2), 3227–3246.

Saastamoinen, J. (1973). Contributions to the theory of atmospheric refraction, Bull. Geod., 107, 13–34, doi:10.1007/BF02521844.

Stephens, G. L. and Greenwald, T. J. (1991). The Earth's radiation budget and its relation to atmospheric hydrology. 1. Observations of the clear-sky greenhouse effect. J. Geophys. Res., 96, 15311–15326.

IL MODELLO GEMMA: REALIZZAZIONE, VALIDAZIONE E DISTRIBUZIONE

D. Sampietro[1], M. Reguzzoni[2]
[1] *GReD srl, Como*
[2] *DICA, Politecnico di Milano, Milano*

Introduzione. La missione satellitare GOCE (Drinkwater *et al*., 2007), dell'Agenzia Spaziale Europea, ha permesso di osservare il campo gravitazionale terrestre a livello globale con una risoluzione e accuratezza senza precedenti. In particolare questo è stato reso possibile dall'innovativo strumento di misura a bordo del satellite GOCE (un gradiometro elettrostatico triassiale) e dall'orbita estremamente bassa (solamente 250 km di quota) del satellite stesso. Tra le varie applicazioni scientifiche di questi nuovi dati, come ad esempio il miglioramento dei modelli climatici (grazie alle nuove conoscenze sulla circolazione oceanica e sul livello medio dei mari) o l'unificazione del *datum* d'altezza a livello globale, anche lo studio della discontinuità tra la crosta e il mantello terrestre, classicamente modellata come una superficie chiamata discontinuità di Mohorovičić o Moho (Fowler, 1990), ne può trarre giovamento.

Per avere un'idea dell'accuratezza del *dataset* fornito dalla missione GOCE, si può pensare ad esempio al fatto che tali dati sono in grado di osservare variazioni di profondità della Moho (considerando solamente l'errore d'osservazione e trascurando l'errore dovuto all'uso di modelli geofisici per la riduzione dei dati) dell'ordine di 0.1 km con risoluzione migliore di 1°x1° (Braitenberg *et al*., 2011; Reguzzoni e Sampietro, 2012a). Questo miglioramento nella precisione e risoluzione della descrizione del campo gravitazionale terrestre deve tuttavia essere seguito da un miglioramento parallelo nella modellazione e nell'ipotesi sottostanti al calcolo della profondità della Moho da osservazioni di gravità. I modelli di Moho derivati dall'inversione del campo gravitazionale, come quelli presentati in Sunkel *et al.* (1985), Moritz (1990), Sjöberg (2009) e Reguzzoni *et al.* (2013), sono infatti di solito basati su ipotesi molto semplificate, ad esempio spesso viene trascurata la dipendenza della densità della crosta terrestre dalla profondità o ancora la densità viene considerata addirittura costante ovunque. Inoltre, il problema di introdurre informazioni sismiche in modelli di Moho calcolati da osservazioni gravimetriche, come ad esempio in Sjoberg e Bagherbandi (2011) e, più recentemente in Sampietro e Reguzzoni (2011) o Sampietro *et al.* (2013), è un compito impegnativo in quanto le ipotesi alla base dei metodi sismici e gravimetrici sono, in generale, diverse e complementari. Come se non bastasse questo compito è reso più complicato dal fatto che una descrizione completa degli errori delle diverse fonti di informazione non è generalmente disponibile.

In questo lavoro viene presentato un nuovo modello globale di crosta terrestre. Tale modello si basa su dati della missione GOCE, su una descrizione accurata della struttura della crosta e su alcune informazioni a priori derivanti dalla sismica. In particolare, l'algoritmo di inversione è costituito da cinque fasi differenti: nella prima fase la griglia di derivate seconde radiale del potenziale gravitazionale calcolata da dati GOCE è ridotta all'effetto gravitazionale dell'ondulazione della Moho, cioè l'effetto gravitazionale delle masse tra la Moho reale e una Moho di riferimento a profondità costante; nella seconda fase un operatore di analisi in armoniche sferiche viene applicato alla griglia ridotta al fine di stimare un *set* di coefficienti di armoniche sferiche δT_{nm}, in particolare essi sono calcolati come in Colombo (1981) o Reguzzoni (2004). Nella terza fase viene applicato l'operatore di inversione: tale operatore si basa su un'espressione linearizzata (Strang van Hees 2000; Reguzzoni *et al.* 2013) che permette di ricavare, a partire da δT_{nm}, i coefficienti $\delta\omega_{nm}$ di un funzionale $\delta\omega(\varphi,\lambda)$ definito come il prodotto tra l'ondulazione della Moho $\delta D(\varphi,\lambda)$ e il contrasto di densità tra crosta e mantello $\Delta\rho(\varphi,\lambda)$:

$$\delta\omega(\varphi,\lambda) = \delta D(\varphi,\lambda)\Delta\rho(\varphi,\lambda) \qquad (1)$$

Ricordando che l'ondulazione della Moho è riferita ad una Moho sferica di raggio $R_E - \bar{D}$ (dove R_E è il raggio medio terrestre e $\bar{D}$ è la profondità media della Moho) si ottiene:

$$\delta\omega_{nm} = \rho_E \left(R_E - \bar{D}\right)\beta_n \delta T_{nm} \qquad (2)$$

$$\beta_n = -\frac{(2n+1)}{\left(1-\frac{\bar{D}}{R_E}\right)^{n+3}} \qquad (3)$$

dove ρ_E è la densità media della Terra. A partire dai coefficienti $\delta\omega_{nm}$ viene stimata una griglia geografica di $\delta\omega(\varphi,\lambda)$ attraverso una sintesi armonica (quarta fase); la profondità della Moho viene quindi calcolata dividendo tale griglia per il contrasto di densità (quinta fase). Per maggiori dettagli sull'algoritmo di inversione e sulla stima dei corrispondenti errori il lettore può fare riferimento a Reguzzoni *et al.* (2013).

Stima della Moho: Considerando le osservazioni GOCE, il principale input per l'algoritmo di inversione è rappresentato da una griglia di derivate seconde radiali del potenziale gravitazionale alla quota media del satellite (circa 250 km). Tale griglia è calcolata utilizzando tutti i gradienti di gravità osservati lungo l'orbita attraverso il cosiddetto approccio *space-wise* (Reguzzoni e Tselfes 2009; Migliaccio *et al.*, 2011).

Come indicato nel paragrafo precedente, prima di applicare l'algoritmo di inversione è necessario rimuovere dalle osservazioni il segnale di tutte le masse anomale a parte quelle dovute all'ondulazione della Moho. Per questo viene dapprima sottratto dalle osservazioni GOCE il contributo del potenziale normale. Il segnale residuo può essere quindi considerato come l'effetto di anomalie di densità all'interno di ogni strato e l'effetto di confini non ellissoidali tra strati contigui (Fig. 1). È importante sottolineare che, poiché non conosciamo la distribuzione di densità che genera il potenziale normale (il potenziale normale può essere infatti interpretato come l'effetto di infiniti modelli di Terra con strati ellissoidali), una volta che i dati sono ridotti non è più possibile stimare la profondità media della Moho.

Il contributo gravitazionale di qualsiasi massa anomala, dalla topografia (comprese le calotte glaciali) ad una superficie di riferimento nel mantello superiore, è quindi ulteriormente rimosso dai dati:

$$\delta T_{rr} = T_{rr}^{GOCE} - T_{rr}^{ICE} - T_{rr}^{OCE} - T_{rr}^{SED} - T_{rr}^{CRUST} - \delta T_{rr}^{MANTLE} \qquad (4)$$

dove: T_{rr}^{GOCE} è la derivata seconda radiale del potenziale anomalo alla quota media del satellite, T_{rr}^{ICE} è l'effetto delle calotte glaciali assumendo una densità costante del ghiaccio $\rho_{ICE} = 980\,kg/m^3$ e la geometria delle calotte da ETOPO1 (Amante e Eakins, 2009), T_{rr}^{OCE} è l'effetto delle masse oceaniche supponendo una densità dell'acqua costante $\rho_{OCE} = 1020\,kg/m^3$ e prendendo la batimetria da ETOPO1, T_{rr}^{SED} è l'effetto dei sedimenti assumendo una densità $\rho_{SED} = \rho_{SED}(\varphi,\lambda,r)$, con confini e densità tratti dal modello sviluppato da Laske e Master (1997),

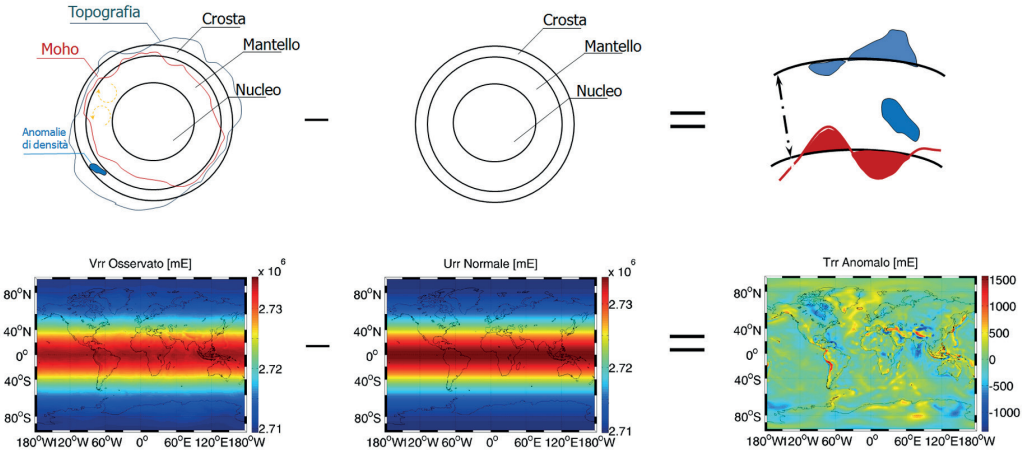

Fig. 1 – Schematizzazione della riduzione del segnale gravitazionale espresso in termini di potenziale; unità [mE].

T_{rr}^{CRUST} è l'effetto della crosta cristallina fino a una certa Moho di riferimento supponendo di conoscere $\rho_{\mathrm{CRUST}} = \rho_{\mathrm{CRUST}}(\varphi,\lambda,r)$ e T_{rr}^{MANTLE} è l'effetto del mantello superiore dalla Moho di riferimento fino ad una certa profondità costante, qui pari a circa 120 km, ipotizzando una densità $\rho_{MANTLE} = \rho_{MANTLE}(\varphi,\lambda)$ da Simmons *et al.* (2010). Si noti che gli effetti delle variazioni di densità laterali della parte restante del mantello e dentro il nucleo possono essere trascurati poiché sono ordini di grandezza inferiore a quelle dovute alle masse crostali ed inoltre sono concentrate principalmente nelle basse frequenze del segnale gravitazionale (Hager, 1985). Va sottolineato che la scelta di ρ_{CRUST} è un fattore critico nella procedura di inversione, infatti esso è richiesto non solo per ridurre le osservazioni GOCE (come tutti gli altri modelli densità), ma anche per definire il contrasto di densità tra la crosta e il mantello da utilizzare nell'inversione dell'Eq. 1. Nel presente lavoro ρ_{CRUST} è stata modellata nel seguente modo: prima di tutto la Terra è stata divisa in province geologiche secondo la mappa USGS (Exxon, 1985), questo ha permesso di creare un set di 139 aree geologicamente omogenee, ognuna delle quali classificata come uno degli otto principali tipi crostali (scudo, piattaforma, crosta orogenetica, bacino sedimentario, grande provincia ignea, crosta estesa, crosta oceanica e dorsale medio oceanica). Per ciascun tipo di provincia è stata quindi definita una funzione tra profondità e densità. In particolare, queste funzioni sono derivate dalle tabelle 3 e 8 di Christensen e Mooney (1995) per la crosta continentale e dalla tabella 2 di Carlson e Raskin (1984) per la crosta oceanica.

Come sottolineato in precedenza una volta che il potenziale normale è stato rimosso dalle osservazioni non è più possibile stimare la profondità assoluta della Moho, ma solo l'ondulazione della Moho rispetto ad una Moho media incognita. Per risolvere questo problema l'algoritmo d'inversione è stato modificato aggiungendo un termine costante μ_ω. È stato anche inserito un fattore di scala h_i per la funzione di densità di ogni provincia geologica. In questo modo provincie geologiche appartenenti allo stesso tipo di crosta possono avere funzione di densità leggermente diverse. Nel presente lavoro sia il termine μ_ω che i fattori di scala h_i sono stimati utilizzando come osservazioni aggiuntive le profondità della Moho CRUST2.0 (Mooney *et al.*, 1998; Bassin *et al.*, 2000), adeguatamente pesate in una soluzione ai minimi quadrati. In questo senso la presente soluzione può essere considerata come una soluzione gravimetrica debolmente combinata con dati sismici (debolmente perché solo 140 parametri vengono stimati da 90x180 osservazioni presenti nel modello CRUST2.0). I pesi utilizzati nella stima, ovvero la mappa dell'errore del modello CRUST2.0, sono stimati come somma di due termini: uno pari al 10% dello spessore della crosta (secondo quanto affermato in Christensen e Mooney, 1995), l'altro funzione della distribuzione spaziale delle osservazioni sismiche usate all'interno del modello CRUST2.0 (Sampietro e Reguzzoni, 2011). Per dettagli sulla procedura di inversione il lettore si può riferire a Reguzzoni e Sampietro (2012b).

Per quanto riguarda l'errore della Moho è stato calcolato come la somma dell'errore di osservazione GOCE propagato in termini di Moho (circa 0.1 km), dell'errore di linearizzazione nell'Eq. 2 (circa 1 km), dell'errore di stima della Moho media e dei fattori di scala (ottenuto dalla compensazione ai minimi quadrati) e degli errori di modello. Quest'ultimo termine, che è quello dominante, è dovuto agli errori nelle funzioni di densità usate e all'errore nella forma delle province geologiche ed è stato empiricamente modellato. Il modello stimato di Moho (chiamato GEMMA Moho) e la corrispondente deviazione standard dell'errore sono riportati in Fig. 2.

Il modello GEMMA: primi confronti. In questa sezione viene fatta una prima valutazione della qualità del modello globale di Moho calcolato. Questa valutazione non è un compito facile a causa della piccola quantità di osservazioni dirette, (ottenute ad esempio da tecniche sismiche) e per il loro livello di precisione limitato.

Il modo più semplice è quello di confrontare il modello GEMMA con altri modelli a scala globale o regionale. In particolare per i confronti sono stati considerati il modello CRUST2.0 (C2 nel seguito), il modello CRUST1.0 (C1 nel seguito), un modello di Moho sviluppato dall'

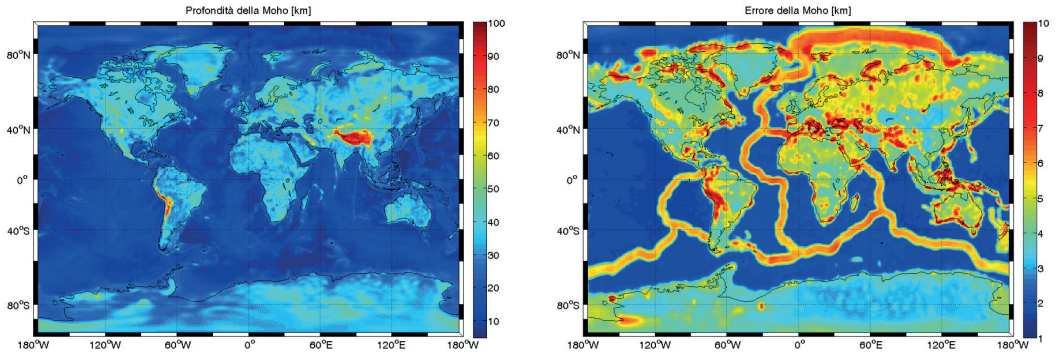

Fig. 2 – Profondità della Moho del modello GEMMA (sinistra) e rispettivo errore di stima (destra); unità [km].

Università di Utrecht (Meier *et al.*, 2007, M7 nel seguito), il modello europeo (Grad e Tiira 2009, ESC nel seguito), il modello australiano (Kennett *et al.*, 2011, AusMoho nel seguito) e quello nordamericano (Gaherty *et al.* 2009, CEUS nel seguito). Per GEMMA, per i modelli M7, ESC e AusMoho sono disponibili le relative mappe della deviazione standard dell'errore, mentre per il modello C2 sono stati considerati i pesi discussi nella sezione precedente. Al modello CEUS è stata assegnata la stessa mappa degli errori di C2. Per poter confrontare i diversi modelli è stato utilizzato un semplice test statistico: considerando che tutti i modelli descrivono la stessa quantità, ovvero la profondità della Moho, e supponendo che i modelli siano indipendenti sia ha:

$$\Delta D_i^{m_1,m_2} = D_i^{m_1} - D_i^{m_2} = 0 \qquad (7)$$

$$\sigma^2\left(\Delta D_i^{m_1,m_2}\right) = \sigma^2\left(D_i^{m_1}\right) + \sigma^2\left(D_i^{m_2}\right) \qquad (8)$$

dove m_1 e m_2 sono una coppia di modelli, i è il nodo della griglia considerato. A questo punto dopo aver interpolato tutti i modelli su un grigliato di 2°x2° è possibile testare per ogni nodo della griglia se l'ipotesi Hp_0:

$$\Delta D_i^{m_1,m_2} = 0 \qquad (9)$$

sia verificata a un livello di significatività del 95%. I risultati di questo test sono riassunti nella Fig. 3 e mostrano come il modello GEMMA sia congruente con M7 su circa 81% del mondo, mentre è congruente con C2 per circa 95% e con C1 per circa 97%.

Si può notare come le differenze maggiori rispetto a C2, C1 e M7 sono nella zona dell'Himalaya e dell'altopiano tibetano. Queste differenze sono dovute all'effetto della collisione tra la placca indiana e quella eurasiatica che provoca, proprio in queste regioni, la frammentazione della Moho e la presenza di Moho multiple. Pertanto la discrepanza può essere spiegata come una conseguenza del fatto che una netta separazione tra crosta e mantello non è un'approssimazione accettabile della struttura effettiva della litosfera in questa regione. Un modello completo dovrebbe includere la subduzione della litosfera e le variazioni di densità a livello della crosta inferiore. D'altra parte, questo risultato dimostra che, in linea di principio, le discrepanze tra il modello GEMMA e i modelli derivati da osservazioni sismiche possono essere utilizzati per rilevare la presenza di anomalie di densità. Un'altra incongruenza si riscontra al confine tra il bacino euroasiatico la piattaforma continentale del mare di Laptev ed è probabilmente dovuta a una modellazione errata delle province geologiche artiche. Le ulteriori incongruenze rispetto a M7 sono invece situate soprattutto nelle zone di passaggio tra crosta continentale e crosta oceanica e nella crosta oceanica recente. Le prime anomalie sono probabilmente dovute alla diversa risoluzione dei due modelli e a leggere differenze nella posizione del limite tra crosta continentale e crosta oceanica, mentre le seconde sono dovute alla non perfetta modellizzazione dei *ridge* medio oceanici nel modello GEMMA.

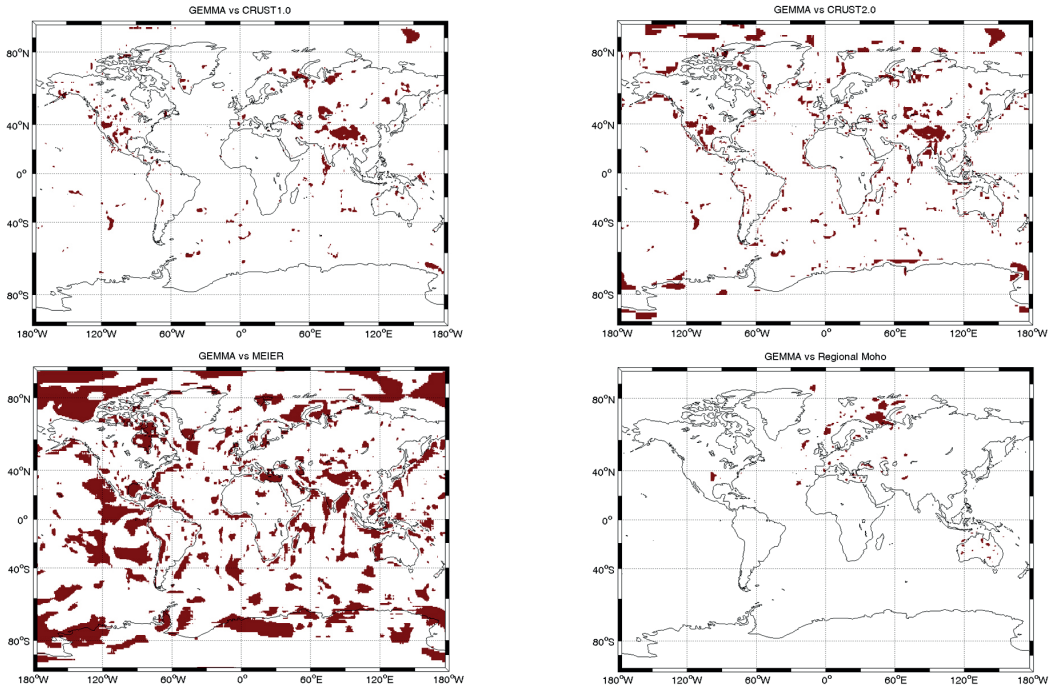

Fig. 3 – Confronto tra il modello GEMMA e i diversi modelli considerati: in rosso i pixel in cui i modelli non sono coerenti.

In ogni caso da questa prima validazione è possibile affermare che il modello GEMMA rappresenta un miglioramento nella descrizione della crosta terrestre rispetto ai modelli esistenti, soprattutto rispetto al modello C2, perché gli strati più superficiali della crosta sono stati aggiornati con dati più precisi e a più alta risoluzione, la crosta rimanente è stata modellata secondo la stesse densità crostali ma nuovamente con un dettaglio maggiore. Inoltre la soluzione è vincolata con i dati di gravità GOCE e comprende parzialmente C2 (dove giudicato attendibile). Tuttavia il miglioramento più importante del nuovo modello è che il modello crostale calcolato è ben coerente con l'effettivo campo di gravità, superando così una delle principale limitazione dei modelli globali derivati da osservazioni sismiche.

La distribuzione dei dati. Per favorire la distribuzione dei dati relativi al progetto GEMMA è stato sviluppo, in collaborazione con il Laboratorio di Geomatica del Politecnico di Milano, un *web processing service* (http://gocedata.como.polimi.it). Tale servizio permette l'acquisizione e lo sfruttamento dei dati del progetto GEMMA attraverso procedure standard definite dell'Open Geospatial Consortium (OGC). Nel dettaglio il servizio WPS è stato realizzato utilizzando il *software free* e *open source* GRASS per gestire e interpolare i dati e pyWPS per gestire le richieste dell'utente e le risposte del *server*.

Il WPS permette di scaricare, interpolare e visualizzare non solo il valore stimato della profondità della Moho ma anche l'intero modello di crosta terrestre (sedimenti, calotte glaciali, oceani, crosta cristallina e mantello superiore). Per ogni *layer* il WPS fornisce la profondità del confine superiore e inferiore, la densità e l'effetto gravitazionale (al momento in termini di derivata seconda radiale del potenziale all'altezza media del satellite GOCE, ma in futuro anche in termini di anomalie di gravità a una quota arbitraria). Per quanto riguarda la crosta cristallina il WPS fornisce, le funzioni densità-profondità ricavate da Christensen e Money, la mappa delle provincie geologiche e i fattori di scala stimati. È inoltre possibile scaricare sia i

dati locali che quelli globali, interpolati dinamicamente dal WPS su un'area e a una risoluzione definite dall'utente oppure valutare il modello in corrispondenza di un insieme di punti sparsi.

Riconoscimenti. La presente ricerca è stata parzialmente finanziata dall'ESA nell'ambito del programma STSE attraverso il progetto Goce Exploitation for Moho Modelling and Applications (GEMMA project), contratto n. 4000102372/10/I-AM.

Bibliografia

Amante C. e Eakins B., W.; 2009: *ETOPO1 1 Arc-Minute Global Relief Model: Procedures, Data Sources and Analysis*. NOAA Technical Memorandum NESDIS NGDC-24.

Bassin C., Laske G. e Masters G; 2000: *The Current Limits of Resolution for Surface Wave Tomography in North America*. EOS Trans AGU, 81, F897.2.

Braitenberg C., Mariani P. e Pivetta T.; 2011: *GOCE observations in exploration geophysics*. In Proc. of the 4th International GOCE User Workshop, ESA SP-696, Munich, Germany.

Carlson R., L. e Raskin G., S.; 1984: *Density of the ocean crust*. Nature, 311, 555–558.

Christensen N., I. e Mooney W., D.; 1995: *Seismic velocity structure and composition of the continental crust: A global view*. Journal of Geophysical Research, 100, 9761–9788.

Colombo O., L.; 1981: *Numerical Methods for Harmonic Analysis on the Sphere*. Report No. 310, Department of Geodetic Science, The Ohio State University, Columbus.

Drinkwater M., R., Haagmans R., Muzi D., Popescu A., Floberghagen R., Kern M. e Fehringer M.; 2007: *The GOCE gravity mission: ESA's first core Earth explorer*. In Proc. of the 3rd international GOCE user workshop, 6-9 November 2006, Frascati, Italy, SP-627.

Exxon Production Research Company; 1985: *Tectonic Map of the World, 18 sheets, scale 1: 10,000,000*. Prepared by the World Mapping Project as part of the tectonic map series of the world. Exxon, Houston, Texas.

Fowler C., M., R.; 1990: *The solid Earth*, Cambridge Univ. Press, New York.

Gaherty J., B., Dalton C. e Levin V.; 2009: *Three-dimensional models of crustal structure in eastern North America*. USGS NEHRP Grant 07HQGR0046 Technical Report.

Grad M., Tiira T. e ESC Working Group; 2009: *The Moho depth map of the European Plate*. Geophysical Journal International, 176, 279–292.

Hager B., H., Clayton R., W., Richards M., A., Comer R., P. e Dziewonski A., M.; 1985: *Lower mantle heterogeneity, dynamic topography and the geoid*. Nature, 313, 541–545.

Kennett B., L., N., Salmon M., Saygin E. e Group; 2011: *AusMoho: the variation of Moho depth in Australia*. Geophysical Journal International, 187, 946–958.

Laske G. e Masters G.; 1997: *A Global Digital Map of Sediment Thickness*. EOS Trans AGU, 78, F483 (1997).

Meier U., Curtis A. e Trampert J.; 2007: *Global crustal thickness from neural network inversion of surface wave data*, Geophysical Journal International, 169, 706–722.

Migliaccio F., Reguzzoni M., Sansò F., Tscherning C., C. e Veicherts M.; 2011: *GOCE data analysis: the space-wise approach and the first space-wise gravity field model*. In Proc. of the ESA Living Planet Symposium, 28 June – 2 July 2010, Bergen, Norway, ESA SP-686.

Mooney W., D., Laske G. e Masters T., G.; 1998: *CRUST 5.1: A global crustal model at 5°x5°*. Journal of Geophysical Research, 103, 727–747.

Moritz H; 1990: *The figure of the Earth: theoretical geodesy and the Earth's interior*. Wichmann, Karlsruhe (1990).

Reguzzoni M.; 2004: *GOCE: the space-wise approach to gravity field determination by satellite gradiometry*. PhD Thesis, Politecnico di Milano, Italy.

Reguzzoni M. e Tselfes N.; 2009: Optimal multi-step collocation: application to the space-wise approach for GOCE data analysis. Journal of Geodesy, 83, 13–29.

Reguzzoni M., Migliaccio F. e Sampietro D.; 2010: Il primo modello di gravità calcolato con l'approccio space-wise dai dati del satellite GOCE e un esempio di applicazione geofisica sull'arco alpino. Atti del XXIX Convegno Nazionale GNGTS, 26-28 Ottobre 2010, Prato, Italia, 524–527.

Reguzzoni M. e Sampietro D.; 2012a: *Moho estimation using GOCE data: a numerical simulation*. In International Association of Geodesy Symposia, "Geodesy for Planet Earth", Kenyon, S., Pacino, M.C. & Marti, U. (Eds.). 136, 205–214.

Reguzzoni M. e Sampietro D.; 2012b: *A new global crustal model based on GOCE data grids*. Presentato a First International GOCE Solid Earth workshop, Enschede, The Netherlands.

Reguzzoni M., Sampietro D. e Sansò F.; 2013: *Global Moho from the combination of the CRUST2.0 model and GOCE data*. Geophysical Journal International, 195(1), 222–237.

Sampietro D. e Reguzzoni M.; 2011. *Global Moho from the combination of the CRUST2.0 model and GOCE data*. In Atti del XXX Convegno Nazionale GNGTS, 14-17 Novembre 2011, Trieste, Italia, 535–538.

Sampietro D., Reguzzoni M. e Braitenberg C.; 2013: *The GOCE estimated Moho beneath the Tibetan Plateau and Himalaya*. In: International Association of Geodesy Symposia, 139 (In print).

Simmons N., A., Forte A., M., Boschi L. e Grand S., P.; 2010: *GyPSuM: a joint tomographic model of mantle density and seismic wave speeds*. Journal of Geophysical Research, 115, B12310.

Sjöberg, L., E.; 2009: *Solving Vening Meinesz-Moritz inverse problem in isostasy*. Geophysical Journal International 179(3), 1527–1536.
Sjöberg L., E. e Bagherbandi M.; 2011: *A method of estimating the Moho density contrast with a tentative application by EGM08 and CRUST2.0*. Acta Geophysica, 59, 502–525.
Strang van Hees G., L.; 2000: *Some elementary relations between mass distributions inside the Earth and the geoid and gravity field*. Journal of Geodynamics, 29, 111–123.
Sünkel H.; 1985: *An isostatic Earth model*. Report No. 367, Department of Geodetic Science and Surveying, The Ohio State University, Columbus.

INTEGRATED GEOPHYSICAL INVESTIGATIONS IN GLACIAL ENVIRONMENT WITH SPECIAL ATTENTION TO IMAGE ANALYSIS

A. Tonelli[1], S. Castellaro[2], F. Zandonai[1], F. Finotti[1]
[1] Fondazione Museo Civico Rovereto, Rovereto, Italy
[2] Università di Bologna, Dipartimento di Fisica e Astronomia, Bologna, Italy

Introduction. On March and May 2012 a working group formed by Museo Civico di Rovereto Foundation, Dpt. of Civil, Environment and Mechanical Engineering Trento University, Meteotrentino of Provincia di Trento, Physics Dpt. Bologna University, carried out a series of tests in a periglacial and glacial environment. The team performed direct and indirect measurements, both on snow trench faces and on subsoil section (snow, ice, rock) in the snow-covered area of Passo Paradiso (Monticello Lake and Presena weather station) on the Presena Glacier (Fig. 1).

Meteotrentino (*functional center for civil protection*) monitors, in several Trentino mountain sites, the state of the snow against the risk of avalanches. Driven by Meteotrentino various geophysical methods have been applied and tested to give a complementary support to the classical nivological direct survey. Aim of the experimental campaign is the setting up of a reliable, rapid way (accounting also for a multitemporal approach), to characterize snow and subsoil.

Complementary geophysical methods, such as remote sensing, geoelectrical and seismic prospecting, suitable for applications in extreme environments, have been chosen to study the complex system given by snow, water, ice and "soil", in terms of seismic and electrical impedance, and snow - light interaction (temperature, reflectance and polarization).

The seismic and electrical prospecting involved a cross section of Lake Monticello (covered by snow), while thermal imaging and photometry interested two fresh snow walls modeled in trenches.

The following section shows, in a schematic way, the characteristics and parameters of geophysical measurement, the field observations with the problems arisen and finally the results. The geophysical data were then correlated and compared with the results of data available about the local morphometry and, for the snow trenches, direct observations and sampling conducted by Meteotrentino and the Hydrogeology group of the Trento University.

Fig. 1 – The test site on the Presena Glacier. Panoramic view and on the right an aerial image.

Remote sensing approach to characterize the snow wall. Measurements of radiating temperature (thermal infrared), reflectivity in the intervals of visible and near infrared and of light polarization have been performed on the vertical wall of trench, roughly 1.8 m high, facing north (on March) and, respectively, south (on May). The measurements were performed immediately after the execution of the trenches to limit as much as possible the alteration caused by excavation and by the exposure to the external environment. The field of radiating temperature has been acquired by means of a thermal camera operating in the 8÷12 μm range while a digital photocamera - provided by polarizing rotating filter - has been used for the visible (0.4÷0.7 μm) and near infrared (0.7÷0.8 μm) bands and to show the polarizing property of the snow. The thermal camera has gathered data on the radiating temperature field, function of contact temperature and of surface emissivity (ratio between the actual radiance and the one emitted at the same temperature by the ideal black body).

The snow colour has also been analysed, comparing the reflectance in the region of green (high transparency) with the one in the near infrared (very low transparency). For the analysis of polarization, the polarizing property of snow has been described taking into account the intensity of the reflectance in the interval of red (0.6÷0.7 μm) for different positions of a polarizing filter put in front of the photocamera. Starting from an arbitrary initial orientation the filter was rotated by steps, 15° each, till reaching the final 135° angle. From the frames acquired, the value of maximum and minimum intensity (*max* and *min*) have been extracted and compared. The zones where *max* - *min* = 0 have isotropous behaviour while where *max* – *min* ≠ 0 polarization occurs. For such a reason, in the polarization analysis, was selected areas where max - min ≠ 0, corresponding to anomalous response. On the snow surface facing North, in absence of direct sun illumination (early morning), the vertical thermal profile puts in evidence an anomalous variation around the depth of 45 cm which can be explained as the resulting seepage of "greenhouse effect". The snow cover partially transparent to sunlight radiation at some extent, is completely opaque to the re-emitted thermal infrared radiation, thus some heat remains trapped inside the snow mass with the consequence of generating a clear discontinuity around a depth of 45 cm. This effect, highlighted by the thermal profile, is confirmed by analysis of the polarization of the light too (Fig. 2). On the snow wall facing South, with direct sun illumination, data within the bands of blue, green, red and near infrared have been collected with selective filters applied on a digital open spectrum photocamera (Sony, provided by "night shot" configuration and Kodak Wratten 87 filter for visible-light rejection). The analysis of the polarization of the solar light impinging on the wall facing South confirms the presence of a discontinuity around the depth of 40 cm.

The temperature trend and the polarization behaviour seem to be important for the analysis of the first package of snow, which is interesting for risk assessment. The shooting in the visible have provided data on the reflectivity in the regions of the red, green and blue, while polarization analysis gives information on the state of aggregation of the snow. Further information can be obtained from the multispectral analysis; on the wall facing South the profile of reflectance in near infrared (high opacity) contrasts with that in the green (high transparency). The operating conditions of detection of the walls facing north and south were, of course, different. The wall facing North was minimally influenced by the exposure to the external environment, at the same time, however, it was impossible to collect useful data in the near infrared for the lack of direct solar radiation. The wall facing South was strongly affected by the exposure to the external environment due to the intense radiation of the sun, that determined an external water film, altering the thermal infrared emissivity value. On the other side, the sun light allowed the acquisition of near infrared images, visible and polarization with an excellent signal to noise ratio.

Electrical and seismic prospecting to characterize the first subsoil. Measurements of electrical and seismic data, in passive and active mode, were made on March along a transect crossing the frozen and snowy Monticello Lake, including banks, in order to verify if the

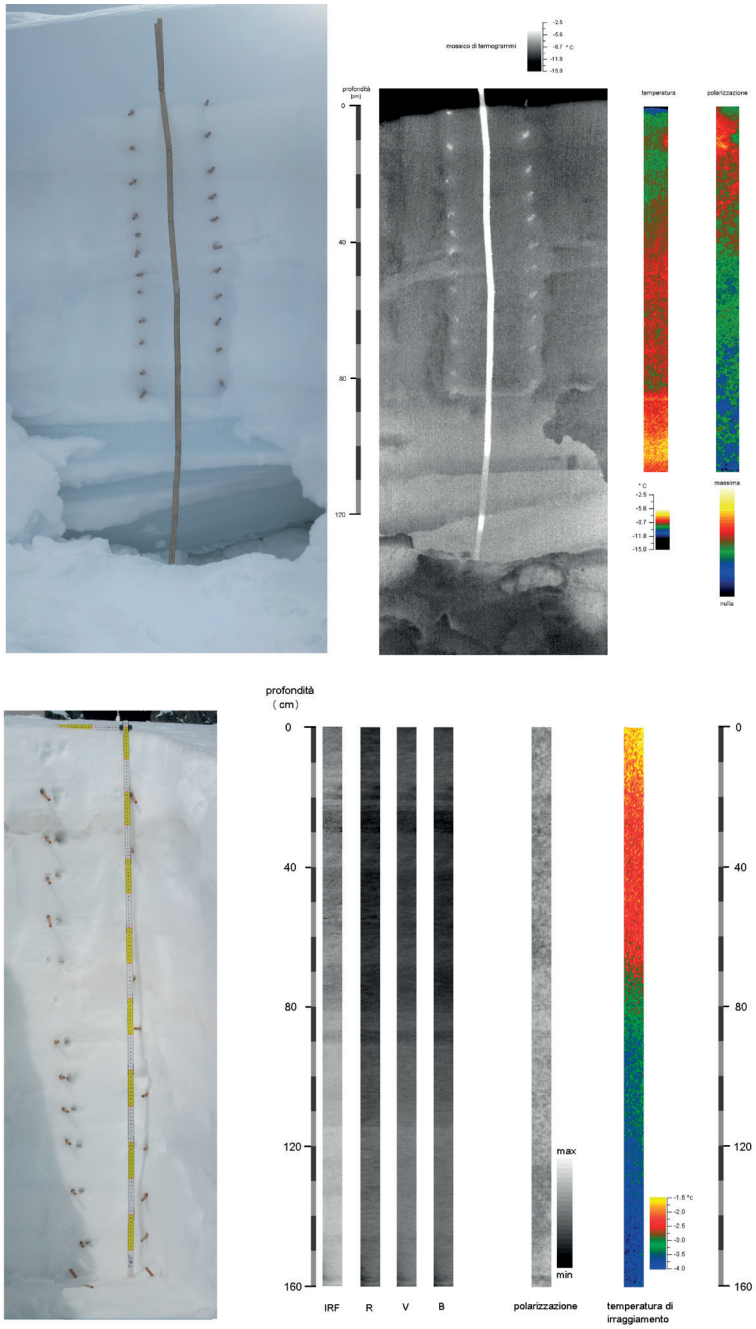

Fig. 2 – Photograph of the snow wall. Top: facing north showing the reference woody nails arranged to have reference points for the thermal pictures acquired immediately after the excavation of the trench. Follows the mosaic of thermograms (note the woody nails and the meter which were previously heated by the hands of the operator). The vertical radiant temperature profile shows a variation around the depth of 45 cm as a consequence of "greenhouse effect". On the right the trend of light polarization (from the surveys of March 8th 2012). Bottom: facing south showing the reference woody nails arranged to have reference points for the thermal pictures acquired immediately after the excavation of the trench. Middle: reflectance profiles in the near infrared interval (IRF), red (R), green (V) and blue (B). Right: trend of light polarization (within red interval) and temperature profile coded in colours (from the surveys of May 24th 2012).

transitions among different media could be detected: "soil" – snow, on the banks, and "soil" - water - ice - snow over the lake. To this aim we used: the resistivimeter Electra, the seismometer SoilSpy Rosina and five tromographs Tromino. The average stratigraphy on the lake, known from an *in situ* probe, was: 0.7 m snow, a thin water layer (0.07 m), 0.45 m thick ice and finally 16 m of water.

Constrained by the environmental conditions, room at disposal, and the necessity to made all the measurements in a short time lapse, the electrical acquisition sensors were disposed in the snow with a interval of 3 m (as the sensor for the multichannel seismics). For the geoelectrics this step would allow a certain depth of investigation and, at the same time, a vision, albeit crude, of the snow level. Some operational difficulties made impossible to achieve more detailed data (e.g., inter-electrode space 0.5 m). Interferences of water with the electrical parts forced us to work on shorter a profile (93 m), limited to 32 electrodes.

Despite the operative and technical conditions and the strong contrast between the various media, to which the air in small crevasses (cracks evident also on the snow surface) has to be added, the measures are reasonably repeatable and meaningful. The measured range of apparent resistivity is very wide, ranging from low values (around 50 Ω·m) corresponding to more conductive means, referable to water and melting snow, up to extremely high values (thousands of Ohm meter), which represent the presence of practically insulating media (probably air inside the surface cracks). An intermediate resistive response is associated with what is most likely the compact substrate; in particular a stratigraphic transition (probably with the substrate) is clearly marked at the lake bottom (roughly 40 m from the lake bank) by a sharp increase in resistivity (around 1300 Ω·m).

Although the amount of data collected was less than what was planned to adequately describe the site, it was also possible to recognize high resistive anomalies at the small crevasses in the first part of the array (corresponding to the bank of the lake). The presence of snow, water, ice and water again, is the cause of a complex response characterized by heterogeneous and also abrupt steps.

The wide range of resistivity observed and the jumps among lateral and vertical resistivities do not help in the inversion processes with usual software, which results in models with high error.

Regarding the seismics, both active and passive acquisitions, in single-station and in array, were carried out, consisting of: active MASW (Multichannel Analysis of Surface Waves), passive ReMi (Refraction Microtremor), passive ESAC (Extended Spatial AutoCorrelation) and mainly 11 acquisitions (20' at 128 Hz) of microtremor in free field (along a line of 100 m).

The surveys allow to estimate the velocity of shear waves (Vs) of the snow (around 80 m/s) from the velocity of the surface waves (Rayleigh in the case of this study); to measure the resonance frequencies of the site and to rebuild a seismic stratigraphy in 1D and in 2D. For the 2D reconstruction, the individual HVRS (Horizontal to Vertical Spectral Ratio) curves have been converted from the frequency domain to the depth domain, exploiting the results of the tests in arrays as a constraint.

It can be observed at the extremes of the seismic section (Fig. 3) the seismic bedrock outcrops, while in the central part there is a large inversion velocity linked to the presence of water under the ice surface (the thin red level close to the surface). The data seem to suggest a thickness of the lake in order of 20 m and then an anomaly in the middle of the profile, as in the electrics, that would require further investigation.

The seismics and electrics results are coherent, in relation to the common depth of investigation.

Conclusion. We have tested the performance of geoelectrical, seismic and remote sensing prospection in the detection of the characteristics of the first subsoil in glacial and periglacial environmental as in the Presena Glacier area. The greatest effort was addressed towards the collection of local data about the physical status of the snowpack. In particular, for detailed

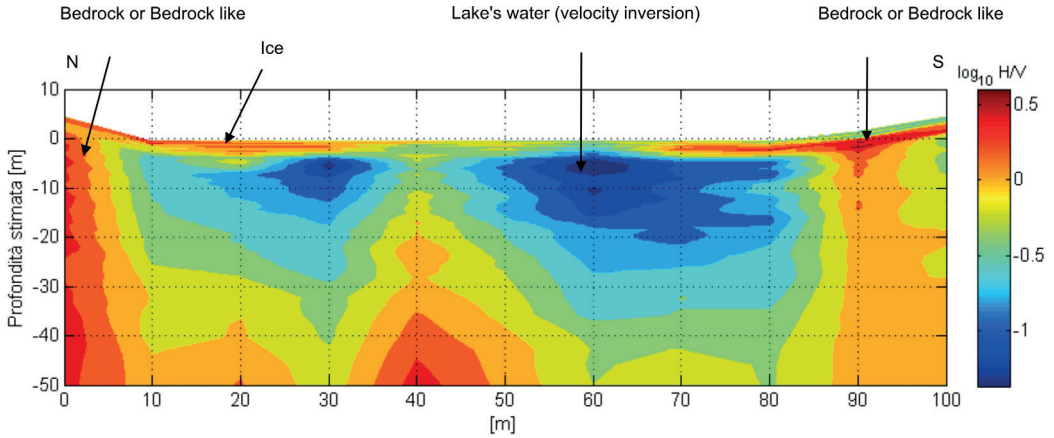

Fig. 3 – Synthetic view of the HVSR in the depth domain illustrating the lake section, from bank to bank. The reddish colours indicate positive impedance contrasts (increased rigidity). On the contrary blue tones means softer media.

data, a remote sensing analysis was carried out on walls facing, respectively, North and South, with measures of temperature, light polarization and spectral response in the visible and in the near infrared bands.

First results are promising and for the future we wish to develop a simple system, usable by non-specialist, to acquire information on the state of aggregation of snow, also on vertical profiles made accessible by trenches, as normally used in the classical nivological survey.

Acknowledgements. The authors wish to thank the whole team that conducted these test sessions on the Presena Glacier: the Hydrology group of the Professor A. Bellin, Department of Civil, Environmental and Mechanical Engineering Trento University; A. Trenti, Director of the Forecasting and Planning Office, Provincia of Trento, with the technical working group of Meteotrentino. And, for the support, the Consorzio Adamello Sky that manages the ski lifts facilities on the Presena Glacier.

References

Finotti F., Zandonai F., Tonelli A., Castellaro S.; 2006: Rassegna di alcune correnti metodologie per lo studio dell'estensione e spessore di ghiacciai e proposta di applicazione della sismica passiva a stazione singola. Atti III Workshop di Geofisica, 67-79, Ed. Museo Civico di Rovereto, 2007.

French H. K., Hardbattle C., Binley A., Winship P., Jakobsen L.; 2002: Monitoring snowmelt induced unsaturated flow and transport using electrical resistivity tomography. Journal of Hydrology 267, 273–284, 2002.

Huggel C., Haeberli W., Kääb A., Hoelzle M., Ayros E., Portocarrero C.; 2002: Assessment of glacier hazards and glacier runoff for different climate scenarios based on remote sensing data: a case study for a hydropower plant in the peruvian Andes. EARSeL e-proceedings n. 2, March 11 – 13, 2002.

Indice degli autori

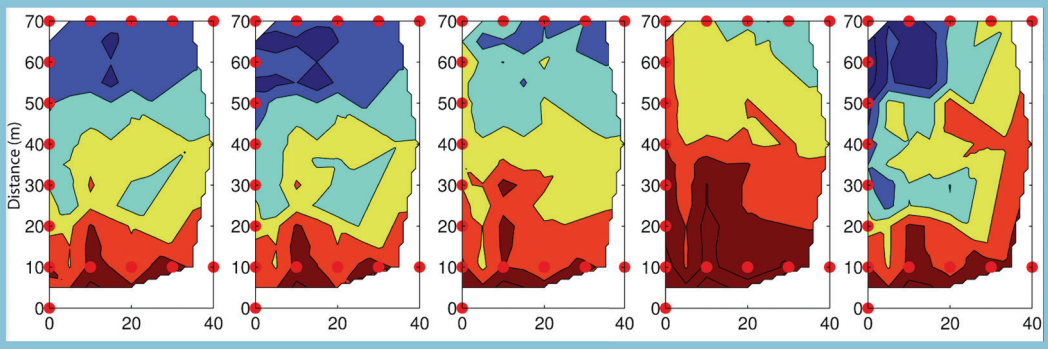

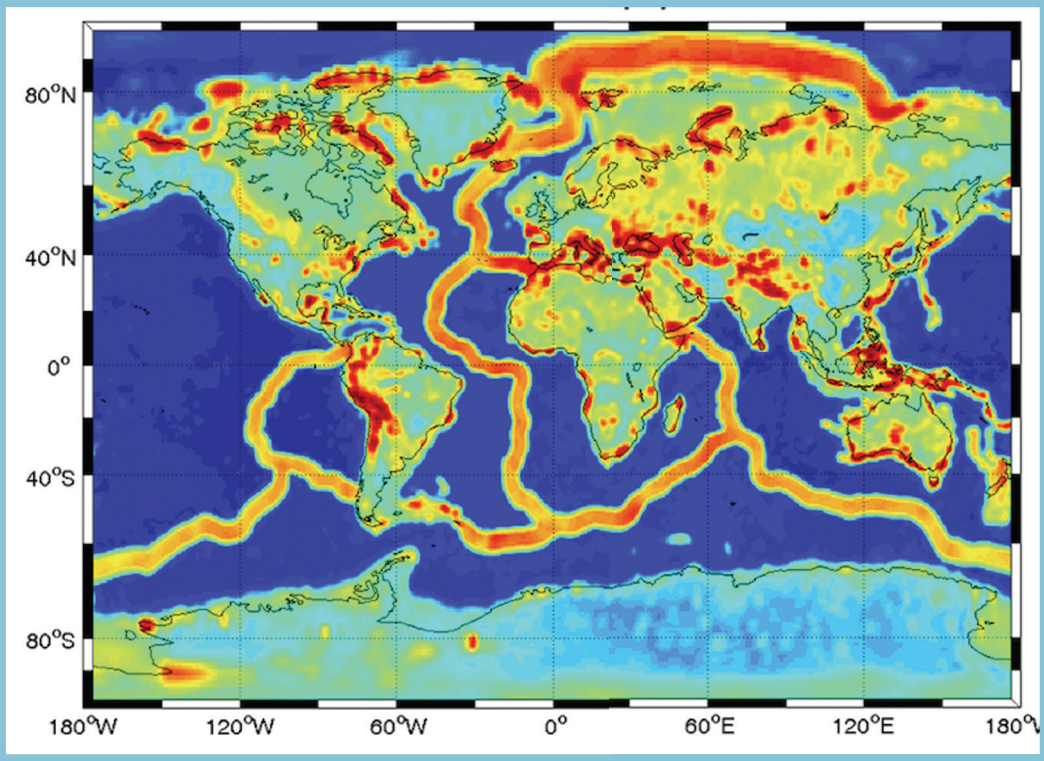

con la sponsorizzazione di:

EAGE
EUROPEAN ASSOCIATION OF GEOSCIENTISTS & ENGINEERS
SEZIONE ITALIANA

13° Convegno Nazionale

CODEVINTEC
Tecnologie per le Scienze della Terra

volume ISBN 978-88-902101-8-1
raccolta ISBN 978-88-902101-9-8